# A Bio-Inspired Approach to Functional Composite Crystals

Stephanie Elizabeth Foster

Submitted in accordance with the requirements for the degree of

Doctor of Philosophy

The University of Leeds

Faculty of Engineering and Physical Sciences

School of Chemistry

August 2022

The candidate confirms that the work submitted is her own and that appropriate credit has been given where reference has been made to the work of others.

## Acknowledgements

Firstly, I have to thank Professor Fiona Meldrum for the opportunity to do this PhD, and for her supervision and guidance which has been so instrumental. Thank you for helping me push through the tough parts. I must also thank Dr Yi-Yeoun Kim, whose mentorship through my MChem made me stay on for a PhD, for teaching me so much and who pushed me to be a better scientist. Dr Alex Kulak, my favourite specialist, thank you for the support you continually provided me, for the parties, for the fun open days/art exhibition installations/group Christmas gift shopping trips.

A massive thank you goes to the large and vibrant community of past and present Meldrum group members I have had the pleasure of knowing. The sharing of advice, sounds of laughter, and forging of friendships that has taken place in 2.71 ("Our Office") has made my experience unforgettable. There are a few whose contribution I really must highlight and would like to thank especially: Dr Ouassef Nahi, whose advice was invaluable for my research and who patiently helped at a time when I was completely lost. Dr David Green, for always asking the most important questions, for his help and advice on anything and everything, and, of course, his dad dancing during lab cleans. Dr Yifei Xu, for his help with all things TEM, his kind patience during the many hours spent at ABSL, for sharing his wealth of expertise in microscopy with me and whose guidance made me a better microscopist. Dr Helen Freeman and Dr Martha Ilett, who have patiently spent so much time working with me on the LCTEM, sharing their passion for microscopy and going along with the bizarre ideas I randomly sprang on you in middle of sessions.

I also want to thank Stuart Micklethwaite, Dr Zabeada Aslam and John Harrington, who always made my trips over to LEMAS such an enjoyable escape from the lab, and whose passion for microscopy has inspired me so greatly. All of your help has been so crucial for my work and I couldn't have done it without your support.

Thank you to the team at Imerys, Dr Andy Findley, Des Payton and Nigel Jarvis, who have given me fantastic advice during my PhD on all things PCC, and whose enthusiasm always made me excited to crack-on with my projects.

To my collaborators Dr Gianni Jacucci and Professor Silvia Vignolini at the University of Cambridge, for their friendly help and guidance on the structural colour project and for always making my visits to Cambridge fun.

Perhaps one of the greatest thanks I owe is to the rheumatology team and vasculitis clinic across Leeds Teaching Hospitals, and the incredible Professor Ann Morgan. I would certainly not be here to write this, let alone complete my PhD, if it were not for the early diagnosis and treatment I received under your care. I will always be so, so grateful.

I want to thank my parents, who always believe in me, empower me to carry on and back me unconditionally. Thank you to Mad, Dan and little Noah, for lifting my spirits with their banter (or in Noah's case, cheeky smiles and squeaks) and the rest of my family for their encouragement. To my second family, the Higginbottoms, who have supported me throughout the last few years. The drive to make all of you proud has carried me through so much of this PhD.

I certainly would not have been able to complete this PhD without the love and absolute support of my partner Cal. You have always picked up the slack when I was at my worst and helped me shine brighter when I was at my best. You have always kept me going and I can't wait to start my next chapter with you.

## Abstract

This thesis explores how crystallisation can be used as a tool to synthesise and optimise the properties of composite materials for diverse applications. It also examines an important industrial process, the carbonation of calcium hydroxide to yield calcium carbonate. The first experimental chapter focuses on the incorporation and subsequent removal of organic additives in calcite single crystals for the purpose of creating highly scattering, porous crystals that exhibit structural colour. A particular goal was to create crystals that were extremely white, therefore satisfying the need to replace current $TiO_2$ pigments with environmentally-friendly materials. Optimisation of the synthesis delivered porous single crystals of calcite with varying levels of porosity and pore sizes. The introduction of 25 – 200 nm pores into the calcite crystals increased their reflectance in a broadband fashion and delivered bright white particles.

The second experimental chapter investigates the carbonation of $Ca(OH)_2$ to gain insight into the mechanism of $CaCO_3$ formation in industrial settings. Time-resolved conventional TEM, cryo-TEM and cryo-electron tomography (cryo-ET) were combined to obtain time-resolved information about how $Ca(OH)_2$ crystals convert to $CaCO_3$. Liquid-cell TEM (LCTEM) studies revealed the dynamics of the reaction in real time in solution, and confirmed that the conversion of $Ca(OH)_2$ to crystalline $CaCO_3$ occurred via a dissolution-precipitation reaction pathway. Skeletal hexagonal structures were observed as key intermediates and were attributed to the precipitation of pseudomorphic amorphous calcium carbonate (ACC) on the basal faces of hexagonal $Ca(OH)_2$ plates.

The synthesis of porous manganese oxide (MnOx) crystals and their application as photocatalysts in the water splitting reaction is described in the final chapter. $Mn_2O_3$ was produced by thermal decomposition of precipitated manganese carbonate, where the porosity could be controlled by manipulating the heating regime, while highly porous core-shell $MnO_2$ crystals were synthesised using a hydrothermal route. More complex porous materials were also synthesised using $MnCO_3$ single crystals occluded with gold nanoparticles as a precursor. Annealing these materials yielded porous Au-$Mn_2O_3$ and Au-$MnO_2$ nanocomposites in which the nanoparticles were uniformly distributed throughout the crystal host. Porous $Mn_2O_3$ crystals were the

most efficient photocatalysts for water splitting, where the heating regime strongly influenced the catalytic efficiency, due to its effect on the composition, crystallinity and surface area of the crystal products. Manganese oxides containing Au nanoparticles were poor photocatalysts for water splitting, suggesting that the Au nanoparticles inhibited the recycling of electrons between the co-catalysts and charge carriers. Overall, this study demonstrates two facile and versatile strategies for synthesising novel photocatalyst materials with porosities that can be controlled and easily optimised.

# Table of Contents

# List of Tables

# List of Figures

# Chapter 1 | General Introduction

This chapter provides a general introduction to crystalline materials and crystallisation. Due to the diverse nature of the themes explored in this thesis, each of the experimental chapters is prefaced by a dedicated introduction and methods section that is tailored specifically to the work detailed in that chapter. As calcium carbonate is relevant to both Chapters 3 and 5, it is also introduced in this chapter.

## 1.1 Crystalline Materials

### 1.1.1 Defining Crystalline Materials

A crystal consists of atoms or ions that are regularly arranged into a lattice. The smallest possible representation of the crystal is known as the unit cell (Figure 1.1), which is repeated to make up the overall crystal structure. A unit cell can take one of seven 3D shapes, which are described by the seven crystal systems (Table 1.1). Each crystal system can be distinguished by its symmetry elements. There are also different ways in which the atoms in these unit cells may be packed, which can be described using one of the fourteen permitted Bravais lattices.

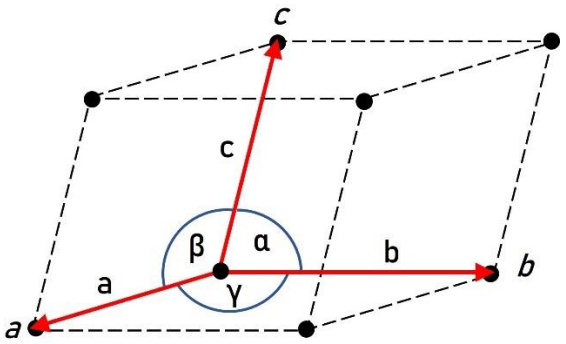


**Figure 1.1 A 3D unit cell labelled with the crystallographic axes *a, b, c*, and the lattice parameters, including vectors a, b, c, and angles α, β, and γ.**

| Crystal System | Axial Lengths and Angles | Bravais Lattices |
|---|---|---|
| Cubic | **$a = b = c$ $\alpha = \beta = \gamma = 90°$** | **P, I, F** |
| Tetragonal | **$a = b \neq c$ $\alpha = \beta = \gamma = 90°$** | **P, I** |
| Orthorhombic | **$a \neq b \neq c$ $\alpha = \beta = \gamma = 90°$** | **P, I, C, F** |
| Rhombohedral/trigonal | **$a = b = c$ $\alpha = \beta = \gamma \neq 90°$** | **R** |
| Hexagonal | **$a = b \neq c$ $\alpha = \beta = 90°$, $\gamma = 120°$** | **P** |
| Monoclinic | **$a \neq b \neq c$ $\alpha = \gamma = 90°$ $\beta \neq 90°$** | **P, C** |
| Triclinic | **$a \neq b \neq c$ $\alpha \neq \beta \neq \gamma \neq 90°$** | **P** |

**Table 1.1 The seven crystal systems, where the Bravais lattices are P = primitive, I = body-centred, C = base-centred and F = face-centred.**

Virtually all crystals possess imperfections known as defects. This can occur when foreign atoms disrupt the lattice by incorporation as a substitutional or interstitial impurity. On the other hand, defects may also arise due to vacancies caused by missing atoms or ions in the lattice. A Schottky defect describes a pair of vacancies (anion and cation), whereas Frenkel defects are those created when a cation occupies an interstitial site, leaving its original site vacant. All of these defects are known as point defects. Extended defects such as dislocations can also occur, which consist of a line of defects through the lattice caused by applied shear stress. Edge dislocations are formed by an additional half-plane of atoms, which causes localised lattice distortion. Screw dislocations are produced by the displacement of atoms perpendicular to the applied shear stress, which forms a step on the surface by its dislocation. As a result, screw dislocations play a significant role in growth and dissolution (discussed in detail in Section 1.2.2.2), where growth at this step occurs in a helicoid fashion to produce a spiral hillock. Another type of extended defect found in crystalline materials are grain boundaries. They lie between crystallites and are associated with disorder and misorientation along this border. Crystals composed of two or more crystallites separated by grain boundaries are known as polycrystalline materials. Conversely, a single crystal is one which does not possess any grain boundaries.

### 1.1.2 Describing Crystalline Materials

The structure of crystalline materials can be described using Miller indices to label expressed crystal faces, planes or crystallographic directions. The reciprocal of the positions at which a face or plane intercepts each axis is taken to yield *h, k* and *l*, which correspond to the *a, b* and *c* axes respectively. Depending on what is being described, different notations are used to frame the *hkl* values. A single plane is expressed as *(hkl)*, whereas {hkl} is used when describing a family of symmetry-related planes. A single direction can be conveyed using *[hkl]*, while symmetrically equivalent directions are expressed as <*hkl*>.

### 1.1.3 Polymorphism and Morphology

Many crystalline materials can exist in more than one crystal structure, which is termed polymorphism[1]. While the chemical composition does not differ between polymorphs, they can exhibit contrasting physical properties such as melting point, solubility, density, electrical conductivity and optical activity. It is therefore important to understand the conditions that give rise to specific polymorphs such that pure forms of individual polymorphs can be synthesised for a desired application. Each polymorph has its own thermodynamic stability and kinetics of formation, and the polymorph that is obtained will depend on whether crystallisation is under kinetic or thermodynamic control. Under thermodynamic control, the most stable polymorph is obtained. If crystallisation is chiefly governed by the kinetics, metastable phases may form first, followed by a cascade of further transformations into phases with increasing thermodynamic stability. This is known as Ostwald's step rule and is represented in Figure 1.2. Kinetic control can be induced by high supersaturations, elevated temperatures, confined crystallisation environments, additives, and mixed solvents[2, 3], which can lead to the metastable or less stable polymorphs being obtained, though these will ultimately convert to the stable form.

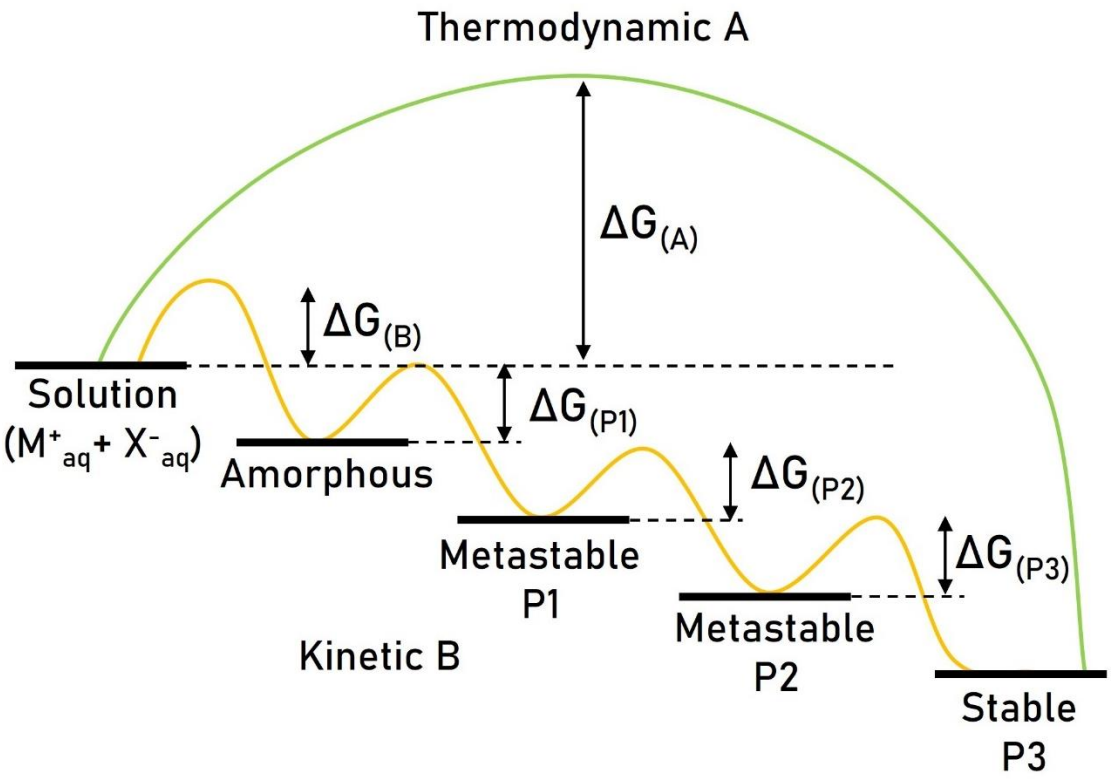


**Figure 1.2 Ostwald's rule of stages, showing a one-step thermodynamic pathway and a multi-step kinetic cascade, where the free energy of activation, ΔG determines which route is followed. Adapted from ref.[4]**

Polymorphic crystals may or may not share the same morphology. Crystals with the same unit cell may take various morphologies, since morphology is affected by both crystal structure and the conditions experienced during crystal growth[5]. The faces that are ultimately expressed in a crystal are those that grow most slowly, whereas the fastest growing faces are lost completely. Therefore, any change in crystallisation conditions that results in the promotion or suppression of a growing crystal face can change the morphology. Such effects can be described using the term *Tracht* (the German word for costume), used to distinguish situations where the crystal shape is the same (i.e. the crystal habit), but the faces are developed to a different extent.

## 1.2 The Crystallisation Process

### 1.2.1 Supersaturation

In order for crystallisation to occur, there must be a sufficient driving force for this phase transition. This is termed the supersaturation. For crystallisation in a binary solution, this is achieved when the concentration of a solute surpasses the solubility limit, causing the equilibrium position to become unbalanced. The supersaturation, $\Delta\mu$, can be described using Equation 1.1,

$$\Delta\mu = \mu_s - \mu_c \tag{1.1}$$

which represents the difference in the chemical potentials of molecules in solution ($\mu_s$) and molecules in a crystal ($\mu_c$). In thermodynamic terms, supersaturation can be expressed in Equation 1.2,

$$\Delta\mu = k_B T \ln(S) \tag{1.2}$$

where $k_B$ is the Boltzmann constant and $T$ represents temperature, while $S$ is supersaturation as defined by one of the following:

$$S = \frac{AP}{K_{sp}} \quad or \quad S = \frac{c}{c*} \tag{1.3}$$

where $AP$ is the activity product of the constituents, $K_{sp}$ represents the solubility product (which is different for each polymorph), $c$ represents the molarity and $c^*$ represents the equilibrium concentration.

A supersaturated system has $\Delta\mu > 0$ or $S > 1$, where the equilibrium position is $\Delta\mu = 0$ or $S = 1$ and crystallisation is probable. Conversely, an undersaturated system will have $\Delta\mu < 0$ or $S < 1$ and crystallisation will not occur. The system can also exist in a metastable zone, where nucleation does not occur readily but growth would occur on a seed crystal exposed to the system[6]. In the saturation diagram shown in Figure 1.3, the metastable zone occupies the region between the solubility and supersolubility curves, known as the Ostwald-Miers region. Control over the supersaturation of a system can allow a particular polymorph to be isolated, due to the difference in the solubility products.

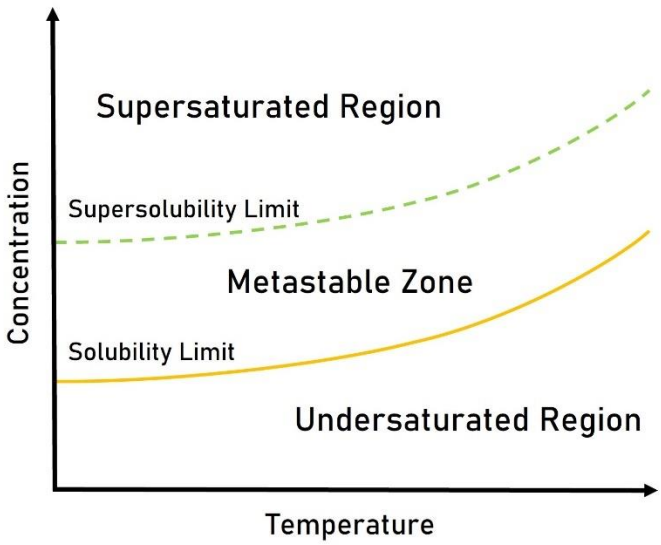


**Figure 1.3 Supersaturation as a function of temperature and concentration.**

## 1.2.2 Classical Crystallisation

### 1.2.2.1 Classical Nucleation Theory

Crystallisation begins with nucleation, where the new phase forms and a nucleus is established. It can be further defined as homogeneous or heterogeneous nucleation, where homogeneous nucleation occurs spontaneously in an impurity-free system whilst heterogeneous nucleation is induced by impurities or surfaces which lower the total energy cost of nucleation. Nucleation can also be described as primary or secondary, where secondary nucleation is typically used to describe a second burst of nucleation that occurs in a system.

A nucleus is constructed by the assembly of atoms, ions or molecules into a cluster. However, the particles will associate and dissociate from the cluster until a critical size is reached. This occurs by chance and up to this point complete dissolution of the cluster can occur, so a higher supersaturation will increase the likelihood of such clusters forming due to the increased amount of solute. Once the critical size threshold has been passed, the cluster is stable and will undergo growth.

The formation of a cluster above the critical nucleus size is associated with a certain critical Gibbs free energy[7], which is the sum of two components, as shown by the following equation

$$\Delta G = \Delta G_v + \Delta G_s \qquad (1.4)$$

where $\Delta G_v$ reflects the energy reduction associated with assembling the particles and $\Delta G_s$ reflects the gain in energy associated with formation of the cluster surface. Each of these components can be substituted to give the following

$$\Delta G = -n\Delta\mu + 4\pi r^2\gamma \tag{1.5}$$

where $r$ is radius and $\gamma$ is interfacial tension. Assuming clusters are spherical, this can be better represented by substituting the volume contribution to yield

$$\Delta G(r) = -\frac{4}{3}\frac{\pi r^3}{V}\Delta\mu + 4\pi r^2\gamma \tag{1.6}$$

where $V$ is the volume. The volume and surface components are proportional with $r^3$ and $r^2$, respectively, and the overall relation between Gibbs free energy and the cluster radius is depicted in Figure 1.4.

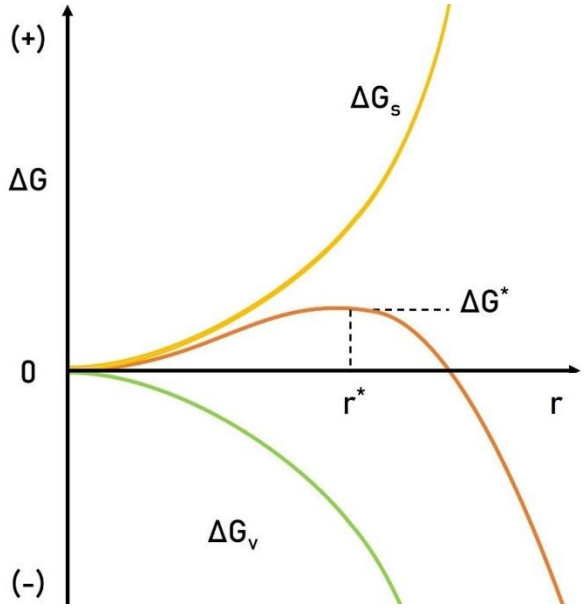


**Figure 1.4 Gibbs free energy as a function of cluster radius, where $r^*$ is the critical cluster radius and $\Delta G^*$ is the critical Gibbs free energy. Adapted from ref.[8]**

Initial formation of the cluster is disfavoured due to the energy cost in forming the surface, as reflected in the steep curve for the surface component at small $r$. With growing $r$, the volume component will have a greater effect as its value sharply increases at higher $r$. The critical nucleus size is represented by $r^*$, which has the critical energy $\Delta G^*$ and is the highest Gibbs free energy experienced by the system. Beyond this critical size, the nucleus is stable and growth will occur since this will reduce the Gibbs free energy of the system and is thus favoured until the equilibrium

is balanced. The radius of the critical nucleus, $r_c$, can be established by differentiation of Equation 1.6 to give

$$\frac{d\Delta G}{dr} = \frac{4\pi r^2}{V}\,\Delta\mu + 8\pi r\gamma \tag{1.7}$$

which can set be to 0, since $\Delta G^*$ is the maximum $\Delta G$ value, leaving Equation 1.8.

$$r_c = \frac{-2\gamma V}{\Delta\mu} \tag{1.8}$$

Crystallisation is more likely to occur if the critical energy $\Delta G^*$ involved can be reduced. By substituting $\Delta\mu$ in Equation 1.6 using the relationship in Equation 1.2, Equation 1.9 can be derived.

$$\Delta G(r) = -\frac{4}{3}\frac{\pi r^3}{V}\,k_B T \ln(S) + 4\pi r^2\gamma \tag{1.9}$$

This equation reflects the influence of supersaturation, whereby a higher supersaturation gives rise to a smaller critical nucleus. Temperature has a significant effect on $\Delta G^*$ as it appears in the volume component and also inherently factors into the supersaturation of the system. A decrease in temperature therefore decreases the overall critical energy $\Delta G^*$ required for the formation of a stable nucleus. On the other hand, the surface component becomes more favourable when smaller interfacial tensions are involved. This explains why heterogeneous nucleation occurs more readily than homogeneous nucleation, as the presence of a surface or an interface with foreign particles will reduce interfacial tension. The ability of a surface to effectively lower the energetic barrier for nucleation can be estimated by the wettability of the solution on the substrate. Nucleation will be promoted to a greater extent on surfaces that exhibit low contact angles with solution, indicating their high wetting ability which reduces the interfacial tension.

An experimental measure of the efficiency of nucleation processes is the nucleation rate, as shown in Equation 1.10, and can be estimated experimentally by measuring induction time, which is the time required before crystals are observed. The nucleation rate ($J$) is commonly expressed as the number of nuclei formed per unit volume, per unit time, and can be calculated using the Arrhenius-type equation

$$J = A\exp\left(-\frac{\Delta G^*}{k_B T}\right) \tag{1.10}$$

where *A* is a rate constant that is dependent on the nucleation rate mechanism. This equation shows that the nucleation rate is defined by the temperature of the system and the critical free energy $\Delta G^*$. As seen in Equation 1.9, the critical free energy $\Delta G^*$ depends on the supersaturation of the system, and as a result faster nucleation rates occur at high supersaturation.

#### 1.2.2.2 Classical Growth Theory

Once a stable nucleus is established, it is favourable for it to grow larger. In classical crystallisation theory, this is described as the attachment of growth units to a surface. This occurs first by diffusion of the atoms through solution to the growing crystals, followed by a series of surface processes. The crystal surfaces are classified into different "sites" using Kossel's model[9], based on the environment they provide and the surface energies associated with them. These are known as terrace, step and kink sites and are capable of forming 1, 2 or 3 bonds with the incoming growth unit, respectively. As kink sites will share 3 bonding surfaces with the new unit, this is the most stable site for attachment.

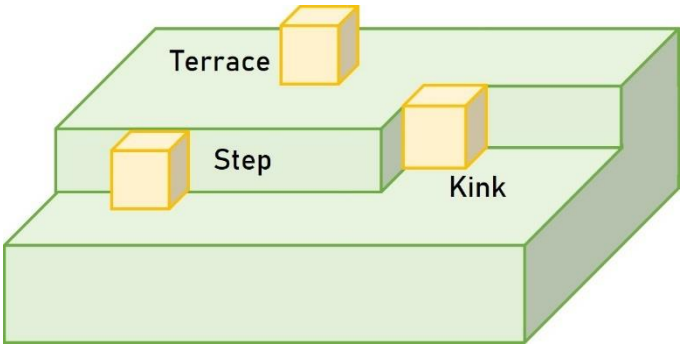


**Figure 1.5 Growth units adsorbed at terrace, step and kink sites.**

It is evident that the growth conditions are highly influential on the resulting crystal morphology[10]. The growing crystal faces can be classified using Hartman and Perdock's periodic bond chain theory[11], which defines the crystal faces as flat (F), stepped (S) or kinked (K). It states that the lattice consists of uninterrupted in-plane periodic bonding chains (PBCs) composed of growth units. The K, S and F faces contain 0, 1 and 2 or more PBCs, respectively, rendering the F faces the most stable and the K faces the least stable. As the incorporation of growth units will therefore occur rapidly at K faces, this face will grow at the fastest rate until it is completely removed from the crystal morphology.

After growth units have diffused through solution to the growing crystal, they can attach at terrace, step or kink sites. In order to improve the stability of the system, growth units attached at terrace or step sites may detach and reattach to kink sites. Once all kink sites are filled, growth units at terraces will detach and reattach at step sites. This process will eventually result in a complete layer being formed and is therefore termed the layer-by-layer growth model.

At very low supersaturations, layer-by-layer growth is unlikely to occur due to the energetic cost of forming a new layer. It does occur in practice, however, via the spiral growth mechanism (also known as BCF model, named after Burton, Cabera and Frank who devised it)[12] (Figure 1.6). This proceeds at screw dislocations, which provide a supply of step edges and kink sites and therefore lower the energetic barrier to growth. Sustained growth by this mechanism results in the formation of a spiral of steps on the crystal surface.

In systems with moderate supersaturation, nucleation rates are higher and growth may occur by a birth and spread or polynuclear growth model. In this model, monolayers grow outwardly with additional growth units attaching to the surface of the spreading layers.

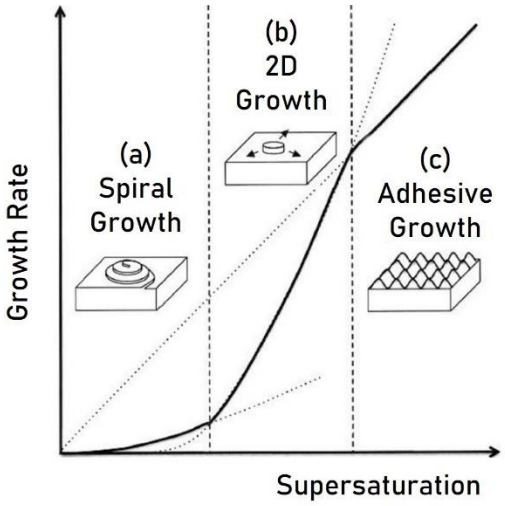


**Figure 1.6 The growth models followed at different levels of supersaturation. Adapted from ref.[13]**

Thus far, we have described crystal growth that is limited by kinetics, i.e. the supply of growth units to the crystal surface. At very high supersaturations, growth units are more abundant and therefore growth of the crystal is instead limited by diffusion, i.e.

the transport of the growth units to favourable surface sites. High supersaturation also cause the growing crystal to exhibit rough interfaces[10]. This is unlike the previous growth models discussed, in which interfaces are atomically smooth. The presence of rough interfaces facilitates adhesive growth, where the attachment energy required is isotropic[14]. The instability exhibited by the interface will therefore result in morphological instability, promoting the formation of increasingly polycrystalline dendritic and spherulitic crystals[10]. This is shown by Figure 1.7, which also shows that an intermediate stage exists between the conditions that yield polyhedral and dendritic crystal morphologies, where hopper crystals are obtained. These are formed when 2D growth is dominant but there is a large enough supersaturation for the reaction to be diffusion limited, causing anisotropic growth that occurs faster at crystal corners and edges than the faces[15]. This ultimately results in the central face of a crystal being lower than edges and corners, forming a unique hopper morphology[10].

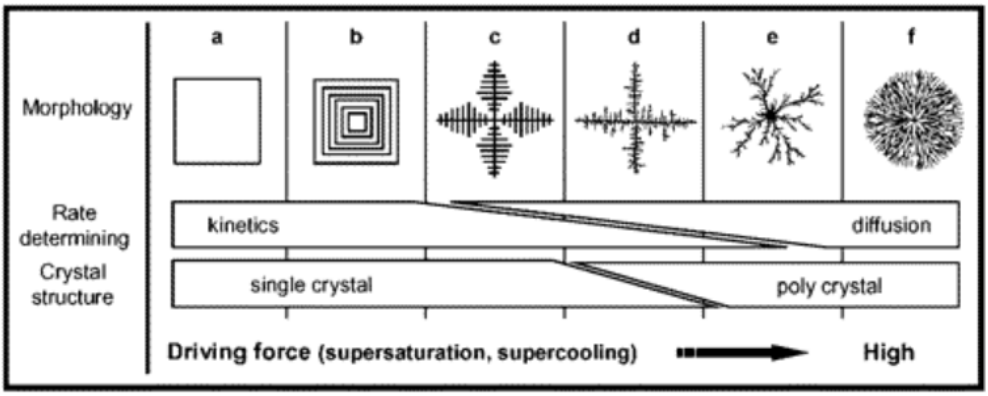


**Figure 1.7 The effect of reaction driving force on crystal morphology, showing (a) a polyhedral crystal, (b) a hopper crystal, (c) a dendritic single crystal, (d) a dendritic crystal with a single crystal centre and polycrystalline branches (e) a polycrystalline dendritic crystal. Reproduced from ref.[16]**

### 1.2.2.3 Dissolution

Dissolution is often thought as the reverse of crystal growth, however this is not strictly true, as observed by comparing the rates of each process. Growth typically occurs at a much slower rate than dissolution, which readily proceeds at low supersaturations or undersaturation. However, there is still a symmetry between the mechanisms involved in growth and dissolution, particularly with respect to their

relationship with supersaturation[17]. As discussed in the previous section, classical growth models state that growth occurs by spiral growth, 2D nucleation, and birth-and-spread mechanisms with increasing supersaturation of the system. In dissolution, the same general mechanisms are employed and occur in the same order with increasing undersaturation[18], as shown in Figure 1.8. Instead of the 2D nucleation of growth units, the nucleation of vacancy "islands" takes place. These are formed by numerous etch pits created in the crystal surface during dissolution, which can only be produced by surpassing the associated energy barrier (as for growth)[19]. This energy barrier is reduced by increasing the undersaturation of the system.

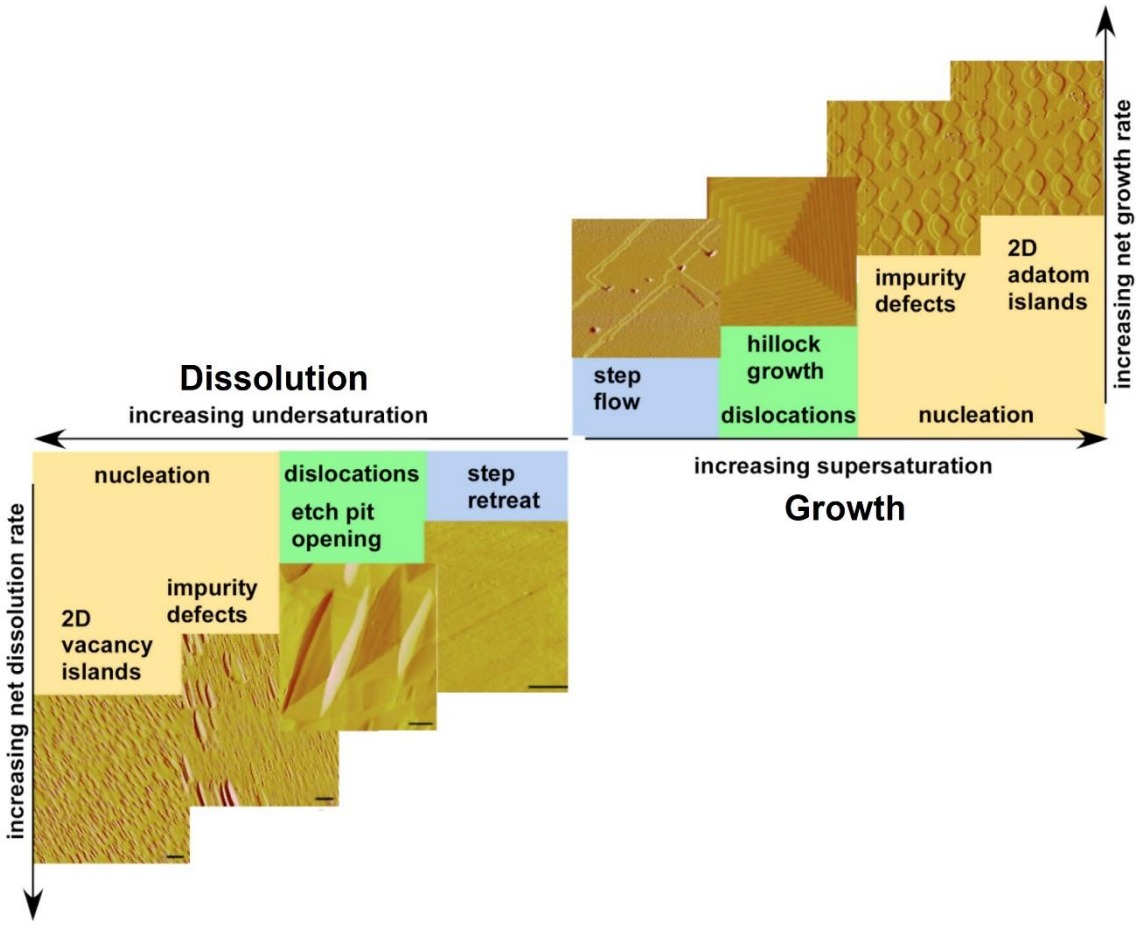


**Figure 1.8 Dissolution and growth mechanism illustrated using AFM images of quartz (dissolution images) and calcite (growth images). Scale bars are equal to 1 µm. Adapted from ref.[18]**

Simultaneous dissolution and growth can occur amongst crystals of different sizes. This is known as Ostwald ripening[20]. Smaller crystals undergo dissolution due to the

unfavourable surface energy involved, making growth units freely available to participate in the growth of larger crystals, which is energetically favoured. Therefore, the average crystal size will increase over time.

## 1.2.3 Non-Classical Crystallisation

### 1.2.3.1 Non-Classical Nucleation Theory

As discussed in the previous section, classical nucleation theory (CNT) relies on stochastic fluctuations in the composition of a system in order for a critical nucleus to be produced by the consecutive addition of atoms, ions or monomers[21, 22]. However, nucleation rates calculated using CNT have been found to be many magnitudes higher than rates obtained experimentally[23], indicating that CNT is not an adequate model for describing crystallisation in real systems, particularly those with high or low supersaturations. It also leaves unclear how structural changes can occur during the phase transition in terms of density and order, for example when crystallisation is performed from a gaseous phase[23]. To address these shortcomings, non-classical nucleation theories have been developed.

Non-classical nucleation is generally thought to proceed via two main pathways. In two-step nucleation, the nucleation event is preceded by the formation of a dense liquid phase[24]. This arises due to density fluctuations in the system, followed by the formation of a nucleus[25]. The second pathway proposed involves the formation of prenucleation clusters (PNCs) (Figure 1.9). PNCs consist of ions which are bound together in solution and possess a phase interface. They are thought to aggregate and ultimately precipitate amorphous and crystalline phases[22].

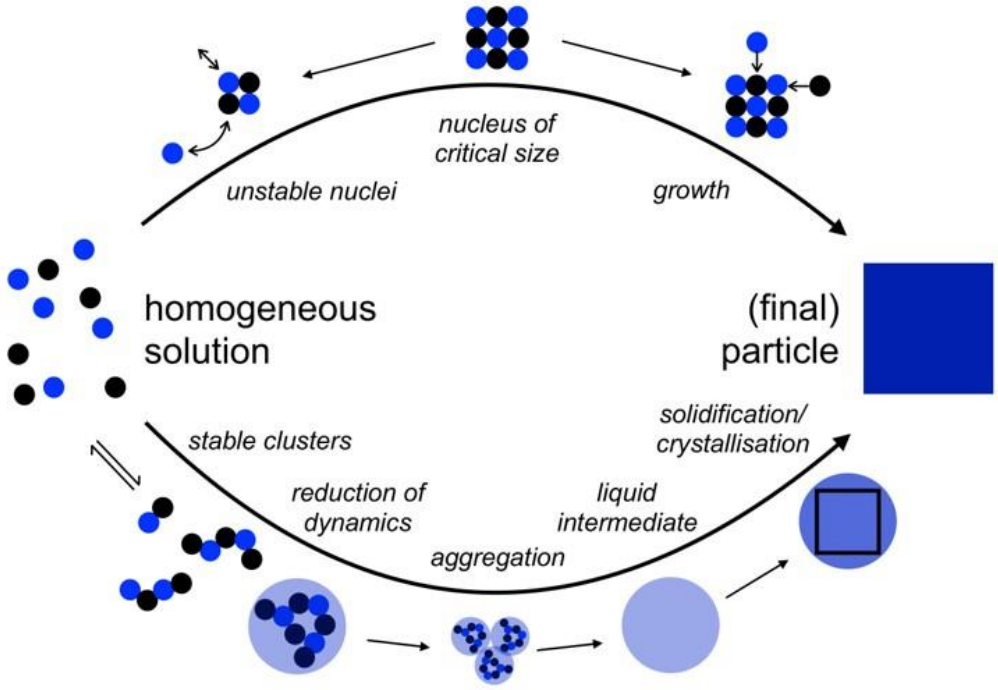


**Figure 1.9 The proposed prenucleation cluster (PNC) pathway (bottom) compared to classical nucleation theory (top). Reproduced from ref.[26]**

Spinodal decomposition is a spontaneous phase transition that occurs when the composition of a fluid phase becomes unstable[6]. This occurs when the system approaches the solubility limit. There is no energy barrier to spinodal decomposition as the process is controlled by diffusion rather than being reliant on thermodynamic fluctuations. In order for spinodal decomposition to proceed, the system must pass through the metastable region to the unstable region without nucleation, as illustrated by the points A, B and C on the arrow in Figure 1.10. Typically, this is unlikely to happen, so for spinodal decomposition to occur the system must be quenched. Heterogeneous nucleation can then proceed at the interface between the two phases formed in spinodal decomposition[27].

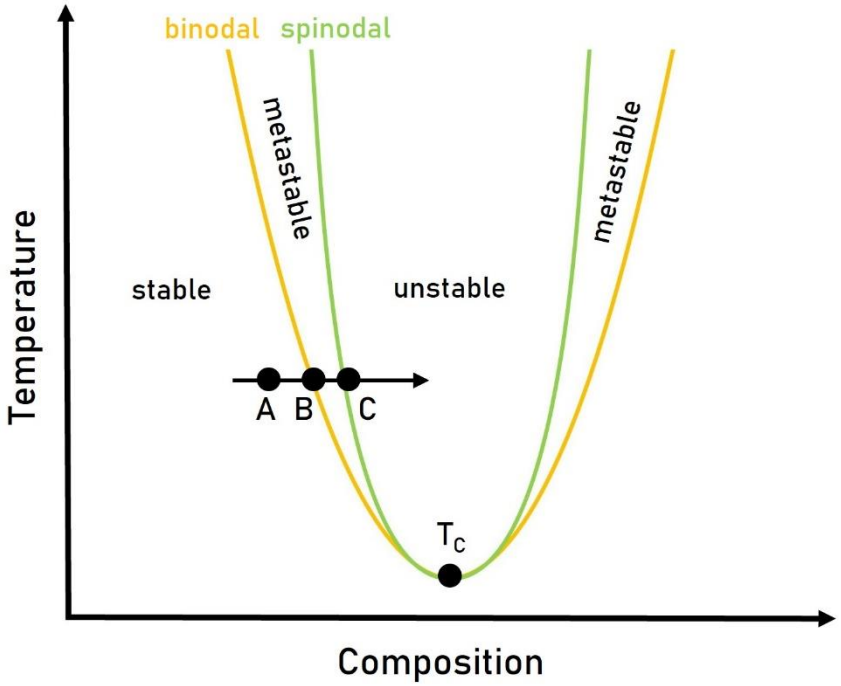


**Figure 1.10 Phase diagram for a two-phase system, illustrating the binodal and spinodal curves, where $T_c$ is the lower critical solution temperature.**

### 1.2.3.2 Non-Classical Growth Theory

Non-classical growth does not involve the attachment of individual growth units as for classical growth, but rather proceeds by the aggregation of nanoparticles[28]. Oriented attachment describes the alignment and assembly of nanoparticles to form a larger single crystal[29]. In order to achieve this common orientation, the nanoparticles rotate and align themselves prior to contact occurring and subsequent fusion (Figure 1.11).

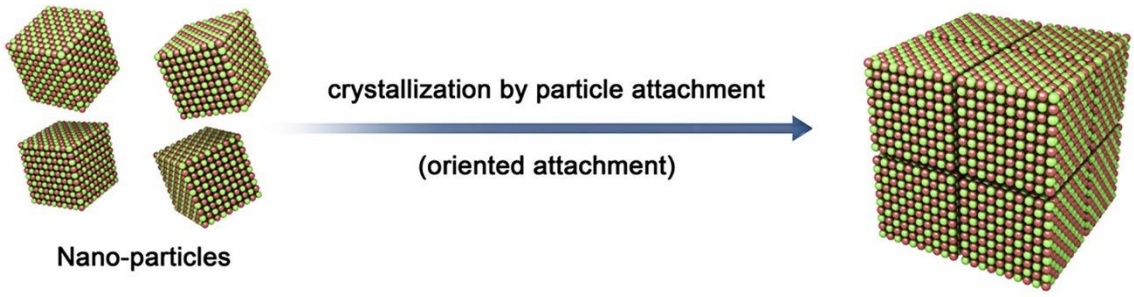


**Figure 1.11 The oriented attachment growth mechanism compared with classical growth by addition of growth units. Adapted from ref.[30]**

If oriented aggregation of nanoparticles occurs to generate single crystals in which the individual units maintain their individual surfaces and are not fused, they are termed “mesocrystals”.[24] This is energetically unfavourable, so the mesocrystals exist as intermediates before fusion yields a perfect single crystal[31]. Polymers therefore often preserve the mesocrystal structure by adsorbing onto the surfaces of the precursor particles[32, 33]. Oriented attachment can give rise to a wide range of anisotropic morphologies[34] that could not form via classical crystal growth mechanisms[35-38].

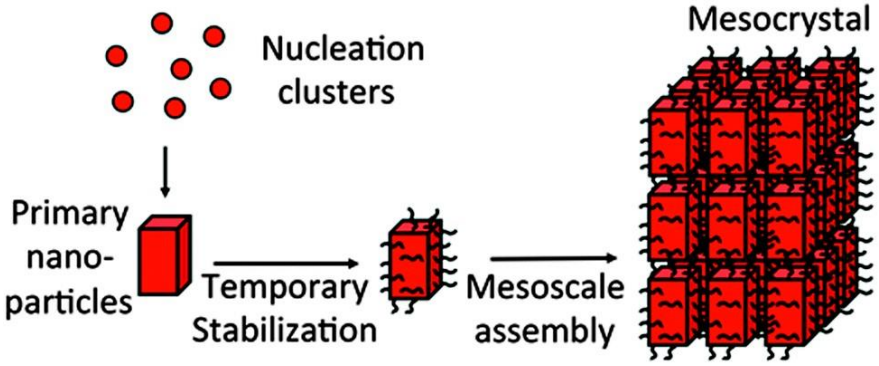


**Figure 1.12 Formation of a mesocrystal by oriented attachment. Reproduced from ref.[39]**

## 1.3 Calcium Carbonate

Calcium carbonate ($CaCO_3$) is a highly versatile mineral which is important in many natural processes, and common in man-made materials. The formation of $CaCO_3$ deposits is a crucial step in the carbon lifecycle, which is essential in regulating both atmospheric $CO_2$ and the pH of our oceans[40]. Numerous marine organisms mineralise $CaCO_3$[41], such as molluscs, corals, crustaceans, and planktons[42], making it one of the most predominant biominerals[43]. This has led to significant research interest into the crystallisation of $CaCO_3$[44], to improve understanding of biomineralization and exploit the advantageous properties exhibited by these organisms through biomimicry[45]. Since the Stone Age, humans have used $CaCO_3$ as a building material[46], even using it to create works of cultural importance such as the Great Pyramid of Giza and the Colosseum[47]. Today, $CaCO_3$ is a universal filler ingredient in paper, paint, plastic, and rubber, and has also found application in a range of household, medical and personal care products.

Calcium carbonate is commonly explored as a model crystallisation system and is used in two of the three chapters in this thesis. There are three polymorphs of anhydrous $CaCO_3$, which are calcite, aragonite and vaterite. There is also an amorphous form (amorphous calcium carbonate, ACC), and two hydrated crystalline forms (ikaite, $CaCO_3.6H_2O$, and monohydrocalcite, $CaCO_3.H_2O$).

### 1.3.1 Calcite

Calcite is the most thermodynamically stable polymorph of $CaCO_3$ and is most commonly observed experimentally during crystallisation in additive-free solutions under ambient conditions. It has a trigonal lattice and is described by either a rhombohedral unit cell (Figure 1.13) or a hexagonal unit cell. The structure of calcite can be described as a distorted rock salt (NaCl) structure. In the unit cell each $Ca^{2+}$ ion is octahedrally co-ordinated to 6 $CO_3^{2-}$ ions, each of which bond with 1 oxygen atom, and a layered structure of $Ca^{2+}$ and $CO_3^{2-}$ ions is apparent in the hexagonal unit cell. Calcite crystals produced experimentally typically possess rhombohedral morphologies, which are bound by non-polar (104) faces that contain equal numbers of $Ca^{2+}$ and $CO_3^{2-}$ ions.

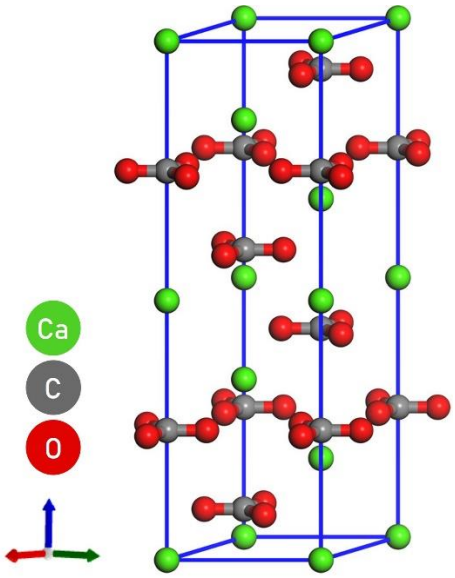


**Figure 1.13 The unit cell of calcite. Adapted from ref.[48]**

### 1.3.2 Aragonite

Following calcite, the polymorph aragonite is next in terms of thermodynamic stability. However, it is generally only formed in small quantities under ambient

conditions in the absence of additives as it is poorly stable. It can be precipitated at elevated temperatures of 50 °C or greater[49]. It is also more dense than calcite and therefore forms at high pressure[50]. However, following Ostwald's rule of stages, it will eventually convert into calcite over time if left under ambient conditions. Precipitation in the presence of $Mg^{2+}$ ions has also been shown to promote the formation of aragonite by suppressing calcite growth faces and increasing its solubility[51].

Aragonite possesses an orthorhombic unit cell (Figure 1.14) and has a pseudohexagonal arrangement of the cations[52]. Each $Ca^{2+}$ is co-ordinated to 6 $CO_3^{2-}$ ions, as for calcite. However, 3 of these are bonded with 2 oxygen atoms while the rest are bound through 1 oxygen, giving a coordination number of 9. This results in two layers of carbonate ions rather than the alternating structure in calcite. Crystals of aragonite typically possess acicular morphologies.

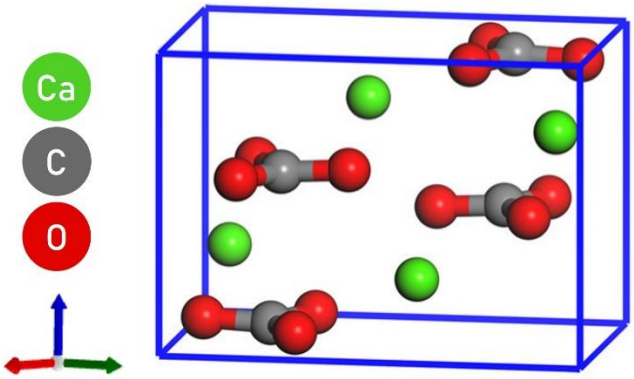


**Figure 1.14 The unit cell of aragonite. Adapted from ref.[48]**

### 1.3.3 Vaterite

Vaterite is the least stable of all the crystalline $CaCO_3$ polymorphs and is rarely observed in nature[53]. Although it is highly metastable and rapidly transforms into calcite in solution, it is not unusual to observe experimentally that vaterite crystals have readily precipitated in the presence of organic molecules[54]. It is the least dense of all the crystalline $CaCO_3$ polymorphs and cannot be stabilised relative to other crystalline polymorphs by controlling temperature or pressure during crystallisation[55].

Vaterite possesses a hexagonal unit cell with alternating layers of $Ca^{2+}$ and $CO_3^{2-}$ ions, where the latter are oriented parallel to the c-axis rather than perpendicular, as occurs for aragonite and calcite[45]. Crystals of vaterite are most commonly observed as polycrystals with spherical morphologies. However, hexagonal plates of vaterite

may also be produced in the presence of ammonium ions, which can stabilise the high energy (00-1) faces[56].

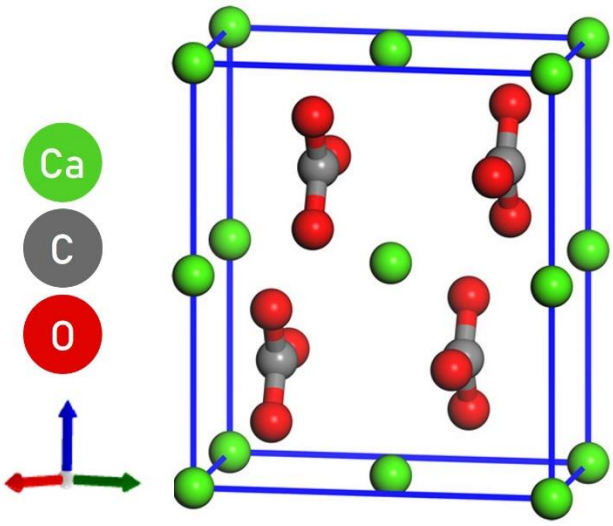


**Figure 1.15 The unit cell of vaterite. Adapted from ref.[48]**

### 1.3.4 Amorphous Calcium Carbonate (ACC)

Amorphous calcium carbonate (ACC) may be formed as a precursor to the anhydrous $CaCO_3$ polymorphs in aqueous solution. It precipitates rapidly at low and ambient temperatures and is highly unstable. Left in solution it will dissolve and reprecipitate into calcite, aragonite or vaterite[57]. ACC exists in solution as spherical nanoparticles which possess no long-range order, with a chemical composition thought to be $CaCO_3.xH_2O$, where x is ≈ 1 – 1.5[45, 58].

However, a distinction has been made between transient and stable ACC in biomineralization, where the former is dehydrated and the latter hydrated[59]. Experiments have shown that transient ACC phases may crystallise via structural arrangements occurring during dehydration, mediated by the expulsion of structural water[60, 61]. This has developed our understanding of biomineralization in sea urchin spicules, which grow using vesicles of transient ACC devoid of bulk water[62, 63]. Indeed, ACC has been shown to be an important phase in biomineralization[64], where its amorphous, space-filling nature allows it to be moulded into any arrangement. This has led to the precipitation of anhydrous $CaCO_3$ crystals which retain complex morphologies after being transformed from ACC held in constrained volumes[65, 66]. There is also interest in the stabilisation of ACC, which has been achieved using a number of additives[67, 68], including ions such as $Mg^{2+}$,[69, 70] $Sr^{2+}$,[71] $PO_4^{3-}$,[72, 73] in

addition to proteins[73, 74], and polymers[75]. The stabilisation of ACC using polymers was particularly significant as this led to the discovery of a polymer-induced liquid precursor (PILP)[76, 77].

The role of ACC in non-classical nucleation has also been explored[78-81], where studies have indicated that aggregation of the prenucleation clusters (PNCs) results in the nucleation of ACC[81, 82]. Nanosized crystalline domains have been observed within ACC by Clark *et al.*, who highlighted the similarity between the size of the domains with that of PNCs at 1 – 4 nm[79, 83, 84]. Furthermore, studies into the structure of ACC have shown that it can possess short-range order reminiscent to the anhydrous $CaCO_3$ polymorphs[85, 86]. These ACC sub-types, or polyamorphs, are known as proto-calcite, proto-aragonite and proto-vaterite[85, 87]. Crystallisation is thought to occur by the aggregation and subsequent dehydration of the proto-structures, resulting in precipitation of the corresponding polymorph[80].

### 1.3.5 The Hydrates of Calcium Carbonate

There are two well-established hydrates of $CaCO_3$, which are ikaite ($CaCO_3.6H_2O$)[88] and monohydrocalcite ($CaCO_3.H_2O$)[89]. Monohydrocalcite can be precipitated using additives such as $Mg^{2+}$ in highly supersaturated solutions[90]. Both monohydrocalcite and ikaite have been discovered in marine sediments and sea ice, though ikaite is considered more common[91, 92]. Synthetic studies have shown that ikaite can be formed under high pH and low pressures and temperatures[93 94], or using additives known to suppress calcite such as $Mg^{2+}$ and $PO_4^{2-}$ (which also suppresses aragonite formation)[92, 95].

## 1.4 Investigating the Crystallisation of $CaCO_3$ Using Cryo-TEM and LCTEM

Calcium carbonate has been widely explored as a model crystallisation system and to broaden our understanding of biomineralization, with a large number of such investigations employing advanced transmission electron microscopy (TEM) techniques[96]. Cryogenic TEM (cryo-TEM) has allowed the structure and properties of $CaCO_3$ phases to be examined at high magnifications while avoiding damage induced by the electron beam, in addition to facilitating time-resolved studies[97, 98]. By allowing samples to tolerate repeated imaging, cryogenic electron tomography (cryo-

ET) can also be conducted to determine the spatial relationship between particles and gain additional information on their 3D structure[99]. Liquid cell TEM (LCTEM), also known as liquid phase TEM (LPTEM) allows us to monitor reactions in-situ, unlocking a wealth of information on the dynamics of a reaction or process[100, 101]. Furthermore, a combined approach harnessing several of these TEM techniques has been illustrated as a powerful strategy in elucidating the reaction pathways involved in crystallisation[102, 103]. In this section, the use of cryo-TEM and LCTEM for the study of $CaCO_3$ formation will be summarised.

The earliest reported cryo-TEM study of $CaCO_3$ crystallisation was performed by Rieger *et al.*, who used the technique to probe the role of polymeric additives in scale inhibition[104]. This was built upon in later work[105], where the authors identified a spinodal phase separation prior to ACC formation. Further insight into the reaction mechanism was gained by Pouget *et al*., who studied the early stages of $CaCO_3$ formation on a stearic acid monolayer template using cryo-TEM[79, 106]. At high resolution, they observed ≈ 1 nm prenucleation clusters at the onset of aggregation (Figure 1.16)[79]. Further reaction yielded 30 nm amorphous nanoparticles, consistent with the formation of ACC. Intriguingly, PNCs were still observed following nucleation, which contrasted with previous studies conducted using titration[22]. The monolayer template had a stabilising effect on local ACC particles, which grew to larger sizes than the ACC in solution. At extended reaction times of 10 – 20 min, vaterite crystals were observed, whilst a template-free control yielded both vaterite and calcite. These observations allowed the authors to deduce the reaction pathway for template-directed $CaCO_3$ crystallisation shown in Figure 1.16, deepening our understanding of the template-controlled precipitation strategies exhibited in biomineralization.

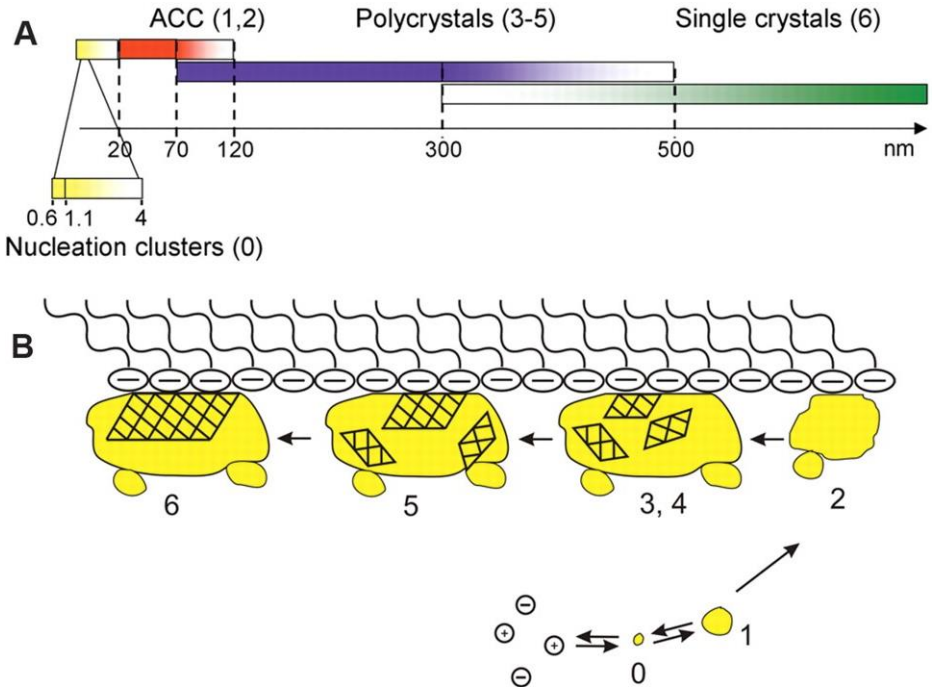


**Figure 1.16 Template-directed crystallisation of calcium carbonate, (A) the particle sizes of the products formed at each stage, (B) the proposed stages involved, which are (0) the formation of PNCs, (1) the formation of ACC by aggregation of PNC clusters, (2) clustering and growth of ACC, (3,4) initial formation of poorly crystalline particles, (5) template-stabilised growth of a crystallisation domain, and (6) the formation of a single crystal. Reproduced from ref.[79]**

Cryo-TEM has made it easier to examine beam-sensitive phases at high magnifications[99], and has therefore facilitated a number of in-depth studies involving ACC[75, 107]. Nudelman *et al*. investigated the effect of poly(α,β)-DL-aspartic acid (pAsp) on ACC stability and found that ACC particles with sizes under 100 nm could be stabilised[107]. They deduced that the coating of pAsp on ACC particles inhibited their growth, thus allowing them to remain stable for longer periods. Additionally, it was possible to identify PNCs in the vitrified solution using electron diffraction, due to the shift in their diffraction peaks relative to water. The interaction of ACC with pAsp was further studied by Xu *et al.* using cryo-TEM and cryo-ET to reveal new insights behind the polymer-induced liquid precursor (PILP)[75]. The authors examined the formation of PILP using pAsp, double-stranded DNA, and poly(allylamine) (pAH), and found that it consisted of polymer-ACC nanoparticles which contained ≈ 2 nm clusters of ACC. These clusters were formed via interaction of $CO_3^{2-}$ ions with $Ca^{2+}$

ions from solution that have bound to the polymeric chains, resulting in the precipitation of ACC within the matrix. Cryo-ET revealed the structure of the polymer-ACC nanoparticles to be highly granular spheres with rough surfaces, accounting for the granular morphology of $CaCO_3$ thin-films induced by PILP, as seen using SEM.

Cryo-TEM has also been used to study the transformation pathway of ACC into anhydrous crystalline forms[56, 108]. The role of ACC in the formation of hexagonal vaterite particles using ammonium ($NH_4^+$) ions was established by Pouget *et al.*[56]. By combining cryo-TEM and cryo-ET imaging techniques, they determined that ACC undergoes a solid-state transformation to form polycrystalline vaterite, where $NH_4^+$ ions stabilise the (00-1) face. This inhibits growth at this face and induces the formation of hexagonal single crystals of vaterite. A solid-state transformation of ACC into aragonite has also been observed by Walker *et al*. in the presence of ethanol[108]. Initial formation of ACC occurred to yield interconnected networks in solution, which aggregated to form larger ACC particles of ≈ 300 nm. These formed linear arrangements and subsequently precipitated needle-like aragonite crystals through a solid-state transformation, rather than dissolution-precipitation.

The advent of LCTEM has allowed the mechanism underlying $CaCO_3$ crystallisation to be studied dynamically, and for further information on the earliest stages of reaction to be revealed. A LC with mixing capabilities was first used to investigate $CaCO_3$ formation by Nielsen *et al*.,[78] who performed a range of experiments directly mixing aqueous $CaCl_2$ and $NaHCO_3$ solutions in-situ, employing different solution concentrations and flow rates. Electron diffraction was used to confirm the identities of the products, though this was only possible when the liquid layer had thinned during an experiment and the scattering from solution was minimal. During the in-situ reactions, both direct and multistep pathways were observed. Although the direct pathway yielded ACC and all three of the anhydrous crystalline phases, the multistep pathway began with ACC and only transformed into aragonite or vaterite, with calcite never being observed. This study also highlighted different dissolution behaviours of ACC particles following continuous exposure to the beam. One dissolution mechanism involved shrinkage of the ACC particle until it was no longer visible, whereas another mechanism involved saw the ACC particles become solid-like, roughening and forming pits on the surface before eventually disappearing.

It should also be noted that confinement effects can influence LCTEM studies due to the small dimensions of the liquid cell[109] (illustrated in Figure 1.17), which may result in reduced reaction kinetics[102], altered polymorph selectivity and other changes to the crystal properties[110]. The effect of the confined environment provided by the liquid cell on $CaCO_3$ crystallisation has been deduced by Kröger and Verch[109], who used simulations to show that the ion transport was restricted. They deduced that this lowers the concentration of available ions, which in turn reduces the stability of $CaCO_3$ phases.

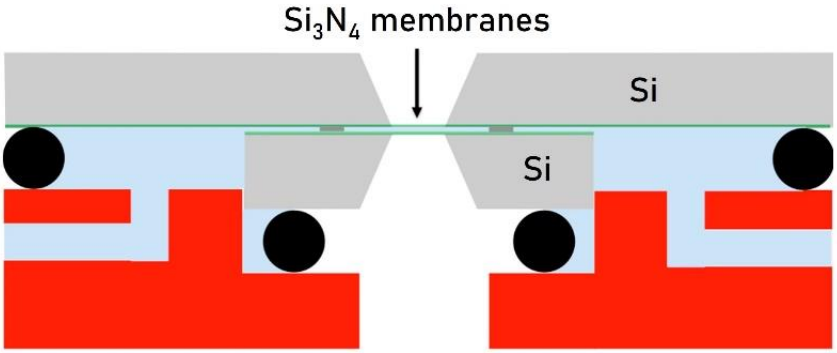


**Figure 1.17 Schematic of a liquid cell TEM holder, showing the O-rings used to seal the cell in black, and the spacers in dark grey (typically 100 – 500 nm in depth depending on model) between the green silicon nitride chips. Adapted from ref.[109]**

LCTEM can also be used to explore the role of additives on $CaCO_3$ formation. The effect of polystyrene sulfonate (PSS) on $CaCO_3$ crystallisation was investigated by Smeets *et al.* using LCTEM in order to understand how a charged polymer matrix may influence biomineralization[111]. Upon mixing of PSS and $CaCl_2$ solutions in the LC, globular hydrated Ca-PSS complexes were formed. Diffusing $(NH_4)_2CO_3$ vapour through the cell led to the nucleation of ACC in or on the Ca-PSS globules, but not in solution (though vaterite eventually precipitated in solution after 2 hours of sustained diffusion). These findings were attributed to the generation of a high local supersaturation, caused by the complexation of $Ca^{2+}$ ions with $SO_3^-$ groups on the immobilised PSS matrix.

Further insight into biomineralization has been gained using LCTEM by investigating the effect of $Mg^{2+}$, sodium citrate, and sodium poly-acrylate (PAA) on $CaCO_3$ crystallisation[112], which are thought to regulate the transformation of transient ACC

during biomineralisation[113, 114]. The authors found that in the presence of sodium citrate and PAA, ACC transformed into anhydrous polymorphs via a dissolution-reprecipitation process. However, the transformation pathway of ACC in the presence of $Mg^{2+}$ varied with [$Mg^{2+}$], where low [$Mg^{2+}$] (≤ 2.5 mM) resulted in a direct transformation and larger [$Mg^{2+}$] led to a dissolution-reprecipitation pathway being followed. Calcite precipitated by the direct transformation route was found to preserve the shape of the ACC precursor, imparting further insight into how morphology is controlled in biomineralization.

It is challenging to ensure that the earliest stages of a reaction are captured during LCTEM, as the flow inlet is located away from the viewing window. A novel liquid cell design was reported by Kelly *et al.*,[115] who created a 2D heterostructure mixing cell with two liquid pockets that are isolated by a thin layer of $MoS_2$ that can be pierced by prolonged electron beam exposure (Figure 1.18). The authors used this method to initiate mixing of aqueous $CaCl_2$ and $Na_2CO_3$ solutions directly at the viewing window, and observed the rapid formation of irregularly shaped, dense globules. It was deduced that these were products of spinodal decomposition, with further imaging showing dehydration and shrinkage of the globules to form smaller particles, indicating that the spinodal mixture was equilibrating towards a binodal composition. From these smaller particles, the authors observed the formation of smooth ACC particles with greater densities than the aforementioned precursors. In a beam-blanked experiment, the authors also reported the formation of calcite from the dense globules, revealing an indirect pathway not previously seen in LCTEM studies of the $CaCO_3$ system.

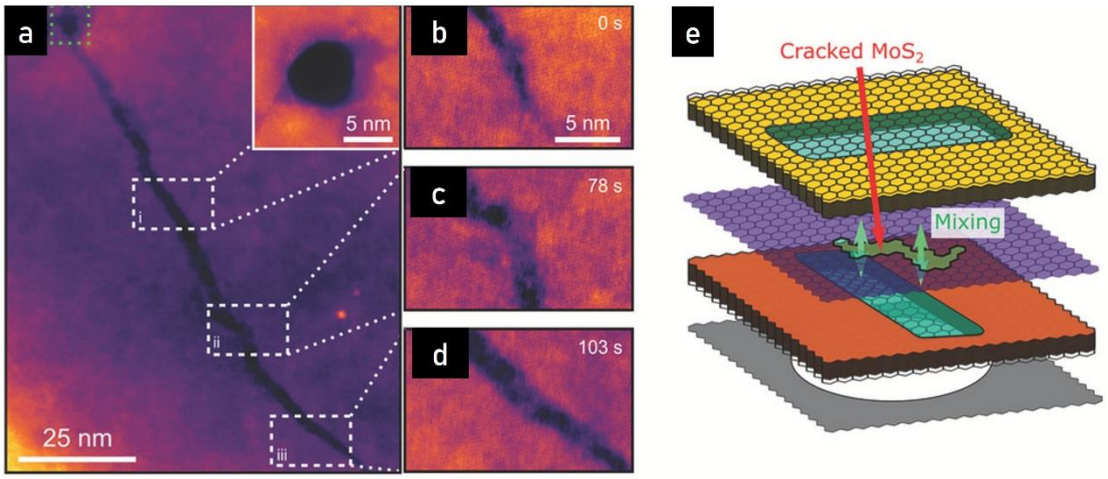


**Figure 1.18 The 2D heterostructure-based liquid cell, (a) the beam induced pore, (b – d) time series images of the formation of a crack from the pore, (e) schematic of the cell after mixing. Adapted from ref.[115]**

Very recent studies of $CaCO_3$ crystallisation using LCTEM have further evidenced a multistep pathway that begins with the formation of a dense liquid phase. In a study by Ramnarain *et al.*, the effect of aspartic acid (Asp) on the early stages of $CaCO_3$ formation was investigated using LCTEM and correlated with hyperpolarised solid-state NMR analysis[116]. In the absence of Asp, they found that nucleation occurred via a phase separation mechanism. The authors observed the formation and subsequent disappearance of droplets of a dense liquid phase. They determined that this was caused by dehydration of the droplets, resulting in the precipitation of ACC. However, in the presence of Asp a different pathway was observed, starting with the formation of PNCs. The aggregation of PNCs resulted in larger clusters that showed surprising stability and high conformational flexibility, which led the authors to deduce that they were DOLLOP-like in behaviour. This refers to simulation-based work by Demichelis *et al.* that proposed that PNCs consist of ionic polymer species[83], the so-called ordered liquid-like oxyanion polymer (DOLLOP), which have highly dynamic structures that readily undergo structural rearrangement. Using hyperpolarised solid-state NMR, Ramnarain *et al.* showed that these effects were caused by the complexation of Asp with $Ca^{2+}$ and $CO_3^{2-}$ ions, which stabilises the PNCs[116].

A LCTEM study by De Yoreo *et al*. also indicates that the early stages of $CaCO_3$ formation occurs via a dense liquid phase (currently available as a preprint)[117]. The

authors used in-situ liquid-state NMR techniques and IR spectroscopy to identify the species formed upon mixture of aqueous $CaCl_2$ and $NaHCO_3$ solutions in the presence of PAA or *de novo-designed* helical repeat (DHR) proteins. They observed the formation of dense liquid droplets, where certain solution concentrations resulted in an interconnected network. This dense liquid phase was found to undergo a solidification process to produce ACC by two different pathways. In the first pathway, hollow particles are produced with a thick shell, whereas the second pathway formed ACC by densifying from the centre of the dense liquid droplet outwardly. This occurred for both the additive and additive-free solutions, where the additives had a stabilising effect on the dense liquid phase.

In summary, LCTEM has provided an ideal platform for conducting the numerous investigations of $CaCO_3$ discussed in this section, which have led to substantial developments in our understanding of the mechanisms involved in biomineralization.

### 1.4.1 An Overview of the Themes Explored in the Thesis

The work described in this thesis broadly explores crystallisation as a tool for preparing functional crystals suitable for a range of applications. It also investigates the mechanism behind an important industrial crystallisation reaction using advanced electron microscopy techniques. Chapter 2 provides a description of the analytical and microscopy techniques used in the thesis. The work described in Chapter 3 centres around the use of additives in calcite crystallisation to form porous crystals capable of exhibiting structural colour. Therefore, Chapter 3 begins with an introduction to additive-controlled crystallisation, synthesis routes for porous calcium carbonate, and structural colour. In Chapter 4, the mechanism behind the carbonation of calcium hydroxide for producing precipitated calcium carbonate (PCC) is investigated using conventional, cryo-, and liquid cell TEM. The introduction to this chapter reviews the industrial synthesis of PCC, the current understanding of the carbonation reaction mechanism, and the methods used to control PCC properties during synthesis. In Chapter 5, a range of porous manganese oxides were synthesised from precipitated manganese carbonate precursors as photocatalysts for the water splitting reaction. The chapter begins by reviewing photocatalytic water splitting and introduces the manganese carbonate system and its thermal

decomposition into manganese oxides. Finally, Chapter 6 concludes the thesis by drawing together the key findings and provides some original ideas for future study.

# Chapter 2 | Characterisation and Analytical Techniques

## 2.1 General Methods

### 2.1.1 Cleaning Techniques

All labware was thoroughly cleaned prior to use to eliminate impurities and cross-contamination of experiments. Glassware was immersed in a base bath (1 M KOH in iPA), rinsed with water, then immersed within an acid bath (1 M HCl). Final rinsing was performed with deionised Milli-Q water before drying in an oven at 60 °C. Aqua regia was used to remove metallic impurities, which was typically required following water splitting experiments using heavy metal catalysts in Chapter 5. This was prepared using a mixture of HCl and $HNO_3$ in a 70:30 ratio, which was left for several hours for reaction to cease before removing the mixture and rinsing thoroughly with DI water.

Glass slides used as crystallisation substrates were prepared by cutting microscopy slides and cleaned using piranha solution. Piranha solution was prepared using a mixture of $H_2SO_4$ and $H_2O_2$ in a 75:25 ratio, and upon completion of the reaction, the slides were rinsed repeatedly with DI Milli-Q water and stored in DI Milli-Q water until required.

## 2.2 Microscopy Techniques

### 2.2.1 Optical Microscopy (OM)

Optical or light microscopy has been used throughout this thesis as a rapid way of observing crystals. The sample is illuminated by a lamp and is made into an image by a system of lenses and apertures. A condenser lens and aperture are positioned close to the light source, and are used to focus and control the amount of light that reaches the sample. Positioned above the sample is an objective lens and aperture. A range of objectives with different focal lengths can be used which give the user a choice of magnifications while viewing. The image produced by the objective is inverted, and so furthest from the sample is the projector lens, which adjusts the image and projects it to the viewing piece or camera.

This setup generally describes a microscope configured for illumination and viewing in transmission mode, which is best for observing thin translucent samples. For

larger samples whose surface is being examined, reflectance mode may be more appropriate. In this setup, a lamp is typically positioned above and to the side of the sample, using a beam-splitter to aim the light at the sample. The light reflected from the sample is received by the objective and passed through to the viewing binoculars or camera.

In this work, a Nikon Eclipse LV100 was typically used, in both reflectance and transmission mode.

### 2.2.2 Scanning Electron Microscopy (SEM)

The scanning electron microscope (SEM) is used to examine samples at higher magnifications, with a spatial resolution approaching 1 nm for high-performance microscopes[118]. Instead of light, electrons are used to illuminate a specimen. Although this allows the resolution limit to be reduced, electrons are highly scattered in gases, so the microscope must be kept under vacuum with a pressure of at least $10^{-10}$ Pa to ensure the electrons reach the sample. A beam of electrons is produced by a thermo-ionic gun or more commonly, a field emission gun (FEG). A FEG operates by applying a voltage to a sharp tip, producing a strong electric field that causes the emission of electrons. Like the light microscope, a series of lenses are used to focus the beam (Figure 2.1), but in this case the lenses are electromagnetic coils which can be easily manipulated using the microscope computer. The beam position is also controlled and will scan across a sample, producing signals from electron interactions which are collected using detectors.

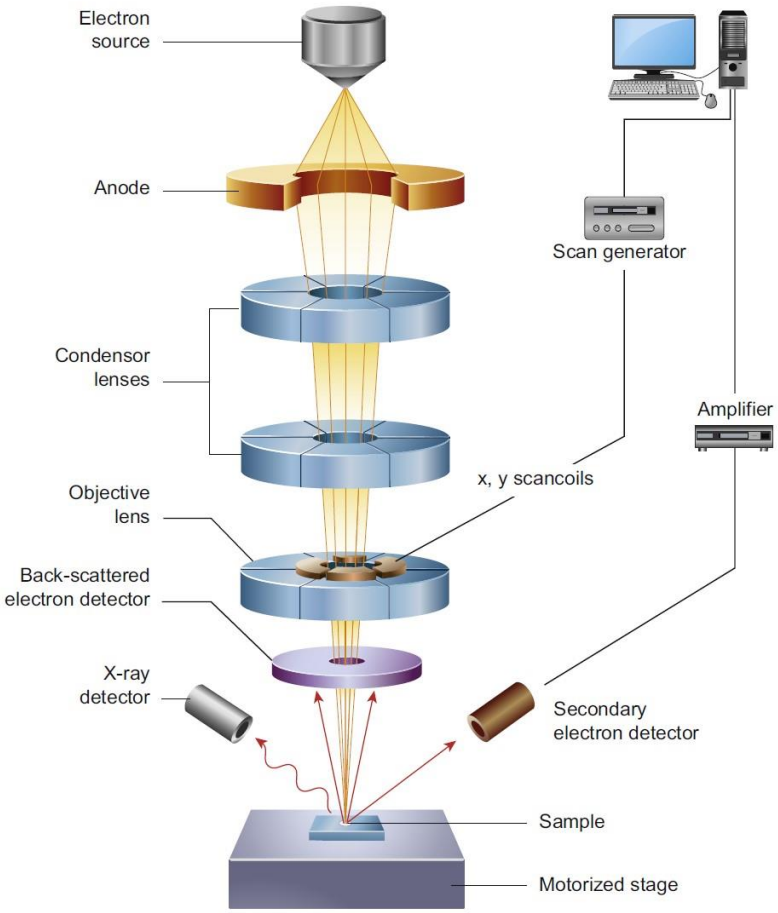


**Figure 2.1 The components of a SEM microscope. Reproduced from ref.[119]**

Electrons can interact with a sample in various ways, and by selectively detecting different interactions it is possible to examine different parts of a sample. The bulk of the interactions originate from electrons that have been inelastically scattered from the surface and top layer of the sample, and typically have low energies < 50 eV [118]. By imaging with a secondary electron detector, topological features are more defined, and the surface of the sample can be observed in detail. Backscattered electrons can also be detected. These are primary electrons (part of the incident beam) that have interacted with a partial volume of the sample before leaving it, and so they still possess a high energy. These interactions are not as prevalent as secondary electron interactions, and so the signals produced are not as strong, but it is more sensitive to compositional changes within the material. Imaging with a backscattered electron detector can be useful for studying samples containing multiple elements and crystallographic orientations.

X-rays are also emitted by the sample following interaction with the electron beam. This allows the use of a qualitative technique called energy dispersive analysis of X-rays (EDAX or EDX), which detects the emitted X-rays and their energies. This reveals the elements present, which can be interpreted to give the overall composition of the mixture of elements present or overlayed with SEM images to form an elemental map.

Due to the vacuum conditions required when operating the microscope, samples must be dry and well-fastened to the sample stub. Samples can also be coated with a thin conductive layer to improve the interaction of electrons with the sample, as non-conductive samples can suffer “charging” effects that affect image quality. Iridium and platinum are widely used as coatings for this purpose, which can be applied to a desired thickness using a sputter coater.

In this work, SEM samples were coated with iridium to a thickness typically 2 – 4 nm, using a Cressington 208HR High Resolution Sputter Coater. Samples were typically prepared on glass substrates, which were affixed to the stub using carbon paint or tabs. SEM images were taken using an FEI Nova NanoSEM 450 fitted with a FEG.

### 2.2.3 Focused-Ion Beam Scanning Electron Microscopy (FIB-SEM)

A dual-beam FIB-SEM allows for simultaneous modification and imaging of a sample. The SEM microscope is fitted with an ion beam which is produced by applying a voltage to a sharp gallium tip. Interaction of the ions with the sample produces secondary electrons and so images can be formed by collecting these signals as in SEM. By applying a stronger probe current, the ions possess enough energy to disrupt a sample by knocking out atoms[118]. As the beam can be precisely controlled, specific areas can be selectively milled to modify a sample as required. This process can be used to ablate entire regions of a sample, precisely etch upon a surface, or perform fine polishing steps. To prevent milling of regions outside of the selected area, a protective coating can be applied using the gas injection system. Organometallic gas is flowed through a needle positioned close to the sample, which will be deposited where the ion beam is directed. Commonly used GIS needles deposit metals such as platinum, tungsten and carbon, in addition to specific chemical mixes that can be used while etching semiconductors. These coatings can be used to protect a sample from excess beam damage and uneven ablation of

material, which can lead to defects known as curtaining. This is caused from the non-uniform redeposition of ablated particles, resembling irregular pillars or curtains that can hinder image analysis or result in uneven thickness across a lamella.

Another component of the FIB-SEM is the micromanipulator. This is essential when using FIB to construct thin lamella as TEM samples; after using milling and polishing processes to create the lamellae, the micromanipulator is used in conjunction with the GIS needles to remove it from the bulk sample and attach it to a sample “chip”.

An FEI Helios G4 CX DualBeam was used in this work to prepare cross-sections of crystals. FIB-SEM samples were attached to SEM stubs using carbon paint applied underneath the glass sample substrates, with edges and corners also coated to improve conductivity and ensure it was well fastened. Samples for FIB-SEM were coated with 20 nm of iridium using an Agar Scientific High Resolution Sputter Coater. Specific details regarding the probe currents and protocol used to obtain FIB-SEM cross-sections are provided in Chapter 3.

### 2.2.4 Transmission Electron Microscopy (TEM)

A TEM is used to examine the internal structure of a sample, and has many of the same components as an SEM (Figure 2.2). A FEG is used as the electron source, although the voltage applied to the tip is generally 10 times larger than for SEM. The beam is focused by 2 condenser lenses, referred to as the C1 and C2 lenses, and a C2 aperture. The sample is placed onto a holder which positions the specimen into the optical axis within the pole pieces of the objective lens. This is the strongest and most important lens, which produces the first image [120]. Rays that pass through the sample form a diffraction pattern in the back focal plane, before forming an inverted image in the image plane. Depending on whether an imaging or diffraction mode is selected by the user, the intermediate lenses focus on either the image or the back focal plane, respectively. Additionally, apertures can be inserted to improve the image or pattern produced. The objective aperture can be inserted into the back focal plane to remove the contributions of electrons that have been scattered by large angles, which improves the contrast in the image. Alternatively, a selected-area electron diffraction (SAED) aperture can be inserted into the image plane. This is essential for viewing diffraction patterns, as the intensity of the diffraction pattern for a large area will damage the viewing screen or camera. The SAED aperture provides

an easy way to limit the number of electrons passing through, and hence reduces the chance of damaging the camera or screen.

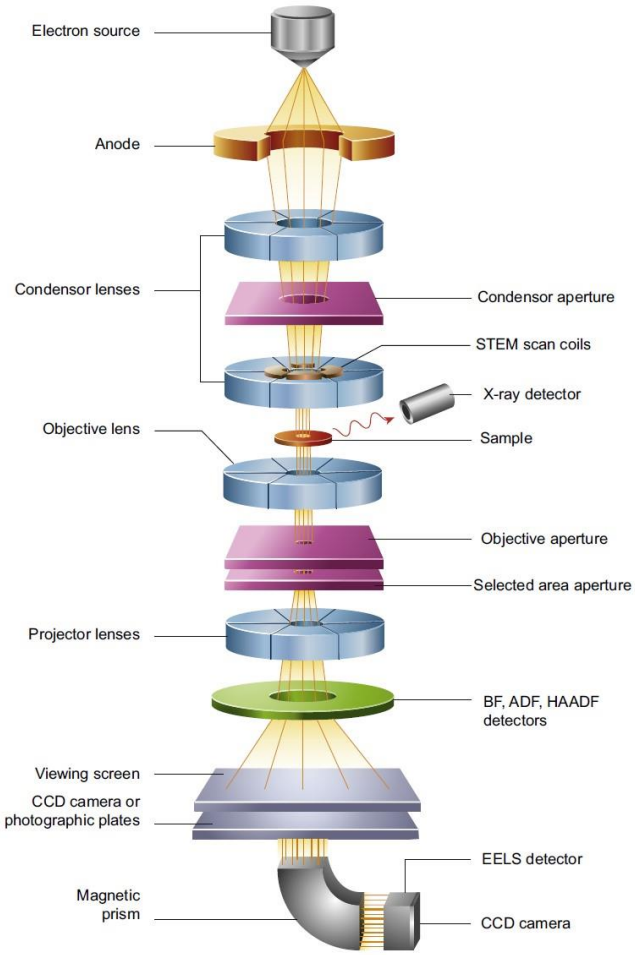


**Figure 2.2 The components of a TEM microscope. Reproduced from ref.[119]**

The projected image is viewed on a fluorescent screen visible through a window at the bottom of the microscope. A camera is positioned below the screen, which is typically a CCD (charge-coupled device) camera. High-performance microscopes may also contain an energy filter, which will remove the contribution of inelastically scattered electrons. This is essential for imaging in high resolution, but can also be used for quantitative microscopy, e.g. to perform electron energy loss spectroscopy (EELS). EDX (mentioned above in Section 2.2.2) can also be used in conjunction with TEM.

TEM samples are prepared on grids that are usually made of a conductive metal such as copper or gold. The grid is placed on a specimen holder which fits into the

objective lens pole pieces. Depending on the analysis required, different holders can be used, which allow the user to tilt the sample, or heat and cool in situ.

For the majority of the work in this thesis, an FEI Tecnai TF20 was used, which is a FEG TEM operating at 200 kV. It is fitted with a Gatan Orius SC600A CCD camera and an Oxford Instruments INCA 350 EDX system with 80 mm X-Max SDD detector. For some of the work in Chapter 4, a Titan$^3$ Themis 300 was used (typically where TEM work was performed on the dry liquid cell and in the additive study). This is an X-FEG S/TEM microscope which operates at 300 kV and is fitted with a Gatan OneView CCD, HAADF/ADF/BF STEM detectors and also an FEI Super-X EDX system. TEM samples were prepared on Quantifoil grids (either Cu or Au) with R 2/2 film size and mesh size 200.

### 2.2.5 Cryogenic Transmission Electron Microscopy (Cryo-TEM)

In standard TEM, the specimen must be dry as the sample is placed directly within the vacuum of the microscope. This is a problem if the user wishes to examine wet or aqueous samples, as structural changes often occur during dehydration. Cryo-TEM was developed to solve this problem, allowing many biological and liquid-based samples to be analysed using TEM by freezing the sample in a hydrated state.

Sample preparation is crucial for attaining high quality images using cryo-TEM. In light of this, recent developments in this area have transformed the ability to study biological specimens. The 2017 Nobel prize in Chemistry was jointly awarded to Dubochet, Frank and Henderson for their developments in cryo-TEM[121], where Dubochet's research was focused on sample preparation techniques[122].

Freezing a sample involves careful consideration of the different polymorphs of ice. Crystalline ice will produce a diffraction pattern, which will interfere with the diffraction pattern of the sample. Therefore, vitreous ice is required and is made by rapid freezing of water. This is typically achieved using commercial or homemade plunge freezing devices (Figure 2.3). The TEM grid is held using a pair of tweezers that connect to a moving arm. This arm is moved up into a chamber with controlled temperature and humidity, allowing the sample to be pipetted onto the grid through a side door. This is blotted between filter papers for a set time using a set amount of force, before the grid is plunged downwards into a bucket of liquid ethane, which is kept cold by liquid nitrogen. Liquid ethane is used for vitrification as it has a higher

boiling point than liquid nitrogen. This avoids an insulating layer of gas being produced upon plunging, which delays the freezing process and can affect sample quality. The sample must then be kept cold by storing under liquid nitrogen, as any change in temperature will introduce cubic ice contamination and may even destroy or thaw the sample.

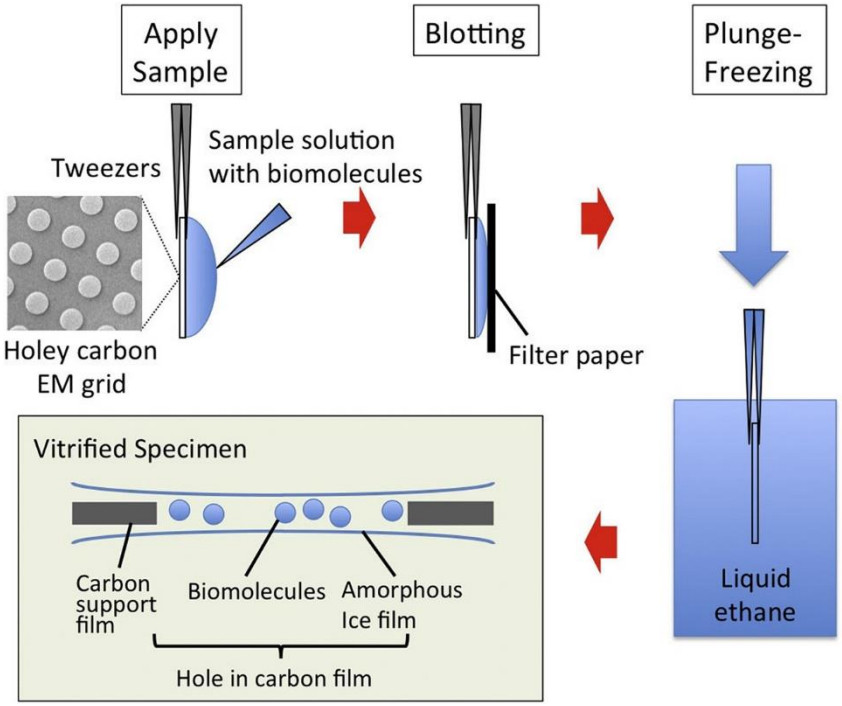


**Figure 2.3 Overview of the plunge-freezing process used to prepare grids for cryo-TEM. Reproduced from ref.[123]**

For cryo-TEM, a commonly used TEM grid style is the Quantifoil grid, which has a set mesh size, coated with a holey thin carbon film. Alternatively, a lacey carbon film can be used where the size of the sample varies or is unknown, as the holes have a wide distribution of sizes.

In this work, a Thermo Fisher Titan Krios G2 with X-FEG and autoloader was used. This was operated at 300 kV and fitted with a Thermo Fisher Falcon 4 direct electron detector and a TFS Ceta (used for diffraction). All cryo-TEM samples were prepared on Au Quantifoil grids with R 2/2 film size and mesh size 200, and vitrified using an FEI Vitrobot Mk. IV, using a blot time of 6 s and blot force of 6.

### 2.2.6 Liquid Cell Transmission Electron Microscopy (LCTEM)

To visualise dynamic processes, it is important to examine samples in solution. This can be done by using LCTEM, which uses a specialised specimen holder to contain liquid samples in a fully closed cell or flow cell (Figure 2.4). A standard cell design consists of two silicon chip "walls" with transparent windows, with a spacer placed between the chips to form the cell [100]. It can be sealed with adhesive or using O-rings depending on whether a closed or flow cell is desired. Samples are loaded into the cell during assembly, which will then be tested for leaks under vacuum. This will identify if there is a break or any misaligning parts before the cell holder is put into the TEM.

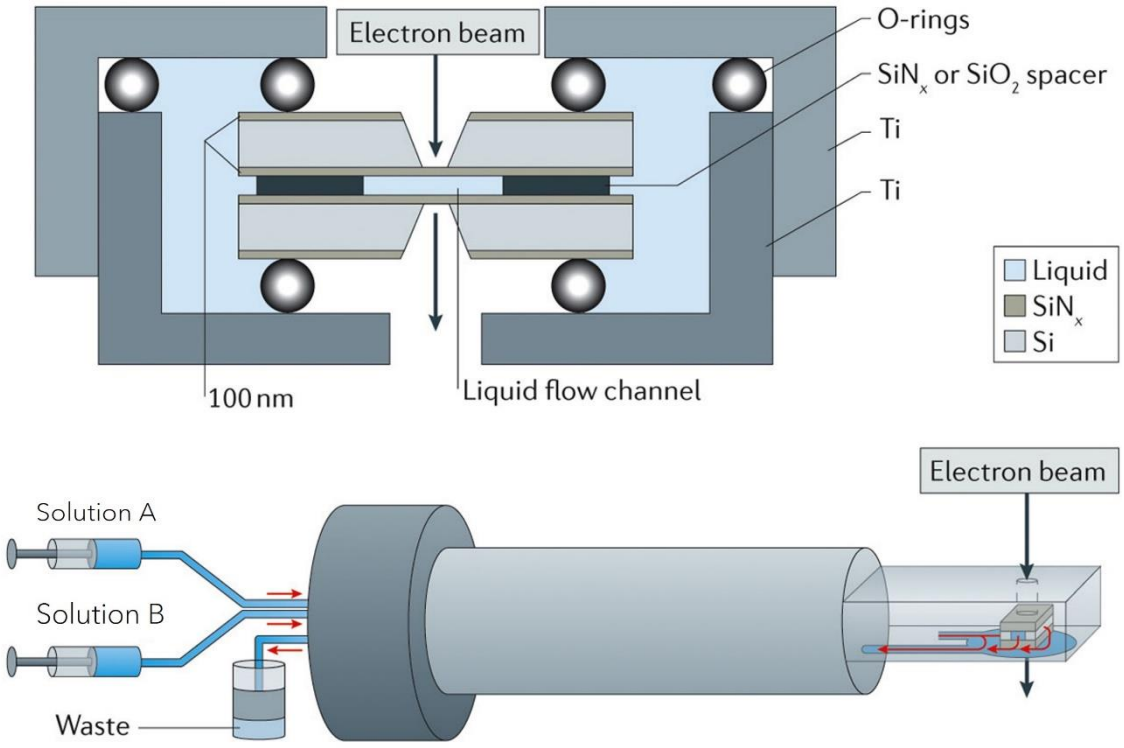


**Figure 2.4 A liquid-cell TEM holder with flow setup. Adapted from ref.[98]**

Several considerations must be made when using the TEM to examine a liquid sample. Exposure of water-based samples to the electron beam can cause radiolysis which may result in a rise in pH, changing the sample environment[124]. Additionally, the liquid layer scatters the beam to some extent and so the resolution is not as high as achievable in dry or cryo-TEM. Imaging of the LC is usually conducted in STEM mode, which offers the best resolution for liquid samples[125].

In this work, a Titan FEI Titan$^3$ Themis 300 was used in both STEM and TEM modes (for full microscope specification see Section 2.2.4 above). A Hummingbird Scientific LCTEM holder with dual-flow capabilities was used, which was fitted with SiN chips with windows (also SiN) that are 200 x 50 µm in size and 50 nm thick. The spacers between the chips were 250 nm. Plasma cleaning of the chips was conducted under $Ar/O_2$ using a Henniker Plasma HPT-100 for 60 s to initially clean them and then 20 s after loading the sample to help it adhere onto the chip. Leak-checking was performed using a Hummingbird Scientific Pfeiffer Vacuum DCU, where a pressure of $10^{-6}$ mbar had to be achieved to pass. After installing the LC holder into the TEM, the tubing was connected to a syringe pump in order to perform in-situ experiments.

## 2.3 Analytical Techniques

### 2.3.1 Raman Spectroscopy

Raman spectroscopy allows molecules to be identified by the distinct way they interact with light. When photons collide with a molecule, there are several ways they can scatter depending on whether this occurs elastically or inelastically. Rayleigh scattering describes the elastic scattering of light, where the molecule is excited to a higher state before relaxing to the original state[126]. Inelastic scattering occurs when a molecule reaches a final energy state that was higher or lower than the original energy state. This can be further classified into Stokes and anti-Stokes scattering. Stokes scattering occurs when the emitted photon has less energy than the incident photon. When a photon is emitted with more energy, this is described as anti-Stokes scattering. Raman spectroscopy measures Stokes scattering, so for a molecule to be “Raman-active” it must undergo a change in polarizability after interaction with light[127]. The data obtained in Raman can be compared with reference values to characterise the peaks and identify a material.

Early work in this thesis that used Raman for basic confirmation of chemical composition was performed using a Renishaw 2000 Raman microscope with a 785 nm laser. The majority of the Raman data, particularly that presented in Chapter 3, was obtained using a Horiba LabRam HR Evolution Raman instrument with confocal optical microscope, fitted with both 532 and 785 nm lasers. Data was typically collected with the 532 nm laser, using an edge filter and an 1800 grooves/mm grating.

### 2.3.2 Thermogravimetric Analysis (TGA)

Thermogravimetric analysis (TGA) gives information on the compositional changes of a material during heating. The sample is continually weighed during heating under air or an inert atmosphere, generating a thermogravimetric curve graph. From this curve, the step heights can be used to calculate the stoichiometry and reaction conversion, in addition to the moisture content[128]. TGA is particularly useful for investigating thermal decomposition reactions, where the exact temperature that transitions occur at can be identified, as well as exploring the effect of the heating rate during a decomposition reaction. TGA instruments are often coupled with differential scanning calorimetry (DSC) capabilities to give information such as the heat flow, which is useful for identifying phase changes. This technique can also be coupled with mass spectroscopy (TGA-MS), to determine the identity of any gaseous species that are formed during decomposition.

In this work, a TA Instruments SDT Q600 instrument was used and samples were heated in air or under nitrogen.

### 2.3.3 Powder X-ray Diffraction (pXRD)

Powder X-ray diffraction (pXRD) is an important technique in solid state chemistry that is used to identify crystalline materials. By measuring the interaction of X-rays with a crystalline solid, the arrangement of the lattice in space can be determined (Figure 2.5).

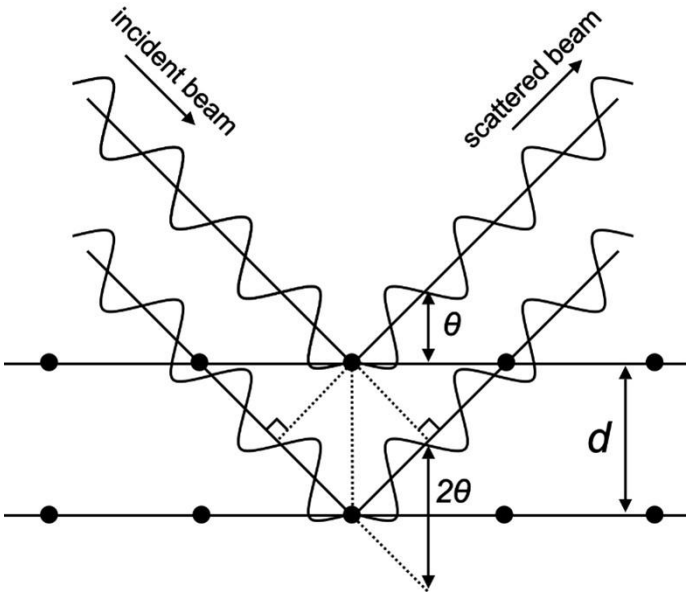


**Figure 2.5 Interaction of X-rays with the crystal lattice, demonstrating Bragg's Law, where *d* represents the atomic spacing between crystal planes and *θ* represents the angle between the atomic plane and the beam.**

This is shown by the relationship outlined by the Bragg equation (Equation 2.1), where *n* represents an integer, *λ* the beam wavelength, *d* the atomic spacing between crystal planes, and *θ* the angle between the atomic plane and the beam.

$$n\lambda = 2dsin\theta \tag{2.1}$$

For Braggs Law to be satisfied, *n* must be an integer. This reflects the fact that for the scattered X-rays to be detected, they must undergo constructive interference during interaction with the lattice to ensure the waves are in-phase. This can only occur when the path lengths between X-rays scattered by adjacent planes differ in value by an integer[129]. In powder X-ray diffraction, many differently oriented crystals are exposed to the X-rays, and reflections are obtained from a range of different planes, allowing a characteristic pattern to be obtained. This can be indexed by comparing the pattern to reference patterns. Although pXRD is mainly used to identify crystalline materials, it can also be used to establish purity or to determine crystallite size[130].

In this work, powder XRD measurements were obtained using a Bruker D2 Phaser, fitted with a copper K-α anode (*λ* = 1.5406 Å) and a LynxEye detector operating in Bragg-Brentano reflection geometry. The range of 2θ values collected was varied

depending on the material being measured (generally between 5 – 80°), while the step size was generally fixed at 0.02°.

# Chapter 3 | Porous Calcium Carbonate Crystals for Structural Colour

## 3.1 Introduction

### 3.1.1 Aims and Overview

The development of porous crystalline materials is of significant interest due to their potential for diverse applications such as water treatment, energy storage, and drug delivery. An exciting, new potential application of porous crystals is their use as highly scattering materials that exhibit structural colour, whereby colouration is achieved by the interaction of light with micro- or nano-scale features. However, the synthesis of porous crystals often requires complex templating strategies. The aim of the work outlined in this chapter was to develop a facile method for creating porous single crystals of calcite by the occlusion of organic additives and their subsequent removal via thermal decomposition. It was also important to identify and optimise the influential parameters behind these processes, such as additive concentration and heating temperature, to highlight how the porosity could be controlled. The final goal of study was to demonstrate that the generation of porosity greatly increased the light scattering ability of the crystals, exhibiting structural colouration to appear bright white. This has exciting implications for calcite applications such as paper and paint, which typically require additional pigments to achieve a desired finish, where porous calcite may provide a cheap, non-toxic alternative.

In order to meet these objectives, single crystals of calcite were occluded with a range of organic additives including aspartic acid (Asp), glycine (Gly), polystyrene microspheres (PS) and PMAA-PBzMA vesicles (Ves), and the incorporation efficiency was optimised. The composite crystals were heated to remove the occluded organic material using a variety of temperatures, heating rates and annealing times in order to establish their effect on the porosity. Cross-sections of the porous crystal were prepared using FIB-SEM and the porosity was quantified in terms of both pore size distribution and filling fraction using image analysis techniques. Finally the reflectance of the porous crystals was measured using a spectrometer, which showed that intense, broadband reflectance of > 70 % was

observed for Asp-, Gly- and Ves-calcite crystals, making them suitable as structurally coloured pigments.

### 3.1.2 The Effect of Additives on $CaCO_3$ Crystallisation

For many synthetic chemists, crystallisation is a purification tool to be used for the expulsion of impurities from the bulk phase. However, the presence of impurities often has profound effects on the crystallisation process and the properties of the crystals produced. This has led to the purposeful addition of such impurities, repurposed as functional additives, during crystallisation in order to control the polymorph, morphology, size, and both nucleation and growth rates[131]. Additives have therefore become essential in many industrial crystallisation processes where specific crystal properties are crucial for their application[3, 132]. For example, polymorph control is imperative for the crystallisation of active pharmaceutical ingredients (APIs), since different polymorphs may possess drastically different stabilities, solubilities, and bioavailabilities that may alter the overall efficacy of the drug[133, 134].

As more is revealed about biomineralization processes, we see that additives also play a key role in the formation of biominerals with advantageous properties for the host organism[135]. In fact, the process of biomineralization is reliant on soluble macromolecules to direct crystallisation to control morphology and polymorph[135, 136]. These reactions occur within the structural matrix, which consists of insoluble organic molecules that provide a confined crystallisation environment where the composition of the system can be controlled by the organism[137]. The fascinatingly complex hierarchical structures formed during biomineralization serve as strong motivation to mimic Nature's crystallisation strategy synthetically[138]. In order to successfully achieve this, first there must be an understanding of how different additives influence crystallisation.

For centuries it has been known that the presence of additives during crystallisation can induce a change in the crystal *Tracht*[139]. This is brought about by a change in the growth rate of one or more crystal faces compared to their growth rate under normal conditions[140]. Considering only crystals that grow via the spiral growth mechanism (since it is via this mechanism that the expected *Tracht* is obtained), the growth rate of crystal faces are dictated by the step height, separation, and

advancement rate (step velocity). Additives can interfere with these factors by interacting with the crystal surfaces, and may do so selectively if they have varying affinities for different crystal faces. The adsorption of an additive onto a crystal face reduces its surface energy and suppresses the growth rate of the face. As discussed in Chapter 1, the faces that are ultimately exhibited by the crystal are those which grow most slowly, therefore the selective adsorption of additives can be used to control morphology.

On a crystal face, additives may interact with the surface at step or kink sites and there are several established effects this may have upon the crystal, such as step pinning and kink blocking. Step pinning occurs when an adsorbed additive prevents further growth of the step edge, which is the case when the growing step cannot advance (or proceeds more slowly) around an additive that is adsorbed onto the adjacent surface. According to the Cabrera-Vermileya (C.V) model[141], whether growth around the additive can continue depends on whether the spacing between additive ions/molecules exceeds the critical radius of the step curvature[142]. If the additive spacing is smaller, dissolution of the step is favoured. If the additive spacing is greater, then growth may continue. The spacing of the additive is dictated by its concentration, where higher concentrations result in smaller spacings. On the other hand, the critical radius of the step is influenced by supersaturation, where a low supersaturation results in a larger critical radius. Therefore, low supersaturations and high additive concentrations favour step pinning. The range of supersaturations at which growth cannot proceed is known as the “dead zone”. Where the step can advance, this often gives rise to a curved step edge that appears roughened.

As the C.V model relies on rapid thermal fluctuations to continually generate kink sites[141], further explanation has been sought for systems where the solute is poorly soluble (such as calcite)[143, 144], and so has fewer fluctuations and there is a low kink density[145]. This is because the formation of kink sites is rate-limiting in these systems, rather than the attachment of growth units at kink sites, which occurs relatively rapidly[145]. This finding has highlighted the significance of additive interactions at kink sites on crystal growth[146], namely kink blocking. Kink blocking occurs when additives become adsorbed at or temporarily occupy kink sites[147], and can result in total inhibition of growth if both sides of the kink site are blocked, which is more likely to occur at increased additive concentrations[146]. Adsorption of

additives at kink sites can also change the properties of the step edges, such as step height, separation, and step velocity. This gives rise to an effect known as step bunching or pile-up[148], that presents as roughening of the crystal surface. These effects are clearer in crystals with large sizes, which possess a greater number of kink sites, and so kink blocking can be more important[149].

Incorporation of an additive occurs following adsorption at kink sites, step edges or terraces, when growth can advance around the additive causing it to become entrapped in the host crystal[142]. The result is a composite, or hybrid crystal, which may possess elevated properties relative to the individual components, such as increased mechanical strength[150-152] or optical properties[153, 154], and so occlusion has become an exciting strategy for the engineering of novel crystalline composites for diverse applications. Generally, the incorporation efficiency of an additive is increased at increased supersaturation due to the greater density of steps that are formed at higher supersaturations[155]. The occlusion of additives is known to induce strain in the crystal lattice[156], which makes it increasingly soluble. This reduces the effective supersaturation and lowers the step velocity compared to an additive-free system[142].

In addition to adsorption and incorporation, a final, less invasive way in which additives may affect crystallisation is by changing the properties of the liquid phase. This can occur if an additive alters the supersaturation of the system, changing the solubility characteristics of a phase [6], or by complexation of ions in solution[157]. Finally, there is also interest in studying the combined effects of different additives, where two or more additives may have cooperative or antagonistic influences on the growing crystal, or one can act as a chaperone[158, 159].

Focusing now on the role of additives in controlling the crystallisation of calcite, it is first necessary to understand the faces and steps exhibited by pristine calcite. Pure calcite crystals are bound by six {104} faces, with two acute steps (in the $[-441]_-$ and $[48\text{-}1]_-$ directions) and two obtuse steps (in the $[-441]_+$ and $[48\text{-}1]_+$ directions), which have heights of ≈ 3 Å (Figure 3.1). Calcite crystals exhibit glide-plane symmetry along the c-axis, about which the acute and obtuse steps are paired. In an additive-free system, the growth of calcite proceeds via spiral growth from dislocations at supersaturations lower than 0.8, where much higher supersaturations of ≈ 1.5 results in 2D island nucleation[160]. Once calcite crystals reach a size greater than 1 μm,

spiral growth is favoured over 2D island nucleation as the reduced diffusion kinetics result in a reduction of the supersaturation[161].

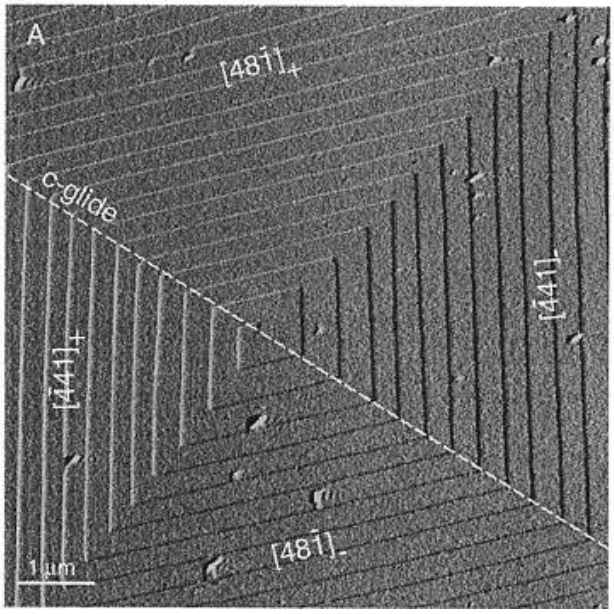


**Figure 3.1 AFM image of a spiral hillock on a calcite (104) face. Reproduced from ref.[160]**

Small inorganic ions such as $Mg^{2+}$, $Sr^{2+}$, $Li^{+}$ have been shown to interact with growing calcite crystals, where they are of special interest due to their presence in natural $CaCO_3$ deposits and biominerals[50, 162]. Crystallisation of calcite in the presence of $Mg^{2+}$ ions leads to incorporation of the ions[163], increasing the width of terraces and reducing the step density[164]. The occlusion of $Mg^{2+}$ increases the solubility of calcite and as a result inhibits the growth of calcite faces[165]. At low [$Mg^{2+}$], where growth is not inhibited, roughening of the acute crystal step edges is observed due to the preferential binding of $Mg^{2+}$ at these sites[166], and elongation of the *c*-axis leads to a significant change in the calcite morphology[167]. Conversely, $Sr^{2+}$ ions bind preferentially to the obtuse step edges and can also increase the growth rate of calcite at low concentrations[168]. Calcite crystals with tabular morphologies are precipitated in the presence of $Li^{+}$ ions, due to the stabilisation of the {001} faces[169]. AFM studies have shown that $Li^{+}$ ions adsorb onto the obtuse steps, causing them to curve and resulting in a fan-shaped hillock[170]. The $Li^{+}$ ions also reduce the step density along the acute directions ([-441]- and [48-1]-, by decreasing the free energy of these steps and subsequently increasing the terrace widths[170].

It has been demonstrated that a broad range of organic additives can be incorporated within single crystals of calcite[149, 171], including polymers[172, 173], single organic molecules[174], dyes[175-177] and gels[178, 179]. The incorporation of organic soluble additives such as amino acids within calcite has been extensively studied to gain insight into biomineralization[174, 180-182]. One of the most well-explored amino acids, that is utilised in this chapter, is aspartic acid (Asp). Mollusc shells are composed of biogenic calcium carbonate containing acidic macromolecules that are rich in Asp within their organic matrix[183], where the negatively charged Asp domains have been shown to be crucial for interacting with calcium ions[184]. The effect of aspartic acid (Asp), a chiral amino acid, as an additive in synthetic calcite crystallisation has been investigated in detail by Orme *et al.* using atomic force microscopy (AFM)[185] (Figure 3.2). The authors showed that Asp binds to the acute <44-1> and <44-8> steps preferentially, which appear roughened at high concentrations of Asp and form the curved edge of the cap facets. Asp can interact with calcite steps by direct bonding of the carboxyl groups with $Ca^{2+}$ ions and hydrogen bonding between the protonated amino group and the carbonate sites[186]. As Asp does not interact with the obtuse steps, these remain straight in the cap facets, exhibited at the apex of the crystal. Molecular dynamics simulations have suggested that disordered water at the acute steps may stabilise Asp by interacting with the carboxyl groups[187]. Depending on whether the D- or L-enantiomer of Asp is present, binding occurs at the (01-4) or (-1-14) step edges respectively to maximise the stereochemical fit and allow coordination of both carboxyl groups[188].

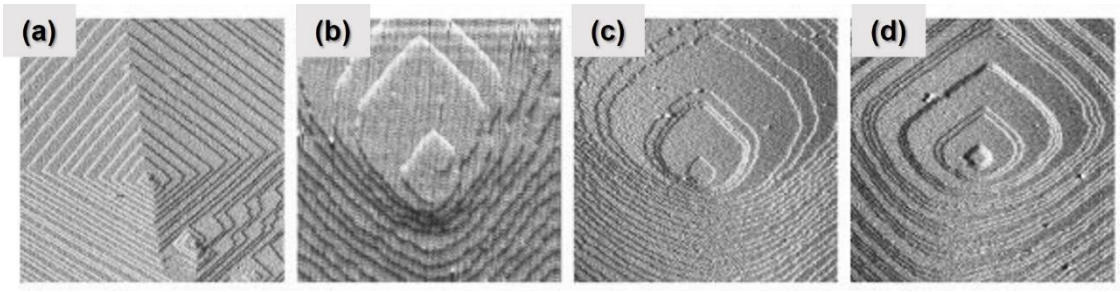


**Figure 3.2 AFM images of hillocks on calcite (104) faces with amino acids, (a) pure calcite, (b) glycine, (c) D-aspartic acid and (d) L-aspartic acid. Adapted from ref.[185]**

In contrast, the other amino acid utilised in this chapter, glycine (Gly), is a non-polar amino acid which has only a hydrogen atom as a side chain. However, it exhibits a

similar adsorption free energy to Asp[189]. X-ray diffraction (XRD) and modelling studies have indicated that Gly does not directly interact with the surface, but does participate in the hydration layers of water surrounding the crystal[190]. Regardless, effective incorporation of Gly within calcite crystals has been achieved[151], which suggests that some direct absorption does occur following displacement of water, though this requires further study to clarify the underlying mechanism[159]. Compared to Asp, Gly does not pack as efficiently[174], and induces stronger inhibitory effects at high additive concentrations[151].

The effect of amino acids on the early stages of calcite precipitation has been investigated to identify their potential interactions with ACC[191] and prenucleation clusters (PNCs)[192, 193]. Tobler *et al.* found that the addition of Asp or Gly prolonged the lifetime of ACC by adsorbing onto the surface of ACC particles, and subsequently delayed the precipitation of crystalline phases. At very high concentrations of Asp, ACC formation was inhibited and direct precipitation of calcite and vaterite was observed. This was not observed for Gly using the concentrations tested, which binds less strongly. The influence of amino acids on the formation of prenucleation clusters was explored by Picker *et al.*, who found that several of them (glutamic acid, aspartic acid, serine, threonine and tyrosine) stabilised the clusters by interaction with the carboxylate/hydroxide side chains[192]. Gly was found to retard nucleation and increased the solubility of ACC, which was thought to occur due to potential incorporation of Gly within ACC. Molecular dynamics simulations performed by Finney *et al*. looked further into the role of Asp, arginine (Arg) and Gly on calcite crystallisation, and found that Asp bound more strongly with $Ca^{2+}$ ions than Gly or Arg, which are neutral and positively charged respectively[193]. However, $HCO_3^{2-}$ bound more strongly with Arg than Gly and Asp, emphasising the role of the charge on the amino acid for interaction with clusters.

The occlusion of amino acids within calcite with high incorporation efficiencies has been investigated as a method of synthesising hybrid materials with increased functionality[174], such as enhanced mechanical strength[151]. Kim *et al.* showed that occlusion of Asp and Gly elevated the hardness of synthetic calcite to those of biogenic calcite[151]. Mijowska *et al.* showed that occlusion of Asp was elevated to 6.12 mol% by crystallising Asp-calcite under hydrothermal conditions (134 °C, 0.4 MPa)[194]. The authors also found that incorporation of Asp within calcite increased

the thermal expansion coefficient, resulting in twice the volumetric expansion coefficient of pure calcite. This lead to the formation of cracks in Asp-calcite annealed at 350 °C.

A vast number of polymer-calcite composites have been synthesised due to the ease with which polymeric structures with diverse shapes and properties can be prepared. Aside from their use in colloidal crystal templating[195] (described in detail later in Section 3.1.3), polystyrene microspheres have been shown to incorporate effectively within calcite when their surfaces are functionalised with high acid-content carboxylate chains[196]. Carboxylate-coated PS microspheres without the high acid-content showed that particles were only entrapped in the surface and outer region of the crystals, indicating poor interaction between the growing crystal and the additive particles[197]. Removal of the organic beads, which was achieved by dissolving them in tetrohydrofuran (THF) or calcination at 500 °C, created pores on the surfaces of the calcite crystals.

Block-copolymers with varied compositions, shapes and functionalisation have been shown to efficiently incorporate with single calcite crystals [198-200]. There is particular interest in di-block copolymer micelles and vesicles due to their potential in encapsulation[201-203]. The occlusion of such vesicles within calcite was explored by Ning *et al.*, who found that the level of incorporation was increased for vesicles which were functionalised with negatively charged carboxylate groups[204, 205]. Three key steps have been proposed for the occlusion of anionic di-block copolymer vesicles within calcite: (i) desorption following initial attachment to {104} faces, (ii) hovering above growing step edges and (iii) final incorporation within the growing crystal[206]. The incorporation step was studied using AFM to reveal some preference for adsorption onto acute steps, and also that they underwent compression during occlusion and eventually extended towards the free surface to form ellipsoidal shapes[155].

However, it should be noted that despite recent focus on the use of anionic functional groups for efficient occlusion in additives, positively charged functional groups have also been found to facilitate high levels of incorporation[207]. Although they interact relatively weakly with the growing calcite crystals[208], positively charged additives do not complex with $Ca^{2+}$ ions, unlike negatively charged additives, which means that higher supersaturations and additive concentrations can be explored

without aggregation occurring[207]. By lifting these restrictions on crystallisation conditions, exceptionally high levels of occlusion have been achieved for a range of cationic additives[207].

### 3.1.3 Synthesis of Porous Calcium Carbonate

Calcium carbonate is an attractive crystalline material for biomedical and food applications due to its biocompatibility and biodegradability. Facile routes of synthesising porous calcium carbonate crystals have therefore been explored for their use in bone-scaffolding[209-211], drug delivery[212, 213], and waste water treatment[214]. Porous vaterite crystals have been most widely studied due to its inherent porosity and polycrystallinity[215-217], and control over the porosity has been achieved using polymers and solvents as additives in the crystallising solution[218-220].

An exciting use of porous calcium carbonate materials is for the encapsulation of active compounds for specific applications where direct application or ingestion is undesirable. Calcium carbonate is a non-toxic material which is stable at physiological pH[221] and will dissolve at gastrointestinal pH. Such high biocompatibility has made porous calcium carbonate an ideal candidate for drug delivery applications. To exploit this advantageous property, functionalised calcium carbonate was synthesised by Ridgeway *et al.*[222] and been commercialised as a highly versatile pharmaceutical excipient, where the porous framework provides a surface for loading drug molecules onto[223-225]. The highly porous (60 % v/v) particles were synthesised from ground calcium carbonate (GCC), which was reprecipitated in the presence of inorganic mineral salts to create a new porous surface[226].

In addition to facilitating encapsulation, the pores can provide additional benefits. This was demonstrated by researchers loading $CaCO_3$ with flavouring compounds such as vanillin, who exploited the confined environment within the pores to avoid unwanted crystallisation of the flavouring compound[227]. Another example where the porosity was advantageous was in the delivery of powder-form insulin, which was more rapidly absorbed when simultaneously administered with porous $CaCO_3$ particles compared to non-porous $CaCO_3$[228]. The prospect of using porous calcium carbonate for slow-release of a loaded compound has been explored not only for drug molecules[229], but also herbicides, where porous $CaCO_3$-starch composites

allow better adhesion to the plants and reduced undesired leaching of the herbicide into the soil[230].

Fewer studies focus on creating porosity within calcite crystals. This has typically been achieved using templates such as colloidal crystals. Li and Qi formed porous single crystals of calcite by adding ACC to a colloidal dispersion of polymer microspheres and drying, before removing the template by dissolving the beads in THF and heating at 450 °C[195]. The ACC filled the interstitial areas between the polymer beads before crystallising with an inverse opal structure to yield a highly porous, mesh-like single crystal. A similar study by Hetherington *et al.* employed a wedge setup to form larger prismatic porous single crystals of calcite via direct precipitation, demonstrating that both methods can be used to form structurally complex crystals[231].

Highly porous calcite crystals have also been prepared using the naturally porous sea urchin skeleton to make a polymer template, then using a U-tube apparatus to perform crystallisation inside the membrane template via double diffusion[232, 233]. The template was removed by dissolution in solvents (chloroform or a hot mixture of 1:1 THF:EtOH) or heating at 500 °C to generate single crystals of calcite with sponge-like porosity.

In addition to templating strategies, additive incorporation is also a viable method of producing porous calcite. As highlighted in Section 3.1.2, the incorporation and subsequent removal of functionalised PS particles in calcite created pores on the crystal surfaces[197]. The occlusion of agarose hydrogel within calcite crystals was found to cause porosity via the incorporation of gel fibres throughout the crystal structure[179]. A mixture of calcite and vaterite was obtained by Li *et al.* who used performed the crystallisation in gelatin[234]. The vaterite was converted into the stable calcite polymorph on annealing at 550 °C to remove occluded gelatin, yielding porous calcite crystals. The porosity facilitated a higher loading of doxorubicin and the controlled, slow release of the drug compared to the non-porous control.

However, the incorporation of additives is not essential for the formation of porosity within calcite. Yu *et al.* decomposed calcium carbonate at 1000 °C to yield porous calcium oxide, which slowly reacted with air upon cooling to form porous calcium carbonate[235]. The same strategy was used with calcium citrate ($C_{12}H_{10}Ca_3O_{14}\cdot 4H_2O$)

and calcium lactobionate ($C_{24}H_{42}CaO_{24}\cdot 2H_2O$), where larger pores were observed with increasing size of the organic side chains[236].

In the present study, porous calcium carbonate is produced by thermal decomposition of organic additives occluded within calcite. The thermal behaviour of calcium carbonate has been well-studied as calcination is a key stage for the formation of calcium oxide from natural sources such as limestone[237, 238]. As highlighted previously, many animal shells comprise biogenic calcium carbonate, which contains organic macromolecules. While studying the thermal decomposition of avian eggshell, Tsuboi *et al.* showed that delicate structural features and pores were created by heating biomineralized $CaCO_3$[239].

A detailed study of the evolution of porosity during thermal decomposition of sea urchin spine and plate sections by Albéric *et al.* provided insight into the mechanism of pore formation[240]. They found that pores were formed during two main processes: (1) crystallisation of residual ACC at 170 – 300 °C and (2) the decomposition of organic molecules occluded within the crystals at 300 – 400 °C. The authors hypothesised that the formation of pores by removal of organics in the spine and plate proceeded via different mechanisms. They suggested that both the micro- and nano-porosity in the spines relied on bulk diffusion, whereas the plate pores which were controlled by surface diffusion. This was explained by identifying a “percolation” threshold, which dictated the pore density required for surface diffusion to be the predominant mechanism. The plates possessed a far greater pore density which surpassed this threshold, providing a lower activation energy for surface diffusion. This was not the case for the spines, suggesting that bulk and surface diffusion possess similar activation energies.

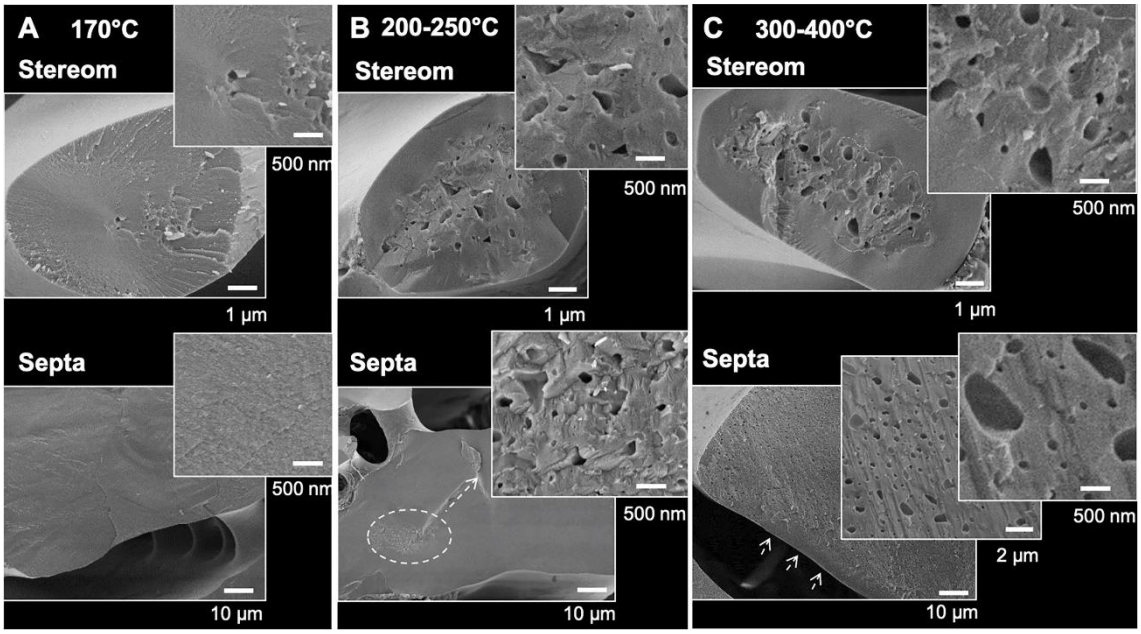


**Figure 3.3 SEM images of fractured laminar stereom and septa regions of *P. lividus* sea urchin annealed at (a) 170 °C, (b) 200 – 250 °C, (c) 300 – 400 °C, where the arrows in (c) highlight the outer layer that has no observable pores. Reproduced from ref.[240]**

Overall, porous calcium carbonate has been produced for a range of applications, but the porosity has not been explored for enhancing optical properties. In this chapter, the ability of porous calcite to scatter light and yield a bright white colour via structural colouration is investigated.

### 3.1.4 Structural Colour

Structural colour describes a fascinating phenomenon whereby colour is produced through the interaction of light with nanoscale features on the surface of an object. Structural colour is prevalent within Nature, and a multitude of flora and fauna use this phenomenon to display bright colours or iridescent effects (Figure 3.4).

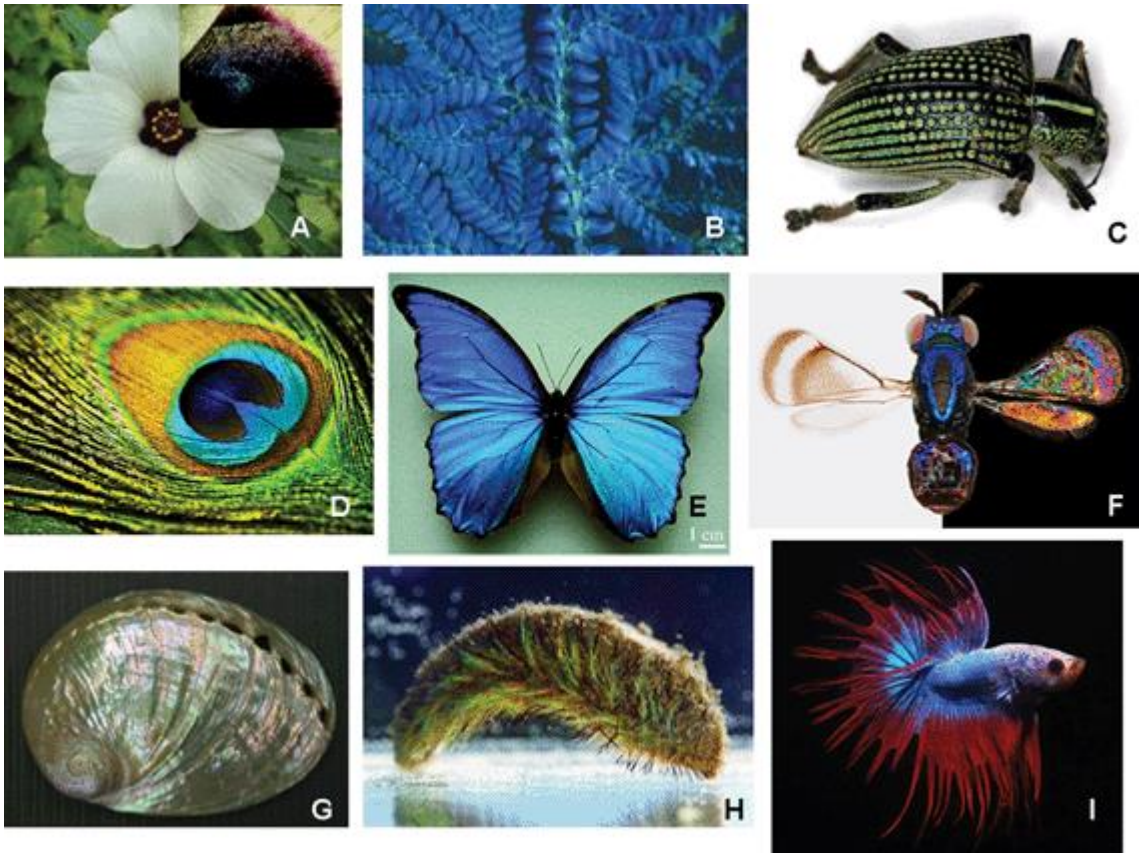


**Figure 3.4 Examples of structural colour in nature, (a) iridescent *H. trionium* petal, (b) the blue iridescent fern *Selaginella*, (c) green photonic crystals in the elytra of the diamond weevil beetle *Entimus imperialis*, (d) iridescent structural colour in a male peacock tail feather, (e) blue structural colour in the butterfly *Morpho rhetenor*, (f) thin-film interference in the wings of the insect *Clostereocerus coffeellae*, (g) iridescence in the shell of the mollusc *Haliotis glabra*, (h) iridescent structural colour in the bristles of the sea mouse *Aphrodita aculeata*, (i) in male Siamese fighting fish *Betta splendens*. Reproduced from ref.[241]**

There are a number of mechanisms by which structural colour is achieved, which can be broadly categorised into six main, non-exclusive types (Figure 3.5). The first two mechanisms are thin-film and multi-film interference. These occur when light is reflected by each interface of a thin-film or multiple thin-film layers, where increasing the number of layers will boost reflectance and can create a metallic appearance[242]. The third mechanism involves periodically grooved surfaces known as diffraction gratings. This occurs by constructive interference, as for the film interference mechanism, but unlike film interference, the wavelength of light reflected is different

at each reflector site (or each groove in a diffraction grating). The fourth and fifth mechanisms describe coherent and incoherent scattering. Coherent scattering broadly includes the mechanisms already discussed, in which the incident and scattered light are related to each other[241]. Incoherent scattering describes the reflection or refraction of light which is caused by randomly oriented features. This is the case for Mie, Rayleigh and Tyndall scattering, which involve incoherent scattering by small particles and molecules[243]. Disordered, anisotropic scatterers are also key in producing a bright white appearance in Nature[244]. This can be optimised by maximising the difference between the refractive indices of the scatterer and surrounding medium[242]. The final way in which structural colour is achieved is through periodically structured photonic crystalline materials. Photonic crystals are 1D, 2D or 3D composites built using materials with contrasting refractive indices[245]. These include opal and inverse opal structures exhibited by some beetle and butterfly species[241]. The photonic bandgap of these materials dictates their optical activity.

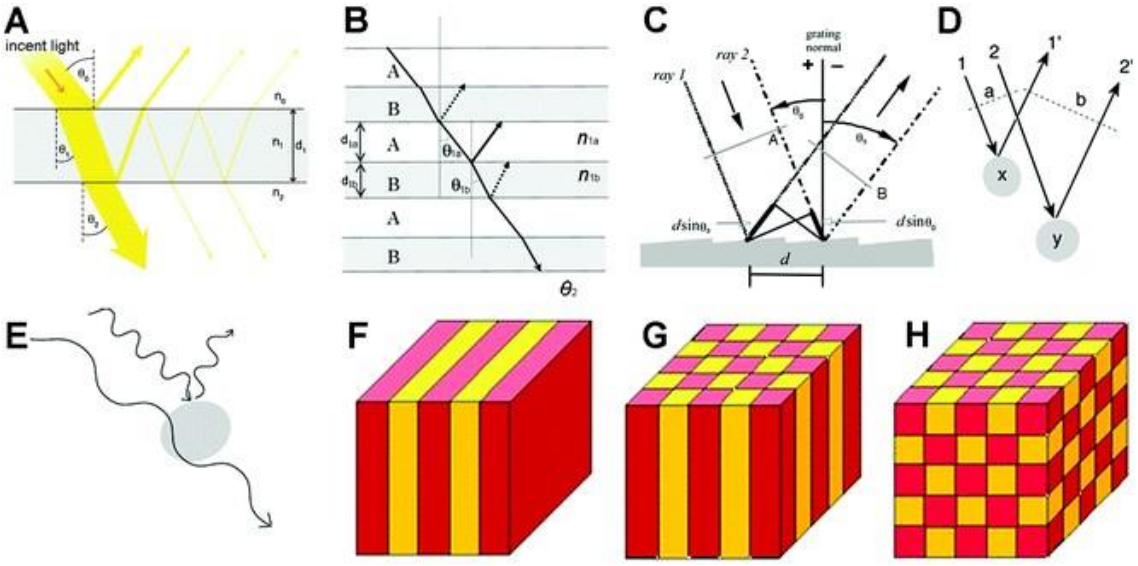


**Figure 3.5 Structural colour can be produced by (a) thin-film interference, (b) multi-film interference, (c) diffraction grating, (d) coherent scattering, (e) incoherent scattering, (f – h) 1D, 2D and 3D photonic crystals. Reproduced from ref.[241]**

It is common for both animals and plants to exhibit not just one but a combination of these mechanisms to achieve their iconic visual effects. Using mechanisms which reflect light at different periodic distances, such as in multi-film inference and

diffraction gratings, will cause the resulting optical effect to have an angular dependence. This means that depending on the illumination and viewing angle of the feature surface, different colours or iridescence may be observed.

In this chapter, the mechanism used to create structural colour was incoherent scattering, with the aim of creating bright white calcite crystals by exploiting the contrasting refractive indices of calcite with the air-filled pores ($\lambda_{590\ nm}$ = 1.658 and 1.00 respectively[246]). Calcite is widely employed as a filler compound in products such as paper, plastic, rubber and paint. Highly scattering calcite with bright white appearance could remove the need to use additional white pigments in these products, the most popular of which ($TiO_2$) has been newly classified as a carcinogen by the European Chemicals Agency[247], due to recent findings on its toxicity[248-250]. Additionally, the optical properties of highly reflective materials can be exploited in thermal protection systems and solar cells.

A desire to mimic the optical effects shown in Nature has led to researchers exploiting structural colour mechanisms through the fabrication of nanoscale features[245, 251-253]. However, few of these efforts have focused on creating bright white materials. In the literature, polymers have typically been used to prepare porous structures which are capable of scattering light in a broadband fashion to appear white[254-256]. Drawing inspiration from the *Cyphochilus sp.* beetle, PMMA films with bright white appearance were prepared by Syurik *et al.* using a solvent-evaporation method to create highly disordered networks capable of scattering light[257] (Figure 3.6). Indeed, the chitinous scales of the *Cyphochilus sp.* reflect diffuse, broadband light so effectively that they appear brilliant white despite being only half the thickness of comparable synthetic materials[258, 259]. Further replication of the disordered chitin network has been achieved using cellulose nanofibrils, where a wide range of pore and nanofibril sizes were crucial for ensuring superior reflectance.

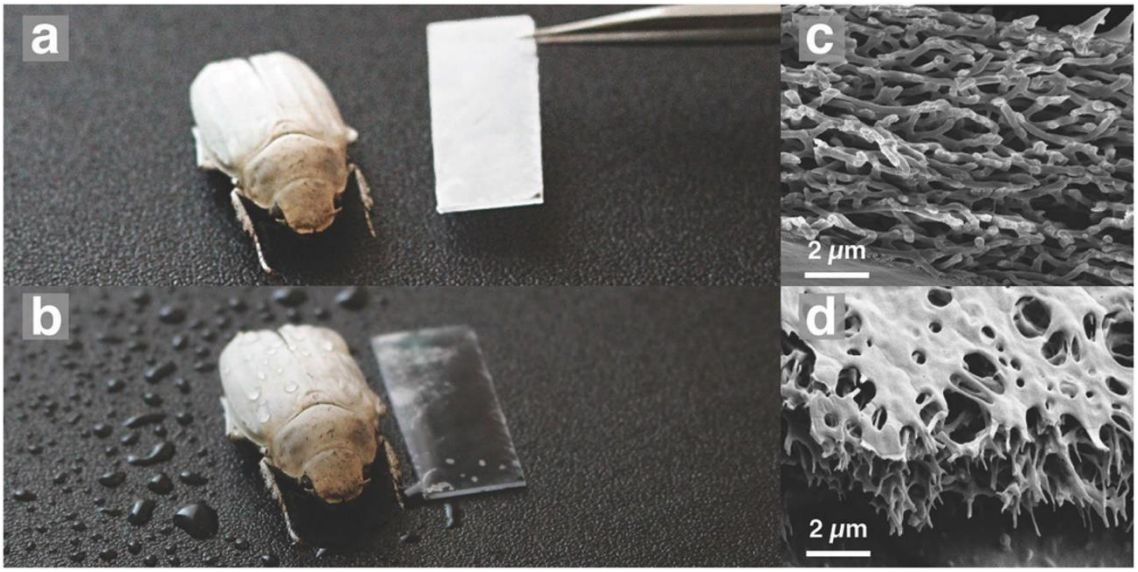


**Figure 3.6 Mimicking the *Cyphochilus insulanus* beetle using microstructured PMMA films (a). After wetting, the beetle is the same colour whereas the polymer film becomes transparent (b). SEM images of a cross-section of a *Cyphilochilus sp.* scale (c) and the PMMA film. Reproduced from ref.[257]**

Structural colour has also been observed in calcium carbonate crystals in nature. The coccolithophore *Emiliania huxleyi* produces calcite crystal plates called coccoliths that cover the cell. Stacks of coccoliths appear iridescent and when subjected to a magnetic field, the periodicity between discs will change to give rise to different colours[260]. In some molluscs, the shells possess multiple layers with a thick layer of nacre (which is composed of 95% aragonite[261]). Interaction of light with the spacings between the plates in this layer creates either a white or iridescent appearance, depending on their thicknesses[242]. A similar phenomena is displayed in the single-celled organisms Foraminifera, which contain layers of calcium carbonate material with voids, resulting in structural colouration to yield a bright white appearance[262].

The present study investigates the optical properties of porous calcite prepared via occlusion and removal of organic additives, namely their ability to scatter broadband light efficiently to achieve a bright white colour. This relies on the incoherent scattering mechanism of creating structural colour. By using different additives, porous calcite could be produced with varying pore size distributions and filling fractions. This allowed the effect of these pore properties on the crystal reflectance to be studied. Inspired by the use of calcium carbonate in Nature to give a bright

white appearance, this chapter aims to demonstrate how porous calcite may offer an exciting alternative to pigments for achieving optical effects.

## 3.2 Experimental

### 3.2.1 Synthesis and Preparation of Materials

#### 3.2.1.1 Materials

The following materials were obtained from Sigma Aldrich: calcium chloride dihydrate $CaCl_2.2H_2O$, ammonium carbonate $(NH_4)_2CO_3$, L-aspartic acid (Asp), glycine (Gly). High-acid content carboxylate-functionalised 0.51 µm polystyrene (PS) microsphere dispersions were obtained from Bangs Labs Inc. and the size distribution was measured as 445 ± 21 nm. Anionic diblock copolymer vesicles composed of poly(methacrylic acid)-poly(benzyl methacrylate) (PMAA-PBzMA) (Ves) with size distributions 365 ± 120 nm were synthesised and supplied by Dr Ouassef Nahi. Chemical structures of the additives used are shown in Figure 3.7. All aqueous solutions were prepared using deionised water from a Millipore Q Water system operating at 18 Ω.

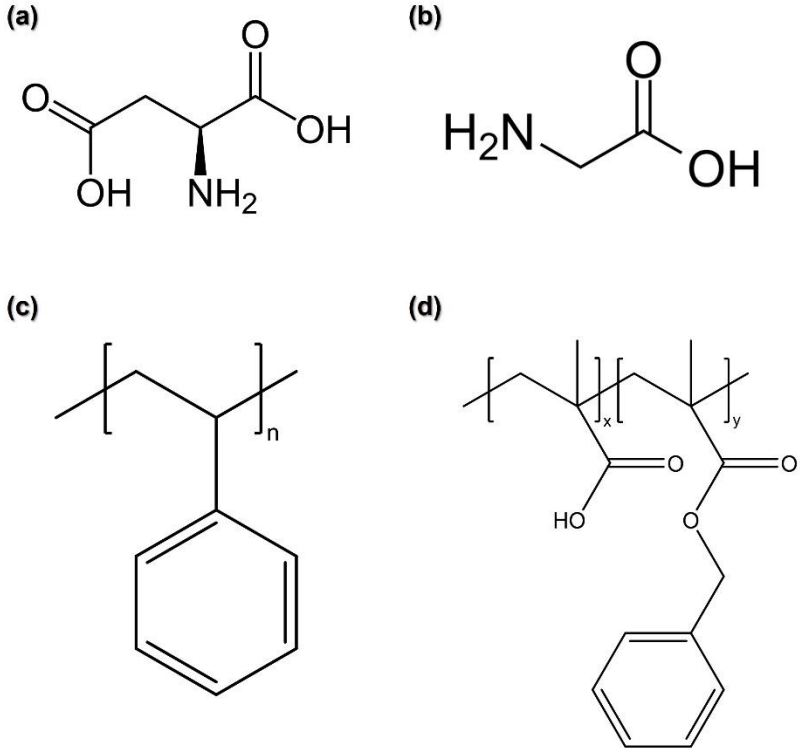


**Figure 3.7 Chemical structures of the additives occluded within calcite, (a) aspartic acid, (b) glycine, (c) polystyrene, (d) poly(methacrylic acid)-poly(benzyl methylacrylate (PMAA-PBzMA).**

### 3.2.1.2 Synthesis of Additive-$CaCO_3$ Composite Crystals

In this project, Asp-, Gly- and PS-calcite composites were prepared by precipitating calcite in the presence of additives using the ammonia diffusion method. Aqueous solutions of $CaCl_2$ of were pipetted into a multi-well plate containing several glass slide pieces in each well. Additive solutions were then added to the well plate and gently mixed. A range of [$Ca^{2+}$] and additive concentrations were used to prepare Asp-, Gly- and PS-calcite (Table 3.1, Table 3.2 and Table 3.3, respectively). The well plate was placed in a desiccator accompanied by a petri dish containing ≈ 3 g ammonium carbonate powder, which was covered with Parafilm and pierced several times. The desiccator was left undisturbed for a minimum of 48 hours. Following crystallisation, the glass slides were removed from the solution and rinsed thoroughly with DI water and EtOH. The glass substrates were subsequently dried in a 60 °C drying cabinet.

The amino acids Asp and Gly were firstly chosen as an additive as they are both well-known to occlude effectively within single calcite crystals with high incorporation efficiencies. Additionally, Asp and Gly are cheap and readily available chemical compounds, and therefore would demonstrate the most potential for application purposes. PS microspheres were chosen as an additive as they have uniformly spherical sizes which facilitated and simplified simulations of the ideal void size and filling fraction. Vesicles were then chosen as an unfilled analogue of the PS microspheres, in order to avoid the undesired absorbance effects caused by carbon remnants that persisted inside the crystals following heat treatment. A combination of PS and Gly was trialled in an attempt to obtain porosity with mixed pore sizes and shapes. Finally, sea urchin spine provided a natural analogue to the Asp- and Gly-calcite composites and were subjected to the same heat treatment to allow comparison.

| $[Ca^{2+}]$ / mM | [Asp] / mM |
|---|---|
| 1.25 | 10 |
| | 20 |
| | 50 |
| 5 | 10 |
| | 20 |
| | 50 |
| 10 | 10 |
| | 20 |
| | 50 |

**Table 3.1 The range of final $[Ca^{2+}]$ and [Asp] used for the crystallisation of Asp-calcite via ADM.**

| $[Ca^{2+}]$ / mM | [Gly] / mM |
|---|---|
| 1.25 | 100 |
| | 200 |
| 5 | 100 |
| | 200 |
| 10 | 100 |
| | 200 |

**Table 3.2 The range of $[Ca^{2+}]$ and [Gly] used to crystallise Gly-calcite.**

| [PS] / wt.% |
|---|
| 0.005 |
| 0.01 |
| 0.1 |
| 0.5 |
| 1 |
| 2 |
| 3 |
| 4 |
| 5 |

**Table 3.3 The range of [PS] used to obtain PS-calcite.**

Calcite incorporating PMAA-PBzMA vesicles were synthesised using a direct mixing strategy. 10 mM $CaCl_2$ solutions were prepared and mixed with the vesicle dispersion (Table 3.4), before adding 20 mM $Na_2CO_3$ solution. The well-plate was left undisturbed for 48 hours and the glass slide substrates were removed and washed as before.

| [Ves] / wt.% |
|---|
| 0.05 |
| 0.1 |
| 0.25 |
| 0.5 |

**Table 3.4 The range of [Ves] used to obtain Ves-calcite.**

### 3.2.1.3 Thermal Decomposition of Occluded Additives in Calcite

The glass substrates supporting the crystals were placed on a ceramic tray crucible and heated in a muffle furnace at a controlled rate. The heating parameters were varied to determine their effect on porosity and whether the pore properties could be controlled via heating rate, temperature, and heating time (Figure 3.8). It should be noted that the heating time refers to the time spent at the target temperature, and is not inclusive of the time spent heating up to it.

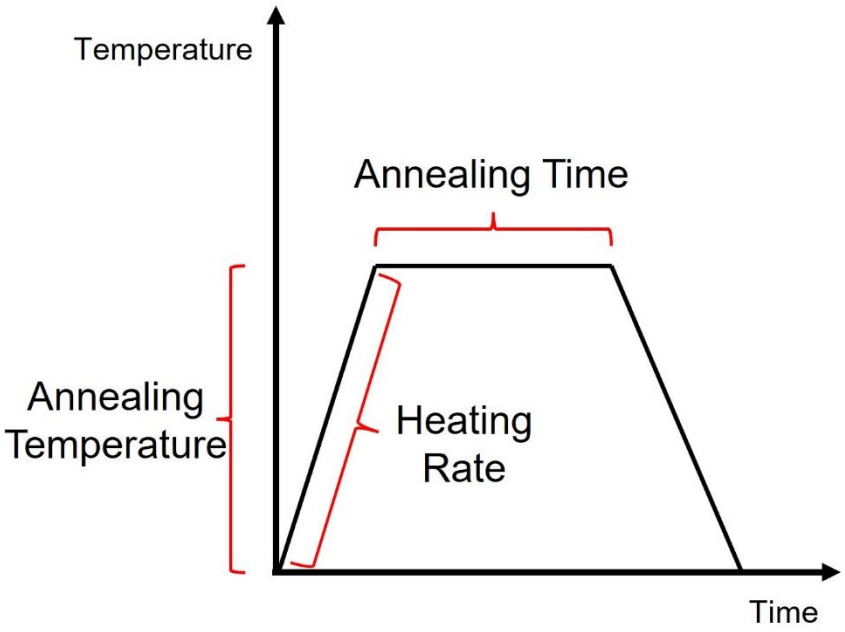


**Figure 3.8 The heating parameters investigated for thermal degradation of occluded organic additives in calcite crystals.**

Preliminary work was undertaken using TGA to confirm the temperature at which $CaCO_3$ transforms into CaO (Equation 3.1), cited in literature typically at 600 °C (Figure 3.9).

$$CaCO_{3\,(s)} \xrightarrow{\Delta} CaO_{(s)} + CO_{2\,(g)} \qquad (3.1)$$

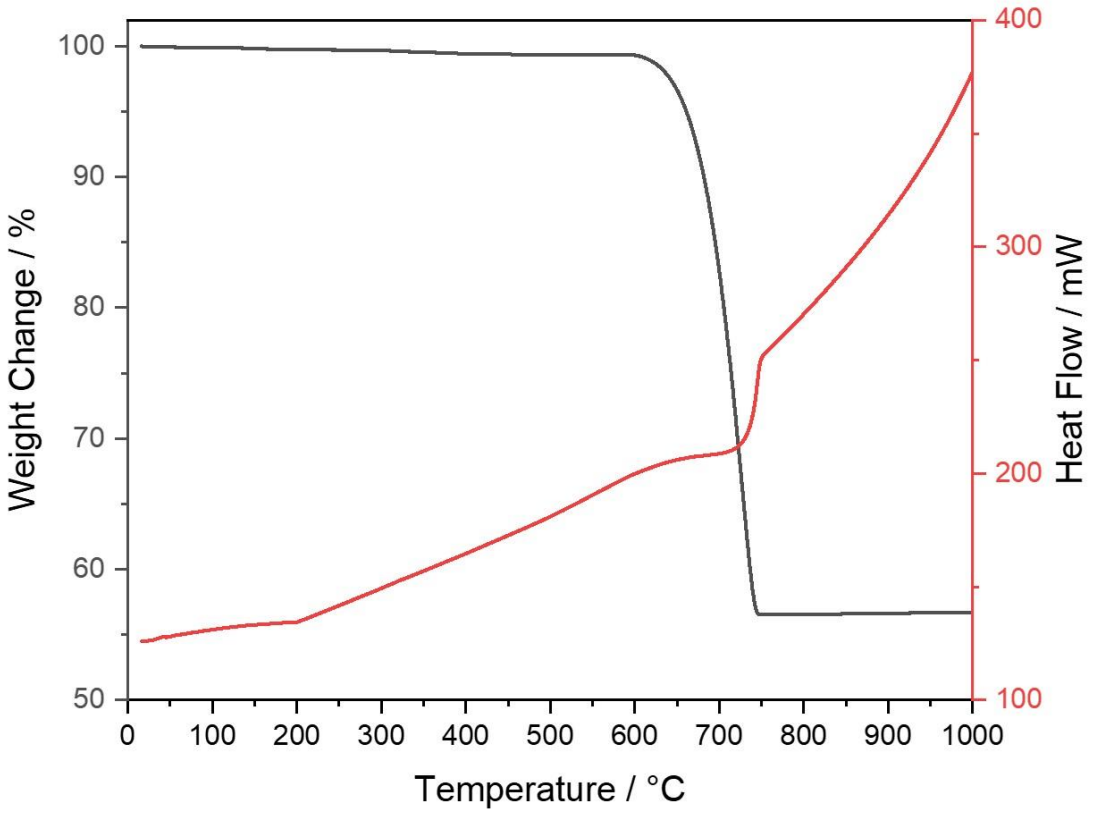


**Figure 3.9 Thermogravimetric profile for calcite, heated using a rate of 5 °C min$^{-1}$.**

The TGA profile for calcite shows a major weight loss that occurs at 600 °C until 750 °C. The reduction in weight to 56 % of the initial weight reflects the change in molar mass from 100 to 56 gmol$^{-1}$ as $CaCO_3$ decomposes into CaO, releasing $CO_2$. This confirmed that the calcination process occurs at 600 °C, and so this was considered the upper temperature limit for heating calcite to create porosity. The degradation of organic additives was expected at temperatures > 200 °C[200, 263, 264]. Therefore, this formed the lower bound of suitable heating temperatures. The full range of heating parameters used are shown in Table 3.5. It should be noted that the annealing time refers to the time that samples were subjected to the target temperature for, and is not inclusive of the time required to achieve the target temperature.

| Heating Rate / °C min$^{-1}$ | Temperature / °C | Length of time / min |
|---|---|---|
| 5 | 300 | 30 |
| 5 | 400 | 30 |
| 5 | 500 | 30 |

| | | |
|---|---|---|
| 5 | 600 | 30 |
| 5 | 500 | 10 |
| 5 | 500 | 4 h |
| 5 | 500 | 8 h |
| 1 | 500 | 30 |
| 10 | 500 | 30 |

**Table 3.5 Heating parameters investigated for their effect on porosity formation within Asp-Calcite.**

## 3.2.2 Analytical Techniques

### 3.2.2.1 Amino Acid Quantification via Fluorometric Assay

The amount of Asp and Gly occluded within AA/calcite crystals was quantified using a plate reader, using a modified version of the high-throughput quantification strategy outlined by Green *et al.* [265] Firstly, the crystals were cleaned using NaOCl to remove organic material, chiefly the surface-bound amino acids but also any remnants of ammonia which can react with the derivatisation solution. The crystals were immersed in NaOCl solution and left overnight. The crystals were then washed thoroughly, filtered under vacuum and left to dry in air overnight prior to loading into a 96 well plate. Each of the [Asp]/[Gly] and [$Ca^{2+}$] conditions were measured and had a total of 3 repeats per condition, with 2 mg of AA/calcite loaded per well. A microbalance was used and the exact mass was recorded for each well to use later in the mole calculations. In order to release the occluded amino acid molecules, the calcite crystals were dissolved in 150 µl of 200 mM EDTA solution and shaken on a microplate mixer at 600 rpm for 2 hours.

The well plate was also loaded with Asp and Gly control solutions of known concentration (0.02 – 5 mM), in order to create calibration curves for both amino acids. The resulting solution was loaded with 100 µl IBLC (isobutyryl-L-cysteine)/OPA (*o*-phthaldialdehyde) derivatisation solution. OPA is a fluorescent molecule which reacts with nucleophiles such as primary amines and thiols (e.g. IBLC), the latter of which has been shown to boost fluorescence when mixed with OPA prior to addition of amino acids[266]. The IBLC/OPA was prepared using 1 M potassium borate solution at pH 10.4, to further ensure optimum fluorescence

intensity, with final concentrations of 26 mM IBLC and 17 mM OPA. Following derivatisation, the well-plate was loaded into a Perkin Elmer EnVision 2103 well plate reader and the fluorescence intensity was measured using $\lambda_{ex}$ = 230 nm, $\lambda_{em}$ = 445 nm.

By comparing the fluorescence of the amino acid solutions against a calibration curve, the moles of occluded amino acid could be obtained. This allowed the efficiency of the occluded additive across different [$Ca^{2+}$] and [Asp]/[Gly] to be evaluated in terms of mol% (where the total moles of AA-calcite was calculated from the recorded masses loaded into the well-plate).

#### 3.2.2.2 Measurement of Optical Properties using a Spectrometer

The optical properties of the crystals were measured in the Bioinspired Photonics Lab at the University of Cambridge by Dr Gianni Jacucci, under the supervision of Professor Silvia Vignolini.

A Zeiss Axio Scope A1 microscope, configured with an Avantes HS2048 spectrometer and Avantes FCUV50-2-SR (50 µm core size) optical fibre, was used to measure the optical properties of the crystals. The fibre size used was chosen to allow a single crystal to be measured, which typically ranged from 10-100 µm in size. The reflection spectrum across the visible light wavelength region (400 – 700 nm) in bright field was collected for 3-5 crystals for each sample set. A silver mirror (PF05-03-P01, Thorlabs) was used to normalise the reflectance values. Microscope images were taken and annotated to record the crystal measured, so that they could be located with SEM using a tilted stage to measure the z-height or “thickness” of the crystal. The crystal thickness was recorded in order to determine whether it was attributable for changes in optical behaviour between different samples.

#### 3.2.2.3 FIB-SEM for Cross-Section Preparation and Imaging

In order to examine the porosity within the crystals, cross-sections were prepared and imaged using FIB-SEM. The glass substrates were fixed to SEM stubs using carbon paint and coated with 20 nm of iridium before placing into the microscope chamber. After taking low magnification SEM images, a single crystal was selected and high magnification images were collected. The stage was tilted to 52° to bring the crystal substrate perpendicular to the ion beam. Using the GIS needle, platinum was deposited selectively onto a central region perpendicular to the long axis of the

crystal using an ion beam current of 0.23 – 0.43 nA. This was applied to form a layer of 0.5 – 2 µm thickness depending on the size of the crystal, in order to protect the crystal surface and outer regions from the ion beam during milling. The unwanted edge of the crystal was removed using ion beam currents of 21 – 2.5 nA, milling into the platinum coated region. This was followed by polishing steps using lesser ion beam probe currents of 0.79 nA – 7.7 pA until a smooth, curtain-free cross section was obtained. Images of the cross-section were taken using the electron beam and backscatter detector to mitigate charging, which was prevalent around pore edges.

#### 3.2.2.4 Cross-Sectional Image Analysis

After obtaining SEM images of the cross-sections, image analysis was conducted to investigate the properties of the pores. FIJI was used first to crop and select the crystal area from the image background[267]. The crystal area was measured and the contrast of the image was adjusted to clarify the pore regions against the crystal. The resulting image file was exported to ilastik and the object classifier programme was used[268]. The classier was first trained to recognise the pores, crystal and background as three separate objects. This was done by manually labelling these features until the object classifier was optimised and applied to the full image. This generated a segmented image which was exported into FIJI once more. The “Analyse Particles” function was used to select the pores and generate quantitative data describing the pore properties.

The main data collected from the image analysis were the area of each pore. The distribution of the pore areas was graphically represented using violin box-plots. This method was chosen as it shows the kernel density plot, which helps to identify clusters of data points amongst the population, unlike typical box-plots. Additionally, the data did not possess a normal distribution and was highly positively skewed. This suits a non-parametric statistical method such as the kernel density estimation. Though both were calculated, the median pore area was preferred over the mean, as the median provides a better reflection of the central tendency for skewed data such as this[269]. The interquartile range (IQR), which is the range where 25 – 75 % of the data population lies, was also calculated as a measure of the spread. The filling fraction of the porosity was quantified by calculating both the pore area and the pore density, where the pore area describes the proportion of the crystal area occupied by

pores (%) and the pore density represents the number of pores per unit area of crystal ($\mu m^{-2}$).

## 3.3 Results

### 3.3.1 Crystallisation of Calcite with Additives

A range of organic additives were trialled for the formation of porous calcite. For ease of reference, a nomenclature will be used to differentiate between samples prepared using different $Ca^{2+}$ and additive concentrations. The sample names take the form “X, Y additive-calcite”, where X indicates [$Ca^{2+}$]/ mM, Y indicates [additive]/ mM and “additive” will be replaced with Asp/Gly/PS/Ves. For example, “10, 20 Asp-calcite” refers to the calcite samples occluded with aspartic acid using [$Ca^{2+}$] = 10 mM and [Asp] = 20 mM.

#### 3.3.1.1 Crystallisation of Asp-Calcite

Calcium carbonate crystals were grown in the presence of Asp via the ammonia diffusion method, using [$Ca^{2+}$] = 1.25, 5, and 10 mM and [Asp] = 10, 20 and 50 mM. While a perfect rhombohedral shape was observed at low [$Ca^{2+}$] and [Asp], the crystal morphology showed increasingly pronounced {104} faces, surface roughening and slight elongation along the [001] direction with increasing [Asp] and [$Ca^{2+}$] (Figure 3.10).

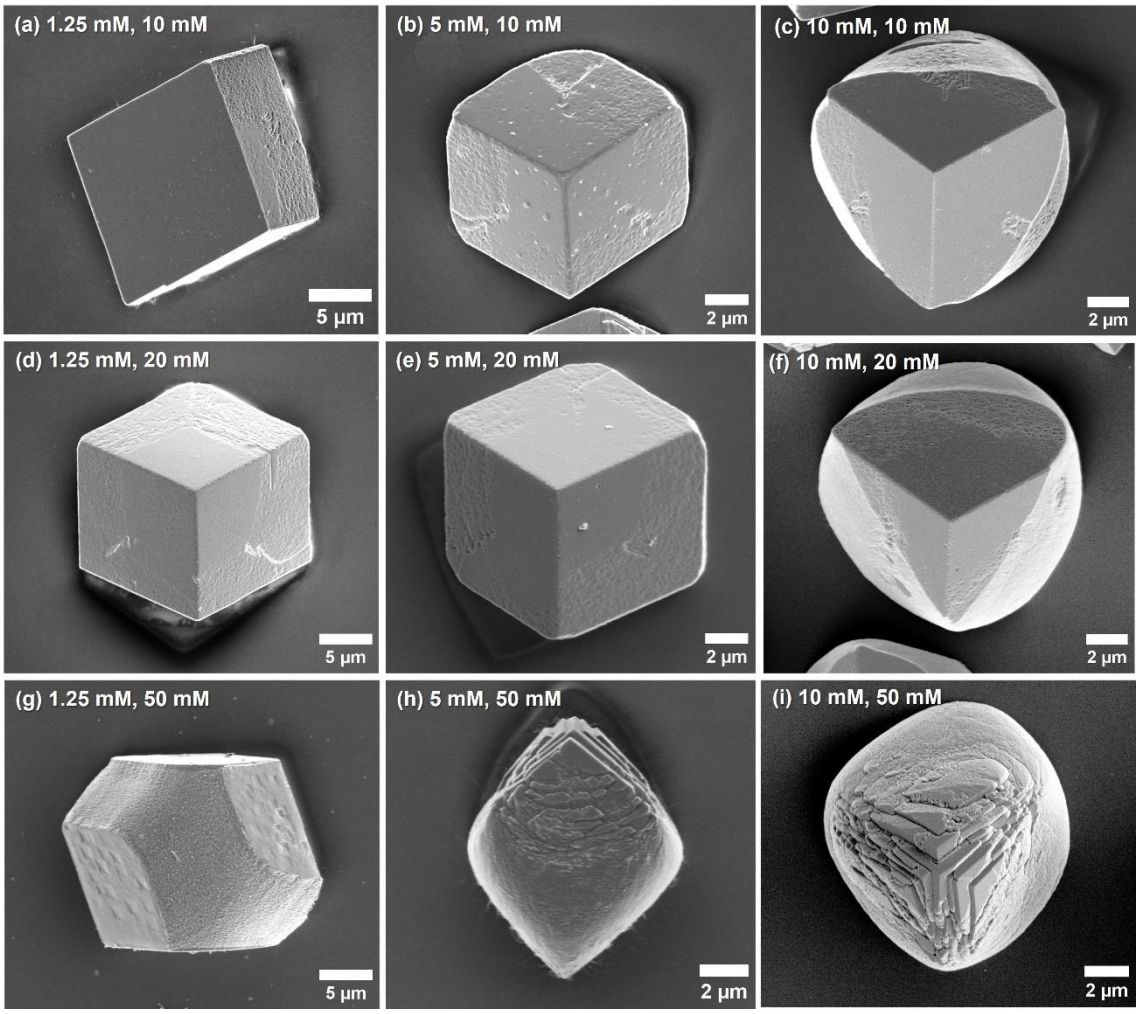


**Figure 3.10 SEM images of Asp-calcite, prepared with varying [Asp] and [$Ca^{2+}$].**

Raman spectroscopy confirmed that calcite was obtained (Figure 3.11), with all characteristic peaks present (Table 3.6).

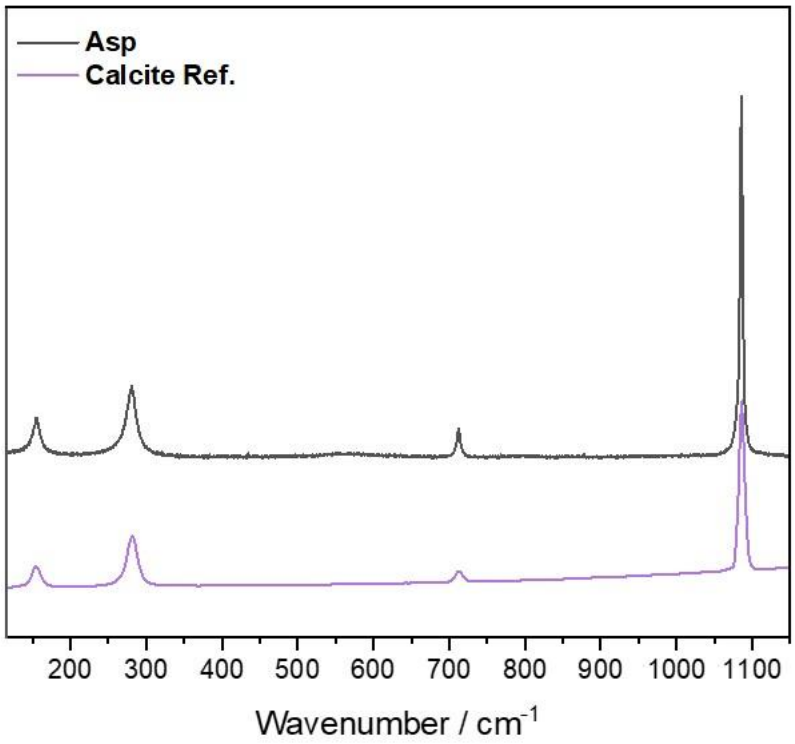


**Figure 3.11 Raman spectrum of Asp-calcite, compared with a reference spectrum for calcite obtained from RRUFF[270] (RRUFF ID: 040070).**

| Peak Position / $cm^{-1}$ | Peak Assignment |
|---|---|
| 1083 | $v_1$, $CO_3^{2-}$ stretching mode |
| 710 | $v_4$, $CO_3^{2-}$ out-of-plane bending mode |
| 280 | L, $CO_3$ external mode |
| 154 | T, $CO_3$ external mode |

**Table 3.6 Raman peaks observed for calcite crystals and their assignments.**

The amount of Asp occluded within the calcite crystals was quantified using a fluorescence assay, using a calibration curve of known concentrations as described in Section 3.2.2.1. The efficiency of amino acid occlusion was determined in mol% and compared across the range of [$Ca^{2+}$] and [Asp] (Figure 3.12).

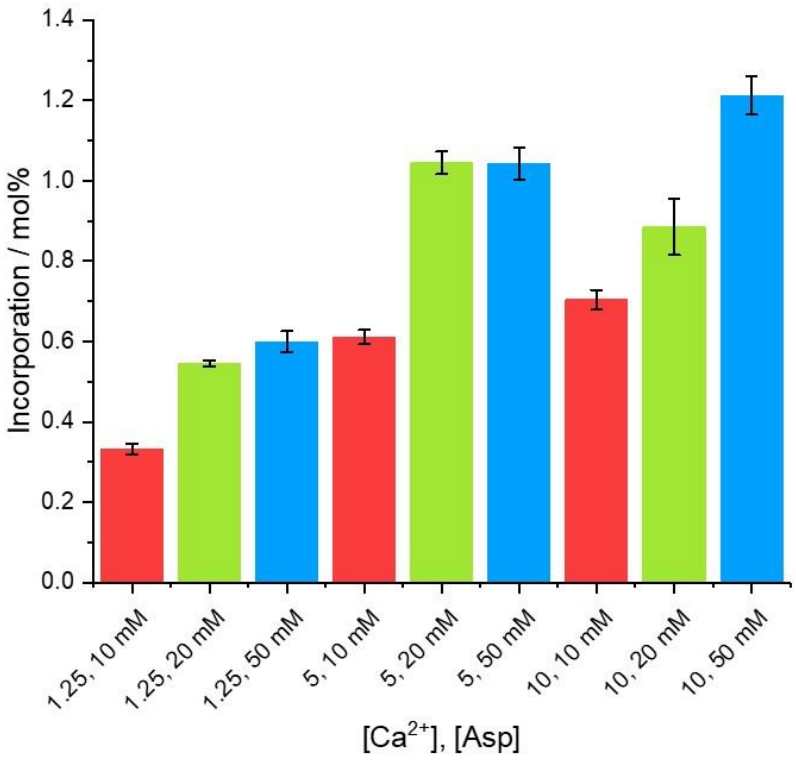


**Figure 3.12 The incorporation efficiency of Asp within calcite crystals in mol% across different [Asp] and [$Ca^{2+}$].**

Asp-calcite showed greater occlusion of Asp at higher [Asp] and [$Ca^{2+}$], indicating that incorporation scales with both addition concentration and supersaturation. This was expected as the greater number of step edges created at higher supersaturation facilitates greater interaction and occlusion[155]. However, there was little increase in Asp incorporation between the 1.25, 20 mM and 1.25, 50 mM samples, or the 5, 20 mM and 5, 50 mM samples. This could be attributed to the steep increase in [Asp]/[$Ca^{2+}$] between these conditions. Overall, the highest level of incorporation was achieved for [$Ca^{2+}$] 10 mM, [Asp] = 50 mM, which had 1.2 mol% of Asp occluded within the crystals.

### 3.3.1.2 Crystallisation of Gly-Calcite

Gly-calcite was precipitated using [$Ca^{2+}$] = 1.25, 5, 10 mM and [Gly] = 100 and 200 mM. Rhombohedral calcite crystals were obtained, which also showed increasingly pronounced {104} faces at each apex with [Gly] and [$Ca^{2+}$] (Figure 3.13).

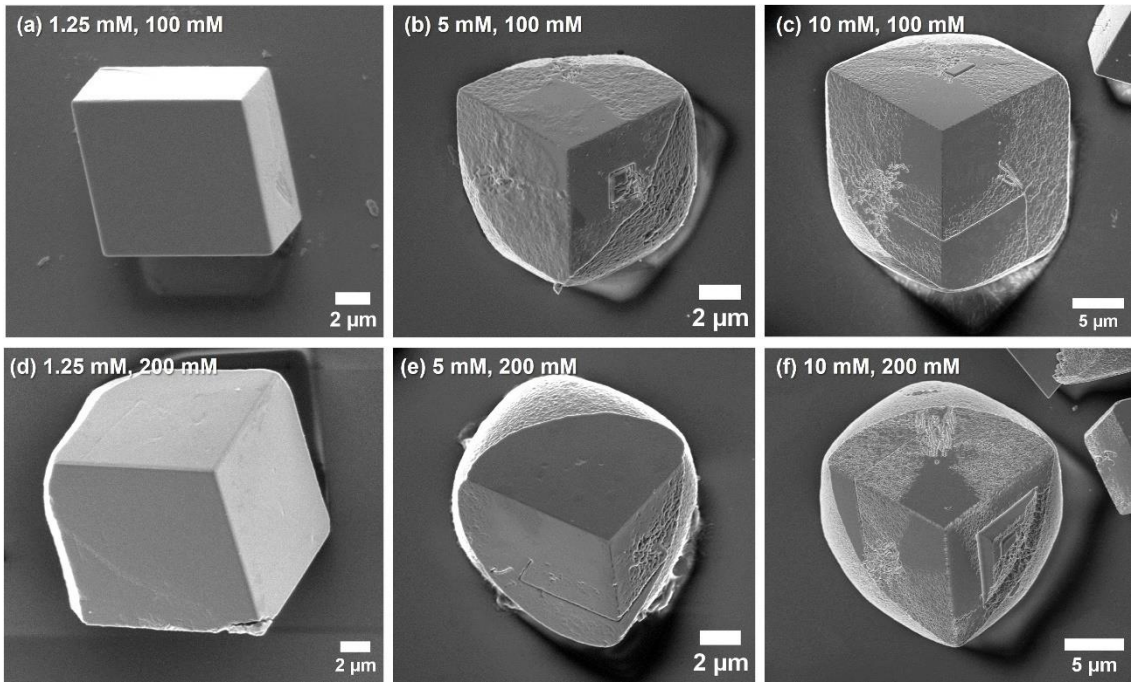


**Figure 3.13 SEM images of Gly-calcite prepared using varying [Gly] and [$Ca^{2+}$].**

Raman spectroscopy confirmed that calcite was obtained (Figure 3.14).

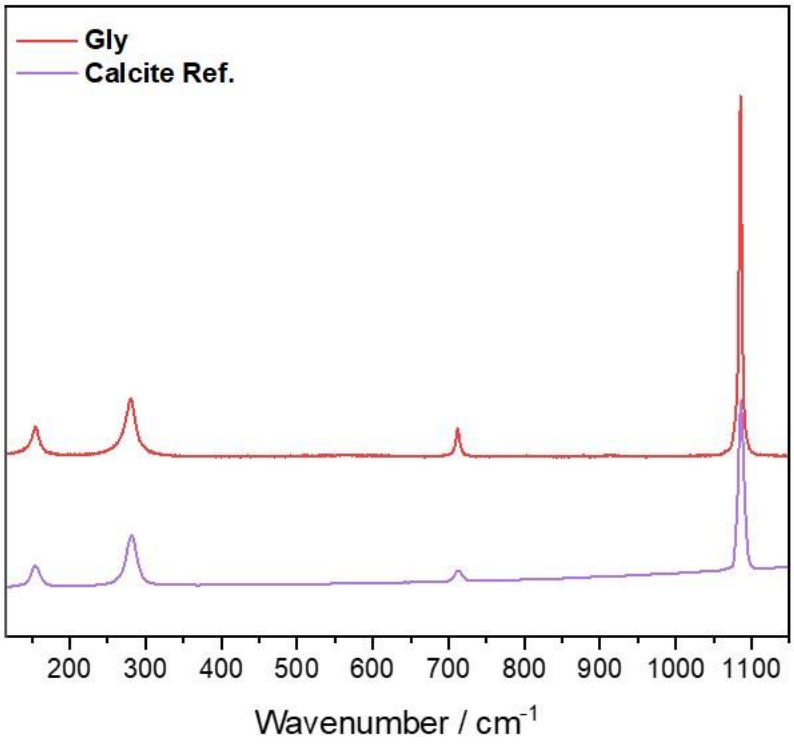


**Figure 3.14 Raman spectra of Gly-calcite, compared with a reference spectrum for calcite obtained from RRUFF[270] (RRUFF ID: 040070).**

The incorporation efficiency of Gly within calcite crystals was quantified, as for Asp-calcite, in mol% for crystals prepared with a range of [$Ca^{2+}$] and [Gly].

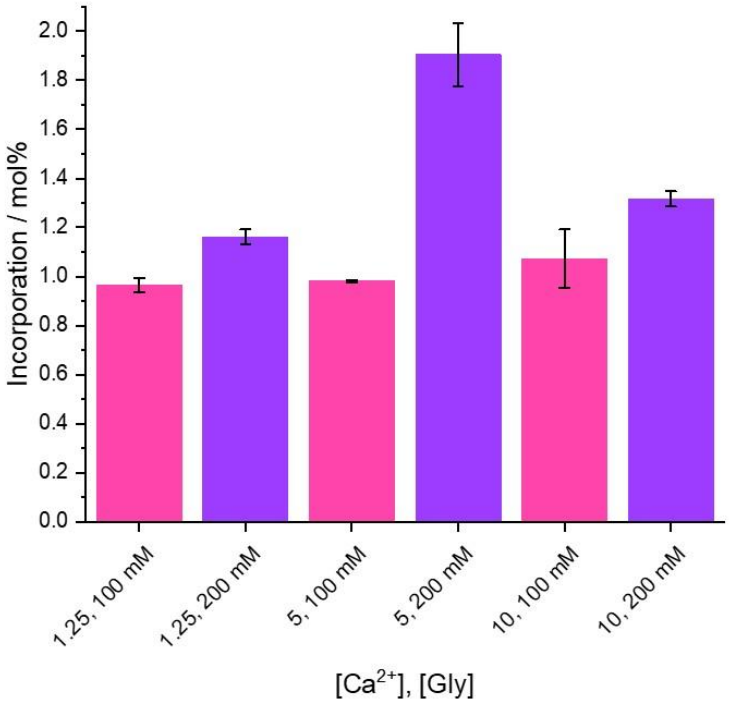


**Figure 3.15 The incorporation efficiency of Gly within calcite crystals in mol% across different [Gly] and [$Ca^{2+}$].**

Higher Gly incorporation occurred with increasing [Gly], though there was a more complicated relationship with [$Ca^{2+}$]. There was little increase in Gly incorporation with increasing [$Ca^{2+}$] at [Gly] = 100 mM. However, there was a drastic increase in incorporation between [$Ca^{2+}$] = 1.25 – 5 mM for [Gly] = 200 mM, before ultimately decreasing between [$Ca^{2+}$] 5 – 10 mM. This change suggests that at [$Ca^{2+}$] = 10 mM the $Ca^{2+}$ ions are so freely available that there is a competition effect, and so less occlusion of Gly is observed. It was also noted during synthesis that very low yields of calcite were obtained using [$Ca^{2+}$] = 1.25 mM, indicating that nucleation was inhibited by the Gly molecules. Overall, the highest level of occlusion (1.89 mol%) was obtained for 5, 200 Gly-calcite, which is slightly greater than for Asp-calcite (1.2 mol%).

### 3.3.1.3 Crystallisation of PS-calcite

Functionalised polystyrene microspheres are commercially available in a variety of sizes. Initial simulations were therefore performed by Dr Gianni Jacucci to determine

the most appropriate size for enhancing light scattering. The amount of scattering generated by a 3D box filled with spherical voids of varying diameter was modelled (Figure 3.16). This showed that the ideal diameter of the voids for maximum scattering was 500 nm. Further simulations testing the ideal packing efficiency showed that the optimum filling fraction of the voids within the simulated crystal was 30 %. Various concentrations of PS were therefore tested to attain this filling fraction experimentally.

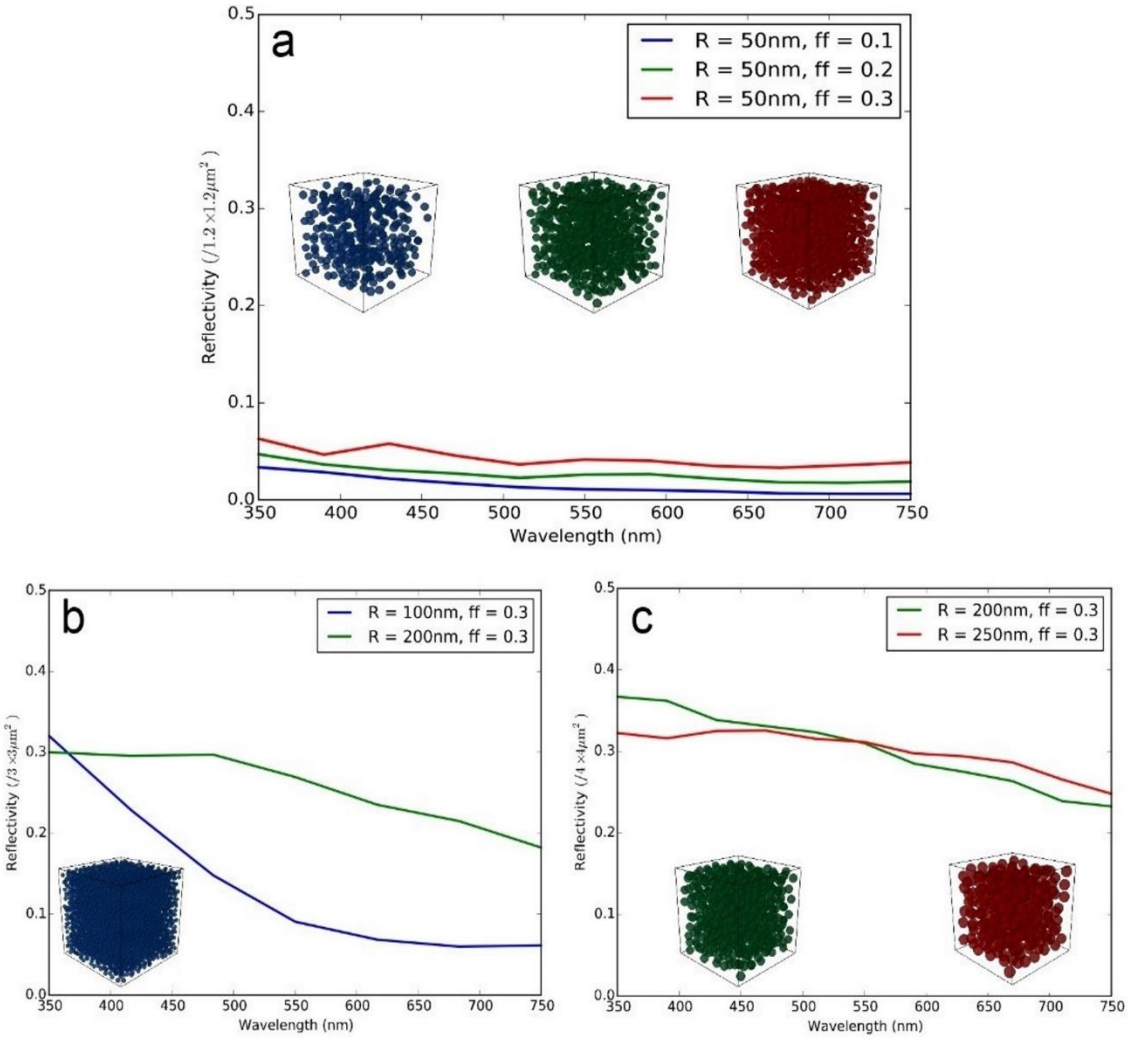


**Figure 3.16 Simulated scattering of voids in a 3D, where R represents the radii of the voids and ff represents the filling fraction, (a) scattering by voids with 50 nm radii and filling fractions of 10 – 30 %, (b) scattering by voids with 100 and 200 nm radii and a filling fraction of 30 %, (c) scattering by voids with 200 and 250 nm with a filling fraction of 30 %.**

Calcium carbonate was precipitated in the presence of PS, using [PS] = 0.005, 0.01, 0.1, 0.5, 1, 2, 3, 4, 5 wt.% and fixed [$Ca^{2+}$] = 1.25 mM. All conditions produced crystals with PS microspheres incorporated onto the external faces (Figure 3.17). At low concentrations of 0.005 and 0.01 wt.%, rhombohedral calcite crystals were obtained. Above these concentrations, the particles became elongated along the [001] direction.

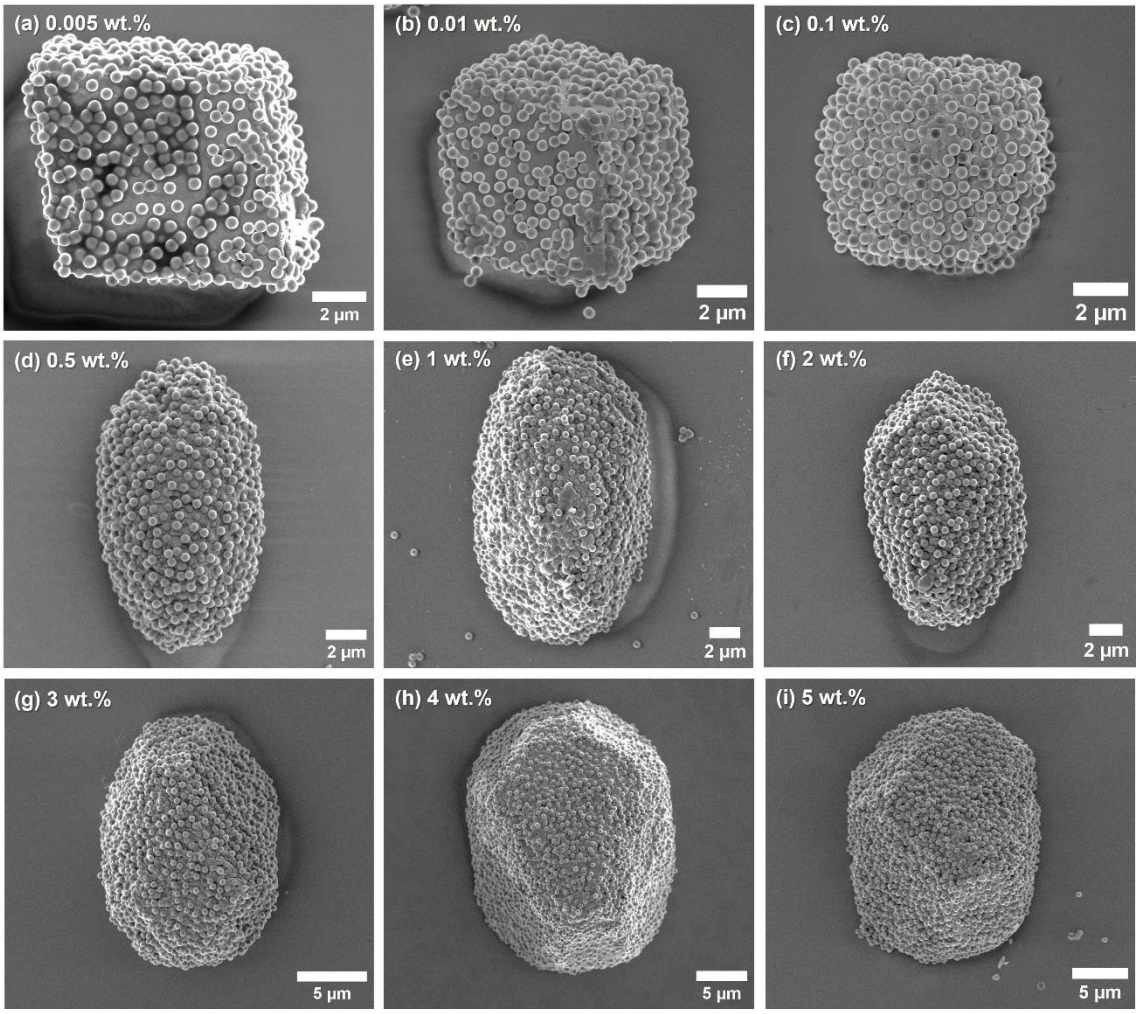


**Figure 3.17 SEM images of PS-calcite prepared with varying [PS].**

The Raman spectrum showed that calcite was produced, however there were several additional peaks present that could be attributed to the occluded PS beads (Figure 3.18).

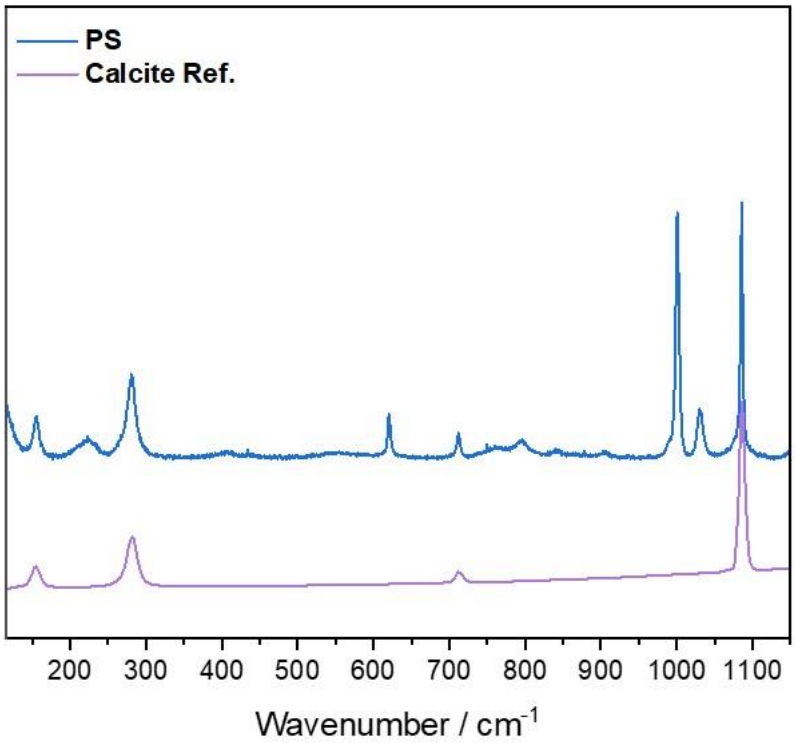


**Figure 3.18 Raman spectra of PS-calcite, compared with a reference spectrum for calcite obtained from RRUFF[270] (RRUFF ID: 040070).**

Quantification using TGA was not performed for PS-calcite as surface bound additives could not be removed from the crystals, which prevented accurate analysis of the incorporation using this method. However, the level of incorporation can be gauged using the porosity analysis described later in this chapter, since the sizes of the pores and the size of individual PS microspheres are comparable.

### 3.3.1.4 Crystallisation of Ves-calcite

Ves-calcite was synthesised by precipitating calcium carbonate in the presence of poly(methacrylic acid)-poly(benzyl methacrylate) (PMAA-PBzMA) diblock copolymer vesicles with sizes 365 ± 120 nm using a direct mixing strategy. Vesicles concentrations of [Ves] = 0.05, 0.1, 0.25 and 0.5 wt.% were employed. Rhombohedral crystals were obtained with modified morphologies and polycrystals were obtained for [Ves] = 0.5 wt.% (Figure 3.19), as shown at lower magnification in Figure 3.20.

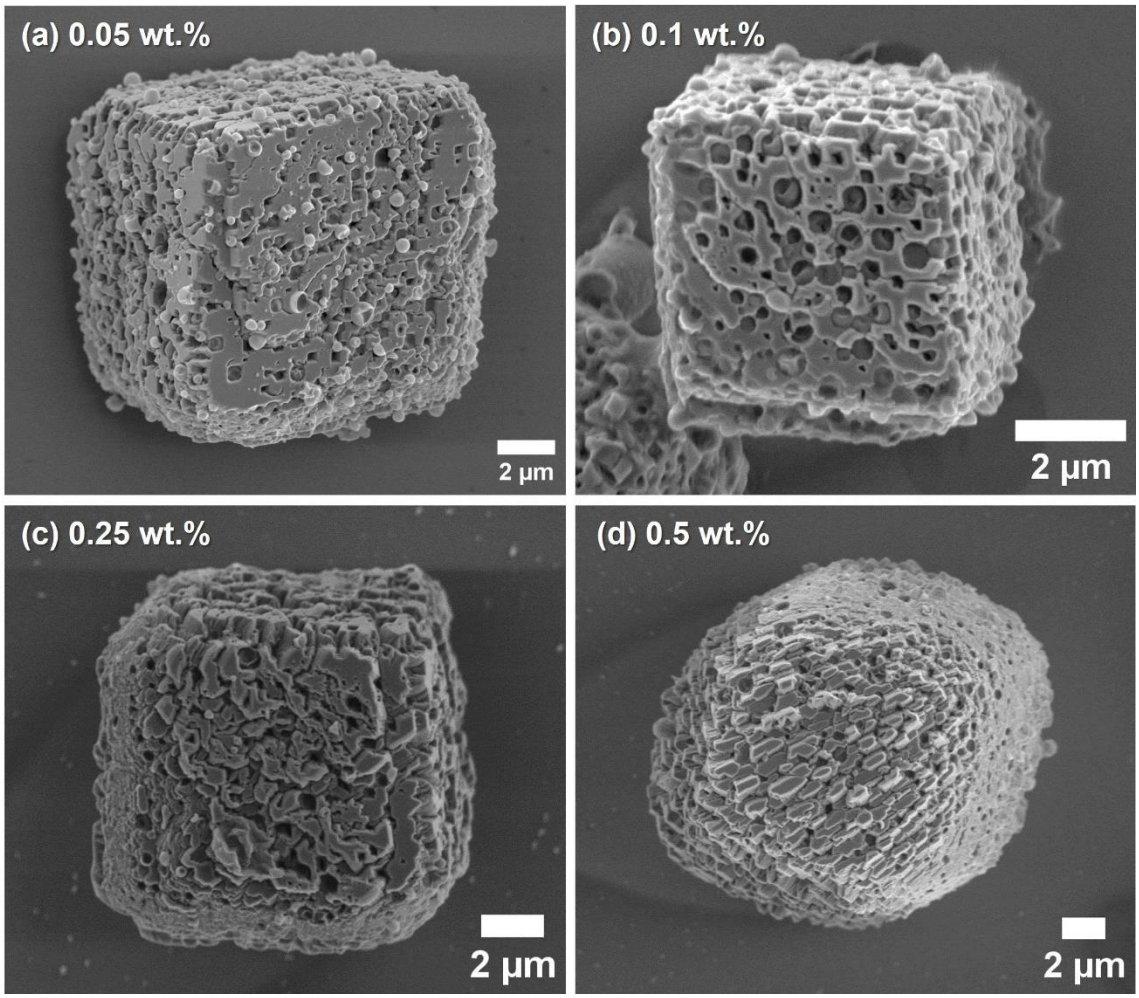


**Figure 3.19 SEM images of Ves-calcite prepared using varying [Ves].**

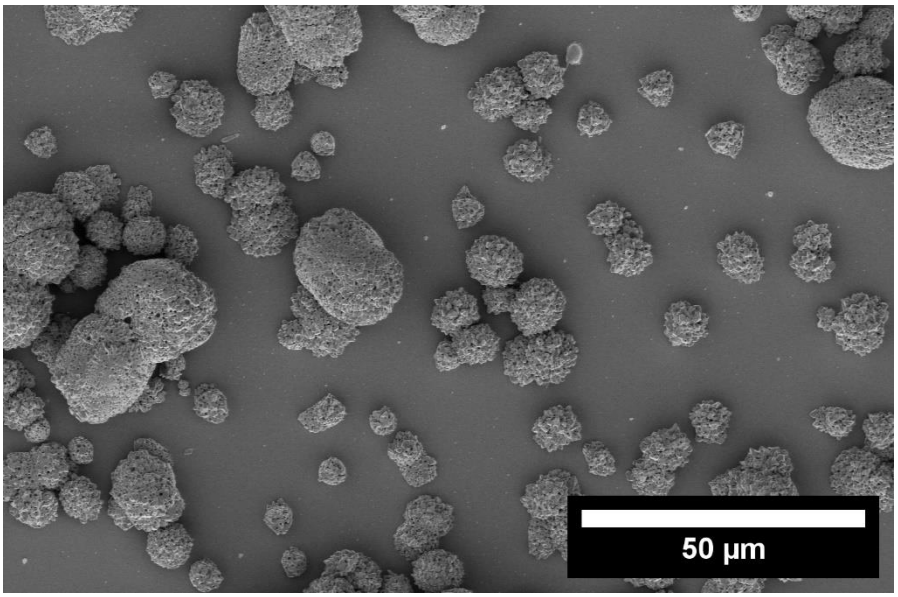


**Figure 3.20 SEM image of Ves-calcite polycrystals using [Ves] = 0.5 wt.%, taken after heating.**

Raman spectroscopy confirmed that calcite was obtained, with some minor additional peaks present due to the occluded vesicles (Figure 3.21).

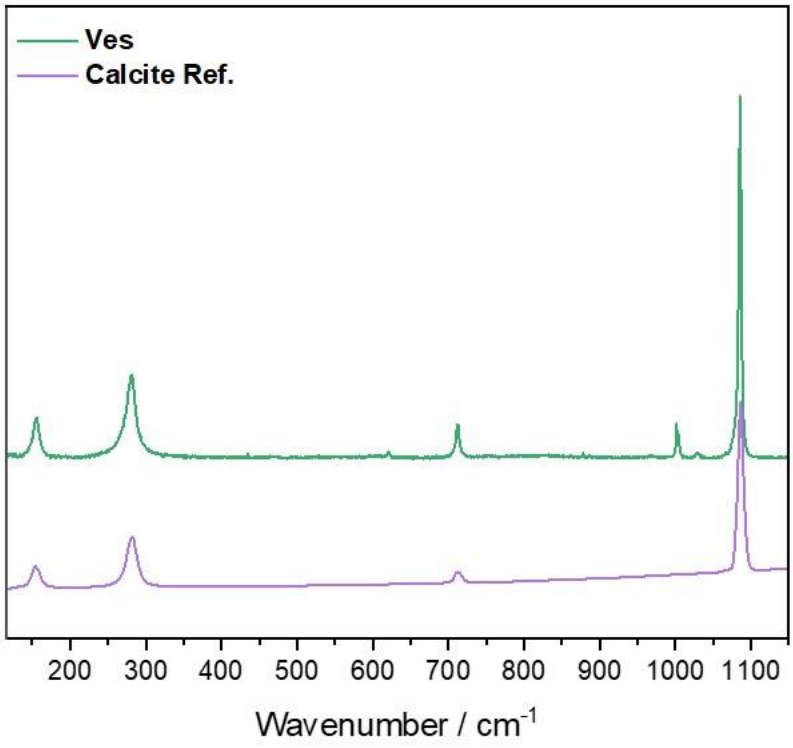


**Figure 3.21 Raman spectra for Ves-calcite, compared with a reference spectrum for calcite obtained from RRUFF[270] (RRUFF ID: 040070).**

As for PS-calcite, the incorporation of Ves-calcite was gauged by porosity analysis described later in the chapter, as surface bound additives could not be removed.

### 3.3.1.5 Crystallisation of PS/Gly-calcite

Calcite was precipitated in the presence of both PS and Gly to determine whether a wider range of pore sizes could be achieved by occluding two additives with contrasting sizes. A fixed [PS] of 1 wt.% was used with [Gly] = 100, 200 mM (Figure 3.22).

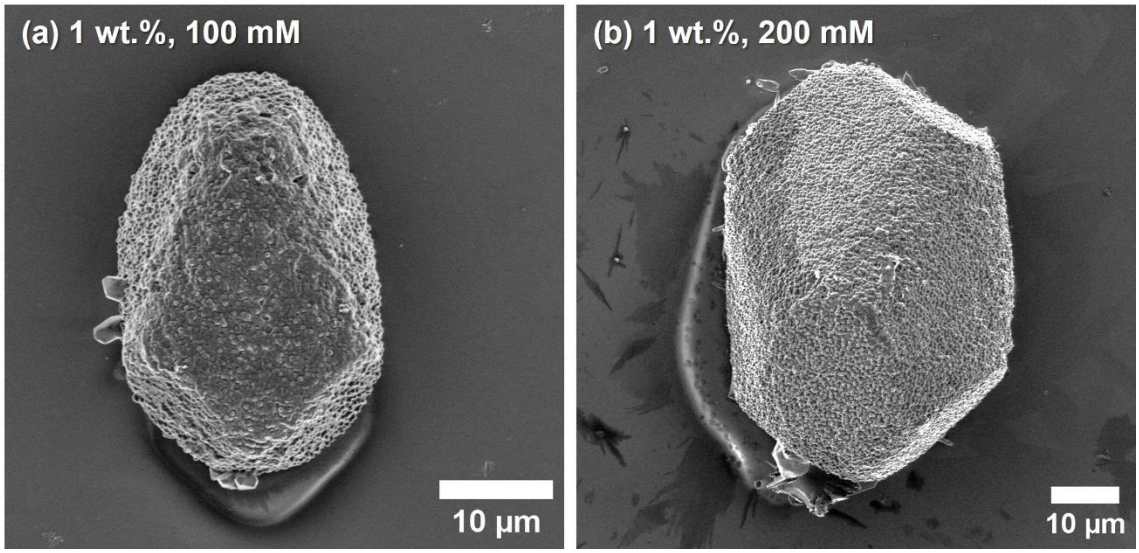


**Figure 3.22 SEM images of PS/Gly-calcite crystals prepared with varying [Gly].**

### 3.3.2 Investigation into the Effect of the Heating Parameters on Porosity

The annealing temperature is critical to the generation of porosity, where it initiates the decomposition of organic additives while avoiding the breakdown of the crystal into calcium oxide. Feasible temperatures fall in the range 200 – 600 °C, as identified using TGA (Figure 3.9) and the literature on thermal degradation of the organic additives used here (discussed in Section 3.2.1.3). Experiments were therefore conducted to determine how the porosity can be controlled within this temperature range, where the ability to tune the pore size distribution and filling fraction is valuable for multiple applications. The effect of the heating rate and annealing time was also investigated.

The annealing experiments were conducted using crystals prepared with [$Ca^{2+}$] = 10 mM and [Asp] = 10 mM, using the heating parameters shown in Table 3.5. Briefly, this explored the effect of 4 different temperatures (300, 400, 500 and 600 °C), 4 different annealing times (10 min, 30 min, 4 hr and 8 hr) and 3 heating rates (1, 5 and 10 °C $min^{-1}$).

Following heating, the samples were allowed to cool to ambient temperature inside the furnace. Cross-sections of the crystals were prepared and imaged using FIB-SEM to assess the porosity, and to analyse the pore size distribution and filling fraction in terms of pore density and pore area.

### 3.3.2.1 Effect of Temperature

The cross-section images in Figure 3.23 show that pores were formed at all temperatures tested. However, they were only uniformly distributed across all areas of the crystal at temperatures above 500 °C. A small number of pores are observable at 300 °C, which are only located within a small region near the top face of the crystal. At 400 °C, the pores are more prevalent, but are localised to the top face and one side. The remaining heating conditions resulted in porosity which presented uniformly across the cross-section.

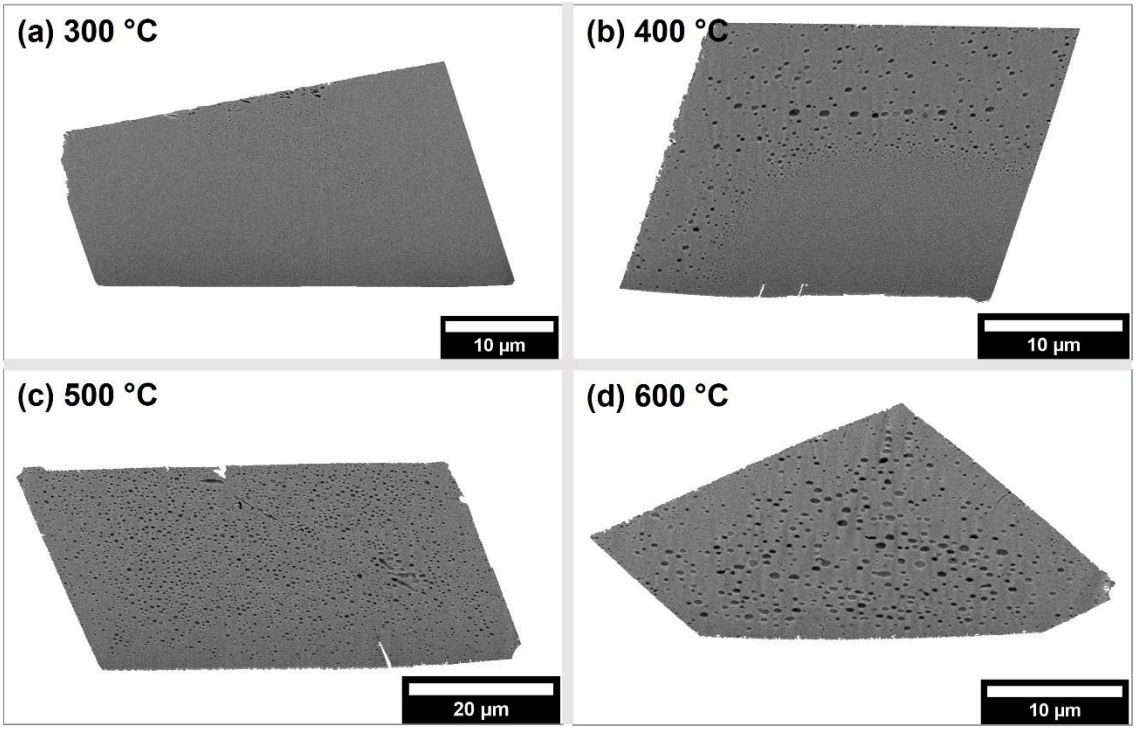


**Figure 3.23 FIB-SEM images of Asp-calcite heated using different temperatures, with a fixed heating rate and heating time length of 5 °C min$^{-1}$ and 30 min.**

The annealing temperature is therefore critical to the generation of uniform porosity. At low temperatures, the pores are only present near the top face of the crystal. They become more abundant in the central and bottom areas of the cross-section as the temperature increases. This indicates that the porosity begins to form at the top face of the crystal. At higher temperatures, this process will occur rapidly such that pores are generated across the entire cross-section within the annealing time. This indicates that for low temperatures, a longer heating time is necessary for widespread pore formation.

The pore size distributions were plotted using violin box plots. The violin box plot incorporates a standard box plot with a population density to provide additional insight into the spread of data[271]. This produces a violin-shaped curve around the box-plot that reflects the shape of the distribution, allowing bimodal, uniform and normal distributions to be distinguished from one another even if the IQR, mean and median are identical. A key advantage of using violin box plots is that they show whether a data population clusters at different values within the IQR, so in this context would reveal whether two distinct pore sizes were formed. Standard box plots were also used to show clearly the IQR and median, which was chosen over mean and standard deviation as a measure of central tendency due to the skewness of the pore size data.

The pore size distribution increases at higher temperatures (Figure 3.24a) as seen in the increase in median pore size with temperature in the range 300 – 500 °C (Figure 3.24b). The IQRs vary between 500 and 600 °C, while there is negligible change in the median in this temperature range. This can be explained using the filling fraction (Figure 3.24c). The pore density increases with temperature until it plateaus at 500 °C, while the pore area increases with every temperature increase. This indicated that additional pores formed but coalesced.

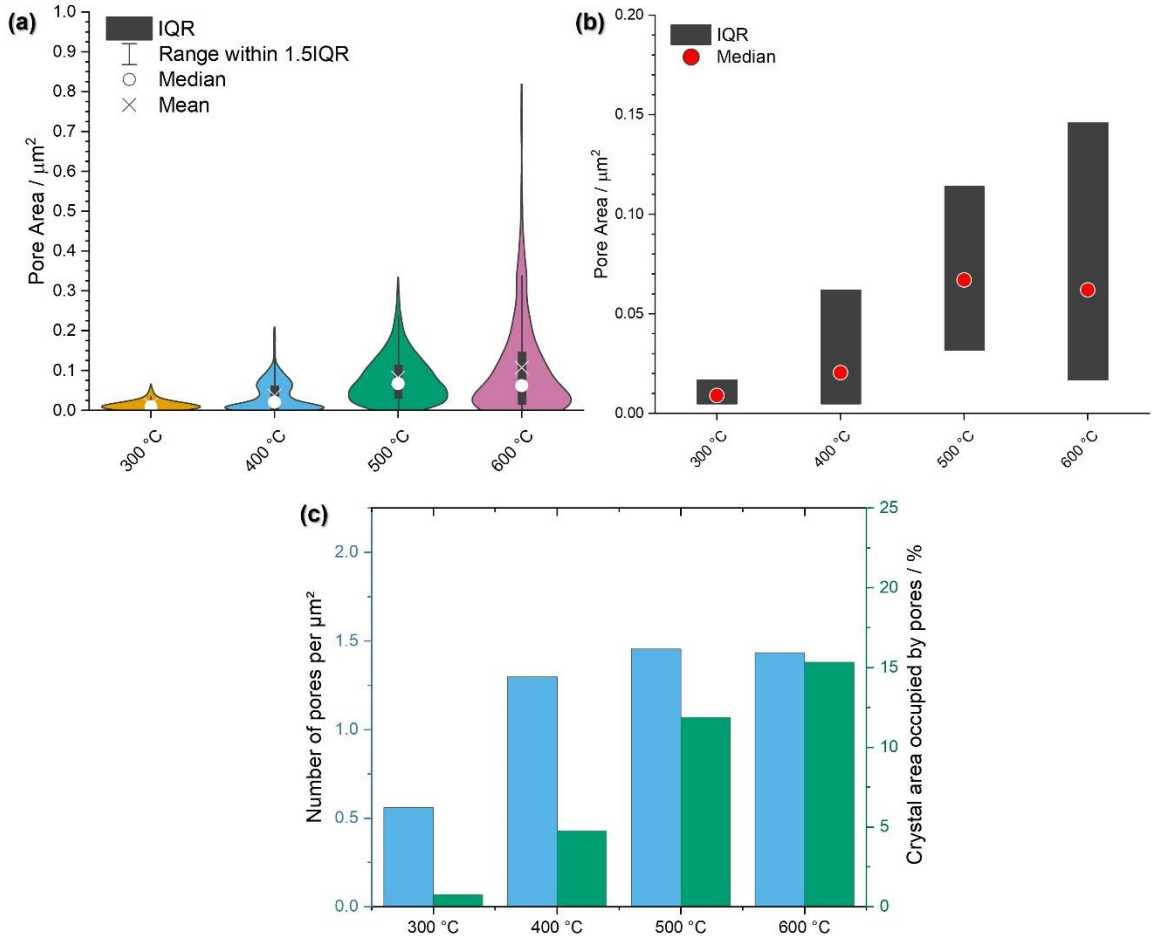


**Figure 3.24 The effect of heating temperature on porosity, (a) violin plot showing the population spread of pore size, (b) box plots of the pore sizes and (c) the filling fraction of pores within the crystal, in terms of pore density ($\mu m^{-2}$) and pore area (%).**

### 3.3.2.2 Effect of Annealing Time

The effect of annealing time (the amount of time that the sample was kept at the target temperature) was studied using a temperature of 500 °C and a fixed rate of 5 °C $min^{-1}$. Initial observations of the FIB-SEM cross-sections showed that all crystals had pores located uniformly through the internal structure, even after only 10 minutes (Figure 3.25).

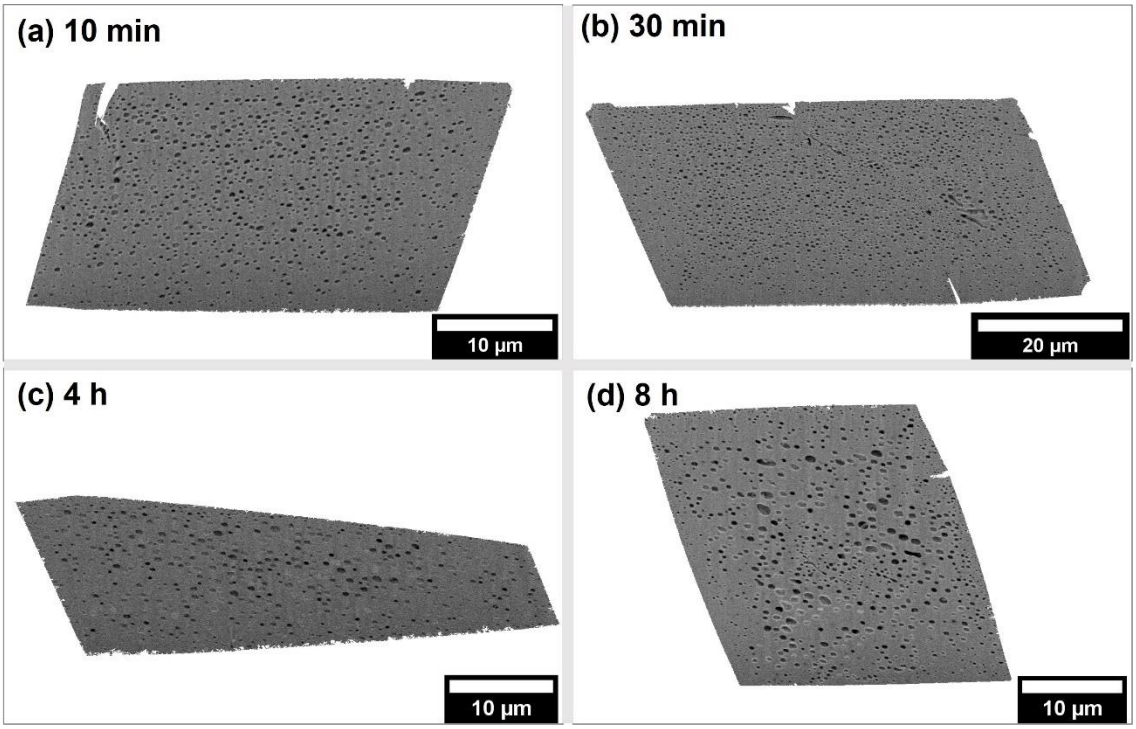


**Figure 3.25 FIB-SEM images of Asp-calcite heated at 500 °C for different time lengths, using a fixed heating rate of 5 °C min$^{-1}$.**

Comparison of the pore size ranges showed a clear distinction for short and long time periods (Figure 3.26a). Crystals heated for 4 – 8 hours possessed a much broader range of pore sizes than those heated for 10 – 30 minutes. This was also the case when comparing median pore sizes (Figure 3.25b), which differed for samples heated for short and long times. This shows that the heating time has a strong influence on the pore size distribution.

The filling fraction also shows two types of behaviour (Figure 3.26c). The pore density and pore area were fairly similar for samples heated for 10 – 30 minutes. Between 30 minutes and 4 hours, the pore density drops and pore area increases. This indicates that both growth and coalescence of the pores occurred. This likely proceeds by the initial growth of pores which eventually merge with neighbouring pores to form a smaller number of larger pores. Between 4 and 8 hours of heating, there is a large increase in the pore area but little change in pore density, suggesting that the pores grew without further coalescence.

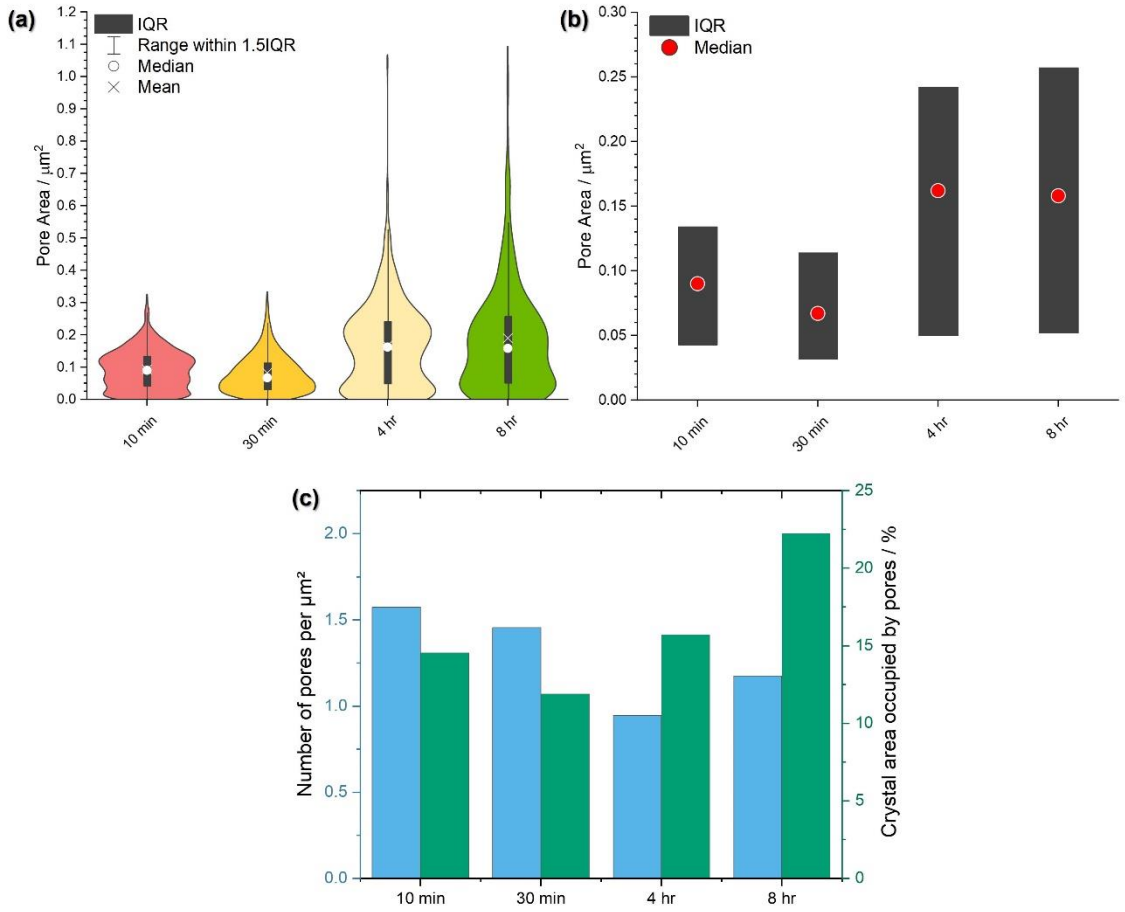


**Figure 3.26 The effect of heating time on porosity, (a) violin plot showing the population spread of pore size, (b) box plots of the pore sizes and (c) pore density (µm$^{-2}$) and pore area (%).**

### 3.3.2.3 Effect of Heating Rate

The effect of the heating rate was firstly investigated using TGA, comparing rates of 1, 5 and 10 °C min$^{-1}$. In the literature, the heating rate has been found to affect the thermal decomposition of $CaCO_3$, where different conversion values occurred between 625 – 850 °C when different heating rates was used[272]. This is a phenomenon known as thermal lag that is underpinned by Newton's Law of Heating/Cooling, which describes the proportional relationship between the temperature rate and the temperature of the sample and environment[273]. It implies that at faster heating rates the sample experiences greater thermal lag. This was also found to be the case for Asp-calcite, where a complete transformation of $CaCO_3$ to CaO occurred at different temperatures depending on the rate used (Figure 3.27). When Asp-calcite was heated at 1 °C min$^{-1}$, this transition began at 570 °C and

completed at 675 °C, compared to 630 – 740 °C for 5 °C $min^{-1}$ and 645 – 770 °C for 10 °C $min^{-1}$. Therefore, the transition occurred at lower temperatures when slower heating rates were used. This behaviour was also observed for the transition that occurred at 450 – 490 °C due to the release of $CO_2$ from the decomposition of occluded Asp molecules. The thermal lag exhibited here, which worsens with increased heating rate, will also be shown when other heating devices are used (such as the muffle furnace) unless there is excellent thermal conductivity and diffusivity[274].

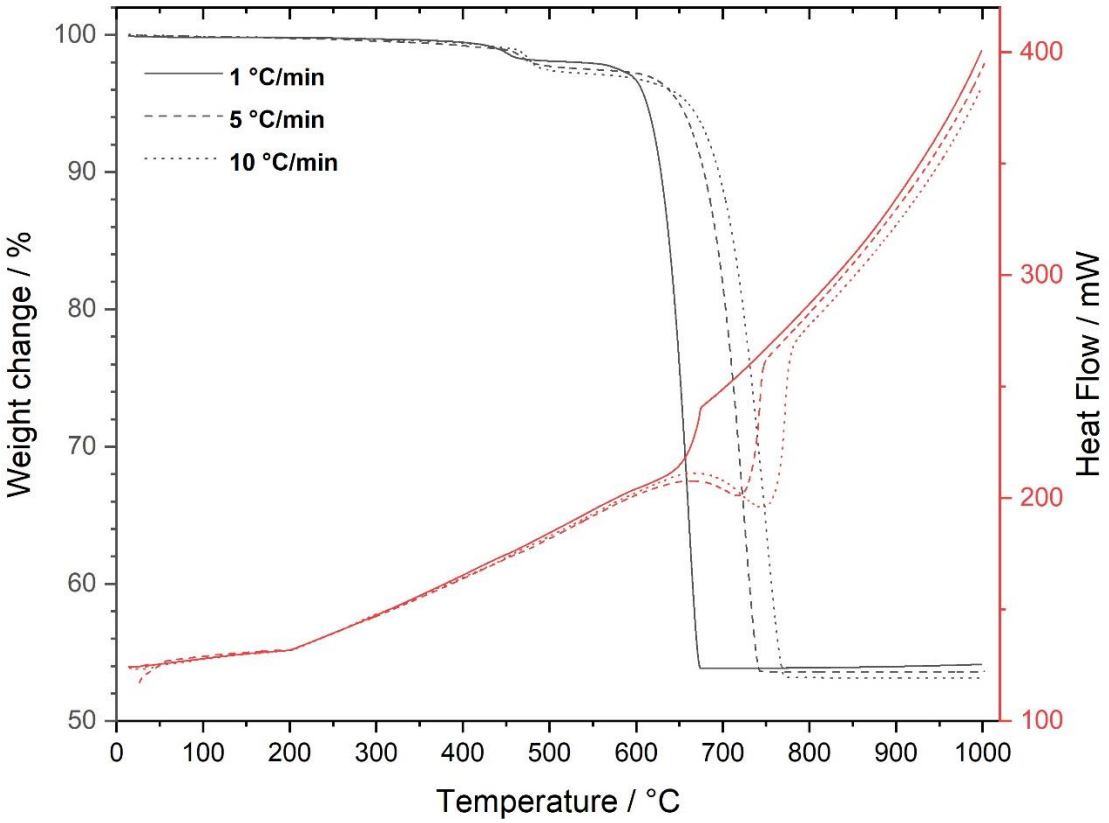


**Figure 3.27 The effect of heating rate on the thermal decomposition of Asp-calcite shown using TGA.**

Calcite was heated at 1, 5 and 10 °C $min^{-1}$ to 500 °C and held at this temperature for 30 minutes. Widespread porosity was observed in crystals prepared at all heating rates (Figure 3.28).

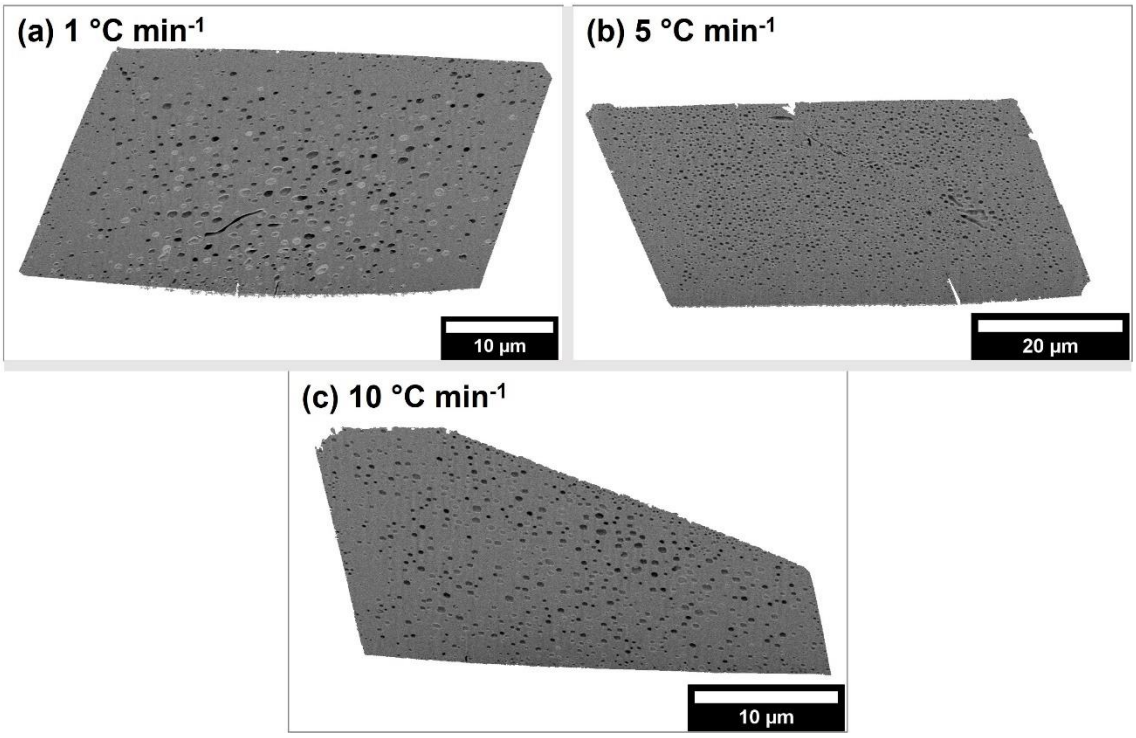


**Figure 3.28 FIB-SEM images of Asp-calcite heated at different heating rates to 500 °C and held for 30 min.**

The slowest heating rate yielded the widest range of pore sizes, with similar ranges obtained using 5 and 10 °C $min^{-1}$ (Figure 3.29a). However, there was little difference in median pore size between heating rates (Figure 3.29b). The pore density increased significantly as the heating rate increased, while there was minimal change in pore area at different rates (Figure 3.29c).

The contrasting pore density and area values combined with the different distribution curves in the violin plots suggest that the heating rate chiefly influences the proportion of large and small pores formed. At slow heating rates, a smaller number of larger pores are formed, whereas at fast heating rates, a larger number of small pores are formed.

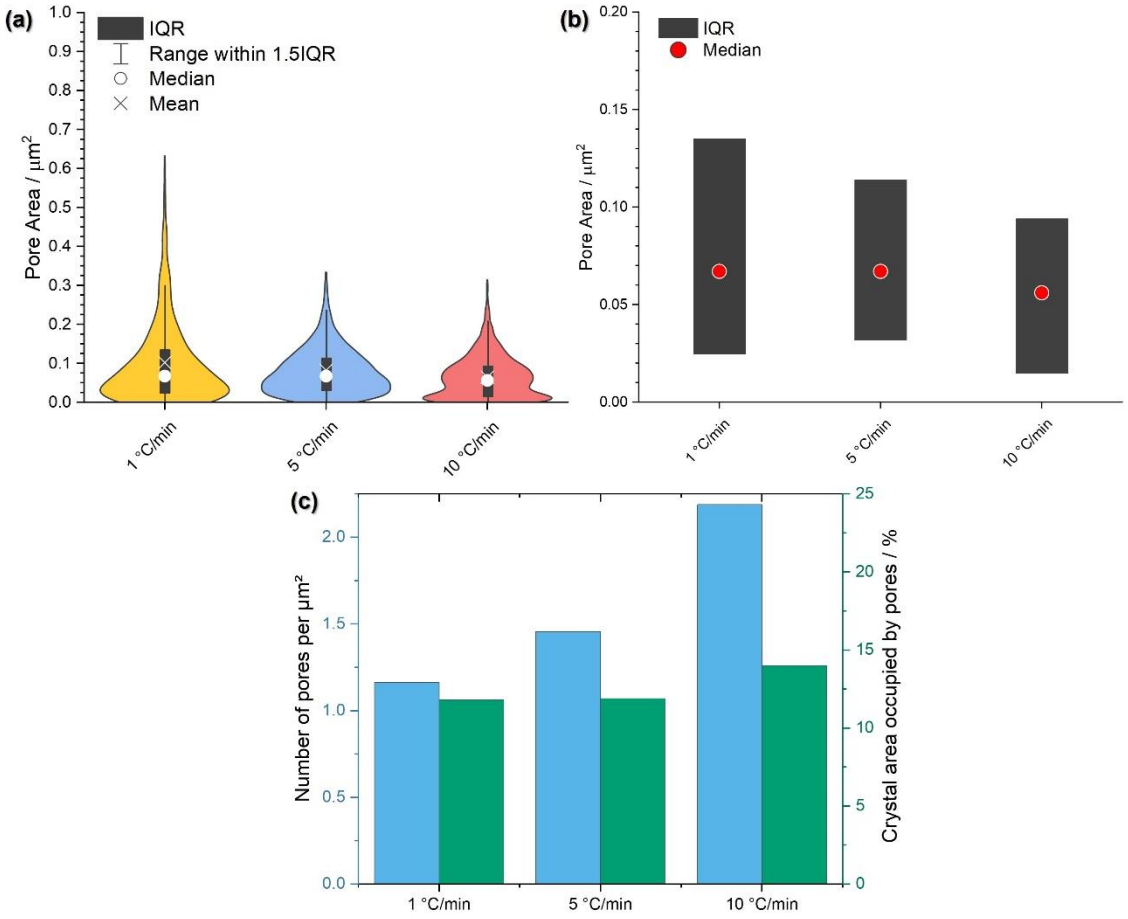


**Figure 3.29 The effect of heating rate on porosity, (a) violin plot showing the population spread of pore size, (b) box plots of the pore sizes and (c) the filling fraction of pores within the crystal, in terms of pore density ($\mu m^{-2}$) and pore area (%).**

### 3.3.2.4 Overview of Heating Conditions

In summary, the properties of the pores formed could be controlled by tuning the heating parameters. Temperatures of 500 °C or greater were required to form uniform porosity (using a heating rate of 5 °C $min^{-1}$ and held for 30 minutes). The sizes of the pores can be controlled via the heating time, where the greatest distribution of pore sizes was formed using long heating periods of 4 – 8 hours (Figure 3.30a). The median pore size roughly doubled in crystals annealed for hours rather than minutes (Figure 3.30b).

The smallest pore size distribution was found for crystal heated at 300 – 400 °C, though both these conditions yielded a non-uniform distribution of pores across the crystal cross-section (Figure 3.30a). The porosity of the crystals obtained using all

other heating conditions had similar pore size distributions and had median pore sizes of 0.05 – 0.1 μm$^2$ (220 – 320 nm diameter) (Figure 3.30b). The pore density was chiefly controlled by the heating rate, where the largest pore density of 2.2 μm$^{-2}$ was obtained using the fastest rate of 10 °C min$^{-1}$ (Figure 3.30c). The pore area increased with annealing time, where the largest pore area of 22 % was observed in crystals heated for 8 hours.

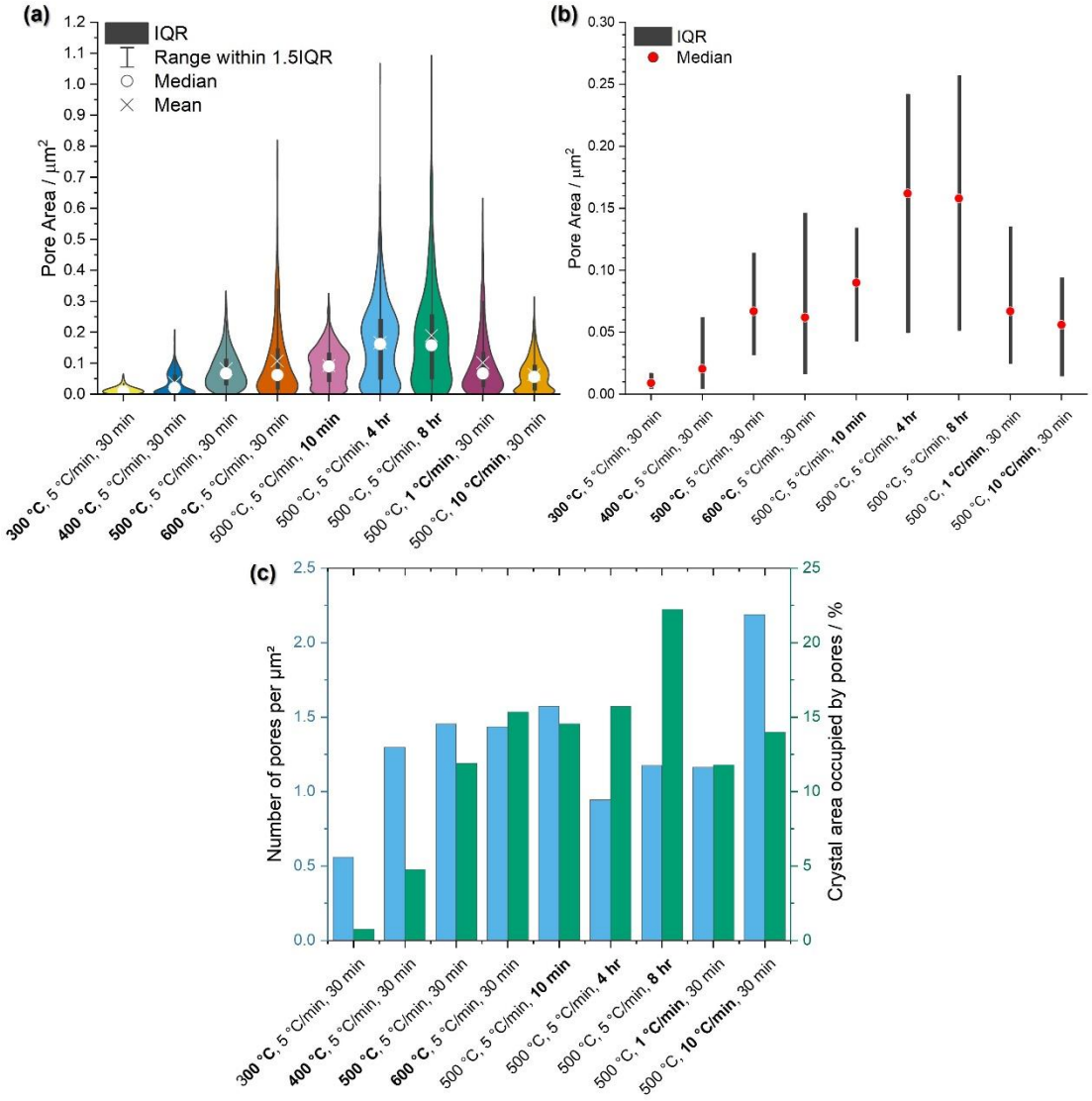


**Figure 3.30 Pore properties for all heating properties tested, (a) violin plot showing the population spread of pore size, (b) box plots of the pore sizes and (c) the filling fraction of pores within the crystal, in terms of pore density (μm$^{-2}$) and pore volume (%).**

Insight into the transformation of the pores during heating can be obtained by considering the change in pore density and area with heating time. The pore density decreased by a third between 30 minutes and 4 hours of heating, while the pore area increased by roughly a third. This could be explained by the expansion of pores over time until neighbouring pores coalesce. Further heating caused the pore area to increase, but gave little change in pore density, indicating that further pore growth occurred between 4 – 8 hours.

As the method of heating is crucial to pore formation, a fixed heating protocol was used to investigate the effect of occluded additives. The chosen protocol was 500 °C, for a period of 30 min using a rate of 5 °C $min^{-1}$, as this condition had the best balance between pore density and area.

#### 3.3.2.5 Low Temperature Heat Treatment

Finally, a low temperature heat treatment was trialled to determine whether long heating periods at low temperatures would also provide uniform porosity. Crystals were heated at 5 °C $min^{-1}$ to 250 °C and were then held at this temperature for 3 hours.

The cross-section for this sample showed that pores were uniformly distributed across the crystal (Figure 3.31). This shows that uniform porosity can be achieved by substituting a low temperature and long heating time for a high temperature and short incubation time.

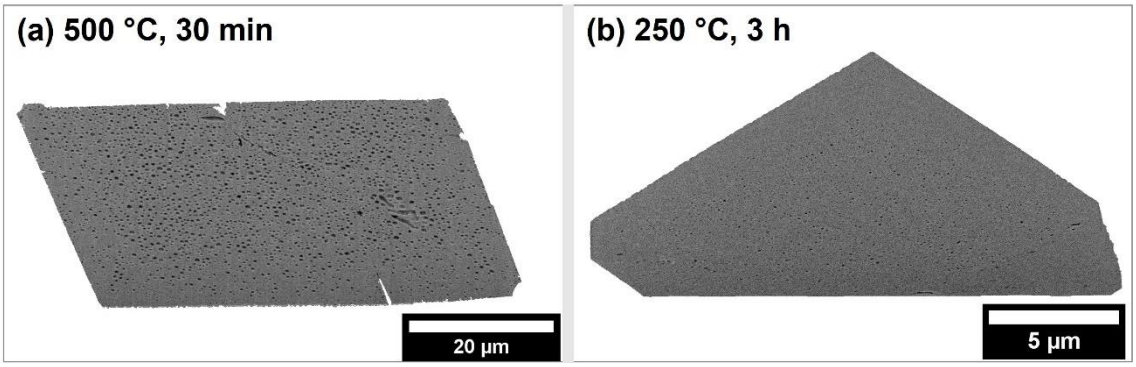


**Figure 3.31 SEM images of Asp-calcite cross-sections prepared by FIB-SEM, comparing low and high temperature heating regimes.**

The porosity was compared with that of crystals prepared using the high temperature regime (500 °C, 30 min, 5 °C $min^{-1}$). The pore size distributions were very different

between the high and low temperature regimes (Figure 3.32a), where the low temperature regime yielded much smaller pores with a very narrow size distribution (Figure 3.32b). The filling fractions were also very different, where the pore density was much higher for the low temperature regime. At 4.5 $\mu m^{-2}$ this was almost twice the value of all other heating conditions trialled. However, the pore area was much larger for the high temperature heating regime. This suggests that although the low temperature heating regime generates a higher pore density, they are so small that the pore area is not comparable to that of the high temperature sample.

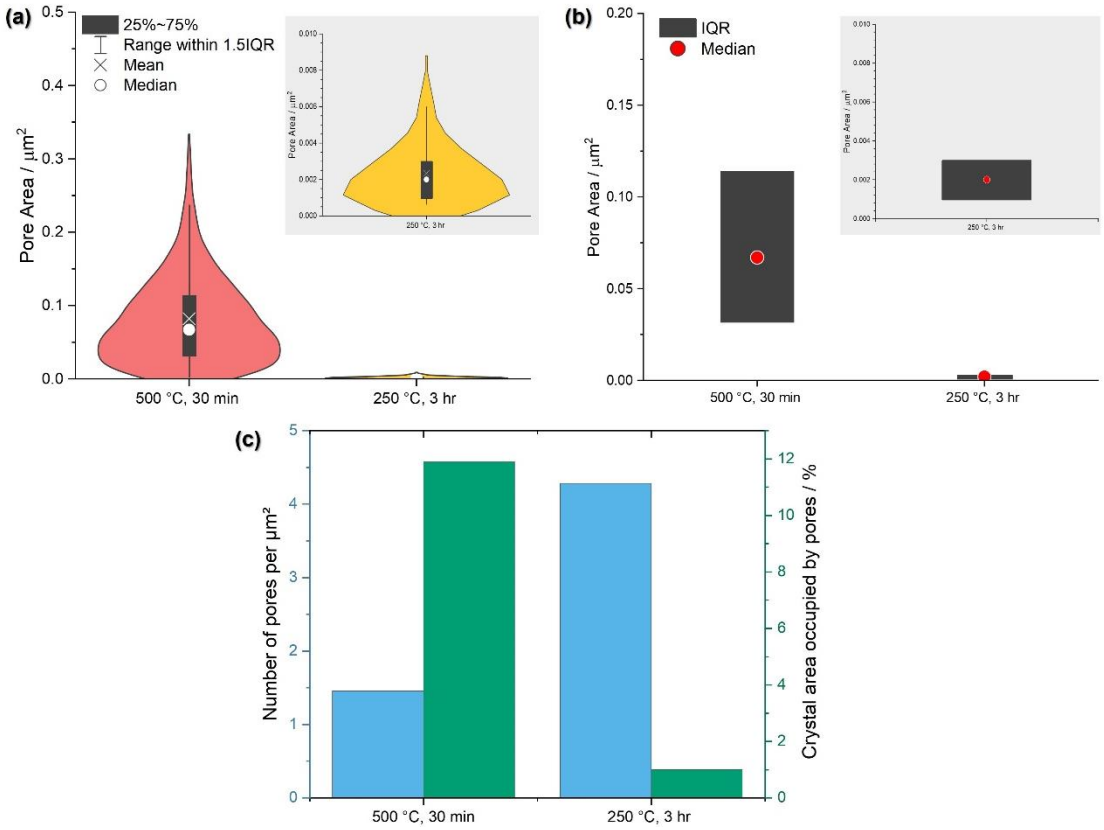


**Figure 3.32 Comparison of pore properties for high and low temperature heating regimes, (a) violin plot showing the population spread of pore size, (b) box plots of the pore sizes and (c) the filling fraction of pores within the crystal, in terms of pore density ($\mu m^{-2}$) and pore area (%).**

In summary, judicious balancing of the heating parameters can ensure that porosity is uniform throughout the calcite crystal even at low temperatures. Contrasting pore properties were obtained between the high and low temperature heating regimes, demonstrating how the porosity can be controlled by tuning the heating parameters.

### 3.3.3 Analysis of Porosity of Annealed Additive/Calcite Crystals

#### 3.3.3.1 Annealed Asp-calcite

The crystals were heated to remove Asp using a heating rate of 5 °C $min^{-1}$ until they reached 500 °C where they were incubated for 30 mins. After heating, the crystals were inspected using OM in reflectance mode (Figure 3.33) and FIB-SEM to examine their porosity (Figure 3.34). The OM images showed that crystals with higher [Asp] and [$Ca^{2+}$] appeared bright white, though there was a yellow hue to the 10, 50 mM Asp-calcite crystals. The cross-section images showed that all conditions yielded porous crystals in which the pores were uniformly distributed.

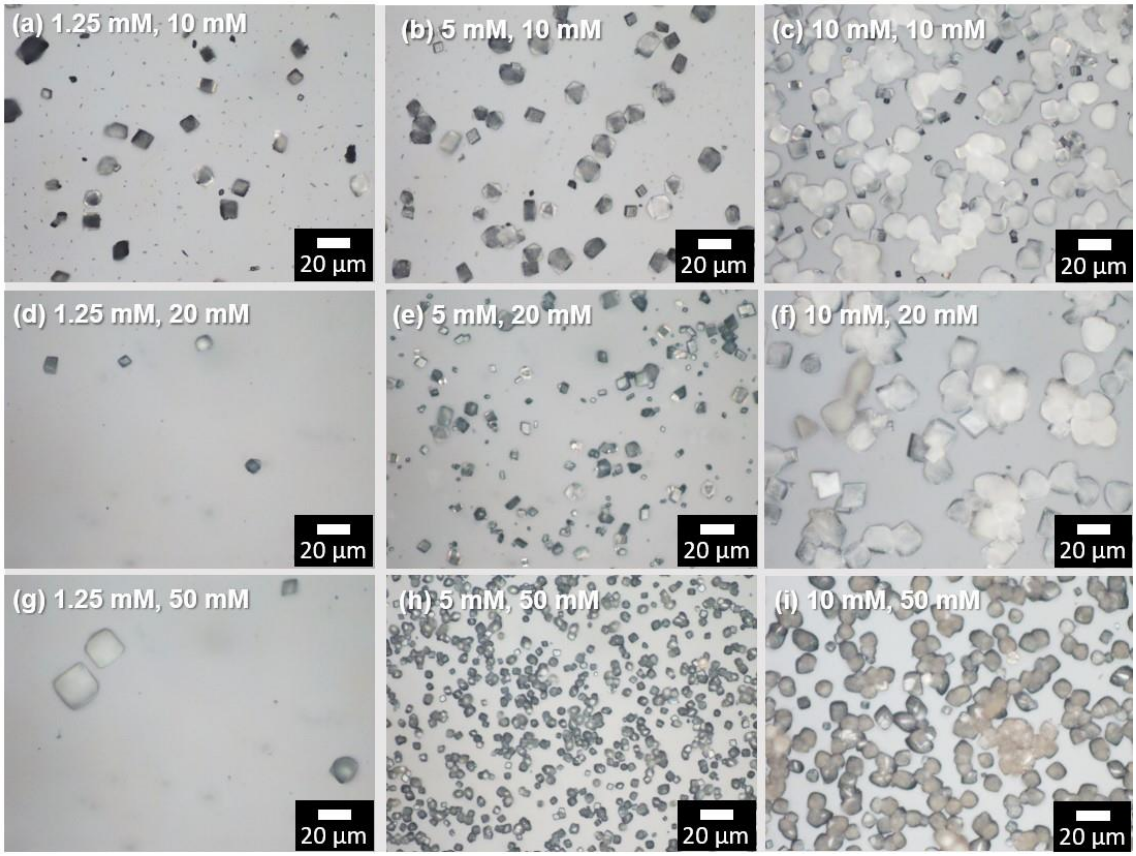


**Figure 3.33 OM images of Asp-calcite after heating, taken in reflection mode.**

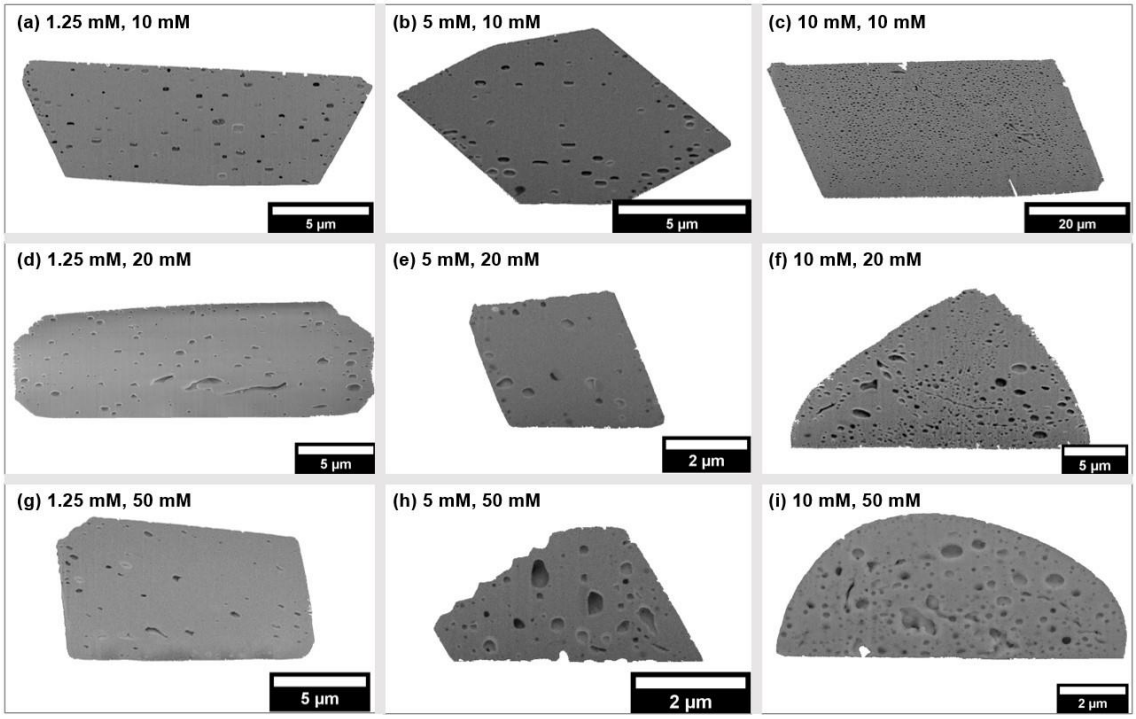


**Figure 3.34 SEM images of Asp-calcite cross-sections prepared using FIB-SEM, annotated with [$Ca^{2+}$], [Asp].**

Porosity analysis showed that the pore size distribution varied in crystals prepared at different [$Ca^{2+}$] and [Asp] (Figure 3.35). However, it is difficult to identify clear trends in the pore size with [$Ca^{2+}$] and [Asp]. Increasing [Asp] for samples with [$Ca^{2+}$] = 1.25 mM led to an increase in median pore size, whilst this brought about a decrease in median for those with [$Ca^{2+}$] = 5 and 10 mM.

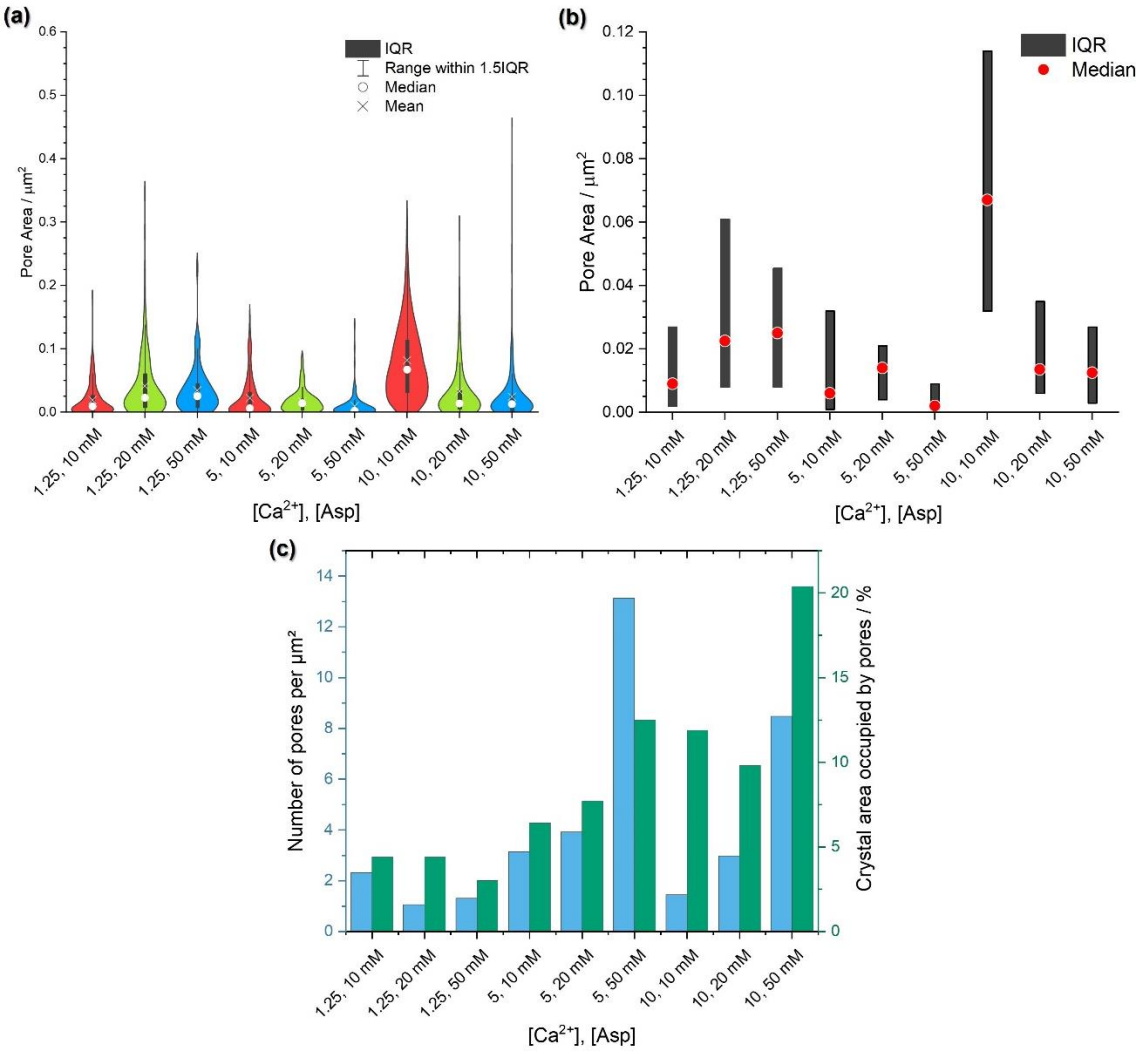


**Figure 3.35 The effect of [$Ca^{2+}$], [Asp] on pore properties of Asp-calcite heated at using the high temperature heating regime, (a) violin plot showing the population spread of pore size, (b) box plots of the pore sizes and (c) the filling fraction of pores within the crystal, in terms of pore density (µ$m^{-2}$) and pore area (%).**

The pore density and pore area generally increased with increasing [Asp] for [$Ca^{2+}$] = 5 and 10 mM. This indicates that more pores were formed with increasing [Asp]. Once again, this trend does not fit with the data for [$Ca^{2+}$] = 1.25 mM, where the pore density and area decreased with increasing [Asp]. The decrease in pore area and volume with [Asp] for [$Ca^{2+}$] = 1.25 mM suggests that fewer pores are formed with increasing [Asp] at this [$Ca^{2+}$].

Considering the effect of [$Ca^{2+}$] on samples with fixed [Asp], the pore area increased with increasing [$Ca^{2+}$]. However, the pore density increased with [$Ca^{2+}$] between 1.25

and 5 mM, while decreasing between 5 and 10 mM. This could be due to higher levels of occlusion at 10 mM, increasing the likelihood of pores forming and coalescing.

Overall, increasing [Asp] created more pores when higher [$Ca^{2+}$] was used, but the opposite trend was observed at low [$Ca^{2+}$]. There was no clear trend for the relationship of [$Ca^{2+}$] with pore size, but the evidence suggested that increasing [$Ca^{2+}$] led to more pores until [$Ca^{2+}$] = 10 mM. At this concentration the pore area increased while the pore density fell, indicating that additional pores were formed but that some coalescence also occurred.

The composition of the Asp-calcite crystals following heating was checked using Raman spectroscopy (Figure 3.36). This was not possible for all samples due to the highly scattering nature of the crystals, which caused saturation of the detector at > 50,000 counts using low laser power settings (at very low laser power, the signal became inadequate with an unacceptably low signal to noise ratio). The Raman spectrum obtained for Asp-calcite after heating showed a very small increase in the contribution from Asp around 550 $cm^{-1}$ and all calcite peaks were present. There would not be any indication of whether calcite had begun to decompose and produce CaO, as CaO is not Raman active. However, this is not expected according to the thermal decomposition profile obtained using TGA, which shows decomposition occurring at 630 – 740 °C when heating at a rate of 5 °C $min^{-1}$ (Figure 3.27). In future work, in-situ heating in TEM of calcite composite crystals could be conducted to determine if CaO was produced and whether this occurred locally at pore sites.

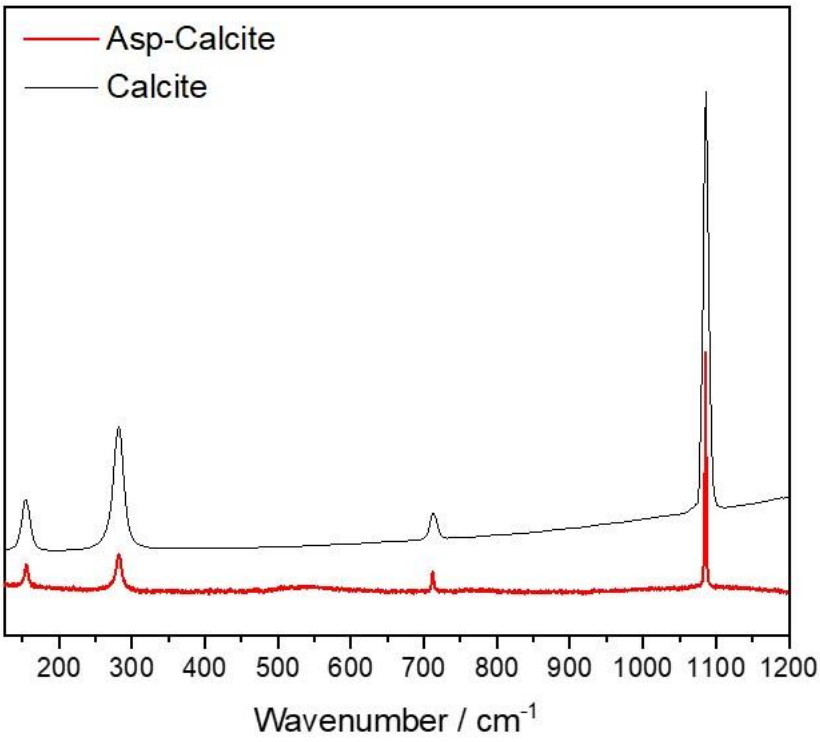


**Figure 3.36 Raman spectrum of Asp-calcite, prepared using [$Ca^{2+}$] = 1.25 mM and [Asp] = 10 mM, after heating for 30 min at 500 °C using a heating rate of 5 °C $min^{-1}$, compared with a reference spectrum for calcite obtained from RRUFF[275] (RRUFF ID: 040070).**

### 3.3.3.2 Annealed Gly-calcite

Gly-calcite was annealed and observed using OM (Figure 3.37) and the cross-section examined using FIB-SEM (Figure 3.38). As for Asp-calcite, the annealed crystals appeared white under OM but the 10, 200 mM Gly-calcite crystals appeared slightly yellow. The porosity was widespread through the crystal for all samples excluding 1.25, 200 Gly-calcite, where pores were localised towards the base and one side of the crystal.

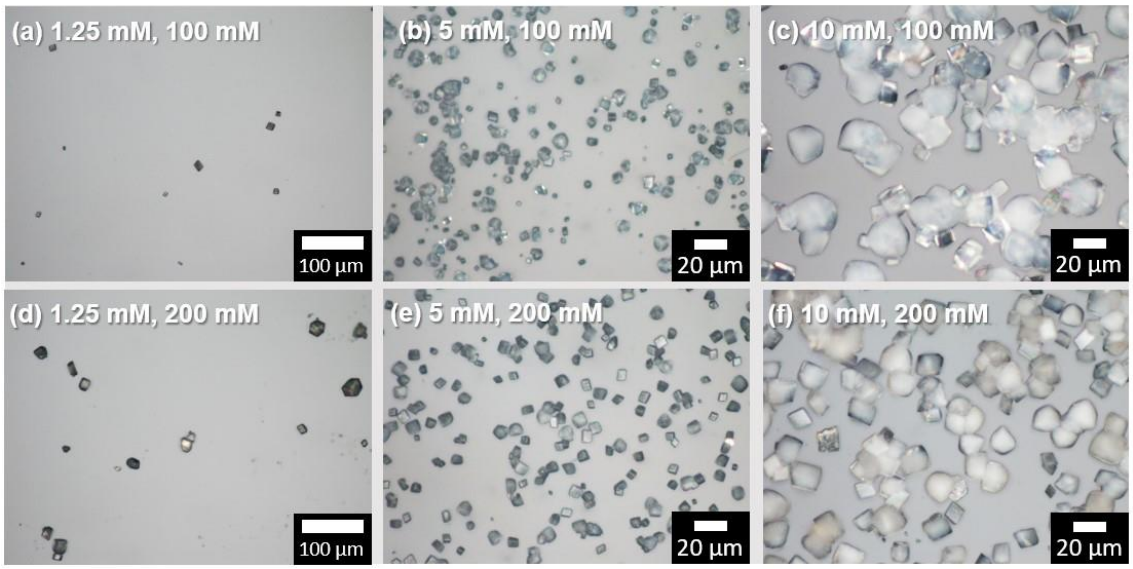


**Figure 3.37 OM images of Gly-calcite after heating, measured in reflection mode.**

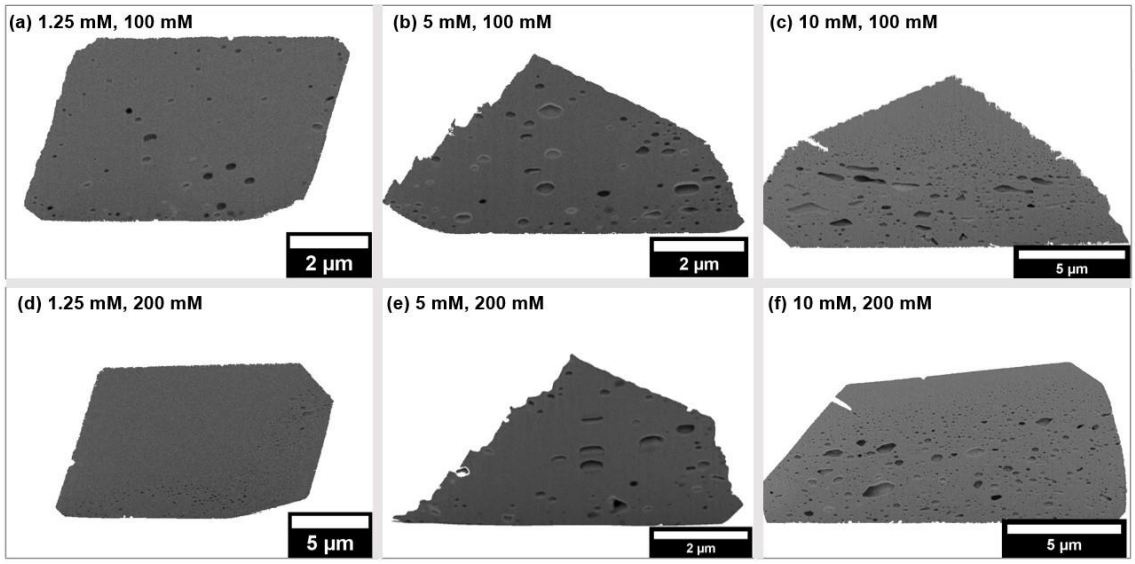


**Figure 3.38 SEM images of Gly-calcite cross-sections prepared using FIB-SEM, annotated with [$Ca^{2+}$], [Gly].**

Overall, the spread of pore sizes did not vary much between different [$Ca^{2+}$] and [Gly] (Figure 3.39a). The median pore size generally decreased with increasing [Gly] and [$Ca^{2+}$] (Figure 3.39b) while both pore density and area increased with increasing [$Ca^{2+}$] (Figure 3.39c). This shows that more pores formed at higher [$Ca^{2+}$]. On the other hand, increasing [Gly] resulted in a smaller pore area, while the pore density differed with [$Ca^{2+}$]. At [$Ca^{2+}$] = 1.25 and 5 mM, pore density increased with [Gly], whereas it decreased with [Gly] for [$Ca^{2+}$] = 10 mM. This suggests that greater

numbers of smaller pores were obtained by increasing [Gly], with the exception of $[Ca^{2+}]$ = 10 mM where increasing [Gly] led to fewer, smaller pores.

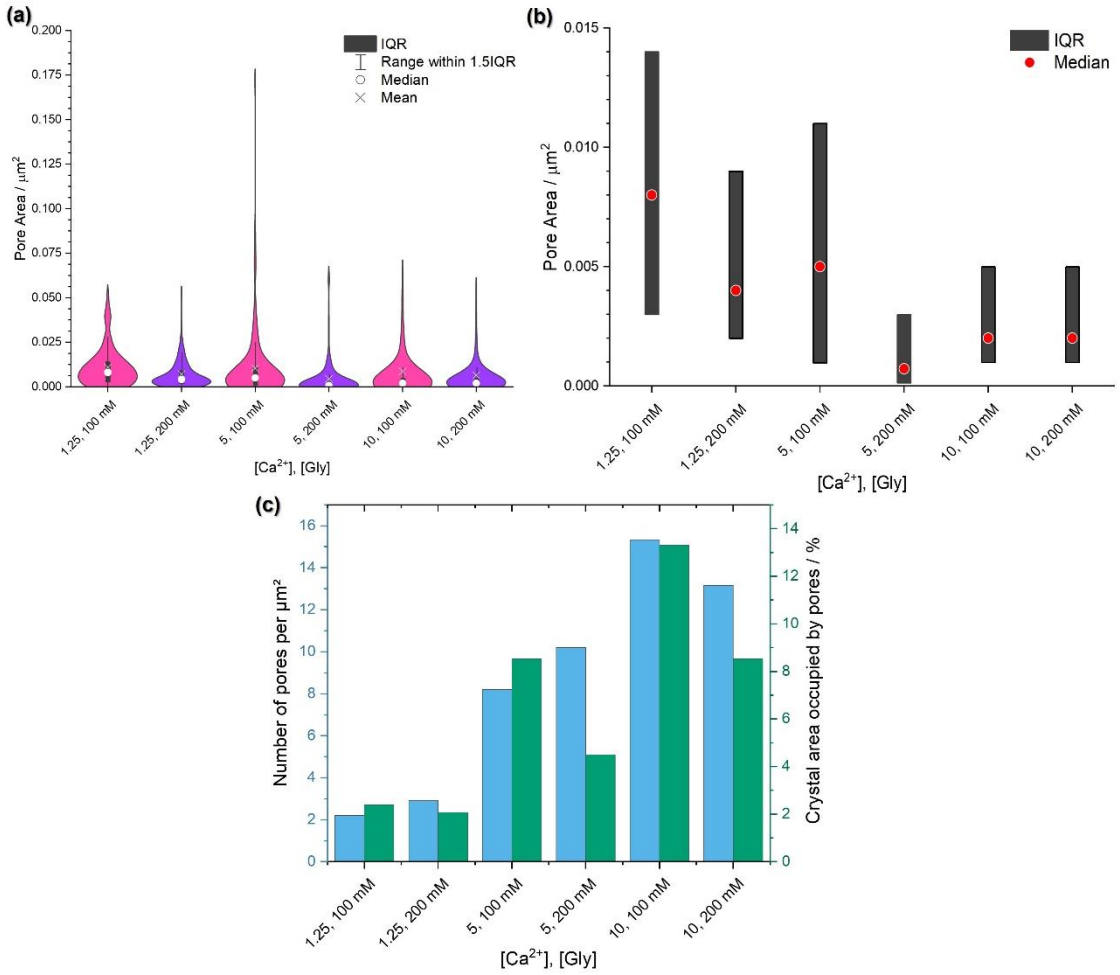


**Figure 3.39 The effect of $[Ca^{2+}]$, [Gly] on pore properties of Gly-calcite annealing using the high temperature heating regime, (a) violin plot showing the population spread of pore size, (b) box plots of the pore sizes and (c) the filling fraction of pores within the crystal, in terms of pore density ($\mu m^{-2}$) and pore area (%).**

### 3.3.3.3 Annealed PS-calcite

Annealed PS-calcite was examined using OM (Figure 3.40) and cross-sections were obtained using FIB-SEM (Figure 3.41). The crystals observed were yellow in colour for all [PS] ≥ 0.1 wt.%. The cross-sections showed that uniform occlusion was achieved for all samples but those prepared using [PS] of < 0.1 wt.%. Very few

microspheres are incorporated into crystals with rhombohedral morphologies, while successful occlusion occurred in crystals with elongated morphologies.

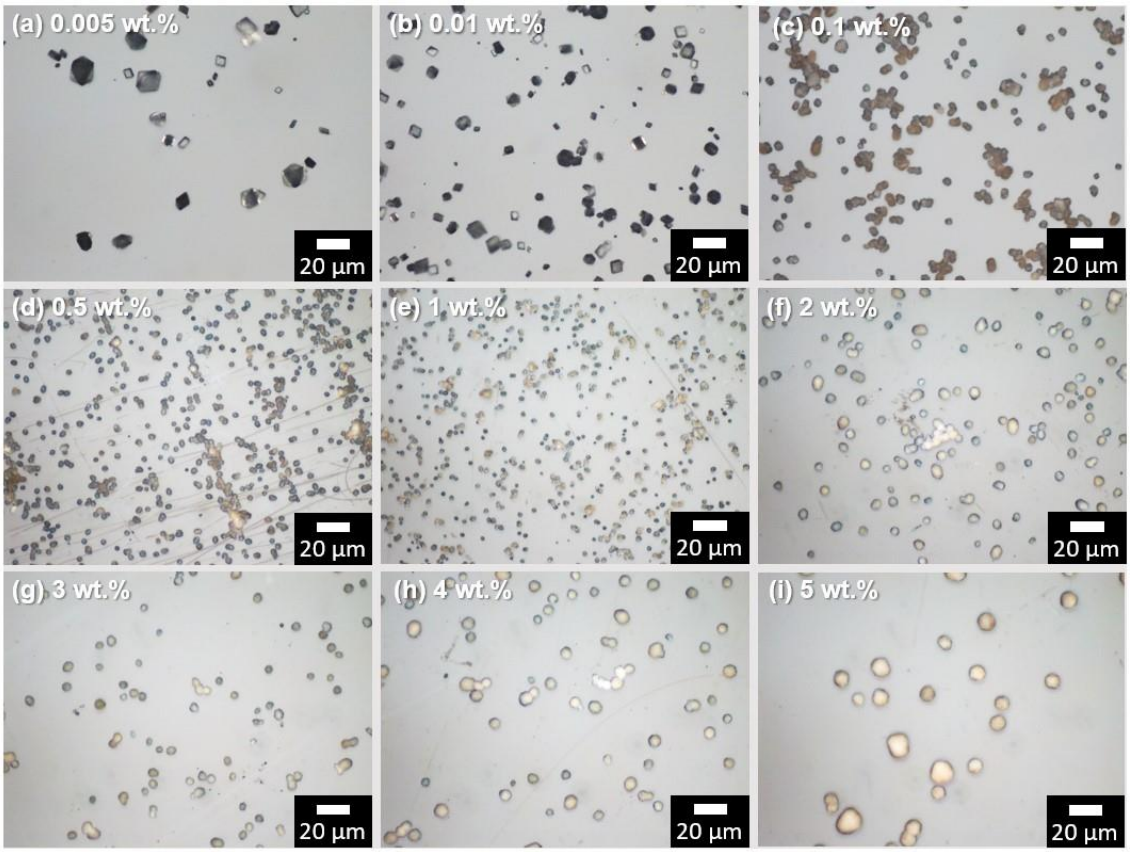


**Figure 3.40 OM images of PS-calcite after heating, taken in reflection mode.**

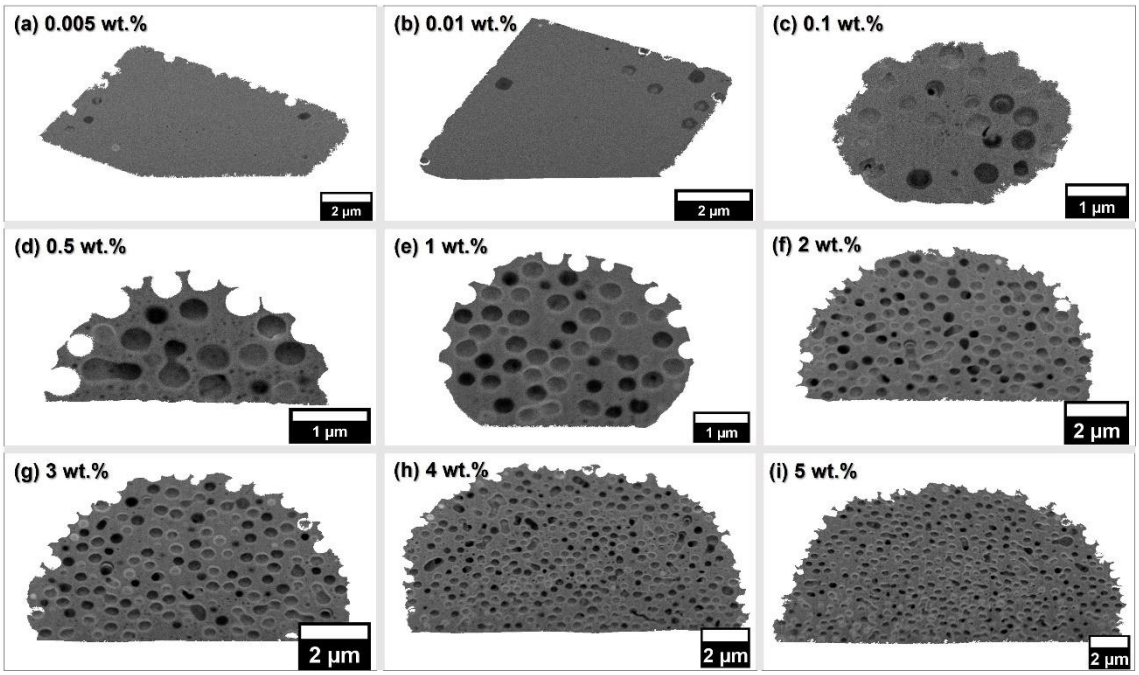


**Figure 3.41 SEM images of PS-calcite cross-sections prepared using FIB-SEM, annotated with [PS].**

The spread of pore sizes in PS-calcite precipitated with different [PS] fall into 2 distinct groups (Figure 3.42a). For [PS] ≤ 1 wt.%, the pore sizes are mostly within a small range centred around the mean and median. However for [PS] ≥ 2 wt.% there are two clear clusters of pore sizes, leading to a wider IQR and larger median (Figure 3.42b). The second larger cluster of pore areas can be attributed to two or more pores having coalesced. This results in a lower pore density but preserves the pore area. This is shown in Figure 3.42c, where the number density of pores is highest for [PS] = 0.1 wt.% and decreases as [PS] increases. This is due to increased incorporation of PS microspheres with increasing [PS], leading to their closer packing within the crystal structure and a higher likelihood of multiple particles being in contact. The similarity in pore properties at [PS] ≥ 2 wt.% indicates that the occlusion of [PS] within calcite is saturated at this level, and increasing the concentration beyond this point does not improve incorporation or porosity formation.

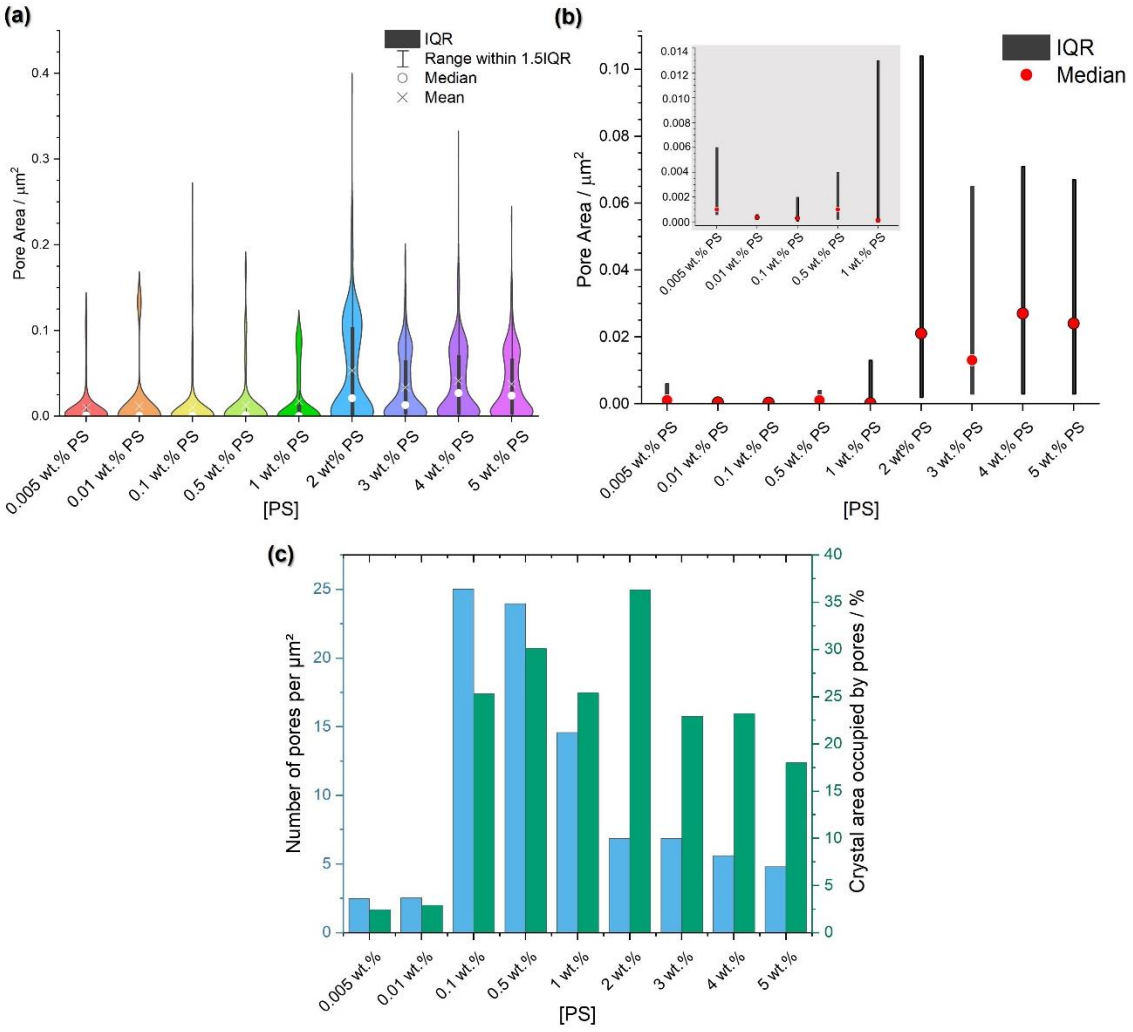


**Figure 3.42 The effect of [PS] on pore properties of annealed PS-calcite, (a) violin plot showing the population spread of pore size, (b) box plots of the pore sizes and (c) the filling fraction of pores within the crystal, in terms of pore density (µm$^{-2}$) and pore area (%).**

Compared to porous calcite created using Asp and Gly, the pores in PS-calcite occupy a much higher proportion of the crystal area. The highest pore area for PS-calcite was obtained at [PS] = 2 wt.% with 36 % of the crystal cross-section being occupied by pores. This is more than twice the highest proportion obtained for Asp-calcite, which was 16 % for [$Ca^{2+}$] = 5 mM, [Asp] = 20 mM, and only 13 % for Gly-calcite, prepared using [$Ca^{2+}$] = 10 mM, [Gly] = 100 mM. The pore density was also much higher in PS-calcite than Asp- and Gly-calcite. In PS-calcite, the largest pore density was 25 µm$^{-2}$ for [PS] = 0.1 wt.% compared to 13 µm$^{-2}$ for 5, 50 Asp-calcite and 15 µm$^{-2}$ for 10, 100 Gly-calcite. This shows that higher filling fractions of pores were generated using PS microspheres than the amino acids Asp and Gly.

However, a limitation of using cross-sections to determine the porosity is that it is just reveals the porosity across one slice of the crystal. If a crystal is full of pores with 500 nm diameter, taking a slice across through the crystal will invariably segment the pores at different points along their circumferences and yield a range of different pore sizes. Depending on the shape, size and uniformity of the pores, the pore size measured can vary considerably from the maximum value. For uniformly spherical pores, it can be assumed that the pore sizes displayed in a cross-section will almost always be smaller than the true value of the mean pore diameter. They will never be larger unless the pores are interconnected, such that two or more pores that are touching will contribute to a larger pore area. This is not the case for non-uniform particles, and if pores possess a quadrilateral shape, the pore size measured may provide a more accurate representation of the overall pore size.

This approach was taken due to the large number of samples involved and prohibitive cost of capturing full FIB tomograms of each crystal. However, the cross-sections obtained in this chapter typically include hundreds or thousands of pores each, and therefore still provide a large sampling volume of the overall crystal to be analysed.

#### 3.3.3.4 Annealed Ves-calcite

The annealed Ves-calcite was observed using OM (Figure 3.43) and FIB-SEM was used to examine the porosity (Figure 3.54). The crystals appeared bright white under OM and the FIB-SEM showed that pores were widely distributed across the cross-section.

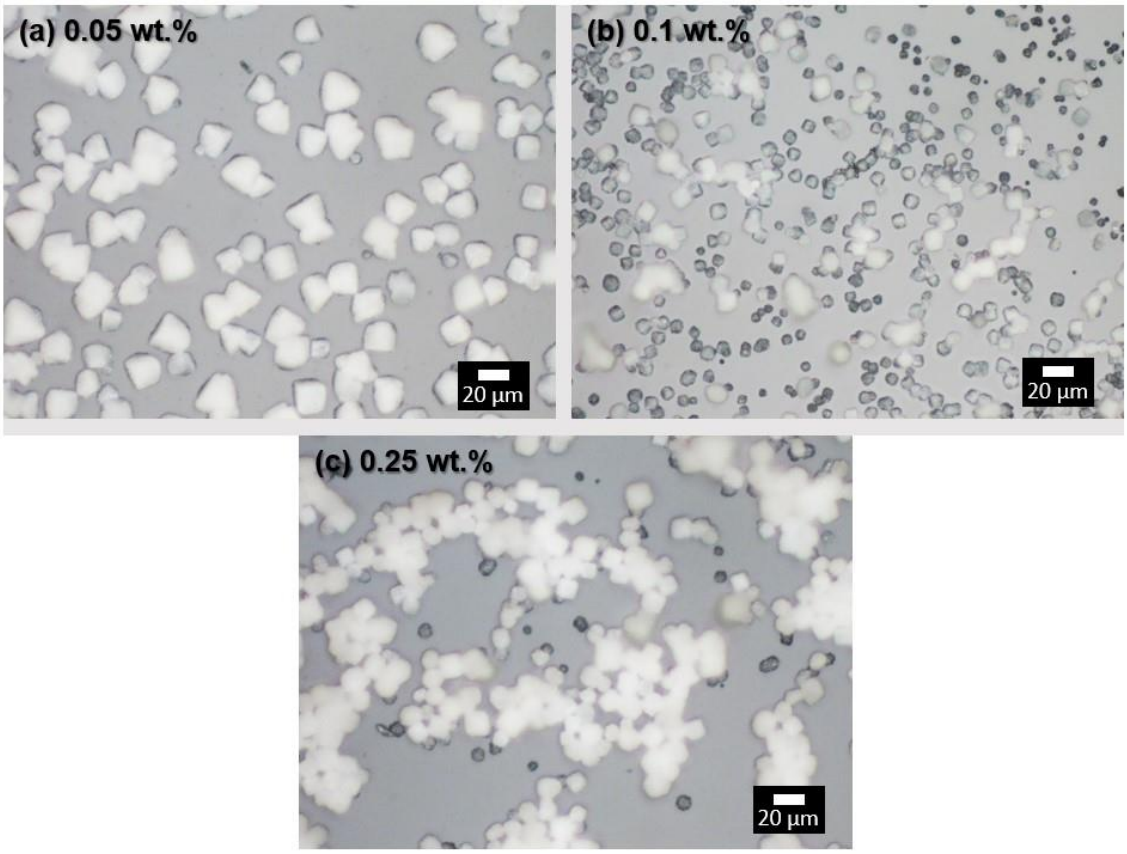


**Figure 3.43 OM images of Ves-calcite after heating, taken in reflection mode.**

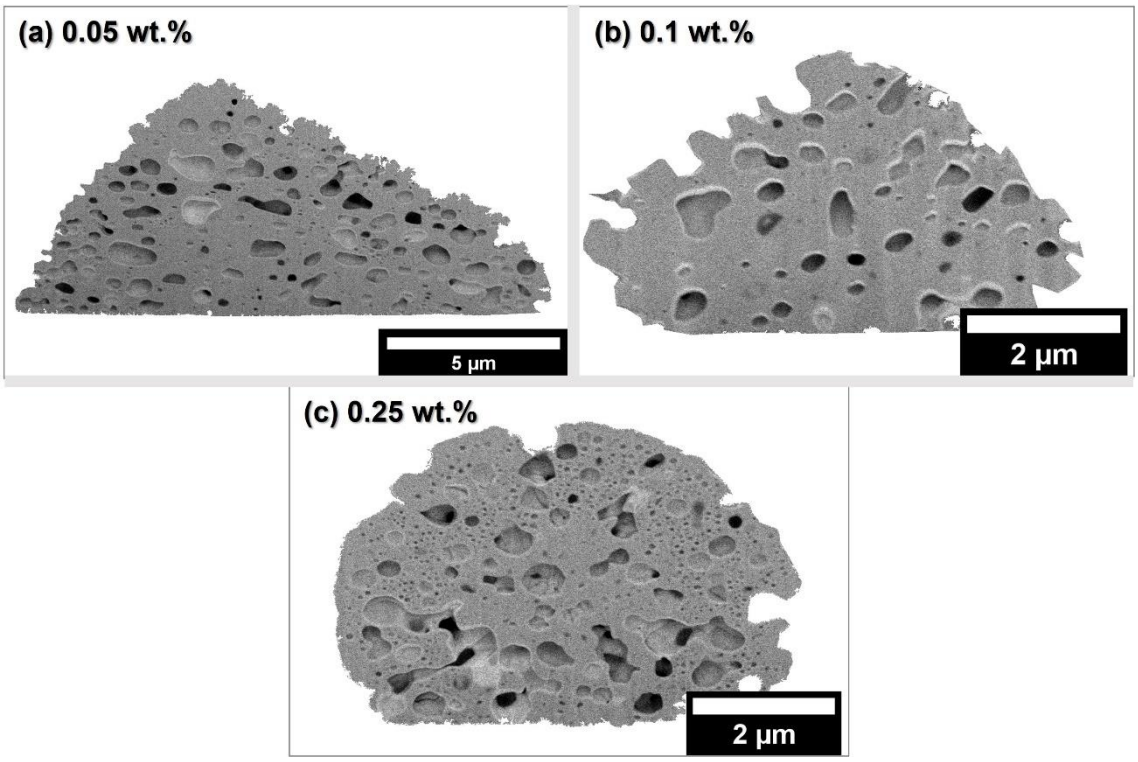


**Figure 3.44 SEM images of Ves-calcite cross-sections prepared using FIB-SEM, annotated with [Ves].**

The pores within Ves-calcite were much more irregular in shape than those obtained for PS-calcite (Figure 3.44). This is to be expected given the hollow structure of the vesicles. The broad pore size distribution reflects the range of vesicle sizes, which were 365 ± 120 nm.

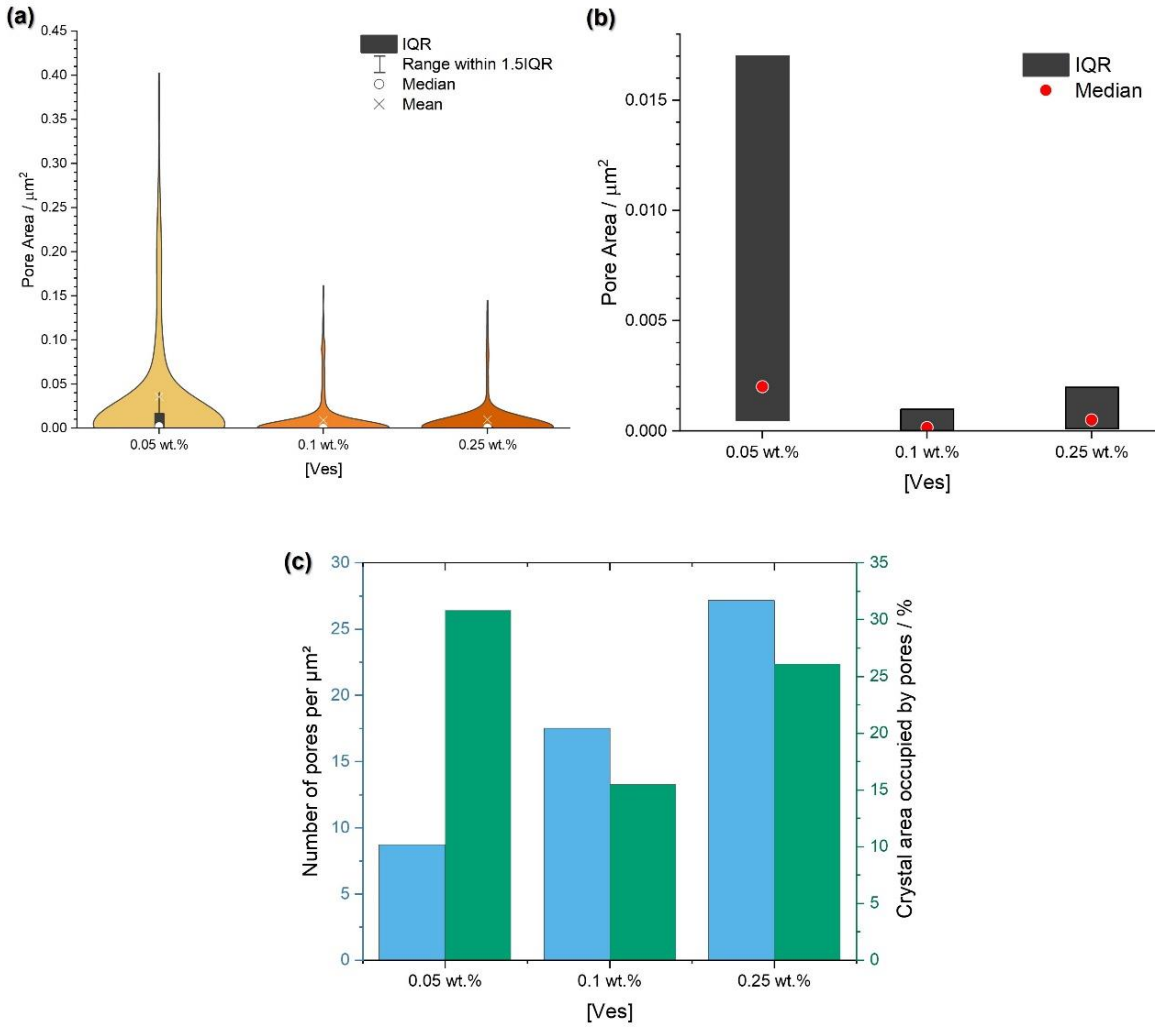


**Figure 3.45 The effect of [Ves] on pore properties of annealed Ves-calcite, (a) violin plot showing the population spread of pore size, (b) box plots of the pore sizes and (c) the filling fraction of pores within the crystal, in terms of pore density (µm$^{-2}$) and pore area (%).**

The IQR and median was markedly higher for [Ves] = 0.05 wt.% than [Ves] = 0.1, 0.25 wt.%, which were very similar. The filling fraction also showed two different behaviours amongst the three [Ves] trialled. At low [Ves], the pore density is low while the pore area is high, indicating that fewer large pores are present. Upon increasing [Ves] to 0.1 wt.%, the pore density increases but pore area drops. This suggests that more, small pores are obtained. However as [Ves] increases further to 0.25 wt.%, both pore density and area increase, indicating that more pores are created.

### 3.3.3.5 Annealed PS/Gly-calcite

The annealed PS/Gly-calcite showed widespread porosity across the cross-section (Figure 3.46).

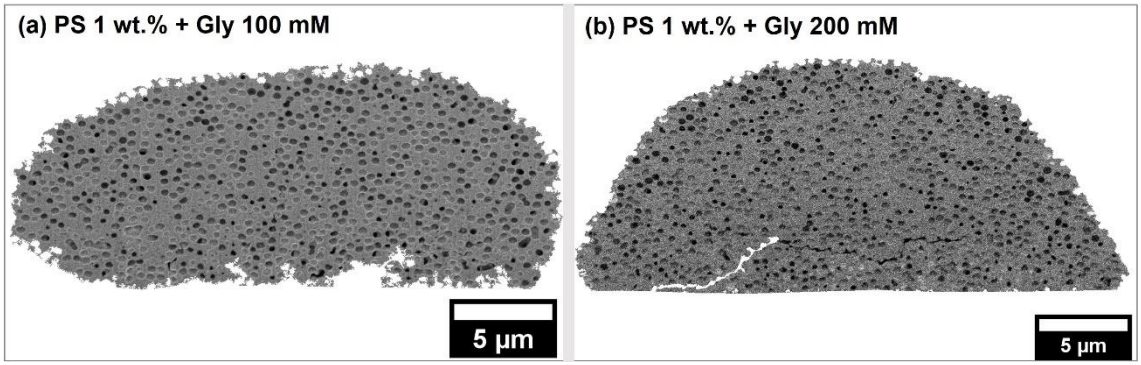


**Figure 3.46 SEM images of PS/Gly-calcite cross-sections prepared using FIB-SEM.**

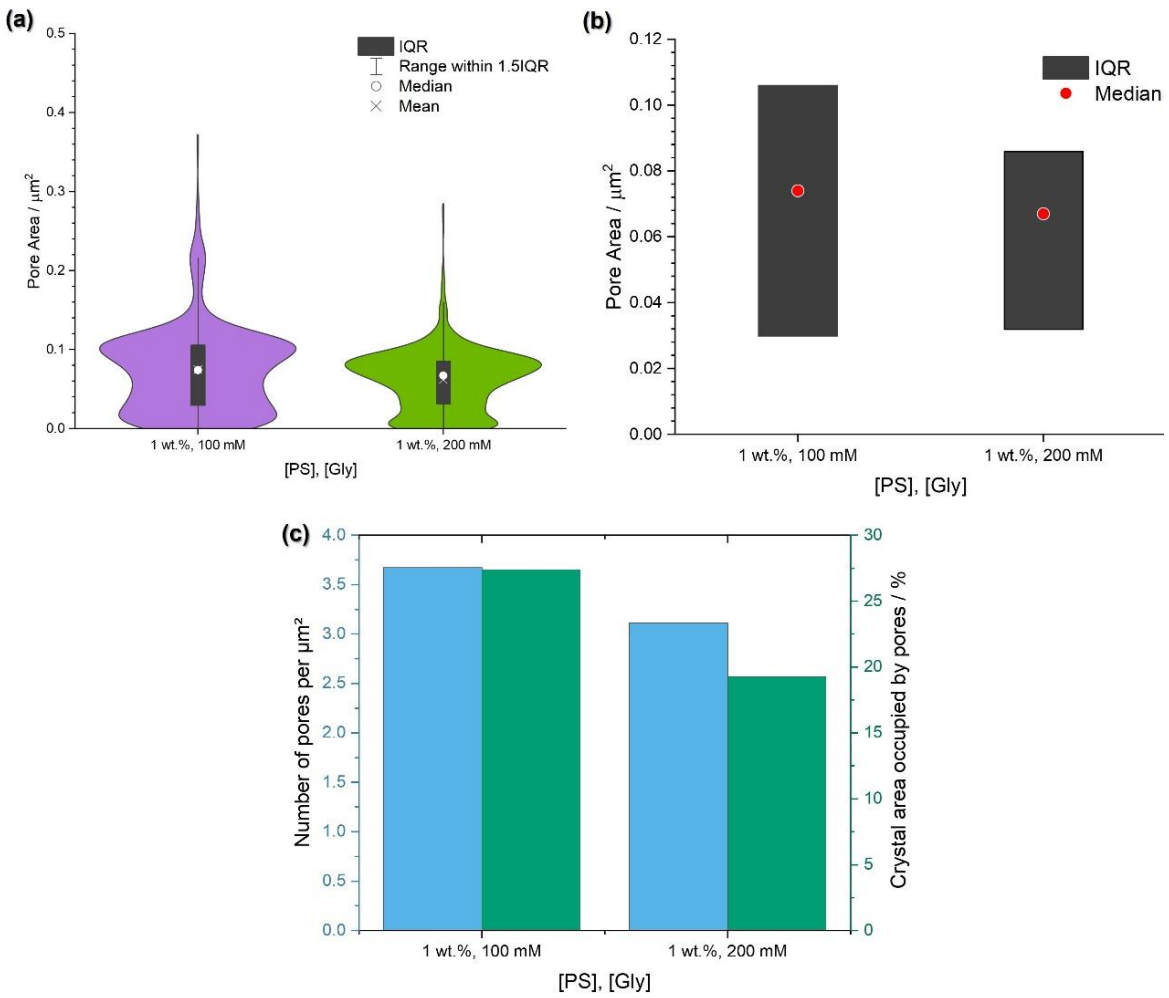


**Figure 3.47 The effect of [Gly] on pore properties of annealed PS/Gly-calcite, (a) violin plot showing the population spread of pore size, (b) box plots of the pore sizes and (c) the filling fraction of pores within the crystal, in terms of pore density (µm$^{-2}$) and pore area (%).**

The violin plot of pore sizes showed two main clusters; one cluster at 0.01 µm$^2$ and a larger cluster at 0.1 µm$^2$ (Figure 3.47). This is attributable to the two different additive sizes. Both [Gly] had similar median pore sizes but [Gly] = 200 mM had a narrower IQR. The filling fraction for [Gly] = 200 mM was lower than [Gly] = 100 mM, in terms of both the pore number density and proportion of pore to crystal area.

### 3.3.3.6 Annealed Sea Urchin Spine

As discussed in the chapter introduction (see Section 3.1.2), biogenic calcium carbonate is occluded with acidic macromolecules such as Asp[183]. It is therefore a natural analogue of our Asp-calcite composite. Sea urchin spine sections were

ground into a powder and annealed using the high temperature heating protocol (500 °C, 30 min, 5 °C $min^{-1}$). Unlike the test plates of sea urchin, the spine is not porous and thus was used in the present study. The annealed spine was examined using FIB-SEM (Figure 3.48) and uniform porosity was observed.

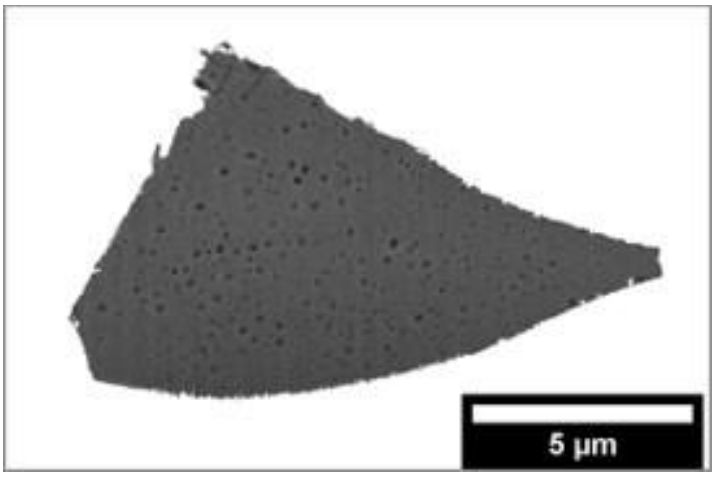


**Figure 3.48 SEM image of a sea urchin spine cross-section prepared using FIB-SEM.**

The IQR of pore sizes was similar to those for the Asp- and Gly-calcite and the pore density and area was comparable to mid-range Asp- and Gly-calcite samples. This confirms that biogenic calcite specimens become porous after heating, as was recently reported by Albéric *et al.* [240] They showed that both ACC crystallisation and degradation of organic material formed porosity at 170 – 250 °C and 300 – 400 °C respectively.

It is possible to compare the present data with their serial FIB-SEM analysis of the septum of the spine heated at 450 °C for 1 hour (the heating rate was not disclosed). They reported pore sizes of 30 nm – 2.6 µm, which is much larger than the IQR found here which spanned 60 – 110 nm. The pore density and volume was found to be 10 $\mu m^{-3}$ and 5.5 vol.%, compared to the 2D data collected here which yielded a pore density of 3.7 $\mu m^{-2}$ and pore area of 6 %. Overall, the porosity observed was similar, despite differences in the heating conditions. It should also be noted that Albéric *et al.* explicitly sampled the septum of the spine, whereas this study did not distinguish between the septum and stereom.

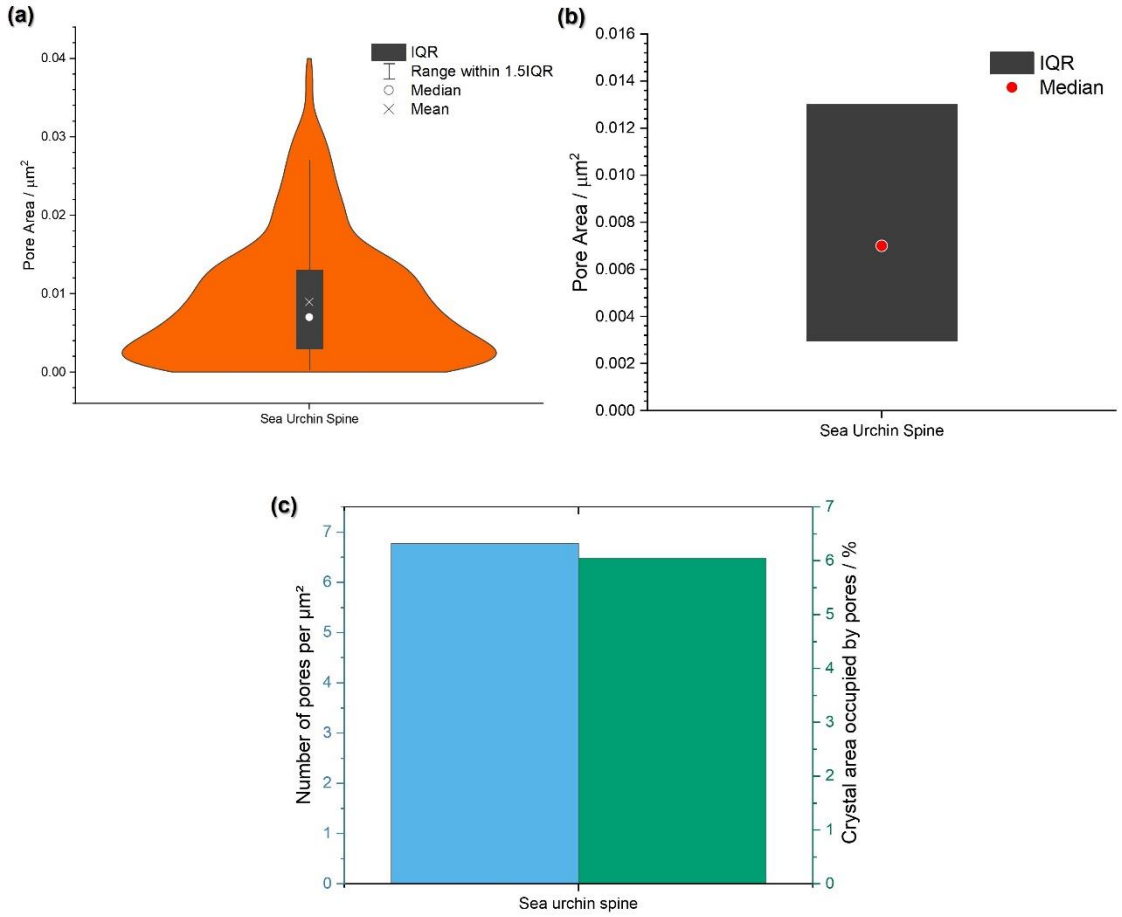


**Figure 3.49 The pore properties of annealed sea urchin spine, (a) violin plot showing the population spread of pore size, (b) box plots of the pore sizes and (c) the filling fraction of pores within the crystal, in terms of pore density ($\mu m^{-2}$) and pore area (%).**

## 3.3.4 Low Temperature Heat Treatment for Porosity Formation

### 3.3.4.1 Asp-Calcite Annealed Via Low Temperature Heating Route

The low temperature heating protocol described in Section 3.3.2.5 was trialled on Asp- and Gly-calcite. The heating rate was kept at 5 °C $min^{-1}$, but instead of heating at 500 °C for 30 mins, samples were annealed at 250 °C for 3 hours. As previously, the cross-sections were examined using FIB-SEM and showed widespread porosity for all conditions (Figure 3.50).

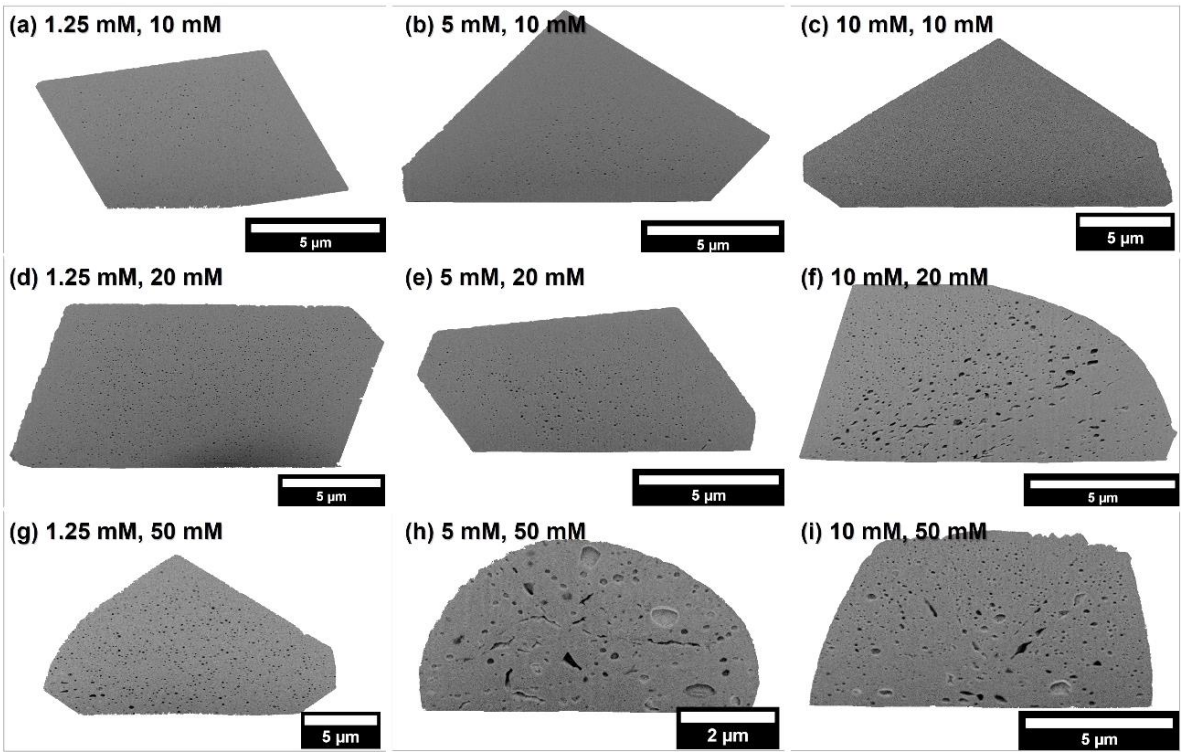


**Figure 3.50 SEM images of Asp-calcite cross-sections prepared using FIB-SEM, heated using a low-temperature heat treatment, annotated with [$Ca^{2+}$], [Asp].**

The pore sizes were at least an order of magnitude smaller in samples prepared using the low temperature heating regime compared to the high temperature protocol (Figure 3.51a). Increasing [Asp] generally resulted in larger pore sizes, a greater size distribution and larger median values, where this was particularly evident at [Asp] = 50 mM. Similar IQR and median values were observed when [$Ca^{2+}$] was varied.

For samples prepared with [$Ca^{2+}$] = 5 and 10 mM, both pore density and area increased with increasing [Asp], indicating that more pores formed at higher [Asp]. This is not the case for [$Ca^{2+}$] = 1.25 mM, where pore density peaked at [Asp] = 20 mM while the pore area increased with [Asp]. This suggests that initially more pores are produced, in keeping with the above trend, but that their close proximity results in their eventual coalescence, reducing the overall pore density.

Different filling fractions in annealed Asp-calcite were generated using the high and low temperature heating regimes. All samples had higher pore densities when heated using the low temperature regime. However, the high temperature heating protocols led to greater pore areas in the majority of the samples. Both of these

properties reflect the difference in pore sizes obtained using the different heating regimes.

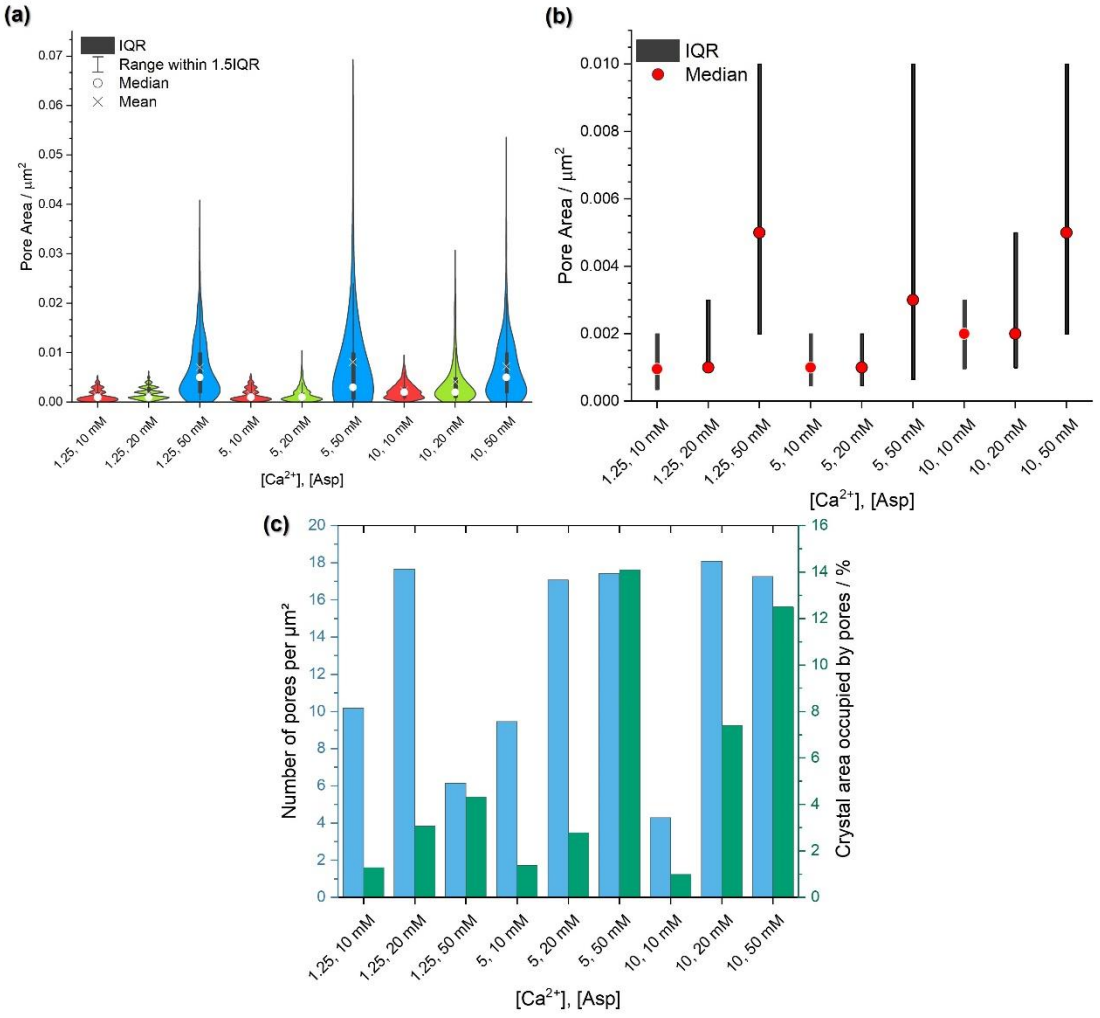


**Figure 3.51 The effect of [$Ca^{2+}$], [Asp] on pore properties of Asp-calcite using the low temperature regime (a) violin plot showing the population spread of pore size, (b) box plots of the pore sizes and (c) the filling fraction of pores within the crystal, in terms of pore density (µ$m^{-2}$) and pore area (%).**

### 3.3.4.2 Gly-calcite Annealed via Low Temperature Heating Route

The low temperature heating regime was also used to anneal Gly-calcite. Samples prepared at [$Ca^{2+}$] = 1.25 mM exhibited localised porosity as seen using the high temperature regime (Figure 3.52). The porosity was generally uniform for all other conditions.

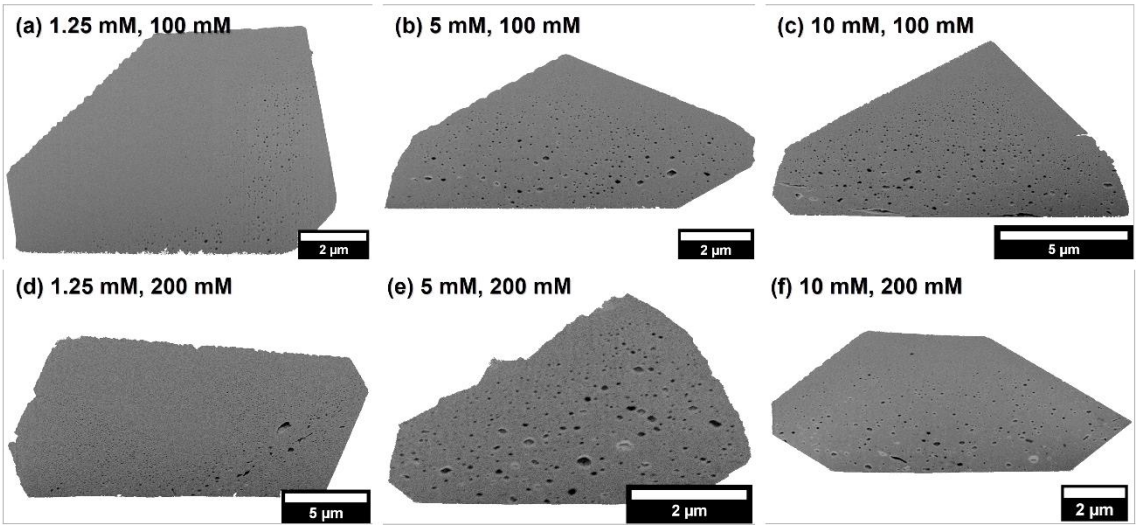


**Figure 3.52 SEM images of Gly-calcite cross-sections prepared using FIB-SEM, heated using a low-temperature heat treatment, annotated with [$Ca^{2+}$], [Gly].**

As for Asp-calcite, the pore sizes were much lower for Gly-calcite after annealing at the low temperature rather than the high temperature regime (Figure 3.53a). The pore sizes increased with both [Gly] and [$Ca^{2+}$] (Figure 3.53b), while the pore density decreased with [Gly] whereas the pore area generally increased with [Gly] (Figure 3.53c). This indicates that increasing [Gly] creates more pores that are close enough to coalesce. Compared to the high temperature regime, a higher pore density and lower pore area was achieved. Interestingly, this was the opposite to Asp-calcite.

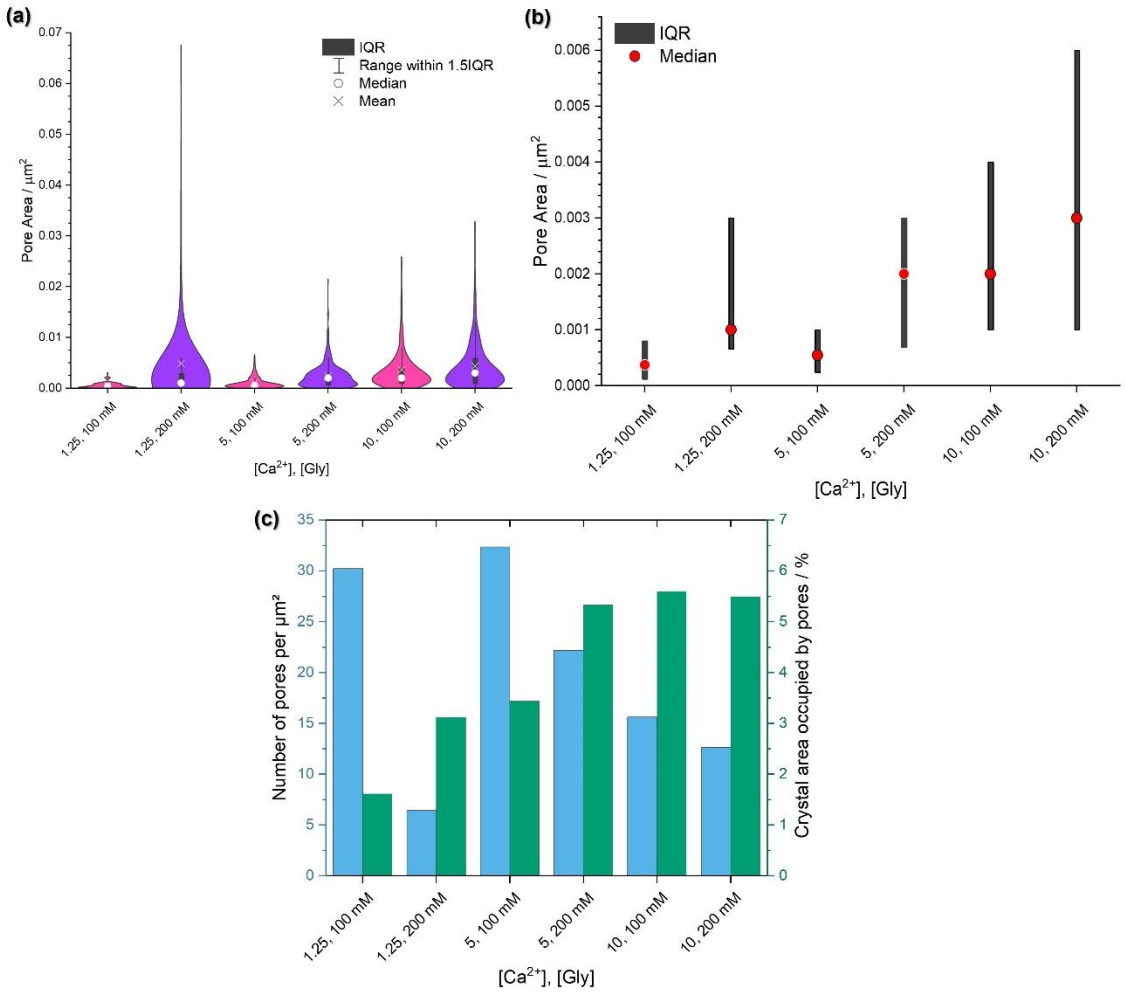


**Figure 3.53 The effect of [$Ca^{2+}$], [Gly] on pore properties of Gly-calcite heated at T2, (a) violin plot showing the population spread of pore size, (b) box plots of the pore sizes and (c) the filling fraction of pores within the crystal, in terms of pore density (µ$m^{-2}$) and pore area (%).**

### 3.3.5 Effect of Crystal Orientation

The calcite crystals were present in a range of orientations on the glass substrate. When choosing a crystal to create a cross-section from using FIB-SEM, it is possible to select differently oriented crystals due to their defined morphologies. This was done for crystals of Asp-calcite, comparing crystals that had grown with the [001] plane parallel to the substrate against those with it perpendicular to the substrate. Two crystals with these orientations were chosen for cross-section preparation and the resulting images were analysed to compare the effect of crystal orientation on the properties of the pores (Figure 3.54).

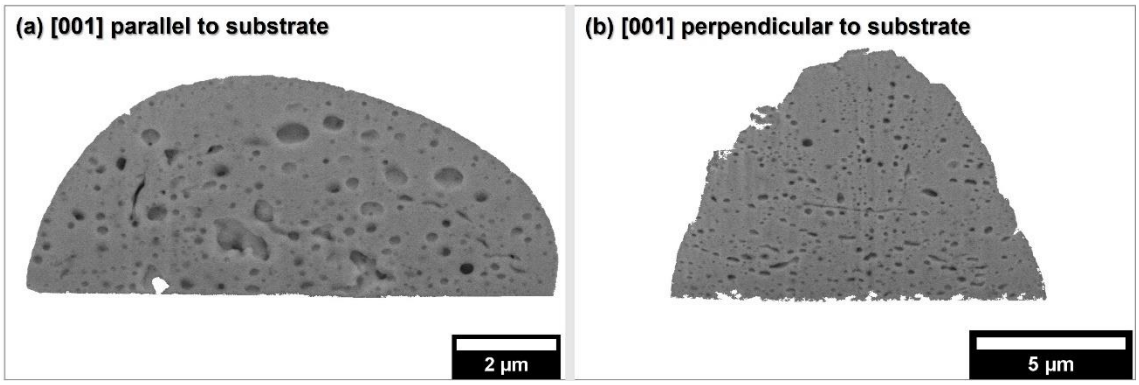


**Figure 3.54 SEM images of Asp-calcite cross-sections prepared using FIB-SEM, slicing through crystals with different orientations, with the [001] direction parallel (a) or perpendicular (b) to the glass substrate.**

A broader range of pore sizes were obtained for the parallel section despite both orientations having similar median pore sizes (Figure 3.55 a, b). Comparison of the filling fractions shows that there is negligible difference between the pore densities, while the pore area was lower for the perpendicular section. This was due to the difference in pore size, since the parallel section had a broader IQR which included larger pores. Overall, this suggests that the prevalence of the pores was relatively unaffected by the change in orientation, but that the size range of the pores varied somewhat.

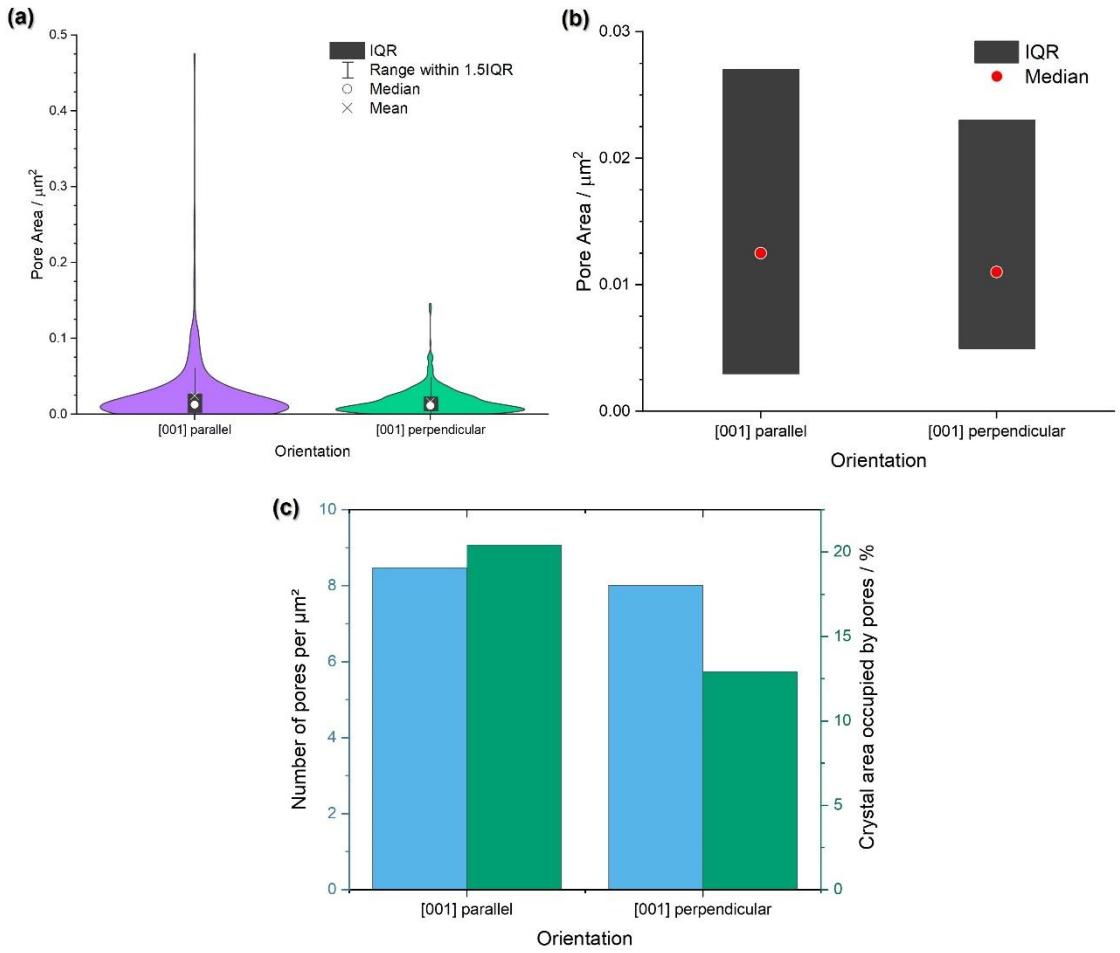


**Figure 3.55 Pore properties measured from cross-sections with different orientations of 10, 50 mM Asp-calcite heated at T1, (a) violin plot showing the population spread of pore size, (b) box plots of the pore sizes and (c) the filling fraction of pores within the crystal, in terms of pore density ($\mu m^{-2}$) and pore area (%).**

## 3.3.6 Optical Properties of Porous Calcite

The reflectance of the porous crystals was measured using the setup described in Section 3.2.2.2.

### 3.3.6.1 Optical Properties of Annealed PS-calcite

Negligible reflectance was observed across all wavelengths in the reflectance spectrum of pure calcite (Figure 3.56). Calcite prepared with 1 wt.% PS and which had not been heated behaved similarly and reflected less than 20 % of the incident light across all wavelengths.

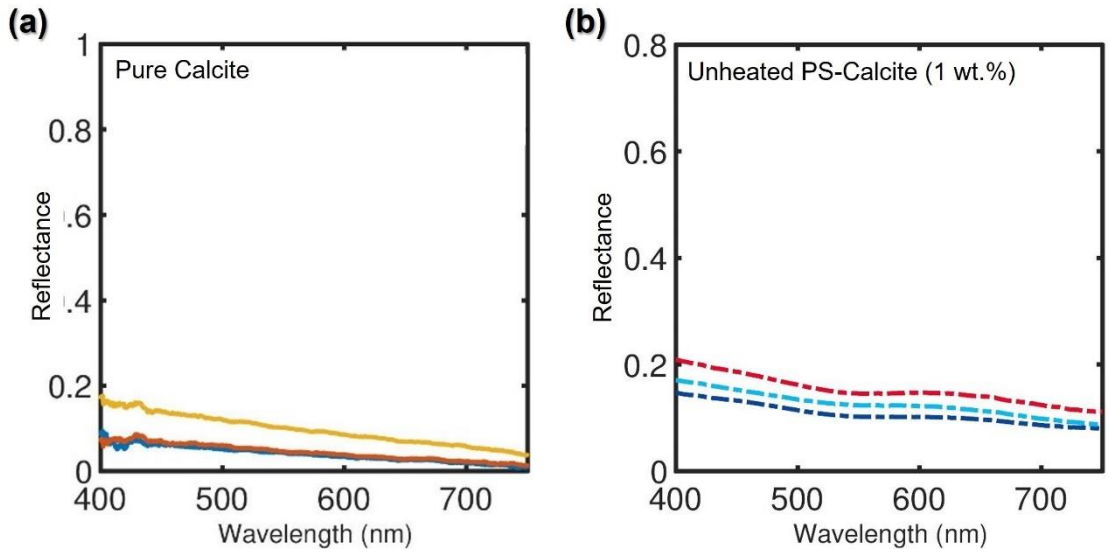


**Figure 3.56 Reflectance spectra for (a) calcite control and (b) unheated PS-calcite.**

Optical measurements of heated PS-calcite with different [PS] showed that a range of reflectance values was achieved (Figure 3.57). PS beads are not incorporated within calcite crystals at very low concentrations of PS (0.005 and 0.01 wt.%) (see Section 3.3.3.3). The internal structures of these crystals are therefore very similar to those of the control calcite, and thus the reflectance is also very similar to the control. Uniform occlusion of PS beads throughout the crystal was achieved using [PS] = 0.1 wt.% and gives rise to an increase in the reflectance.

For annealed calcite with [PS] ≤ 0.1 wt.% and both the calcite and unheated PS-calcite controls, the reflectance profile is mostly broadband with a small slope decreasing from the blue to red wavelengths region. Annealed calcite crystals prepared with [PS] ≥ 0.5 wt.% exhibited an increase in reflectance from the blue to red wavelengths, which was steeper for the high concentrations of 2 – 5 wt.% than for 0.5 and 1 wt.%. The broadband reflectance was lost at [PS] ≥ 2 wt.% as although reflectance intensity increased in the red region with increasing [PS], the maximum intensity observed at λ = 400 nm was for [PS] = 0.1 wt.%. This is likely due to samples with [PS] ≥ 0.5 wt.% absorbing blue light. The absorption of blue light at high [PS] can be explained by the presence of carbon remnants, which are left by the PS microparticles after annealing PS-calcite. Organic carbon is known for absorbing strongly in the 200 – 500 nm wavelength range[276].

Additionally, there was no change in the reflectance behaviour when water was added to the crystals, confirming the lack of interconnection between the pores and the crystal surface. Due to the change in refractive index between water and air, the optical behaviour would be expected to change if the pores were filled with water. This is further evidence that pores on the crystal surfaces do not contribute towards the reflectance.

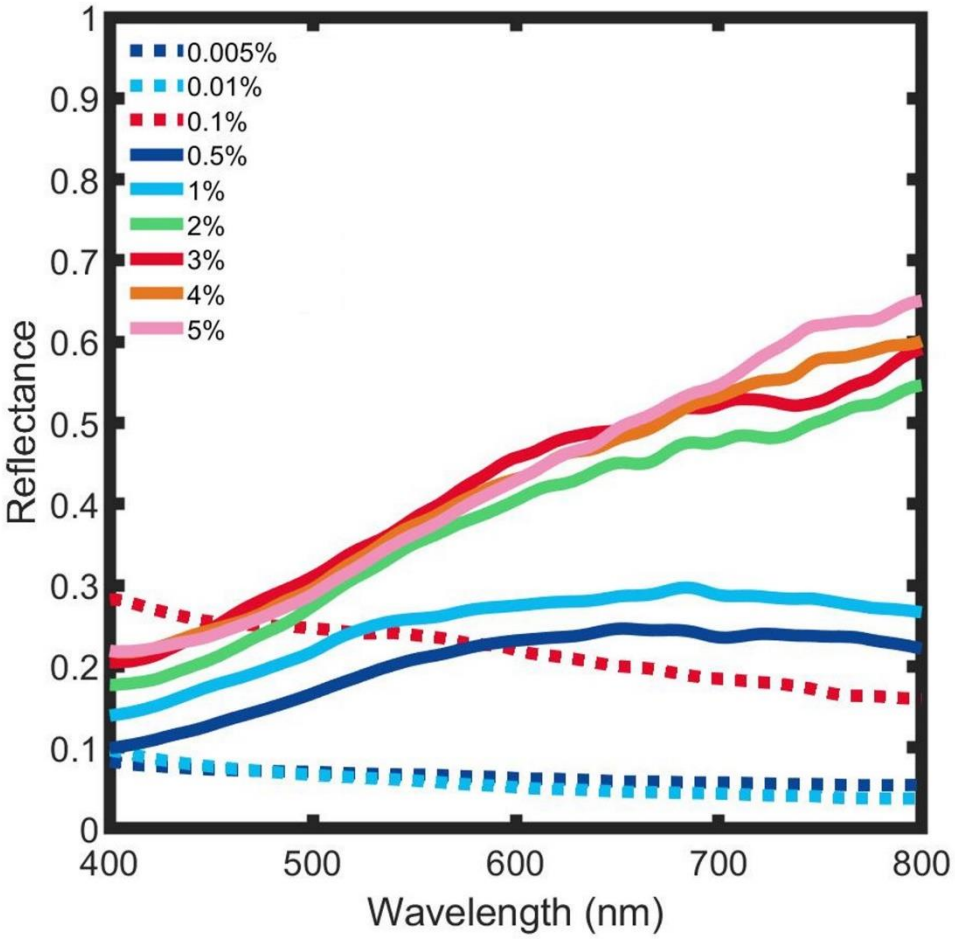


**Figure 3.57 Reflectance spectrum for PS-calcite.**

### 3.3.6.2 Optical Properties of Annealed Asp-calcite

Diverse reflectance behaviour was observed across the range of $[Ca^{2+}]$ and [Asp] tested (Figure 3.58). The highest reflectance was observed for crystals prepared with [Asp] = 10 mM, and increasing reflectance occurred with decreasing $[Ca^{2+}]$. The reflectance intensity for Asp-calcite prepared with [Asp] = 20 and 50 mM decreased from $[Ca^{2+}]$ = 1.25 – 5 mM and increased from 5 – 10 mM. Broadband reflectance was observed for all samples apart from 1.25, 10 mM and 10, 50 mM, which had a

negative and positive slope respectively. These samples also had the lowest and highest amount of Asp incorporation, respectively (see Section 3.3.1.1). The positive slope for 10, 50 mM was due to absorbance of blue light by carbon remnants following decomposition of Asp molecules, as seen for high [PS] PS-calcite samples. A negative slope was observed for the calcite control, and both unheated and low [PS] PS-calcite, which indicates that the negative slope observed for crystals prepared with 1.25, 10 mM was due to low incorporation of Asp.

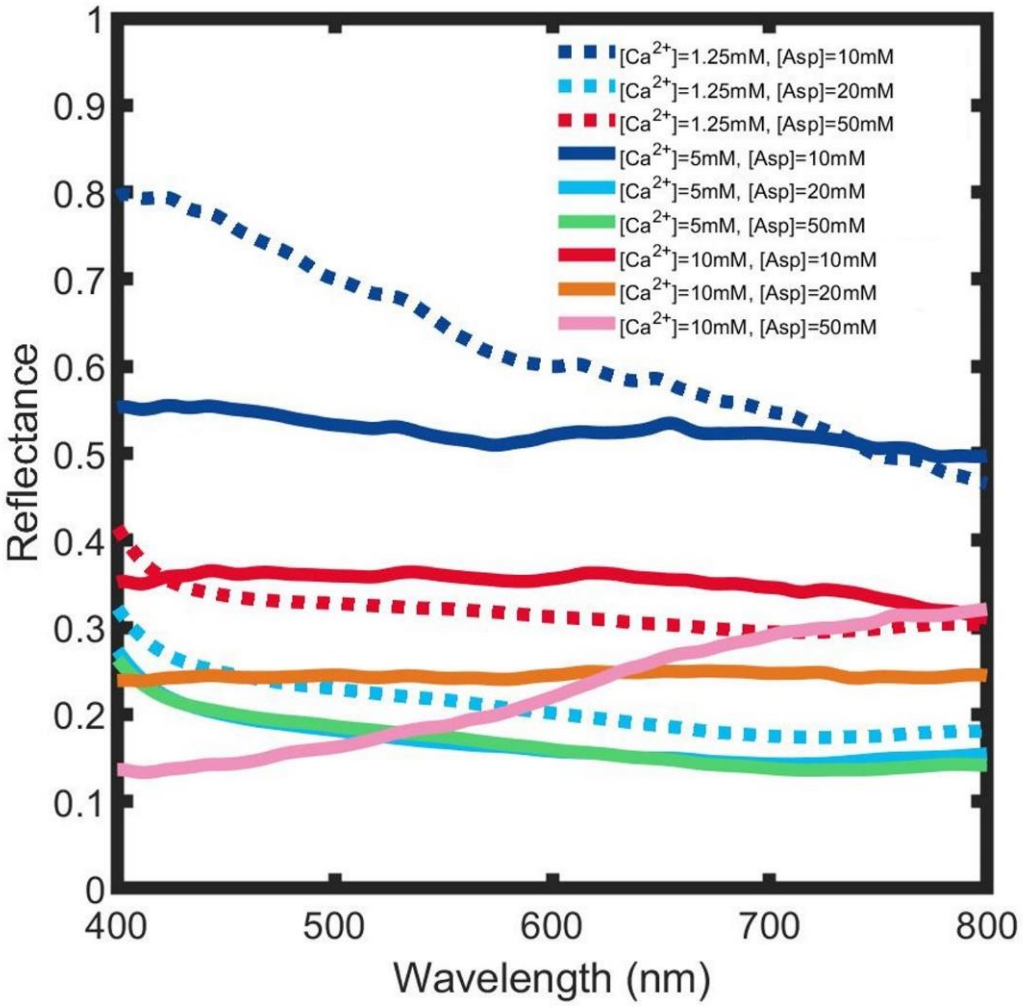


**Figure 3.58 Reflectance spectrum for Asp-calcite heated using the high temperature annealing regime.**

### 3.3.6.3 Optical Properties of Annealed Gly-calcite

As for Asp-calcite, the reflectance spectra varied for different Gly and $Ca^{2+}$ concentrations (Figure 3.59). Interestingly, the most reflective Gly-calcite sample (1.25, 200 mM) also exhibited a negative slope, as was seen for the most reflective

Asp-calcite sample. Few trends were observed between the reflectance and the concentrations at which the samples were prepared. The lowest reflectance values were seen in samples prepared at [$Ca^{2+}$] = 5 mM for both [Gly] = 100 and 200 mM, and were comparable to pure unannealed calcite.

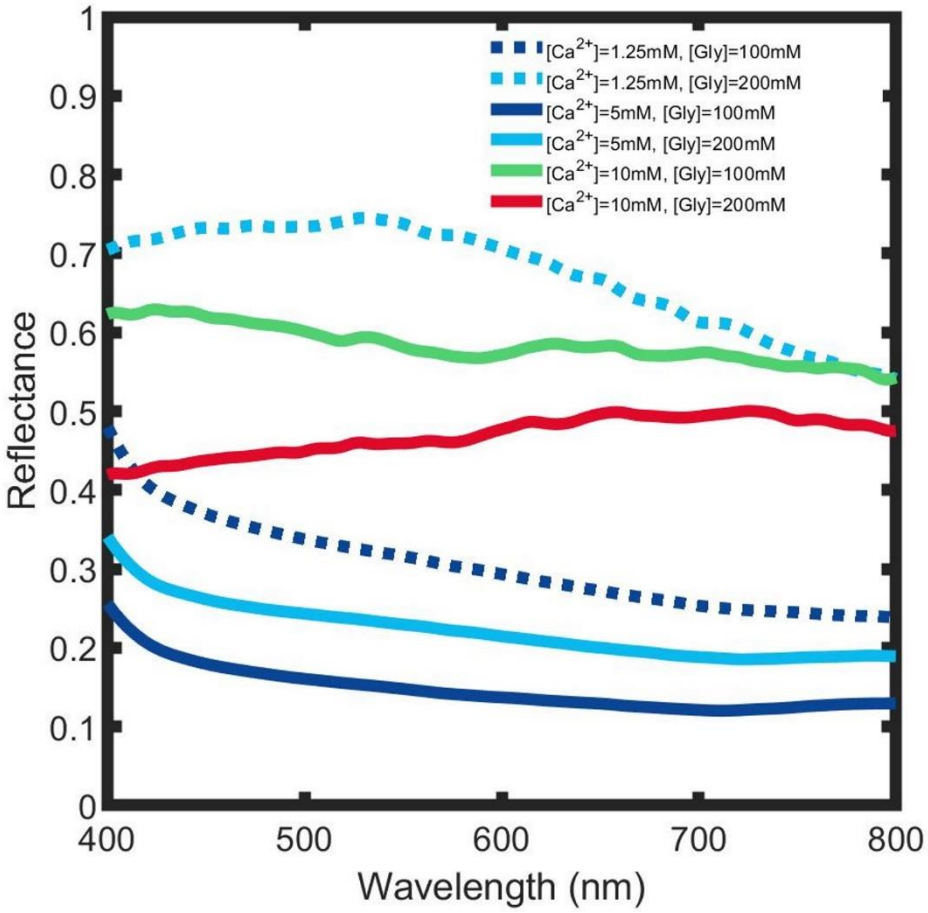


**Figure 3.59 Reflectance spectrum for Gly-calcite heated using the high temperature regime.**

### 3.3.6.4 Optical Properties of Annealed Ves-calcite

The reflectance spectra of Ves-calcite samples showed two types of behaviour (Figure 3.60). The lowest [Ves] displayed the highest reflectance, which was much greater than any other [Ves] tested. The reflectances for [Ves] = 0.1 and 0.25 wt.% were almost identical in the blue region but a negative slope was observed for 0.1 wt.% but not 0.25 wt.%. Importantly, unlike PS-calcite at high [PS], there were no signs of absorbance in the blue region for any of the Ves-calcite spectra.

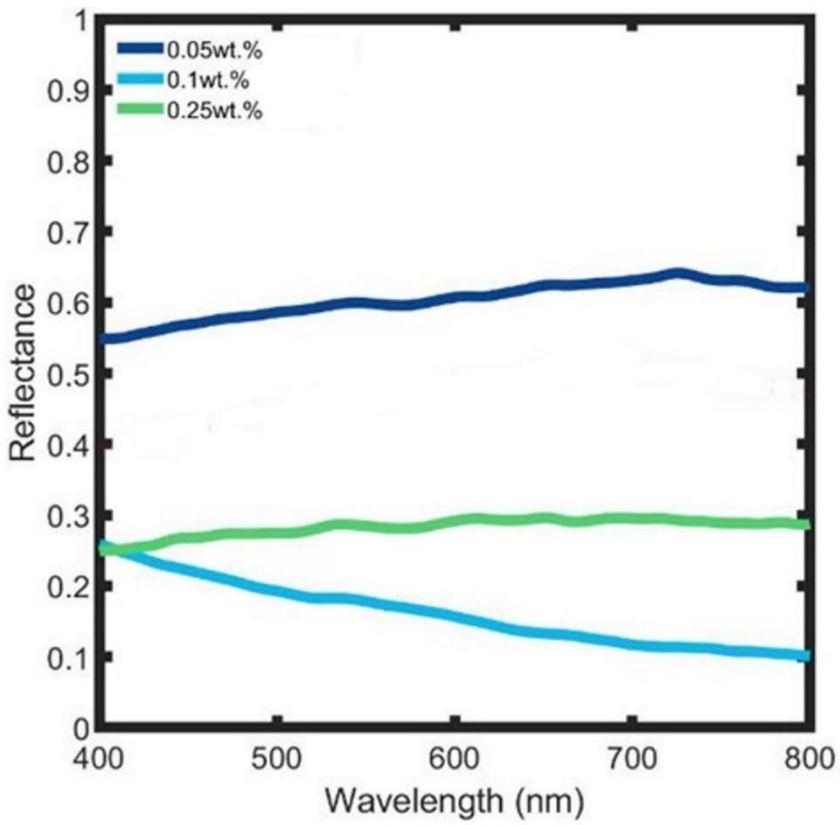


**Figure 3.60 Reflectance spectrum for Ves-calcite.**

### 3.3.6.5 Optical Properties of Low Temperature Annealed Asp-calcite

The reflectance of Asp-calcite annealed using a low temperature protocol was generally lower than Asp-calcite heated using the high temperature treatment (Figure 3.61). However, samples prepared using [$Ca^{2+}$] = 1.25 mM, [Asp] = 20 and 50 mM, and [$Ca^{2+}$] = 10 mM, [Asp] = 50 mM and the high temperature heating regime showed superior reflectance. The change in reflectance was particularly interesting for calcite prepared at [$Ca^{2+}$] = 10 mM and [Asp] = 50 mM; the reflectance in the red wavelength region was lower for the low temperature regime compared to the high temperature regime, despite being higher in the blue wavelength region. As the spectra for the high temperature samples showed signs of absorbance in the blue region, while the low temperature samples do not, this shows that the low temperature heating protocol was more effective at removing all remnants of the additives.

It is also interesting to note that some samples prepared using the low temperature heating regime exhibited very low reflectances, which were similar in intensity to the pure calcite control. This is expected as the pores for many of the samples obtained

by heating with the low temperature regime had IQR's of < 0.0025 $\mu m^2$. Therefore, many conditions did not yield pores greater than the 50 nm size threshold for interacting with visible light.

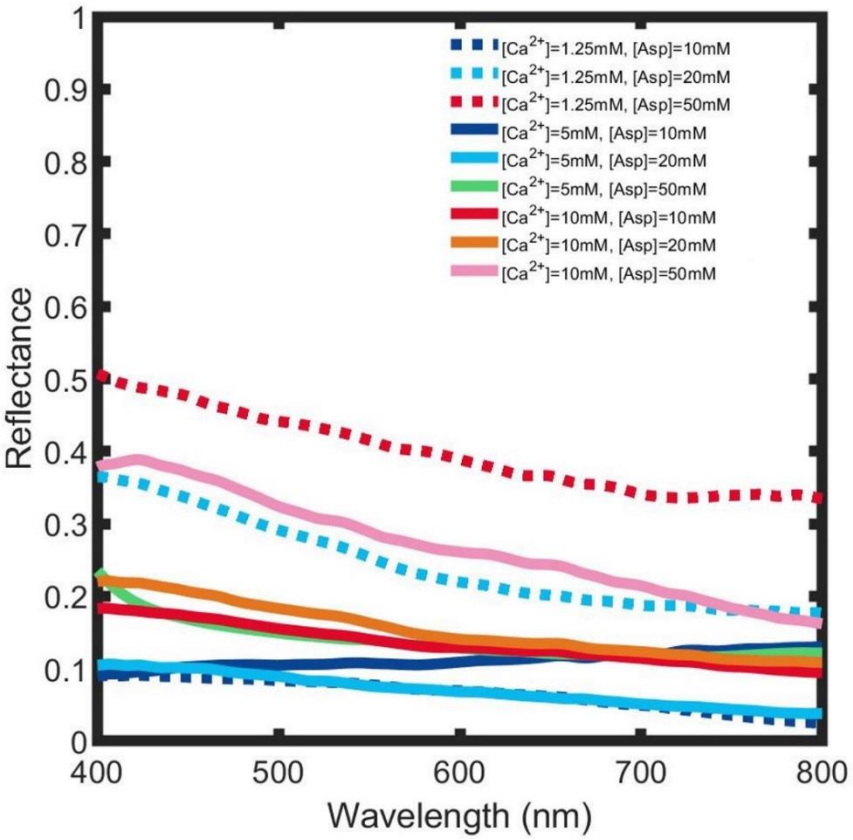


**Figure 3.61 Reflectance spectrum for Asp-calcite, prepared using the low-temperature heating regime.**

### 3.3.6.6 Optical Properties of Low Temperature Annealed Gly-calcite

All Gly-calcite crystals exhibited lower reflectance after heating using the low temperature regime compared to the high temperature regime (Figure 3.62). In fact, many of the low temperature samples exhibited spectra with similar reflectance to pure unannealed calcite. Again, this was expected due to the small pores, which were incapable of interacting with light. There were few differences between the samples prepared under different conditions, and the only condition that displayed a boost in reflectance above the pure calcite control was that with $[Ca^{2+}]$ = 10 mM and [Gly] = 200 mM.

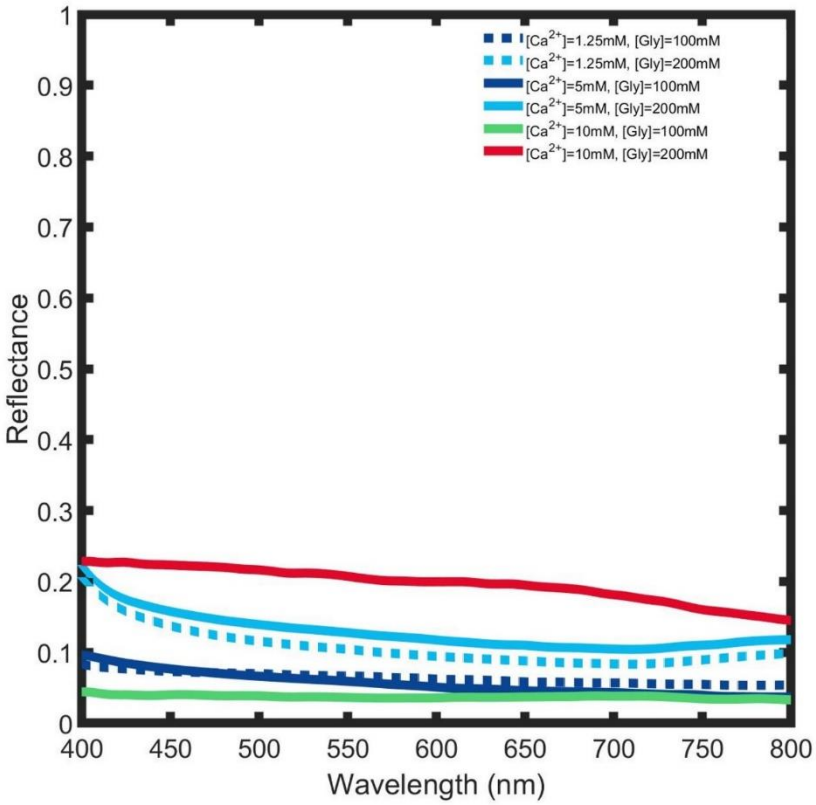


**Figure 3.62 Reflectance spectra of Gly-calcite, heated using a low-temperature heating regime.**

### 3.3.6.7 Optical Properties of Annealed PS/Gly-calcite

Porous crystals prepared using both PS and Gly showed promising reflectance intensities of 0.6 at red wavelengths but showed a steep positive slope towards the blue wavelengths (Figure 3.63). This indicated that blue light was absorbed by the residual carbon left after annealing, as seen for PS-calcite. PS/Gly-calcite prepared with [Gly] = 100 and 200 mM had similar reflectance at red wavelengths, but the higher Gly concentration brought about further absorption of blue light.

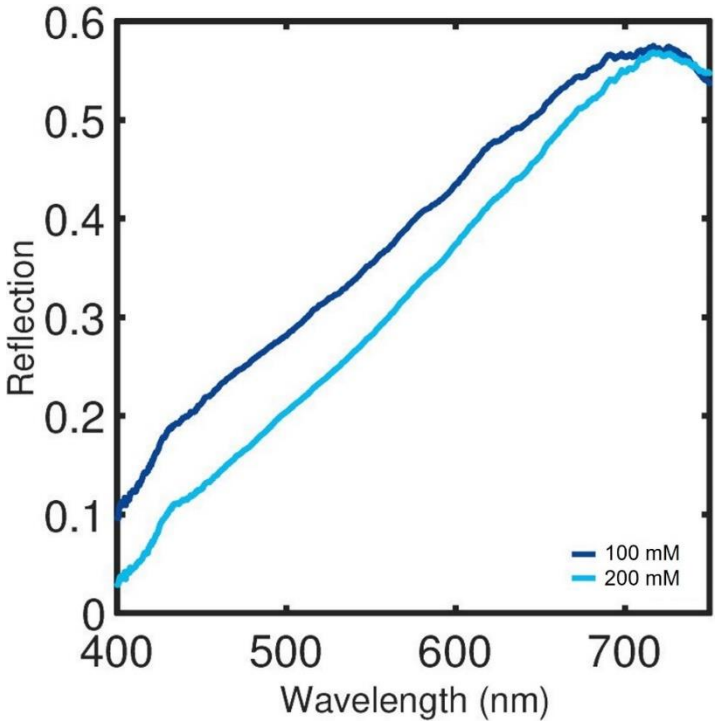


**Figure 3.63 Reflectance spectra of PS/Gly-calcite, with varying [Gly].**

### 3.3.6.8 Optical Properties of Annealed Sea Urchin

Annealed sea urchin spine was highly scattering, and yielded a broadband reflectance intensity of 70 % for wavelengths 400 – 700 nm (Figure 3.64).

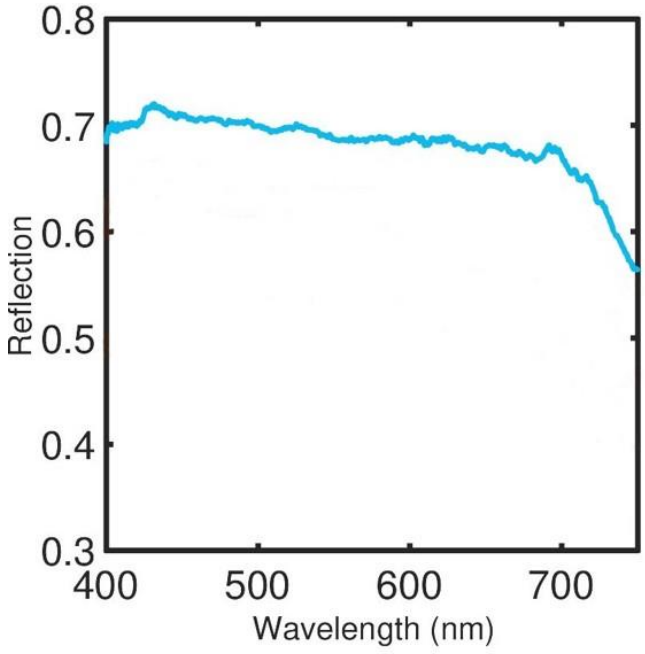


**Figure 3.64 Reflectance spectrum of annealed sea urchin spine.**

### 3.3.6.9 Summary of Optical Properties of Porous Calcite

In summary, porous calcite prepared using different additives and heating methods exhibited diverse reflectance behaviours. PS-calcite showed increasing broadband reflectance with [PS], however increased absorption of blue light by organic remnants caused uneven reflectance across visible light wavelengths in samples with [PS] ≥ 0.5 wt.%. This is shown by the yellow colour of annealed PS-calcite at these concentrations (see Section 3.3.3.3). This detrimental effect was also seen in the reflectance behaviour of PS/Gly-calcite. The absorption of blue light was avoided by substituting PS for Ves, which showed broadband reflectance and appeared white in OM images. The most reflective Ves-calcite sample also showed a similar intensity to that for PS-calcite in the red wavelength region.

It was difficult to establish a consistent trend between the reflectance and porosity in Asp- and Gly-calcite. This is likely due to absorption of blue light by crystals with high [$Ca^{2+}$] and [Asp] or [Gly], which did appear yellow under OM. This resulted in crystals with less occlusion exhibiting greater reflectance. Interestingly, when Asp- and Gly-calcite was heated using the low temperature regime, broadband reflectance occurred at all conditions. This suggested that the low temperature regime was more effective at removing the occluded organic. However, this regime generally resulted in less intense reflectance. This is because the pores formed using the low temperature heating regime were too small to interact with light effectively, as decreasing the size of a scatterer will reduce the intensity of light scattered [277]. Interestingly, the annealed sea urchin spine exhibited intense broadband reflectance of 70 %, which was comparable with the most reflective samples obtained for Asp-, Gly- and Ves-calcite.

Overall, the formation of porosity within calcite enhanced its scattering ability. The complete removal of organic material was crucial for ensuring that reflectance was broadband, due to intense absorbance of blue light by carbon-rich compounds. The impact of this effect on the spectra made it difficult to relate the reflectance values to the porosity or initial composition of the amino acid crystals. However, the choice of heating regime had a drastic effect on the reflectance of these samples, where the small pore size created by the low temperature regime yielded low reflectance. This demonstrated that the pore size must be sufficiently large (beyond a few nanometres) to scatter light effectively.

## 3.4 Discussion

In this study, the heating regime used to remove the organic additives had a significant influence on the crystal porosity. A sufficiently high heating temperature (≥ 500 °C) was crucial in forming uniform porosity throughout the crystals, though low temperatures (250 °C) could be utilised by prolonging the heating time. The size of the pores could typically be increased by using higher temperatures or longer heating times. With increasing temperature, more pores formed with greater sizes, until their close proximities resulted in coalescence at 600 °C. The observed increase in pore size with temperature was in agreement with the data of Albéric *et al.* comparing sea urchin spine heated at 350 and 450 °C [240]. Two different effects on the pores were observed by changing the heating time. Although heating the crystals for 4 h rather than 30 min led to growth and eventual coalescence of the pores, extending the heating time further to 8 h led to the formation of new pores rather than growth. The continued generation of pores with increasing temperature and heating time suggests that removal of the occluded organics was still underway.

The heating rate influenced the pore density and range of pore sizes, where a smaller number of larger pores formed at lower heating rates. Both literature and initial TGA data showed that heating at different rates led to different conversion fractions during decomposition due to the delay in thermal conduction at faster rates[272]. The occluded additives can therefore be decomposed at lower temperatures if slower heating rates are employed, so the removal of the additive is more complete than for samples prepared using fast heating rates at equivalent temperatures and annealing times.

It is well-known that changing the additive concentration affects the level of incorporation. The efficiency of amino acid occlusion was quantified in this study using fluorometric assay, and generally increased at higher [Asp] or [Gly] and [$Ca^{2+}$], in agreement with other studies[151, 265]. The difference in porosity between crystals prepared using different [$Ca^{2+}$] and additive concentrations could also be linked to the efficiency of occlusion, particularly pore density. This was not a straightforward relationship due to coalescence occurring at the highest levels of occlusion as pores form and grow in close proximity.

A clearer relationship between the crystallisation conditions and porosity was observed when a low temperature heating regime was used, where pore size generally correlated with the level of incorporation. The size of the pores formed using the low temperature regime were at least an order of magnitude smaller than those formed via the high temperature regime. This indicated that the annealing protocol was more suitable for tuning pore size than the crystallisation conditions.

As porosity measurements were conducted via image analysis of cross-sections, this relies heavily upon the accuracy of the segmentation method. Image segmentation of FIB-SEM cross-sections can be particularly challenging due to the presence of pore-back (also known as pore shine) artefacts. These arise when the back wall of a pore has similar grayscale values to the rest of the crystal volume, rather than appearing as a dark void. The lack of contrast between the pore and background therefore obscures the pore from standard filters used to segment the image. As a result, under-segmentation can occur where obvious pores are overlooked or over-segmentation can occur when adjustment of the threshold to include overlooked pores then includes unacceptable amounts of noise. As for all image segmentation methods, a balanced approach was used for filtering and edge features were used to improve the segmentation of the pores.

The introduction of porosity into the calcite crystals was shown to enhance their reflectance. As the pore properties were influenced by both [$Ca^{2+}$] and additive concentration, the reflectance was also affected. Higher levels of occlusion were found to increase crystal reflectance. However, this was limited by the presence of residual carbon left after incomplete decomposition of the additive during annealing, which worsened as the additive concentration increased. Carbon compounds absorb light at low wavelengths in the UV and near-UV visible light range (~400 nm), which corresponds to the drop in reflectance exhibited by crystals with high additive concentrations. This effect was particularly evident in PS- and PS/Gly-calcite, as PS was the most carbon-dense additive trialled, but was also noted in Asp- and Gly-calcite crystals with the highest levels of Asp/Gly. The affected crystals tended to appear yellow under OM rather than bright white, further evidencing the absorbance of blue light.

Two ways in which this effect could be mitigated were identified; the use of a low temperature annealing regime for Asp- and Gly-calcite and the substitution of the

densely-filled PS microspheres with vesicles. The reflectance spectra for Asp- and Gly-calcite annealed using the low temperature heating regime showed constant reflectance intensity at blue wavelengths for all the [$Ca^{2+}$] and [Asp/Gly] trialled. Although using the low temperature regime rectified this issue, it led to the formation of smaller pore sizes than the high temperature regime. This reduced the median pore size for some conditions to less than 50 nm, lessening their ability to scatter light effectively and resulting in reflectance intensities similar to pure calcite.

Using polymeric vesicles as a low-carbon analogue of PS microspheres also avoided unwanted absorbance of blue light. The vesicles are expected to contain less carbon-based material since they are not filled with polymer chains and were also generally smaller in size than the PS microspheres.

The reflectance modelling indicated that the highest level of reflectance could be achieved with voids of 250 nm radius and a filling fraction of 30 %, therefore these criteria were treated as target porosity properties to produce synthetically. PS microspheres were used as an additive to recreate the simulated pore shapes, which were uniformly spherical voids. The desired pore size was achieved by incorporating PS microspheres with a size distribution of 445 ± 21 nm, creating pores with an average radius of 223 nm. This was acceptable compared to the original target of 250 nm, as the 200 nm simulated voids had similar reflectance intensity but was less broadband. The simulated filling fraction of 30 % (which is the percentage of the crystal area occupied by the voids) was achieved by using [PS] = 0.5 wt.%. Calcite crystals precipitated with [PS] of 0.1, 1 and 2 wt.% also had similarly high filling fractions, of 25, 25 and 36 %, respectively.

Though both of the target porosity properties were met synthetically, it is difficult to directly compare the simulated and measured reflectance as the residual carbon absorbed light and affected the reflectance spectra of PS-calcite. The measured reflectance increased with [PS] in the red wavelength region, but suffered increasing absorbance in the blue wavelength region from [PS] = 0.5 wt.%. While the simulations showed that reflectance increased as the filling fraction increased from 10 to 30 %, this was not found to be the case for the measured reflectance spectra. Considering only the regions of the measured reflectance spectra unaffected by absorbance, reflectance intensity increased with [PS] while the filling fraction peaked at 25 – 36 % for mid-level [PS] of 0.5 – 2 wt% and decreased at high [PS] of 3 – 5

wt.%. This discrepancy in the dependence of reflectance on filling fraction between the simulations and experimental work may be explained by the fact that the filling fraction simulations were conducted using a smaller void radius size of 50 nm, compared to the average pore radius size of 223 nm. This could be addressed in future work by conducting filling fraction simulations using larger pore sizes which more closely match those obtained experimentally.

This study identified several ideal pore properties for achieving high levels of broadband reflectance in porous calcite; (i) the pore size should be within the range of 50 – 500 nm, and should have a broad size distribution within this range to ensure that sufficiently intense light may be scattered, (ii) the pores should be free of any organic remnants that may contribute to absorbance and detract from the overall scattering performance, and finally (iii) the porosity should be uniformly distributed throughout the crystal. Excellent broadband reflectance of 70 % or more was exhibited by Asp-, Gly- and Ves-calcite produced using at least one of the crystallisation conditions tested. The high level of reflectance for porous synthetic calcite was similar to that exhibited by annealed sea urchin spine, which demonstrated that this strategy could also be utilised to remove organic molecules within biogenic calcite for the purpose of creating highly scattering materials.

It is also intriguing that despite relatively small amounts of an additive being incorporated into the crystal, the resulting crystal is highly porous. This could be due to partial decomposition of the calcite at the pore sites and other defects present within the crystal. It is also possible that decomposition of the additive and the subsequent generation of $CO_2$ within the crystal could create sufficient internal pressure to bring about expansion. This could also be worsened by the occlusion of water molecules alongside additives such as Asp and Gly. The TGA profile for Asp-calcite showed that at 500 °C, 97.72 % of the initial weight remained (Figure 3.27). Taking into account the loss of 0.12 % at 100 °C that can be attributed to residual water, this means that only 2.16 % is lost during heating up until 500 °C. It should be noted that this is not directly equivalent to the furnace heat treatment, where samples are kept at 500 °C for 30 minutes, as the temperature continued to increase during TGA tests to 1000 °C without a holding period at 500 °C. The incorporation study revealed that crystals prepared with $[Ca^{2+}]$ = 1.25 mM and [Asp] = 10 mM contained 0.7 mol% of Asp, which equates to 0.93 wt.%. This leaves 1.23 % of the

TGA weight loss unaccounted for, indicating that material other than occluded Asp decomposed during heating to 500 °C. This may be attributable to decomposition of calcite to calcium oxide, which may occur on a small scale locally at the pore sites. Further investigation using an in-situ technique, such as in-situ heating in TEM as previously discussed, is needed to observe the process and confirm whether CaO is evolved. This will also allow the effect of cooling, which may facilitate rearrangement of the crystal into a stable configuration, to be deconvoluted from the heating process. Future work could also include evaluating the strain on the crystal lattice using Raman spectroscopy or XRD, which would allow the initial strain caused by occlusion of the additive to be compared with the further strain created during heating and formation of the porosity.

## 3.5 Conclusions

In summary, porous calcite has been generated via the thermal decomposition of organic additives occluded within calcite crystals. This chapter has shown how simple molecules like amino acids and particles such as functionalised polymers can be used for this purpose. The porosity achieved using different heating regimes and additive systems was analysed and their effect on pore properties was explored.

Control over the heating parameters used to heat the composite crystals was paramount in creating porosity. In order to ensure uniform porosity, the temperature and heating time had to be well-balanced. The heating parameters were also highly influential on the pore size distribution. Increasing temperature increased the pore size, whilst slower heating rates led to a broader range of pore sizes. Varying the heating time provided useful information about the pore behaviour during heating; initial growth of the pores was followed by coalescence between 30 minutes – 4 hours, with continued heating leading to further expansion of the pore.

The crystal composition also affected porosity, as porous calcite produced by occlusion of Asp, Gly, PS and Ves each showed different pore size distributions and filling fractions that varied with both [$Ca^{2+}$] and additive concentration. These properties could be linked to the degree of Asp/Gly occlusion for Asp- and Gly-calcite, which was quantified by fluorometric assay. The efficiency of occlusion for PS and Ves could be adequately established from FIB-SEM cross-sections alone due to their large sizes.

Finally, the porosity within calcite crystals was found to enhance scattering relative to non-porous calcite. The reflectance of the crystals varied across the range of occluded additives, with broadband reflectance behaviour and a bright white appearance exhibited by many of the porous calcite samples that would render them suitable for application as white pigments. The results in this chapter showed that all additives trialled led to optically-active porous calcite at an optimised [$Ca^{2+}$] and additive concentration, using the high temperature heating regime. Overall, a facile strategy of preparing highly scattering porous calcite was demonstrated, which can be easily applied using organic additives that readily incorporate within the crystal and decompose using temperatures of ≤ 500 °C. The versatility of this approach implies that it could be employed across a diverse range of crystalline materials to form novel porous composites with functional optical properties.

# Chapter 4 | An Investigation into the Mechanism of Formation of Precipitated Calcium Carbonate

## 4.1 Introduction

### 4.1.1 Aims and Objectives

Precipitated calcium carbonate (PCC) is an important mineral for production of numerous materials, such as paper, plastic and rubber, in addition to being a ubiquitous component of many household products. In order to synthesise the vast quantities required, industrial manufacturers synthesise PCC by the carbonation of calcium hydroxide ($Ca(OH)_2$). However, the underlying mechanism of the carbonation reaction is still debated, and clarification is needed on whether a solid-state or dissolution-precipitation pathway is followed. The aim of this chapter was to use TEM techniques such as cryo-TEM, LCTEM and conventional TEM to study the reaction mechanism involved in the carbonation reaction. By combining insight obtained from both static (cryo-TEM) and dynamic (LCTEM) microscopy techniques, the goal was to monitor and capture the carbonation reaction to elucidate whether it proceeded by a solid-state or dissolution-precipitation mechanism.

In order to achieve these aims, synthesis of the starting reagent, $Ca(OH)_2$, was optimised to yield thin, hexagonal plates which would be easily recognised and of a compatible size for TEM techniques. The carbonation reaction was first investigated using conventional TEM to characterise the products at different stages of the reaction and establish the reaction timescale. Cryo-TEM studies revealed that the morphology of calcite varied with $[Ca^{2+}]/[CO_3^{2-}]$, where scalenohedral calcite was obtained at excess $[Ca^{2+}]$ and became increasingly rhombohedral-like in environments with higher $[CO_3^{2-}]$. Cryo-ET was used to examine the structure of partially-dissolved $Ca(OH)_2$ plates and calcite crystals at an early growth stage. The dynamics of the carbonation reaction was investigated using LCTEM, which showed that the dissolution of the $Ca(OH)_2$ occurred first at the basal faces of the plates. This led to the formation of hexagonal, skeletal structures by the pseudomorphic replacement of $Ca(OH)_2$ by precipitated ACC, when then dissolved prior to calcite precipitation. Finally, the effect of two common PCC additives, citric acid and

gypsum, on the carbonation reaction was explored using conventional TEM and cryo-TEM, demonstrating how these techniques can be used to further our understanding of additives in PCC production.

### 4.1.2 Industrial Production of Precipitated Calcium Carbonate (PCC)

Calcium carbonate is a versatile mineral that is essential as a filler in paper, plastic, paint, sealants and construction materials[278], in addition to being a ubiquitous component in numerous household products[279]. Industrial manufacturers of calcium carbonate supply it in two main forms: “ground calcium carbonate” (GCC) and “precipitated calcium carbonate” (PCC). GCC is formed via an elementary processing method by crushing limestone rock to a desired particle size[280]. Natural limestone contains ions such as $Mg^{+}$ and $Mn^{2+}$, which therefore remain as impurities in GCC particles[281]. In addition to the low purity, GCC typically has irregular particle sizes and shapes. However, this is a cheaper material which is suitable for most filler applications where further refinement of the $CaCO_3$ is not necessary for the end use[282].


**Figure 4.1 Applications of GCC and PCC.**

In contrast, PCC production involves multiple processing steps in which several chemical reactions are performed on the mined limestone to re-precipitate $CaCO_3$. This eliminates impurities and refines properties such as particle size and morphology[282]. A three-step synthesis route known as the “carbonation” or “milk of lime” process is used that follows a solid-liquid-gas crystallisation reaction.

Compared to the gas-liquid and liquid-liquid crystallisation pathways used elsewhere in this thesis, industry favours this approach due to the high yield and low cost[278].

The first step in producing PCC occurs at lime quarries, where limestone is extracted from the ground. Limestone is a biogenic sediment that is rich in skeletal remains and thus contains a range of impurities[283]. Large impurities can be separated from the rock mass during crushing, a process which reduces the particle size in preparation for calcination[46]. This step involves heating the crushed limestone particles in a kiln at temperatures > 800 °C, where 900 – 1000 °C is typically used by manufacturers[284]. A large amount of $CO_2$ is released to form CaO, known as "quicklime" (Equation 4.1).

$$CaCO_{3(s)} \xrightarrow{\Delta} CaO_{(s)} + CO_{2(g)} \quad (4.1)$$

Limestone provides an ideal feedstock for PCC production over other natural $CaCO_3$ sources such as marble and chalk, due to the problems that can occur during calcination of the latter materials. Marble is the hardest and fracturing can occur during heating, which can block the $CO_2$ exit channel within the kiln[283]. In contrast, chalk is a very soft material due to the higher content of skeletal remains present, and readily disintegrates during heating. Both of these calcination behaviours present serious production issues for manufacturers, whereas limestone possesses intermediate properties and behaves manageably in the kiln[285]. The difference in decrepitation behaviour between these $CaCO_3$ materials can be attributed to differences in the porosity and crystal size[286].

Following calcination, CaO is mixed with water in a process known as slaking (Equation 4.2). The resulting $Ca(OH)_2$ suspension is commonly referred to as "slaked lime" or "milk of lime". To aid full conversion of the oxide, the reaction is initiated at 35 °C; due to its exothermic nature the end temperature can reach 75 °C[287]. Additives may also be used at this point in the manufacturing process.

$$CaO_{(s)} + H_2O_{(l)} \longrightarrow Ca(OH)_{2(aq)} + \Delta \quad (4.2)$$

The final step of PCC production is carbonation of the slaked lime, which is generally performed using $CO_2$ produced in the calcination step to improve the sustainability and cost-efficiency of the process[288]. This $CO_2$ constitutes a proportion of the required gas for the reaction, while the rest is typically requisitioned through

calcination of limestone to make CaO that is sold commercially, rather than being processed further. Carbon dioxide is bubbled through the slaked lime in an exothermic reaction yielding $CaCO_3$ and water (Equation 4.3).

$$Ca(OH)_{2(aq)} + CO_{2(g)} \longrightarrow CaCO_{3(s)} + H_2O_{(l)} + \Delta \quad (4.3)$$

The overall reaction depicted in (4.3) proceeds via a series of steps, shown below in reactions (4.4), (4.5) and (4.6). Firstly, dissolution of $Ca(OH)_2$ occurs to generate $Ca^{2+}$ and $OH^-$ ions, followed by the dissolution of bubbled $CO_2$ gas. This is the rate limiting step, so effective gas distribution methods must be utilised to encourage dissolution of $CO_2$[289]. Initially, dissolution of $CO_2$ generates carbonic acid, which further dissociates to form bicarbonate and carbonate ions (Equation 4.4 and 4.5). Finally, the $Ca^{2+}$ and $CO_3^{2-}$ ions combine to precipitate $CaCO_3$ (Equation 4.6).

$$Ca(OH)_{2(aq)} \longrightarrow Ca^{2+}_{(aq)} + 2OH^-_{(aq)} \quad (4.4)$$

$$CO_{2(g)} + H_2O_{(l)} \longrightarrow H_2CO_{3(aq)} \longrightarrow H^+_{(aq)} + HCO^-_{3(aq)} \longrightarrow 2H^+_{(aq)} + CO^{2+}_{3(aq)} \quad (4.5)$$

$$Ca^{2+}_{(aq)} + CO^{2-}_{3(aq)} \longrightarrow CaCO_{3(s)} \quad (4.6)$$

The carbonation reaction is continually monitored to ensure that the end point is reached. The influx of ionic species formed during the dissolution of $CO_2$ and dissociation of its products results in an initial increase in electrical conductivity that reduces over time as $CaCO_3$ is formed[290]. A final increase in conductivity is observed after all $Ca(OH)_2$ has dissolved and reacted, as the ions produced by the dissolution of $CO_2$ accumulate and are no longer being consumed by $Ca^{2+}$ to form $CaCO_3$. Therefore, monitoring the electrical conductivity of the reaction allows the end point of the reaction to be determined. Additionally, pH can be used to monitor the reaction[290]. $OH^-$ ions are formed by dissolution of $Ca(OH)_2$ creating an alkaline pH, but as $CO_2$ dissolves into the solution the pH decreases and becomes neutral due to the generation of $H^+$. This fall in pH is only seen towards the very end of the reaction when $Ca(OH)_2$ is depleted and all $OH^-$ ions are consumed. In the industrial manufacturing process, once the end point has been reached the reaction is usually continued for a short period of time to “over-carbonate” and ensure pH stability of the end product[291]. The resulting slurry may then undergo several refining steps, including “dewatering” and milling to a desired particle size[278].

### 4.1.3 Current Understanding of the Mechanism of Formation of $CaCO_3$ via Carbonation of $Ca(OH)_2$

This chapter focuses on the final PCC synthesis step, the carbonation of $Ca(OH)_2$ to form calcite. This reaction is of significant interest due to the diverse applications of $Ca(OH)_2$; it is used as a cementitious material in construction, a restorative treatment for protecting cultural heritage sites[292], and also has a promising role in carbon capture and storage due to its reactivity with $CO_2$[289, 293-295]. Insight into the mechanism behind the carbonation of $Ca(OH)_2$ is also crucial in optimising the industrial manufacture of $CaCO_3$. However, there has been considerably fewer studies into the formation of $CaCO_3$ by this method compared to direct mixing and diffusion methods discussed in Chapter 3.

$Ca(OH)_2$ has the mineral name portlandite and belongs to the trigonal crystal system in the hexagonal scalenohedral class. Each calcium ion is octahedrally coordinated by 6 hydroxide ions as shown in the unit cell (Figure 4.20). Portlandite crystals have hexagonal morphologies consisting of {10-10} prismatic facets and layered {0001} basal facets[296], with weak hydrogen bonds between layers stacked on the basal (0001) plane[297, 298]. The crystals are typically precipitated as micron-sized hexagonal prisms or thin plates, commonly referred to as “nanolime” due to their 10 – 100 nm thicknesses.

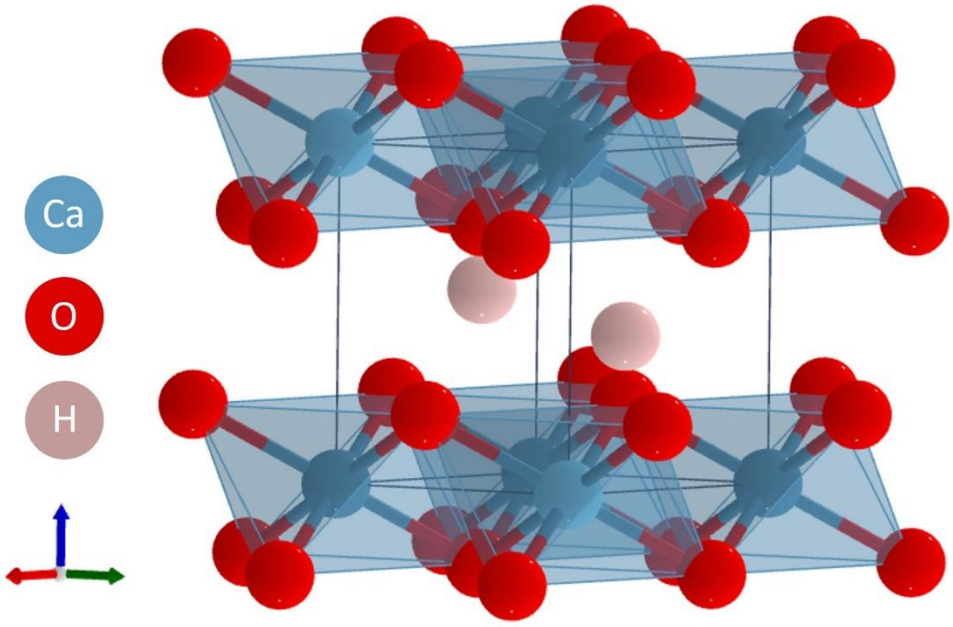


**Figure 4.2 The unit cell of portlandite. Adapted from ref.[299]**

Research into the mechanism behind the carbonation reaction has brought about contrasting findings, namely whether the reaction proceeds via a solid-state transformation[300] or a coupled dissolution-precipitation process[301]. An interface-coupled dissolution-precipitation reaction consists of several key steps which are outlined in Figure 4.3. Firstly, a solid must undergo some degree of dissolution in an aqueous fluid. This may only occur for a few monolayers, and will result in the creation of an interfacial layer of fluid around the dissolving solid. If this layer is supersaturated with respect to another phase, then this phase will precipitate and typically nucleates on the surface of the solid phase. This reaction will eventually be limited as formation of the product phase blocks contact of the interfacial fluid with the reaction front[302]. This can be avoided in cases where a volume deficit is created; this can be achieved when a product phase has a smaller molar volume than the parent phase, or if the parent phase has a lower solubility[303] and can therefore evolve intracrystalline porosity[304]. Fractures can also provide another route for mass transport between the interfacial fluid and the reaction front, and may be generated when the change in molar volume between the parent and product phase induces sufficient local stress. This may also give rise to pseudomorphism, which occurs when a crystalline material takes the crystal system of another crystalline species. This can only be achieved when the dissolution and precipitation processes occur locally to each other and within similar timeframes[302].

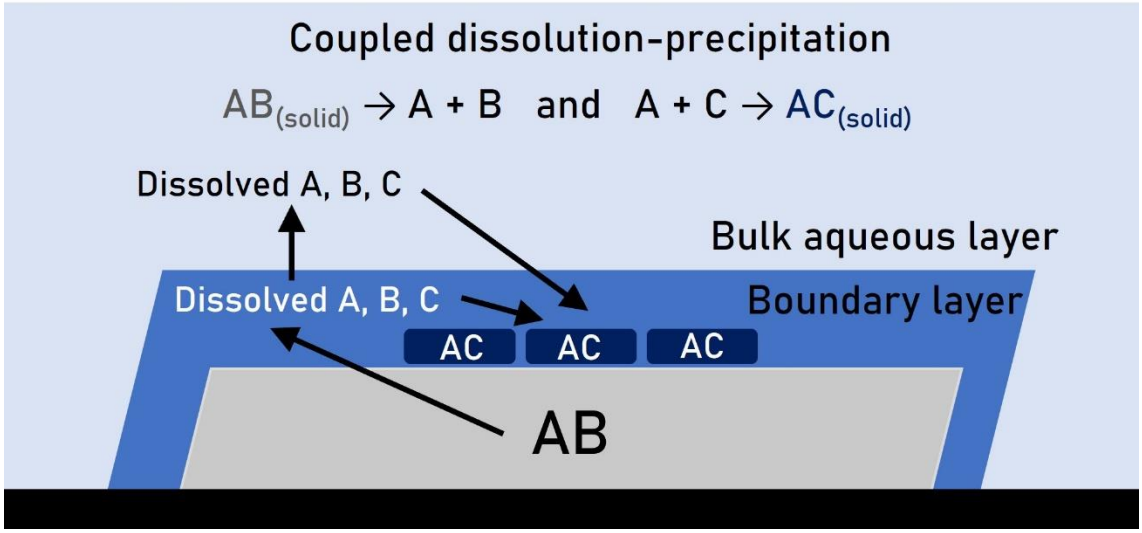


**Figure 4.3 Coupled dissolution-precipitation reaction schematic, where AB is a dissolving mineral, and A is a cation that can bind with C and precipitation to form a new mineral AC. Adapted from ref.[305]**

On the other hand, a solid-state transformation is one which typically occurs in the absence of any solvent, whereby the internal atomic or molecular structure of a solid rearranges to form a new phase[306, 307]. This process relies on the solid-state diffusion of ions and a diffusive front that is able to move freely through the parent phase. In the case of two parent phases forming a product phase (as solid-state transformations are found in a broad range of reactions), the requirements for a solid-state diffusion reaction are similar to those for dissolution-precipitation reactions to occur. Additionally, pseudomorphic replacement can occur in both interface-coupled dissolution-precipitations and solid-state transformations[304, 308]. However, the kinetics of solid-state transformations are much slower than those for dissolution-precipitation reactions, in the absence of high temperatures or indeed a fluid[302]. These slow dynamics generally allow the retention of a textured microstructure that would otherwise coarsen with time, which can provide evidence of the solid-state diffusion mechanism.

The carbonation of $Ca(OH)_2$ was first hypothesised to occur via a dissolution-precipitation mechanism by Powers, while investigating Portland cement paste[301]. Carbonation of the paste led to shrinkage rather than expansion, despite the increase in molar volume associated with the transformation from $Ca(OH)_2$ to $CaCO_3$. Therefore Powers deduced that the reaction must first occur via dissolution of $Ca(OH)_2$ rather than a solid-state transformation. This was later supported by carbonation studies performed by Johnstone and Glasser, which also showed that $CaCO_3$ formed at the surface of $Ca(OH)_2$ crystals[309].

More recent examination of the dissolution and carbonation reaction of $Ca(OH)_2$ has been conducted using AFM[310, 311]. One such study by Ruiz-Agudo *et al.* confirmed that the reaction progressed via a coupled dissolution-precipitation process, and that calcite precipitated in a pseudomorphic fashion on the basal face of the $Ca(OH)_2$ crystal[310]. In order to determine the feasibility of this mechanism, the requirements for an interface-coupled dissolution precipitation reaction were considered. Due to the increase in molar volume during the transformation, no porosity is evolved during the reaction. However, it is clear from the AFM results that the growth of calcite occurs via a 3D island growth model rather than layer-by-layer, which permits the continued mass transport required for the reaction[308]. Additionally, Ruiz-Agudo *et al.* hypothesised that the increase in molar volume during the reaction generates stress

that accumulates and leads to fracture through the prismatic faces of $Ca(OH)_2$, which facilitates further transport of the ions to the reaction site.

Dissolution of $Ca(OH)_2$ crystals occurs fastest at the prismatic {1010} faces, which possess a higher surface energy than the {0001} basal plane and are therefore more soluble[312]. However, the reaction is passivated by the formation of ACC on the surface of the $Ca(OH)_2$ basal faces which hampers diffusion of $CO_2$ to the reaction front[313]. In summary, the reaction is initially controlled by the interface, before the diffusion of $CO_2$ becomes the rate-limiting step after the $Ca(OH)_2$ surfaces become passivated after precipitation of ACC[289].

The role of water in catalysing the reaction has also been well-documented [314-317]. Beruto and Botter showed that $Ca(OH)_2$ had up to 7 monolayers of absorbed water at 20 °C, where only 4 were necessary for a catalytic effect. Ruiz-Agudo *et al.* calculated that 7 monolayers of water was sufficient for the interfacial fluid to become supersaturated with respect to calcite[310].

In contrast, multiple studies have found evidence indicating that the carbonation of $Ca(OH)_2$ is a solid-state reaction. Gillott hypothesised that the reaction occurred via a topotactic process[300], whereby the crystal lattice rearranges whilst retaining at least some of the original crystal orientations[318]. Stepkowska studied the reaction using a combination of pXRD, TGA, IR and mass spectroscopy and interpreted results as the reaction occurring via a solid-state transformation[319]. The author proposed that ageing of $Ca(OH)_2$ paste resulted in a solid-state transformation into hydrated calcium carbonate species, which occurred by the replacement of $OH^-$ ions by $CO_3^{2-}$ ions in the basal face. Conversely, a study by Montes-Hernandez *et al.* conducted using TGA of the carbonation reaction found that a solid-state transformation occurred at high temperatures (> 200 °C) if the relative humidity was ≈ 0%[294].

The carbonation reaction has also been studied to determine whether crystallisation proceeds via a classical or non-classical pathway. The evidence that suggests growth of calcite occurs via a dissolution-precipitation mechanism also indicates that a non-classical route is followed, due to the formation of nanoparticles which later merge and become a layer[320]. Rodriguez-Navarro *et al*. studied the evolution of ACC via the carbonation of $Ca(OH)_2$, and found that it formed via a dense liquid phase[321]. This phase formed almost instantaneously upon exposure of the $Ca(OH)_2$ solution to

air. The authors deduced that the transition from dense liquid phase to ACC occurred by the expulsion of water, which created “shapeless” ACC structures similar to those found by Rieger *et al*. using the direct mixing route (with $CaCl_2$ and $Na_2CO_3$)[105]. Spinodal decomposition, which is the spontaneous demixing of two phases, has been found to occur chiefly in systems with high supersaturations[322]. The carbonation reaction inherently generates a supersaturated system with respect to $CaCO_3$ phases[321], so it is plausible that the threshold could be met for spinodal decomposition to occur[323]. Further study is required as new techniques for identifying such phases are developed.

### 4.1.4 Controlling Properties of PCC During the Carbonation Reaction

PCC with the desired properties can be produced by controlling the reaction conditions or using additives during the carbonation step. Firstly the effect of various reaction parameters on PCC properties will be considered.

One of the most important properties is the polymorph of $CaCO_3$ produced. Calcite is readily obtained over a range of reaction conditions and typically possesses scalenohedral or rhombohedral morphologies, which can be further defined into “fine” or “coarse” grades of particle size. “Ultra-fine” rhombohedral calcite is typically used as a filler material in sealants and plastics, or as a paper coating, whilst scalenohedral calcite is chiefly used as a filler in paper and paint[324]. High temperatures and low $CO_2$ flow rates during carbonation favour the formation of aragonite, which precipitates as needle-like crystals with high aspect ratios that can be used in cosmetics, rubbers and plastics[325]. The metastable polymorph vaterite has found applications in drug delivery and personal care products[215, 326]. However, it must be thoroughly dried within 24 – 48 hours of production or the crystals will transform into a more stable polymorph.

Another crucial property of PCC is the crystal morphologies. An intriguing aspect of the carbonation reaction is that the calcite crystals obtained typically possess scalenohedral morphologies, which are readily formed in the absence of additives. Although scalenohedral or “dog-tooth” calcite is the prevalent form found in nature, the rhombohedral form bounded by {104} is the dominant morphology obtained via synthetic methods such as the gas-liquid diffusion and direct mixing (liquid-liquid) routes explored in Chapter 3.

The preferential formation of the scalenohedral morphology has been attributed to two possible situations by Cizer *et al.*[327]. The first relies again on periodic bond theory as devised by Hartman and Perdok [11, 328]. This assigns crystal facets as flat (F), stepped (S) or kinked (K) to explain the anisotropic behaviour of different faces due to their different energies. Here, the rhombohedral {104} faces are classified as flat (F) while the scalenohedral {214} faces are stepped (S)[329]. This means that the rhombohedral faces are lower in energy and these typically bound the growth form[327]. The authors suggested that under an excess of $Ca^{2+}$ ions, the scalenohedral {214} faces become a stable growth form, due to adsorption of $Ca^{2+}$ at the obtuse steps $[-441]_+$ and $[48\text{-}1]_+$[329] which disrupt the growth of {104} faces[327]. The second explanation given by Cizer *et al.* was that the excess $Ca^{2+}$ ions present attach to the polar scalenohedral {214} faces over the non-polar {104} faces, which stabilises the {214} faces and allows them to become the dominant growth form[327].

This was further explored by García Carmona *et al.,* who investigated the effect of the $[Ca^{2+}]/[CO_3^{2-}]$ content of a slaked lime suspension on the resulting calcite morphology[330, 331]. The $[Ca^{2+}]/[CO_3^{2-}]$ content was monitored by conductivity, where a larger conductivity value indicates a higher ratio of $[Ca^{2+}]$ to $[CO_3^{2-}]$. Scalenohedral calcite was obtained at high conductivities (7 mS/cm) and lowering the conductivity caused the calcite crystals to become more rhombohedral, where amalgamated scaleno-rhombohedral and rhombo-scalenohedral morphologies formed before the pure rhombohedral morphology at 1 mS/cm (Figure 4.4).

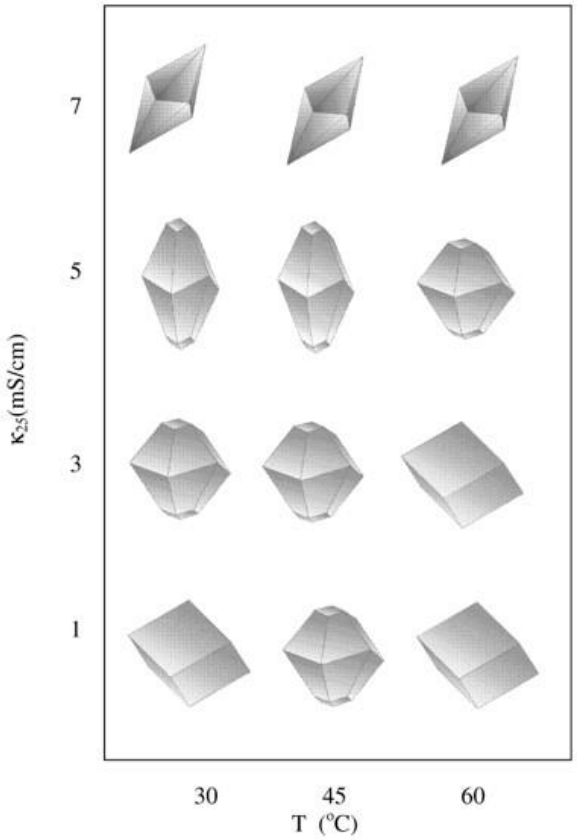


**Figure 4.4 The morphological change of PCC observed with temperature and conductivity, with illustrations of the scalenohedral, scaleno-rhombohedral, rhombo-scalenohedral, and rhombohedral morphologies. Reproduced from ref.[330]**

Similar observations were made in the aforementioned study by Cizer *et al.,* where calcite with different morphologies formed at different depths in carbonated lime paste. Rhombohedral crystals were present in the outermost layer, scaleno-rhombohedral crystals in an intermediate layer and purely scalenohedral crystals were observed at the base of the sample. This was the case regardless of whether carbonation was performed in air or in a $CO_2$ atmosphere. However, the authors attributed this to dissolution-precipitation of scalenohedral calcite into rhombohedral calcite, which is more stable at high relative humidity and a $CO_2$ atmospheres.

The morphology of PCC can also be controlled using temperature, where rhombohedral calcite is usually obtained at low temperatures (20 °C) compared to scalenohedral calcite at mildly elevated temperatures (40 °C)[332-334].

Other important properties of manufactured PCC are the particle size and specific surface area (SSA). High supersaturation levels can lead to increased SSAs, as greater numbers of small crystals nucleate. Control over the supersaturation can be achieved by maintaining an optimum reaction temperature; as $CO_2$ has reduced solubility with increasing temperature, the supersaturation generally decreases with temperature. As a result, maintaining a low temperature during the exothermic reaction can allow PCC with small particles sizes and high SSA to be produced[334]. The particle size is also affected by the gas sparging method and efficiency, as shown by Xiang *et al.* who found that a radial-shaped sparger that provided more efficient gas dispersion led to finer particle sizes than a round gas sparger[335]. This is in agreement with studies employing microbubble generators in the carbonation reaction, which produced smaller calcite crystals and larger SSAs relative to ordinary sparging methods[336, 337].

Additives are commonly used in combination with optimised reaction conditions to control the properties of PCC crystals[278]. Citric acid is a complexing agent that is often used in the production of calcite to supress the formation of aragonite, reduce particle size and increase the SSA[338, 339]. Other complexing agents such as ethylenediaminetetraacetic acid (EDTA), diethylenetriaminepentaacetic acid (DTPA) and pyromellitic acid have also been explored and were found to retard the growth of aragonite and calcite, though did not fully inhibit the formation of aragonite as for citric acid[340]. Polysaccharides such as starch and carboxymethyl cellulose (CMC) may also be used to increase particle size and favour the formation of rhombohedral calcite over scalenohedral calcite[338]. The addition of sucrose or glucose has also been shown to favour the formation of vaterite[341, 342].

Inorganic additives have also been explored as a method of controlling PCC properties. Xiang *et al*. found that PCC particle size was reduced in the presence of $ZnCl_2$. The use of $Mg^{2+}$ is well-established as a method for crystallising aragonite by hindering the growth of calcite[165], and has also been shown to affect the morphology of the aragonite crystals produced, where high concentrations of $MgCl_2$ led to pyramidal morphologies rather than acicular[343]. Gypsum, a polymorph of $CaSO_4$, is also used as an additive during carbonation to control PCC particle size by retarding growth.

The effect of solvents such as ethylene glycol and glycerol on the carbonation reaction has been investigated by Konopacka-Łyskawa *et al*., who compared their effects with pure aqueous phase reactions[344]. The authors showed that the addition of ethylene glycol and glycerol both had an effect on morphology and particle size, where smaller particles with rhombo-scalenohedral morphologies and shorter *c*-axes were produced as compared to the scalenohedral calcite obtained in the control.

After crystallisation, further additives may be used to control the properties of PCC mixture. These include drying agents such as $MgSO_4$[345], or inorganic acids such as phosphoric acid, which is typically used to adjust the pH of alkaline PCC suspensions or partially react with PCC to form a protective layer of $Ca(H_2PO_4)_2$ that inhibits dissolution during paper making[346, 347].

## 4.2 Experimental

### 4.2.1 Synthesis and Preparation of Materials

#### 4.2.1.1 Materials

$Ca(OH)_2$ was obtained from Fluorochem. NaOH, $CaCl_2.2H_2O$, citric acid ($C_6H_8O_7$), $Na_2SO_4$ and Dowex Monosphere 550A ($OH^-$) resin beads were obtained from Sigma Aldrich. Deionised (DI) water was used to prepare all aqueous solutions, which was prepared using a MilliQ system operating at 18 Ω.

#### 4.2.1.2 $Ca(OH)_2$ Synthesis via Aqueous Precipitation

Calcium hydroxide was precipitated via a synthesis route developed by Ambrosi *et al.*[348] . An aqueous solution of NaOH (0.6 M) was added dropwise to an aqueous solution of $CaCl_2$ (0.3 M) with stirring at 90 °C to produce $Ca(OH)_2$ and NaCl (Equation 4.7).

$$CaCl_2 + 2NaOH \rightarrow Ca(OH)_2 + 2NaCl \quad (4.7)$$

The reaction was conducted whilst bubbling under nitrogen to reduce premature carbonation in air. Once all of the NaOH had been added, the flask was left to cool while stirring to ensure complete conversion of the reactants. In order to remove the unwanted NaCl crystals, multiple washing steps with DI water were required. This inevitably led to a minor loss of product and repeated exposure of the aqueous $Ca(OH)_2$ suspension to air. Final washing steps were performed to displace the water with EtOH, in order to prolong the stability of the suspension.

#### 4.2.1.3 $Ca(OH)_2$ Synthesis via Anion Exchange Resin Method

An aqueous solution of $CaCl_2$ (0.2 M in all studies initially and later 0.02 M in LCTEM studies) was added to a beaker containing Dowex Monosphere 550A (OH) resin beads and it was stirred for 30 minutes. The resin beads consist of a styrene-divinylbenzene gel with quaternary amine functional groups and hydroxyl counter-ions. After adding $CaCl_2$ solution to the resin beads, the resin $OH^-$ groups are exchanged for the dissolved $Cl^-$ groups (binding is 22 times stronger for $Cl^-$ than $OH^-$). The $Ca^{2+}$ and $OH^-$ groups form $Ca(OH)_2$ which is poorly soluble and thus precipitates. The exhausted beads were removed using a sieve with 250 µm mesh size and the resulting suspension (1 – 2 ml) was added to a 15 ml vial containing 13

ml EtOH. This $Ca(OH)_2$ suspension was used for the cryo-TEM studies described in Sections 4.3.5.1 and 4.3.5.2.

In later studies, the stability of the suspension was improved by removing residual water. After removing the resin beads, the product was immediately filtered under vacuum using a 100 nm polycarbonate track-etched membrane filter. EtOH was used to rinse the glassware and dry the product on the filter, before fully drying it in a vacuum desiccator. The resulting powder was weighed and a suspension with controlled concentration (mg/ml) was prepared using EtOH, before sonicating for 1 – 2 minutes to break up any aggregated particles. As a suspension of particles was desired the $Ca(OH)_2$ concentration was much higher than the solubility limit of 1.6 mg/ml.

#### 4.2.1.4 Synthesis of $CaCO_3$ via Carbonation of $Ca(OH)_2$

In order to monitor the carbonation of $Ca(OH)_2$ using TEM, the reaction was conducted via two methods: on-grid or in a centrifuge tube, from which aliquots were taken and deposited onto a grid. For conventional dry TEM work, the carbonation reaction was performed on-grid by depositing a known volume of $Ca(OH)_2$ suspension and DI water onto a TEM grid in a 1:1 ratio. The grids were left exposed to air for an allotted amount of time before manually back-blotting them.

For cryo-TEM work, a $Ca(OH)_2$ suspension was added to DI water in a 2.5 ml centrifuge tube in a known ratio (in this chapter the effect of using both a 1:10 and 1:1 dilution ratio were investigated using cryo-TEM). The tube was left exposed to air for an allotted amount of time before removing a 3 µl aliquot and depositing it onto a TEM grid and plunge freezing. Plunge freezing of the grids was performed using a Vitrobot Mk. IV.

#### 4.2.1.5 PCC Additives

Both gypsum and citric acid were used as additives in the crystallisation of $CaCO_3$ via the carbonation of $Ca(OH)_2$. Gypsum was precipitated by mixing 3M $CaCl_2.2H_2O$ with 3M $Na_2SO_4$, and was then vacuum filtered and washed with DI $H_2O$ and EtOH. The product was confirmed to be gypsum using Raman spectroscopy, and an aqueous suspension of $CaSO_4$ was prepared. In order to study the effect of each additive on the carbonation reaction, aqueous additive suspensions were used as the water source for the reaction, which mixed in the same dilution ratio of 1:1 with

the $Ca(OH)_2$ suspension. The amount of additive used was kept in-line with the amount that would be used in industry to control the product; this was 0.1 wt.% gypsum and 0.2 wt.% citric acid of the final PCC weight.

### 4.2.2 Analytical Techniques

#### 4.2.2.1 LCTEM

LCTEM is discussed in Chapter 2. The specific details of the LC experiments conducted in this chapter are detailed here. The lower chip component was plasma cleaned for 20 s and loaded with 2 doses of 2 µL. The EtOH was left to evaporate, leaving the $Ca(OH)_2$ particles dried onto the chip. To improve the adherence of the particles to the chip, the loaded chip was plasma cleaned once more for a further 20 s. The cell was finally assembled and filled with EtOH before leak-testing and placing the holder into the microscope. Imaging of the LC was done in HAADF STEM mode. Water was flowed through the cell at 0.05 ml $min^{-1}$ and the change in the composition of the solvent was monitored using EDX. In order to collect SAED patterns and characterise the particles, air was flushed through the LC to dry it and imaging and diffraction was performed in TEM mode. The LC was not rehydrated once dry.

## 4.3 Results

### 4.3.1 Bulk Precipitation of $CaCO_3$ via Carbonation of $Ca(OH)_2$

The carbonation reaction was first performed in bulk using commercial calcium hydroxide powder. Preliminary tests were performed in litre-volumes and necessitated several hours of carbonation with highly effective gas sparging to ensure the end point was reached. Due to the difficulty in preventing blockages occurring in the gas sparger as $CaCO_3$ crystallised, two smaller batch reactors were constructed to contain millilitre scale slurry volumes (30 ml and 3 ml), and allow shorter carbonation times to be used. The reaction was monitored via pH, where the end point corresponds to a pH of 7-8. The larger setup, which consisted of a 30 ml $Ca(OH)_2$ slurry in a 100 ml glass beaker, allowed the reaction to be easily monitored using a conventional pH probe. The smaller setup housed 3 ml $Ca(OH)_2$ slurry within a 20 ml glass vial, and the pH was monitored by taking aliquots of the reaction mixture and depositing them onto pH indicator paper (Figure 4.5).

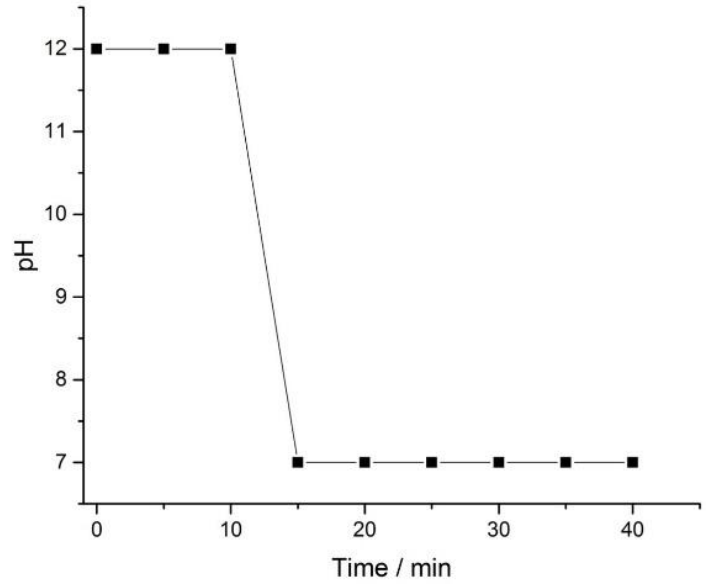


**Figure 4.5 Monitoring the reaction in the 3 ml reactor using pH.**

The final product obtained using the 30 ml setup was filtered and powder XRD was conducted (Figure 4.6). This confirmed that calcite was formed, with no residual portlandite peaks present.

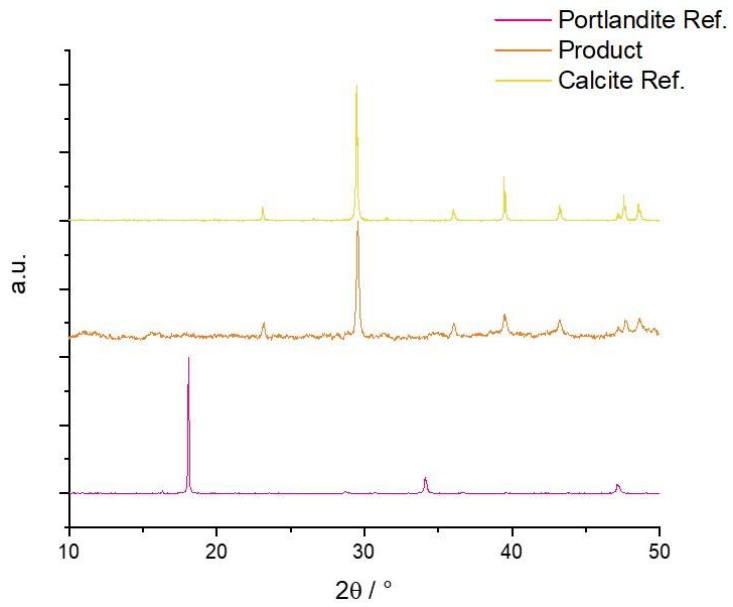


**Figure 4.6 Powder XRD analysis of the product obtained in the 30 ml reactor confirming that calcite was produced, compared with reference spectra obtained from AMCSD[349] (ID: 0000116 (portlandite) and 0000098 (calcite)).**

The crystals were observed using SEM which showed that large aggregates of polycrystals were obtained (Figure 4.7). Individual crystals possessed scalenohedral

morphologies typical of calcite produced via the carbonation method, and were 1 – 2 µm in length.

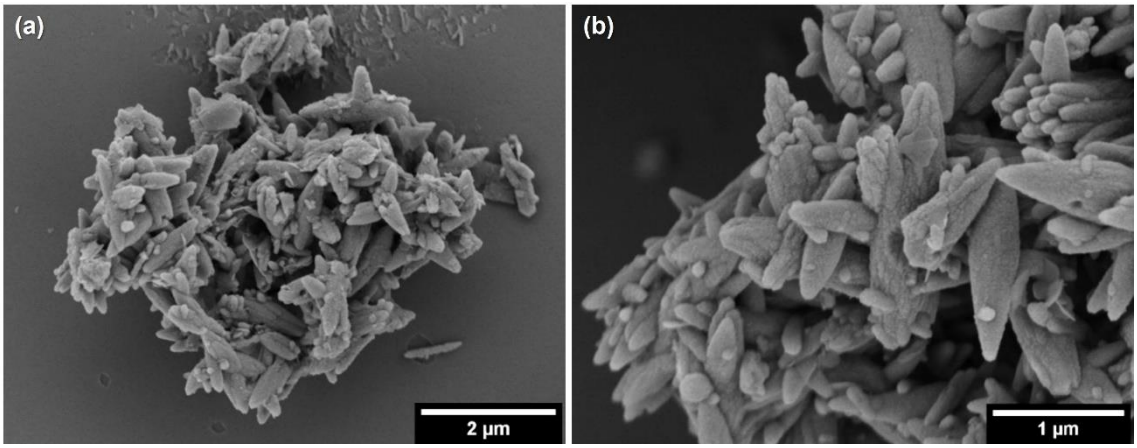


**Figure 4.7 SEM images of the scalenohedral calcite obtained in the 30 ml reactor.**

The progress of the reaction was further characterised by taking aliquots of the reaction at set time points, filtering them and using Raman spectroscopy to characterise the products obtained. Spectra were collected in the 100 – 500 $cm^{-1}$ region, which captured the lattice vibration modes of calcite and portlandite and allowed the analyses to be performed quickly such that further reaction of the sample in air was avoided (Figure 4.8). The peaks at 152 and 278 $cm^{-1}$ were present for all timepoints and can be attributed to the $E_g$ phonons (*T* and *L*, respectively) for calcite. The peaks at 255 and 358 $cm^{-1}$ that disappear over time belong to the $E_g(T)$ and $A_{1g}(T)$ modes of portlandite. This showed that calcite was readily formed, but that longer carbonation periods were required for full conversion of the reactants.

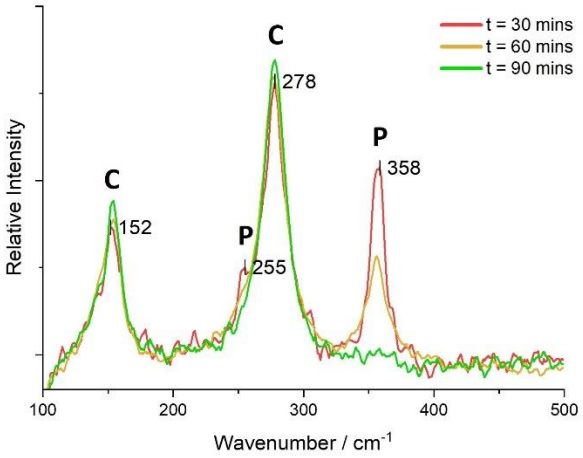


**Figure 4.8 Raman spectroscopy of the product obtained over time from the 30 ml reactor, where peaks corresponding to calcite and portlandite are marked as C and P respectively.**

## 4.3.2 Synthesis of Calcium Hydroxide via Aqueous Precipitation

### 4.3.2.1 Commercial $Ca(OH)_2$ Powder

Bulk reactions were conducted using commercial calcium hydroxide powder, shown in the SEM images in Figure 4.9. The particles had poorly-defined morphologies and formed micron-sized aggregates.

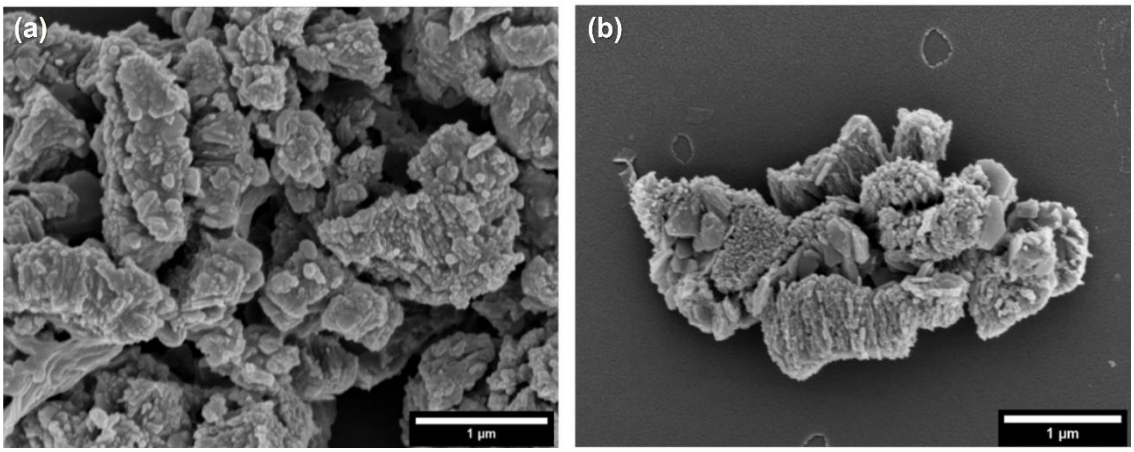


**Figure 4.9 SEM images of commercial calcium hydroxide powder, showing the aggregates formed.**

The commercial $Ca(OH)_2$ powder was dispersed in ethanol and loaded onto a TEM grid for further characterisation (Figure 4.10). Due to the large size of the aggregates it was challenging to find thin particles ideal for TEM imaging. A representative

SAED pattern is shown in Figure 4.10 and contains rings of spots due to the multiple crystals were present. These corresponded to both portlandite and calcite, which shows that carbonation had already begun to occur. This is likely due to exposure of the sample to air on the grid or in the reagent bottle, which would worsen with time. Overall, the irregular morphology of the particles and the large size of the aggregates confirmed that commercial $Ca(OH)_2$ would not be ideal for TEM studies.

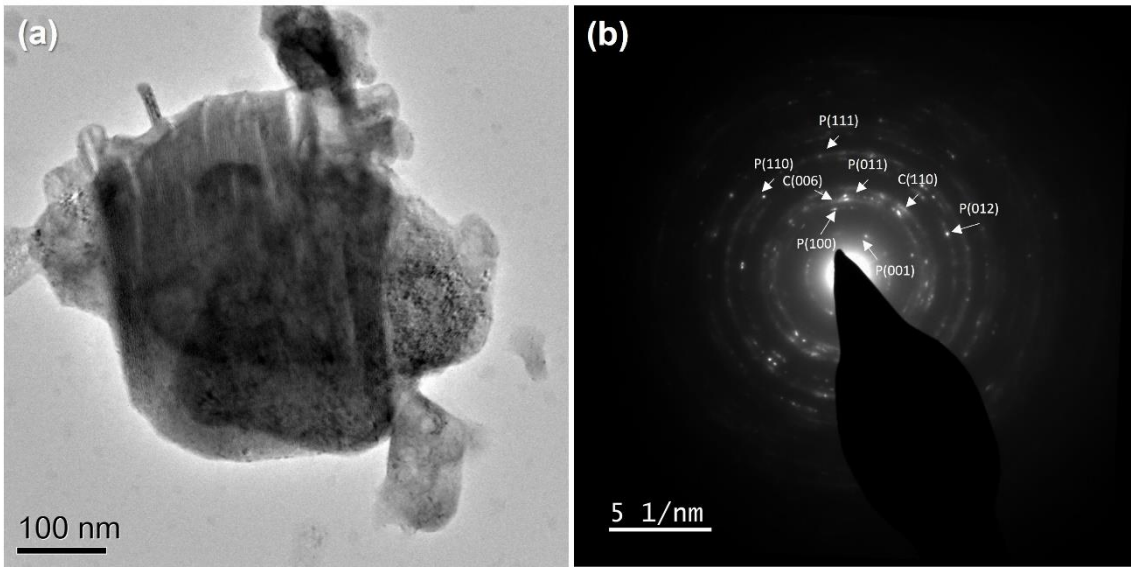


**Figure 4.10 TEM image of commercial $Ca(OH)_2$ particle aggregates (a) and the corresponding SAED pattern (b).**

#### 4.3.2.2 Calcium Hydroxide Synthesis using an Aqueous Precipitation Method

In order to further study the carbonation reaction using TEM, the particles should be well-dispersed, prepared freshly to avoid premature carbonation and ideally possess a recognisable morphology that can be easily distinguished from new phases. To achieve this, other routes of synthesising monodisperse calcium hydroxide particles were explored.

$Ca(OH)_2$ crystals were synthesised using the aqueous precipitation method as described in Section 4.2.1.2. The resulting $Ca(OH)_2$ crystals were examined using SEM (Figure 4.11) by loading a glass slide with the final product and lightly blotting excess solvent. Hexagonal particles were observed, which had sizes of 0.2 – 2 µm. Unlike the commercial $Ca(OH)_2$, the particles were not agglomerated and the individual hexagonal morphologies of the crystals were generally easily recognisable.

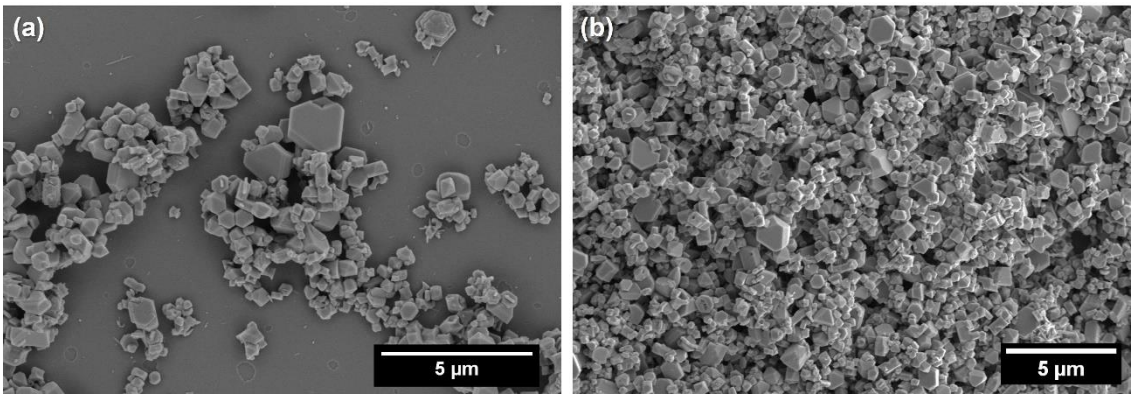


**Figure 4.11 SEM images of calcium hydroxide particles prepared via aqueous precipitation and dispersed in ethanol.**

#### 4.3.2.3 Carbonation of $Ca(OH)_2$ Produced via Aqueous Precipitation

The reaction was performed on a glass slide by adding 3 µl of the $Ca(OH)_2$ ethanol suspension followed by 3 µl of deionised water and leaving it to carbonate in air until it was dry. Different stages of the reaction were observed at different areas on the substrate, as evaluated using SEM (Figure 4.12), which was likely due to the drying process occurring non-uniformly and less densely populated areas drying more quickly. One area contained hexagonal $Ca(OH)_2$ prisms which were partially dissolved (Figure 4.12a), with regions on the basal plane missing while the outer hexagonal edge remained largely intact. Spherical particles with sizes 50 – 150 nm were also present, which is characteristic of amorphous calcium carbonate (ACC). There was also an emerging phase, which took the form of small, needle-like crystals with thicknesses of 20 nm. These were seen both as isolated particles and also protruded from the apexes of larger, rod-like crystals. This suggested that these particles were indeed the early formation of scalenohedral calcite. In contrast, the reaction had reached completion in other areas of the substrate (Figure 4.12b). These regions were densely packed with 3 – 5 µm aggregates of polycrystalline scalenohedral calcite.

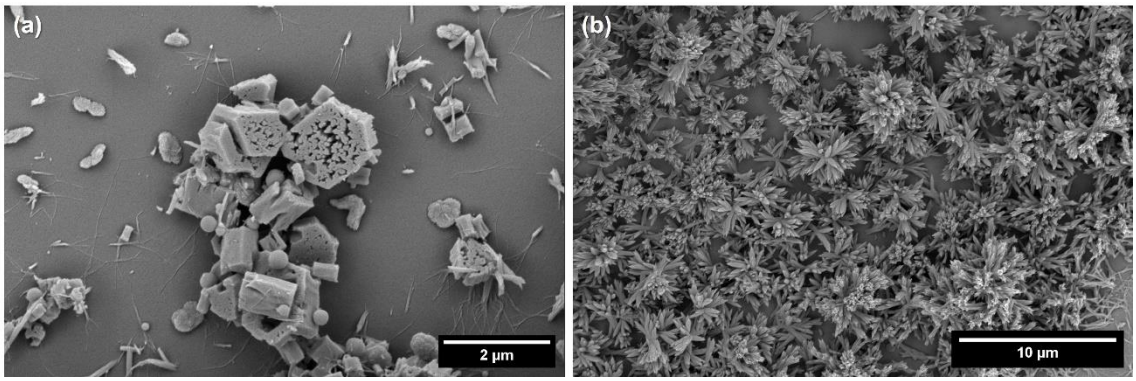


**Figure 4.12 SEM images taken after adding water 1:1 to the calcium hydroxide in ethanol suspension on a glass slide and dried in air.**

The particles were also examined using TEM so that the various crystal morphologies present could be further characterised using SAED. Firstly, the unreacted $Ca(OH)_2$ suspension was analysed and the hexagonal prisms (Figure 4.13) were confirmed as single crystals of portlandite $Ca(OH)_2$ using SAED.

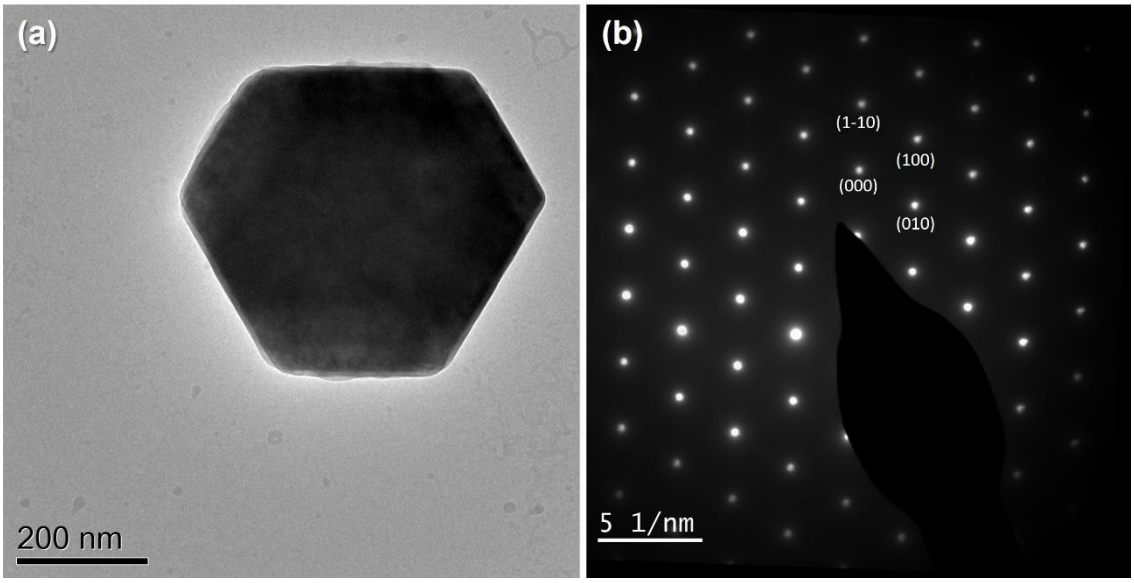


**Figure 4.13 TEM image of a $Ca(OH)_2$ particle (a) and the corresponding SAED pattern (b).**

The reaction was repeated for observation using TEM by loading a TEM grid with 3 µl $Ca(OH)_2$ suspension followed by 3 µl deionised water and leaving it to dry. The major product observed was scalenohedral calcite (Figure 4.14). The corresponding SAED pattern confirmed that the crystals were calcite and that they possessed a polycrystalline structure, due to the clusters of discrete diffraction spots in the same

position. The scalenohedral crystals appeared to be granular in structure, which suggested that small crystallites were commonly aligned within the scalenohedral rod structures. As previously seen in SEM, needle-like features at the apex of calcite crystals were observed, with some measuring as little as 5 nm at the tip.

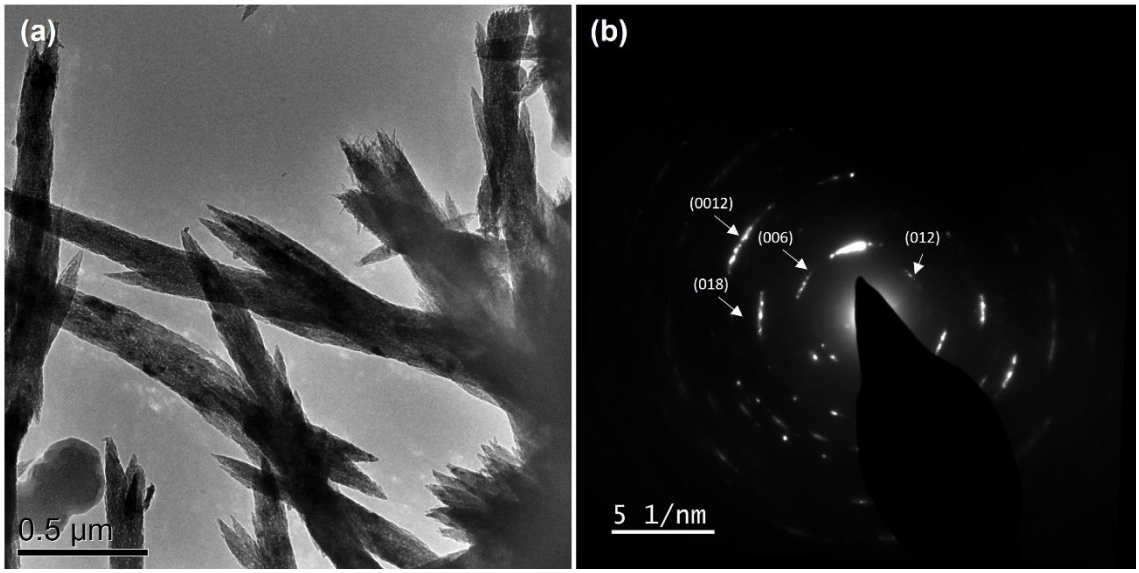


**Figure 4.14 TEM image of calcite crystals exhibiting scalenohedral morphology (a), with corresponding SAED pattern (b).**

The ~200 nm spherical particles previously seen were also confirmed to be amorphous using SAED. This further demonstrated that the particles were ACC.

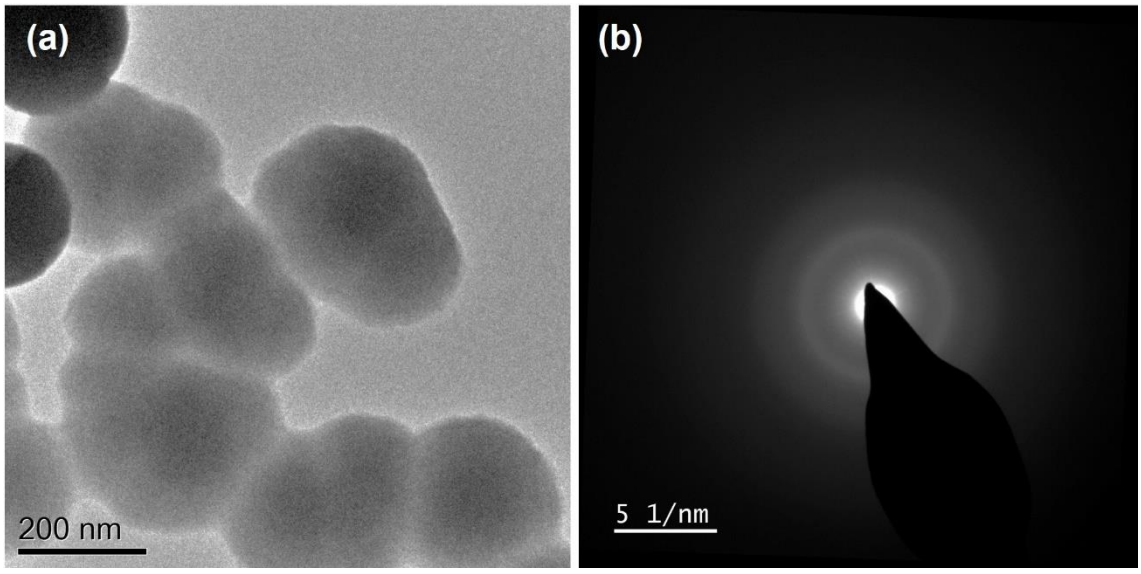


**Figure 4.15 TEM image of ACC particles present after reacting 1:1 $Ca(OH)_2$ suspension and water in air (a), with corresponding SAED pattern (b).**

A small number of 500 nm spherical particles were additionally observed that were not smooth like the ACC particles, but which possessed highly granular structures (Figure 4.16). SAED showed that they were polycrystalline vaterite.

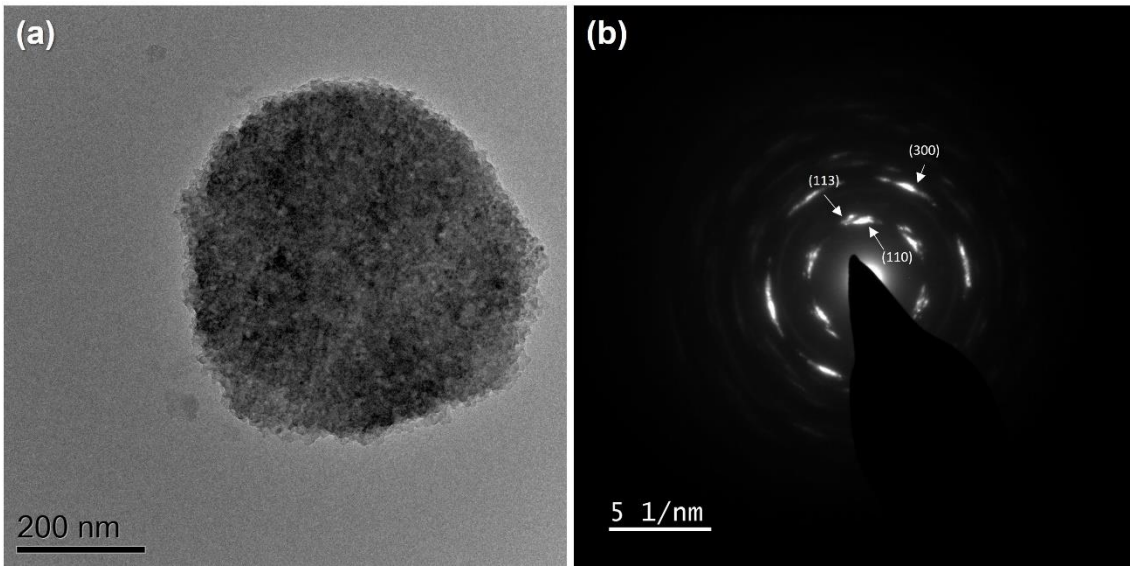


**Figure 4.16 TEM image of vaterite displaying a highly granular structure (a), and corresponding SAED pattern (b).**

### 4.3.3 Time-Resolved TEM Studies of the Carbonation of $Ca(OH)_2$ Synthesised via Aqueous Precipitation

#### 4.3.3.1 Dry TEM Studies using a 1:10 Suspension

Initial time-resolved studies of the carbonation of $Ca(OH)_2$ prepared via the aqueous precipitation method were performed using dry TEM. Firstly, samples were prepared by adding 200 µl of the $Ca(OH)_2$ ethanol suspension to 1.8 ml DI water, creating a 1:10 mixture. This was briefly mixed before taking 20 µl aliquots into centrifuge tubes and leaving them exposed to air for allotted times. The first study was conducted using carbonation times of 5, 10 and 15 minutes, after which 3 µl of the sample was added to the grid before back-blotting with filter paper.

A mixture of amorphous material and dendritic crystals was observed after 5 minutes (Figure 4.17) and SAED of the dendritic crystals (Figure 4.17a) showed that they were crystalline calcite. SAED of the globular material present in the sample showed that they were amorphous (Figure 4.17b) and thus ACC.

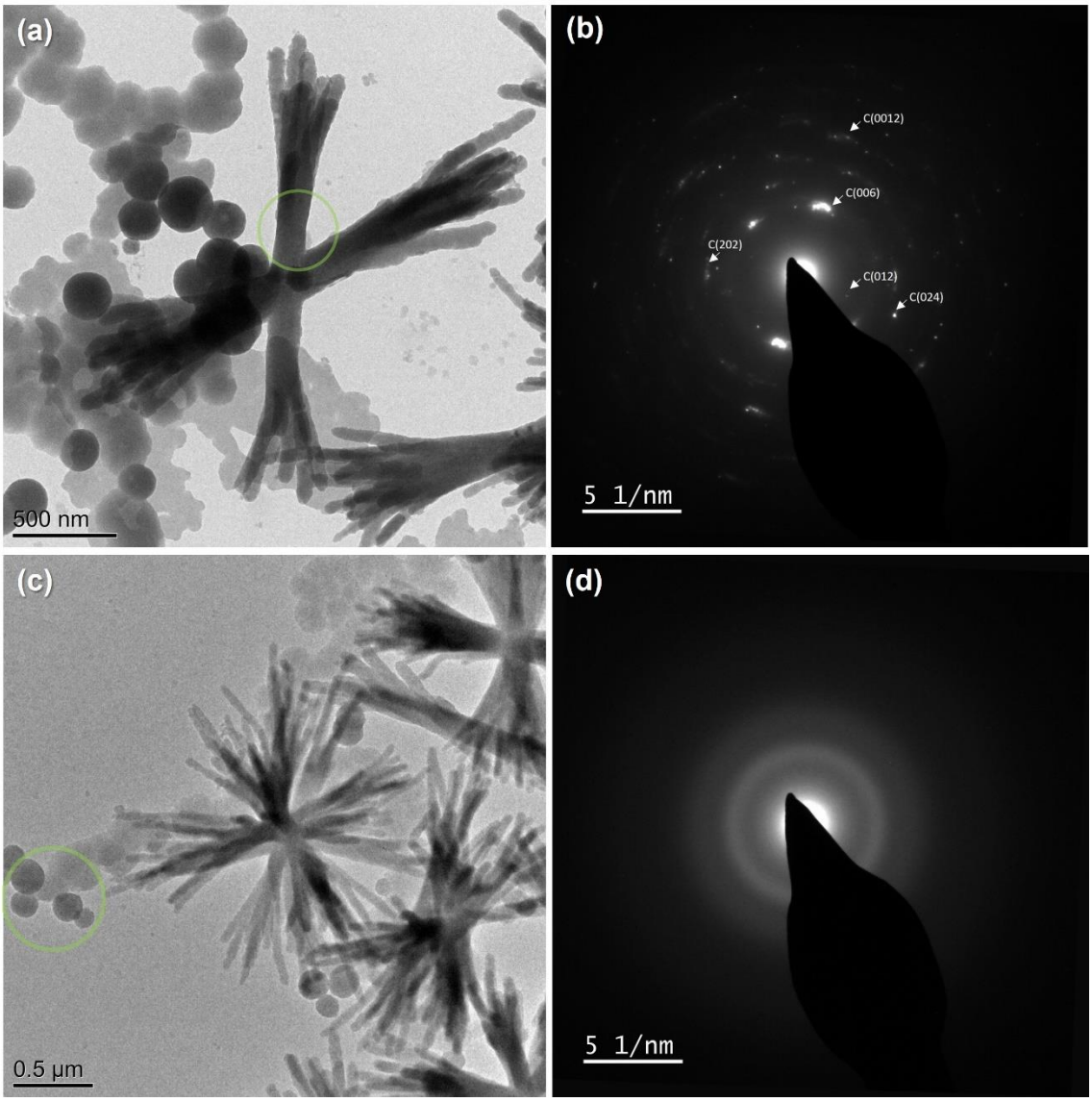


**Figure 4.17 TEM images of the products obtained after reacting 1:10 $Ca(OH)_2$ suspension and water in air for 5 minutes (a, c), with corresponding SAED patterns (b, d).**

Hexagonal plates remained in other areas of the sample, where they were surrounded by amorphous material (Figure 4.18). SAED demonstrated that the plates were portlandite while the other material showed only diffuse rings typical of amorphous materials.

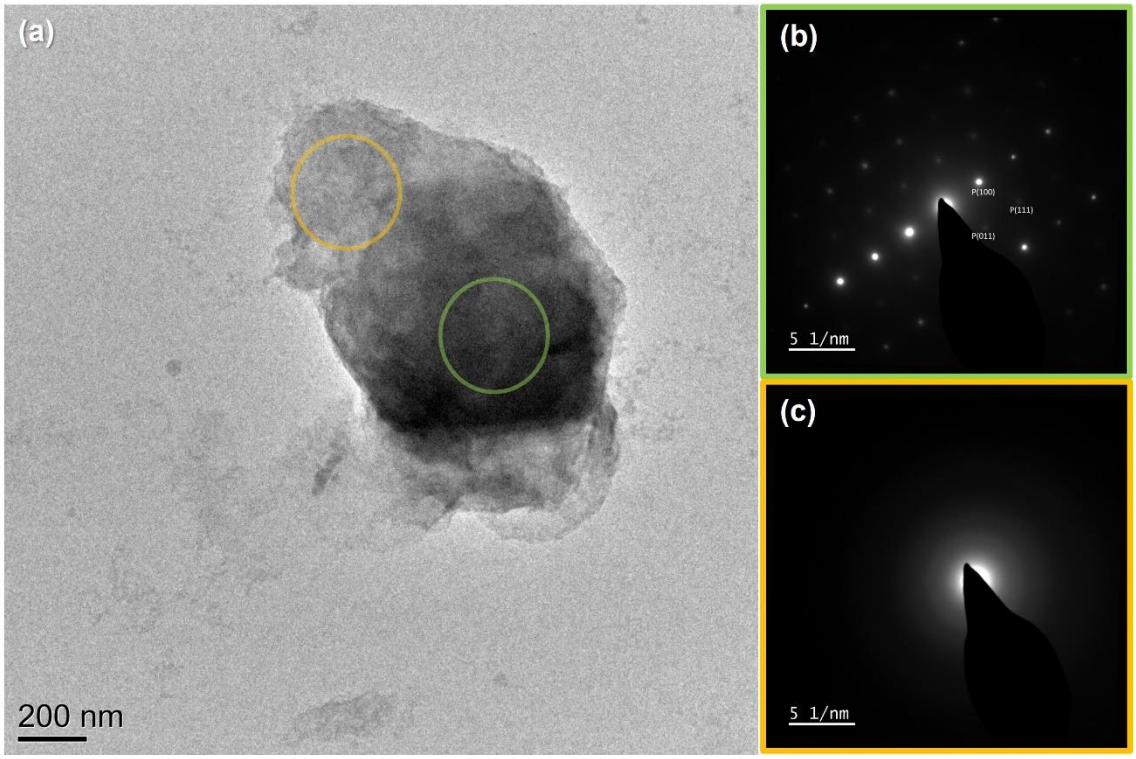


**Figure 4.18 TEM image of a $Ca(OH)_2$ and amorphous material obtained after reacting 1:10 $Ca(OH)_2$ suspension and water in air for 5 minutes (a), with corresponding SAED patterns (b, c).**

Further growth of the dendritic calcite crystals occurred after 10 minutes of exposure to air (Figure 4.19). The crystals emerging from the central nucleation site were thicker and less distinct from each other than after 5 minutes. SAED showed that calcite was produced but also contained diffuse rings indicating the presence of amorphous material. Images taken at high-magnification (Figure 4.18c) showed a central region along the crystal that was darker than the rest of the particle, which indicated that this area was crystalline.

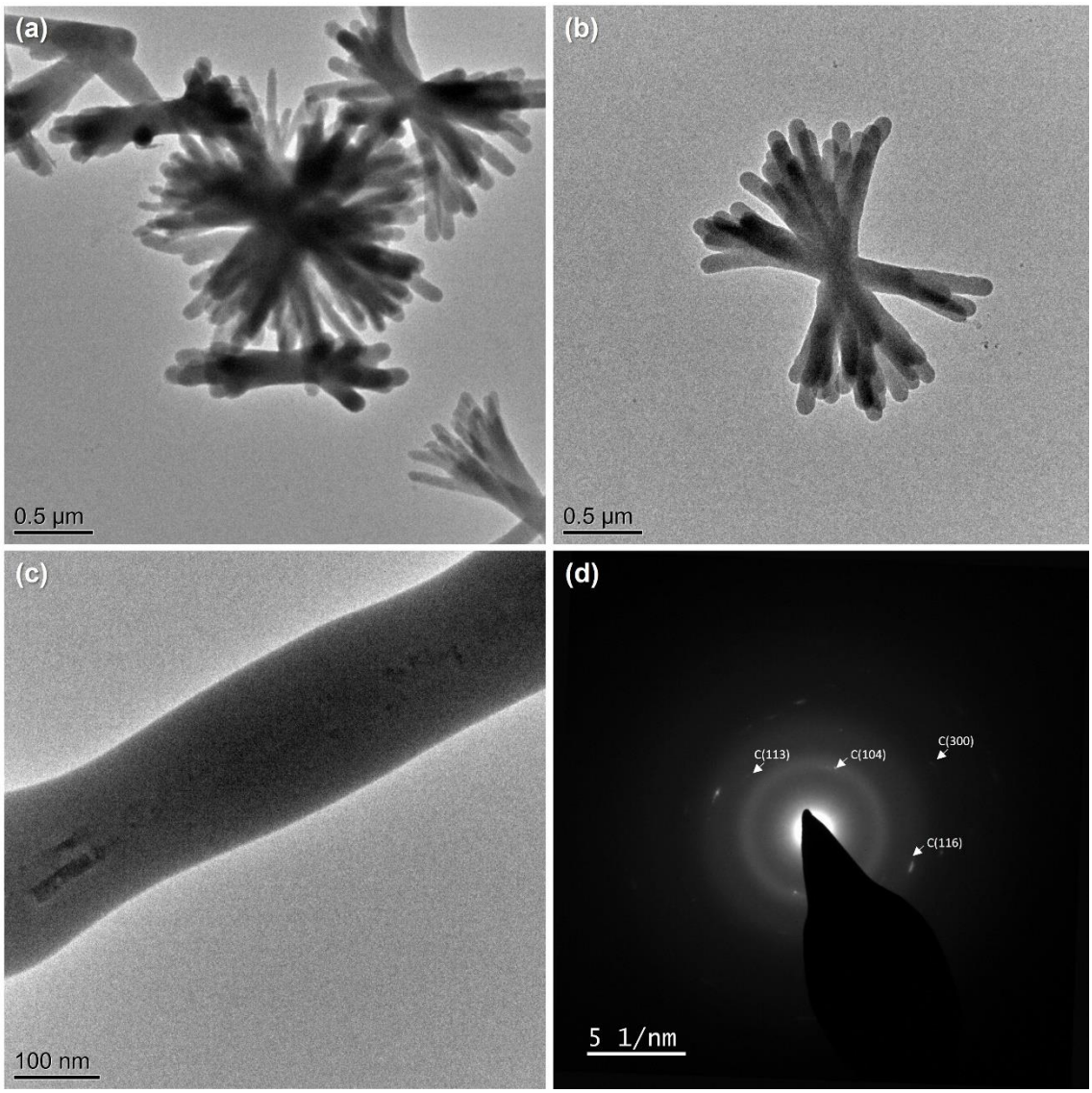


**Figure 4.19 TEM images of a $Ca(OH)_2$ and amorphous material obtained after reacting 1:10 $Ca(OH)_2$ suspension and water in air for 10 minutes (a, b, c), with corresponding SAED pattern (d) of image shown in (c).**

The dendritic structures became more dense after 15 minutes of carbonation, with the individual rods thickening and completely coalescing in the centre. SAED showed that these were crystalline calcite.

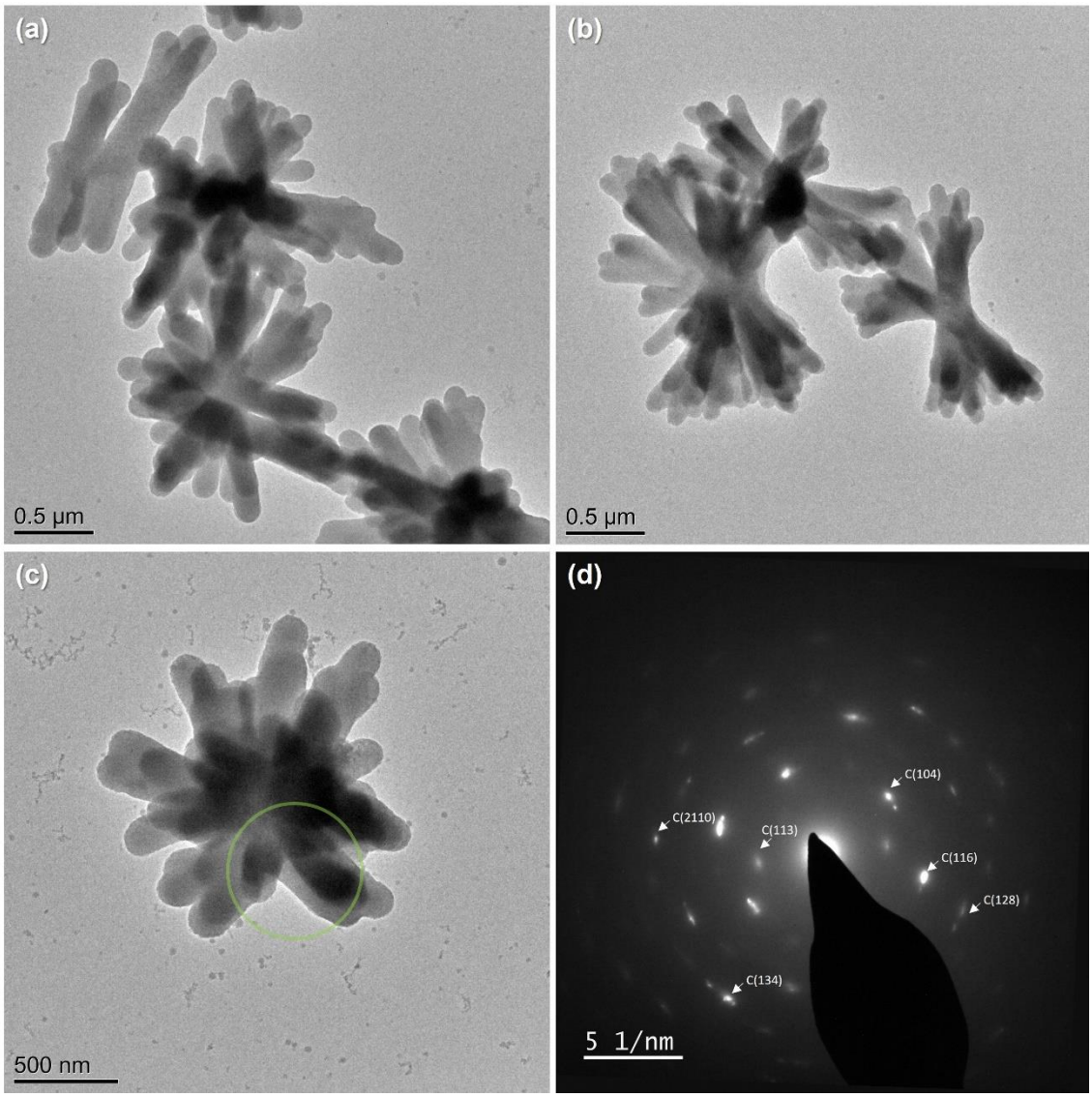


**Figure 4.20 TEM image of a $Ca(OH)_2$ and amorphous material obtained after reacting 1:10 $Ca(OH)_2$ suspension and water in air for 15 minutes (a, b, c), with corresponding SAED pattern (d) for image (c).**

#### 4.3.3.2 Dry TEM Studies using a 1:1 Suspension

A concentrated dispersion of particles optimal for cryo-TEM was created by increasing the ratio of the $Ca(OH)_2$ suspension to water from 1:10 to 1:1. This also slowed down the reaction by reducing the proportion of excess water to $Ca(OH)_2$. The aliquots were removed after shorter time points and the time-resolution was improved by taking aliquots from one solution at intervals rather than preparing separate vials after mixing. A 2 ml 1:1 dispersion was created by adding 1 ml of the

$Ca(OH)_2$ ethanol suspension to 1 ml DI water and mixing. Aliquots were taken at 0, 2 and 5 minutes, deposited onto a TEM grid and back-blotted.

The sample obtained after 0 minutes, which was prepared by taking an aliquot immediately after mixing, contained 0.5 – 2 µm crystals with prism morphologies and hexagonal basal planes (Figure 4.21). SAED pattern confirmed that they were portlandite single crystals. Spherical ACC particles were also observed, the majority of which were 30 nm in diameter with some larger 100 nm particles present.

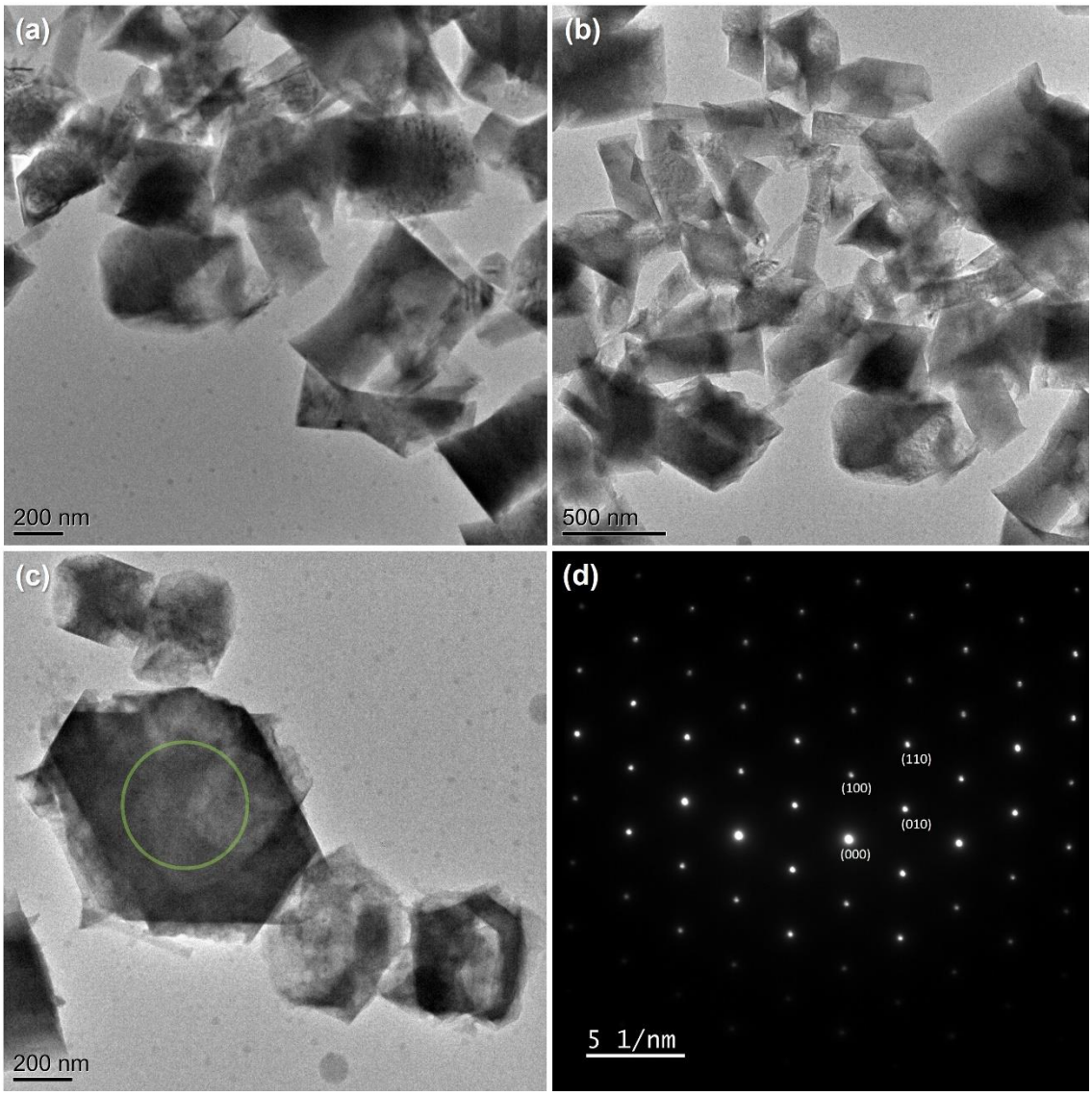


**Figure 4.21 TEM image of a $Ca(OH)_2$ and amorphous material obtained after mixing 1:1 $Ca(OH)_2$ suspension and water (a, b, c), with corresponding SAED pattern (d) for image (c).**

Rod-like particles were observed amongst the $Ca(OH)_2$ crystals after 2 minutes of carbonation (Figure 4.22). SAED showed that portlandite and calcite were present, due to their close proximity in the SA. This confirms that the rod-like particles were the early growths of scalenohedral calcite. The ACC particles previously seen were also present after 2 minutes, and images suggested that some particles had coalesced.

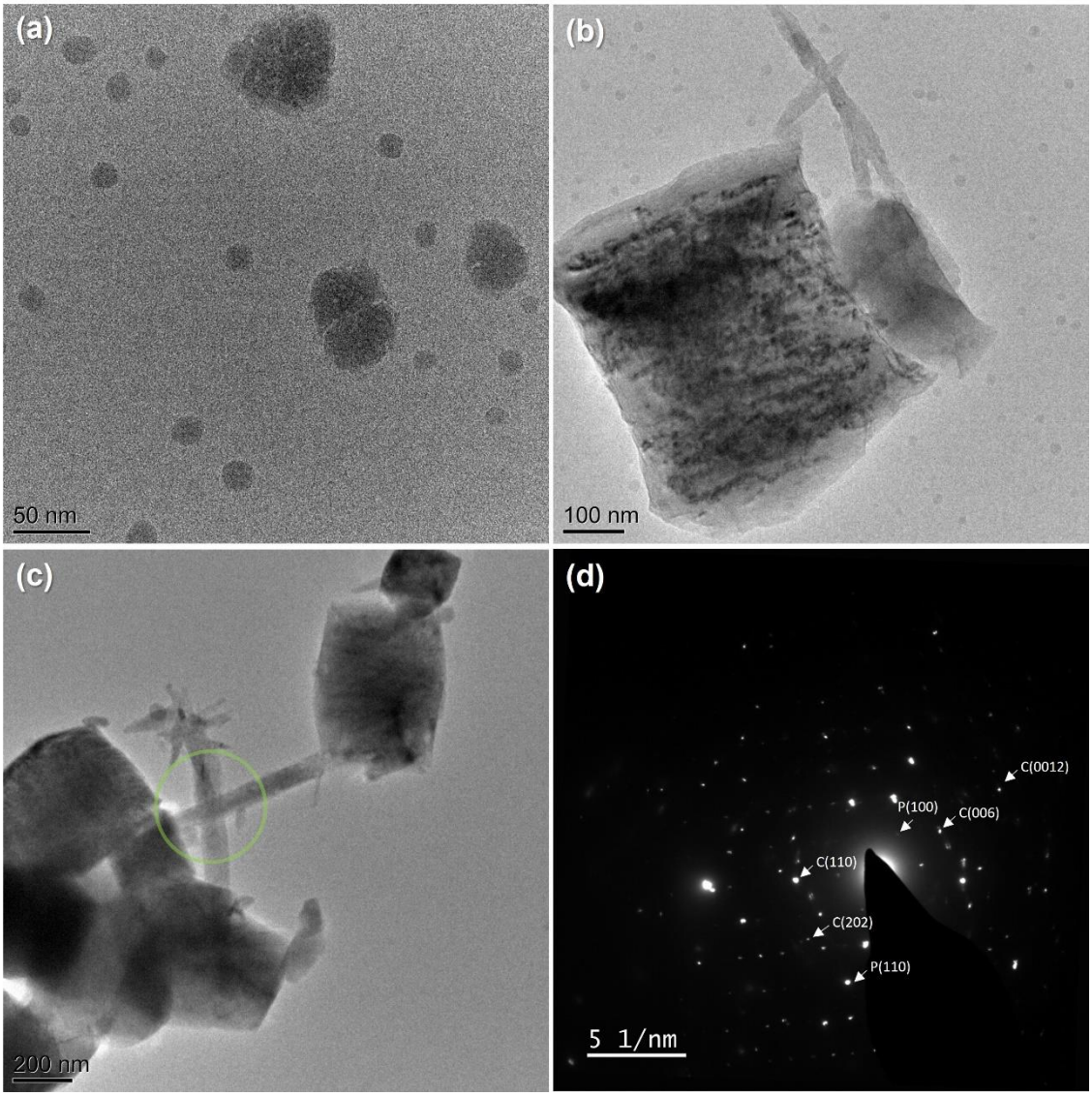


**Figure 4.22 TEM image of a $Ca(OH)_2$ and amorphous material obtained after reacting 1:1 $Ca(OH)_2$ suspension and water in air for 2 minutes (a, b, c), with corresponding SAED pattern (d).**

Carbonating the suspension for 5 minutes also resulted in a mixture of $Ca(OH)_2$, calcite and ACC particles (Figure 4.23). However the calcite crystals had grown further along their long axis, with some crystals being over 1 µm long with clear

scalenohedral shapes. Some of these crystals retained curved edges, as seen in the 1:10 study, although the crystalline area in the centre of the rod was much larger. This area showed an outer layer of amorphous material, indicating that crystallisation was progressing from the centre of the particle outwards.

In some instances the amorphous material adopted an hexagonal shape, suggesting that ACC formed on dissolution of the $Ca(OH)_2$ template. This was in addition to the 30 nm ACC spheres seen after 0 and 2 minutes of carbonation.

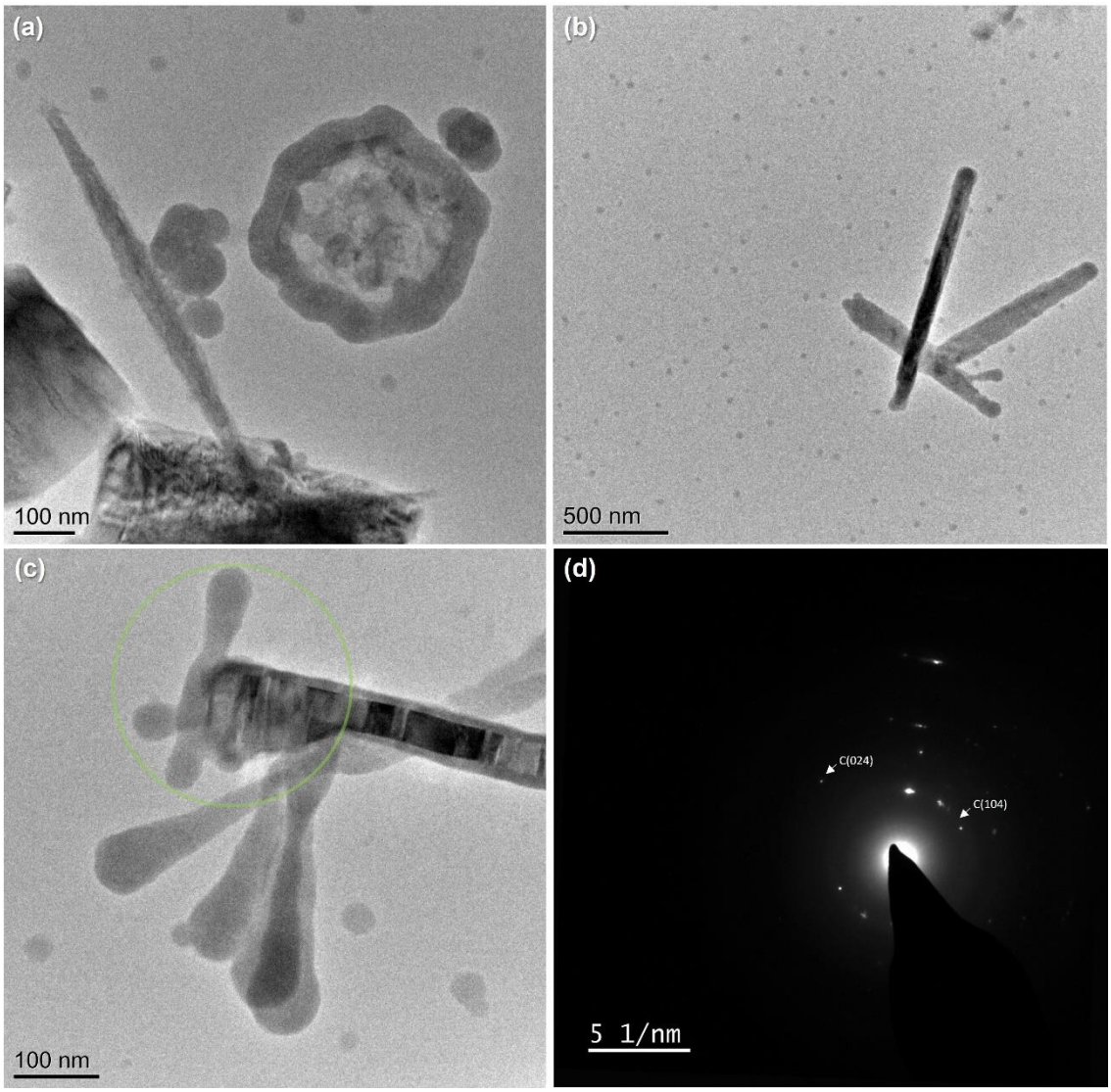


**Figure 4.23 TEM image of a $Ca(OH)_2$ and amorphous material obtained after reacting 1:1 $Ca(OH)_2$ suspension and water in air for 5 minutes (a, b, c), with corresponding SAED pattern (d).**

#### 4.3.3.3 Cryo-TEM Studies

Cryo-TEM was used to achieve greater analysis without causing beam damage, and also to terminate the reaction via plunge freezing. The samples were prepared as previously described and 3 µl aliquots were loaded onto the grid inside the Vitrobot chamber before rapidly plunge-freezing it in liquid ethane.

The 0 minute samples showed signs of premature carbonation as micron-sized scalenohedral calcite crystals were visible as well as the remnants of $Ca(OH)_2$ hexagonal prisms.

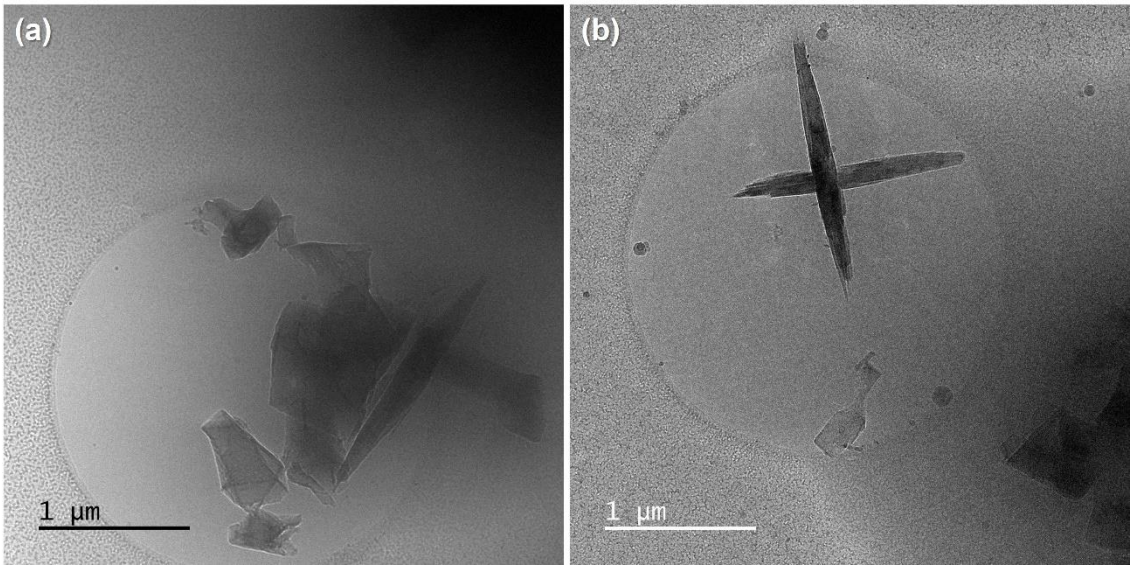


**Figure 4.24 Cryo-TEM images of the product obtained after 0 minutes of carbonation.**

Following 2 minutes of carbonation, the scalenohedral crystals had grown longer and at each apex thin, tendril-like growths were seen (Figure 4.25), as previously observed in SEM and dry TEM. Spherical ACC particles could be seen at calcite apexes that did not have the tendril-like crystal growths. However, it was challenging to distinguish between ACC and ice crystals in these samples due to their similar shapes and sizes.

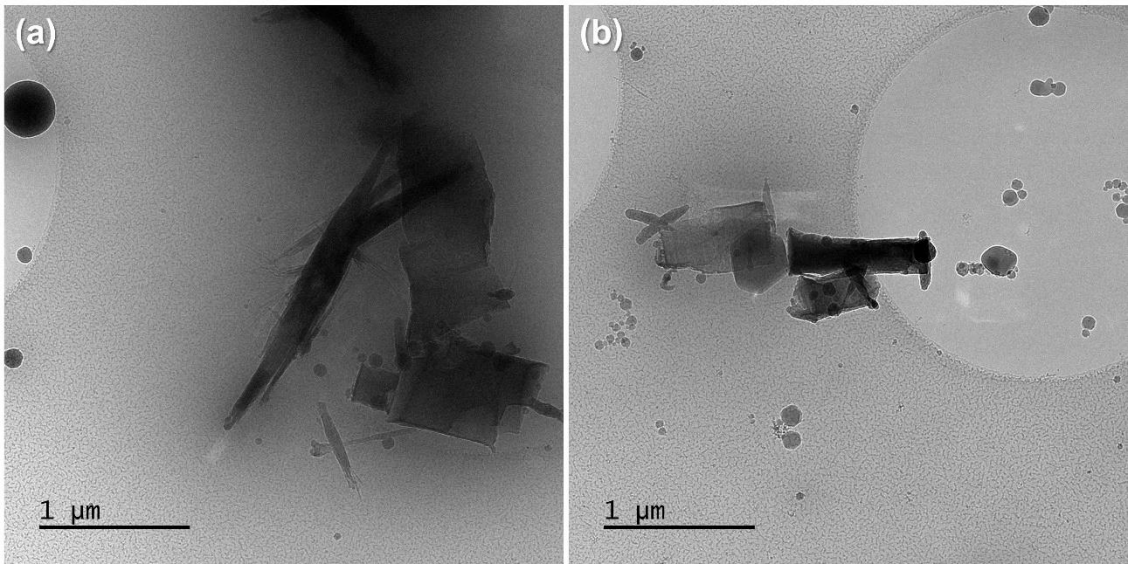


**Figure 4.25 Cryo-TEM images of the product obtained after 2 minutes of carbonation.**

The crystals obtained after 5 minutes of carbonation showed far more mature scalenohedral calcite crystals than those seen at 2 minutes (Figure 4.26). Each particle was highly polycrystalline and larger, with multiple growths occurring from one nucleation site, with the small needle-like features also clearly visible and more prevalent than at 2 minutes. ACC particles were also present around the crystals.

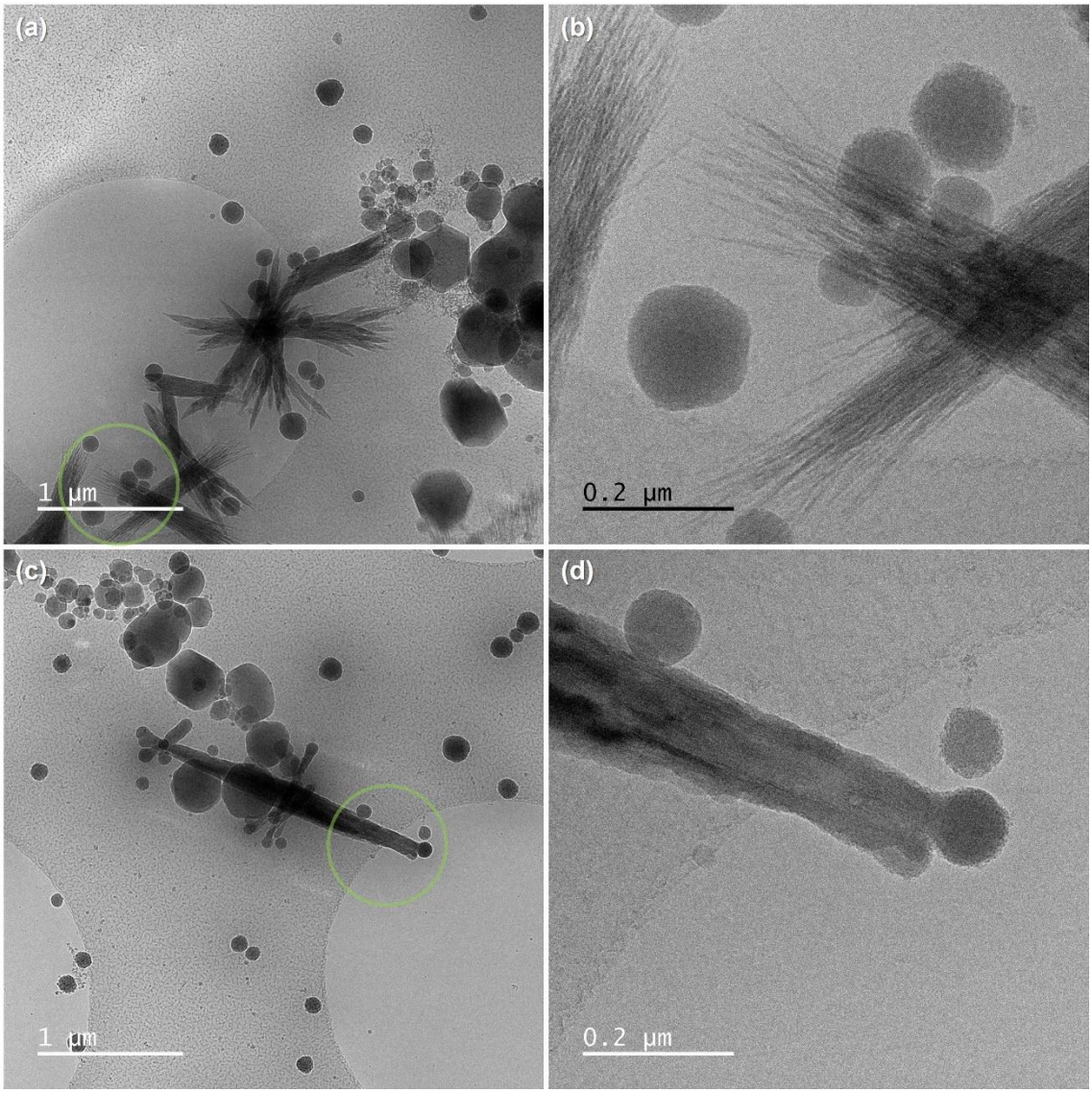


**Figure 4.26 Cryo-TEM images of the product obtained after 5 minutes of carbonation, where the green circles in (a) and (c) indicate the region where (b) and (d) were captured, respectively.**

#### 4.3.3.4 Difficulties in Cryo-TEM Imaging

There were a number of challenges associated with studying the reaction products using cryo-TEM. Achieving a uniform ice layer with a reasonable thickness for imaging was difficult due to large aggregates of particles on the grid. This led to some areas having very thick ice with poor image contrast, whilst grid holes in other areas were dry (Figure 4.27a). This is caused by dewetting of the thin liquid layer, where movement of water molecules towards areas with greater thicknesses occurs to attain more favourable van der Waals' interactions[350]. An extremely thin liquid

layer will evaporate over short times between blotting and plunge-freezing even under humid conditions, which inevitably leads to dry areas forming on the grid.

Initial identification of the different components of the reaction was straightforward due to the distinct morphologies of each material. However, hexagonal ice crystals were occasionally found on sample grids (Figure 4.27b), and were difficult to distinguish from the hexagonal $Ca(OH)_2$ crystals. This highlighted the importance of SAED to verify the composition of crystals.

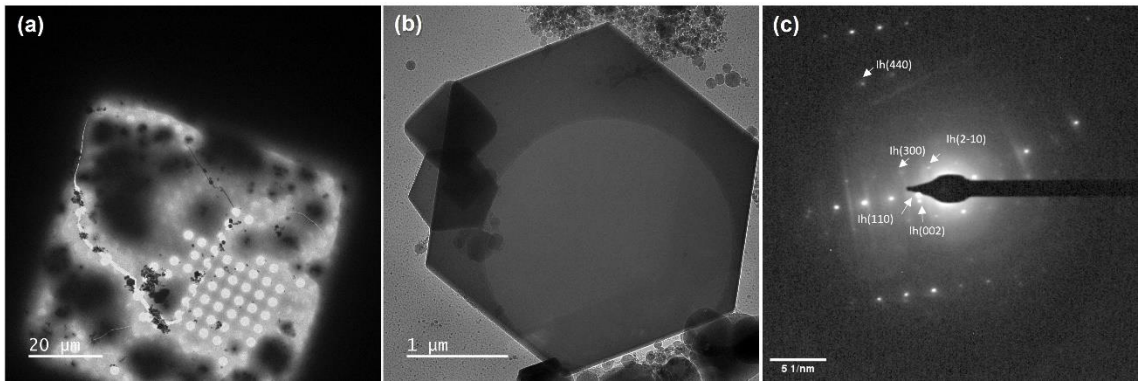


**Figure 4.27 The challenges faced during cryo-TEM: (a) large particles on the grid causing a thick ice layer and dry areas, (b) a hexagonal ice crystal and (c) the corresponding SAED pattern.**

Because of the difficulty in consistently creating high-quality cryo-TEM grids using the $Ca(OH)_2$ suspension prepared using via the aqueous precipitation route, SEM was used to further examine the grids. The SEM images show crystalline aggregates of 5 – 10 µm across much of the grid, which had caused warping and destruction of the holey carbon support film. Although these crystals would certainly be calcite and not the initial $Ca(OH)_2$ particles, it was clear that further optimisation of $Ca(OH)_2$ synthesis was required.

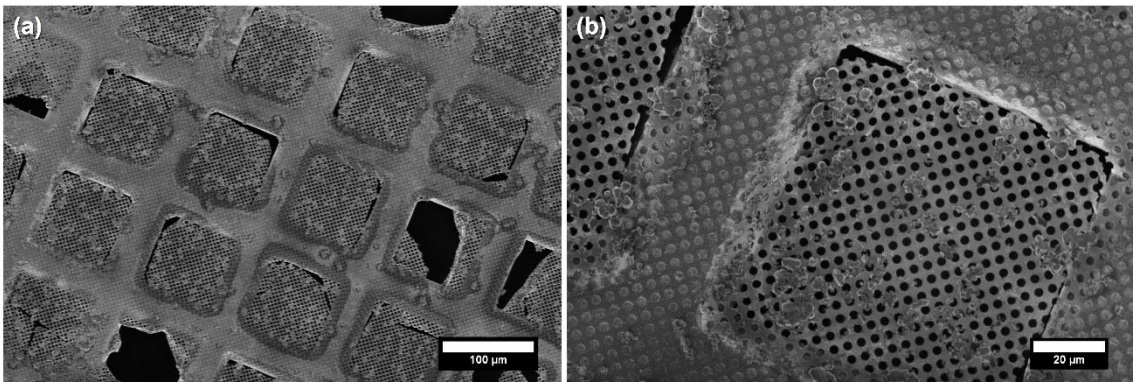


**Figure 4.28 SEM images of a TEM grid after being examined using cryo-TEM.**

### 4.3.4 Synthesis of $Ca(OH)_2$ via Anion Exchange Resin Method

Due to the large particle agglomerates and premature carbonation of the $Ca(OH)_2$ suspension prepared via aqueous precipitation, another synthesis method was trialled. The anion resin exchange method was used (as described in Section 4.2.1.3) to create thin, well-dispersed hexagonal $Ca(OH)_2$ plates which would remain stable for longer periods of time. This yielded well-dispersed suspensions of $Ca(OH)_2$ particles, and avoided repeated exposure to air by negating the washing steps. The product was observed using TEM, which confirmed that ~200 nm hexagonal plates were produced with 20 – 50 nm thicknesses (Figure 4.29).

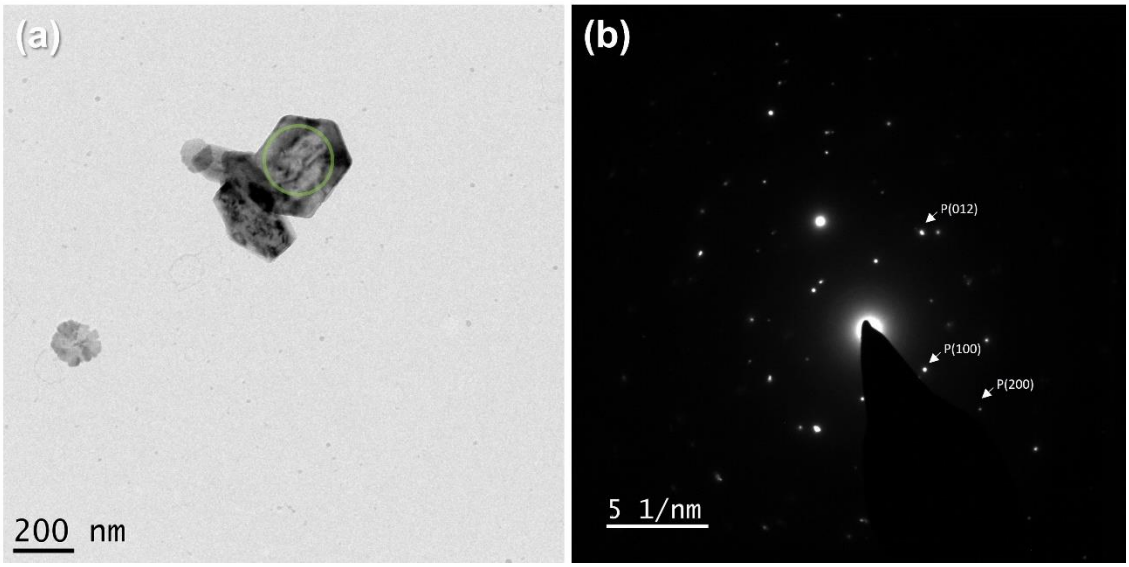


**Figure 4.29 TEM image of the $Ca(OH)_2$ plates produced using the anion exchange resin method (a) and corresponding SAED (b).**

### 4.3.5 Time-Resolved TEM Studies of $Ca(OH)_2$ Synthesised via Resin Method

Time-resolved TEM studies were conducted using $Ca(OH)_2$ prepared with the anion exchange resin to establish whether the difference in thickness between $Ca(OH)_2$ produced by the two methods had an effect on the carbonation reaction.

The grids were loaded with a 3 µl ethanol suspension of $Ca(OH)_2$ and manually back-blotted after 0, 2 or 5 minutes. Thin hexagonal plates which often had central regions missing were present after 0 minutes (Figure 4.30). The holes in the particles were almost exclusively found in the centre of the plates, leaving their outermost edges intact. SAED confirmed that the plates were $Ca(OH)_2$. In some instances, only a ring-like outer edge of the particle remained, which possessed enough of the hexagonal shape to distinguish these particles as $Ca(OH)_2$ plates that had almost completely dissolved. The particles were also found amongst 10 – 20 nm spherical amorphous particles, which were consistent with ACC, with some present on the faces of $Ca(OH)_2$.

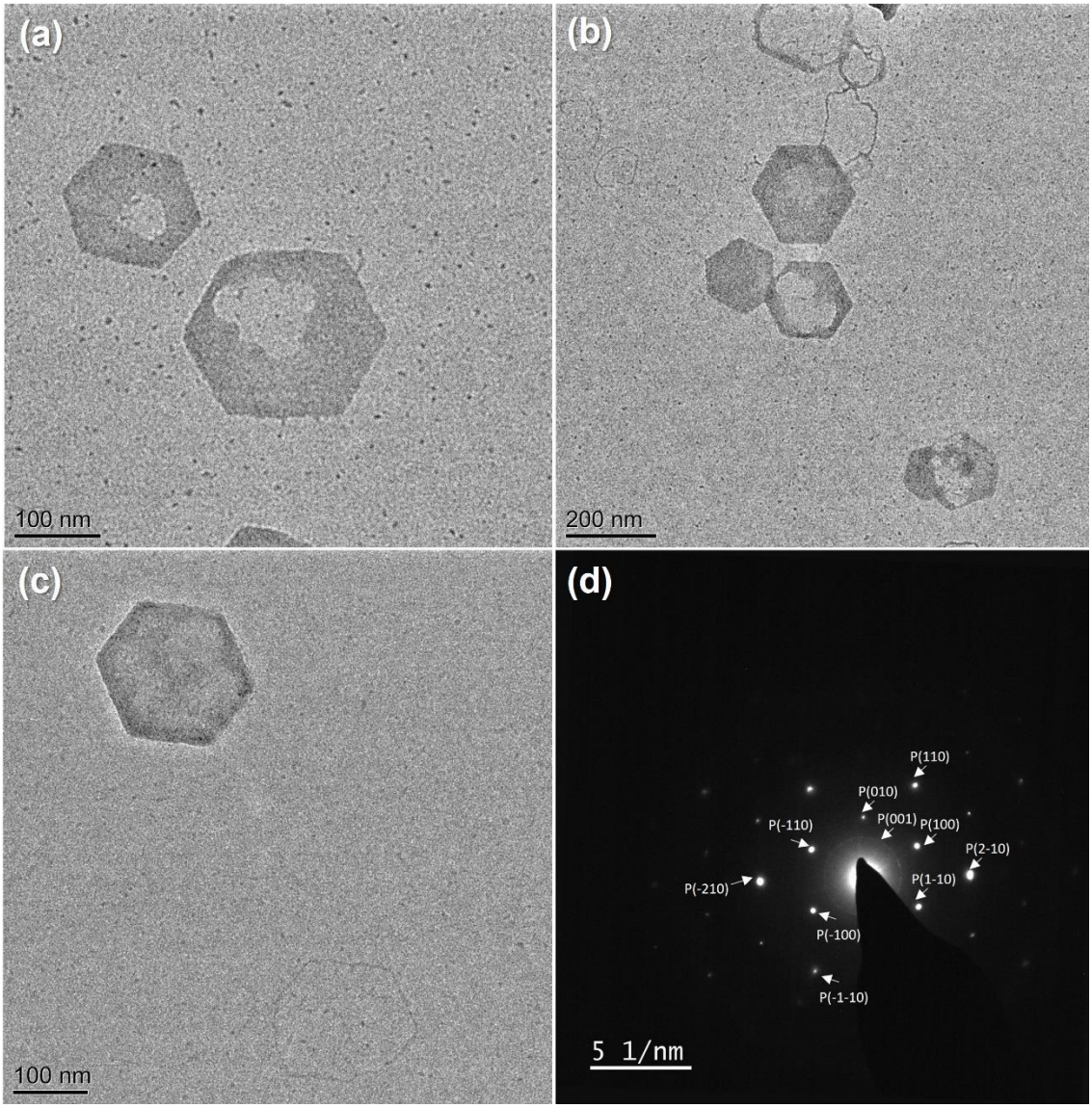


**Figure 4.30 TEM images of the $Ca(OH)_2$ suspension prepared using the anion exchange method following 0 minutes of carbonation (a, b, c), and the corresponding SAED pattern (d) for image (c).**

Few intact $Ca(OH)_2$ plates were visible after 2 minutes carbonation (Figure 4.31). Instead, only the outer edges of these particles remained, appearing as rings which often had a clear hexagonal shape. The spherical ACC particles present were larger than at 0 minutes and were up to 40 nm in diameter. Further, new 100 nm elliptical particles emerged after 2 minutes of carbonation that exhibited much greater contrast due to their crystallinity. These crystals correspond to the early growth stages of scalenohedral calcite.

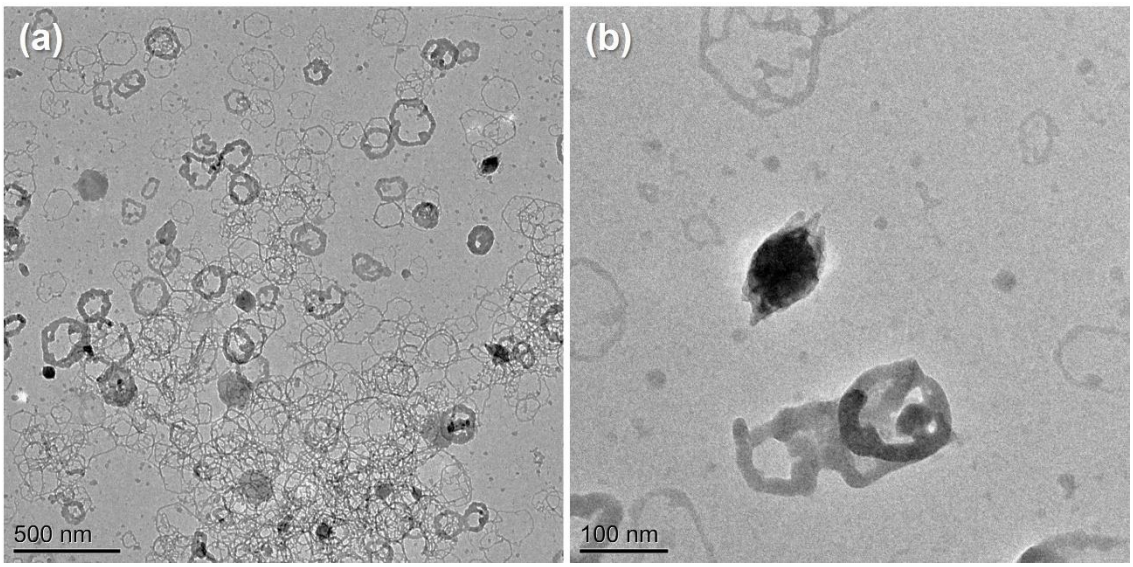


**Figure 4.31 TEM images of the $Ca(OH)_2$ suspension prepared using the anion exchange method, following 2 minutes of carbonation.**

The product obtained after 5 minutes of carbonation was very similar to that obtained after 2 minutes. The early growth stages of calcite were observed, as well as the near completely dissolved $Ca(OH)_2$ rings (Figure 4.32). These showed slightly more advanced dissolution than after 2 minutes, with only the outer edge left in most cases.

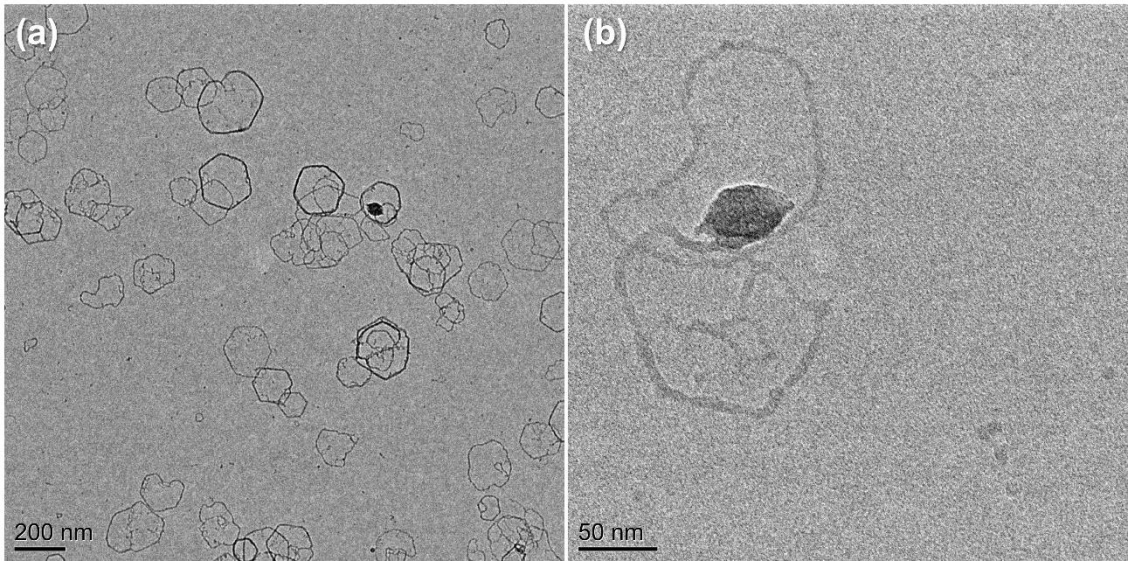


**Figure 4.32 TEM images of the $Ca(OH)_2$ suspension prepared using the anion exchange method, following 5 minutes of carbonation.**

The reaction was repeated in the presence of water by adding a 1.5 µl droplet of DI water to a grid with 1.5 µl $Ca(OH)_2$ suspension (100% EtOH). Following 2 minutes of

reaction, amorphous-like rings of partially dissolved $Ca(OH)_2$ were observed in addition to calcite, which had needle-like growths emerging from the apexes (Figure 4.33). SAED of these growths alone (highlighted in orange) showed that they were individual crystals of calcite, but when the SA was moved to include the central crystal (highlighted in green) a single crystal pattern was observed.

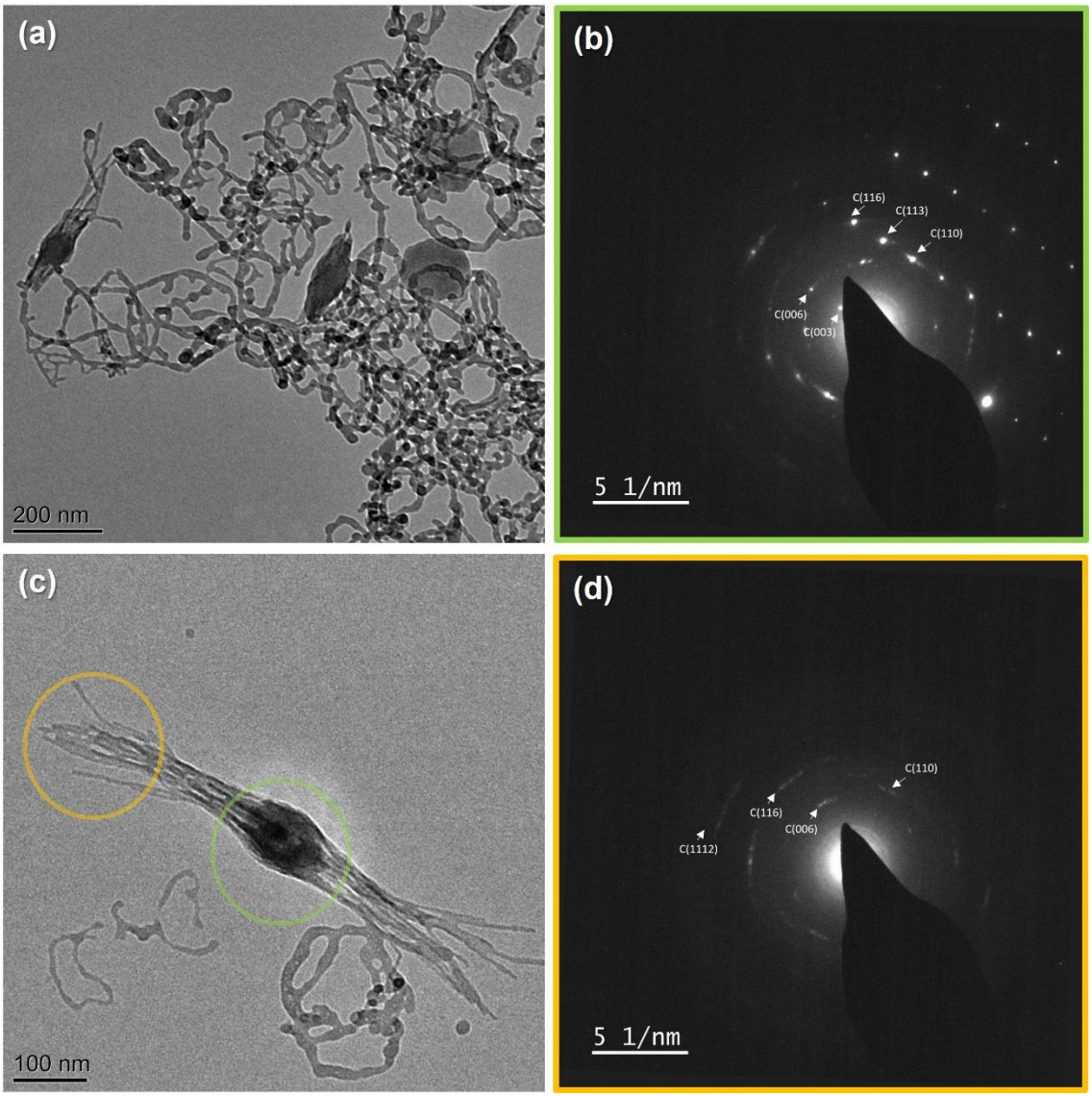


**Figure 4.33 TEM images of the 1:1 $Ca(OH)_2$ suspension and water following 2 minutes of carbonation (a, c), where the orange and green circles indicate the areas corresponding to each SAED pattern (b, d).**

In order to further probe this theory, a calcite crystal was analysed using dark-field imaging (Figure 4.34). Several spots were seen at each lattice point in SAED patterns which shows that several crystallites were present. The diffraction spot

highlighted was selected and upon returning to imaging mode, the majority of the particle appeared bright. This indicated that this entire region of the crystal was responsible for that diffraction spot, further evidencing that the particle was mainly a single crystal with some additional crystallites present.

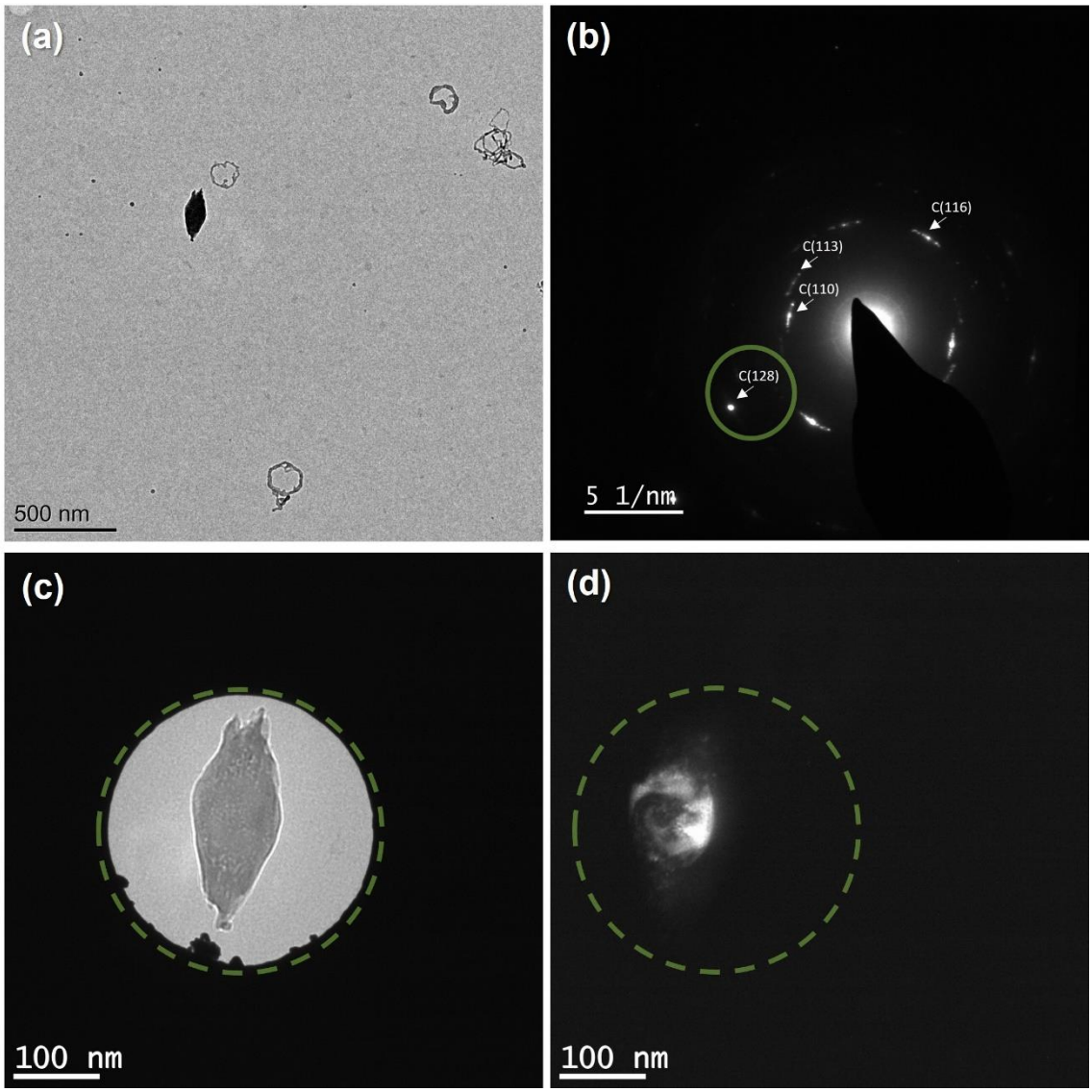


**Figure 4.34 TEM images of the 1:1 $Ca(OH)_2$ suspension and water following 5 minutes of carbonation (a), the obtained SAED pattern with highlighted diffraction spot used for dark field TEM (b), corresponding selected area (c) and dark-field TEM image (d) obtained using the diffraction spot circled in (b).**

The products obtained after 5 minutes of carbonation were again very similar to those obtained after 2 minutes. Scalenohedral calcite was observed as confirmed by SAED (Figure 4.35a) and the individual needle-like growths had consolidated in the

regions nearest to the central crystal, forming an aligned rod. What appeared to be a partially dissolved hexagonal $Ca(OH)_2$ plate was analysed using SAED (Figure 4.35b), which indicated that it was amorphous. This indicates that the structure was not $Ca(OH)_2$, but was instead ACC that has precipitated by pseudomorphic replacement of the $Ca(OH)_2$ plates.

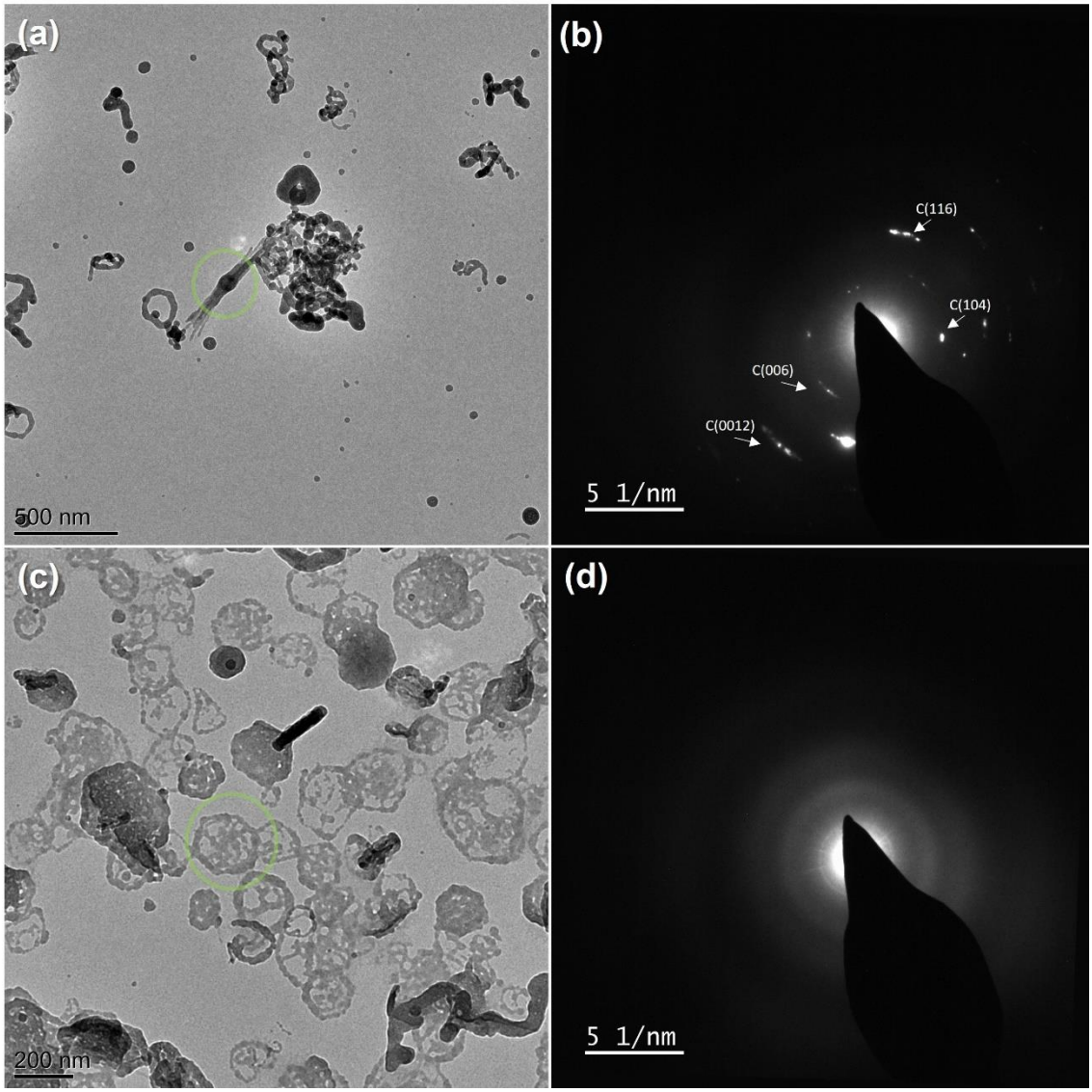


**Figure 4.35 TEM images of the 1:1 $Ca(OH)_2$ suspension and water following 5 minutes of carbonation (a, c), where the green circles indicate the areas corresponding to each SAED pattern (b, d).**

Samples prepared after 10 minutes of carbonation showed advanced growth of the calcite crystals and no remaining $Ca(OH)_2$ (Figure 4.36). The crystals were several microns in length and around 2 µm in thickness.

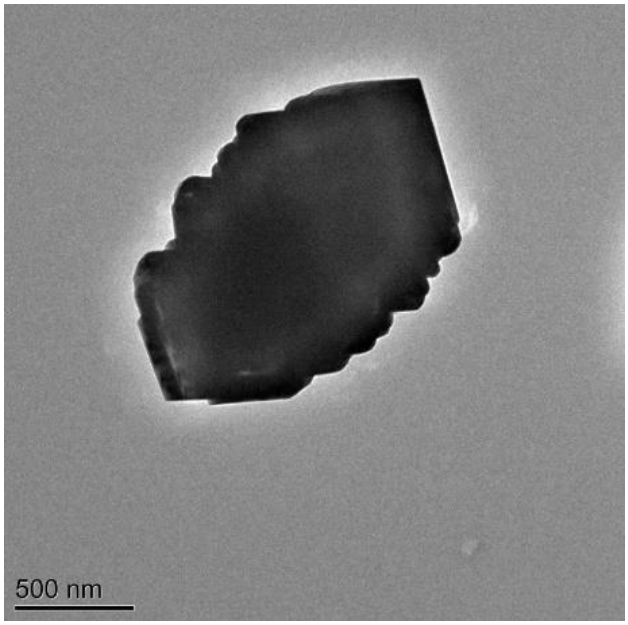


**Figure 4.36 TEM images of the 1:1 $Ca(OH)_2$ suspension and water, following 10 minutes of carbonation.**

#### 4.3.5.1 Cryo-TEM

Time-resolved cryo-TEM was conducted using the new $Ca(OH)_2$ suspension to better isolate each time point of the reaction. Two aliquots were taken for each time point; one from the top of the reaction solution and one after mixing the reaction vial (termed the top and the mixed aliquot respectively). The aim of this was to primarily prepare samples with different particle densities, as the top aliquot would avoid larger particles that settle to the bottom of the vial. However, the top aliquot was also closer to the air-solvent interface and thus the supply of $CO_2$, so this study would determine the influence of this on the rate and products of the reaction. It should also be noted that this study was conducted using the 90% v/v $EtOH/H_2O$ $Ca(OH)_2$ suspension, which was diluted 1:1 with DI water for all samples but the 0 minute carbonation sample.

Thin hexagonal plates were observed as the main product in the 0 minute samples, though some partially dissolved plates that retained their outer edges were also present (Figure 4.37). The SAED pattern confirmed that the plates were $Ca(OH)_2$. At this time point there was no difference in the samples prepared using the two different aliquots.

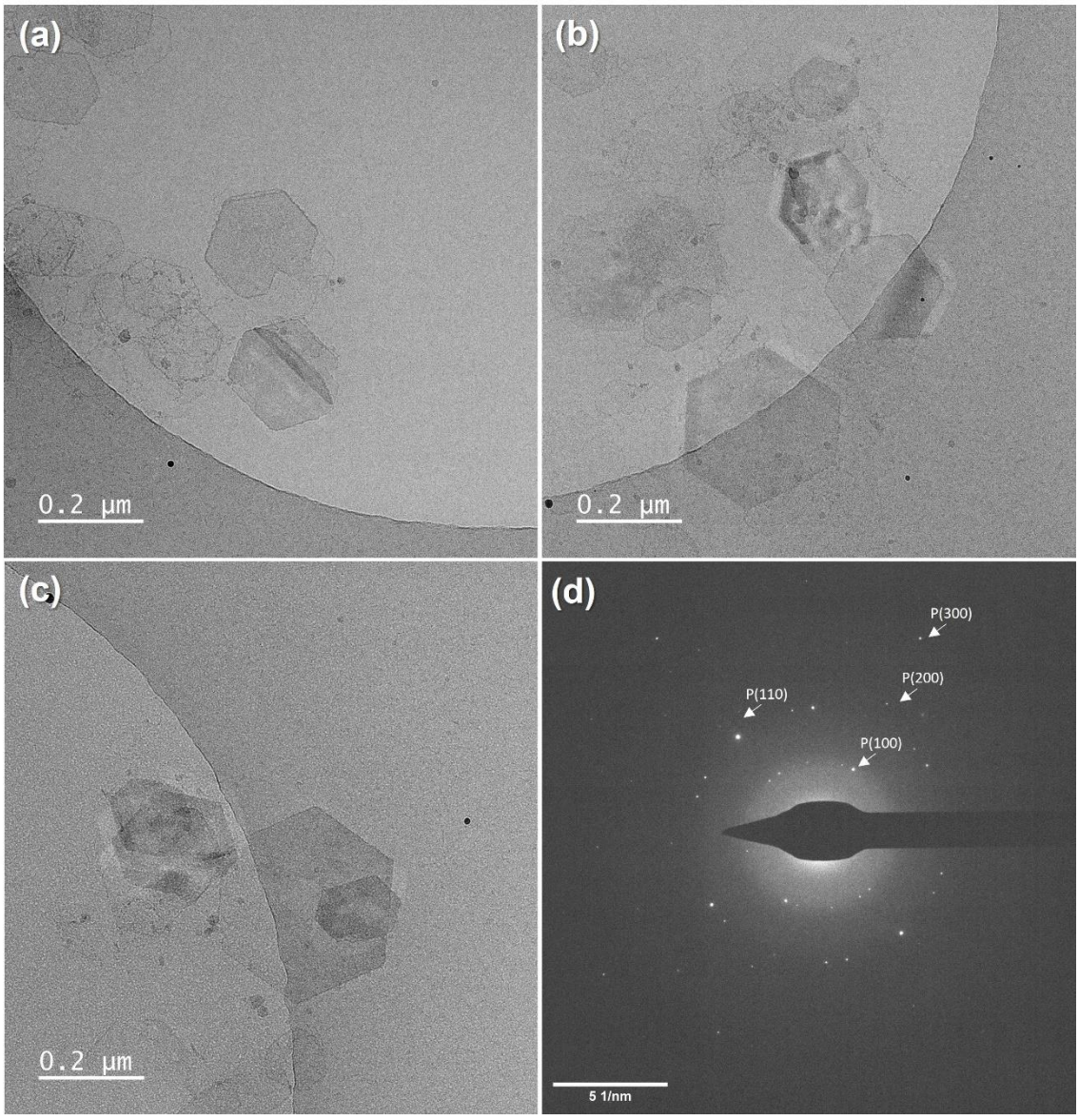


**Figure 4.37 Cryo-TEM images of the 90% v/v EtOH/$H_2O$ $Ca(OH)_2$ suspension (a, b, c), with corresponding SAED pattern (d).**

The top aliquot obtained after 2 minutes of carbonation contained rhombo-scalenohedral particles with obtuse apex angles of ≈ 105° (Figure 4.38). This contrasted with the scalenohedral particles observed in the 2 minute sample obtained from the mixed aliquot, which had acute apex angles of ≈ 60° (Figure 4.39). Both types of particle were around 450 – 600 nm in length, indicating that one was not a later growth stage of the other. This effect on morphology may therefore derive from a difference in the availability of $CO_2$ between the two aliquots, as it has been seen previously in studies varying $[Ca^{2+}]/[CO_3^{2-}]$[330, 332].

The 2 minute sample taken from the top aliquot is closest to the air-solvent interface and as a result the amount of dissolved $CO_2$ will be greatest in this area. This reduces $[Ca^{2+}]/[CO_3^{-2}]$, which as discussed in the introduction, leads to a more rhombohedral-like morphology, referred to as rhombo-scalenohedral[332]. The 2 minute sample from the mixed aliquot yielded scalenohedral particles, as there is less available $CO_2$ relative to the area local to the air-solution interface. This results in a $Ca^{2+}$-rich environment where growth of the non-stoichiometric {21-1} faces is inhibited by adsorbed $Ca^{2+}$ ions.

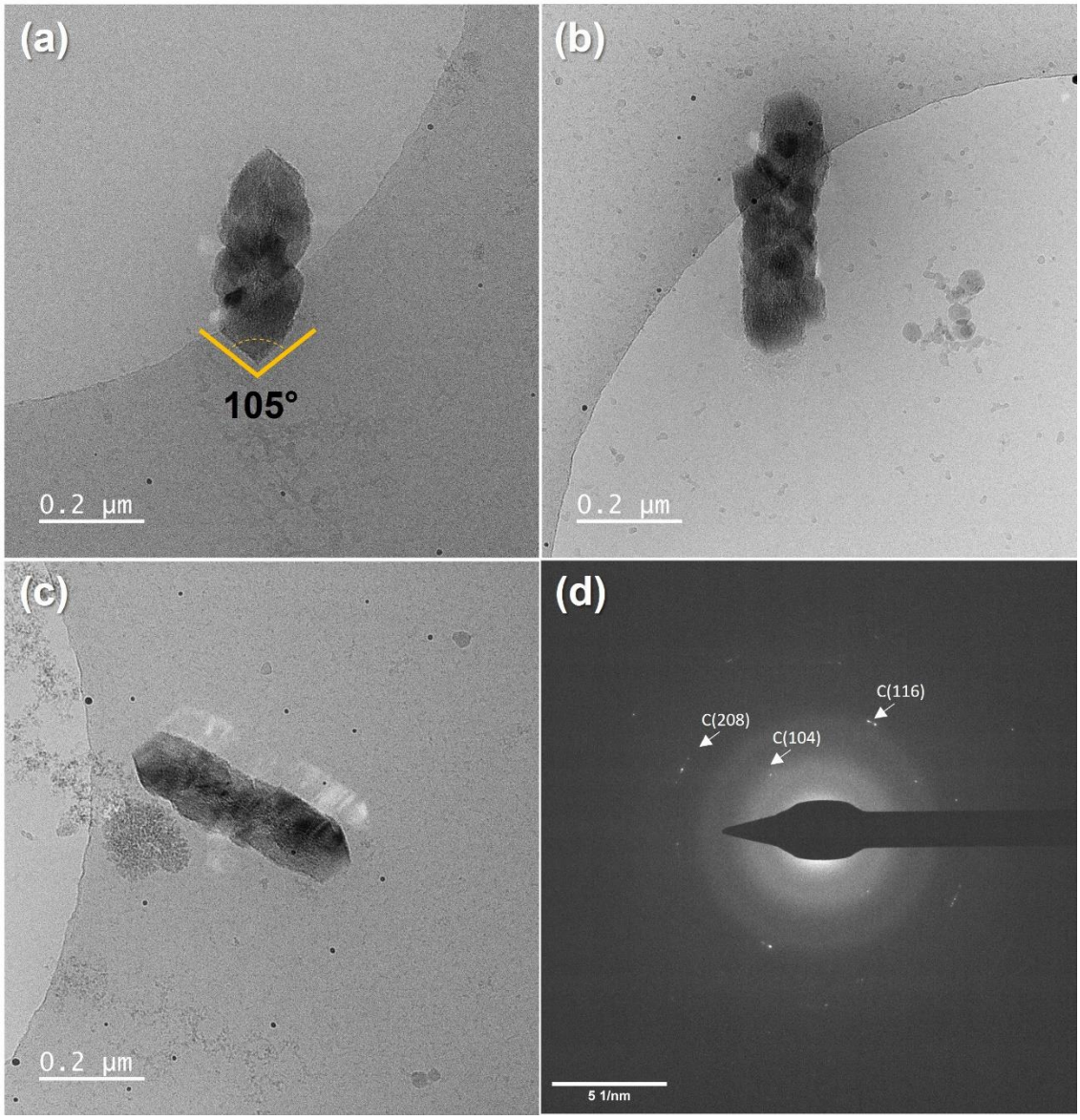


**Figure 4.38 Cryo-TEM images of the top aliquot sample of 1:1 90% v/v EtOH/$H_2O$ $Ca(OH)_2$ suspension and water following 2 minutes of carbonation (a, b, c) and corresponding SAED pattern (d).**

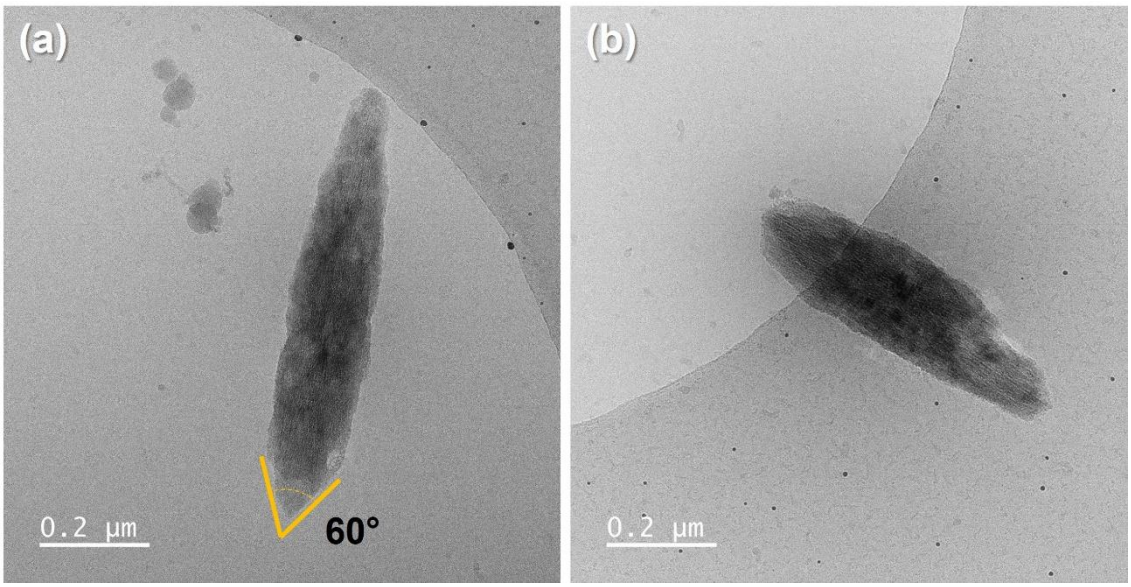


**Figure 4.39 Cryo-TEM images of the mixed aliquot sample of 1:1 90% v/v EtOH/$H_2O$ $Ca(OH)_2$ suspension and water following 2 minutes of carbonation.**

Further growth of the calcite particles was observed in both sample aliquots after 5 minutes of carbonation (Figure 4.40 and Figure 4.41). Calcite crystals with rhombo-scalenohedral morphologies were again observed for the top aliquot, in addition to granular vaterite particles. The sample from the mixed aliquot contained scalenohedral calcite, which had begun to form polycrystals.

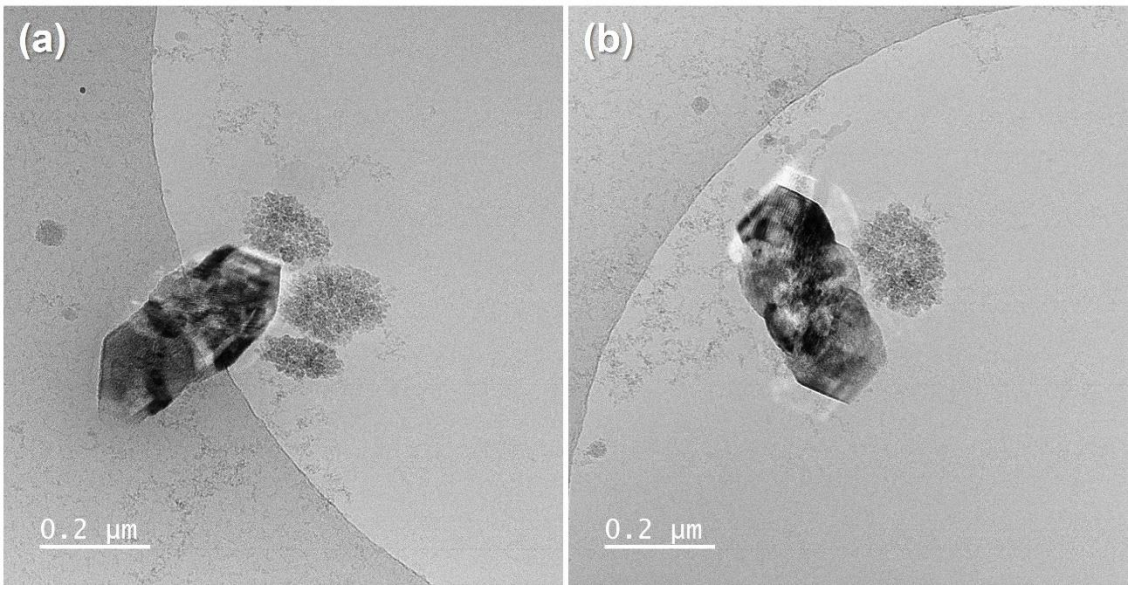


**Figure 4.40 Cryo-TEM images of the top aliquot sample of 1:1 90% v/v EtOH/$H_2O$ $Ca(OH)_2$ suspension and water following 5 minutes of carbonation.**

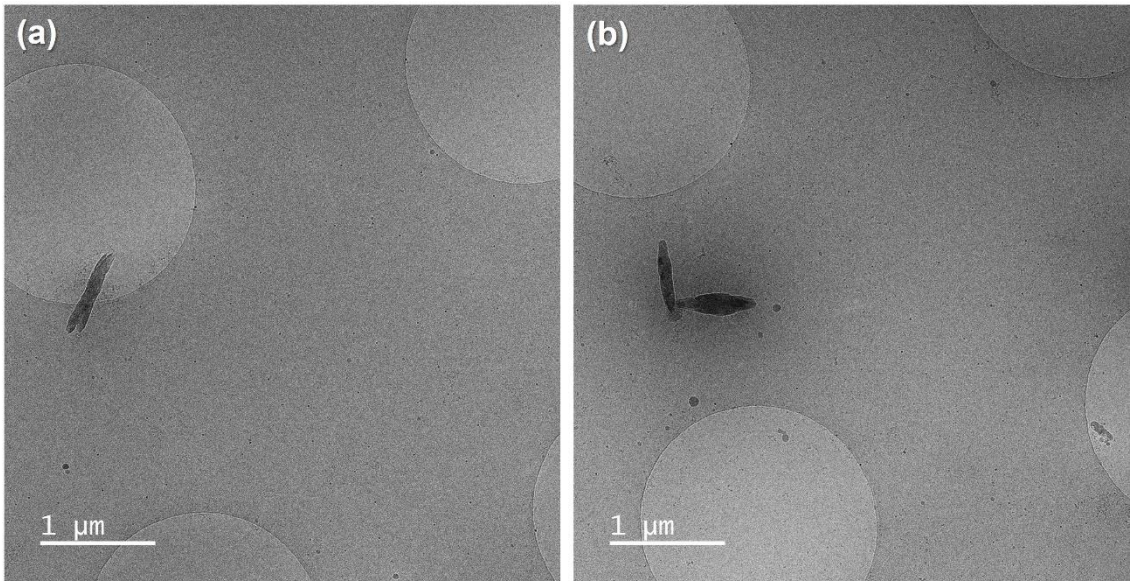


**Figure 4.41 Cryo-TEM images of the mixed aliquot sample of 1:1 90% v/v EtOH/$H_2O$ $Ca(OH)_2$ suspension and water following 5 minutes of carbonation.**

#### 4.3.5.2 Cryo-ET

The mixed aliquot samples were studied using cryogenic electron tomography (cryo-ET) to determine the spatial relationship between the partially dissolved $Ca(OH)_2$ plates and amorphous material, and to study the growing scalenohedral calcite crystals. Tomograms were collected by sequentially tilting and imaging the sample through -60° to +60° using a tilt step of 2°.

To facilitate cryo-tomography, the sample had to tolerate repeated exposure to the electron beam. This was not an issue for the 2 and 5 minute samples which had been diluted with water 1:1, but the undiluted 0 minute sample suffered beam damage after a fluence of 20 $e^-$ $Å^{-2}$, when the total fluence required for the tomograms was 144 $e^-$ $Å^{-2}$. As both the sample and the carbon film were damaged, this was clearly due to the high EtOH content (~90%) rather than any beam-sensitivity of the $Ca(OH)_2$. The issue was resolved by diluting the 0 minute sample 1:1 with water (only ~45% EtOH).

The addition of water to the sample, compounded by the sample loading time using the Vitrobot (at least 13 s), inevitably led to initiation of the reaction prior to plunge-freezing. This can be seen by the partial dissolution of the $Ca(OH)_2$ hexagonal plates in the tilt series (Figure 4.42), whereas full plates were generally the main product in

the cryo-TEM images at 0 minutes (Figure 4.37). The remaining outer edge was reminiscent of the hexagonal $Ca(OH)_2$ plate, which was 20 – 30 nm in thickness and retained 120° angles at each corner. The amorphous globular structures were confirmed as being connected to the hexagonal particle edges by examining the spatial relationship between the two over a range of tilt angles. There were also a number of instances where the outer edge of a $Ca(OH)_2$ plate was preserved and a central region remained intact following partial dissolution (Figure 4.42b). This was previously unclear from the cryo-TEM images, but the tilt series showed that both the central region and outer edge were aligned across all tilt angles, which indicated that they were of the same plate, rather than two stacked plates.

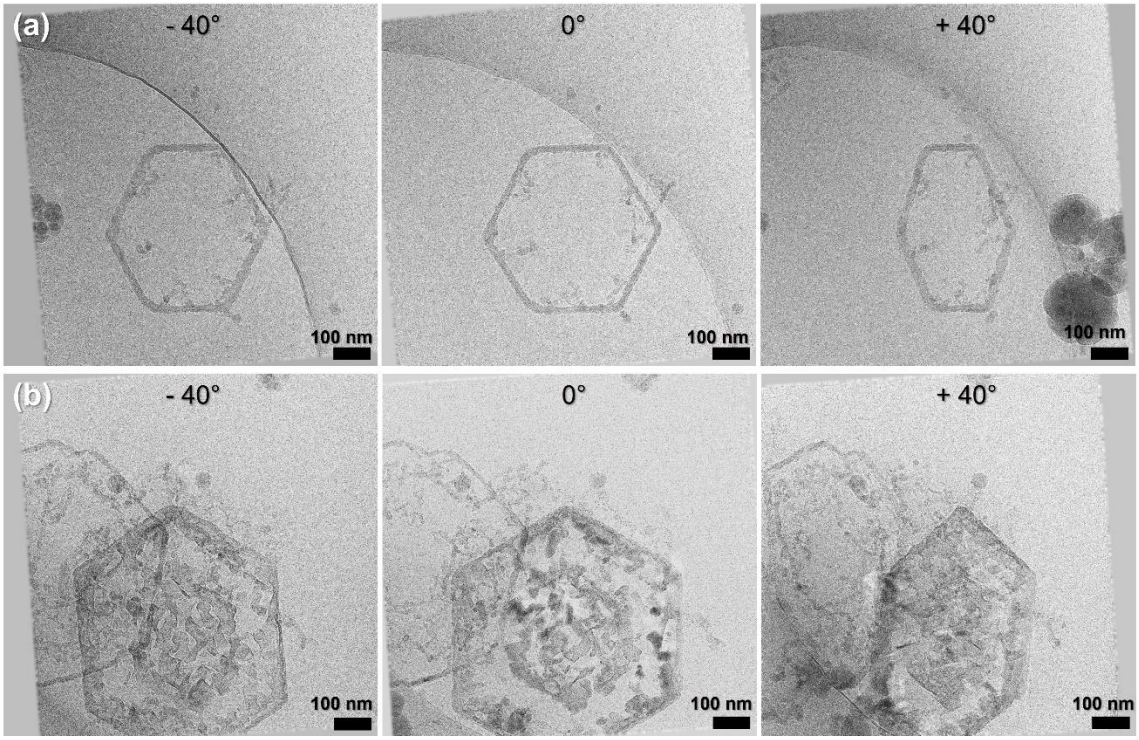


**Figure 4.42 Cryo-TEM tilt series of 1:1 90% v/v EtOH/$H_2O$ $Ca(OH)_2$ suspension and water.**

Calcite crystals were also present in the 0 minute sample, which was expected due to the dilution of the sample with water (Figure 4.43). The crystals were at an early stage of growth and were ~380 nm long with thicknesses of 200 nm. The particles had a granular appearance and individual 5 nm crystallites could be seen aligned along the long axis of the crystal, with the central crystallite being the longest. These were often associated with the amorphous networks seen after dissolution of $Ca(OH_2)$ plates.

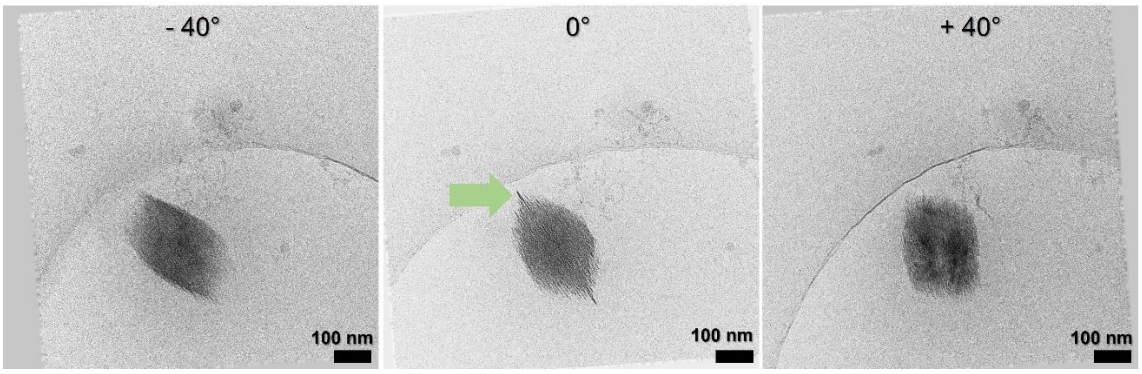


**Figure 4.43 Cryo-TEM tilt series of 1:1 90% v/v EtOH/$H_2O$ $Ca(OH)_2$ suspension and water, where the green arrow highlights the central crystallite.**

Following 2 minutes of carbonation, the calcite crystals had grown further along the long axis to 800 nm but remained approximately 200 nm in thickness (Figure 4.44). This indicated that the formation of the aligned crystallites occurred faster than the growth of the crystallites along the long axis.

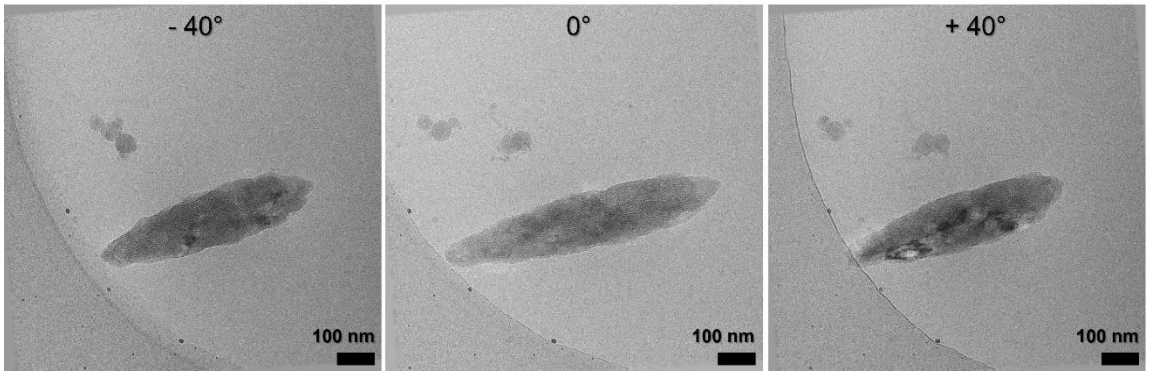


**Figure 4.44 Cryo-TEM tilt series of 1:1 90% v/v EtOH/$H_2O$ $Ca(OH)_2$ suspension and water, following 2 minutes of carbonation.**

Calcite crystals obtained after 5 minutes of carbonation were very similar in size to those formed after 2 minutes, indicating that little growth had occurred between the two time points (Figure 4.45). However, the apex of the crystals had diverged into two separate crystals. This indicated that polycrystals had begun to form.

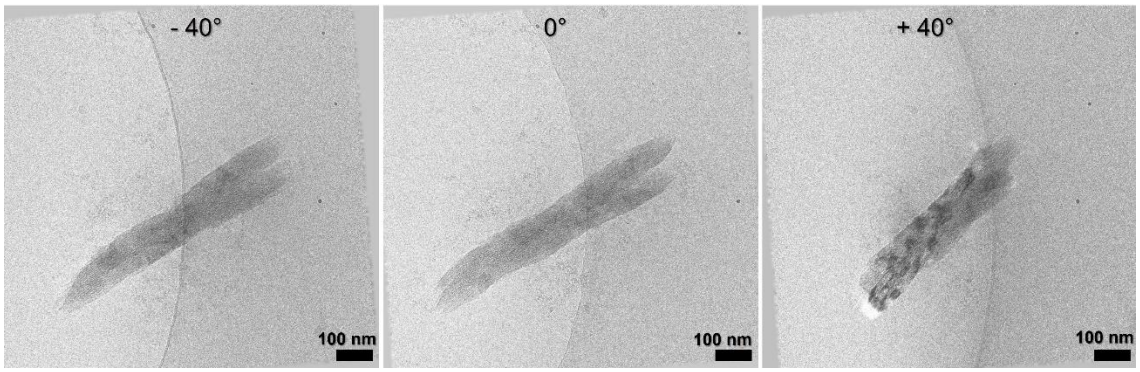


**Figure 4.45 Cryo-TEM tilt series of 1:1 90% v/v EtOH/$H_2O$ $Ca(OH)_2$ suspension and water, following 5 minutes of carbonation.**

## 4.3.6 Dynamic LCTEM Studies of the Carbonation of $Ca(OH)_2$

Time-resolved TEM and cryo-TEM studies revealed the phases present throughout the reaction, but could not directly observe the transformation of these phases. Liquid-cell TEM (LCTEM) was therefore employed to further probe the formation mechanism of calcite via the carbonation of $Ca(OH)_2$ in real time. Briefly, experiments were conducted by loading the cell with $Ca(OH)_2$ particles (from a 100 % EtOH suspension) and filled with EtOH. After loading the holder, water was flowed through the cell at a rate of 0.05 ml $min^{-1}$ until EDX monitoring confirmed that the EtOH was displaced by $H_2O$.

### 4.3.6.1 Dissolution of $Ca(OH)_2$

Initial imaging of the liquid-cell after flowing water into the cell showed the hexagonal $Ca(OH)_2$ plates randomly oriented in solution (Figure 4.46). Continuous imaging of these areas showed that the $Ca(OH)_2$ plates gradually dissolved, and then became brighter and spherical particles emerged. This could be due to the formation of ACC at the site of partially dissolved $Ca(OH)_2$ remnants where there is a high local concentration of $Ca^{2+}$.

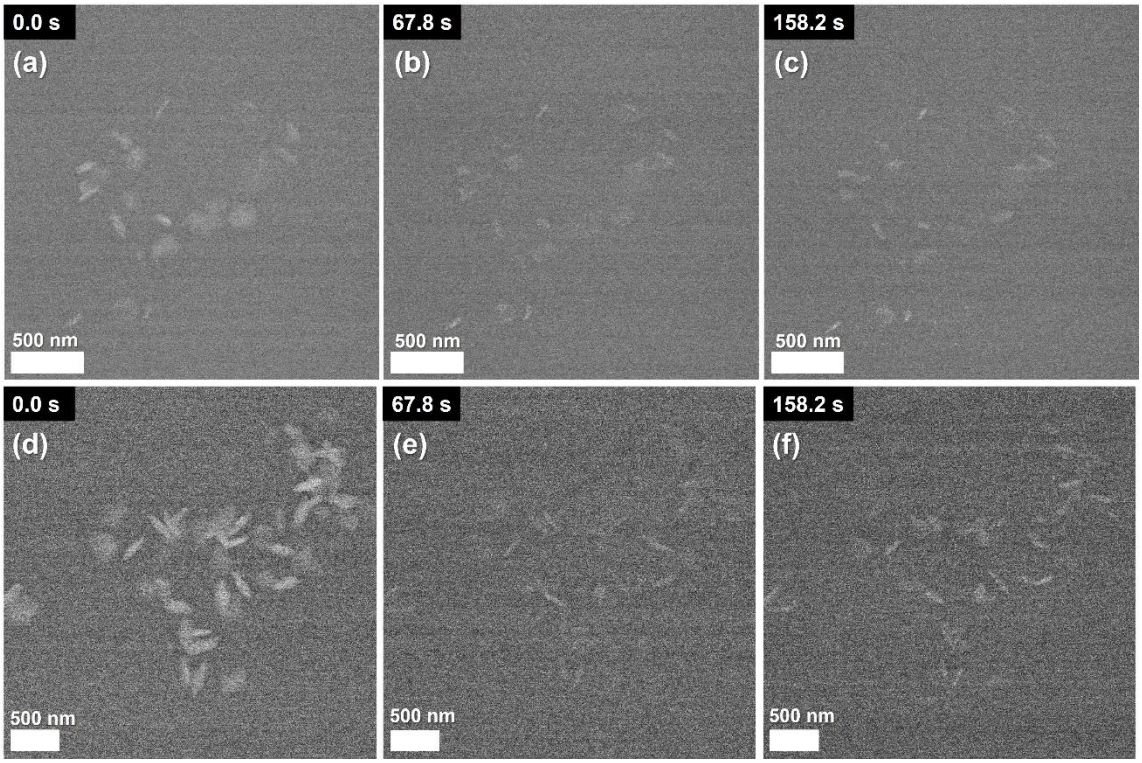


**Figure 4.46 HAADF STEM images taken from a video of the $Ca(OH)_2$ suspension dissolving in the LC, with 2 areas shown in (a-c) and (d-f), where the total fluence at each time point was (a) 32 $e^-$ $Å^{-2}$, (b) 131 $e^-$ $Å^{-2}$, (c) 262 $e^-$ $Å^{-2}$, (d) 13 $e^-$ $Å^{-2}$, (e)167 $e^-$ $Å^{-2}$ and (f) 374 $e^-$ $Å^{-2}$.**

The random orientations of the plates made it challenging to determine whether the dissolution occurred more readily on specific crystal faces, as it was difficult to visually identify the crystallographic planes of the $Ca(OH)_2$ plates. However, an area was found with a $Ca(OH)_2$ plate positioned with the basal face parallel to the chip window (Figure 4.47). Over time the $Ca(OH)_2$ plate dissolved from the centre outwards. As observed previously, the $Ca(OH)_2$ remnants initially faded from view during dissolution, but became brighter as ACC precipitated on the $Ca(OH)_2$ remnants. ACC also formed in solution as 20 nm spherical particles.

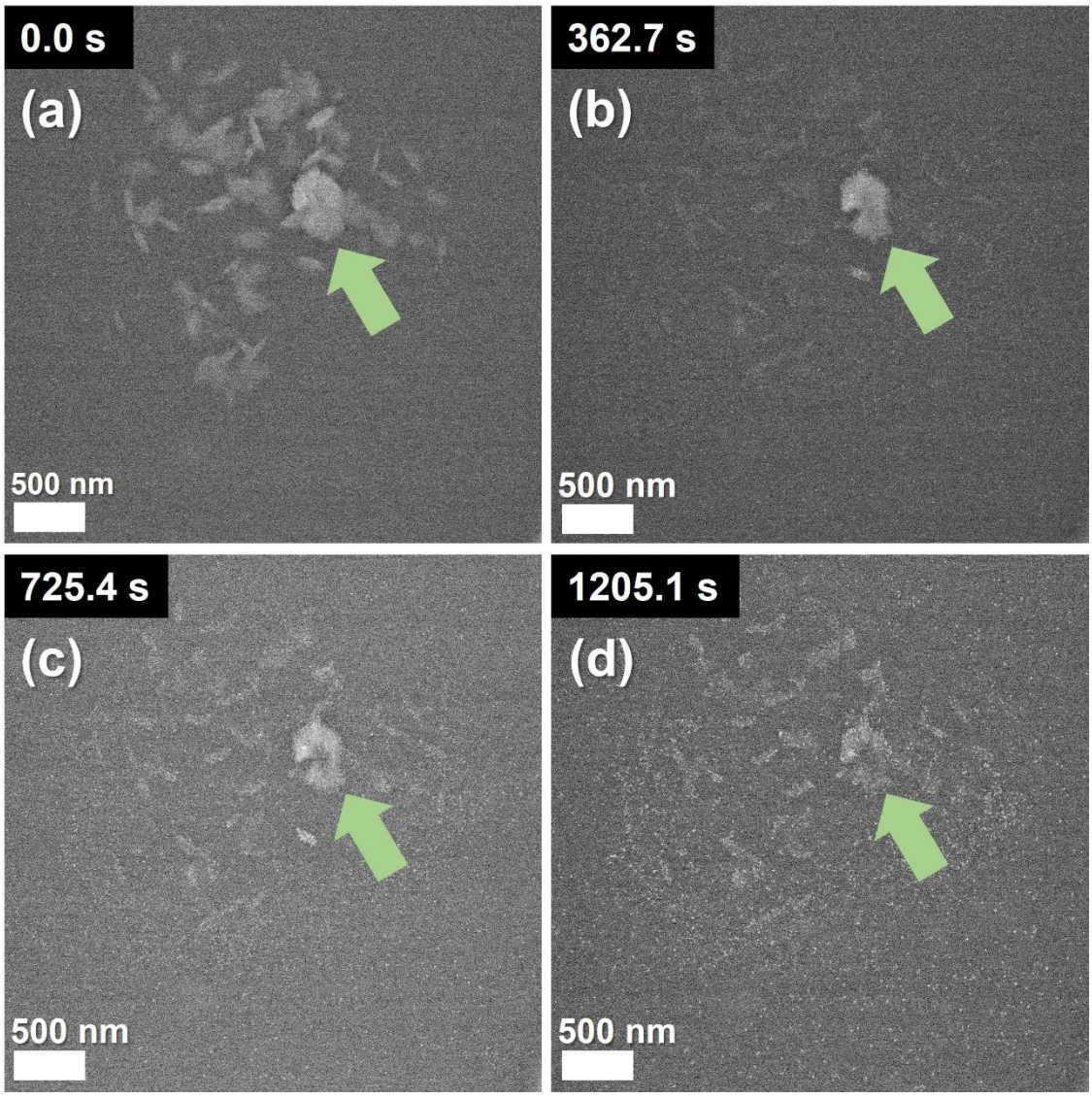


**Figure 4.47 HAADF STEM images taken from a video of the dissolution of a $Ca(OH)_2$ suspension in the LC, where the total fluence at each time point was (a) 4 $e^-$ $Å^{-2}$, (b) 32 $e^-$ $Å^{-2}$, (c) 281 $e^-$ $Å^{-2}$ and (d) 465 $e^-$ $Å^{-2}$.**

In order to ascertain that the dissolution of $Ca(OH)_2$ and emergence of the spherical particles were not induced by continued beam exposure, "snapshot" images were taken of an area at set time intervals. This limited exposure to the electron beam as much as possible whilst monitoring the reaction.

The "snapshot" images showed that the plates dissolved within 6 minutes (Figure 4.48). After 18 minutes, both spherical particles and the brightening of the $Ca(OH)_2$ remnants were observed. Although this confirmed that $Ca(OH)_2$ dissolution and the subsequent formation of the amorphous phase were not beam-induced, these processes did occur faster during continuous imaging. This can be attributed to the

acidifying effect of the beam on aqueous solutions with initial pH > 3, which occurs due to radiolysis of water by irradiation with the beam[124]. As the dissolution rate of $Ca(OH)_2$ increases with decreasing pH[351], prolonged beam exposure will speed up the dissolution of $Ca(OH)_2$ crystals.

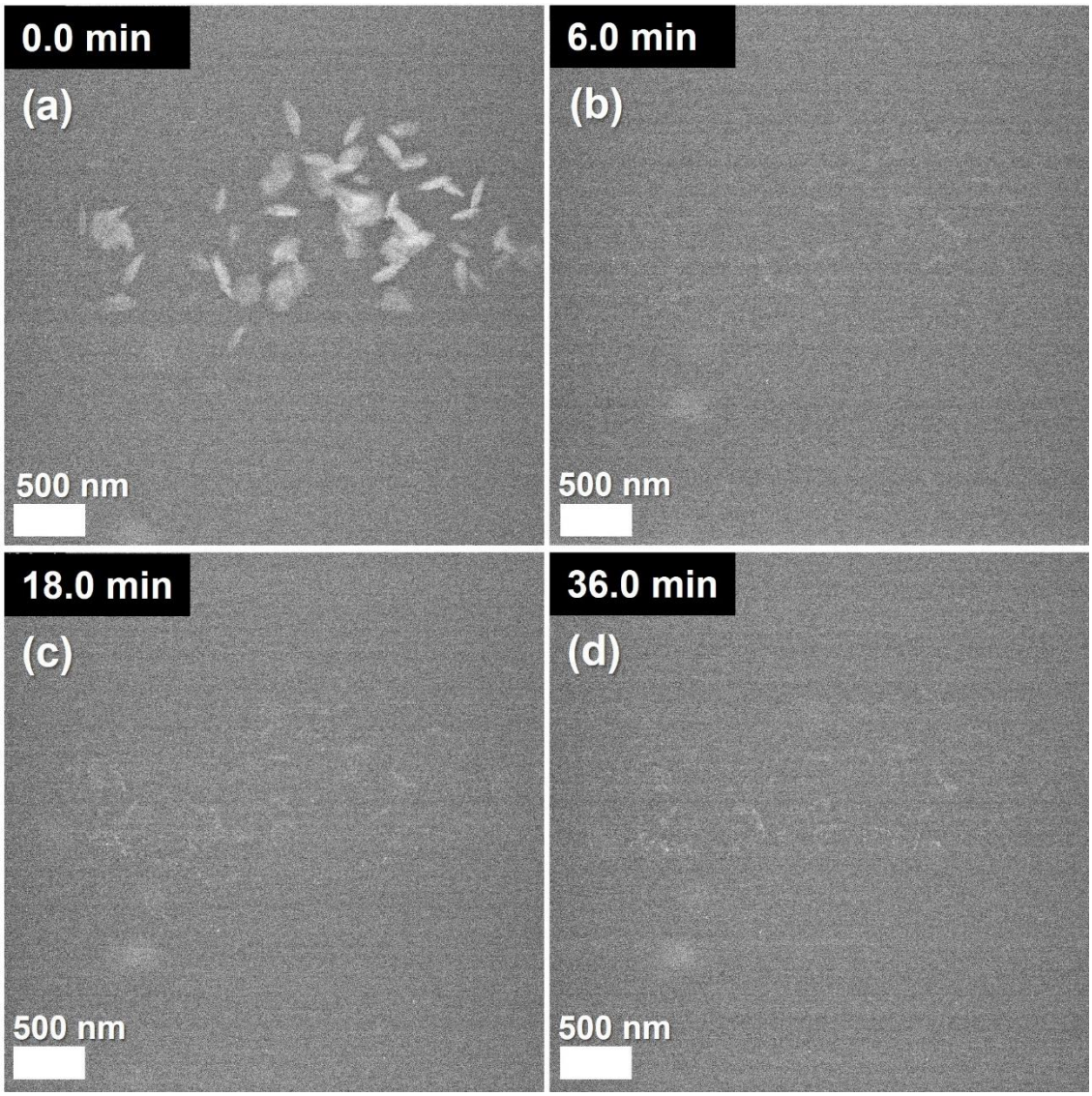


**Figure 4.48 HAADF STEM images taken of the dissolution of $Ca(OH)_2$ particles in a LC. "Snapshot" images were recorded instead of continuous scans to minimise exposure to the electron beam, where the total fluence at each time point was (a) 10 $e^-$ $Å^{-2}$, (b) 60 $e^-$ $Å^{-2}$, (c) 102 $e^-$ $Å^{-2}$ and (d) 143 $e^-$ $Å^{-2}$.**

The liquid-cell experiment was repeated with fresh suspension and larger partially dissolved plates of $Ca(OH)_2$ were observed (Figure 4.49). Despite the low resolution, the outer edges and undissolved central portion of the plates were clearly visible.

Larger intact plates were also found, and are likely to be thicker $Ca(OH)_2$ particles that did not dissolve as quickly.

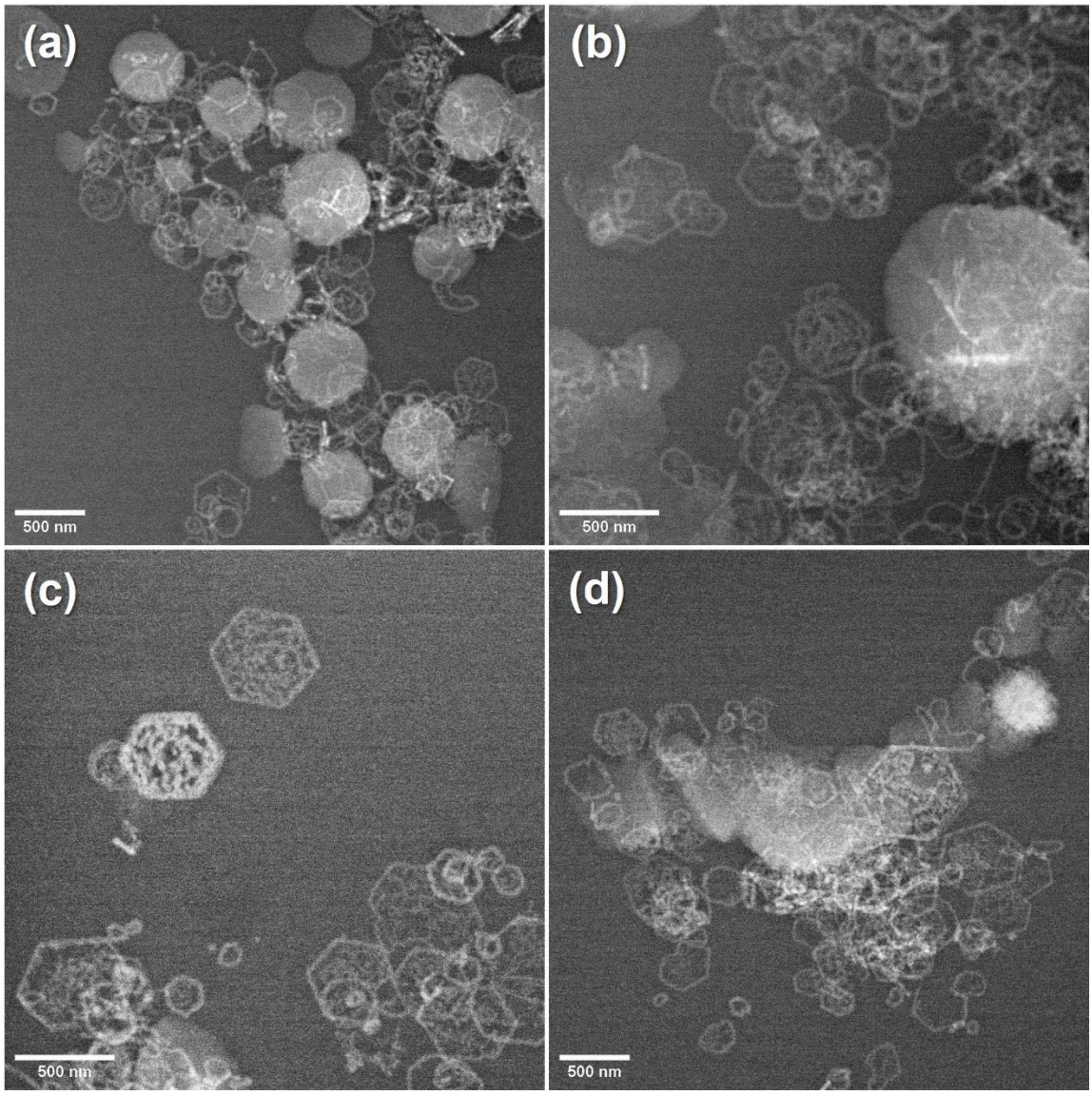


**Figure 4.49 HAADF STEM images of $Ca(OH)_2$ suspension in the LC, where the fluence was (a) 17 $e^-$ $Å^{-2}$, (b) 29 $e^-$ $Å^{-2}$, (c) 33 $e^-$ $Å^{-2}$ and (d) 16 $e^-$ $Å^{-2}$.**

#### 4.3.6.2 Growth of Calcite

In addition to the early stages of the carbonation reaction, it was also important to capture the growth of calcite crystals in the LC. Continuous imaging of calcite crystals was challenging due to their inherent susceptibility to beam damage[352, 353] and dissolution in acidic conditions. Beam damage was observed whilst capturing the video of calcite and ACC particles depicted in Figure 4.50, where the contrast of the image changed significantly in response to the changing conditions. During the

video the ACC particles densified in the centre, displaying the same pitting and roughening prior to dissolution as seen in similar LCTEM work by Nielsen *et al.*[78], which they attributed to the ACC becoming solid-like.

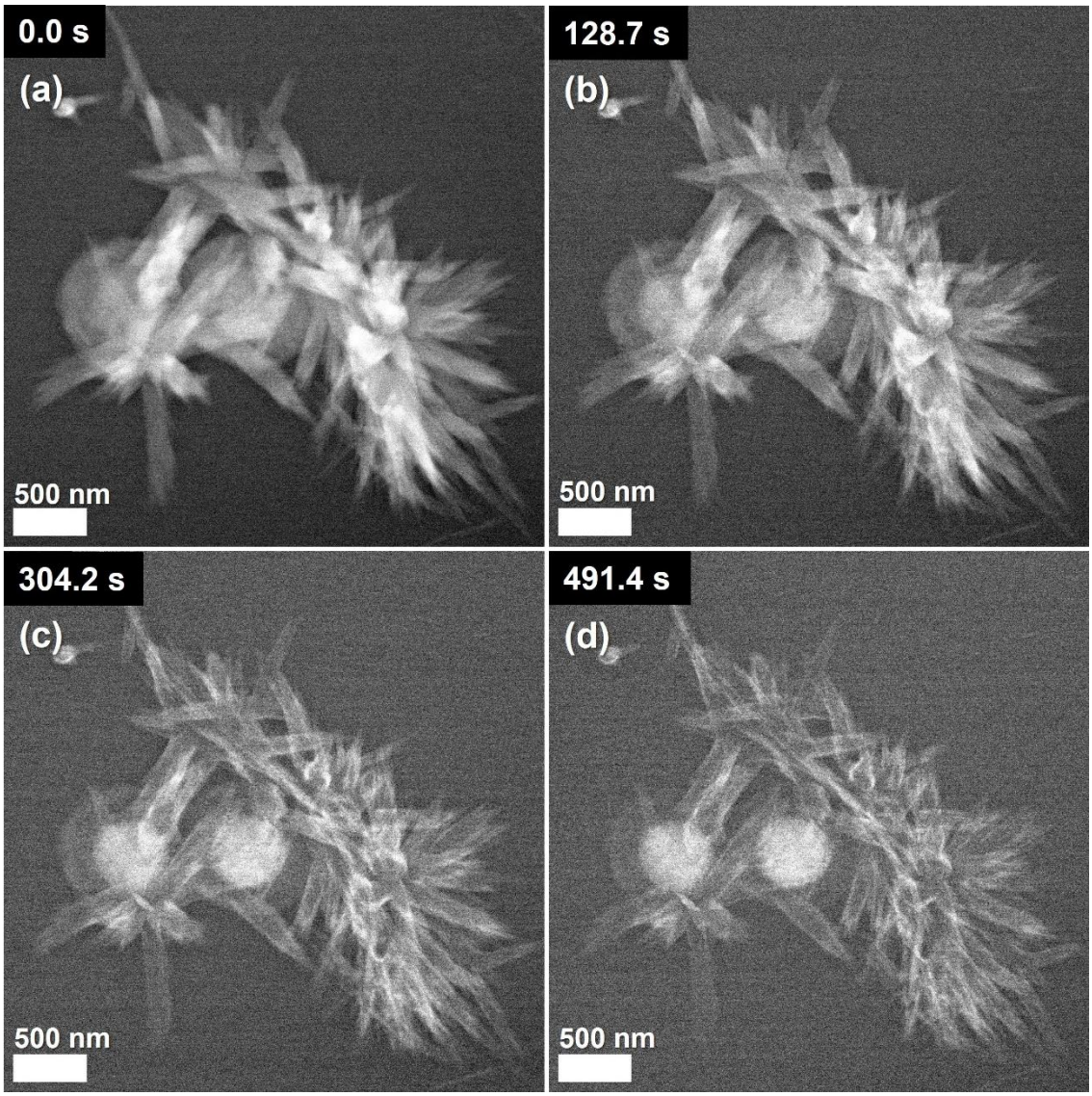


**Figure 4.50 HAADF STEM images taken from a video of calcite crystals suffering from beam damage, where the total fluence at each time point was (a) 7 $e^{-}$ $Å^{-2}$, (b) 84 $e^{-}$ $Å^{-2}$, (c) 189 $e^{-}$ $Å^{-2}$ and (d) 300 $e^{-}$ $Å^{-2}$.**

By carefully optimising the beam dose, continuous imaging was achieved on another area of calcite crystals for a sustained period with no observable beam effects (Figure 4.51).

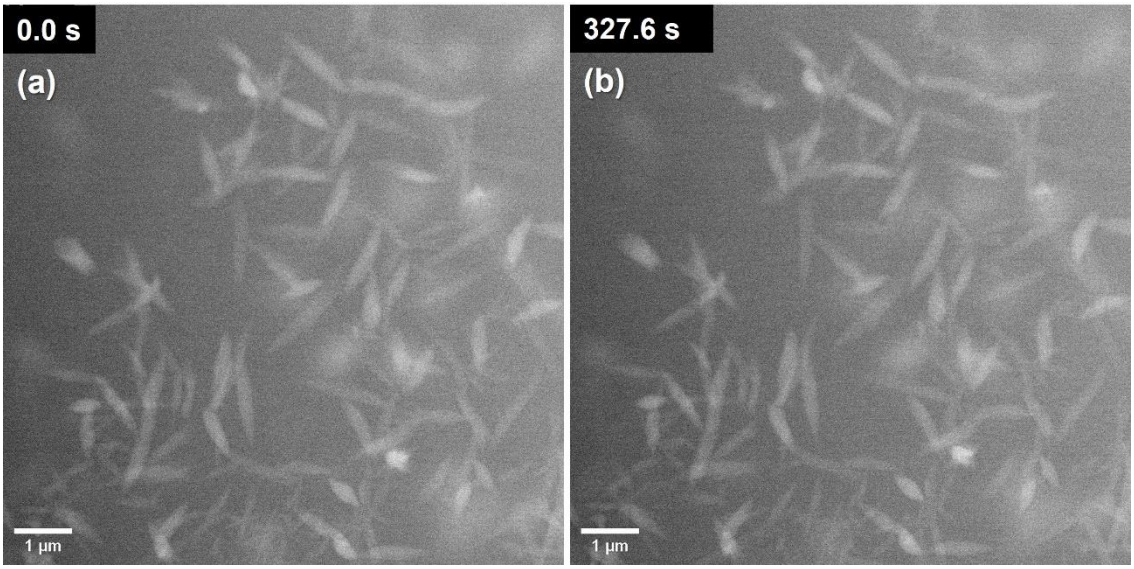


**Figure 4.51 HAADF STEM images taken from a video of calcite crystals with no beam effects, where the total fluence at each time point was (a) 1 $e^{-}$ $Å^{-2}$ and (b) 34 $e^{-}$ $Å^{-2}$.**

Calcite crystals were continuously imaged using the optimised beam dose, and the growth of polycrystals was observed (Figure 4.52). This showed the growth of individual crystals along their long axis.

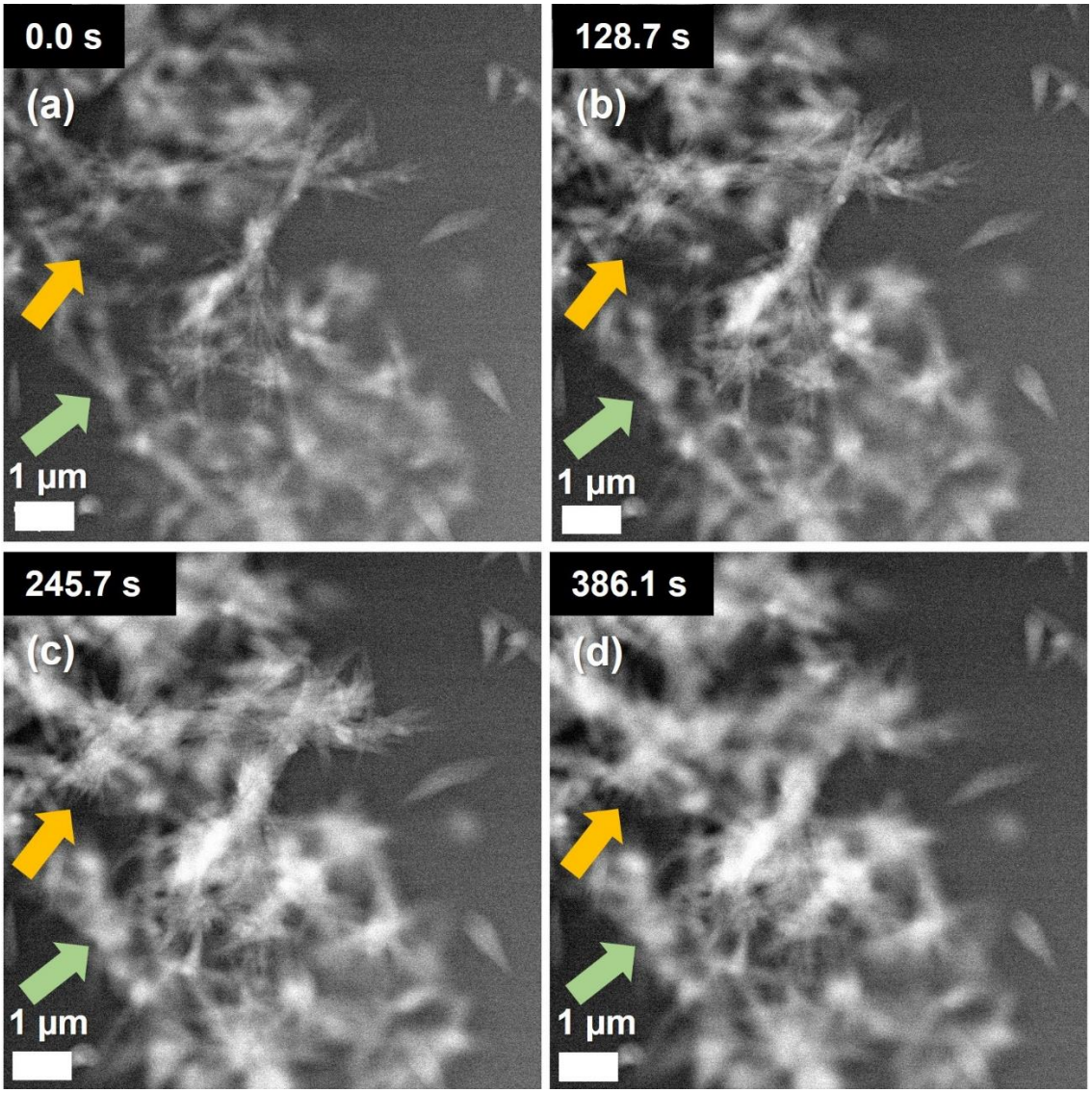


**Figure 4.52 HAADF STEM images taken from a video of growing calcite crystals, where the total fluence at each time point was (a) 1 $e^-$ $Å^{-2}$, (b) 15 $e^-$ $Å^{-2}$, (c) 27 $e^-$ $Å^{-2}$ and (d) 42 $e^-$ $Å^{-2}$. Areas of growth are indicated by orange and green arrows.**

High-magnification imaging in the area where Figure 4.53 was captured showed the small crystallites growing from the crystal apexes (Figure 4.53). The large size of the aggregates made it challenging to achieve focus across the depth of the sample.

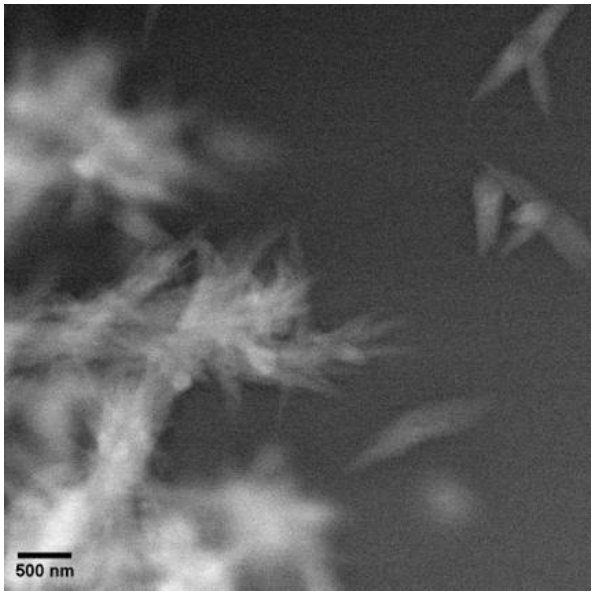


**Figure 4.53 HAADF STEM image of calcite crystals in the area captured in Figure 4.52 at high magnification, showing the needle-like growths at the apex of scalenohedral calcite crystals, where the fluence was 3 $e^{-}$ $Å^{-2}$.**

Although LCTEM allowed the reaction to be followed visually, it was difficult to confirm the composition of the species observed in the LC. EDX was not suitable due to the similar elemental composition of the reactants and products and electron diffraction could not be performed on the LC filled with solution. Therefore, air was flushed through the liquid cell at the end of individual experiments to dry it and allow SAED patterns to be collected. This could only be performed at the end of an experiment, as refilling the LC with solution was generally unsuccessful due to the windows sealing during drying. The scalenohedral crystals were confirmed to be calcite using SAED (Figure 4.54).

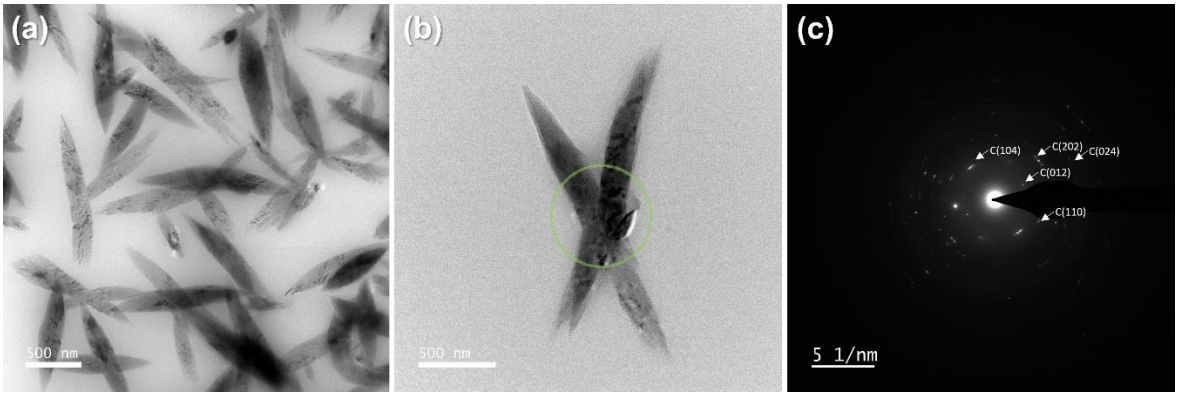


**Figure 4.54 TEM images taken after drying the LC chip of calcite crystals (a, b), with corresponding SAED pattern (c) for circled area in image (b).**

#### 4.3.6.3 Low [$CaCl_2$] Synthesis of $Ca(OH)_2$ via Anion Exchange for LCTEM

The LCTEM studies were often challenging as densely-packed, micron-sized particles were sometimes present (Figure 4.55). This made it difficult to assemble the cell, as the chips would often crack. Further optimisation of the $Ca(OH)_2$ synthesis was therefore needed to ensure that the LC could be loaded successfully.

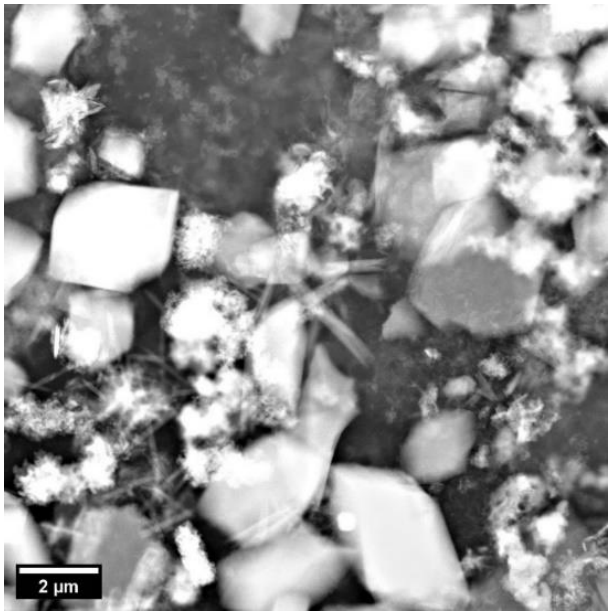


**Figure 4.55 HAADF-STEM image of the LC showing micron-sized particles packed within the viewing window, which were too large for proper characterisation using the LCTEM.**

In order to reduce the particle size of $Ca(OH)_2$, the initial [$CaCl_2$] was reduced, with the best size distribution being achieved at 0.02 M. Dispersions of the $Ca(OH)_2$ in

EtOH were examined using both SEM (Figure 4.56) and TEM (Figure 4.57) and thin hexagonal plates with lengths of 0.1 – 1 µm were observed. SAED confirmed that single crystals of portlandite were obtained.

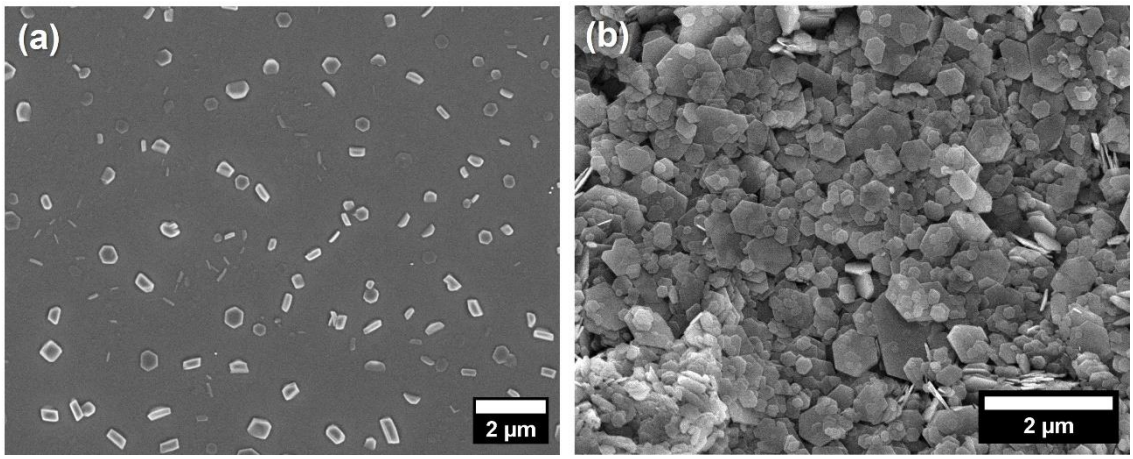


**Figure 4.56 SEM images of $Ca(OH)_2$ plates prepared using a lower $CaCl_2$ concentration of 0.02M in the anion exchange resin method.**

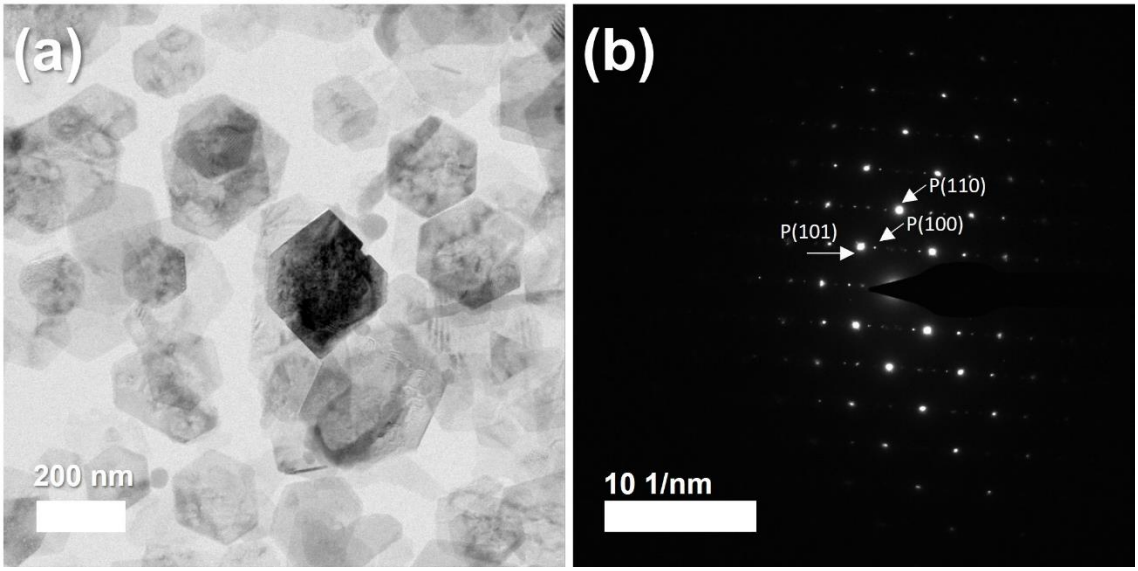


**Figure 4.57 Dry TEM of $Ca(OH)_2$ prepared using a lower $CaCl_2$ concentration of 0.02M in the anion exchange resin method (a), with corresponding SAED pattern.**

The LCTEM studies were repeated with the $Ca(OH)_2$ suspension synthesised using low [$CaCl_2$]. Despite there being a gas bubble in view of the window, continuous imaging showed two hexagonal $Ca(OH)_2$ plates that were preferentially dissolving in the centre, leaving the outer edge intact (Figure 4.58). This confirmed that the

skeletal, hexagonal structures previously seen in static TEM images were formed by the dissolution of the $Ca(OH)_2$.

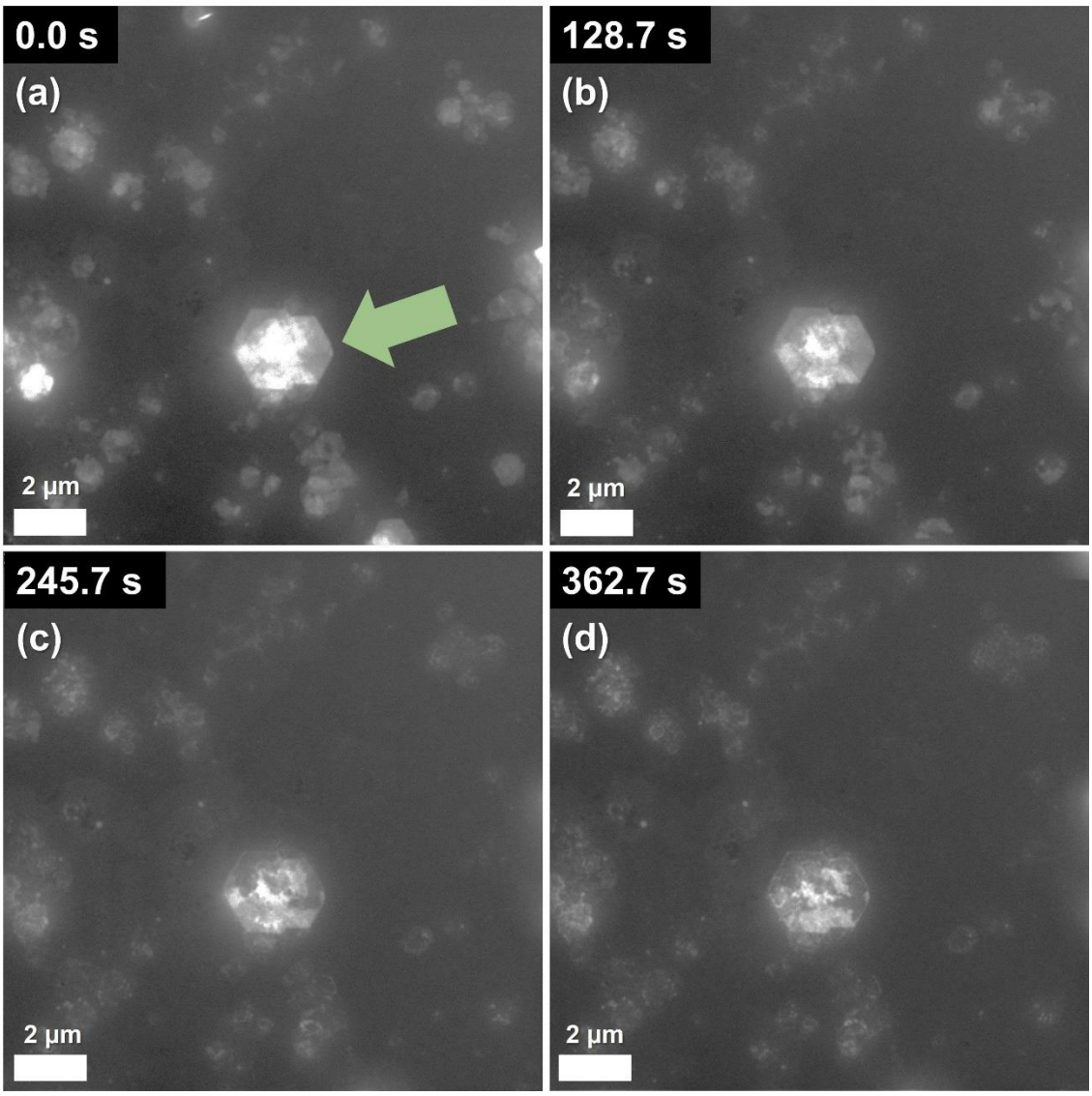


**Figure 4.58 HAADF STEM images taken from a video of the $Ca(OH)_2$ suspension undergoing dissolution in the LC, where the total fluence at each time point was (a) 4 $e^-$ $Å^{-2}$, (b) 45 $e^-$ $Å^{-2}$, (c) 83 $e^-$ $Å^{-2}$ and (d) 121 $e^-$ $Å^{-2}$. The high contrast was due to the presence of a gas bubble over the viewing window.**

Another area on the window that was densely-packed with hexagonal plates was examined over a sustained period and the same preferential dissolution was observed (Figure 4.59). In the final frame in Figure 4.59, the gas bubble once again moved into the viewing window. The greater resolution achieved by imaging through gas rather than liquid highlighted the network of amorphous material between the remnants of different $Ca(OH)_2$ particles.

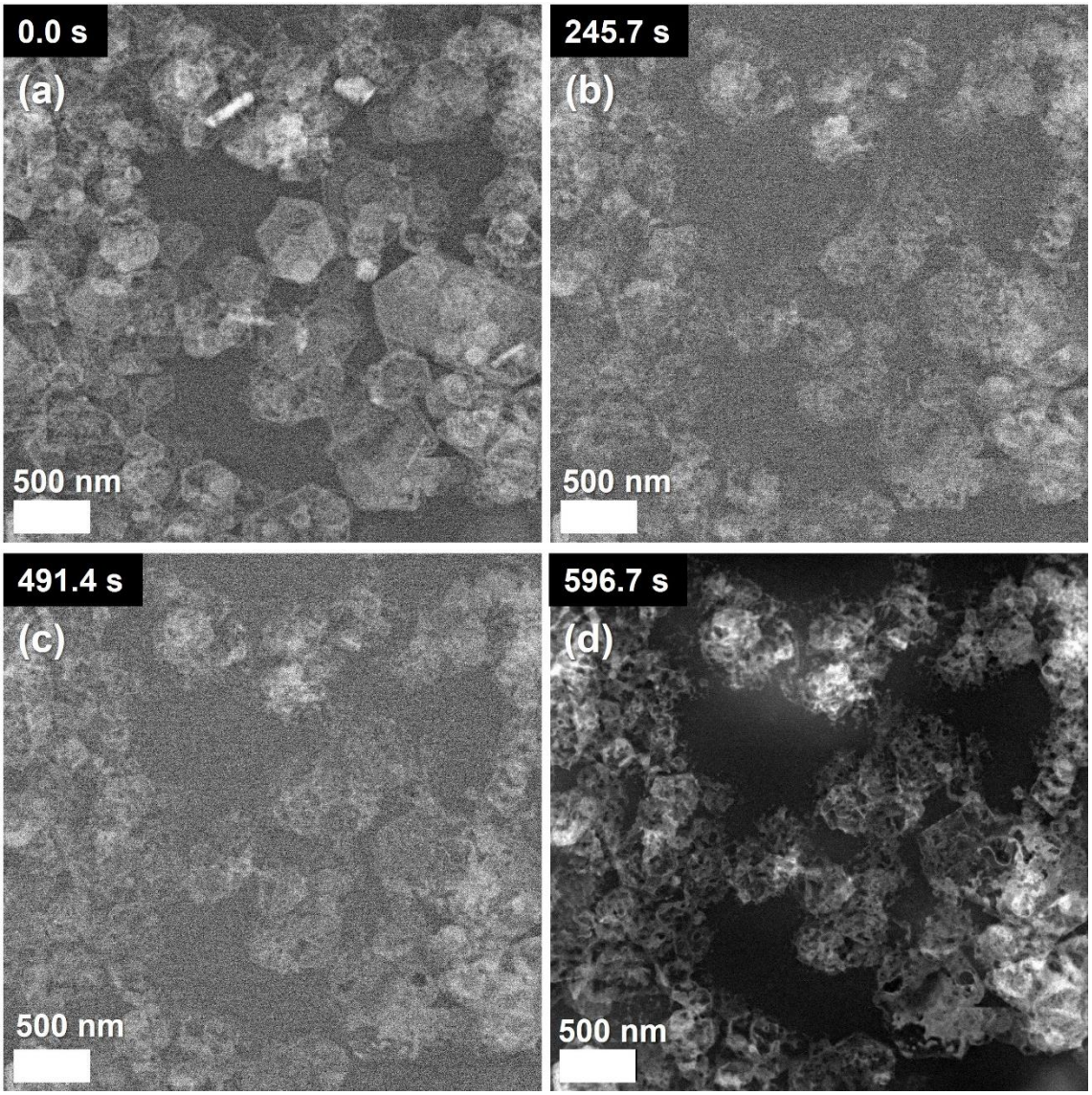


**Figure 4.59 HAADF STEM images taken from a video of the dissolving $Ca(OH)_2$ suspension in the LC with a gas bubble over the viewing window in the last image, where the total fluence at each time point was (a) 5 $e^-$ $Å^{-2}$, (b) 106 $e^-$ $Å^{-2}$, (c) 207 $e^-$ $Å^{-2}$ and (d) 251 $e^-$ $Å^{-2}$.**

Further imaging of this area revealed the transformation of the amorphous material into calcite crystals. This began with a reduction in the network of amorphous material, which occurred faster as the gas bubble caused the sample to be exposed to a greater beam dose (Figure 4.60). The LC partially rehydrated during the video, as evident by the brighter areas in the images, and rod-like calcite crystals could be seen after 5 minutes as highlighted by orange arrows in Figure 4.60b and c. The crystals appeared following the dissolution of the amorphous material. 80 nm spherical features also began to emerge and brightened over time, becoming

prevalent after 10 minutes (Figure 4.60c). This may be attributed to the formation of further ACC, which precipitated as the viewed area of the LC becomes hydrated again, which supplies the area with further ions. Overall, this confirmed that the dissolution of $Ca(OH)_2$ resulted in the precipitation of ACC, which eventually dissolves to crystallise calcite.

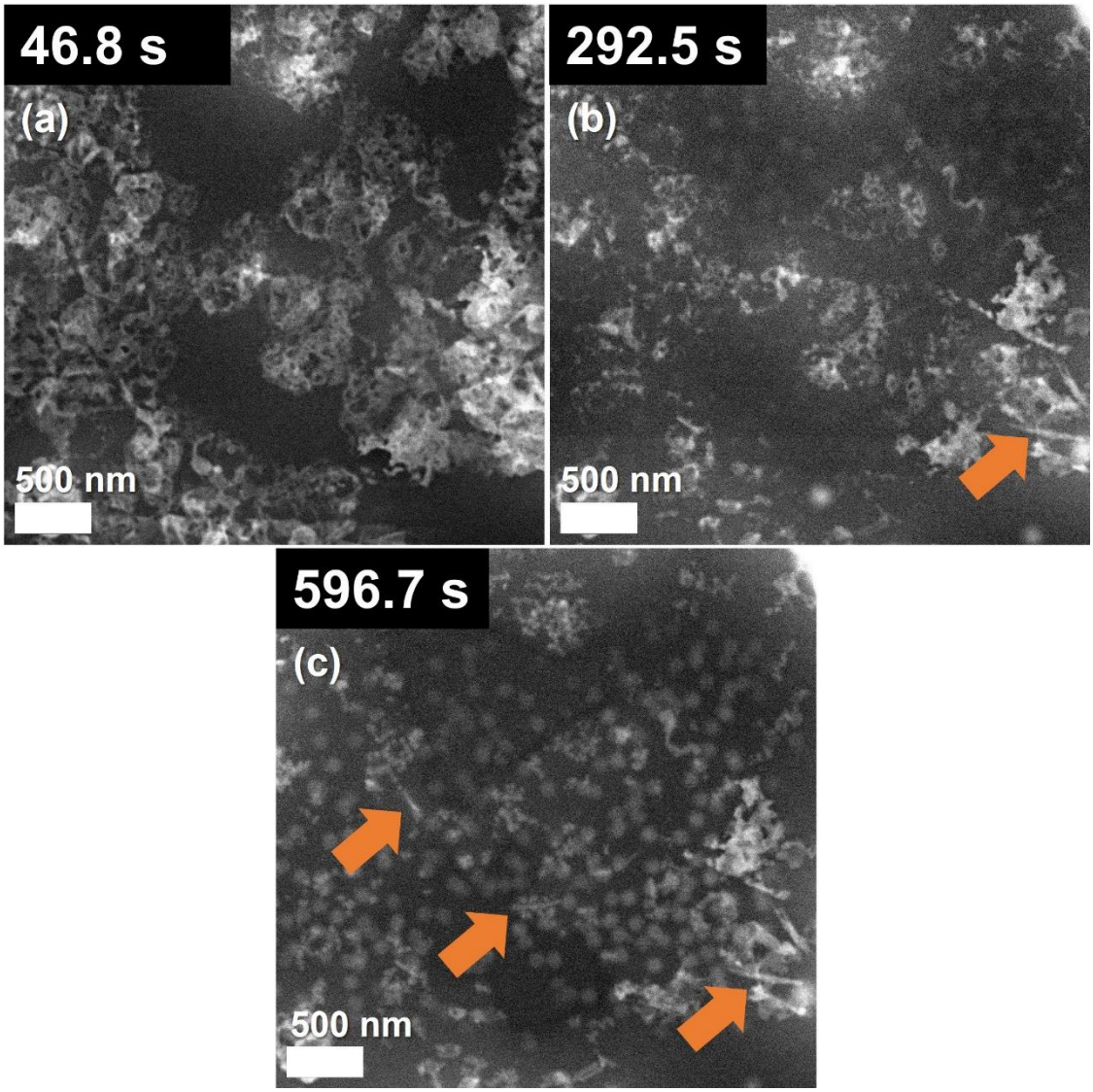


**Figure 4.60 HAADF STEM images taken from a video of the $Ca(OH)_2$ suspension undergoing dissolution in the LC with a gas bubble over the viewing window, where the total fluence at each time point was 324 $e^-$ $Å^{-2}$, 571 $e^-$ $Å^{-2}$ and 876 $e^-$ $Å^{-2}$. The time-stamps correspond to the new video rather than continued from video in Figure 4.59, orange arrows highlight rod-like calcite crystals.**

### 4.3.7 The Effect of Commonly Used PCC Additives on the Carbonation of $Ca(OH)_2$

In the industrial production of PCC, additives are used to control polymorph, morphology, and particle size. The effect of two commonly used additives - citric acid and gypsum - on the early stages of formation was studied using dry TEM, with further study of the citric acid system conducted using cryo-TEM. As discussed in the introduction, both gypsum and citric acid are employed in PCC production to reduce particle size and increase the SSA, while citric acid also suppresses the formation of aragonite.

Suspensions of $Ca(OH)_2$ particles in EtOH were synthesised using the low [$CaCl_2$] route as for the optimised LCTEM samples, and diluted 1:1 with DI water. Samples for dry TEM were prepared using a Vitrobot to plunge-freeze the grids after the allotted carbonation time and brought to room temperature under vacuum. This method was used to pause the reaction as effectively as possible.

#### 4.3.7.1 Additive-Free Control

Firstly, an additive-free sample was prepared to allow a direct comparison of the reaction products at each time point (Figure 4.61). Both 0 and 2 minute samples contained hexagonal $Ca(OH)_2$ plates, with some showing pitted, dissolved regions on the basal faces. Small spherical and liquid-like particles were present at both time points, which can be attributed to the formation of ACC. The rod-like crystals were $Ca(OH)_2$ plates oriented with the basal faces perpendicular to the grid.

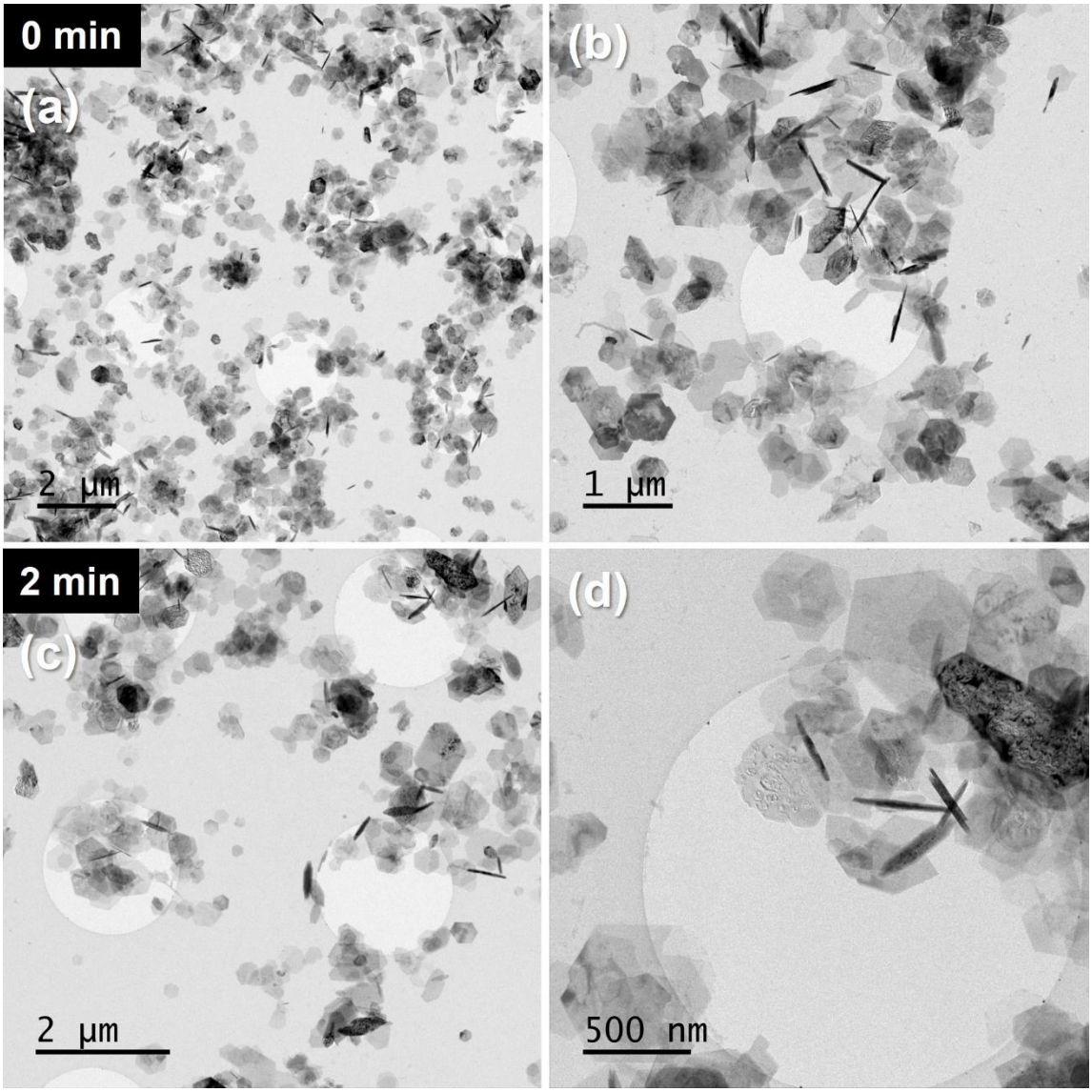


**Figure 4.61 Time-resolved TEM images of additive-free $Ca(OH)_2$ suspensions after 0 min (a, b) and 2 min (c, d) of carbonation, prepared using a Vitrobot.**

Cryo-TEM was also used to observe the products after 0, 2 and 5 minutes of carbonation. The 0 minute sample consisted of thin hexagonal $Ca(OH)_2$ plates (Figure 4.62 a, b). After 2 minutes of carbonation, micron-length scalenohedral calcite crystals were observed (Figure 4.62 c, d), which had grown further by 5 minutes and were increasingly polycrystalline (Figure 4.62 e, f). High magnification imaging of the calcite obtained after 5 minutes showed the granular structure of the calcite, further evidencing the polycrystallinity of the crystals, as well as highlighting the network of amorphous material (ACC) surrounding them.

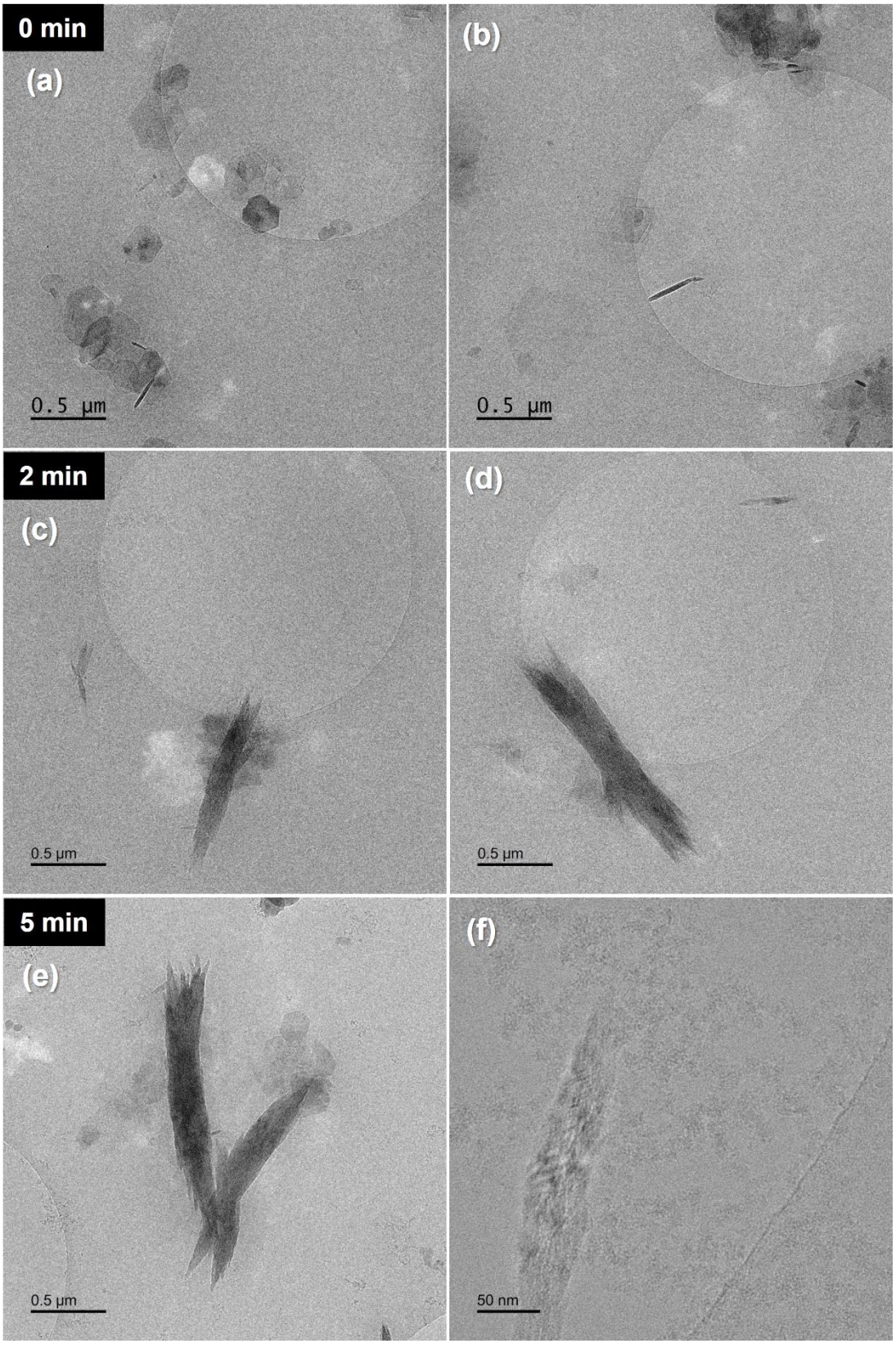


**Figure 4.62 Time-resolved cryo-TEM images of additive-free 1:1 $Ca(OH)_2$ suspensions and water after 0 min (a, b), 2 min (c, d), and 5 min (e, f) of carbonation.**

#### 4.3.7.2 Gypsum

The samples prepared using gypsum as an additive in the $Ca(OH)_2$ suspension did not show any marked differences at 0 or 2 minutes (Figure 4.63 a-d). Dissolution of $Ca(OH)_2$ was observed at both time points, but hardly any amorphous particles were visible in any of the gypsum samples. This could indicate that instead of the rapid precipitation of $CaCO_3$ species, the additional $Ca^{2+}$ supplied in solution by dissolved gypsum causes the equilibrium to shift and the dissolution of $Ca(OH)_2$ to become less favourable.

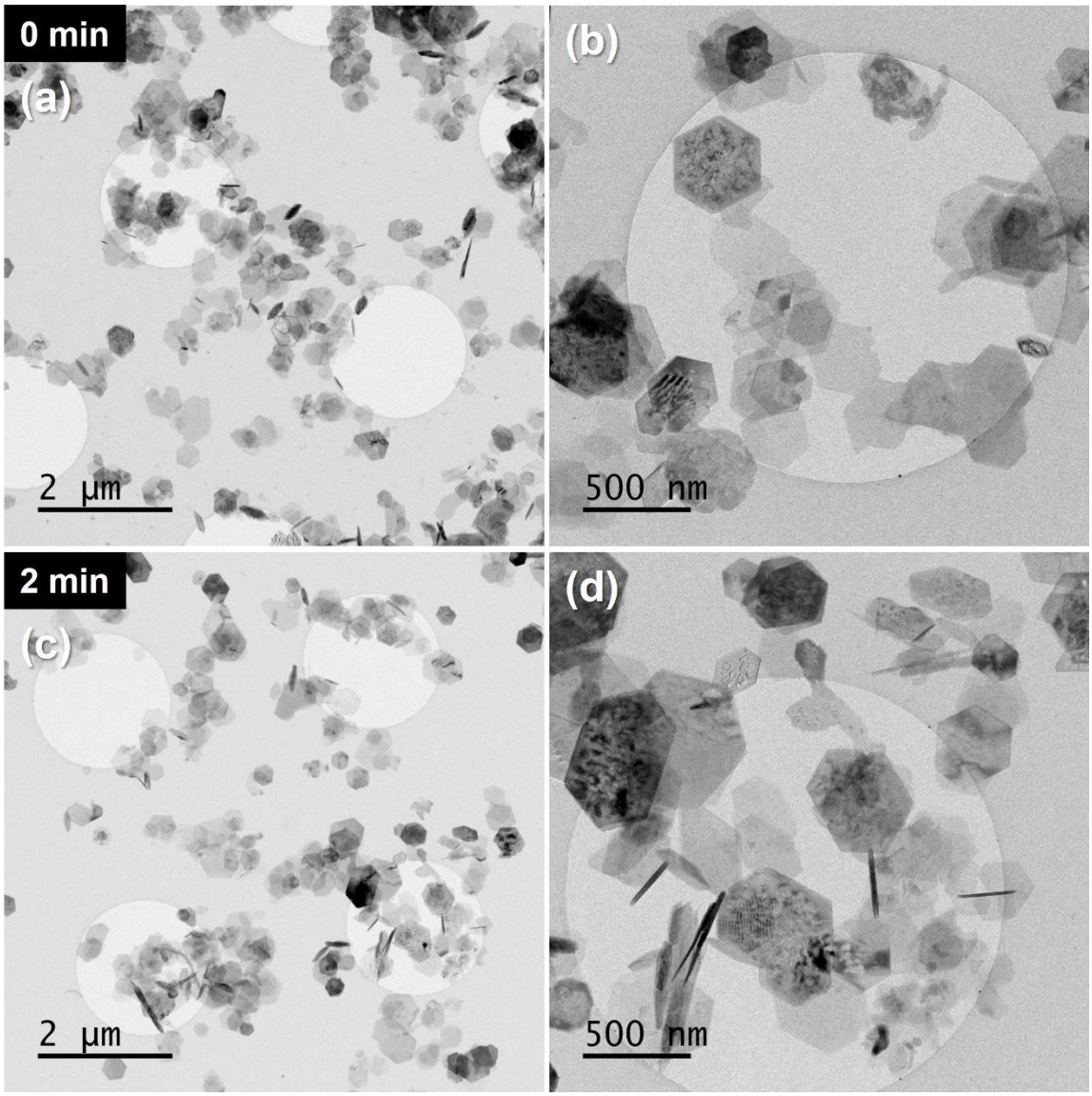


**Figure 4.63 Time-resolved TEM images of $Ca(OH)_2$ suspensions with gypsum after 0 min (a, b) and 2 min (c, d) of carbonation, prepared using a Vitrobot.**

#### 4.3.7.3 Citric Acid

Using citric acid as an additive affected the phases present at 0 minutes, which consisted of $Ca(OH)_2$ plates with varying degrees of dissolution and far more amorphous material (ACC) compared to the control and gypsum samples (Figure 4.64 a, b). The ACC was still present in large amounts after 2 minutes of carbonation (Figure 4.64 c, d), suggesting that it is stabilised by the citric acid, as is consistent with the literature[354].

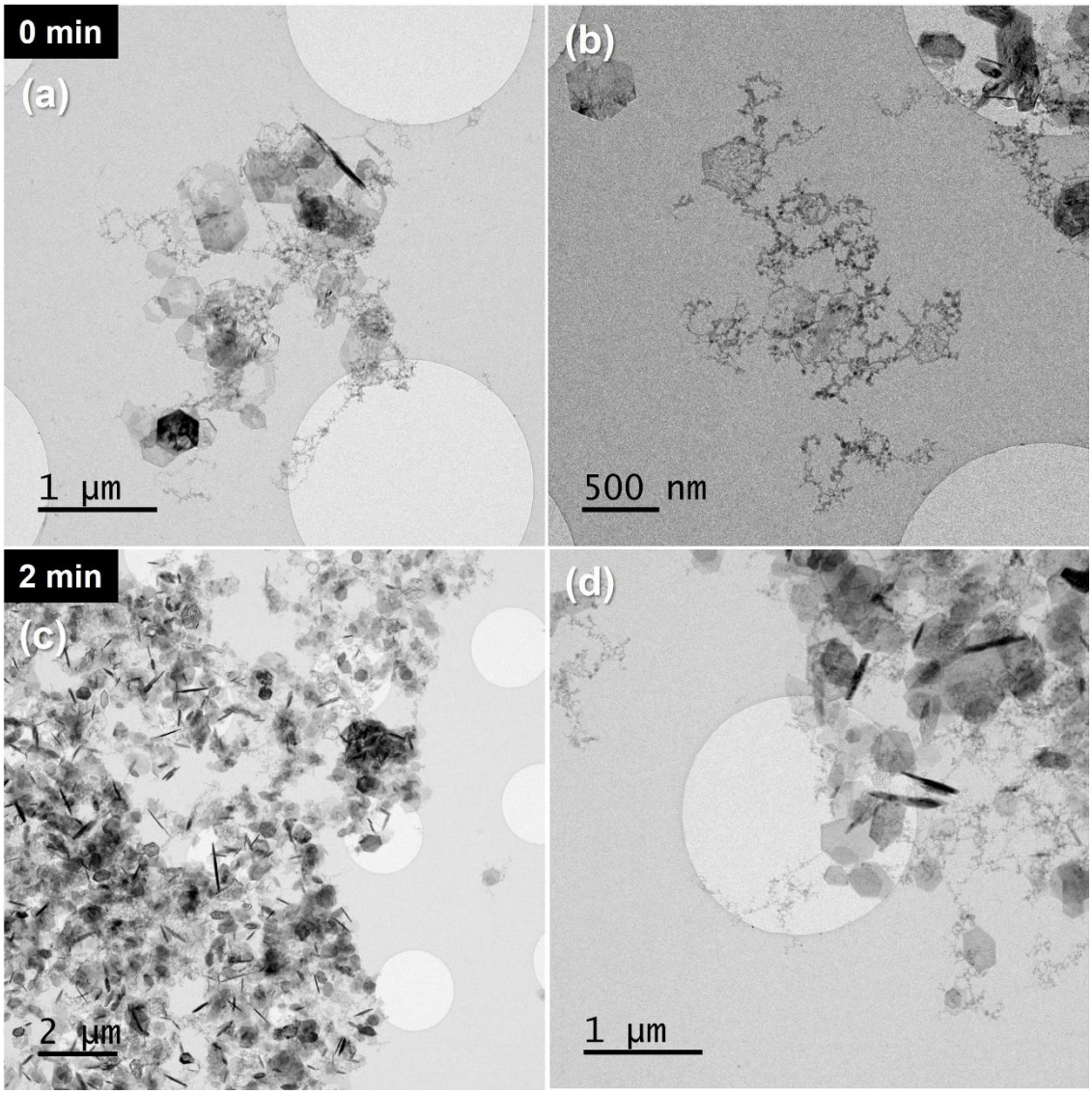


**Figure 4.64 Dry TEM of $Ca(OH)_2$ suspensions with citric acid after different periods of carbonation, prepared using a Vitrobot to pause the reaction.**

Further study was conducted using cryo-TEM (Figure 4.65). As for the dry TEM sample, the presence of citric acid stabilised ACC. Networks of ACC were present after 0 and 2 minutes of carbonation, which clearly retained the hexagonal

framework left by the dissolution of $Ca(OH)_2$ in several areas (Figure 4.65 a-d). The ACC particles were also larger than previously seen for the additive-free sample, reaching almost 100 nm. This agrees with Tobler *et al.,* who found that citrate increased the size of ACC particles[354]. This occurs due to the complexation of $Ca^{2+}$ ions by citrate, which reduces the activity of $Ca^{2+}$ and thereby lowers the supersaturation with respect to ACC. Scalenohedral calcite crystals were not observed until 5 minutes of carbonation (Figure 4.65 e, f), indicating that the induction time is longer for calcite precipitation in the presence of citric acid.

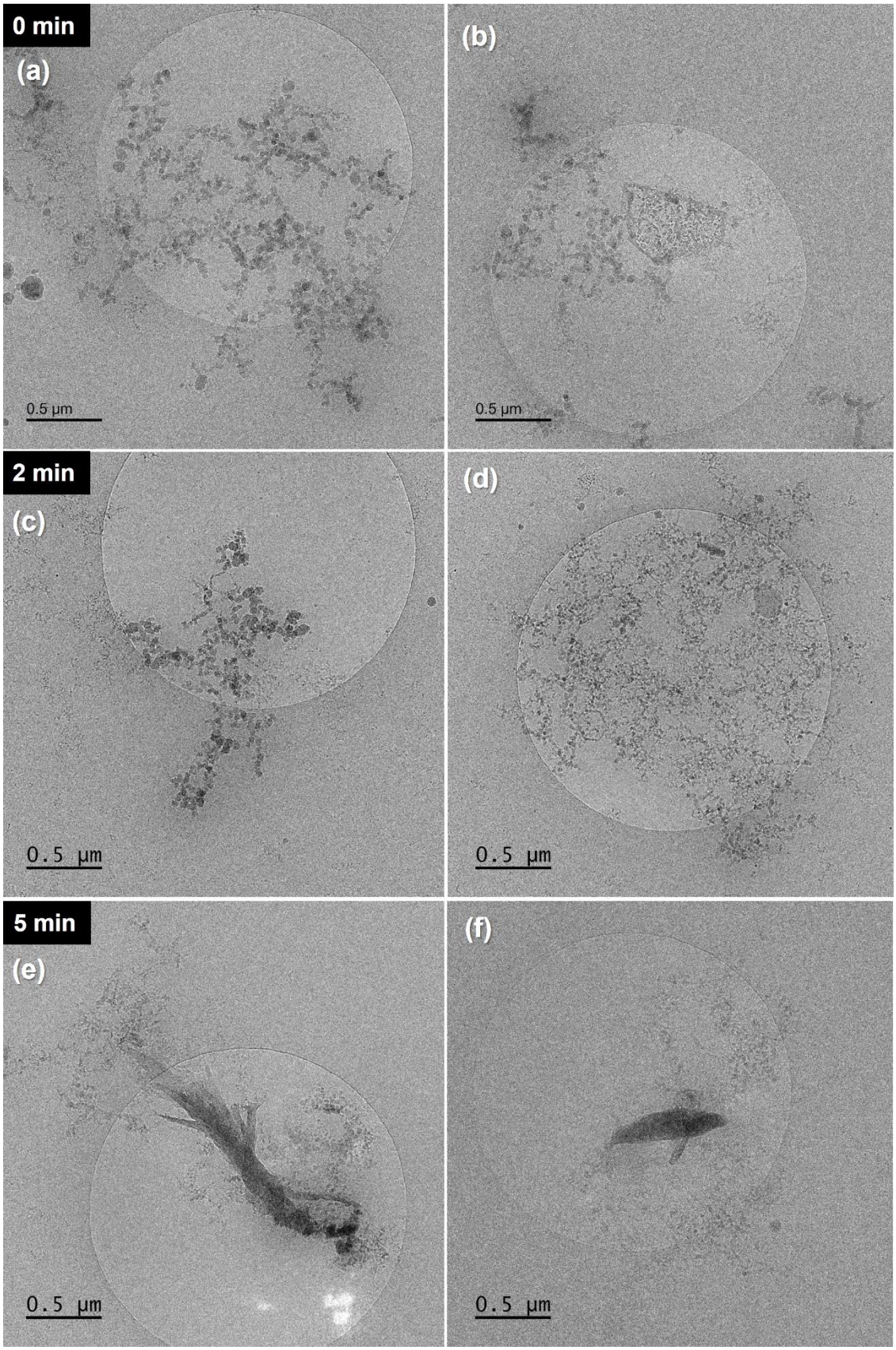


**Figure 4.65 Time-resolved cryo-TEM images of 1:1 $Ca(OH)_2$ suspensions with citric acid and water after different periods of carbonation.**

## 4.4 Discussion

The work in this chapter has explored several key areas of the carbonation reaction of $Ca(OH)_2$, which can be summarised into the following: (i) optimisation of the synthesis of $Ca(OH)_2$ particles suitable for subsequent TEM studies; (ii) the effect of $[Ca^{2+}]/[CO_3^{2-}]$ on the morphology of calcite as observed in cryo-TEM; (iii) insight into the carbonation mechanism as revealed by cryo- and LCTEM; (iv) the effect of additives on the early stages of the carbonation reaction, and (v) the relevance to the industrial carbonation process.

### 4.4.1 Optimisation of the Synthesis of $Ca(OH)_2$ for TEM

Thin hexagonal plates of $Ca(OH)_2$ with defined, recognisable morphologies were required for the TEM studies conducted in this chapter. Commercial $Ca(OH)_2$ was unsuitable for this purpose due to the large particle sizes and high degree of agglomeration. Precipitation of $Ca(OH)_2$ by dropwise addition of NaOH to $CaCl_2$ produced particles with hexagonal prism morphologies that were less agglomerated, but were still fairly thick for observation using TEM. Optimal $Ca(OH)_2$ crystals were produced via an anion exchange resin method. This involved mixing an aqueous solution of $CaCl_2$ with anion exchange resin beads charged with $OH^-$ ions. These ion exchange with dissolved $Cl^-$ ions due to their higher affinity, allowing precipitation of the poorly soluble $Ca(OH)_2$. The synthesis was further optimised for a TEM study by altering the initial $CaCl_2$ concentration to create the best dispersion of particles with ~ 20 nm thicknesses. The method of isolating the $Ca(OH)_2$ was also optimised to avoid premature carbonation following synthesis. This was achieved by immediately filtering the $Ca(OH)_2$ suspension to dryness, washing with EtOH and drying further in a vacuum desiccator before redispersing the particles in pure EtOH.

### 4.4.2 Effect of $[Ca^{2+}]/[CO_3^{2-}]$ on Morphology

Cryo-TEM studies showed that the morphology of the calcite formed during carbonation of $Ca(OH)_2$ suspension in a 2.5 ml vial varied with the proximity of the reaction to the air interface. Aliquots taken from the top of the suspension nearest the air interface yielded calcite with rhombo-scalenohedral morphology, compared to the scalenohedral calcite obtained from aliquots taken at the bottom of the reaction vial. This can be attributed to difference in availability of dissolved $CO_2$ and thus

$CO_3^{2-}$ ions at the two positions in the vial, which results in the environments having different $[Ca^{2+}]/[CO_3^{2-}]$. This ratio is highly influential on calcite morphology, as shown in works by Cizer *et al.*[327] and García Carmona *et al.*[330, 332], where a larger $[Ca^{2+}]/[CO_3^{2-}]$ value favours scalenohedral morphology. As discussed in Section 4.1.4, the scalenohedral morphology is thought to precipitate in the presence of excess $Ca^{2+}$ ions, which may stabilise the polar {214} scalenohedral faces during growth. This is in agreement with the expected differences in $[Ca^{2+}]/[CO_3^{2-}]$ between the two environments in the vial and the observed morphologies present in aliquots extracted from them. At the bottom of the vial, the supply of $CO_3^{2-}$ is limited by diffusion through the suspension and will be readily consumed, so $[Ca^{2+}]/[CO_3^{2-}]$ will be larger and scalenohedral calcite is produced. At the top of the vial, the suspension has an air interface and will have the greatest concentration of $CO_3^{2-}$, so $[Ca^{2+}]/[CO_3^{2-}]$ will be smaller, and rhombo-scalenohedral calcite is obtained.

It should be noted that Cizer *et al*. attributed the difference in morphology across a lime paste sample to a dissolution-precipitation reaction occurring during 60 day ageing, which favours the transformation of scalenohedral calcite into rhombohedral calcite under high relative humidity and $CO_2$ atmospheres[327]. However, the difference in the reaction timeframe and conditions used in the present work indicates that this was not the case here, and can instead be attributed to the change the local $[Ca^{2+}]/[CO_3^{2-}]$ content.

Although this effect on morphology has been previously seen in lime pastes[327] and individual reactors with different conductivities[330, 332], this work demonstrates it can also occur during carbonation of $Ca(OH)_2$ suspension in a reactor where $[Ca^{2+}]/[CO_3^{2-}]$ may not be uniform. This highlights the importance of effective gas dispersion in PCC production to ensure that calcite with consistent morphologies across the batch are obtained.

### 4.4.3 Characterisation of the Partially Dissolved Hexagonal Particles

One of the intriguing observations during the carbonation reaction was the evolution of partially-dissolved hexagonal $Ca(OH)_2$ plates with skeletal structures. The addition of water to ethanolic suspensions of $Ca(OH)_2$ caused their dissolution, which was shown by SEM and TEM to occur preferentially at the {0001} basal faces. The most obvious explanation is that dissolution occurs preferentially at the basal faces of

$Ca(OH)_2$ crystals, leaving prismatic edges in-tact and conserving the hexagonal habit. Conversely, studies of the dissolution rates of portlandite have shown that the prismatic face dissolves more readily than the basal[310, 355], although this was found for micron-sized prismatic crystals rather than the thin plates of $Ca(OH)_2$ prepared here which have very small prismatic faces. Typically, anisotropic dissolution rates for different facets can be attributed to the type of face they are. Both of the dominant faces in portlandite, {0001} and {01-10}, are flat faces, as defined by periodic bond theory[11], which are thought to grow by layer-spreading and do not contain steps and kinks[310]. The growth and dissolution of flat faces occurs more slowly than faces which are populated with steps and kinks, but as both faces in portlandite are flat the preferential dissolution of {0001} cannot be attributed to this.

The preferential dissolution may also arise from an anisotropic distribution of dislocations between the two dominant faces. If the {0001} face possessed a greater number of etch pits, dissolution would occur more readily at this face. At a high level of undersaturation, etch pits can be formed. Dissolution can proceed via a spiral mechanism at low undersaturations, but at high undersaturations the dissolution can occur by 2D nucleation of etch pits[356]. One possibility is that the synthesis method for $Ca(OH)_2$ generates lattice defects specific to this face, which will facilitate rapid dissolution. The type of dissolution seen here is similar to the hollow-core dissolution exhibited by hexagonal prism crystals of hydroxyapatite, which dissolve preferentially on the basal face to form a hollow through the *c*-axis of the prism when exposed to acid[357]. This stems from an unusual “hollow-core” dislocation[358], which has been attributed to a large Burgers vector (which describes the displacement of a dislocation from the perfect lattice) and is typically found in the basal [0001] faces of hexagonal materials[357, 359]. These dislocations become unstable at a critical undersaturation and will develop into etch pits at the open surface[360, 361]. In order to verify this, a surface measurement technique such as atomic force microscopy (AFM) is required to scan the faces and determine their topography. The dissolution of the $Ca(OH)_2$ could also be studied further by performing 3D X-ray micro-tomography (XMT) of a crystal after different lengths of exposure in water. This technique would allow the effect of dissolution on each face to be measured effectively, as outlined in studies by Noiriel *et al.*[362, 363]. However, a relatively large

crystal would be required and preventing further dissolution of the $Ca(OH)_2$ in aerobic conditions during measurement would be challenging.

The partially-filled hexagonal structures have also been seen in work by Kudłacz[364] and Rodriguez-Navarro *et al.*[321, 323, 365]. Kudłacz observed the hexagonal "residual rims" after exposing a suspension of hexagonal $Ca(OH)_2$ plates to air bubbling. The structures yielded diffuse rings in SAED, and Kudłacz highlighted their similarity to ACC spheres. Earlier works of Rodriguez-Navarro into the carbonation of $Ca(OH)_2$ showed ring-like ACC that clearly possess hexagonal shapes reminiscent of the hexagonal $Ca(OH)_2$ plates[321, 323]. The authors determined that these were hexagonal-shaped ACC pseudomorphs formed during the early stages of $Ca(OH)_2$ carbonation via an interface-coupled dissolution-precipitation mechanism[323]. This fits in agreement with the data presented in this chapter, which showed that the $Ca(OH)_2$ plates began to dissolve and left the hollow-core structure as observed in LCTEM.

Finally, it should also be considered that in a recent study Rodriguez-Navarro *et al.* observed the same structures in aliquots taken during the synthesis of $Ca(OH)_2$ plates by mixing $CaCl_2$ and NaOH[365]. However, the authors identified the structures as being amorphous calcium hydroxide (ACH), a precursor phase formed during the crystallisation of $Ca(OH)_2$, though they acknowledge that the existence of ACH has been disputed and multiple studies have refuted the possibility of a hydrated calcium hydroxide phase[366, 367]. It is also unclear how the ring-like hexagonal shape can be assembled from ACH, though the authors suggest that this could occur via a pre-existing portlandite protostructure, as has been suggested in literature for ACC and $CaCO_3$ polymorphs[368]. In this work, $Ca(OH)_2$ readily precipitated from solution using the anion resin exchange method and the reaction was sustained for 30 minutes to ensure completion, whereas the study by Navarro *et al.* only allowed the reaction to run for a couple of minutes. Therefore, the partially-complete hexagonal particles seen here are unlikely to be due to the formation of ACH, which would not remain stable over the relatively long reaction period. In contrast, $Ca(OH)_2$ readily dissolves in air and is catalysed by the presence of only four adsorbed water layers. Pausing this reaction has been an on-going challenge in this chapter. It is more likely that the dissolution-precipitation reaction initiated prematurely, and that the pseudomorphic precipitation of ACC on the surface of $Ca(OH)_2$ basal faces created the intricate structures and retained the outer hexagonal edges.

### 4.4.4 Elucidating the Carbonation Reaction Mechanism

By correlating the findings from TEM, cryo-TEM, and LCTEM studies, the following dissolution-precipitation mechanism is proposed (Figure 4.66). Firstly, dissolution of the thin, hexagonal plates $Ca(OH)_2$ occurred upon addition of water. As discussed in Section 4.4.3, cryo-TEM and LCTEM showed that this initially caused holes to form on the basal faces of $Ca(OH)_2$. This was not seen to occur on the prismatic faces of the $Ca(OH)_2$, indicating that dissolution occurred preferentially at the basal faces. This results in a local boundary layer surrounding the $Ca(OH)_2$ plates to become increasingly saturated with $Ca^{2+}$ and $OH^-$ ions, which can undergo reaction with $CO_2^{3-}$ ions. At this point, ACC precipitated in solution and on the remaining basal surfaces of $Ca(OH)_2$, as seen using cryo-TEM. Continued dissolution of the $Ca(OH)_2$ fed the growth of surface-adsorbed ACC, which resulted in the pseudomorphic replacement of the hexagonal $Ca(OH)_2$ plate with ACC. This was evidenced by SAED, which confirmed that the skeletal hexagonal structures were amorphous, and cryo-ET, which showed that the nearby ACC particle networks were connected to them. This strongly supports the theory that the carbonation of $Ca(OH)_2$ follows an interface coupled dissolution-precipitation reaction pathway. LCTEM confirmed that dissolution of the hexagonal pseudomorphic ACC structures and spherical ACC particles led to the precipitation of calcite.

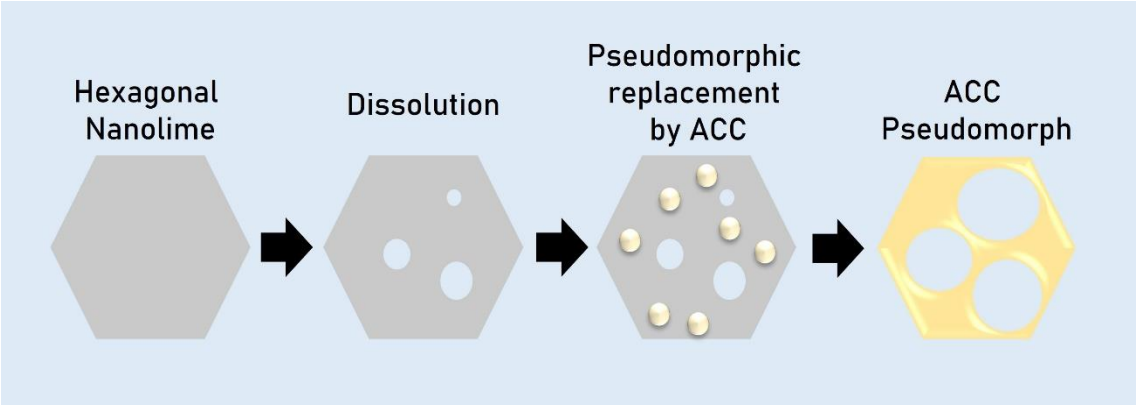


**Figure 4.66 Proposed steps of the dissolution-precipitation mechanism in the carbonation of $Ca(OH)_2$. ACC undergoes a further dissolution-precipitation reaction to form scalenohedral calcite crystals.**

Several stages of calcite growth have been identified using the correlative TEM techniques employed in this work (Figure 4.67). The earliest calcite crystals

capturing using cryo-TEM were highly granular, elliptical crystals which were ≈ 100 nm. Growth predominantly occurred along the long axis, causing needle-like growths to emerge from the apexes of the crystals. The fully developed scalenohedral morphology was evident at the later stages of growth, where continued growth resulted in polycrystals.

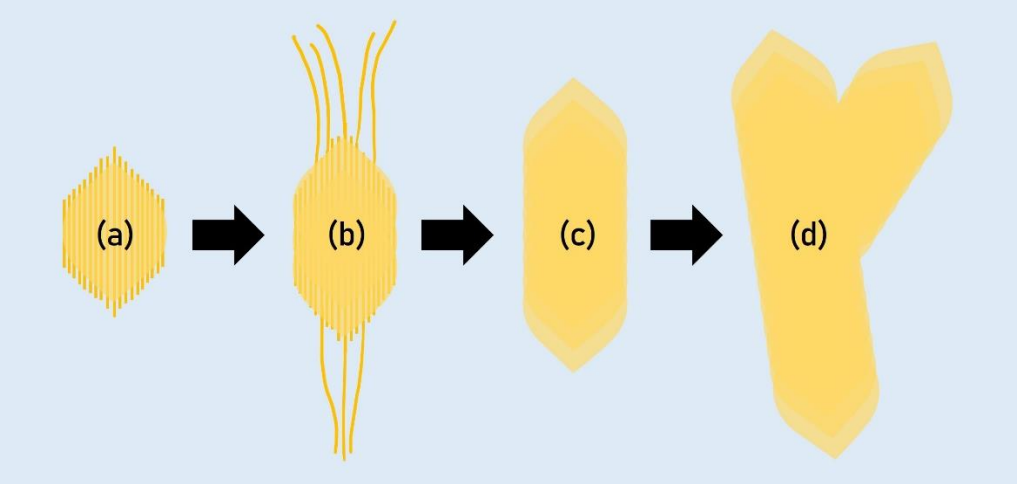


**Figure 4.67 The stages of growth for scalenohedral calcite, (a) initial elliptical crystals with granular structure and crystallites protruding from the apexes, (b) elliptical crystals with needle-like growths at the apexes, (c) scalenohedral calcite, and (d) polycrystalline calcite.**

### 4.4.5 Comparison of the Effects of Cryo-TEM and LCTEM on Reaction Kinetics

Overall, the reaction pathway and both the morphology and polymorph of the product was consistent across both cryo-TEM and LCTEM. However, there were some clear differences in the kinetics of the carbonation reaction observed by each method. Calcite crystallised faster in the cryo-TEM work, which was conducted in a vial with aliquots taken at set intervals, compared to the LCTEM reactions, where reactions occurred within a LC. The reaction is expected to occur at a slower rate in the LC as it is driven by dissolved $CO_2$ within the water that is flowed through the cell, which is vastly less than the amount available when exposed to air as for the cryo-TEM experiments. The implications of the confined environment provided by the LC on the reaction kinetics should also be considered. The effects of confinement on crystallisation have been well-documented and include slower rates of nucleation and growth, longer induction times, and can also change the size, orientation,

morphology, and polymorph of the crystals obtained compared to in bulk[110]. Although the crystals obtained in the LC had similar physical properties to those observed in cryo-TEM, the dynamics of the precipitation reaction were reduced in the confined LC.

On the other hand, the electron beam increased the rate of dissolution of the $Ca(OH)_2$ plates. Prolonged exposure of the aqueous reaction solution to the electron beam causes radiolysis of water, lowering the pH of the solution which in turn promotes dissolution of $Ca(OH)_2$. This was controlled as much as possible by maintaining a low beam current during imaging. Overall, the combination of confinement and beam effects meant that the dissolution occurred quickly, while there was a longer induction time for the precipitation of calcite relative to the bulk reaction performed for cryo-TEM. Calcite dissolution is also promoted at acidic pH and may therefore prevent stable calcite nuclei from forming in the LC. Typically, this effect may be avoided by continuously flowing water through the cell during exposure which prevents the build-up of acidic radiolysis products. However, in this case it is necessary to pause flow after $Ca(OH)_2$ dissolution occurs to ensure that $Ca^{2+}$ and $OH^-$ ions are kept within the viewing area and are not flushed of the LC. These issues could be resolved by speeding up the total reaction time, which would inherently reduce beam exposure and bring down the total fluence without having to reduce the temporal resolution or change the imaging conditions. Increasing the $CO_2$ concentration in the LC would achieve this and make the system more comparable to the cryo-TEM benchtop experiments, as well as helping to counteract the confinement effects that slow down the reaction. One way of increasing $[CO_2]$ in future work would be to saturate the water flowed through the LC with $CO_2$ prior to the experiment.

Although the effects of the electron beam were reduced by using cryo-TEM, it was difficult to isolate the reaction at set reaction time points. As the cryo-TEM samples required pre-mixing of $Ca(OH)_2$ and water, and pipetting of an aliquot onto the grid before blotting and vitrification, the plates had often begun to dissolve even at the T0 time point. This was due to the ~13 s required to mix and load the sample followed by ~6 s to blot and then plunge freeze. This could be reduced in future by using a rapid vitrification device and even earlier time intervals could be collected reliably.

### 4.4.6 The Effect of Additives on the Carbonation Reaction

Finally, the effect of additives in the carbonation reaction was explored using citric acid and gypsum. Both additives are commonly used in the carbonation step of PCC production to control the properties and polymorph of the PCC. In the presence of gypsum, there was little evidence of ACC formation at either of the observation time points, suggesting that the equilibrium shifted towards $Ca(OH)_2$ rather than dissolution in the presence of additional $Ca^{2+}$ ions. In order to gain a fuller picture of the effect gypsum on the carbonation reaction, longer carbonation periods should be used, as calcite crystallisation was not observed for the gypsum or control samples within 2 minutes. However, the effect of citric acid on ACC was evident even during the short carbonation period. ACC particles obtained in the presence of citric acid were larger in size and had longer lifetimes compared to the additive-free control, as shown by both dry and cryo-TEM.

### 4.4.7 Relevance to the Industrial Carbonation Process

Although this study centres around the industrial route of preparing $CaCO_3$, the reaction was adapted in several ways. Firstly, the starting material had to be adapted, and ultimately $Ca(OH)_2$ plates with 20 nm thicknesses were produced. This is very different to $Ca(OH)_2$ used in the industrial-scale reaction, which consists of highly aggregated micron-sized particles with no defined morphology. The reaction was initiated by adding water to the $Ca(OH)_2$ suspension and exposing it to air, whereas the industrial reaction is conducted using by bubbling $CO_2$ through large volumes of $Ca(OH)_2$ slurry at a controlled flow rate. Despite the experimental differences, this study illustrates that the initial $Ca(OH)_2$ starting material is highly influential in the reaction, since it follows an interface-coupled dissolution precipitation mechanism. The study also begins to explore two additives which are used in the industrial reaction, citric acid and gypsum, and highlights the influence of both on ACC.

## 4.5 Conclusions

In summary, the precipitation of calcite via the carbonation of $Ca(OH)_2$ was studied using a range of microscopy techniques. The synthesis of $Ca(OH)_2$ was optimised to prepare a dispersion of thin hexagonal plates ideal for observation using TEM, where the anion exchange method with low $CaCl_2$ was found to yield the best $Ca(OH)_2$

dispersions in terms of size. Initial work was conducted using dry TEM to establish the proper time scale of the reaction and to optimise the method used to purge the reaction after allotted carbonation periods. The reaction was typically found to proceed in under 5 minutes for both reactions performed on-grid and in a vial. However, it was challenging to fully isolate the time points and ensure further reaction did not occur in air. This was improved by using plunge-freezing techniques to prepare grids, and so this was later used to prepare the grids in the additive study for conventional TEM.

Study of the cryo-TEM samples, which were prepared by taking aliquots from two different positions in the reaction vial, revealed that different $[Ca^{2+}]/[CO_3^{2-}]$ environments could be created from the same reaction container and that this had a strong effect on calcite morphology. At the bottom of the vial, where a high $[Ca^{2+}]/[CO_3^{2-}]$ can be expected due to the distance from the air interface (and thus source of $CO_2$), scalenohedral calcite was observed, as opposed to the rhombo-scalenohedral calcite which was obtained in aliquots taken from the top. This finding has implications for PCC production, where control over product morphology is paramount and failure to ensure adequate gas dispersion and $CO_2$ delivery may result in inconsistent morphologies being attained across a single batch.

LCTEM was also used to follow the reaction dynamically and allowed us to observe the dissolution of $Ca(OH)_2$ and precipitation of calcite. In addition to the qualitative information gained by recording images, the cell could also be dried in-situ by pushing air through, which allowed SAED patterns to be collected. Both the cryo-TEM and LCTEM observations were in agreement with a dissolution-precipitation reaction mechanism occurring during the carbonation reaction. The dissolution of $Ca(OH)_2$ appeared to occur preferentially at the centre of basal faces and led to the pseudomorphic precipitation of ACC, which retained the hexagonal edge and often left intricate structures on the basal face intact following complete dissolution of $Ca(OH)_2$.

Finally, the effect of gypsum and citric acid, common additives in PCC synthesis, on the carbonation reaction were studied using conventional TEM and cryo-TEM. Gypsum was found to slow the dissolution of $Ca(OH)_2$ by the addition of $Ca^{2+}$ ions which pushed the equilibrium position toward $Ca(OH)_2$. Citric acid was shown to stabilise ACC particles, which had longer lifetimes. The size of ACC was also

increased, which likely occurred by the reduction in supersaturation caused by the complexation of citric acid with $Ca^{2+}$. Overall, both additives were shown to be highly influential on the early stages of the carbonation reaction, and further demonstrates that TEM techniques can be utilised to provide useful insight into the role of additives used in PCC production.

# Chapter 5 | Synthesis of Porous Manganese Oxides for Photocatalytic Water Splitting

## 5.1 Introduction

### 5.1.1 Aims and Overview

Photocatalytic water splitting is a sustainable way of producing hydrogen using sunlight, which has drawn increasing attention due to the rising demand for clean, renewable energy sources. Inspired by photosynthesis, water splitting research has focused on the development of photocatalysts that can outperform the low efficiencies exhibited by nature to make it a viable alternative to current $H_2$ synthesis routes. However, at present it is highly challenging to develop photocatalytic materials that simultaneously fulfil the requirements of being low-cost, abundantly available, with exceptional solar-to-hydrogen (STH) conversion efficiencies. The aim of the work described in this chapter was to use facile synthesis strategies to prepare highly porous manganese oxide crystals and explore their potential as water splitting photocatalysts. Two synthesis routes were investigated, using precipitated manganese carbonate ($MnCO_3$) as a precursor to yield $Mn_2O_3$ and δ-$MnO_2$ crystals with different porosities. The same approach was applied using $MnCO_3$ occluded with gold nanoparticles, in order to determine whether the incorporation of a noble metal boosted photocatalytic efficiency.

The $Mn_2O_3$ crystals produced by thermal decomposition of precipitated $MnCO_3$ were analysed using pXRD, SEM, FIB-SEM, and BET, which revealed that the annealing conditions were highly influential on the porosity, crystallinity and composition. Similar analysis was performed on δ-$MnO_2$ crystals, which were obtained by hydrothermal reaction of $Mn_2O_3$, to examine how the reaction time affected the surface area of δ-$MnO_2$ crystals. The water splitting reaction was performed using the porous manganese oxides and gold-occluding manganese oxides as photocatalysts, where the highest catalytic efficiencies were observed using $Mn_2O_3$ crystals. Intriguing results were obtained using the gold-occluding manganese oxides, where the occlusion of gold nanoparticles worsened the catalytic performance of both $Mn_2O_3$ and δ-$MnO_2$. Overall, the results obtained in this chapter demonstrate that manganese oxides with controlled porosity for photocatalytic water

splitting can be prepared using the straightforward synthesis strategies outlined therein. Furthermore, these results may inform future design of noble metal-doped metal oxide photocatalysts, by suggesting that accessible interfacial sites and an optimised density of metal nanoparticles are key for ensuring adequate recycling of electrons during reaction.

### 5.1.2 Introduction to Water Splitting

Sustainable energy is an increasingly important area of research due to the continually growing global energy demand[369]. One of the major areas under development in this effort is the renewable sourcing of hydrogen, which is used in oil refining and for the production of fundamental materials such as iron, steel, ammonia, and methanol[370]. Hydrogen fuel cells hold significant potential as a clean and efficient way of powering electric vehicles and other modes of transport[371]. At present, the majority of all hydrogen produced is from steam-methane reforming (SMR)[372]. This process requires natural gas, high temperatures and pressures, and produces $CO_2$ as a by-product. Renewable synthesis routes for hydrogen production include the electrolysis of water, though this is not cost-competitive compared to SMR and would put significant demand on electricity and water resources[370], and photobiological production, which uses photosynthetic microorganisms to break down water[373]. However, there are challenges in scaling up production using this method, as well as the relatively low yields of hydrogen and lengthier time scales involved[374].

In recent years there has been surmounting research focus on another renewable route to hydrogen production: solar-driven water splitting[375]. In this process, sunlight is used to "split" water into molecular hydrogen and oxygen in the presence of a photocatalyst (Equation 5.1). The positive Gibbs free energy associated with the water splitting reaction indicates that there is a large thermodynamic barrier, as the complex rearrangement of bonds required is less favoured energetically than the reverse reaction.

$$H_2O \rightarrow H_2 + \frac{1}{2}O_2 \qquad \Delta G = +238\ kJ\ mol^{-1} \tag{5.1}$$

Photocatalytic water splitting occurs via a three-step mechanism (Figure 5.1): (i) the semiconductor absorbs light with sufficient energy to excite an electron in the

valence band into the conduction band, which creates a hole in the valence band, (ii) the charge carriers (electrons and holes) must diffuse through the particle to reach active sites on the surface of the photocatalyst, and (iii) the photo-generated holes oxidise water molecules and electrons reduce protons to yield molecular oxygen and hydrogen, respectively (Equation 5.2 and 5.3).

$$2H_2O \rightleftharpoons O_2 + 4H^+ + 4e^- \quad E^\circ = +1.23\,V \tag{5.2}$$

$$4H^+ + 4e^- \rightleftharpoons 2H_2 \quad E^\circ = 0\,V \tag{5.3}$$

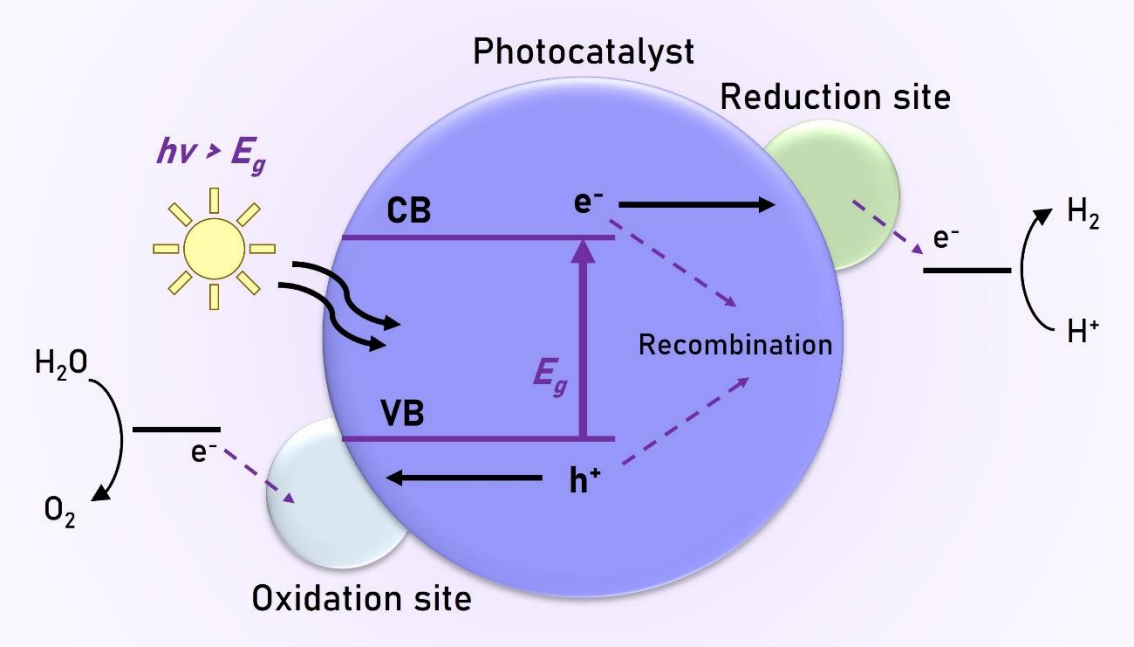


**Figure 5.1 Schematic of the photocatalytic water splitting reaction for a simple particulate photocatalyst. Adapted from ref.[376]**

For each step of the mechanism, various criteria must be met to ensure that the reaction can proceed. In the photoexcitation step, the photon energy must be greater than or equal to the photocatalyst band gap (the difference in energy between the filled lower valence band and the vacant upper conduction band of the semiconductor). As photon energy and wavelength are inversely related, according to the well-known relationship $E = hc/\lambda$ (where $h$ is Planck's constant and $c$ is the speed of light), photons with smaller wavelengths (e.g. UV region) have greater energy. Although numerous photocatalysts have demonstrated excellent water splitting catalysis under UV radiation, this constitutes only 5% of light emitted by the sun[377]. As a larger proportion of sunlight (≈ 40%) is visible light, photocatalysts that can absorb visible light utilise solar energy more efficiently. In order to ensure that

visible light can initiate the reaction, ideally the band gap should not be greater than 3 eV (which corresponds to λ ≈ 400 nm) to have the maximum utilization efficiency of incident solar energy[378].

The band gap is also crucial in ensuring that the reaction between the photocatalyst and water molecules can occur thermodynamically. Both of the redox potentials for the half reactions must be satisfied to allow overall water splitting (Figure 5.2), which means that the band gap cannot be narrower than 1.23 eV. Therefore, the overall band gap should be within the range of 1.23 – 3 eV. Additionally, the energy levels occupied by the valence and conduction bands are crucial in facilitating the redox reactions: the valence band should be more positive than +1.23 V while the conduction band should be more negative than 0 V.

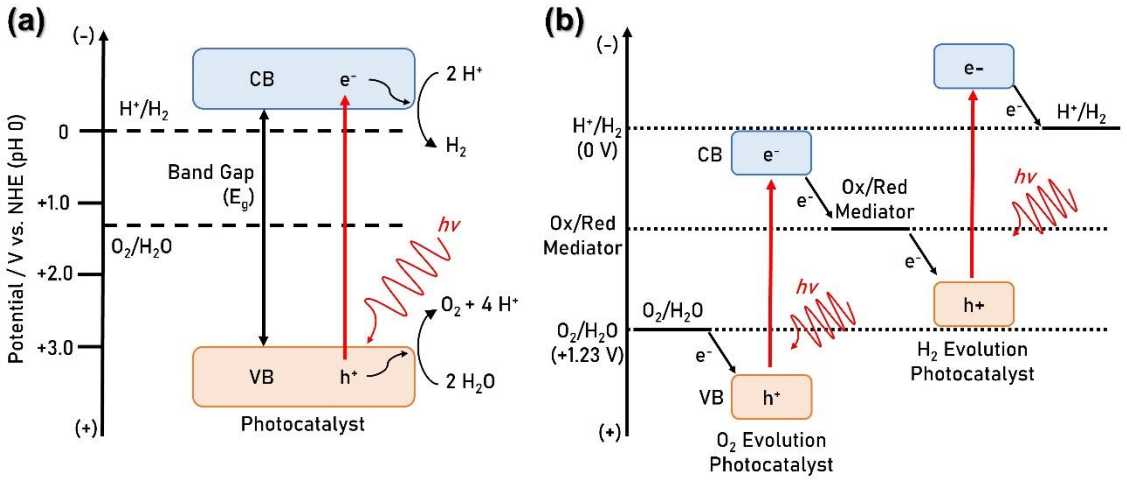


**Figure 5.2 Energy diagrams for (a) one-step excitation photocatalytic water splitting and (b) two-step excitation water splitting. Adapted from ref[379].**

One of the major challenges that arises during the second step of the photocatalytic mechanism is avoiding recombination of the electron-hole pairs. In order for water splitting to occur, the charge carriers must successfully migrate to the catalyst surface. However, the recombination of electron-hole pairs is highly favoured and may be promoted by various properties of the photocatalyst. The most obvious factor involved in this process is the catalyst particle size, where the charge carriers in small particles have shorter distances to the surface[380]. This effect can also be achieved by increasing the surface area or density of the active sites available on the photocatalyst[381]. The crystallinity of the catalyst is also crucial in avoiding the

recombination of electron-hole pairs, as defects within the crystal lattice can provide recombination sites.

Water splitting can be performed using one of two mechanisms: photocatalysis or photoelectrochemical (PEC) catalysis. PEC catalysis requires an electrolyte solution and electrodes, which are typically coated in a thin layer of a semiconductor material or contain immobilised semiconductor particles on the surface[382]. An electron-hole pair is formed following photon irradiation at one of the electrodes, which will then undergo reaction with water molecules. In n-type semiconductors, the overall charge is negative due to the main carrier species being electrons, whereas p-type semiconductors predominantly contain holes and are positively charged. Therefore, depending on whether an n- or p-type semiconductor electrode is used, the reaction of water at the electrode yields either oxygen or hydrogen respectively, followed by production of the other at the counter electrode[383]. This allows better separation of $O_2$ and $H_2$, which is advantageous as it reduces the likelihood of the backward reaction occurring (synthesis of water), which is thermodynamically favoured.

In this work, the photocatalytic route for water splitting was used. In photocatalytic systems, the semiconductor is distributed as a powder throughout an aqueous medium[382]. Electron-hole pairs are generated at the surface of the suspended particles and co-catalysts are often used to boost catalytic efficiency. Photocatalysis is generally fulfilled via a one or two-step excitation process. One-step excitations involve one photocatalyst, whereas two-step excitations utilise two different photocatalysts which each conduct one of the half reactions. Therefore, each catalyst only needs to fulfil the band gap requirements for the half reaction it will perform, allowing a broader range of materials to be employed. Redox shuttles (also known as mediators) are required to enable electrons to be channelled between the photocatalysts[379]. A well-known two-step excitation process is the Z-scheme utilised during photosynthesis[384], which is a natural analogue of photocatalytic water oxidation. Although water oxidation comprises just one half of the water splitting reaction, this generates the supply of protons and electrons required for the reduction reaction and is therefore of interest for overall water splitting. The active photocatalyst in photosynthesis, referred to as photosystem II (PSII), contains proteins and molecules of the pigment chlorophyll arranged around an inorganic cluster of $Mn_4O_5Ca$ known as the oxygen-evolving complex (OEC)[385-387]. This highly

efficient, natural photocatalyst has inspired considerable research into the synthesis of photocatalysts that mimic the complex structure and photoactivity of PSII and OEC[388-390].

Metal oxides have been widely explored as water splitting photocatalysts due to their stability, straightforward synthesis and low cost[391]. In these compounds the conduction band typically consists of *n*s orbitals and the valence band contains O 2p orbitals[392], which have strongly positive energies. This causes metal oxides to have broad band gaps that can reduce their ability to work using visible light. In the first study of photocatalytic water splitting, Honda and Fujishima identified $TiO_2$ as a potential photocatalyst[393]. Since then, there have been numerous studies exploring the use of $TiO_2$ and trying to improve its photoactivity. One of the main issues is that the band gap of $TiO_2$ is too broad for it to harvest visible light, which has been tackled using additional components in the reaction such as dyes and sacrificial agents[394]. Furthermore, recombination of the electron-hole pairs occurs rapidly in $TiO_2$, requiring the addition of electron donors to the system to facilitate separation of electrons and holes.

In this chapter, the photocatalytic efficiency of porous manganese oxide crystals is investigated. Manganese oxides are of particular interest due to the role that manganese plays in PSII. As manganese can exist in various oxidation states (+2, +3, +4), multivalent phases of manganese oxide can be obtained, with many occurring naturally[395]. Manganese oxides can also take a variety of structures, which can be exploited in order to synthesise nanoparticles with high surface areas that can provide a greater density of active sites for catalysis[396]. On the whole, manganese oxide-based catalysts offer a versatile platform of compounds that can be readily modified to boost their catalytic performance. Although manganese oxides typically possess a broad band gap (*ca*. 3.6 – 3.8 eV for MnO; 4.1 – 5.12 eV for $Mn_2O_3$; 2.3 eV for $Mn_3O_4$; 1.3 – 3.26 eV for $MnO_2$)[397], they can still be utilised as photocatalysts under visible light by using a dye-sensitiser, as demonstrated by Harriman *et al.* [398, 399]. Since then, $[Ru(bpy)_3]^{2+}$ has become well-established as a dye-sensitiser for water splitting[398, 400, 401], and is often employed with electron acceptors such as $S_2O_8^{2-}$ or $[Co(NH_3)_5Cl]^{2+}$ to regenerate it from the excited +2* state to +3 [402]. As $[Ru(bpy)_3]^{2+}$ and $[Co(NH_3)_5Cl]^{2+}$ are used in this study and the full

mechanistic details underpinning the reaction are explained in detail later in Section 5.2.1.4.

The high level of interest in manganese oxides for water splitting has led to the devising of criteria for efficient photocatalytic activity. Robinson *et al.* tested a range of manganese oxides and investigated the link between catalytic properties with crystal structure[403]. The catalytic activity was ranked $Mn_2O_3$ > $Mn_3O_4$ >> λ-$MnO_2$, where α-, β-, δ-, R-$MnO_2$ and $LiMn_2O_4$ showed negligible oxygen evolution. The authors deduced that the flexibility of the $Mn^{3+}$–O bonds in edge-sharing octahedra present in both $Mn_2O_3$ and $Mn_3O_4$ led to superior catalytic efficiency. Unlike $Mn^{3+}$–O bonds, which are destabilised due to Jahn-Teller distortion, the $Mn^{4+}$–O bonds in $MnO_2$ are shorter and less flexible. However, in a separate study by Boppana and Jiao, α- and β-$MnO_2$ were found to possess good catalytic properties which were chiefly controlled by surface area rather than morphology or crystal structure[404]. Indeed, variation in the catalytic performance is often found in the literature due to differences in the way the reaction is conducted, particularly with light sources, oxygen measurement systems, and oxidation methods. Pokhrel *et al.* tested nine manganese oxides using three different oxidation methods and found that their catalytic performance varied widely between the different methods[405]. This highlights the need to exert caution when comparing between methods and studies.

Diverse synthetic strategies have been used to prepare manganese oxide photocatalysts. In a study by Menezes *et al.*, MnO, $Mn_2O_3$ and $Mn_3O_4$ were produced via thermal degradation of manganese oxalate[406]. The authors monitored the generation of oxygen over time and found that $Mn_2O_3$ exhibited the highest rate of oxygen evolution. In a similarly facile synthesis strategy, Najafpour *et al.* formed α-$Mn_2O_3$ nanoparticles by heating an aqueous solution of manganese nitrate at 100 °C, which showed efficient water oxidation activity[407].

Mesoporous silica scaffolds have been used to synthesise manganese oxide clusters for water splitting by Frei *et al*. [408]. They deduced that the presence of silica in the cluster structure made it resilient to the surface restructuring that may occur during photocatalysis, allowing the clusters to maintain a high density of active sites throughout the lifetime of the catalyst. It was also hypothesised that separation of the protons was boosted by the presence of proton-permeable silica walls, which reduces the likelihood of the recombination reaction occurring.

Hybrid manganese oxide materials have also attracted interest. Layered $[Ru(bpy)_3]^{2+}$/manganese(III, VI) oxide hybrid structures have been prepared as photocatalysts via the self-assembly of $[Ru(bpy)_3]^{2+}$ particles between manganese oxide nanosheets[409]. In the $[Ru(bpy)_3]^{2+}$ dye sensitizer system, the rate-determining step is the transfer of electrons from the sensitizer to the metal oxide catalysts[410]. By combining both components, the total yield and rate of evolved oxygen was therefore improved[409].

Additionally, metal nitrides and sulfides have been studied as potential photocatalysts. Metal sulfide photocatalysts suffer from photocorrosion, where the liberated holes oxidise $S^{2-}$ ions and the lifetime of the catalyst is diminished[411]. In contrast, metal nitrides still hold potential as efficient photocatalysts. Their band gaps are generally smaller than metal oxides due to the N 2p orbitals being higher in energy than O 2p orbitals[412]. Therefore metal nitrides have found greater success in photocatalysis under visible light,[413] such as GaN:ZnO[414] and $Ta_3N_5$[415].

Noble metals have been used as co-catalysts due to their activity in the reduction reaction to form $H_2$ to ensure overall water splitting is achieved[416]. One of the most notable studies employing noble metals as co-catalysts is that by Maeda *et al.*, who synthesised core-shell particles consisting of $Rh/Cr_2O_3$ deposited on a GaN:ZnO support[417]. Although Rh nanoparticles alone suffered from water re-forming at their surface, coating the nanoparticles with a $Cr_2O_3$ shell led to an increase in the evolved $H_2$. This demonstrated the need to avoid the backward reaction when noble metals are used, in order to optimise their catalytic efficiency for water splitting. Additionally, metallic nanoparticles such as Au, Ag, and Pd have been trialled as co-catalysts, where they can act as electron traps and aid separation of the photo-generated charge carriers[412, 418]. Such metal nanoparticles can exhibit surface plasmon resonance (SPR), which occurs when electrons in the conduction band of a metal oscillate under electromagnetic radiation. SPR can boost catalysis in several ways (Figure 5.3): via direct electron transfer (DET)[*419*], local electromagnetic field enhancement (LEMF)[420] and resonant energy transfer (RET)[421]. This has led to the use of Au and Ag as co-catalysts in $TiO_2$ photocatalytic systems to improve its water splitting activity under visible light[416, 422, 423].

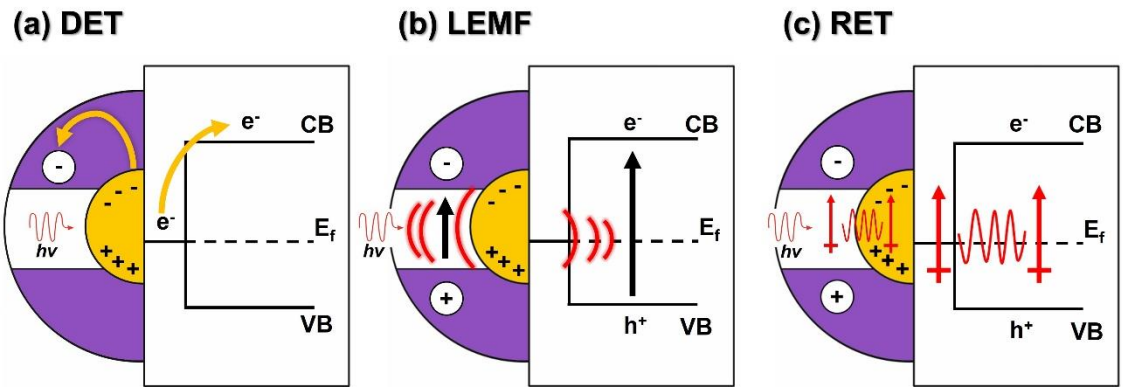


**Figure 5.3 Charge separation mechanisms for metal nanoparticle-semiconductors, (a) direct electron transfer (DET) from the metal to the semiconductor, (b) local electromagnetic field enhancement (LEMF), and (c) resonant energy transfer (RET) from the metal SPR dipole to the semiconductor charge carriers. Adapted from ref.[421]**

A number of studies have found that Au nanoparticle co-catalysts enhance the catalytic performance of manganese oxides[424-426]. This has generally been achieved by surface deposition of Au nanoparticles onto $MnO_x$ films. Seitz *et al.* trialled different layered structures in Au-$MnO_x$ films and found that there was no improvement in catalytic properties for the PEC reaction if the Au layer was fully covered by MnO. This suggests that accessible interfacial sites between Au-$MnO_x$ are imperative for improving catalytic performance[426]. A detailed study by Kuo *et al*. sought to identify the exact role of Au nanoparticles in water splitting by manganese oxides. Au was deposited on the surface of α-, δ-$MnO_2$ and $Mn_2O_3$ crystals[424]. Both α- and δ-$MnO_2$ doped with 1 – 6 wt.% Au showed enhanced water splitting activities via both photocatalytic and PEC reactions. However, Au-doped $Mn_2O_3$ showed no improvement in catalytic efficiency as compared to pure $Mn_2O_3$.

As control experiments showed that Au nanoparticles alone or mixed with $MnO_2$ were not active in water splitting, the authors established that a change in surface properties was chiefly responsible for boosting the catalytic activity of Au-doped $MnO_2$. Using X-ray photoelectron spectroscopy (XPS), they found that the oxidation state of Mn in Au-doped $MnO_2$ was reduced from 3.91 to 3.84 compared to pure $MnO_2$. Additionally, UV-Vis analysis of Au-doped $MnO_2$ in an aqueous solution of $Na_2S_2O_8$ (the electron acceptor co-catalyst) showed that the 3+ oxidation state evolved over time. Overall, it was deduced that the Au nanoparticles improved

electron transfer and promoted the formation of the $Mn^{3+}$, which is most active for water splitting.

### 5.1.3 Introduction to Manganese Carbonate

Manganese carbonate (rhodocrosite), possesses a rhombohedral morphology and belongs to the calcite mineral group (Figure 5.4)[427]. It is readily precipitated by direct mixing of aqueous solutions of manganese chloride or sulfate with sodium bicarbonate or carbonate. There is only one crystal polymorph. There is also some evidence of an amorphous manganese carbonate phase (AMnC), though current research into AMnC is limited[428-430].

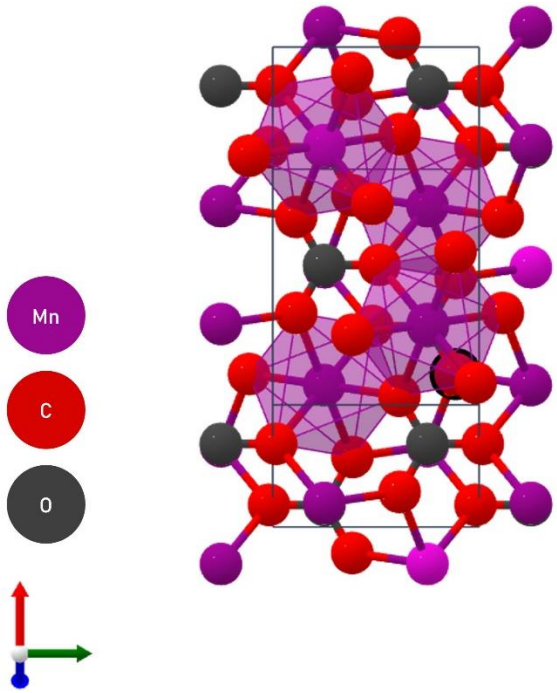


**Figure 5.4 The unit cell of manganese carbonate. Adapted from ref.[299]**

The growing list of applications for $MnCO_3$ include drug delivery[431-433], biosensing[434, 435], supercapacitors[436, 437] and lithium energy storage[438-440]. However, manganese carbonate is also a useful precursor to multivalent manganese oxides[441, 442], which can be readily formed following the thermal decomposition of $MnCO_3$ crystals. The thermal behaviour of manganese carbonate has been well-characterised, with a number of reaction steps being identified when heating under air[443, 444]. Manganese carbonate initially forms $MnO_2$ during heating, around 300 – 400 °C. A large step is seen in the TGA as $CO_2$ is released (Figure 5.16). However, $MnO_2$ is quickly reduced by $O_2$ in air to form $Mn_2O_3$ (Equation 5.4). This is stable but will undergo

further reduction with atmospheric $O_2$ if heated above 850 °C, forming $Mn_3O_4$ (Equation 5.5).

$$2MnCO_{3(s)} + \frac{1}{2}O_{2(g)} \xrightarrow{\Delta} Mn_2O_{3(s)} + 2CO_{2(g)} \quad (5.4)$$

$$3Mn_2O_{3(s)} \xrightarrow{\Delta} 2Mn_3O_{4(s)} + \frac{1}{2}O_{2(g)} \quad (5.5)$$

In a study by Lian *et al.*, $MnCO_3$ was precipitated in the presence of urea and ethanol via a solvothermal method, and the crystals were annealed at temperatures 380 – 575 °C to yield porous manganese oxides. However, the work in this chapter will demonstrate that such templating and co-precipitation methods are unnecessary for the formation of porous manganese oxides via thermal degradation, due to the natural evolution of porosity as $CO_2$ is expelled and the molar volume mismatch between the carbonate and oxide.

## 5.2 Experimental

### 5.2.1 Synthesis and Preparation of Materials

#### 5.2.1.1 Manganese carbonate synthesis

Manganese carbonate was precipitated using two methods: a direct mixing strategy and a diffusion method. For the direct mixing strategy, aqueous solutions of $MnCl_2$ and $NaHCO_3$ were prepared and mixed in 2 L Teflon beakers and left to crystallise for 48 hours. A range of [$MnCl_2$] and [$NaHCO_3$] were explored as shown in Table 5.1. Crystals were collected via vacuum filtration using a 0.45 µm Millipore filter, rinsed with EtOH and finally dried in a drying oven at 60 °C.

| $MnCl_2$ / mM | $NaHCO_3$ / mM |
|---|---|
| 0.25 | 5 |
| 0.5 | 20 |
| 1 | 50 |
| 2 | 100 |
| 5 | 200 |

**Table 5.1 The final concentrations of $MnCl_2$ and $NaHCO_3$ used to prepare manganese carbonate via the direct mixing strategy.**

For the diffusion method, aqueous solutions of $MnCl_2$ were added to a well-plate containing several pieces of glass slide, using [$MnCl_2$] = 0.25, 0.5, 1, 2 and 5 mM. The well-plate was placed in a desiccator accompanied by a petri dish containing ≈ 3 g of $(NH_4)_2CO_3$ powder which was sealed using Parafilm and pierced several times with a needle. The solution was left to crystallise for 48 hours before the substrates were removed and rinsed with DI water and EtOH and allowed to dry in a 60 °C drying oven.

$MnCO_3$ crystals occluded with gold nanoparticles (4 nm) with 40 wt.% loading were synthesised and supplied by Dr Ouassef Nahi. The gold nanoparticles were coated with polyethyleneimine (PEI) to ensure occlusion with $MnCO_3$ crystals[207]. Au-$MnCO_3$ was precipitated using a modification of the diffusion method, where PEI-functionalised gold nanoparticles (0.2 wt.%) were added to the crystallising solution containing [$MnCl_2$] = 2 mM and [$NaHCO_3$] = 100 mM.

#### 5.2.1.2 Thermal Decomposition of Manganese Oxides

Manganese oxides were prepared by heating manganese carbonate crystals in a muffle furnace, contained within a ceramic crucible, following the reaction shown in Equation 5.6.

$$xMnCO_{3(s)} \xrightarrow{\Delta} Mn_xO_{y(s)} + CO_{2(g)} \quad (5.6)$$

A range of heating rates, temperatures and lengths of time were explored to examine their effect on the manganese oxide synthesis (Figure 5.5), as shown in Table 5.2. It should be noted that the annealing time stated here is the time spent at the target temperature and is not inclusive of the time taken to reach it.

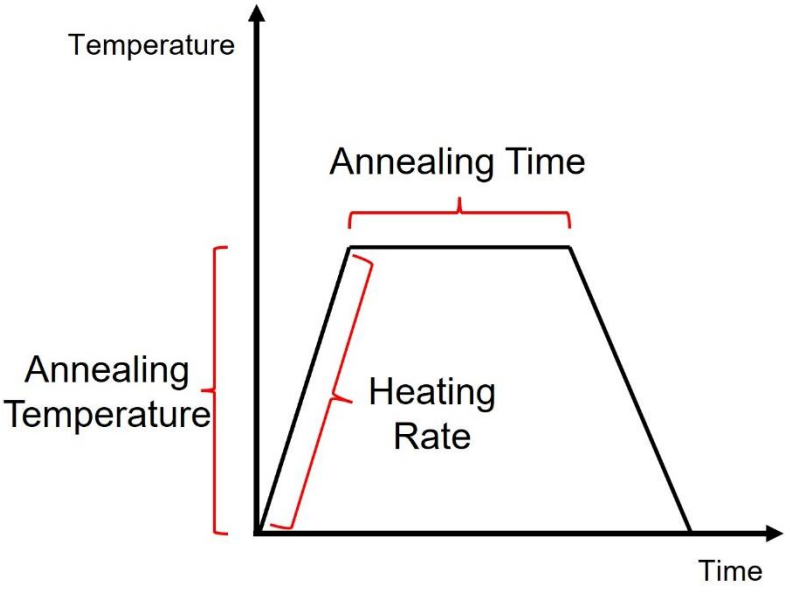


**Figure 5.5 The heating parameters investigated to prepare manganese oxides.**

| **Temperature / °C** | **Time Period** | **Heating Rate / °C min$^{-1}$** |
|---|---|---|
| **450** | 30 min | 5 |
| **500** | 30 min | 5 |
| **550** | 30 min | 5 |
| **600** | 30 min | 5 |
| 450 | **3 h** | 5 |
| 500 | **3 h** | 5 |
| 550 | **3 h** | 5 |
| 600 | **3 h** | 5 |
| 550 | 30 min | **1** |
| 550 | 30 min | **10** |

**Table 5.2 Heating parameters varied to explore their effect on porosity formed during the thermal decomposition of manganese carbonate into manganese oxide.**

#### 5.2.1.3 Hydrothermal Synthesis of Manganese Oxides

$Mn_2O_3$ crystals that were prepared by heating precipitated $MnCO_3$ at 450 °C for 30 minutes at 5 °C min$^{-1}$, were added to 10 M NaOH and sealed within a hydrothermal Teflon beaker[445]. The sealed apparatus was heated at 170 °C for 1, 2, 3 or 6 days

and left to cool. The basic solution was acidified using dilute HCl and neutralised by repeatedly diluting with DI water, centrifuging to separate the supernatant, removing it and replacing with further water, until pH 7 was reached. The resulting suspension was filtered using a Millipore filtration system and 0.45 µm filter paper before finally drying the product in a drying oven at 60 °C.

#### 5.2.1.4 Co-catalyst System

In this work, $[Ru(bpy)_3]Cl_2.6H_2O$ and $[Co(NH_3)_5Cl]Cl_2$ were used as co-catalysts to achieve two-step water splitting (Figure 5.6). These were chosen as together they are a well-used co-catalyst system which does not suffer from photo-corrosion[446].

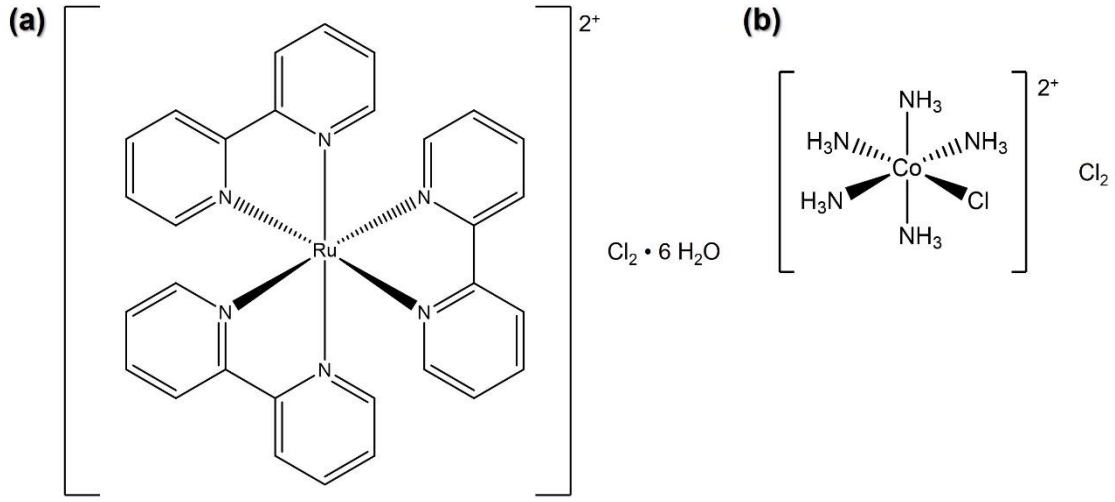


**Figure 5.6 The skeletal formula of (a) $[Ru(bpy)_3]Cl_2.6H_2O$ and (b) $[Co(NH_3)_5Cl]Cl_2$ co-catalysts.**

$[Ru(bpy)_3]^{2+}$ acts as a light sensitiser and initiates the reaction by accepting a proton from the light source (Figure 5.7). $[Ru(bpy)_3]^{2+}$ absorbs light in the blue region with a $\lambda_{max}$ of 454 nm, and therefore allows the catalysis reaction to occur under visible light, rather than UV as is common for most photocatalysts[447].

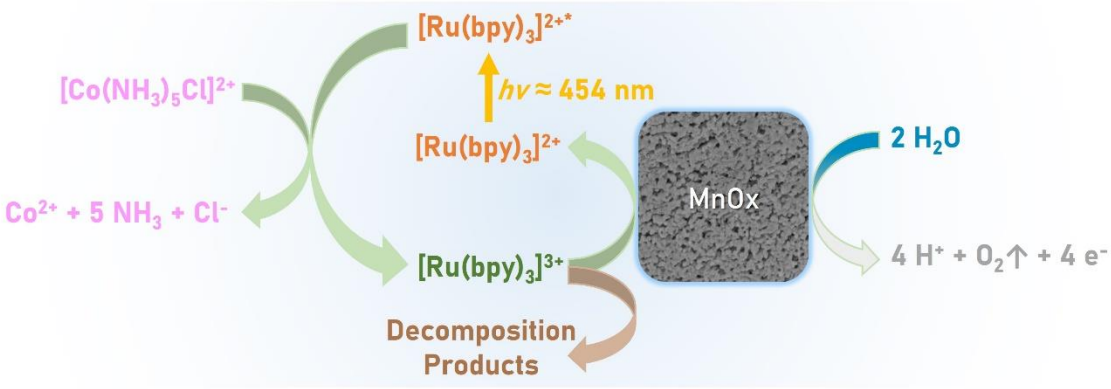


**Figure 5.7 The reaction scheme for photocatalytic water oxidation using manganese oxide and $[Ru(bpy)_3]^{2+}$ and $[Co(NH_3)_5Cl]^{2+}$ co-catalysts. Adapted from ref.[448]**

After absorbing a photon, metal-ligand charge transfer (MLCT) occurs in $[Ru(bpy)_3]^{2+}$, as an electron is transferred from a metal $t_{2g}$ orbital to a ligand π*orbital. This exists in a short-lived singlet state before intersystem crossing (ISC) occurs to yield the triplet excited state, $[Ru(bpy)_3]^{2+}$*. This state is quenched by the sacrificial electron acceptor, $[Co(NH_3)_5Cl]^{2+}$, to form $[Ru(bpy)_3]^{3+}$ which is dark green. This step therefore results in an observable colour change in the reaction mixture from a bright orange-pink to a dark brown colour. The experimental catalyst, which in this project is a manganese oxide, then donates an electron to the Ru-complex to regenerate $[Ru(bpy)_3]^{2+}$. The loss of an electron causes the oxidation of surface-bound water molecules on the experimental manganese oxide catalyst. This reaction is outlined in Equation 5.7. A molecule of gaseous oxygen and 4 protons are released into the buffer solution, and the 4 liberated electrons are taken up by the electron acceptor, $[Co(NH_3)_5Cl]^{2+}$.

$$2H_2O + 4hv \rightarrow O_2 + 4H^+ + 4e^- \qquad (5.7)$$

The reaction is expected to eventually slow and terminate after 30 minutes of light exposure. One reason for this is the decomposition of the electron acceptor, $[Co(NH_3)_5Cl]^{2+}$, which undergoes the reaction shown in Equation 5.8.

$$[Co(NH_3)_5Cl]^{2+} + [Ru(bpy)_3]^{2+*} \rightarrow [Ru(bpy)_3]^{3+} + Co^{2+} + 5NH_3 + Cl^- \qquad (5.8)$$

Another degradation effect is seen in the breakdown of the organic bipyridine ligands as a result of the prolonged oxidative conditions. The ligands become detached from the ruthenium metal centre and will then form deposits on the glass flask. These

have been shown to contain both bipyridine and hydroxylated-$Ru(bpy)_2^{2+}$ material[449]. The decomposition of the bipyridine rings can also lead to the evolution of $CO_2$ gas, which can affect the measurement of the total oxygen concentration within the sealed reaction flask[450].

The degradation of $[Co(NH_3)_5Cl]^{2+}$ further exacerbates the decomposition of $[Ru(bpy)_3]^{2+}$ by creating a basic environment as ammonia is released. In order to minimise this effect, an acetate buffer with mildly acidic pH (4 – 5.2) is typically employed as the reaction medium for this co-catalyst system[451].

#### 5.2.1.5 Catalytic Testing Setup

The main reaction apparatus was housed inside a dark chamber to prevent exposure to external light sources. A 25 ml dual-necked round bottomed flask with magnetic stirrer was held using a clamp stand above a stirrer plate and positioned 10 cm away from an LED lamp. The range of emitted light from the lamp was 430 – 500 nm, where $\lambda_{max}$ = 462 nm, as shown in Figure 5.8.

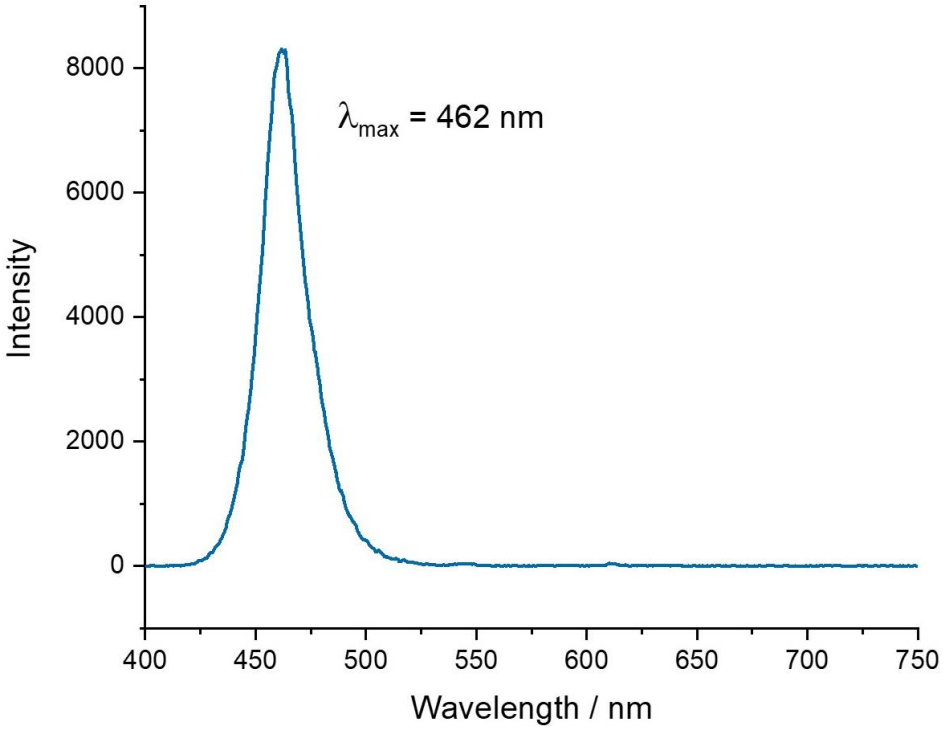


**Figure 5.8 The range of light emitted by the lamp used to initiate the water splitting reaction.**

One neck of the flask hosted the oxygen sensor and accompanying temperature probe, which were securely held in place using a rubber bung. The other neck was

used to load the reagents before finally sealing with a rubber bung. Each test run was set up using the following protocol, adapted from a method outlined by Walsh *et al.*[452, 453].

An aqueous buffer solution of 50 mM sodium acetate (NaAc) was freshly prepared using sodium acetate trihydrate obtained from Merck. Prior to testing, 50 ml NaAc buffer was degassed by continuously flushing with nitrogen gas for a minimum of one hour. The reaction flask was wrapped in aluminium foil, fitted with a magnetic stirrer bar and a bung containing both the oxygen and temperature probes was inserted into the top neck. The Pyroscience oxygen sensor software began logging as soon as the sensor was in place. The co-catalysts were weighed and kept in sealed vials (where the vial containing the light-sensitive $[Ru(bpy)_3]^{2+}$ was covered in aluminium foil to reduce light exposure). Multiple successive aliquots of NaAc buffer solution were used to fully disperse the powders and introduce them into the reaction flask. Three aliquots of 4, 4 and 2 ml each were used to add the $[Co(NH_3)_5Cl]Cl_2$, followed by four aliquots of 4, 4, 4 and 3 ml for the Ru co-catalyst. The second neck of the flask was then sealed using a rubber bung and the co-catalysts were left under stirring for 20 minutes before the addition of the experimental catalyst. 20 mg of the experimental catalyst was dispersed in three aliquots of 5, 3 and 2 ml of buffer solution, which was added to the flask via a syringe. An additional needle was temporarily added to the bung to equalise the pressure as the additions were made. The mixture was left stirring for 10 mins before the reaction was initiated by turning on the lamp. This timepoint was recorded as the T0 point for data processing. The reaction was continuously monitored for at least 1 hour before ceasing data collection, which was long enough to ensure termination of the reaction had occurred.

In addition to the total number of moles of $O_2$ evolved during the reaction, the turnover frequency (TOF) and quantum yield (Φ) were calculated. The turnover frequency was calculated using the fastest rate sustained for 20 s (to remove any noise), and is defined as the moles of $O_2$ produced per second per moles of active metal (in this study, Mn) (Equation 5.9).

$$TOF\ (s^{-1}) = \frac{fastest\ rate\ of\ O_2\ production\ \left(\frac{\mu mol}{s}\right)}{moles\ of\ active\ catalyst\ (\mu mol)} \qquad (5.9)$$

The Φ value was calculated by firstly obtaining the total number of $O_2$ molecules produced, by multiplying the $O_2$ yield in moles at t = 25 min by Avogadro's constant. The energy of a photon emitted with λ = 462 nm was calculated using the relationship $E = hc/\lambda$ (where $E$ is photon energy, $h$ is Planck's constant, c is the speed of light and $\lambda$ is wavelength). The total power absorbed by the system by t = 25 min was calculated by multiplying the light intensity by the incident surface area (1.3 mW/cm$^2$ x 30 cm$^2$ = 39 mW), and then multiplying this by the total time in s (Equation 5.10).

$$\phi\,(\%) = number\ of\ O_2\ molecules\ produced\ \cdot \left(\frac{power\ absorbed\ (J)}{photon\ energy\ (J)}\right) \cdot 400\% \qquad (5.10)$$

## 5.2.2 Analytical Techniques

### 5.2.2.1 Surface Area BET Analysis

BET analysis, named after the scientists Brunauer, Emmett and Teller who developed the method[454], is an important technique for determining the surface area of a solid[455]. A sample of known mass is loaded onto the manifold and degassed to remove any adsorbed contaminants. A known volume of an inert gas, typically nitrogen or argon, is pumped into the sample cell and the quantity of un-adsorbed material is determined using pressure sensors to yield a physisorption isotherm[456]. The amount of adsorbed material, or BET monolayer capacity, is then derived from this plot using the BET equation (Equation 5.11), where $V$ is volume of absorbed material, $V_m$ is the volume of gas adsorbed when the surface is covered by a monolayer, $C$ is the BET constant linking the heat of adsorption of two layers on a surface, $P/P_0$ is the pressure over saturated vapour pressure. The fundamental principles of BET are underpinned by Langmuir's theory of gas adsorption while taking into consideration multilayer adsorption[457], and assumes that: (i) the adsorption sites have equivalent adsorption energy, (ii) adsorbed molecules do not interact with each other or other layers, (iii) once adsorbed the molecule is immobile until detachment.

$$\frac{\frac{P}{P_0}}{V\left(1-\frac{P}{P_0}\right)} = \frac{1}{V_m C} + \frac{C-1}{C} \cdot \frac{\frac{P}{P_0}}{V_m} \qquad (5.11)$$

BET analysis of porous manganese oxide samples was conducted to determine their BET surface area. A Micrometrics ASAP 2020 Plus was used to take all BET measurements, using nitrogen as an adsorbate.

#### 5.2.2.2 Oxygen Optical Sensor

The progress of the water oxidation reaction was followed using an oxygen optical sensor. This allowed the catalytic efficiencies of the prepared manganese oxides to be evaluated. The sensor apparatus consisted of:

- Pyroscience FireSting® $O_2$ 1 channel fibre-optic oxygen meter, with integrated pressure and humidity sensors and logging software
- Pyroscience robust oxygen probe
- Pyroscience temperature probe for FireSting

Both the oxygen and temperature probe were suitable for in-situ measurements. The oxygen meter contains an LED which emits the red excitation light with wavelengths of 610 – 630 nm[458]. It is emitted in a known, sinusoidal fashion. The sensor indicator material, which is contained within a polymeric matrix on the optical fibres within the probe, becomes excited and causes it to luminesce. The luminescence, or emission light, occurs in the near infrared region (NIR) with wavelengths of 760-790 nm, and so will be phase-shifted relative to the excitation light. The collision of the sensor material with surrounding oxygen molecules results in quenching of the luminescence. Therefore, the resultant luminescence is dependent on the partial pressure of oxygen. The photodiode within the oxygen meter will detect the luminescence emission and the amount of oxygen present can therefore be calculated using calibration data taken in 0 and 100 % oxygen saturated environments.

#### 5.2.2.3 FIB-SEM

Cross-sections of the manganese carbonate and oxide compounds were prepared, imaged and analysed using a FIB-SEM and image analysis workflow as described in Chapter 3.

## 5.3 Results

### 5.3.1 Manganese Carbonate Crystallisation

Manganese carbonate crystals were precipitated via diffusion and direct mixing strategies using a range of concentrations in order to identify optimum reaction conditions.

#### 5.3.1.1 $MnCO_3$ Crystallisation via Ammonia Diffusion Method

The ammonia diffusion method, which was used extensively in Chapter 3 to prepare calcium carbonate, was also trialled as a way of making manganese carbonate using [$MnCl_2$] = 0.25, 0.5, 1, 2 and 5 mM. After 48 hours a yellow substance had formed on the substrate. The product was observed using OM which showed crystalline material and small clusters of yellow particles (Figure 5.9). These were thought to be unstable manganese ammonia complexes formed by complexation of ammonia with $Mn^{2+}$ ions[459]. Therefore, this was not a viable method for preparing $MnCO_3$ crystals.

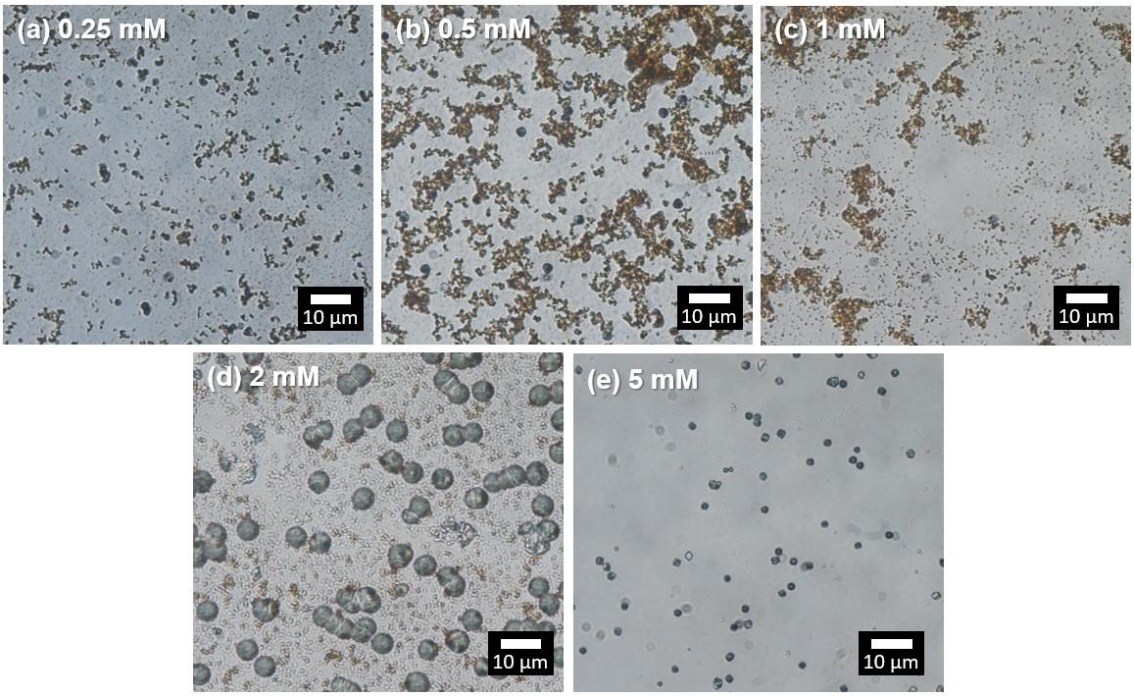


**Figure 5.9 OM images of products obtained via the ammonia diffusion method using various $MnCl_2$ concentrations.**

#### 5.3.1.2 Manganese Carbonate Crystallisation via Direct Mixing Method

The crystals obtained using the direct mixing method were light pink in appearance, as observed using OM (Figure 5.10 - Figure 5.14). The crystals were typically rhombohedral in morphology with some spherical polycrystals present. An overview of the crystallisation outcomes observed is summarised in Table 5.3.

The lowest [$CO_3^{2-}$] trialled (5 mM) only yielded crystals within 48 hours when the highest [$Mn^{2+}$] was used (also 5 mM). Similarly, precipitation within 48 hours was only seen using the lowest concentration of [$Mn^{2+}$] (0.25 mM) when the [$CO_3^{2-}$] was 50 mM or higher. All other conditions trialled resulted in crystallisation and yielded crystals of increasing size when increasing either the [$CO_3^{2-}$] or [$Mn^{2+}$]. Intergrown crystals and polycrystalline aggregates were observed when the highest concentrations of [$Mn^{2+}$] and [$CO_3^{2-}$] were used due to the high levels of nucleation.

| **[$MnCl_2$] mM**<br>**[$NaHCO_3$] mM** | **0.25** | **0.5** | **1** | **2** | **5** |
|---|---|---|---|---|---|
| **5** | X | X | X | X | O |
| **20** | X | O | O | O | O |
| **50** | O | O | O | I/P | I/P |
| **100** | O | O | O | I/P | I/P |
| **200** | O | O | P | P | P |

**Table 5.3 Summary of the crystallisation outcomes for varying final [Mn] and [$CO_3$], where X = no precipitation, O = precipitation occurred, I = intergrown crystals and P = polycrystals present.**

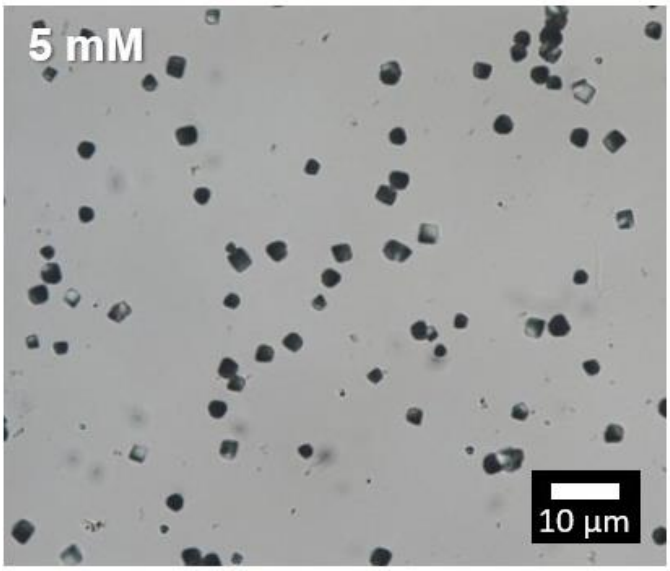


**Figure 5.10 OM image of crystals prepared using [$NaHCO_3$] = 5 mM, [$MnCl_2$] = 5 mM. All other [$MnCl_2$] conditions did not yield crystals.**

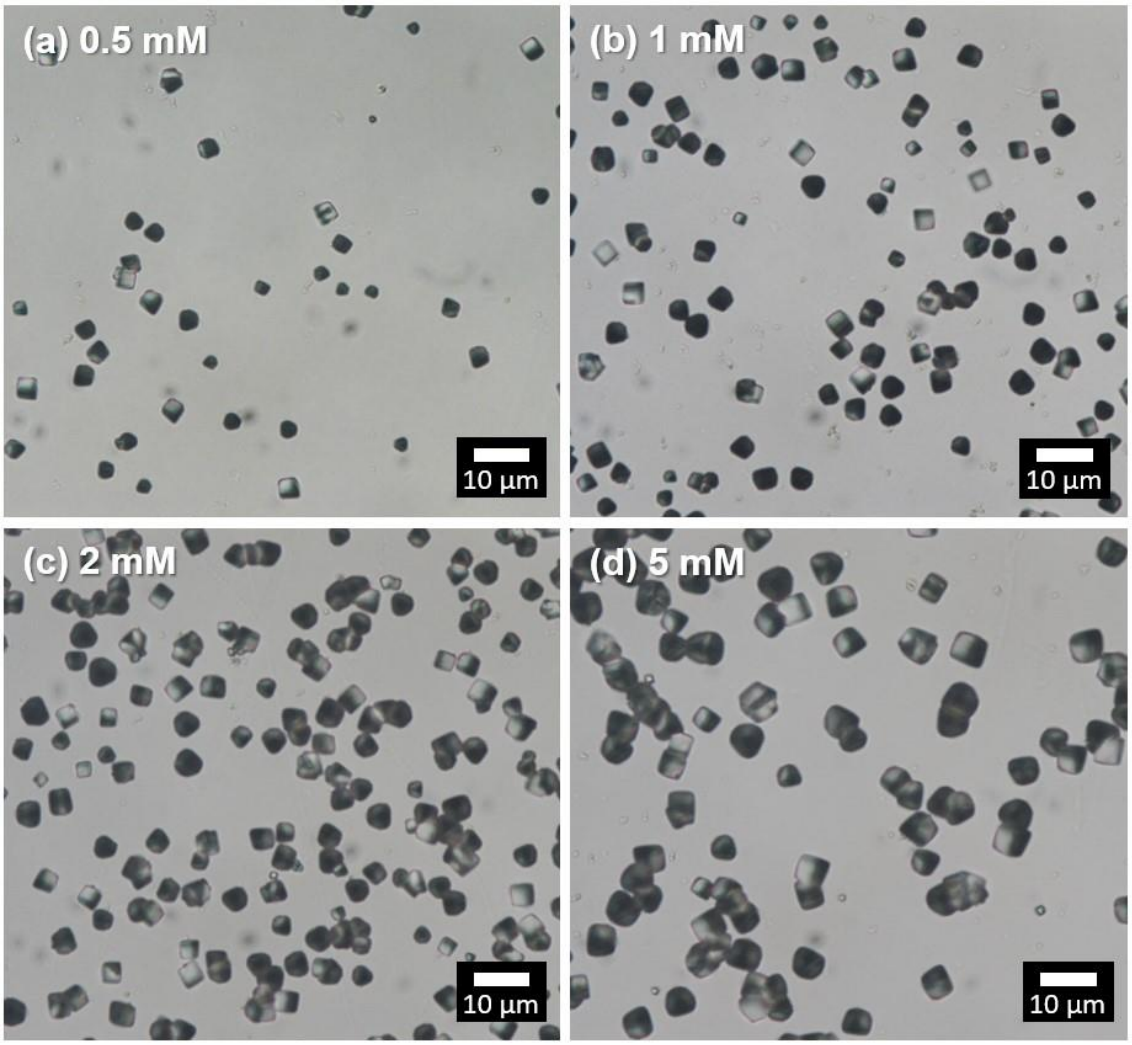


**Figure 5.11 OM images of crystals prepared using [$NaHCO_3$] = 20 mM and varying [$MnCl_2$].**

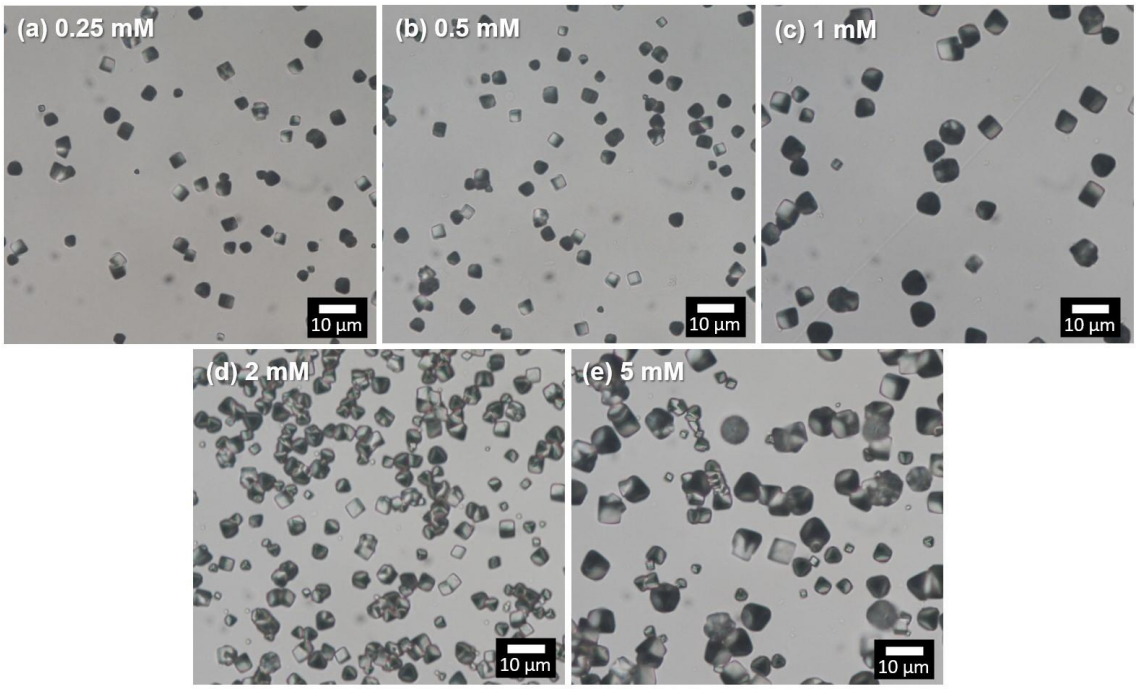


**Figure 5.12 OM images of crystals prepared using [$NaHCO_3$] = 50 mM and varying [$MnCl_2$].**

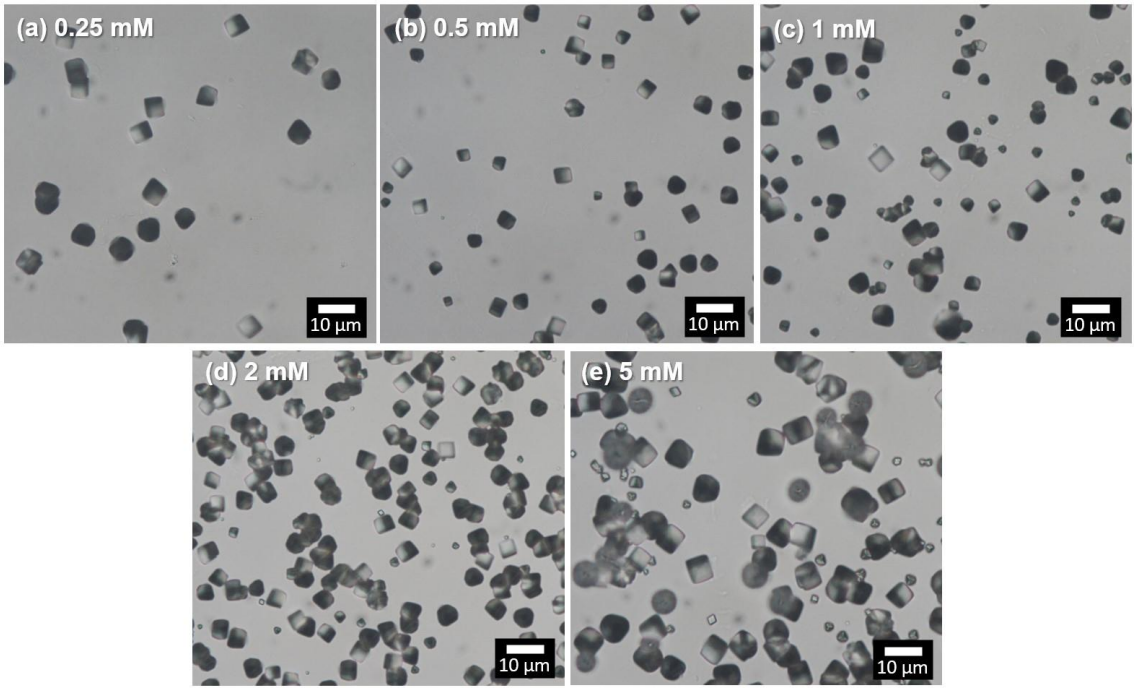


**Figure 5.13 OM images of crystals prepared using [$NaHCO_3$] = 100 mM and varying [$MnCl_2$].**

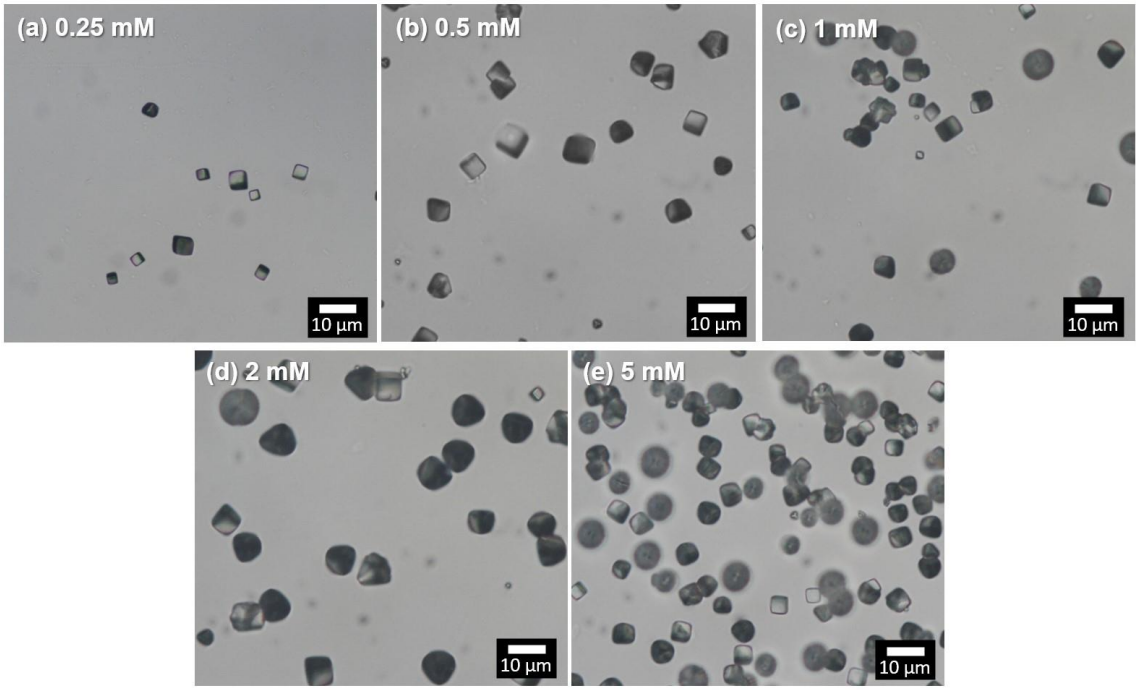


**Figure 5.14 OM images of crystals prepared using [$NaHCO_3$] = 200 mM and varying [$MnCl_2$].**

Several criteria were considered when choosing a reaction condition to prepare $MnCO_3$ and then transform it to manganese oxide: narrow particle size distribution, sufficient yield of crystals, and that the crystals obtained are single crystals rather than polycrystalline or intergrown. Based on these criteria, the condition chosen was [$CO_3^{2-}$] = 100 mM and [$Mn^{2+}$] = 0.5 mM.

### 5.3.1.3 Raman Spectroscopy of $MnCO_3$

Raman spectroscopy confirmed that manganese carbonate was obtained (Figure 5.15), where the active Raman modes observed were assigned in Table 5.4.

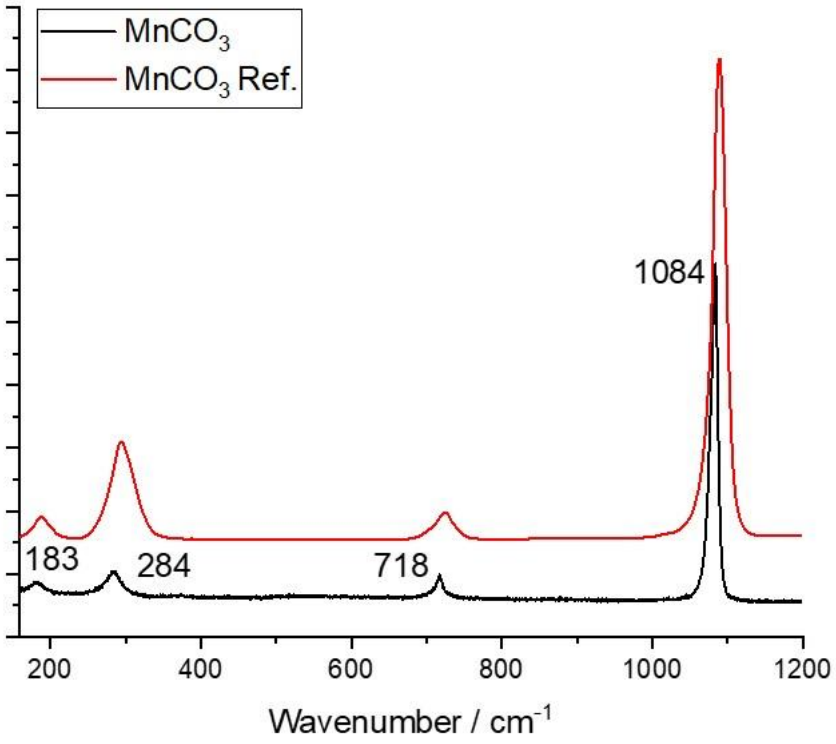


**Figure 5.15 Raman spectrum for $MnCO_3$ crystals, compared with a reference spectrum for rhodocrosite obtained from RRUFF[270] (RRUFF ID: 050019).**

| Peak Position / $cm^{-1}$ | Raman Modes | Assignment |
|---|---|---|
| 183-184 | $E_g(T)$ | Translational lattice mode from $CO_3$ external vibration |
| 287-290 | $E_g(L)$ | Vibrational lattice mode from $CO_3$ external vibration |
| 716-718 | $E_g(v_4)$ | Out-of-plane bending $CO_3$ internal vibration |
| 1083-1085 | $A_{1g}(v_1)$ | Stretching $CO_3$ internal vibration |

**Table 5.4 Assignment of the active Raman modes for $MnCO_3$ within the 100-1200 $cm^{-1}$ range, using reference data[460].**

## 5.3.2 Thermal Decomposition of Manganese Carbonate

The thermal decomposition of manganese carbonate was studied as a route to forming manganese oxides.

### 5.3.2.1 Thermogravimetric Analysis of Manganese Carbonate

Thermogravimetric analysis (TGA) of $MnCO_3$ was conducted to determine the temperature at which thermal decomposition occurred under aerobic conditions. The

TGA profile showed three main transitions during heating from room temperature to 1000 °C at 5 °C $min^{-1}$ (Figure 5.16). The first loss of mass occurred below 200 °C and can be attributed to the loss of residual water from the sample. The largest weight loss was observed at 400 °C and corresponded to 30 % of the initial sample weight. This decomposition step showed a steeper rate of sample weight loss when the sample was heated under nitrogen, and the transition was completed between 400 – 450 °C. When heated under air, the rate at which the transition occurred was slower, and full conversion was not achieved until 500 °C. This is due to the formation of oxidised manganese (most likely $Mn_2O_3$) on the surface of the crystals which blocks the diffusion of $CO_2$ [461]. Additionally, there appeared to be a minor transition (1 – 2 %) in air at 600 – 625 °C, which was not seen under nitrogen. A final transition step was observed at 925 – 950 °C in both atmospheres which corresponded to a 2-3 % loss in sample weight.

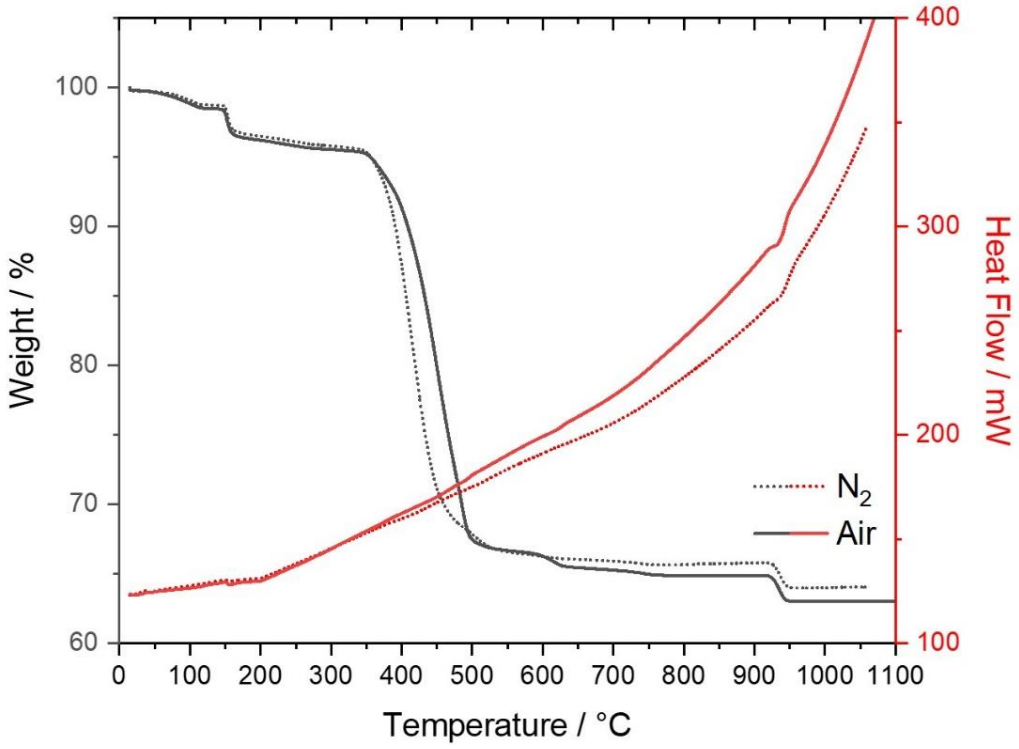


**Figure 5.16 Thermogravimetric analysis of $MnCO_3$, using a heating rate of 5 °C $min^{-1}$, conducted under $N_2$ and air.**

### 5.3.2.2 Characterisation of Manganese Oxides using Powder X-Ray Diffraction

Manganese carbonate samples were heated to the transition temperatures identified in TGA and powder x-ray diffraction (pXRD) was used to characterise the resulting compounds. Temperatures of 500, 700, 850 and 1000 °C were used and the pXRD patterns were compared against reference data to ascertain the oxidation states of the manganese, as shown in Figure 5.17.

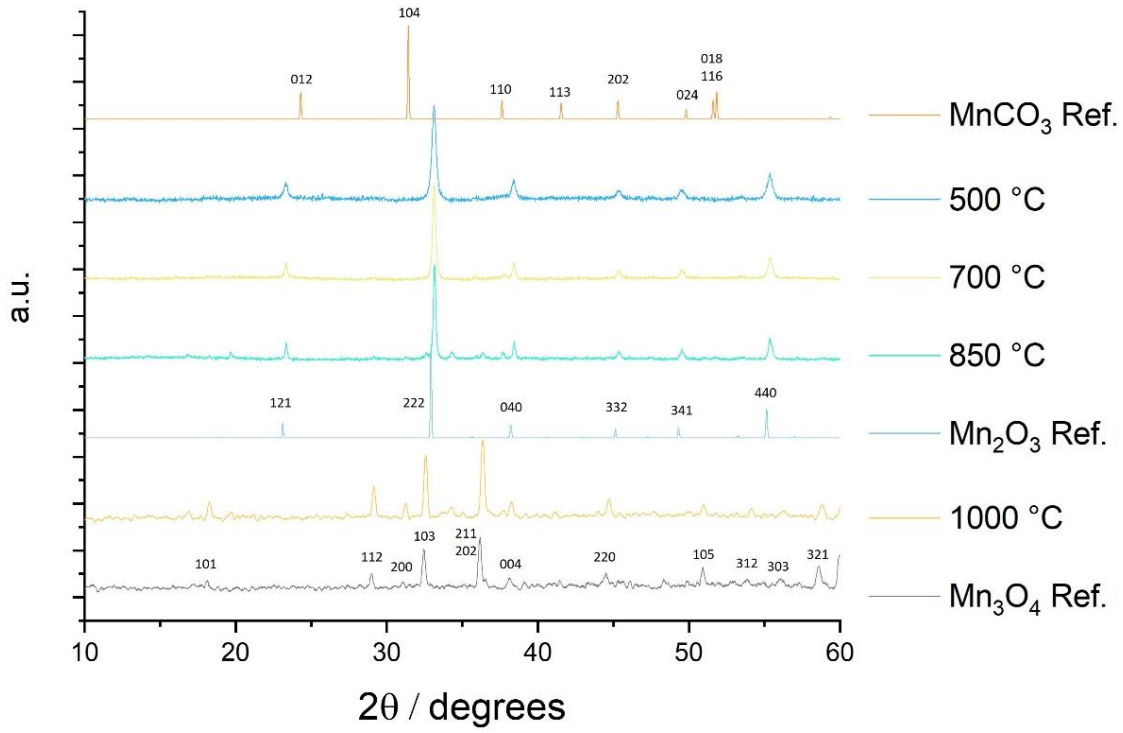


**Figure 5.17 Powder XRD patterns of manganese oxides prepared using the heating conditions corresponding to key transitions observed using TGA, using references obtained from AMCSD[462] (AMCSD ID: $MnCO_3$ 0000100, $Mn_2O_3$ 0009390, $Mn_3O_4$ 0002024).**

The patterns obtained from samples prepared at 500 °C and 700 °C both corresponded to $Mn_2O_3$. Although the TGA profile in air showed that a transition occurred between 500 and 700 °C, the similarity of the pXRD spectra indicated that the product formed at 500 °C was unstable and converted to $Mn_2O_3$ in air during or after cooling. This suggests that α-$MnO_2$ was produced during the transition at 500 – 700 °C[443, 444]. The sample prepared at 850 °C had peaks which belong to $Mn_2O_3$, as well as some additional minor peaks that can be attributed to $Mn_3O_4$. This shows that a small proportion of the $Mn_2O_3$ had begun to be oxidised into $Mn_3O_4$. Further heating to 1000 °C resulted in full transformation to $Mn_3O_4$, and no residual $Mn_2O_3$ peaks were present.

Overall, the pXRD spectra confirmed that the transitions observed using TGA corresponded to the following transformations: (i) the decomposition of $MnCO_3$ and release of $CO_2$, forming α-$MnO_2$, (ii) the conversion of $MnO_2$ into stable $Mn_2O_3$, and (iii) oxidation of $Mn_2O_3$ into $Mn_3O_4$.

#### 5.3.2.3 SEM Images of Manganese Oxides

Crystals obtained at 500 and 1000 °C were imaged using SEM, which showed that both $Mn_2O_3$ and $Mn_3O_4$ were porous and exhibited different levels of porosity. The size of the pores in $Mn_3O_4$ (> 100 nm) was much larger than in $Mn_2O_3$ (< 100 nm), which reflected the predominance of bulk diffusion at higher temperatures to increase the stability of the oxide by reducing surface area[463].

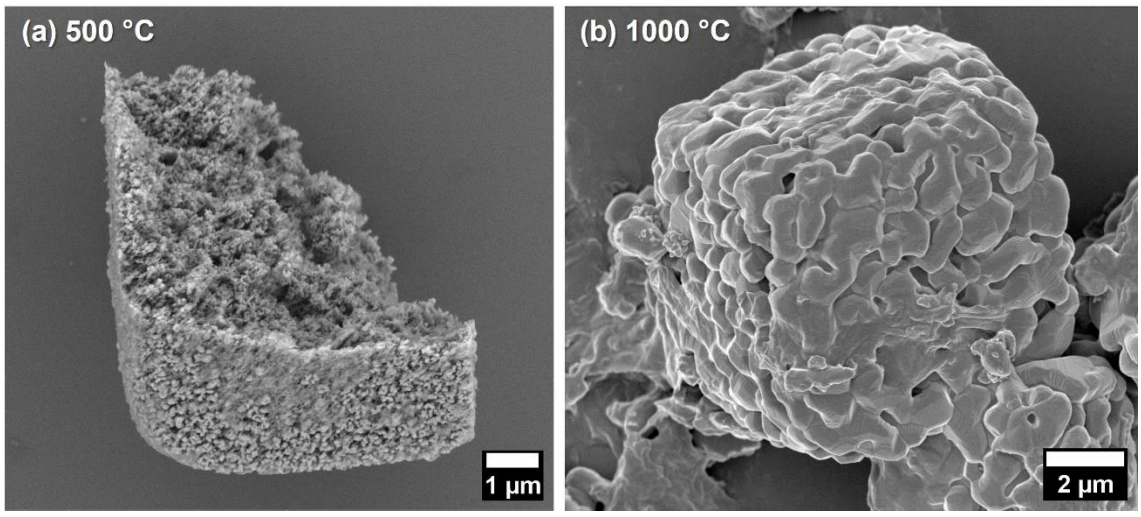


**Figure 5.18 SEM images of the manganese oxides prepared using different temperatures.**

### 5.3.3 Synthesis and Characterisation of $Mn_2O_3$

Following the TGA and pXRD data, 450 – 600 °C was identified as a suitable temperature range for the decomposition of $MnCO_3$ into $Mn_2O_3$. The stability of $Mn_2O_3$ made it preferable over α-$MnO_2$, despite it forming at lower temperatures. $MnCO_3$ was heated using a range of different heating conditions to determine the influence of temperature, heating rate and annealing time on the properties of the product. A total of 10 different heating regimes were used, as summarised in Table 5.2.

#### 5.3.3.1 Powder XRD of $Mn_2O_3$

The annealed crystals were analysed using pXRD, which confirmed that $Mn_2O_3$ was the major product for all heating conditions (Figure 5.19). However, the peaks in the patterns obtained at 450 °C had lower intensities and were broader than the others, indicating that the $Mn_2O_3$ was less crystalline when prepared at this temperature. The broad peak present at 38° for the crystals heated at 450 and 500 °C suggested that a small proportion of unreacted $MnCO_3$ remained at these temperatures.

In contrast, some patterns possessed small peaks at 29 and 36°, indicative of $Mn_3O_4$. This was the case for crystals heated for 3 hours at 500, 550 and 600 °C, and the sample heated for 30 minutes at 550 °C using the slowest heating rate of 1 °C $min^{-1}$. These conditions expose the crystals to the highest amount of thermal energy due to the prolonged heating times, allowing further oxidation to occur.

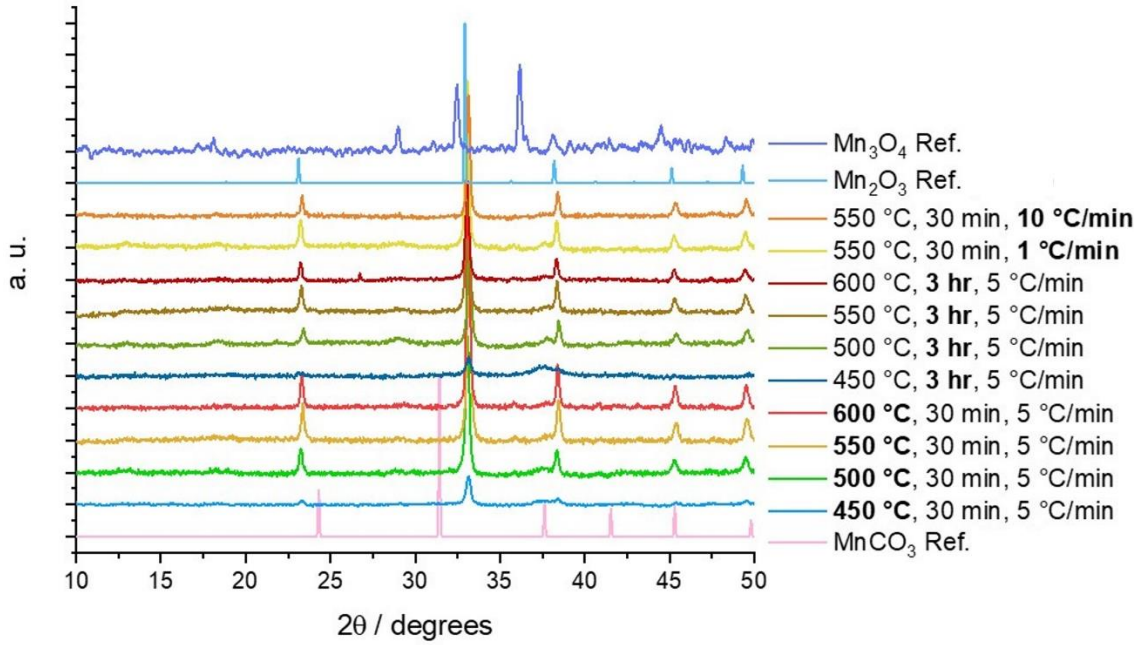


**Figure 5.19 Powder XRD patterns for all manganese oxides prepared using different heating regimes, using references obtained from AMCSD[462] (AMCSD ID: $MnCO_3$ 0000100, $Mn_2O_3$ 0009390, $Mn_3O_4$ 0002024).**

### 5.3.3.2 SEM of $Mn_2O_3$

SEM was used to qualitatively compare the porosities achieved using the different heating regimes. Crystals which were heated to different temperatures using a fixed rate of 5 °C $min^{-1}$ and held at the target temperature for 30 minutes exhibited varying levels of porosity (Figure 5.20). There was no observable porosity at 450 °C, however at temperatures ≥ 500 °C pores were increasingly prominent on the crystal surfaces.

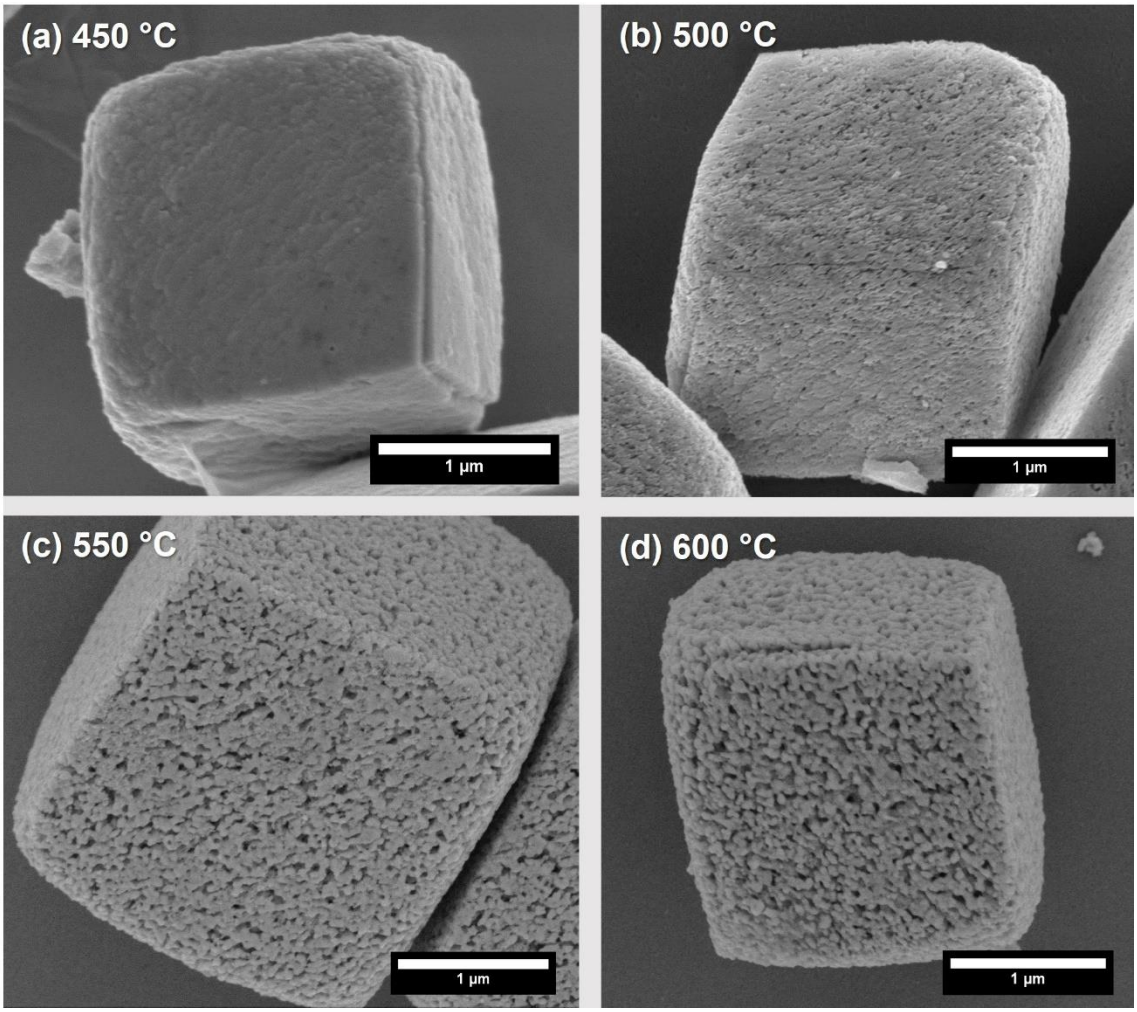


**Figure 5.20 SEM images of $Mn_2O_3$ prepared by heating at different temperatures for 30 minutes using a heating rate of 5 °C $min^{-1}$.**

The experiment was repeated, and the samples were subjected to a longer annealing period of 3 hours (Figure 5.21). Compared to crystals prepared using the shorter annealing period, the crystals heated for 3 hours showed increased porosity. Surface porosity was visible in crystals prepared at all temperatures trialled.

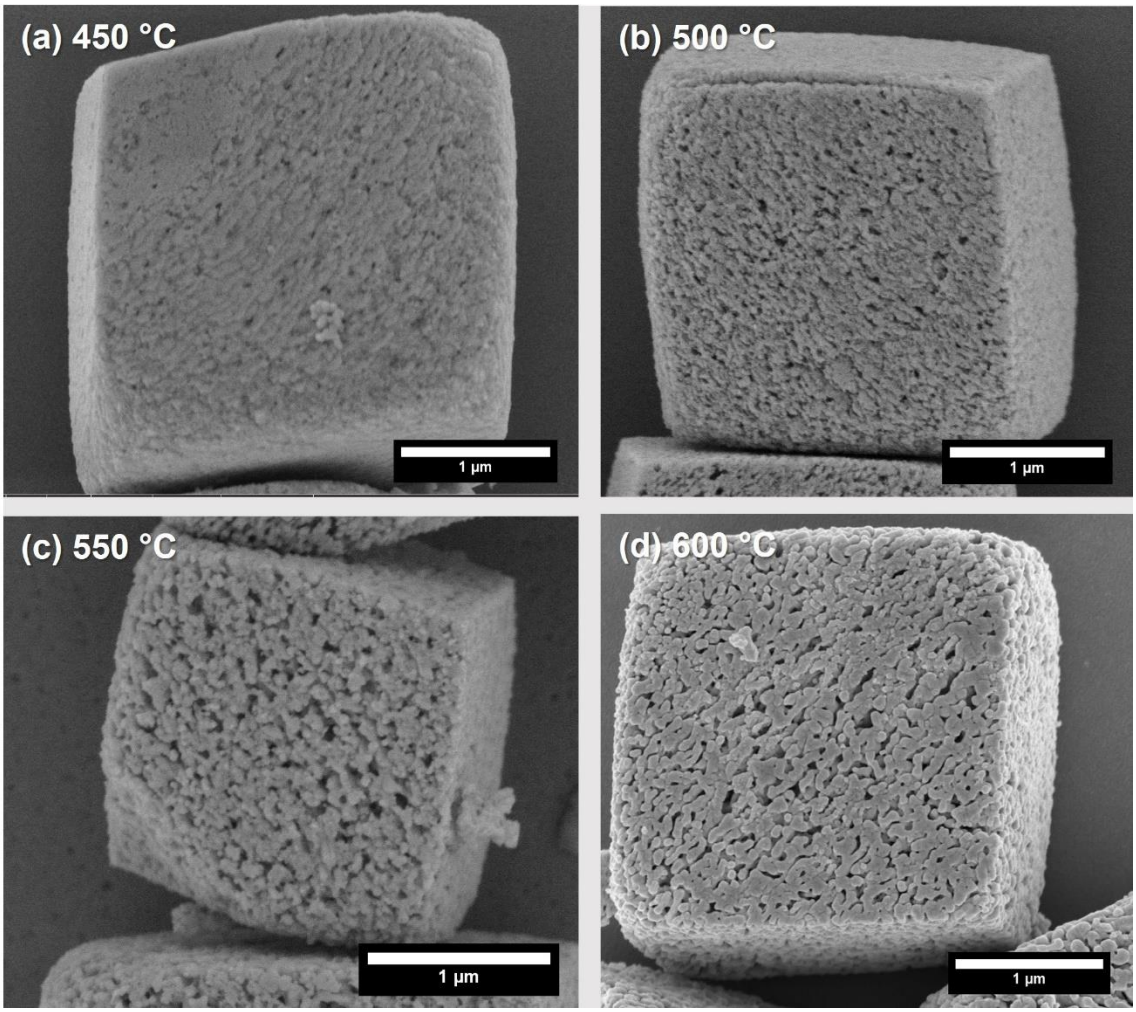


**Figure 5.21 SEM images of $Mn_2O_3$ prepared by heating at different temperatures for 3 hours using a heating rate of 5 °C $min^{-1}$.**

There was little perceivable difference in the surface porosity of crystals prepared using different heating rates and held at 550 °C for 30 minutes, though all were porous (Figure 5.22). Unheated $MnCO_3$ crystals were not porous, confirming that the release of $CO_2$ via thermal decomposition of $MnCO_3$ and formation of the oxide was responsible for generating porosity.

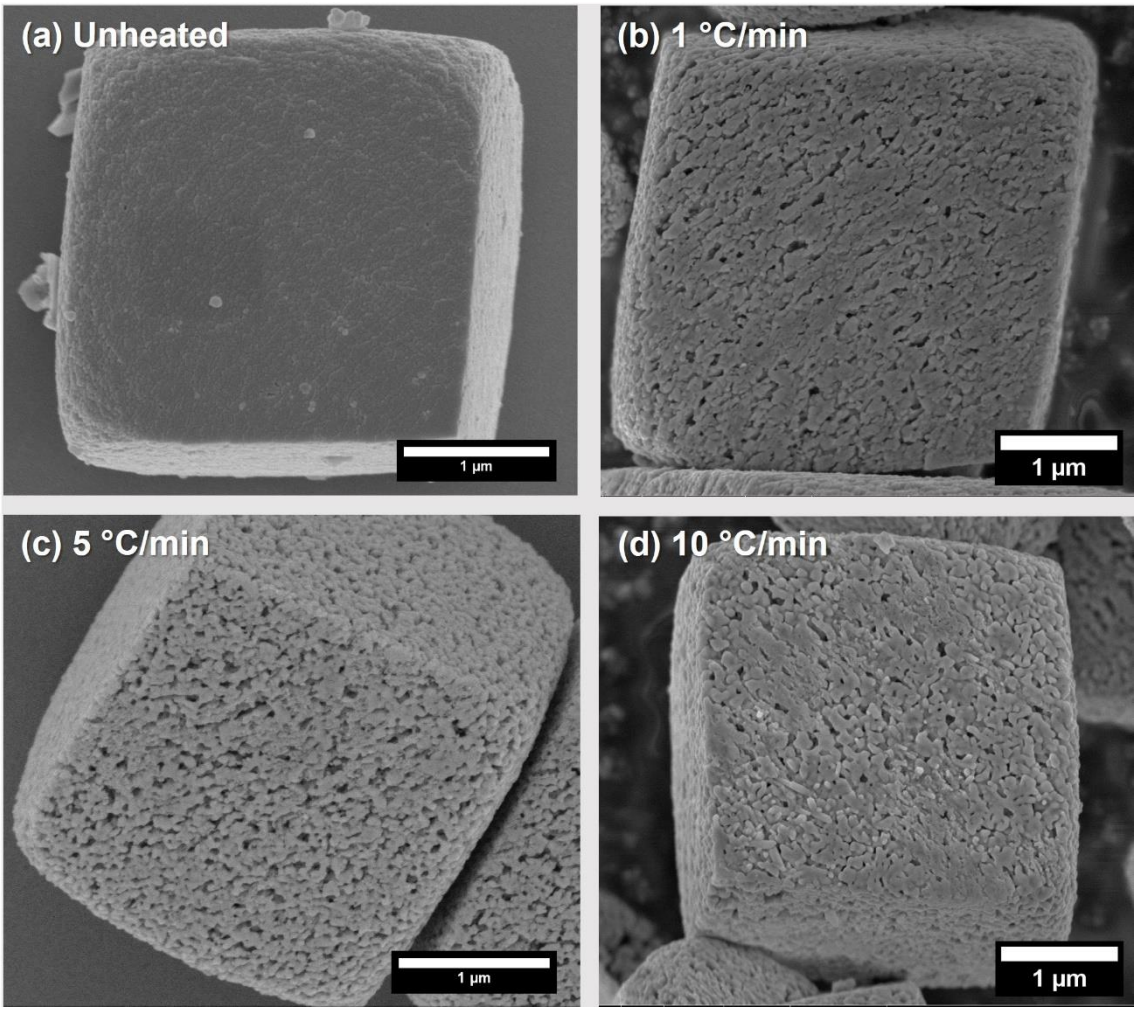


**Figure 5.22 SEM images of $Mn_2O_3$ prepared using different heating rates and unheated $MnCO_3$.**

#### 5.3.3.3 FIB-SEM of Porous $Mn_2O_3$

Quantitative analysis of the porosity was then performed using image analysis of FIB-SEM cross-sections and BET. The FIB-SEM images were segmented and analysed to extract the pore size distribution, pore density ($\mu m^{-2}$) and pore area fraction (%). The pore size distributions were plotted in terms of the pore diameter (nm), and the median pore size and interquartile range (IQR), which is the range between the $25^{th}$ – $75^{th}$ percentile, were calculated.

FIB-SEM images of $Mn_2O_3$ crystals which were prepared at different temperatures using a fixed heating rate of 5 °C $min^{-1}$ and held for 30 minutes showed increasing porosity with annealing temperature (Figure 5.23). Higher temperatures such as 550 and 600 °C yielded interconnected channels of pores, whereas monodisperse pores

were produced at lower temperatures such as 450 and 500 °C. The same trend in porosity with temperature was observed when the annealing time was extended to 3 hours (Figure 5.24). Comparison of the crystals obtained at the same temperature using different heating times showed that more pores were present after longer heating times.

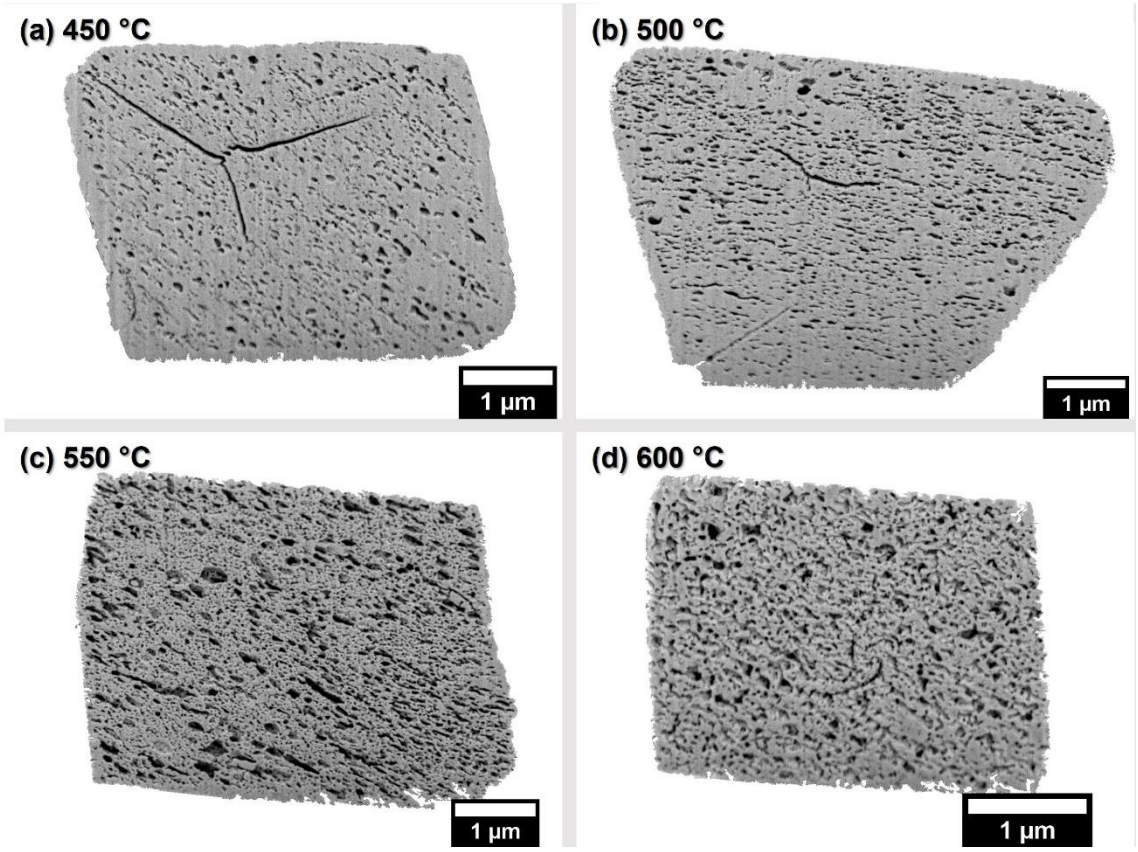


**Figure 5.23 FIB-SEM images of $Mn_2O_3$ formed by heating $MnCO_3$ for 30 minutes using a 5 °C $min^{-1}$ heating rate and the temperatures shown.**

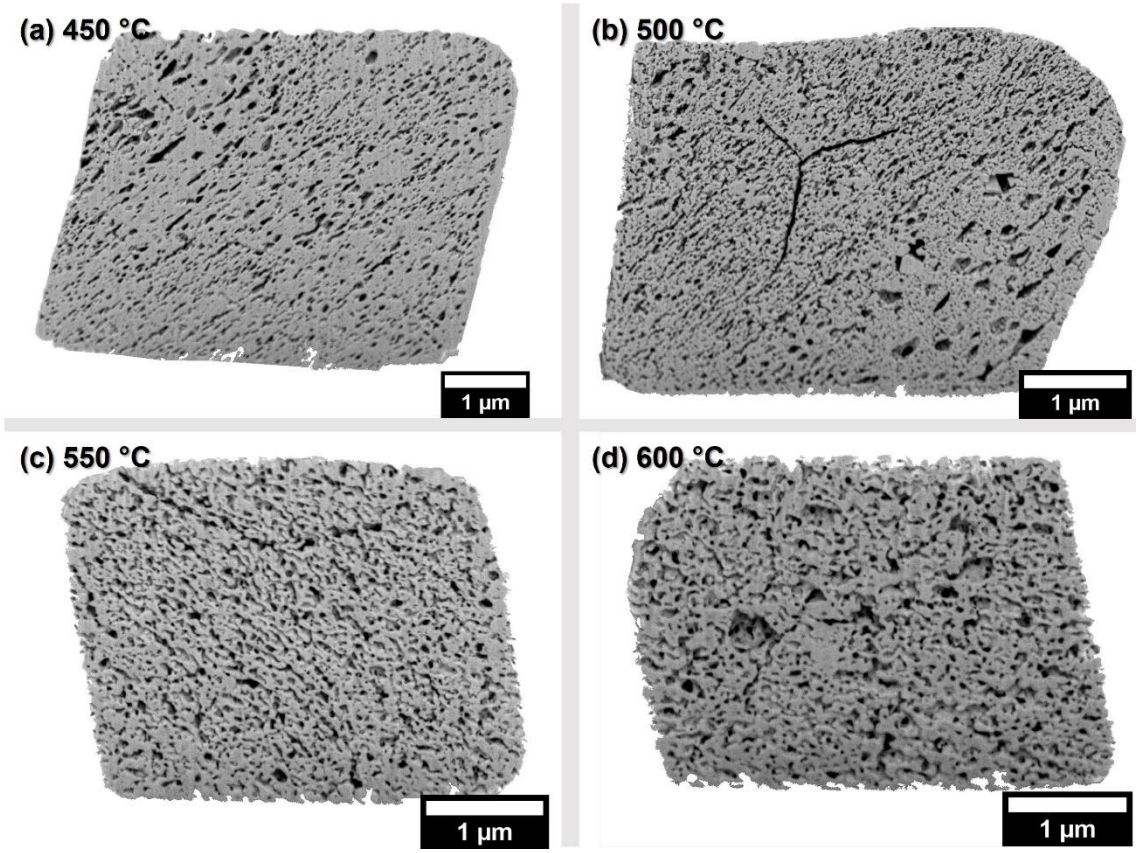


**Figure 5.24 FIB-SEM images of $Mn_2O_3$ prepared by heating $MnCO_3$ for 3 hours using a 5°C $min^{-1}$ heating rate and the temperatures shown.**

Cross-sections through unheated $MnCO_3$ crystals showed that no pores were present, which confirmed that the milling process did not generate porosity (Figure 5.25). It was difficult to qualitatively differentiate between the porosity formed in crystals annealed at 550 °C for 30 minutes using different heating rates, indicating that this parameter may not have a significant effect on the porosity.

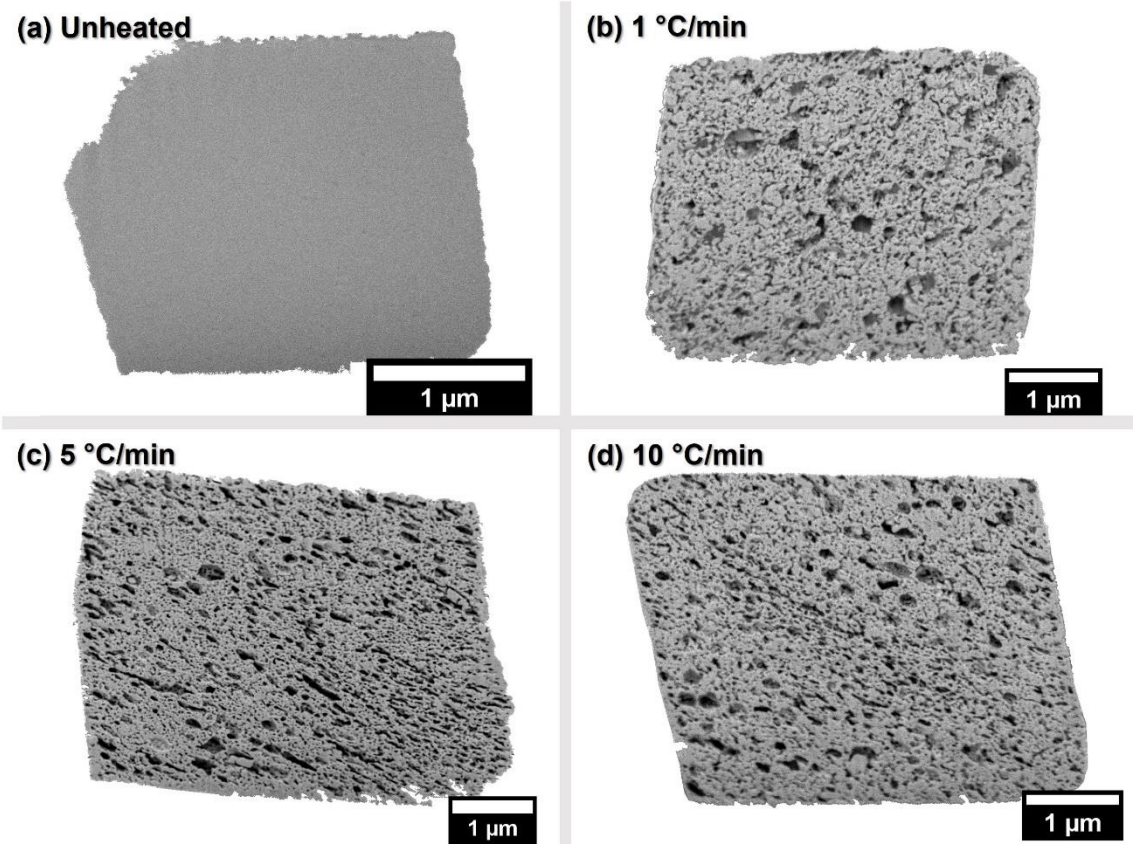


**Figure 5.25 FIB-SEM images of $Mn_2O_3$ prepared by heating $MnCO_3$ for 30 mins at 550 °C using different heating rates, compared to a control of unheated $MnCO_3$.**

#### 5.3.3.4 Pore Size Distribution from FIB-SEM Image Analysis

Firstly, the effect of temperature on porosity for crystals prepared using a fixed heating rate of 5 °C and annealing time of 30 minutes was compared (Figure 5.26). The largest spread of pore sizes was achieved at 500 °C, which had the greatest median pore size and broadest IQR. The median pore size was similar for all other temperatures, but a broader IQR was observed at 600 °C.

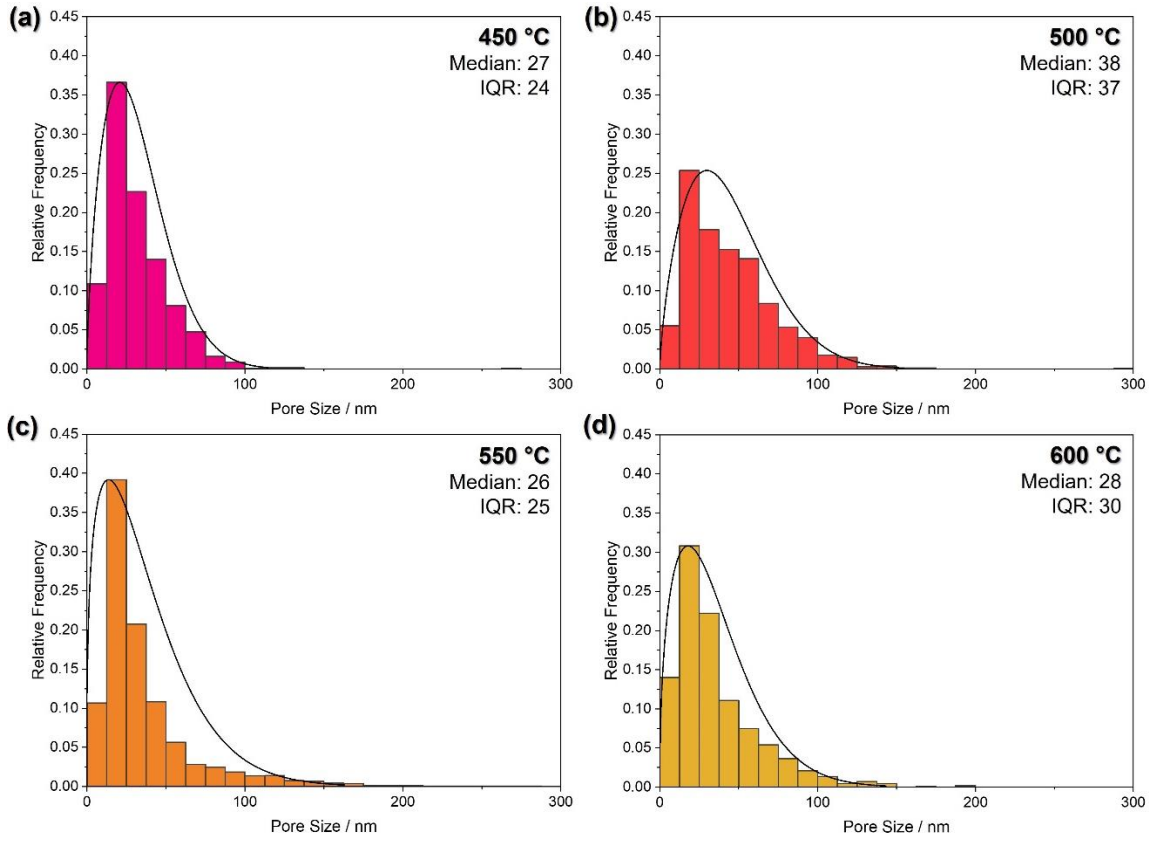


**Figure 5.26 Pore size distribution graphs for $Mn_2O_3$ prepared using different temperatures for 30 minutes at 5 °C $min^{-1}$.**

The density of the pores and the pore area were also calculated (Figure 5.27). The increase in median pore size at 450 – 500 °C was accompanied by an increase in pore area but there was a small decrease in pore density. The combination of these effects indicated that growth of the pores occurred. From 500 – 550 °C, the median pore size decreased while both the pore density and pore area increased. This can be attributed to the evolution of new pores between these temperatures which have small sizes. Finally, the pore area reduced between 550 – 600 °C, while the median pore size and pore density remained relatively unchanged. This could be due to restructuring or "sintering" of the manganese oxide lattice at 600 °C in order to reduce strain caused by the expulsion of $CO_2$[464]. This only occurs at 600 °C due to the energy required for lattice rearrangement and suggests that decomposition occurs via bulk diffusion at this temperature, compared to surface diffusion for temperatures < 600 °C.

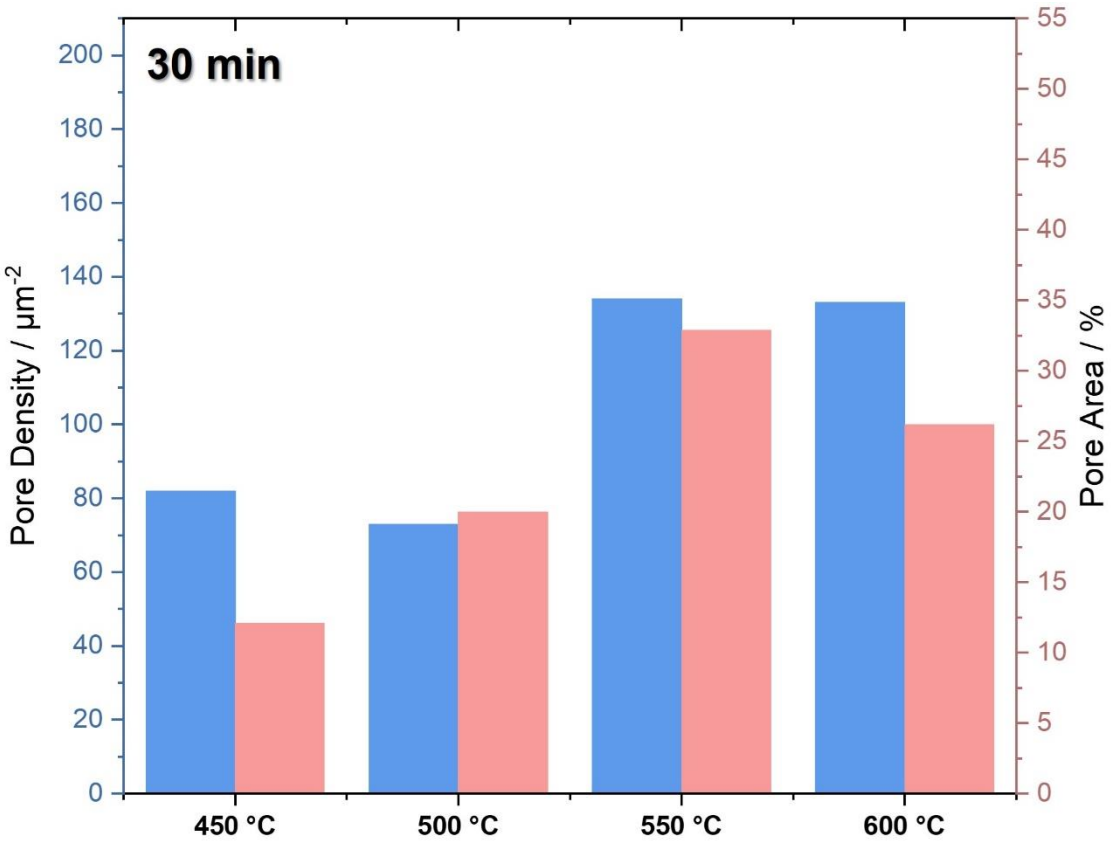


**Figure 5.27 The effect of temperature on porosity in crystals heated for 30 minutes using a heating rate of 5 °C $min^{-1}$, in terms of pore density ($\mu m^{-2}$) and pore area (%).**

The same range of temperatures were used to anneal $MnCO_3$ for an extended period of 3 hours. Compared to the 30 minute samples, higher median pore sizes and wider IQRs were observed (Figure 5.28). This was not the case when comparing $MnCO_3$ heated at 500 °C for 30 min and 3 h, which showed a higher median and broader IQR after 30 minutes.

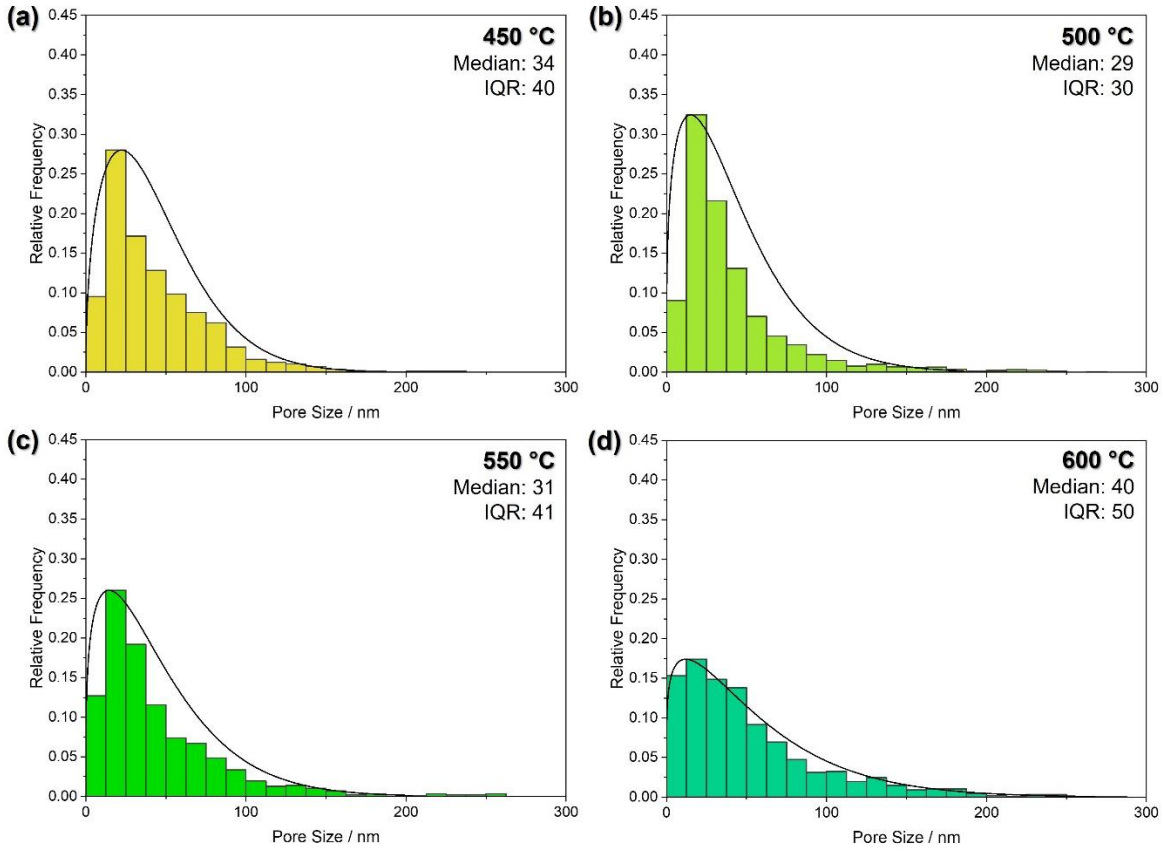


**Figure 5.28 Pore size distribution graphs for $Mn_2O_3$ prepared using different temperatures for 3 hours at 5 °C $min^{-1}$.**

The densities of pores in crystals heated for 3 hours increased with temperature until 500 °C, before decreasing at 550 °C and remained constant at 600 °C (Figure 5.29). The pore area generally increased with temperature, although was comparable for crystals annealed at 500 and 550 °C. As for the samples annealed for 30 minutes, the trend in pore area reflects the different mechanisms that create porosity at different temperatures. From 450 to 500 °C, the observed increase in pore density and area shows that more pores formed with temperature. At 500 to 550 °C the pore area was similar but the pore density falls, indicating that the pores coalesce. Finally, the pore density remains unchanged between 550 and 600 °C while the pore area increases significantly, signifying the growth of pores.

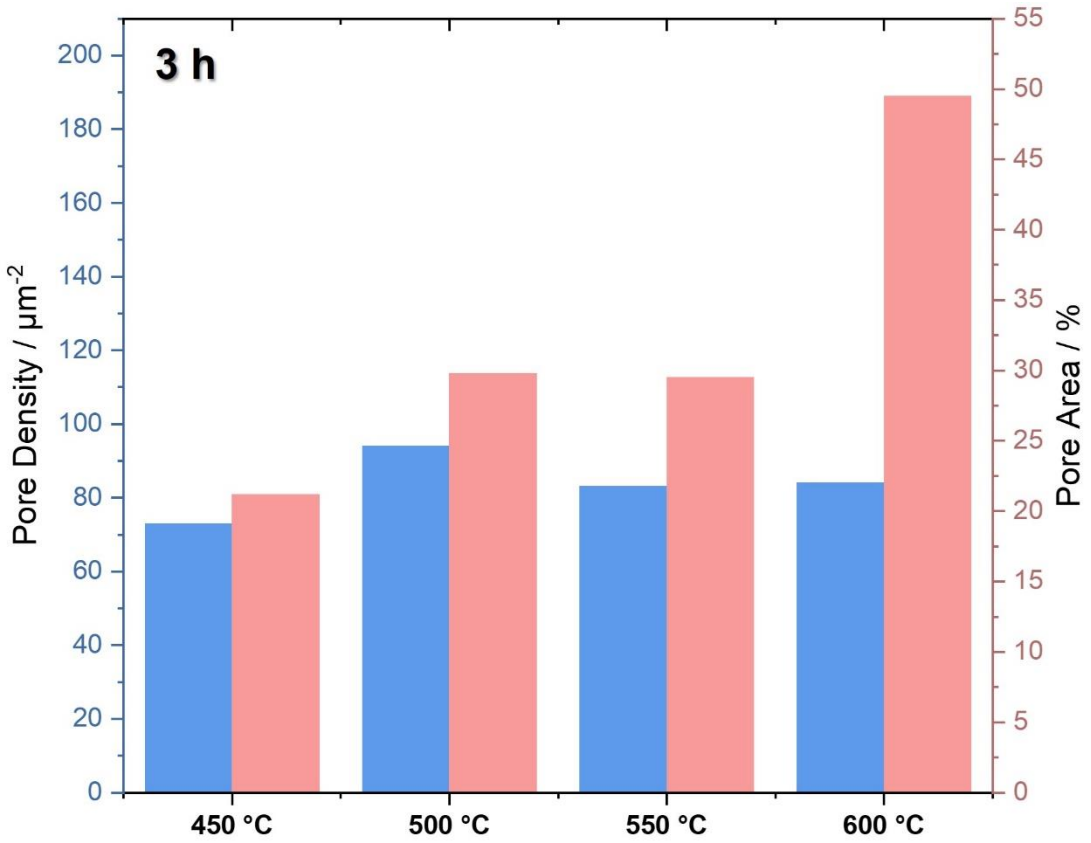


**Figure 5.29 The effect of temperature on porosity in crystals heated for 3 hours using a heating rate of 5 °C min$^{-1}$, in terms of pore density (µm$^{-2}$) and pore area (%).**

The effect of the heating rate on the porosity was also quantified. The crystals heated using a slow heating rate of 1 °C had a higher median pore size and broader IQR of sizes (Figure 5.30) than high heating rates. However, the pore size distribution was very similar between crystals heated at 5 and 10 °C min$^{-1}$.

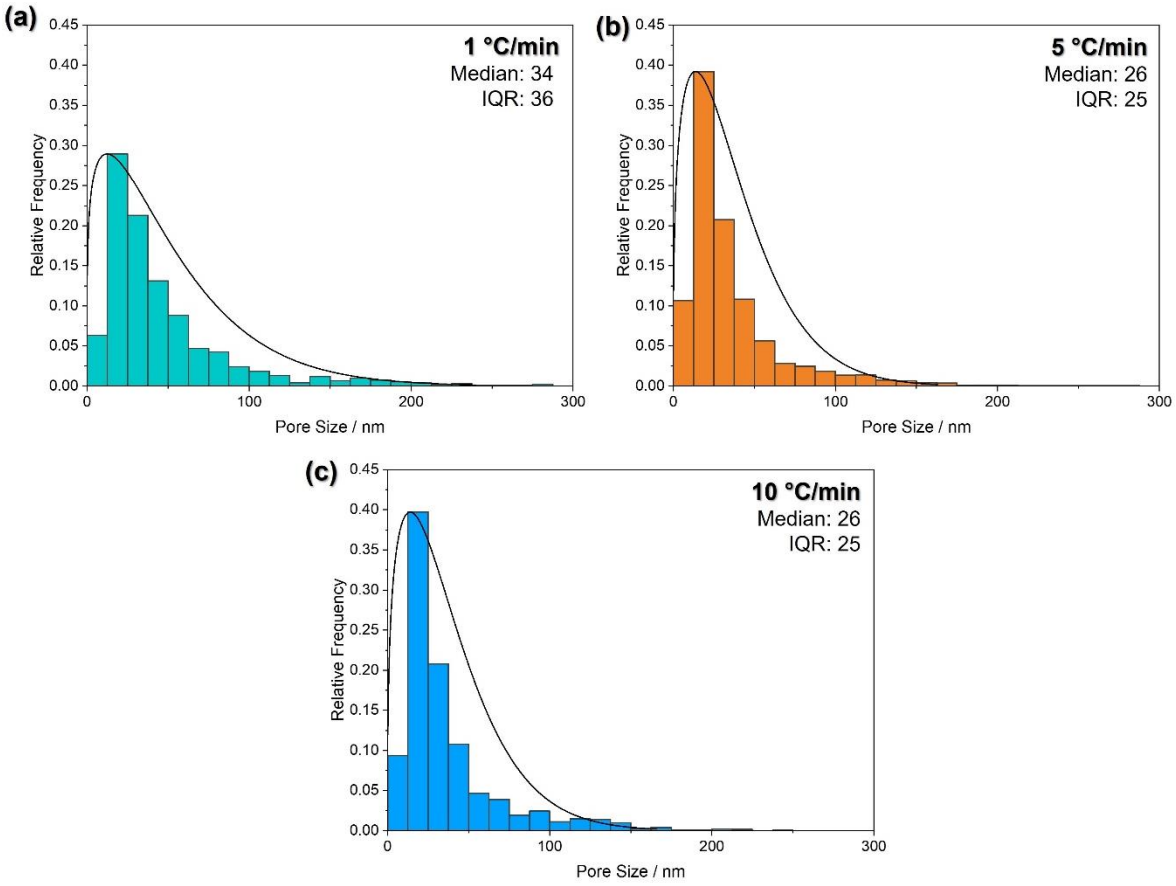


**Figure 5.30 Pore size distribution graphs for $Mn_2O_3$ prepared using different heating rates, at 550 °C for 30 minutes.**

There was little change in pore area for $Mn_2O_3$ heated at different rates (Figure 5.31). The pore density was much lower when a slow heating rate of 1 °C $min^{-1}$ was used and reached a maximum at 5 °C $min^{-1}$. As the slow heating rate involves sustaining high temperatures for the longest period (with ~ 8 h total heating), it is likely that the reduced pore density is caused by sintering of the lattice to accommodate the lattice strain. Although this has been seen previously for samples prepared at 600 °C, the extended heating involved for the 1 °C $min^{-1}$ may allow this to occur here at 550 °C.

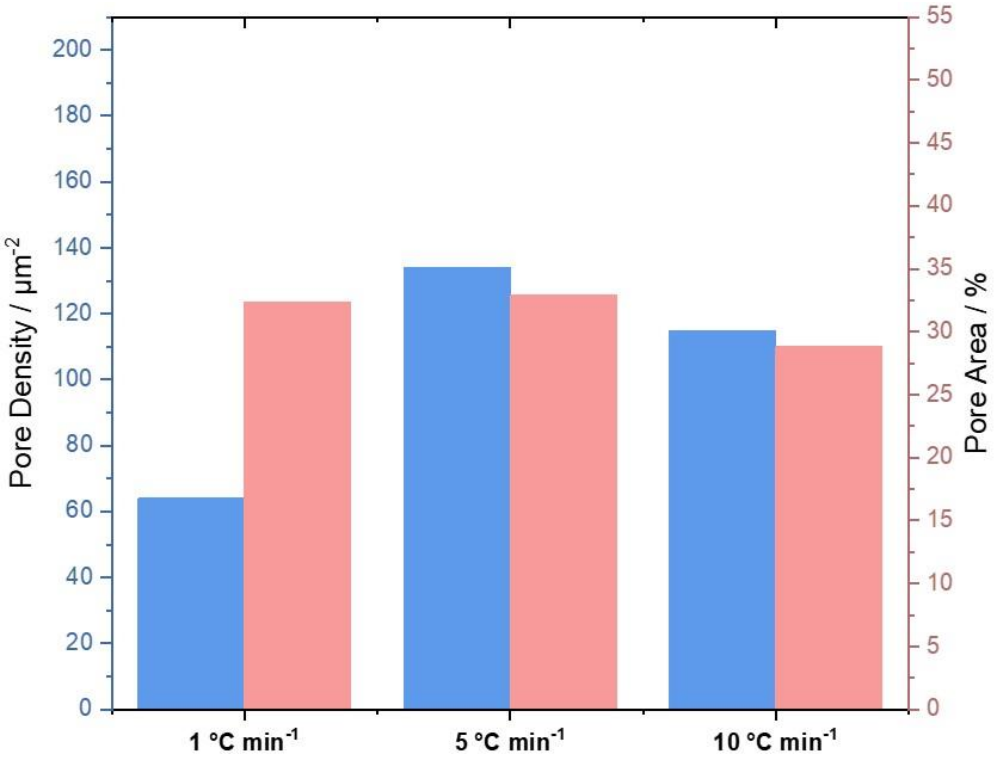


**Figure 5.31 The effect of rate on porosity in crystals heated for 30 minutes at 500 °C, in terms of pore density (µm$^{-2}$) and pore area (%).**

The pore filling fractions of the annealed $Mn_2O_3$ crystals are compared in Figure 5.32. The highest pore densities were achieved in samples heated using high temperatures for short bursts (550 and 600 °C for 30 min). The highest pore area was observed for the sample prepared at 600 °C for 3 h, which was much higher than for any other sample with 50 % of the crystal cross-section occupied by pores.

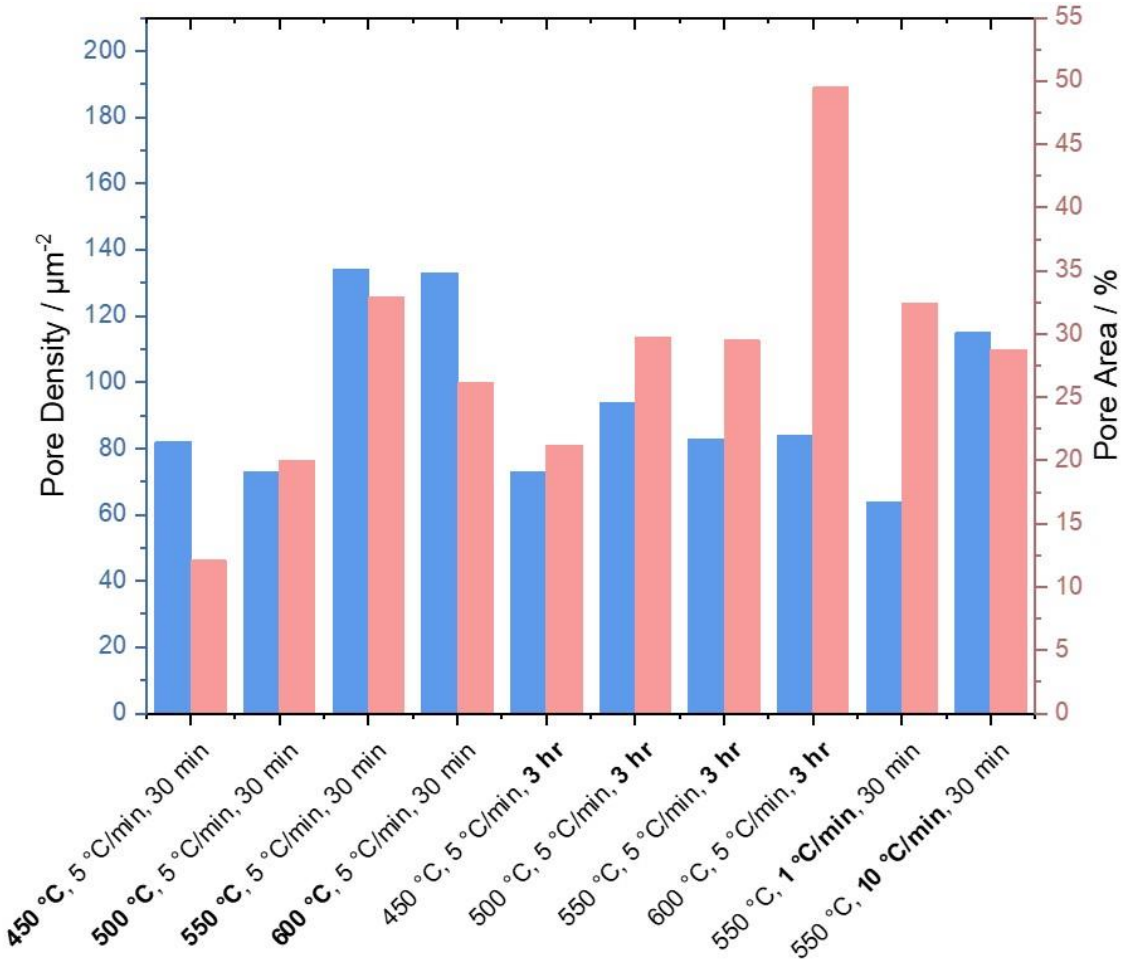


**Figure 5.32 The proportion of the crystal cross-section occupied by pores for $Mn_2O_3$ samples prepared using different heating methods.**

### 5.3.3.5 BET Analysis of Porous $Mn_2O_3$

Analysis using BET revealed that $Mn_2O_3$ prepared at different heating conditions exhibited different surface areas (Table 5.5). Unheated $MnCO_3$ had a very low surface area of 1.1 $m^2\ g^{-1}$ due to the absence of pores. All $Mn_2O_3$ had a greater surface area than the unheated $MnCO_3$. The surface area was highest for $MnCO_3$ heated at 450 °C regardless of the heating time, showing that increasing the temperature beyond 450 °C led to a decrease in surface area. This is expected due to restructuring of the lattice via sintering to reduce strain, which inevitably reduces the surface area and requires higher temperatures to proceed[463, 465].

The surface area was generally larger in samples heated for 3 hours than for 30 minutes. This could be due to the pores produced over long heating periods being more open (connected to the surface) than those obtained using short heating

bursts. As closed pores (which do not connect with the surface) cannot be measured by BET analysis, this would lead to reduced surface area values. The longer period of heating could result in pores with open structures due to greater decomposition and accompanying expulsion of $CO_2$ by diffusion to the surface.

The surface area of $Mn_2O_3$ obtained using different heating rates was very similar between 1 and 5 °C $min^{-1}$, with a slightly higher surface area attained at 10 °C $min^{-1}$.

| **Temperature / °C** | **Time** | **Rate / °C $min^{-1}$** | **BET Surface Area / $m^2 g^{-1}$** |
|---|---|---|---|
| **450** | 30 min | 5 | 37.7 ± 0.2 |
| **500** | 30 min | 5 | 20.5 ± 0.5 |
| **550** | 30 min | 5 | 4.9 ± 0.6 |
| **600** | 30 min | 5 | 1.8 ± 0.3 |
| 450 | **3 h** | 5 | 51.8 ± 0.2 |
| 500 | **3 h** | 5 | 19.3 ± 0.5 |
| 550 | **3 h** | 5 | 16.4 ± 0.2 |
| 600 | **3 h** | 5 | 14.6 ± 0.3 |
| 550 | 30 min | **1** | 7.0 ± 0.8 |
| 550 | 30 min | **10** | 11.0 ± 0.5 |
| **Unheated $MnCO_3$** | - | - | 1.1 ± 0.4 |

**Table 5.5 BET analysis of $Mn_2O_3$ samples prepared using different heating conditions.**

Different trends in porosity were observed based on image and BET analysis. BET analysis showed that the surface area was highest for samples heated at 450 °C. Image analysis of cross-section SEM images showed that the pore area proportion generally increased with temperature. In order to explain this discrepancy, it is important to consider what is actually being measured in each of these methods. The pore area fraction will increase if the pores increase in size but do not change in number. However, in this situation the surface area would decrease. An increase in the size of the pores could therefore explain both the BET and image analysis trends here, as the filling fraction measurements neglect this information.

### 5.3.3.6 Synthesis of Au-$Mn_2O_3$

Manganese carbonate crystals containing gold nanoparticles (Au-$MnCO_3$) were also annealed. The crystals were heated at either 550 or 600 °C for 30 minutes at a rate of 5 °C $min^{-1}$. Powder XRD was used to confirm that $Mn_2O_3$ was produced (Figure 5.33).

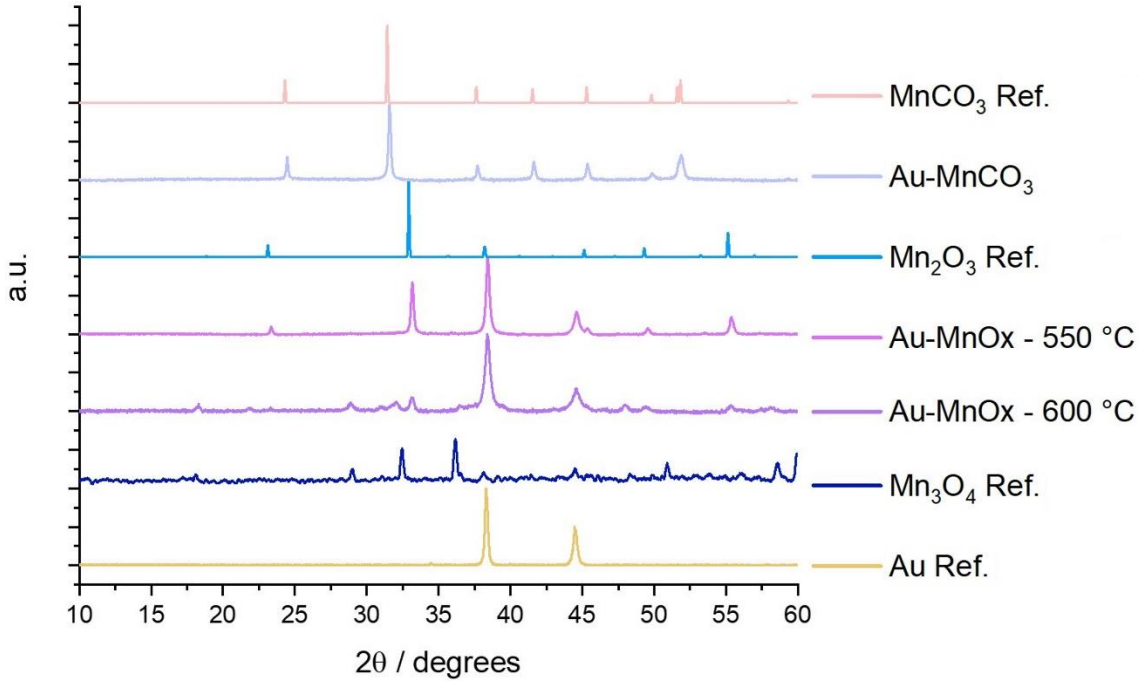


**Figure 5.33 Powder XRD patterns obtained for Au-$MnCO_3$ and Au-$Mn_2O_3$, using references obtained from AMCSD[462] (AMCSD ID: $MnCO_3$ 0000100, $Mn_2O_3$ 0009390, $Mn_3O_4$ 0002024, Au 0011140).**

Unheated Au-$MnCO_3$ displayed all the key peaks for $MnCO_3$ without any additional peaks. Following heating at 550 and 600 °C, the $MnCO_3$ peaks were replaced by peaks corresponding to $Mn_2O_3$ and gold. Interestingly, the gold diffraction peaks at 38 and 44° were not present in the unheated Au-$MnCO_3$. This shows that the gold nanoparticles were originally too small to be detected, but following their aggregation during heating, they became of a sufficient size to be detected.

A range of smaller peaks were also present in the diffraction pattern for Au-$Mn_2O_3$ prepared at 600 °C, which matched the diffraction peaks for $Mn_3O_4$. Interestingly, the pXRD pattern obtained for gold-free $Mn_2O_3$ that was prepared using the same heating conditions did not contain any $Mn_3O_4$. The formation of $Mn_3O_4$ within a shorter time frame than in the gold-free $Mn_2O_3$ can be attributed to the excellent

thermal conductivity of gold[466], which will facilitate efficient heat transfer and allow the energy barrier for the oxidation reaction to be overcome more readily.

#### 5.3.3.7 Gold Nanoparticle Size Measurements using FIB-SEM

As the size of gold nanoparticles is important in ensuring catalytic efficiency[467], it was important to measure the size of the gold particles within the Au-$Mn_2O_3$ crystals after heating. Cross-sections of Au-$MnCO_3$ and Au-$Mn_2O_3$ prepared at 550 and 600 °C were prepared using FIB-SEM (Figure 5.34).

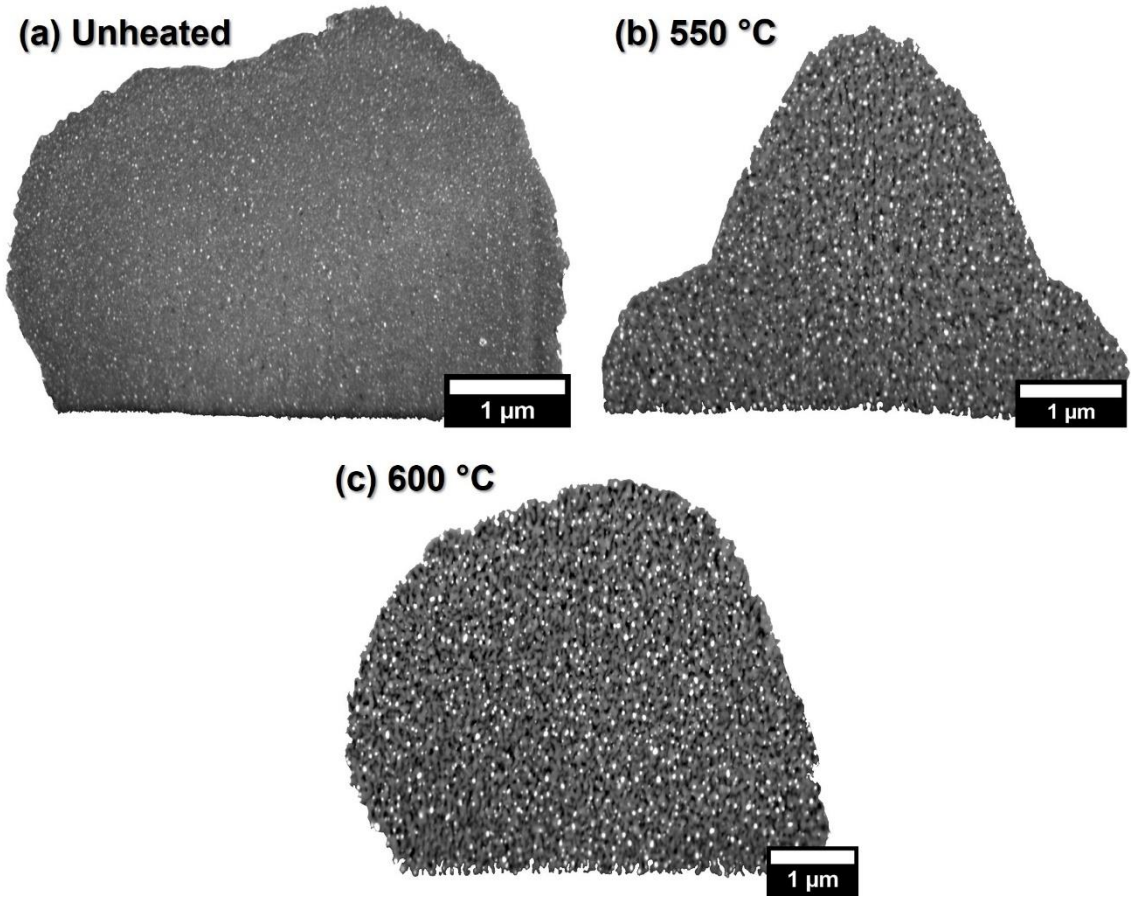


**Figure 5.34 FIB-SEM images of Au-$MnCO_3$ and Au-$Mn_2O_3$ crystals prepared using at 550 and 600 °C.**

The FIB-SEM images showed a distinctive change in the gold particle size. The particles were segmented from the crystal background using the image analysis techniques previously discussed in Chapter 3. The contrast of the gold particles was also enhanced during imaging through the use of a CBS detector, to facilitate clean segmentation of the gold particles from the crystal. The gold particle sizes were

extracted from the segmented image and the particle size distribution was plotted in terms of relative frequency (Figure 5.35).

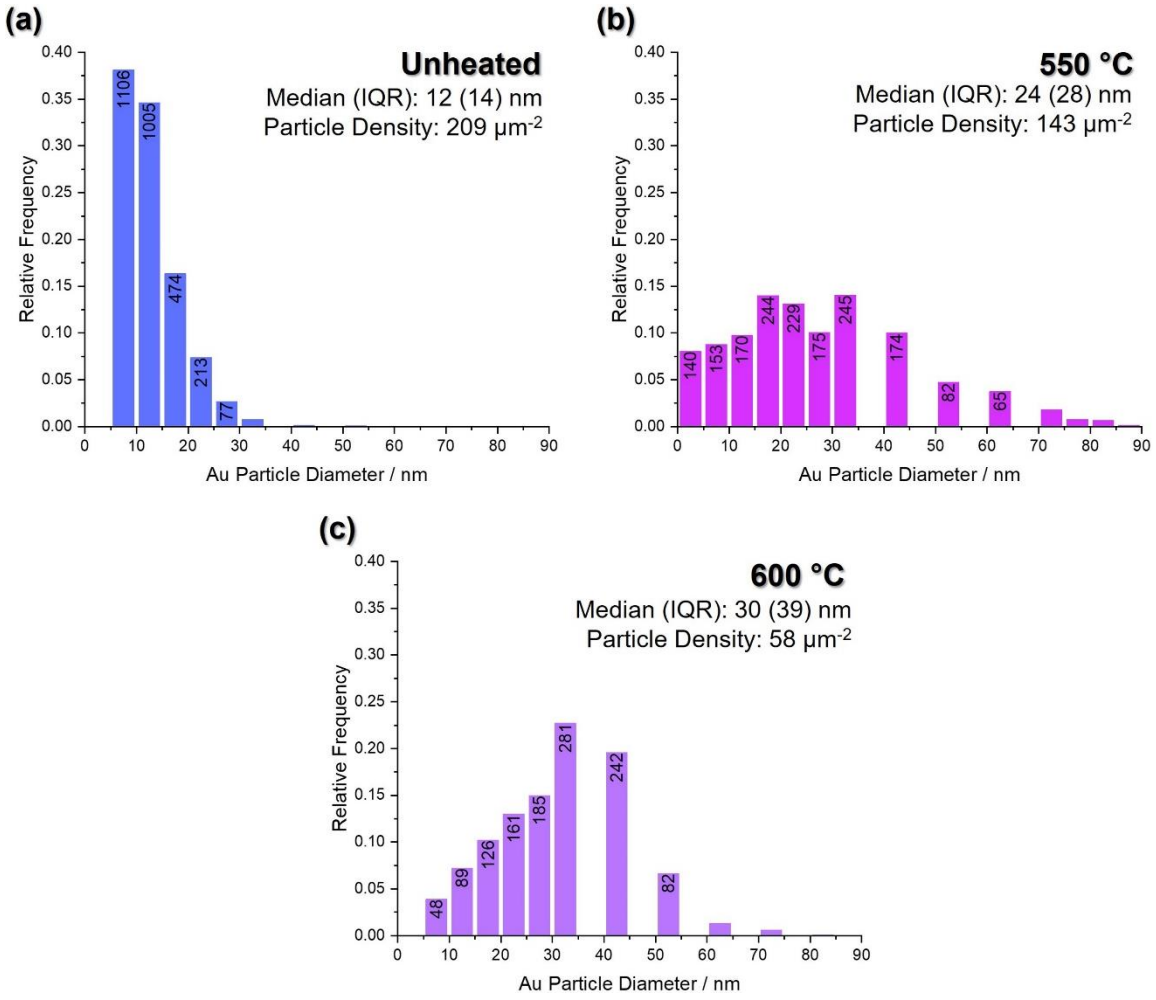


**Figure 5.35 Size distribution of the gold nanoparticles occluded within crystals of unheated Au-$MnCO_3$ and Au-$Mn_2O_3$ heated using 550 and 600 °C.**

The size of the gold nanoparticles occluded within unheated Au-$MnCO_3$ crystals exhibited a positively skewed distribution (Figure 5.35a), indicating that the majority of the particles present had very small pore sizes (< 15 nm). The median size of the nanoparticles doubled from 12 nm to 24 nm after the $MnCO_3$ was heated at 550 °C (Figure 5.35b), and it increased further to 30 nm when Au-$MnCO_3$ was heated at 600 °C (Figure 5.35c). This was also reflected by the shift towards a normal distribution of gold nanoparticle sizes following heating.

The effect of this behaviour on the composition of the Au-$Mn_2O_3$ composites was quantified by calculating the density of the gold nanoparticles across the crystal cross-section. Unheated Au-$MnCO_3$ had the highest particle density of 209 $\mu m^{-2}$,

which fell to 143 $\mu m^{-2}$ after heating at 550 °C. When the crystals were heated at 600 °C, the density of gold nanoparticles reduced further to 58 $\mu m^{-2}$. As the fall in particle density was accompanied by an increase in the size, it is clear that the heating process caused the occluded gold nanoparticles to aggregate. The impact of this aggregation on the catalytic efficiency of the Au-$Mn_2O_3$ photocatalysts will be considered later in the chapter.

### 5.3.4 Synthesis and Characterisation of $MnO_2$

After successfully synthesising $Mn_2O_3$ and Au-$Mn_2O_3$ crystals, manganese oxides of other valencies were considered. While it has already been established that $Mn_3O_4$ can be prepared by heating $MnCO_3$ to 1000 °C, SEM images showed that the pores were very large (> 100 nm). This would also not be a suitable approach for forming Au-$Mn_3O_4$ as the heating temperature required is close to the melting point of gold at 1,064 °C. As the gold nanoparticles occluded within Au-$Mn_2O_3$ aggregated during heating at 600 °C, any further increase in temperature would likely reduce the nanoparticle density further and cause larger aggregates to form. $Mn_3O_4$ was therefore excluded as a suitable catalyst, and instead $MnO_2$ was explored.

Various literature sources have claimed that $MnO_2$ can be synthesised via thermal decomposition of $MnCO_3$ (Table 5.6). Although TGA analysis appeared to show a transition at 400 – 500 °C that could be attributed to the formation of α-$MnO_2$, pXRD of the product obtained at 500 °C confirmed that this was $Mn_2O_3$. To determine whether other heating conditions stated in the literature could yield stable $MnO_2$ under aerobic conditions, the heating conditions used in these publications were trialled. Two further conditions were trialled, 360 °C, 8 hr, 5 °C $min^{-1}$ and 450 °C, 16 hr, 5 °C $min^{-1}$.

| Heating Conditions | Reference |
|---|---|
| 450 °C, 4 hr, 5 °C $min^{-1}$ | Lian *et al.* [468] |
| 400 °C, 4 hr, 5 °C $min^{-1}$ | Li *et al.* [469], Zhao *et al.* [470] |
| 400 °C, 2 hr, 10 °C $min^{-1}$ | Pal *et al.* [471] |
| 380 °C, 4 hr, 5 °C $min^{-1}$ | Lian *et al.* [468] |

**Table 5.6 The heating conditions used in literature to create $MnO_2$ via thermal decomposition of $MnCO_3$.**

### 5.3.4.1 Powder XRD of $MnO_2$ via Thermal Decomposition of $MnCO_3$

The products formed using the different heating regimes were characterised using pXRD (Figure 5.36). The XRD patterns obtained of samples heated at 360 and 380 °C corresponded to $MnCO_3$, while samples heated at 400 °C and 450 °C for 4 hours exhibited patterns corresponding to $MnCO_3$ and also had a small peak at 33°, which can be attributed to the (222) plane of $Mn_2O_3$.

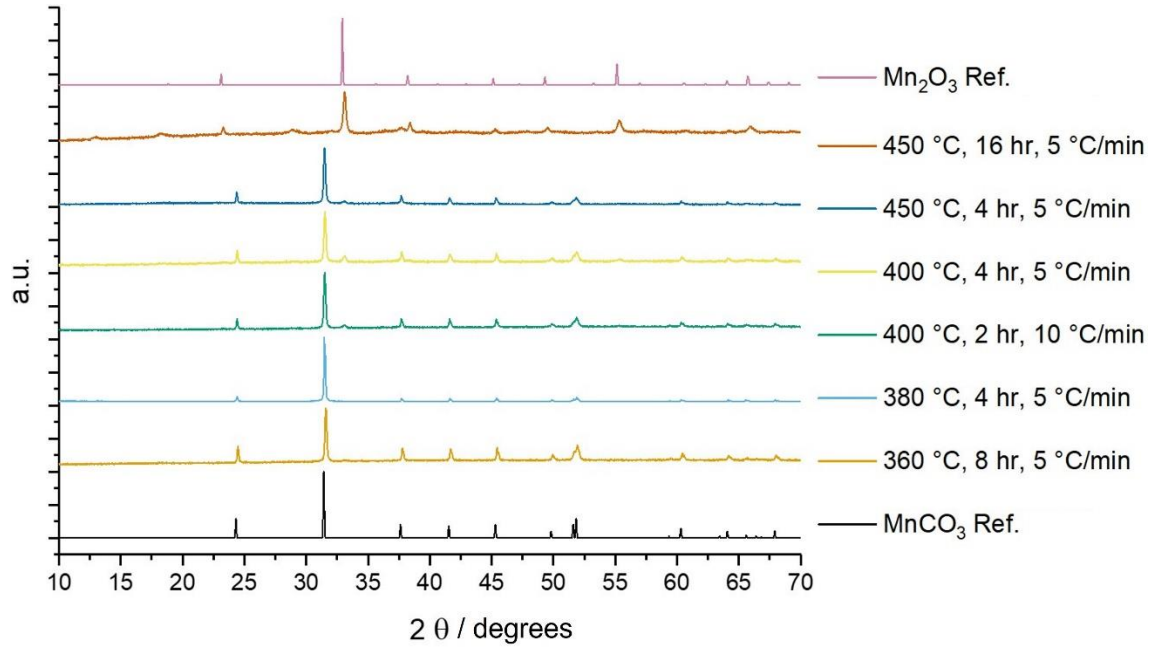


**Figure 5.36 Powder XRD patterns of samples prepared via the heating of manganese carbonate, following various literature protocols to obtain $MnO_2$, compared against controls for $MnCO_3$ and $Mn_2O_3$, using references obtained from AMCSD[462] (AMCSD ID: $MnCO_3$ 0000100, $Mn_2O_3$ 0009390).**

The final condition trialled, 450 °C for 16 hours, displayed all the key peaks for $Mn_2O_3$, but also had small peaks present at 13, 18, and 29° that correspond to the (110), (200) and (310) planes of α-$MnO_2$, showing that the main product was $Mn_2O_3$, with a small proportion of α-$MnO_2$. A very small peak at 38°, which corresponds to the (110) plane of $MnCO_3$, shows that a small fraction of unreacted $MnCO_3$ remained in the sample.

To summarise, only one of the trialled conditions yielded $MnO_2$, which was identified as α-$MnO_2$. As only a small proportion of α-$MnO_2$ was obtained, this was not found to be a reliable method of synthesis for $MnO_2$.

#### 5.3.4.2 Hydrothermal Synthesis of $MnO_2$

As $MnO_2$ could not be reliably synthesised via thermal decomposition of $MnCO_3$, a hydrothermal method was used to form $MnO_2$ through the reduction of $Mn_2O_3$. The starting material, $Mn_2O_3$, was formed by thermal decomposition of $MnCO_3$ at 450 °C for 30 minutes at 5 °C $min^{-1}$. The relatively low temperature conditions used to prepare $Mn_2O_3$ were chosen to reduce the aggregation of the Au nanoparticles. The synthesis route outlined by Ma *et al.* for the formation of $MnO_2$ nanobelts was used[445], with some modifications. The hydrothermal reaction was conducted without stirring with the aim of synthesising 3D structures, using reaction times of 1, 2, 3 and 6 days. An additional reaction was performed with stirring to allow comparison, using a reaction time of 3 days. The hydrothermal reaction was also performed using Au-$Mn_2O_3$ to form Au-$MnO_2$.

#### 5.3.4.3 Powder XRD of $MnO_2$ via Hydrothermal Reduction of $Mn_2O_3$

The products obtained from the hydrothermal reaction using different reaction times were characterised using pXRD (Figure 5.37). All patterns obtained corresponded to birnessite-type δ-$MnO_2$. Increasing the reaction time resulted in a sharpening of the peak at 37° (the -111 plane), suggesting that the conversion was more complete with longer reaction times. This was also seen in the stirred reaction, which possessed a defined peak at 39° for the (-202) plane, unlike the broad (-202) peak exhibited by the non-stirred samples. This indicated that fuller conversion was achieved with stirring.

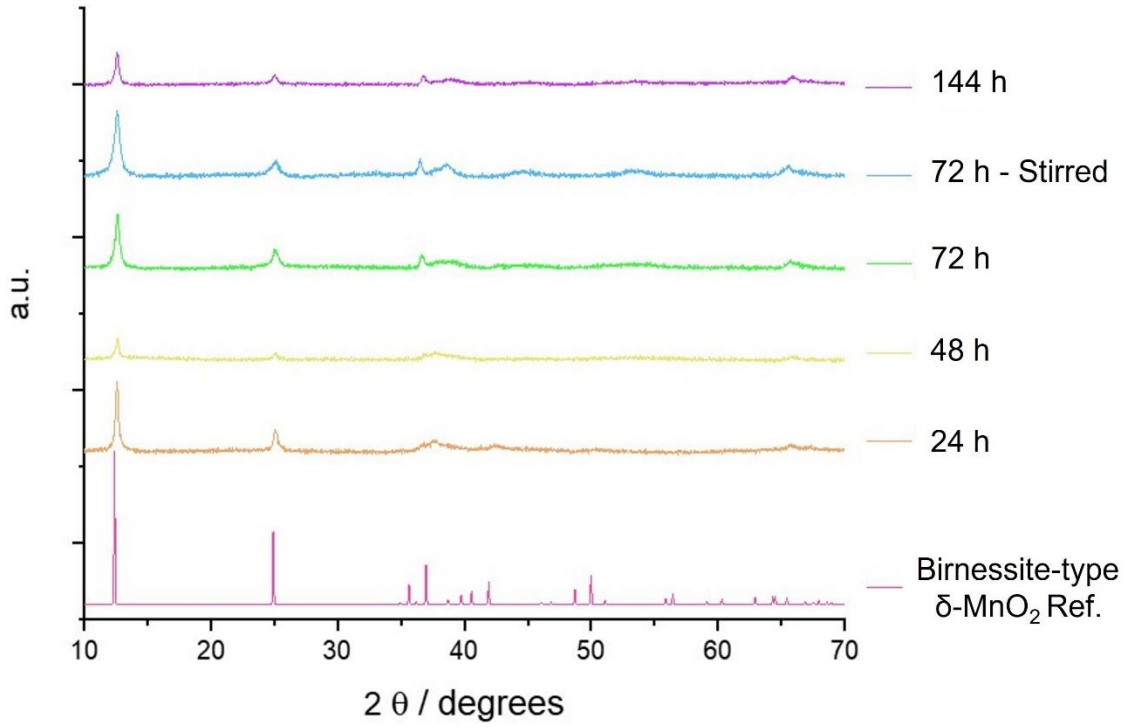


**Figure 5.37 Powder XRD patterns of manganese oxides prepared via hydrothermal synthesis with different reaction times, using references obtained from AMCSD[462] (AMCSD ID: $MnO_2$ 0001300).**

#### 5.3.4.4 SEM of $MnO_2$

The $MnO_2$ samples were observed using SEM to compare the stirred and non-stirred samples (Figure 5.38). The product from the stirred reaction had formed aggregated bundles of nano-sheets, which had a wide range of sizes, but were generally several hundred nanometres in length and ranged from 20-100 nm in thickness, as expected from the literature[445]. The sessile sample, in contrast, consisted of a mixture of nanobelts and rhombohedra. The nanobelts were similar in thickness to the nanosheets present in the stirred mixture (≈ 20 – 100 nm) and were up to 50 µm in length. The rhombohedral particles resembled the $Mn_2O_3$ starting material, but further examination of the structure using the CBS detector revealed that they were composed of fibres and plate-like particles around 200 µm in size. The intergrown fibres and plate structures within the rhombohedral crystals gave them a porous appearance. The composition of the non-stirred reaction mixture was roughly a 50:50 mix of nanobelts and rhombohedral crystals.

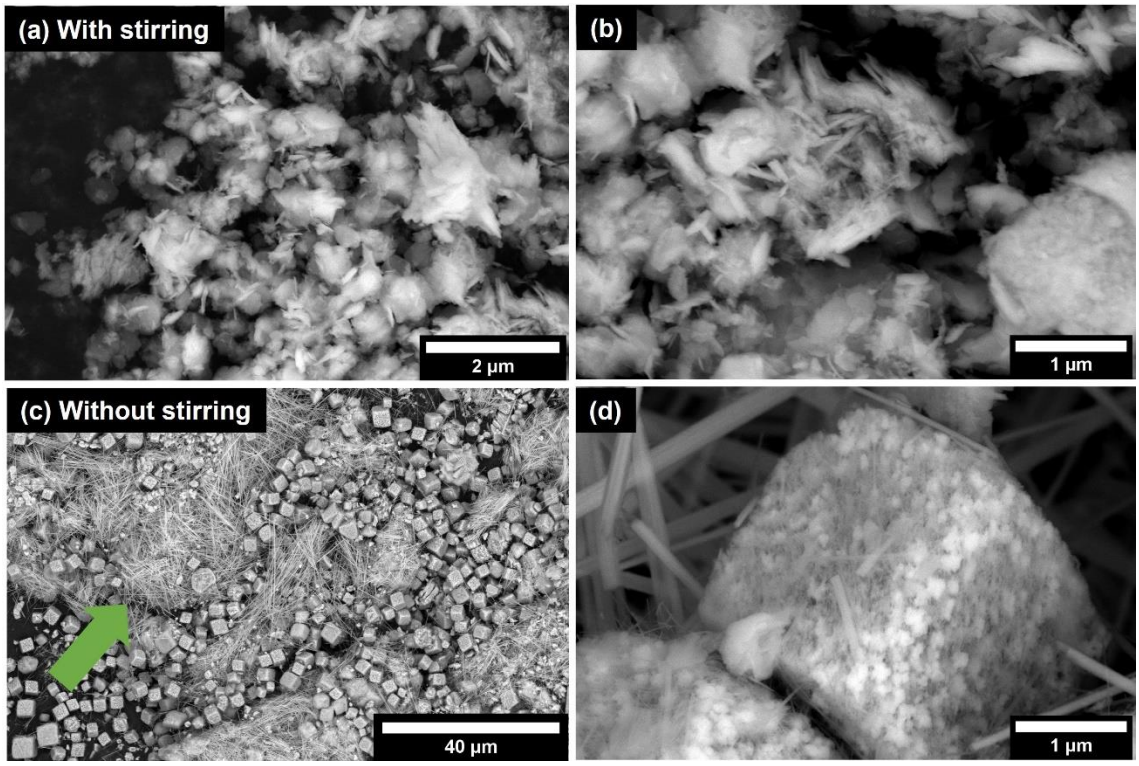


**Figure 5.38 SEM images of the $MnO_2$ prepared with stirring (a, b) and without stirring (c, d), where the green arrow highlights a bundle of nanobelts.**

SEM was also used to examine the products of the reactions at different reaction times, and a crushed sample was prepared for each time point, where gentle pressure was applied to the SEM substrate with a clean glass slide and twisted 90° in order to crush the crystals. This allowed the internal structure of the crystal to be viewed. Rhombohedral crystals were obtained after 24 hours of reaction, (Figure 5.39). The surfaces of the crystals consisted of layers of aligned plates and a small number of nanofibres with < 10 nm thickness. The partially crushed crystals revealed that the plates exhibited a shell-like layer around what appeared to be a core of unreacted $Mn_2O_3$ (Figure 5.39 c-d). The plate shell layer was 200 – 300 µm thick and consisted of individual plates roughly 20 µm in thickness.

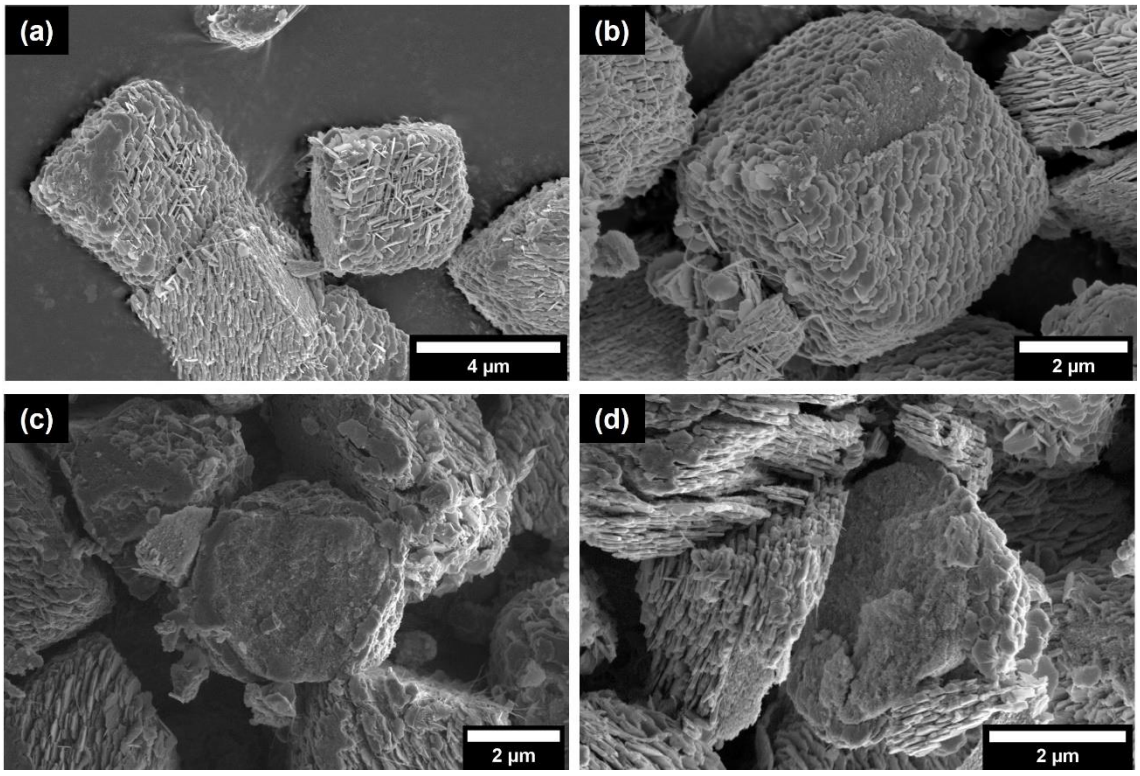


**Figure 5.39 SEM images of $MnO_2$ after 24 hours of reaction, with the bottom row of images showing crushed crystals.**

The crystals produced after 48 hours reaction time were rhombohedral in morphology and possessed intriguing surface structures (Figure 5.40). Some crystals had aligned plates and nanofibres on the surface (Figure 5.40a), as seen in the crystals prepared after 24 h of reaction. There were also crystals that had rod-like structures emerging from the surface (Figure 5.40 b-d). The crushed crystals showed that the shell surrounding the core $Mn_2O_3$ particle was larger than following 24 h of reaction.

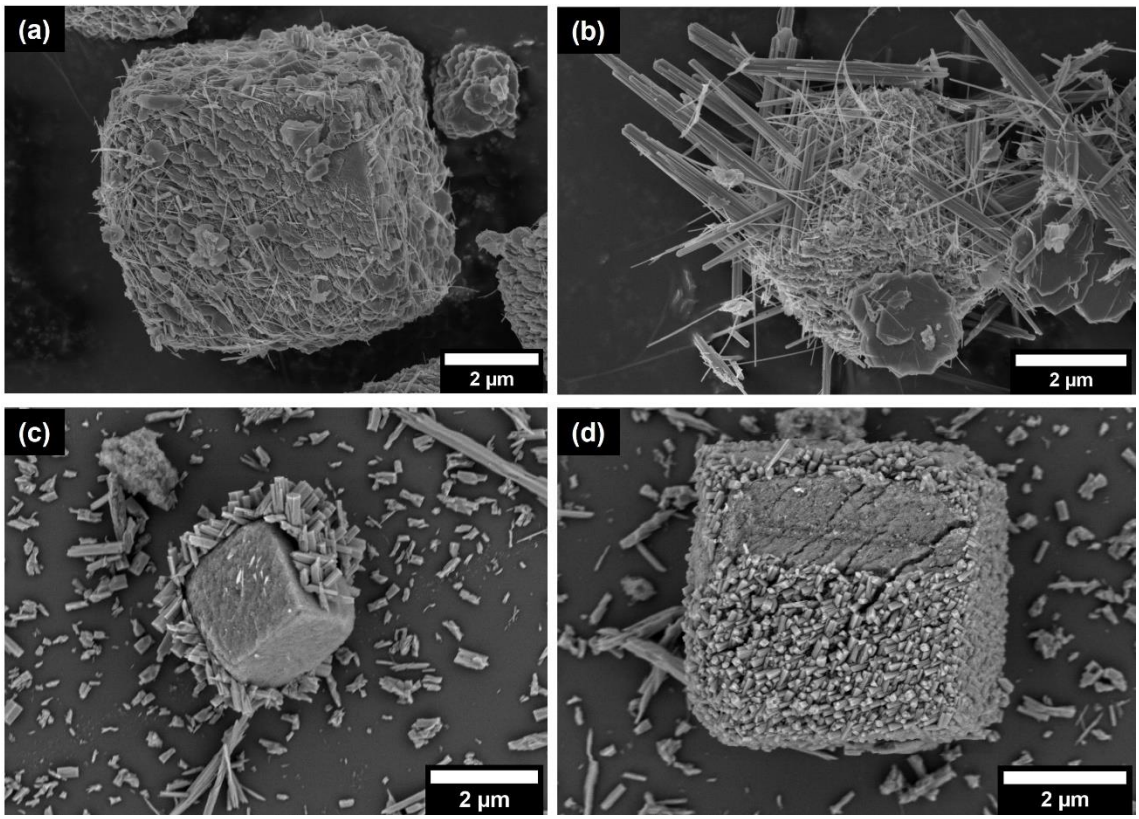


**Figure 5.40 SEM images of $MnO_2$ after 48 hours of reaction, where (c) and (d) show crushed crystals.**

The crystals obtained after 72 hours of reaction were very similar in appearance to those produced after 24 and 48 hours (Figure 5.41). However, the plate shell was thicker than observed after 24 or 48 h of reaction, at ≈ 0.8 µm.

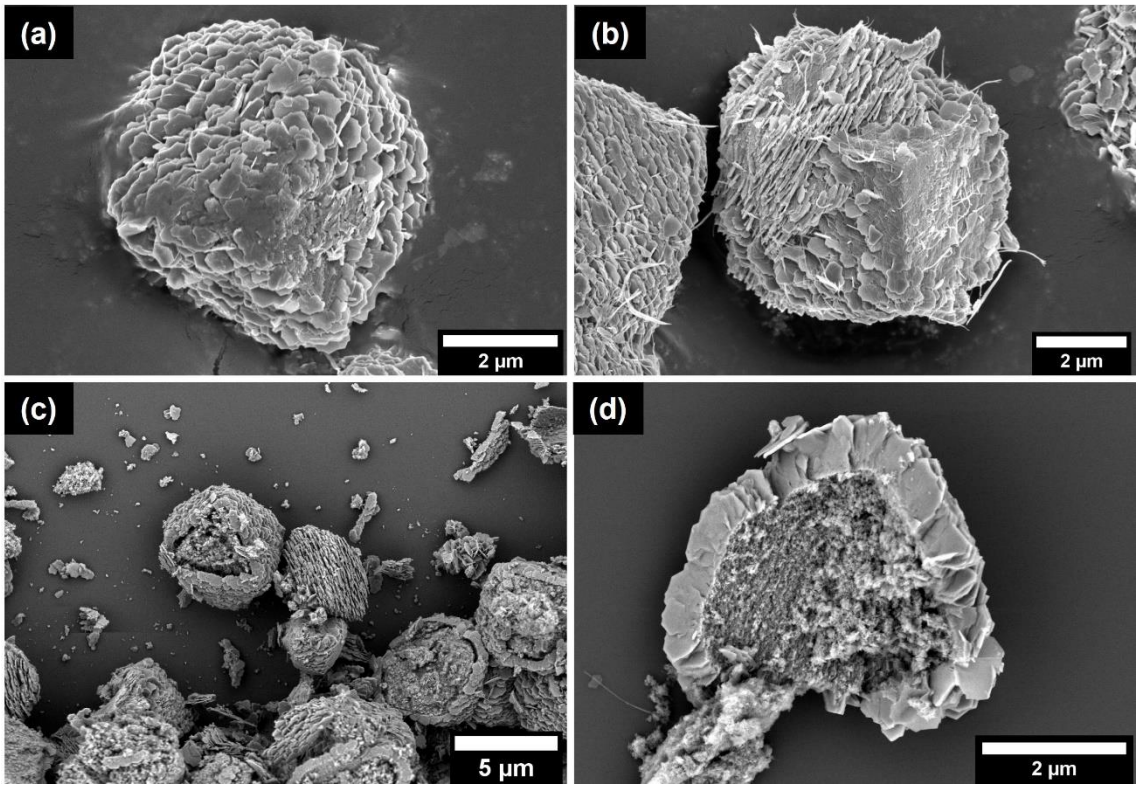


**Figure 5.41 SEM images of $MnO_2$ after 72 hours of reaction, with (c) and (d) showing crushed crystals.**

To summarise, the SEM images show that conversion of $Mn_2O_3$ to the birnessite-type δ-$MnO_2$ occurred first at the surface of the crystals and progressed into the crystal with longer reaction times. In sessile reactions, core-shell particles were formed with porous crystals of $Mn_2O_3$ at the core and shells consisting of aligned plates. The shell thickness increased with reaction time, reaching a maximum of 0.8 µm after 72 h. Stirring the reaction resulted in full conversion of $Mn_2O_3$ to birnessite type δ-$MnO_2$, and yielded nano-sheets that were formed by aggregation of nanobelts. The porosity observed in the core-shell samples produced without stirring was investigated further using BET. FIB-SEM cross-sections for image analysis were not prepared as it was challenging to mill the delicate structures without damaging them.

### 5.3.4.5 BET Analysis of $MnO_2$

The surface area of the hydrothermally synthesised $MnO_2$ compounds was studied using BET analysis (Table 5.7). After 24 h of reaction, the $MnO_2$ had a similar surface area to the starting material ($Mn_2O_3$ prepared by heating $MnCO_3$ at 450 °C

for 30 minutes at 5 °C $min^{-1}$), which was 37.7 $m^2$ $g^{-1}$. However, increasing the reaction time from 24 to 48 hours increased the surface area roughly three-fold to 115 $m^2$ $g^{-1}$. It then further increased to 139.7 $m^2$ $g^{-1}$ when the reaction time was extended to 72 hours, which was the highest surface area measured in any of the manganese oxides.

| Reaction Time | BET Surface Area / $m^2$ $g^{-1}$ |
|---|---|
| 24 hrs | 39.0 ± 3.4 |
| 48 hrs | 115.0 ± 0.2 |
| 72 hrs | 139.7 ± 0.2 |

**Table 5.7 BET analysis of $MnO_2$ samples prepared using different reaction time periods.**

#### 5.3.4.6 Synthesis of Au-$MnO_2$

Au-$Mn_2O_3$ were subjected to hydrothermal treatment for 72 h without stirring, and pXRD confirmed that Au-$MnO_2$ was obtained (Figure 5.42). The pattern obtained for Au-$MnO_2$ was very similar to that for $MnO_2$ at the same conditions, where birnessite-type δ-$MnO_2$ was made. The Au-$MnO_2$ pattern did not contain any diffraction peaks corresponding to gold, which revealed that the nanoparticles were too small to be detected. This is expected as the relatively low temperature used during the hydrothermal synthesis (170 °C) is not sufficient to induce aggregation.

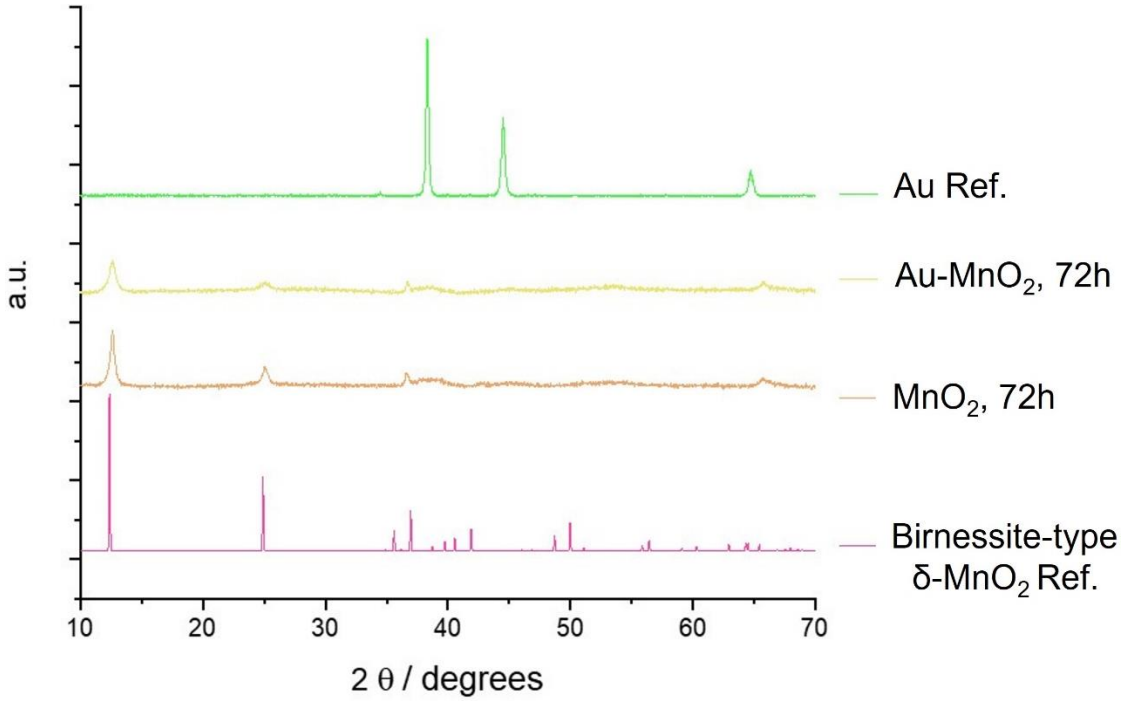


**Figure 5.42 Powder XRD patterns for Au-$MnO_2$, using references obtained from AMCSD[462] (AMCSD ID: δ-$MnO_2$ 0001300, Au 0011140).**

SEM analysis of the Au-$MnO_2$ produced after 72 hours revealed a core-shell structure (Figure 5.43). The gold nanoparticles were uniformly distributed throughout the core of the crystal as for Au-$Mn_2O_3$. However, the size of the gold particles present in the shell was larger than those in the core, indicating that aggregated clusters had formed in this layer.

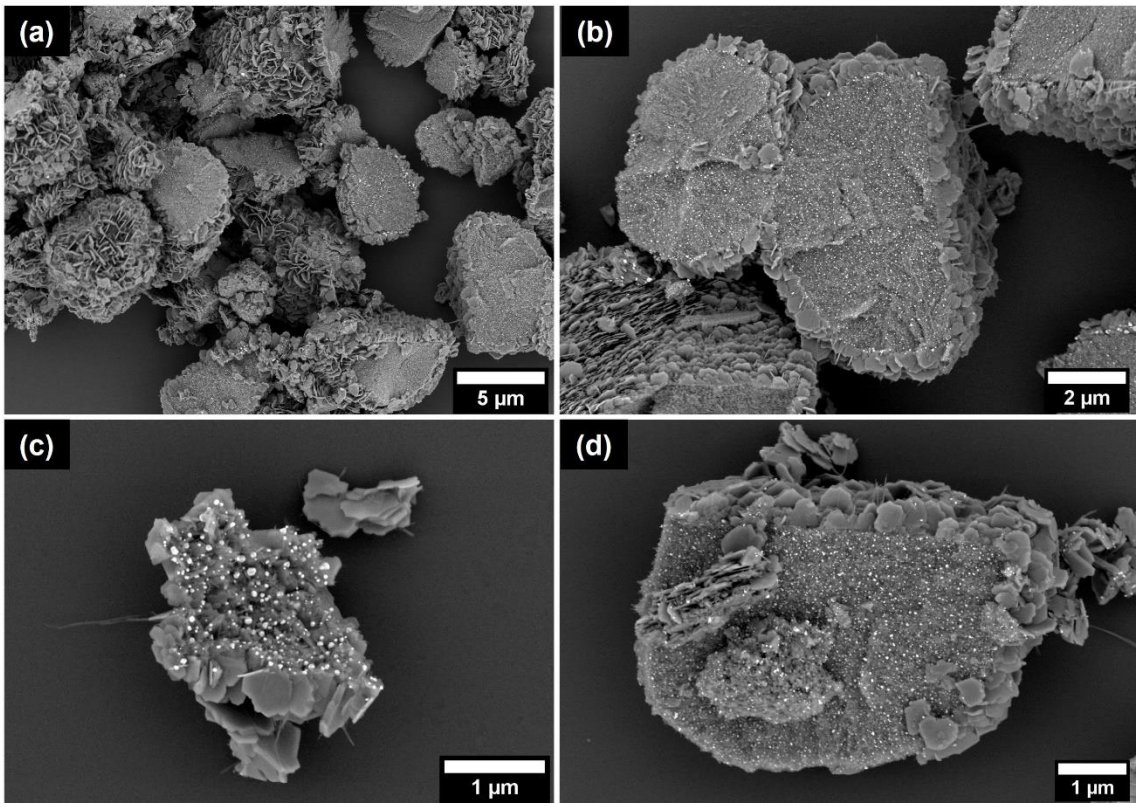


**Figure 5.43 SEM images of Au-$MnO_2$ after 72 hours, where (c) and (d) showed crushed crystals.**

### 5.3.5 Testing the Efficiency of Porous Manganese Oxides for Photocatalytic Water Splitting

The water splitting reaction was conducted using the $Mn_2O_3$ and $MnO_2$ compounds prepared previously.

#### 5.3.5.1 Control Photocatalysis Experiments

Several control experiments were performed, which included:

- No lamp; to demonstrate the light dependency of the catalysis
- No $[Ru(bpy)_3]^{2+}$ complex; to demonstrate that the light sensitizer is necessary
- No experimental catalyst; to demonstrate whether the sample being tested is effective
- $Co_3O_4$ nano-powder (commercial); to use as a well-established photocatalyst against which the experimental catalysts can be compared, and to allow the results obtained to be compared with the literature.

The control without the lamp was set up using the protocol outlined in Section 5.2.1.5, but the lamp was not switched on and the flask was left in darkness inside the isolation box. For both controls without the $[Ru(bpy)_3]^{2+}$ complex or experimental catalyst, the full buffer volume was added to the flask using the same aliquots whilst omitting the $[Ru(bpy)_3]^{2+}$ complex/experimental catalyst material.

No oxygen was produced if the lamp was left off or the $[Ru(bpy)_3]^{2+}$ co-catalyst was omitted (Figure 5.45). There was a slow decrease in oxygen over time, which is attributed to the slight loss of oxygen from the solution into the headspace of the sealed vessel. Oxygen was generated in the control experiment where no experimental catalyst was used, which has been seen in the literature and has been attributed to the formation of active $Co^{2+}$ in situ from the electron acceptor[446]. The amount of oxygen reduces over time, due to the solution-headspace equilibration. Because of this, the turnover number (TON) of the catalyst cannot be accurately established. The focus of these experiments was therefore the turnover frequency (TOF). This could be calculated from rate of the oxygen production prior to equilibration, using the fastest rate measured.

Commercial $Co_3O_4$ nano-powder was tested as a control, which consisted of 50 nm particles in micron-sized aggregates (Figure 5.44). $Co_3O_4$ is commonly used as a reference as direct comparison of data in literature is not meaningful due to differences in setup.

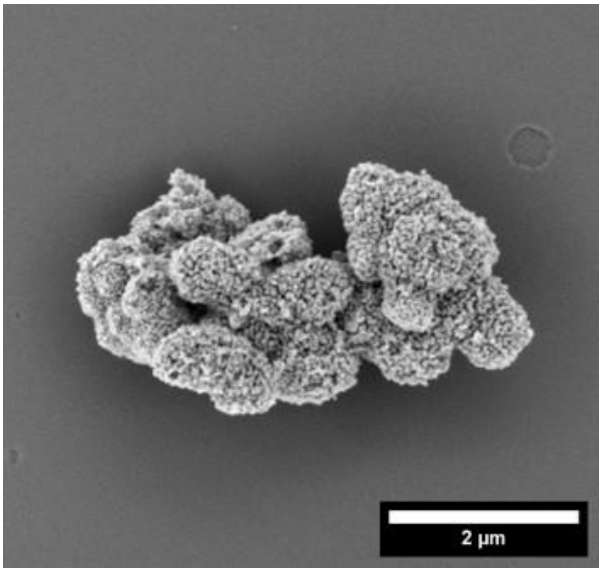


**Figure 5.44 SEM image of commercial $Co_3O_4$ nano-powder.**

The oxygen yield was measured and compared with the various control experiments (Figure 5.45). When either the $[Ru(bpy)_3]^{2+}$ co-catalyst or the lamp were omitted, no oxygen was formed. There was even a slow decline in the oxygen measured; it should be noted that the µmol measurement plotted here is the amount of $O_{2(measured)}$ subtracted from $O_{2(T0)}$, so a negative value for $O_2$ indicates a loss of any residual oxygen in the flask. This is likely due to a minor increase in temperature during measurement, which causes the solubility of oxygen to decrease. The reaction was conducted at room temperature, which was typically 20 °C, and a small increase in temperature from ≈20 to 25 °C was generally observed. This was not caused by the lamp as the control experiments excluding it also showed an increase in temperature, so it is more likely that sealing the metal isolation box around the experiment causes a gradual increase in temperature over time.

The oxygen released during the reaction without any catalyst present reached a maximum of 4.92 µmol and declined steadily after the first 10 minutes. The decline is due to the oxygen probe being held in solution. According to Le Châtelier's principle, the amount of oxygen diffusing into the atmosphere will increase to counteract the increasing amount of oxygen in solution to maintain equilibrium. This effect was reduced as much as possible by reducing the headspace within the flask. Hence, 33 ml of buffer was used in a 25 ml flask.

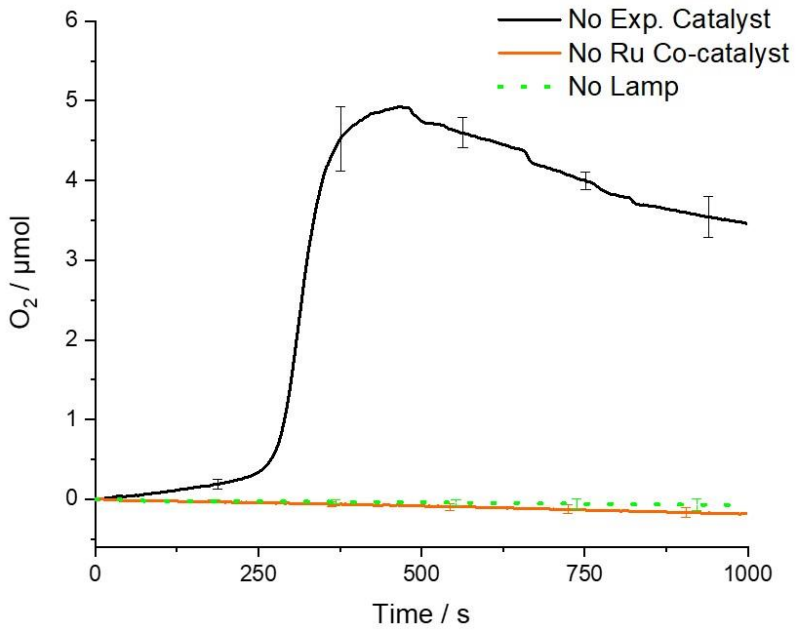


**Figure 5.45 Oxygen measurements during water oxidation using the control conditions.**

The experiment was also conducted using commercial $Co_3O_4$ nano-powder (Figure 5.46). This yielded a maximum of 5.29 µmol oxygen. The amount of oxygen generated was comparable to that found by Duan *et al.*[446], who measured a maximum of 4.96 µmol oxygen using gas chromatography, with the same co-catalyst system and a ruthenium complex as their experimental catalyst.

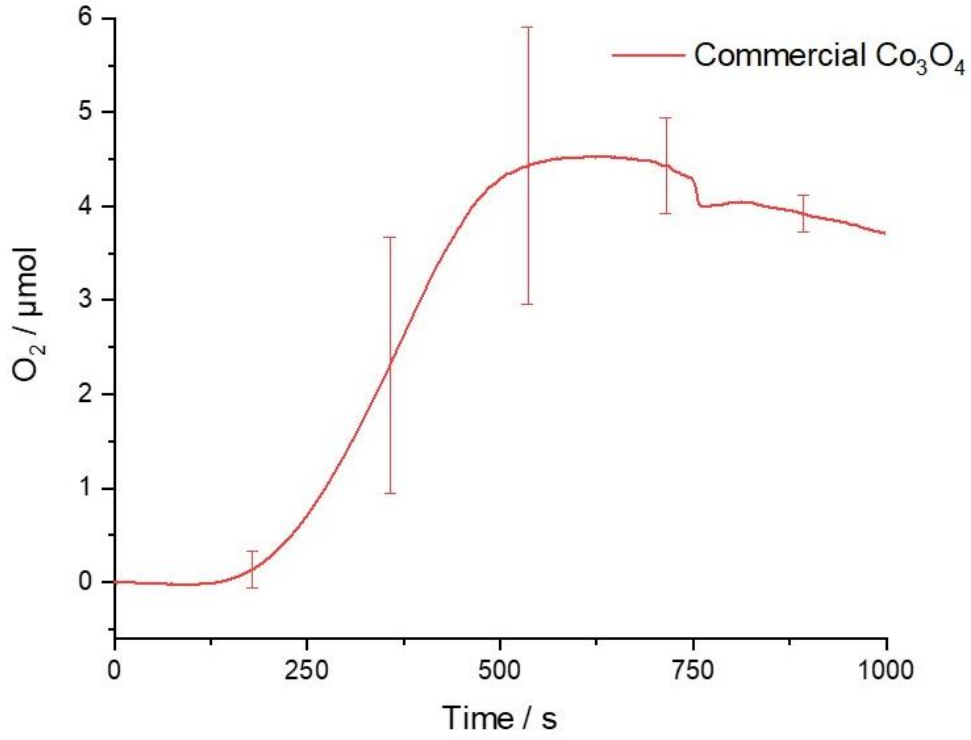


**Figure 5.46 Oxygen measurements during water oxidation using commercial $Co_3O_4$ nano-powder.**

### 5.3.5.2 $Mn_2O_3$ and Au-$Mn_2O_3$ Photocatalysis Experiments

The $Mn_2O_3$ samples that were prepared using 1, 5 and 10 °C $min^{-1}$ heating rates were tested, as shown in Figure 5.47. Overall, there was little difference between the catalytic performances. The $Mn_2O_3$ prepared at 1 °C $min^{-1}$ yielded less oxygen than those samples prepared at 5 and 10 °C $min^{-1}$ (which were very close in performance to each other), but this was not significant due to the considerable overlap in error bars.

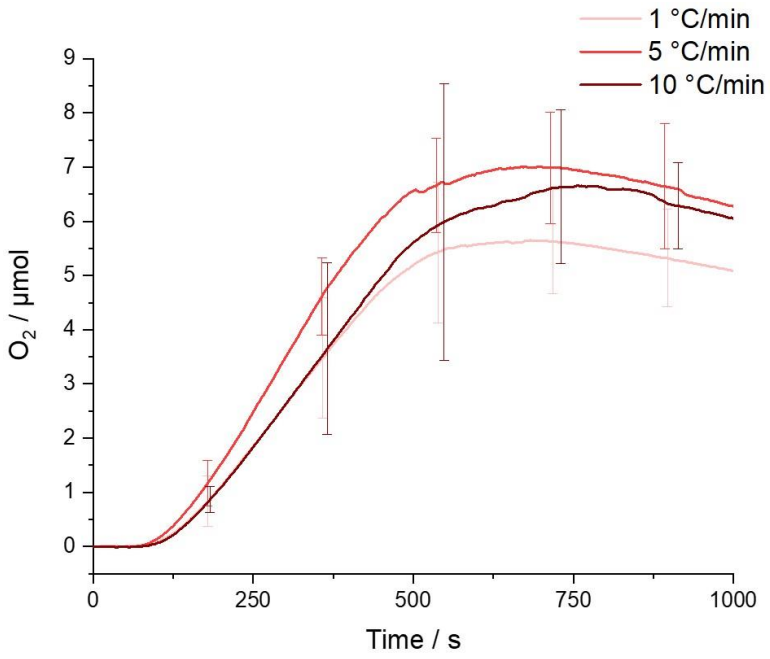


**Figure 5.47 Oxygen measured during water oxidation using $Mn_2O_3$ heated at different rates.**

The $Mn_2O_3$ prepared using different temperatures were tested, and those heated for different lengths of time were compared (Figure 5.48). The trend in oxygen produced was the same for both heating times used; $Mn_2O_3$ prepared at 550 °C yielded the most oxygen, with the 500 and 600 °C samples being indistinguishable from each other. The 450 °C sample produced the least oxygen. Increasing the heating time boosted the oxygen yield for all $Mn_2O_3$ samples, although this was very small for 450 °C. This indicated that extending the heating time had the greatest effect on the samples prepared using 500 °C or higher.

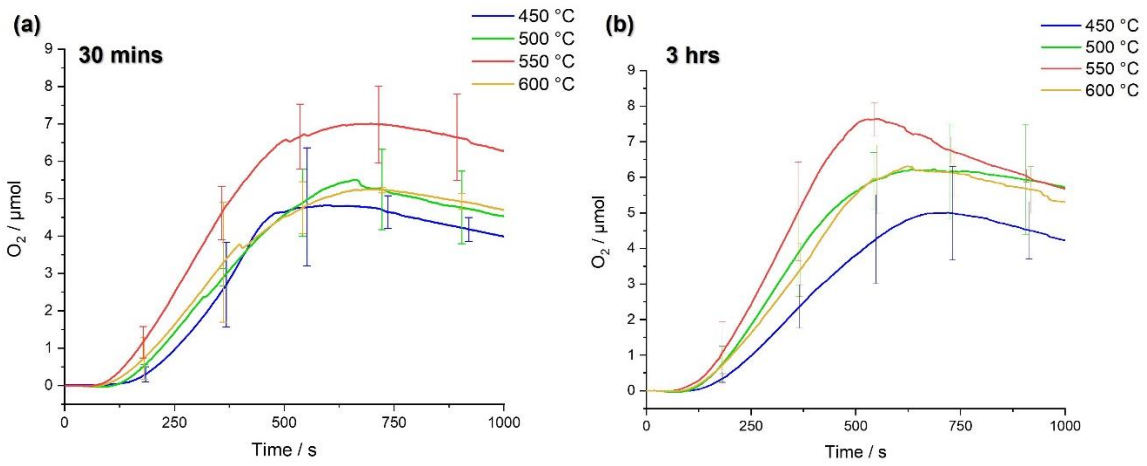


**Figure 5.48 Oxygen measured during water oxidation using $Mn_2O_3$ prepared using different temperatures with both 30 min and 3 hr heating periods.**

Although the oxygen yield provided a general indication of the catalyst's performance, establishing the catalytic efficiency in terms of each active site is essential[472]. Therefore, the turnover frequency (TOF) was calculated for the $Mn_2O_3$ samples (Figure 5.49). The TOF is defined as the number of moles of $O_2$ produced per second per active metal (Mn) site.

Examining first the effect of the heating temperature on the TOF, the trend was the same as for the oxygen yield, where increasing the temperature resulted in faster TOF values to a maximum at 550 °C. The TOF values were very similar for the 500 and 600 °C samples, whereas the 450 °C samples were much slower, regardless of the heating time used. The effect of the heating time period was the same as for the oxygen yield, with the extension of the heating time to 3 hours resulting in faster TOF values for all temperatures trialled. The TOF values for $Mn_2O_3$ prepared using different heating rates were very similar.

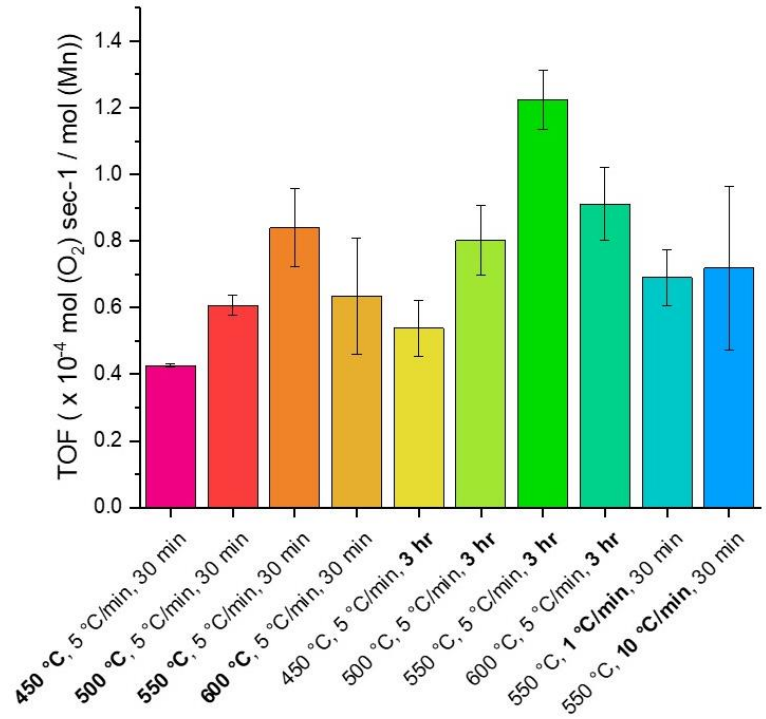


**Figure 5.49 Turnover frequency (TOF) data for $Mn_2O_3$ samples prepared using different heating conditions**

The quantum yield was also calculated. This is a measure of the catalytic efficiency that takes into account the incident photons and is calculated in terms of the oxygen yield per 4 photons (as 4 photons are required to produced 1 $O_2$ molecule). The quantum yield (QY) calculations obtained for $Mn_2O_3$ showed a very similar trend as the TOF calculations and reached values of 9 – 14 % (Figure 5.50).

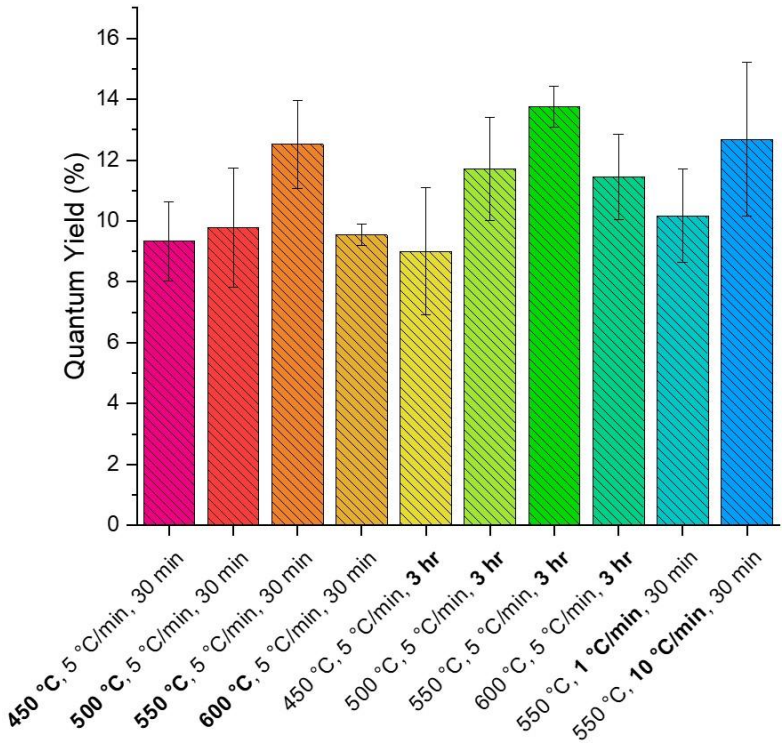


**Figure 5.50 Quantum yield (%) data for $Mn_2O_3$ samples prepared using different heating conditions.**

Au-$Mn_2O_3$ was tested as a photocatalyst to determine whether the presence of the noble metal within $Mn_2O_3$ might boost the catalytic performance. Firstly, the oxygen yield was compared with the analogous $Mn_2O_3$ samples (Figure 5.51). Initial tests were conducted with 20 mg Au-$Mn_2O_3$, as for $Mn_2O_3$ samples. Further testing was conducted using 28 mg, in order to account for the mass of the occluded gold nanoparticles and ensure that the same number of moles of $Mn_2O_3$ were used.

The oxygen yield was much lower for the Au-$Mn_2O_3$ compounds than the corresponding $Mn_2O_3$ compounds. The oxygen produced by Au-$Mn_2O_3$ increased when the annealing temperature increased from 550 to 600 °C. Interestingly, increasing the mass of sample used such that the same number of moles of $Mn_2O_3$ were present reduced the oxygen yield.

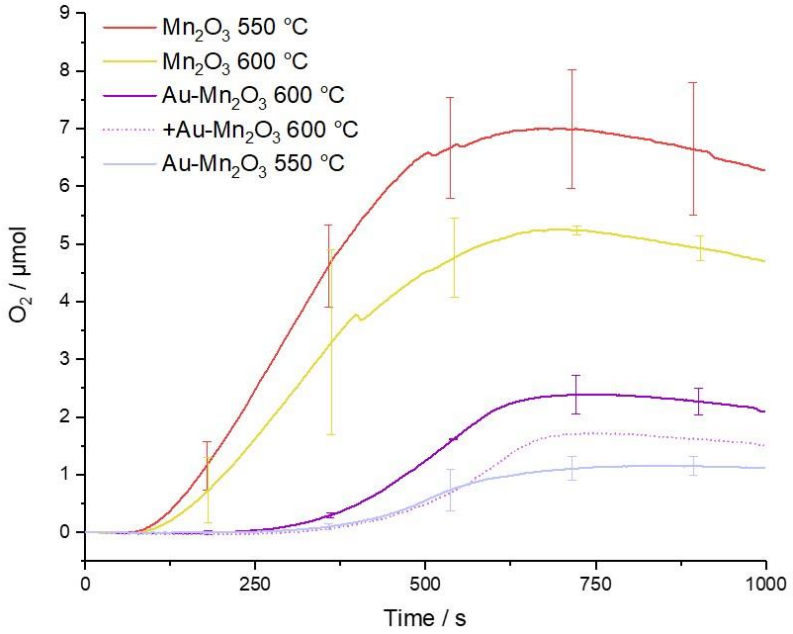


**Figure 5.51 Oxygen measured during water oxidation using Au-$Mn_2O_3$ as a photocatalyst, where +Au-$Mn_2O_3$ indicates that a larger mass was used to take into account the gold content, compared with $Mn_2O_3$.**

The TOF values for Au-$Mn_2O_3$ were also calculated and are presented in Figure 5.52. The different masses of Au-$Mn_2O_3$ used were taken into account when calculating the TOF value for 600 °C. The Au-$Mn_2O_3$ compounds generally had lower TOF values than the analogous $Mn_2O_3$ compounds. Increasing the temperature from 550 to 600 °C slightly increased the TOF values for Au-$Mn_2O_3$. However, this is tenuous due to the large error bars for the 600 °C sample.

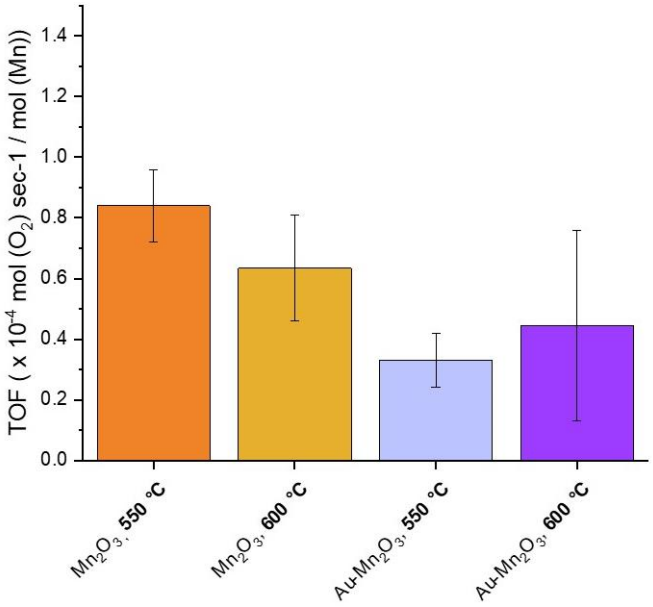


**Figure 5.52 Turnover frequency (TOF) data for Au-$Mn_2O_3$ compounds compared with their $Mn_2O_3$ equivalents.**

A similar trend could be observed in the quantum yield calculations (Figure 5.53), which was much lower for Au-$Mn_2O_3$ than $Mn_2O_3$. The QY was severely diminished for Au-$Mn_2O_3$ after heating to 600 °C and reached only 0.02%, compared to 10 – 12 % for $Mn_2O_3$.

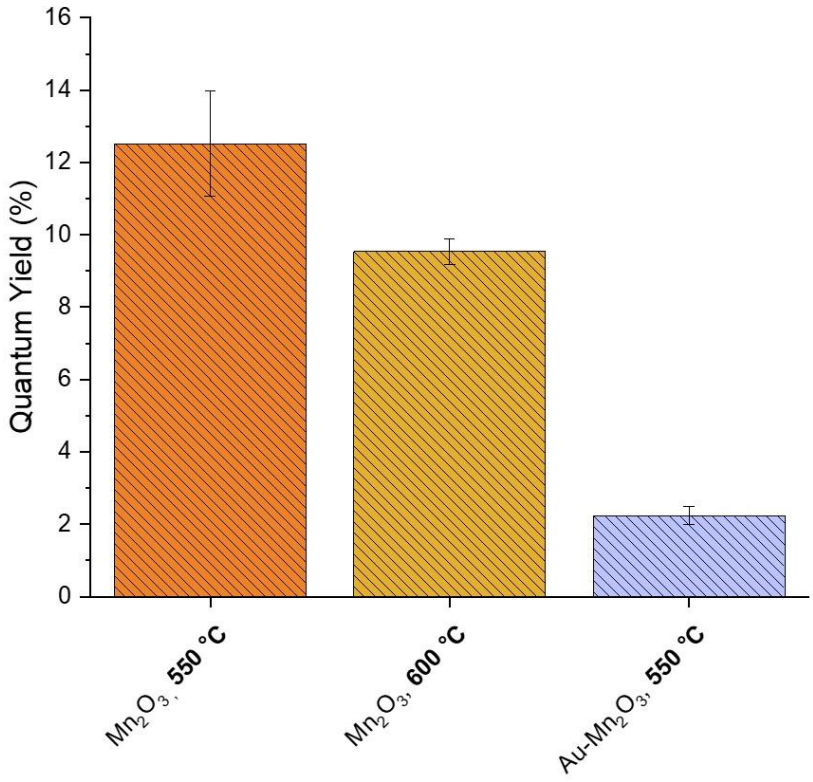


**Figure 5.53 Quantum yield (QY) data for Au-$Mn_2O_3$ compounds compared with their $Mn_2O_3$ equivalents. Au-$Mn_2O_3$ heated at 600 °C (not shown) had a QY of 0.02 ± 0.004 %.**

### 5.3.5.3 $MnO_2$ and Au-$MnO_2$ Photocatalysis Experiments

The photocatalytic properties of the $MnO_2$ and Au-$MnO_2$ compounds were also tested and their oxygen yields were measured (Figure 5.54). The two $MnO_2$ samples had very similar maximum oxygen yields of 1.7 µmol, which were significantly lower than the oxygen yields seen previously for $Mn_2O_3$ (4 – 8 µmol). The Au-$MnO_2$ yielded very little oxygen (0.7 µmol), which was the lowest of any experimental samples tested.

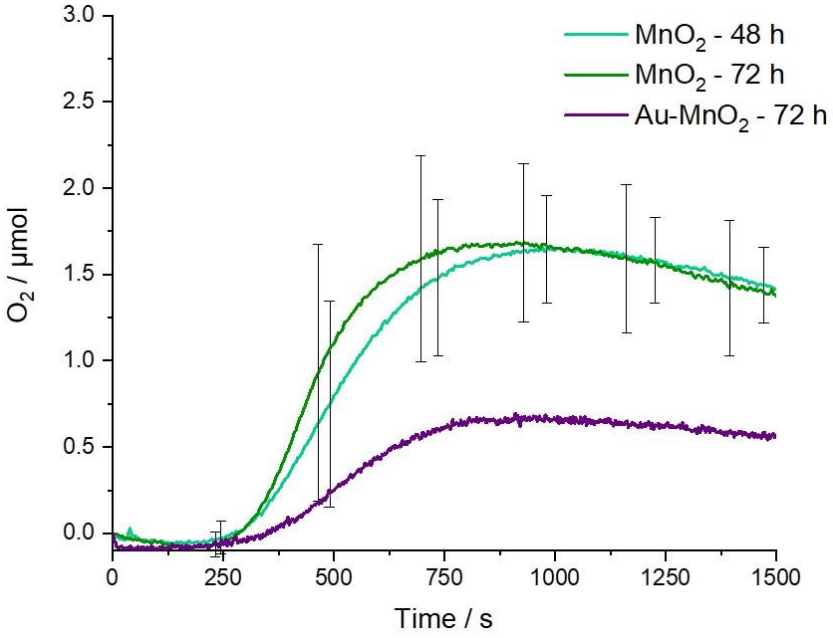


**Figure 5.54 Oxygen measured during water oxidation using $MnO_2$ and Au-$MnO_2$ compounds as photocatalysts.**

The TOF values were also calculated for $MnO_2$ and Au-$MnO_2$, as shown in Figure 5.55. As for the maximum oxygen yields, the TOF values for the two $MnO_2$ samples were very similar. The TOF value obtained for Au-$MnO_2$ was the slowest rate measured.

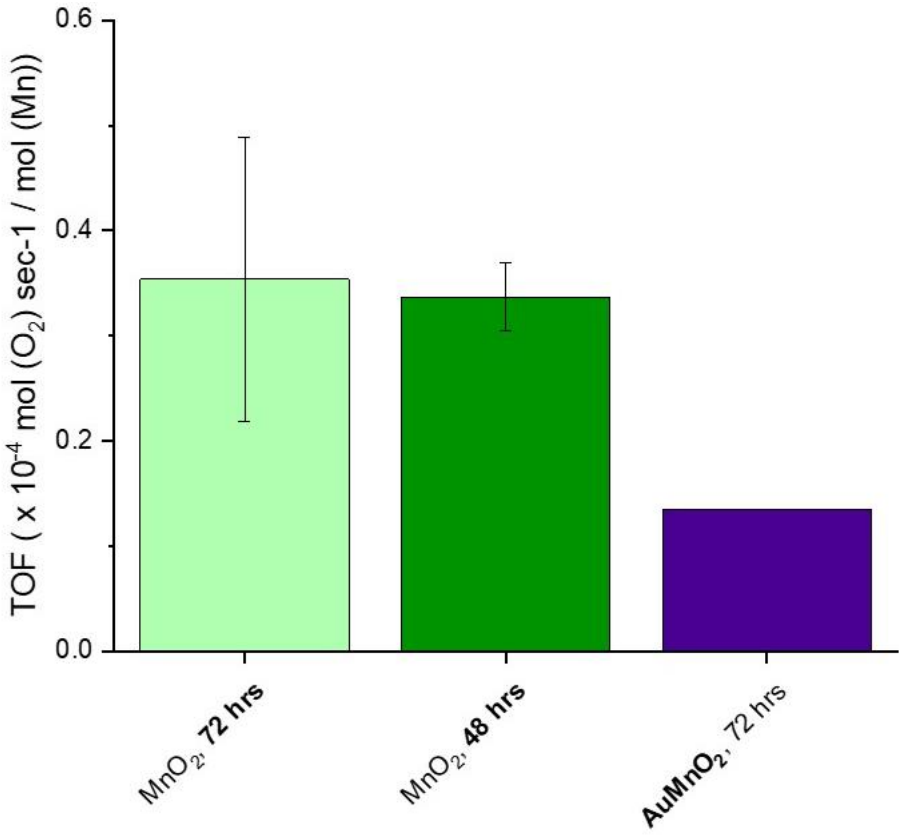


**Figure 5.55 Turnover frequency (TOF) data for $MnO_2$ and Au-$MnO_2$ compounds.**

The same trend seen in the TOF data was observed for the quantum yield (Figure 5.56). Overall, the quantum yield was very low, reaching only 3 % for $MnO_2$ regardless of the reaction time and 1.3 % for Au-$MnO_2$.

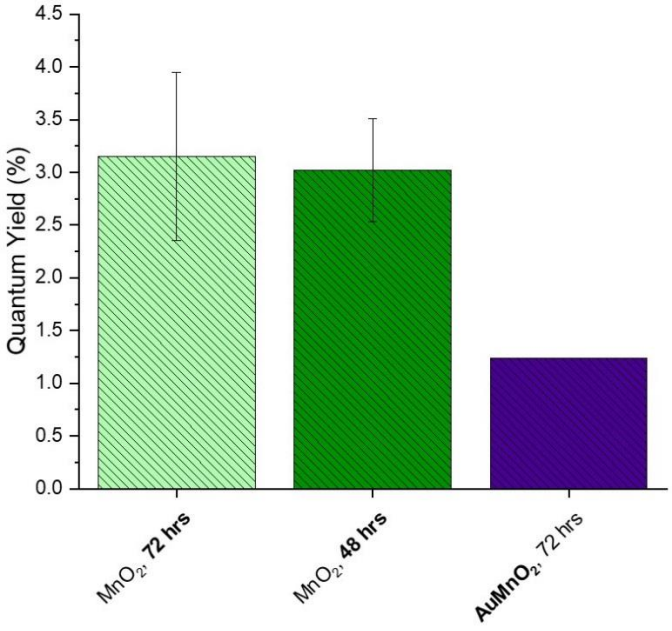


**Figure 5.56 Quantum yield (QY) measurements for $MnO_2$ and Au-$MnO_2$ compounds.**

## 5.4 Discussion

In this project, crystals of $MnCO_3$ were synthesised and annealed using a range of heating parameters to create porous $Mn_2O_3$ crystals. The porosity forms due to the difference in molar volume between $MnCO_3$ and $Mn_2O_3$, which is smaller for the oxide[463]. $CO_2$ is released during the transformation and the porous structure facilitates the expulsion of the gas from the crystal. The parameters used during thermal decomposition are crucial in determining which oxide is produced but also due to their effect on the porosity.

As the mismatch in molar volume between the oxide and carbonate induces strain in the lattice, recrystallisation can occur via adhesion, surface diffusion or bulk diffusion to restore stability[465]. Wüttig deduced that the recrystallisation mechanism for a given system depended on α, the ratio between the experimental temperature used to heat the crystal (T) and the melting point of the substance ($T_m$), giving the relationship $\alpha = T / T_m$[473]. Recrystallisation via adhesion occurs at $\alpha < 0.2$, which describes the coalescence of neighbouring crystallites of converted material. Surface diffusion is predominant at $\alpha \approx 0.2 – 0.4$, where ions of the converted material can be transported across surfaces to increase stability. Bulk diffusion requires a higher

activation energy, so only at $\alpha > 0.5$ is movement of the ions through the bulk lattice permitted.

The α value for $Mn_2O_3$ prepared by heating at 450 and 500 °C is $\alpha = 0.42$ and 0.46 respectively, indicating that the recrystallisation occurred via surface diffusion for these samples. For $Mn_2O_3$ prepared at 550 and 600 °C, the corresponding α value was 0.51 and 0.56, which is sufficiently high for bulk diffusion to proceed. This can explain the differences in porosity observed between the two sets of temperatures and surface area. The coalescence of the crystallites during heating, known commonly as sintering, allows the stability of the lattice to be restored while the surface area is decreased[465]. This correlates with the surface area values measured using BET, which decreased with temperature, and also the increase in pore size with temperature as measured via image analysis of FIB-SEM cross-sections.

Although increasing the temperature allows different mechanisms to become viable, extension of the heating time only permits further progress of the decomposition[465]. Porous $Mn_2O_3$ crystals produced using a long heating time (3 hours) led to larger pore sizes (as measured by image analysis) and BET surface areas. This is likely due to greater numbers of open pores forming during sustained heating, compared to closed pores formed after a short heating burst which therefore cannot contribute towards the surface area. The heating rate did not have as strong an influence on porosity as the temperature or time that the crystals were heated for. The BET surface area was very similar for $Mn_2O_3$ samples formed at different heating rates, while image analysis showed that the slowest rate (1 °C $min^{-1}$) generated larger pores and higher pore densities than the other rates. This is likely due to the longer times that the samples experience high temperatures when slow heating rates are used.

Another manganese oxide, $MnO_2$, was synthesised as a potential water splitting catalyst that could be compared against the range of porous $Mn_2O_3$ crystals. A hydrothermal route was used to form $MnO_2$ as it could not be isolated during thermal decomposition of $MnCO_3$ in aerobic conditions. $MnO_2$ core-shell particles were obtained for all reaction times trialled. The shell consisted of plate or rod-like crystals which encased a porous crystalline core very similar in appearance to the unreacted $Mn_2O_3$ crystals.

The same synthesis routes were used with gold-occluding $MnCO_3$ crystals to yield Au-$Mn_2O_3$ and Au-$MnO_2$. Thermal decomposition led to aggregation of the gold nanoparticles which worsened at higher temperatures. This was evidenced by analysis of the Au-$Mn_2O_3$ cross-sections and also the presence of large gold peaks in the pXRD patterns obtained for both Au-$Mn_2O_3$ samples, which are not present in the patterns for Au-$MnCO_3$ due to their small size. However, less aggregation occurred in Au-$MnO_2$, as evidenced by the absence of gold peaks in pXRD patterns. SEM images of crushed Au-$MnO_2$ showed well-distributed gold nanoparticles throughout the core with some aggregates limited to the inner surface of the shell.

The porous $Mn_2O_3$ crystals formed using different heating regimes had varying photocatalytic efficiencies for the water splitting reaction. The catalytic turnover frequency (TOF) increased with annealing temperature and was maximal at 550 °C. This trend in temperature was observed whether the crystals were heated for 30 minutes or 3 hours. The heating time itself also influenced the TOF; $Mn_2O_3$ crystals heated for 3 hours had higher TOFs than those heated for a shorter time.

As discussed in the introduction to the chapter, there are a number of key properties that are imperative for efficient photocatalysis by powder semi-conductors, such as crystallinity and the oxidation state of the active metal. A high degree of crystallinity can reduce the number of defects within the lattice, which is particularly important in photocatalyst materials as both bulk and surface defects such as dislocations, vacancies and grain boundaries are thought to provide recombination sites for electron-hole pairs. A large surface area is also crucial as water is oxidised on the surface of the metal oxide, and so high surface areas provide more active sites for this oxidation step to occur at. The annealing temperature used to form the oxide had an effect on both the crystallinity and composition of the manganese oxide, and so can explain some of the trends in catalytic ability. $Mn_2O_3$ prepared at 450 °C for 30 minutes had the lowest TOF values and the broad pXRD peaks present in these samples indicated that they were less crystalline than those formed at higher temperatures. There also appeared to be a small amount of $MnCO_3$ in samples prepared at ≤ 500 °C, which could explain the low TOF values obtained for these samples despite their relatively high surface areas. On the other hand, the difference in TOF between samples heated for different lengths of time is likely due to the greater surface area exhibited by $Mn_2O_3$ heated for 3 hours.

The Au-$Mn_2O_3$ catalysts had lower TOFs than the other $Mn_2O_3$ samples, indicating that the presence of the gold particles reduced the catalytic efficiency. This is in agreement with the work of Kuo *et al*., who found that Au nanoparticles offered no enhancement in $Mn_2O_3$, due to their catalytic role being the promotion of $Mn^{3+}$ formation, while $Mn_2O_3$ already exists in the 3+ oxidation state[424].

δ-$MnO_2$ and Au-$MnO_2$ were also poor photocatalysts for water splitting due to their low TOF values, which were lower than any of the $Mn_2O_3$ catalysts trialled. The poor activity of δ-$MnO_2$ concurs with the results of Kuo *et al.*[424] and Robinson *et al.*[403]. One possibility could also be that the intercalation of $Na^+$ in the birnessite-type δ-$MnO_2$ during synthesis worsened the behaviour. However, Boppana *et al.* showed that the catalytic activity of Na-δ-$MnO_2$ was similar to K-δ-$MnO_2$ and better than H-δ-$MnO_2$ due to the stability offered by the cations[474]. The afore-mentioned study by Kuo *et al.* showed that the catalytic properties of δ-$MnO_2$ were vastly improved by doping with small levels of Au nanoparticles[424], whereas Au-$MnO_2$ performed slightly worse than pure $MnO_2$ in the present work.

This could be due to a number of factors. The SEM images of Au-$MnO_2$ showed that the Au particles were distributed evenly throughout the core particle but were limited to the inner boundary of the shell particle, so the interfacial sites between Au and $MnO_2$ were not accessible for mediation of electron-transfer processes, i.e. the oxidation of water molecules and reduction of $[Ru(NH_3)_5Cl]^{3+}$ . Interfacial Au-$MnO_2$ sites were identified by Seitz *et al.* as being highly active in water splitting and their accessibility was found to be crucial for enhancement of the catalytic activity[426].

In the present work, Au-$MnO_2$ was synthesised from Au-$MnCO_3$ with a very high Au loading of 40 wt.% compared to the low doping amounts used in literature, where increasing the amount of doped Au from 0.9 – 5.8 % did not cause an increase in catalytic activity[424]. The increased density of the Au nanoparticles combined with their inaccessible locations within the $MnO_2$ crystals could lead to their increased activity as electron traps, encouraging transfer of the electrons within the crystal instead of with water molecules and co-catalysts. As efficient transfer of the electrons is required for recycling of the photosensitiser, problems in this process leads inevitably to early termination of the reaction. Alternatively, as the oxidation of water occurs due to the loss of an electron from metal oxide as it restores $[Ru(NH_3)_5Cl]^{3+}$ to $[Ru(NH_3)_5Cl]^{2+}$, it could be possible that the high density of Au

nanoparticles allows the $MnO_2$ oxidation state to be rapidly regenerated and reduces the likelihood of adsorbed water molecules becoming oxidised.

The limitations of the photocatalytic measurement setup should also be considered. The positioning of the optical probe made it difficult to measure the total oxygen yield due to loss of oxygen into the headspace. Ideally, a setup could be produced where the oxygen produced could be flushed through a gas chromatography setup. This would have to be done using a spectrometer to record oxygen levels throughout the reaction, in order to follow the production over time and generate TOF data. As flushing through to the GC also results in a drop in oxygen levels, it would have to be carefully set up to flush at the end without losing any of the oxygen collected.

## 5.5 Conclusions

In this chapter, $Mn_2O_3$ and $MnO_2$ were synthesised under different reaction conditions to create a range of manganese oxides with different morphologies and porosities. Porous $Mn_2O_3$ crystals were produced via thermal decomposition of $MnCO_3$ due to the difference in the molar volume between the two compounds. The resulting instability of the lattice is resolved by recrystallisation of the converted material, which can proceed via different mechanisms with different activation energies. The temperature used to convert $MnCO_3$ into $Mn_2O_3$ was therefore fundamental in determining the recrystallisation mechanism; higher temperatures facilitated bulk diffusion while surface diffusion was predominant at low temperatures. The heating time determined the extent of the reaction, where longer heating times led to the formation of larger, open pores compared to the small, closed pores that were obtained by heating for short bursts. The heating rate had little effect on the properties of the $Mn_2O_3$ formed.

A hydrothermal route was used to synthesise core-shell birnessite-type δ-$MnO_2$ particles, which consisted of porous crystalline cores encased in a shell of plate-like crystals. These crystals had high surface areas which increased with the length of the reaction. Both the synthesis of $Mn_2O_3$ and $MnO_2$ could be replicated using $MnCO_3$ incorporated with gold nanoparticles to yield Au-$Mn_2O_3$ and Au-$MnO_2$. Although the thermal decomposition route resulted in aggregation of the gold nanoparticles, this effect was lessened by synthesising Au-$MnO_2$ using a hydrothermal route.

Evaluation of the catalytic efficiencies of the manganese oxides for the water splitting showed that the most effective catalysts were $Mn_2O_3$. The catalytic efficiency relied both on the composition and surface area of $Mn_2O_3$. Residual $MnCO_3$ was a disadvantage for $Mn_2O_3$ prepared at low temperatures, while the larger surface areas exhibited by $Mn_2O_3$ annealed for 3 hours was advantageous for catalysis. The catalytic performance of $MnO_2$ was much lower than that of $Mn_2O_3$, due to the less active $Mn^{4+}$ present in $MnO_2$. The presence of Au nanoparticles worsened the catalytic abilities of both $Mn_2O_3$ and $MnO_2$, indicating that the gold particles may be acting as electron sinks and preventing adequate recycling of the electrons as required for sustained oxygen generation.

# Chapter 6 | Conclusions and Outlook

In the work described in this thesis, crystallisation strategies were used to produce composite crystals with the ultimate aim of imparting advantageous properties suitable for applications such as structurally coloured pigments and water splitting catalysis. The carbonation reaction of $Ca(OH)_2$ was also investigated using a range of electron microscopy techniques to gain insight into the underlying mechanism.

In Chapter 3, porous calcite was produced by occluding organic additives such as amino acids and polymeric beads and subsequently removing them via thermal decomposition. The heating parameters used to remove the additives were highly influential on the pore size distribution, where high temperatures and long heating times led to the formation of large pores. The porosity was also influenced by the choice of additive and the incorporation efficiency, which impacted both the pore size distribution and the filling fraction of the pores. Porous calcite single crystals possessed enhanced scattering capabilities compared to non-porous calcite, with several samples exhibiting excellent broadband reflectance of > 70 %. This was achieved by incorporating Asp, Gly, and di-block copolymer vesicles, where optimisation of both incorporation and thermal decomposition could be used to tune the scattering properties of the product crystals. It was demonstrated that a pore size of 50 – 500 nm was optimal to ensure that scattering could occur, and that a broad size distribution within this range was favourable. Complete removal of the occluded additive was essential for avoiding undesired absorbance, which could be ensured by choosing small molecules or vesicles as additives. Overall, the straightforward synthesis of highly scattering calcite represents an exciting step towards offering feasible, safe alternatives to white pigments such as $TiO_2$.

This work could be further developed to study alternative host crystals such as calcium oxalate ($CaC_2O_4.H_2O$), gypsum ($CaSO_4$), and zinc oxide (ZnO). Alternative organic additives could also be used, provided that they can incorporate within a host crystal and have compatible thermal decomposition properties. Finally, the generation of porosity is associated with a reduction in the density of the host crystal. This was not explored in this work but is an attractive pursuit for manufacturers of crystalline materials, due to the increased volume that could be transported and thus distributed.

In Chapter 4, the mechanism underlying the carbonation reaction of $Ca(OH)_2$ was studied using a range of electron microscopy techniques. The effect of $[Ca^{2+}]/[CO_3^{2-}]$ on the morphology of calcite was observed using time-resolved cryo-TEM, where scalenohedral calcite was prevalent in environments with excess $[Ca^{2+}]$ and became more rhombohedral-like when $[CO_3^{2-}]$ was increased. The findings from cryo-TEM were correlated with dynamic LCTEM studies, which showed that the underlying carbonation reaction occurs via a dissolution-precipitation pathway. Hexagonal, skeletal structures formed during dissolution, which were attributed to the pseudomorphic replacement of the basal $Ca(OH)_2$ faces by ACC. The evidence gleaned from the TEM studies provides strong support for the growing consensus that the carbonation of $Ca(OH)_2$ in solution proceeds by dissolution of $Ca(OH)_2$, which rapidly precipitates ACC pseudomorphically. This is followed by further dissolution and precipitation of scalenohedral calcite. The effect of two common PCC additives, citric acid and gypsum, on the early stages of the carbonation reaction was also examined. Both additives were highly influential, where gypsum slowed $Ca(OH)_2$ dissolution and citric acid stabilised ACC. In summary, this work provides new insight into the mechanism of formation of PCC and the influence of additives on this process. The understanding gained is crucial for improving the manufacturing process and control over PCC properties, which can improve its suitability for a diverse range of applications. This work also demonstrates that correlative static and dynamic TEM techniques can be highly valuable in characterising crystallisation mechanisms.

Future work in this area could include investigation of other additives commonly used in PCC synthesis, and the use of LCTEM to study their effects. There are a wide range of additives utilised by PCC manufacturers and while this has obvious industrial importance, the exact influence of such additives is not well understood. Some of the limitations of this study could also be addressed. Sophisticated methods of spray plunge-freezing after rapid mixing times would directly improve the time resolution of the cryo-TEM work performed here due to the sensitivity of the $Ca(OH)_2$ suspension to air. Finally, the effect of additives such as citric acid and gypsum could be further investigated and quantified using in-flow, time-resolved XRD and Raman spectroscopy. This would allow the intermediate species produced during the

carbonation reaction to be characterised, and the influence of additives on the lifetimes of intermediate species to be qualitatively assessed.

In the final research chapter, porous manganese oxides were produced from precipitated $MnCO_3$ crystals to investigate their catalytic abilities in photocatalytic water splitting. $Mn_2O_3$ crystals were produced by thermal decomposition of $MnCO_3$, where the composition, crystallinity and porosity could be tuned by careful control of the heating parameters, which determined whether the recrystallisation occurred via a surface or bulk diffusion mechanism. The highest surface areas were achieved in crystals that recrystallised via a surface diffusion mechanism, which occurred using temperatures of 450 and 500 °C, whereas the surface area decreased in samples heated at 550 and 600 °C where bulk diffusion is predominant. This highlighted that the recrystallisation mechanism was key to producing desirable porosity properties, as bulk diffusion causes sintering and larger pores are produced. Highly porous core-shell birnessite type δ-$MnO_2$ was produced by a hydrothermal synthesis route, where the surface area could be increased by extending the reaction time. Au-$Mn_2O_3$ and Au-$MnO_2$ was similarly synthesised by using gold nanoparticle occluding $MnCO_3$ crystals, where the nanoparticles were uniformly distributed throughout the host crystal. The $Mn_2O_3$ crystals had the greatest catalytic efficiency, where samples with higher crystallinity and surface areas demonstrated faster turnover frequencies. Manganese oxides with occluded gold nanoparticles exhibited disappointing photocatalytic abilities which were lower than the gold-free catalysts. This can be attributed to poor recycling of the electrons generated by co-catalysts, where the gold nanoparticles may be acting as electron sinks that facilitate recombination of the charge carriers and prematurely terminate the water splitting reaction. This chapter therefore delivered straightforward strategies for preparing porous $Mn_2O_3$ crystals, where the approach could be extended to generate compositionally and structurally more complex $Mn_2O_3$ crystals based on the initial synthesis of $MnCO_3$ composite single crystals occluding noble metal nanoparticles.

The work detailed in the final chapter could be readily extended to synthesise porous manganese oxides containing alternative nanoparticles of noble metals with potential for photocatalysis, such as platinum or silver. It would also be interesting to explore nanoparticles with different sizes. The limitations of the water splitting setup could be improved by incorporating gas chromatography to improve the accuracy of the total

oxygen yield. Notably, only the birnessite-type δ- phase of $MnO_2$ was synthesised in this work, so other phases such as the α- and β- phases could be trialled, since these have been previously highlighted as potential photocatalysts. Other applications for the porous manganese oxides produced in this chapter could also be explored, such as water treatment, energy storage and other catalytic systems.

## Chapter 7 | References


1. Lee, A.Y., Erdemir, D. and Myerson, A.S. Crystals and Crystal Growth. In: Lee, A.Y. et al. eds. *Handbook of Industrial Crystallization*. 3 ed. Cambridge: Cambridge University Press, 2019, pp.32-75.
2. Lee, E.H. A practical guide to pharmaceutical polymorph screening & selection. *Asian Journal of Pharmaceutical Sciences.* 2014, **9**(4), pp.163-175.
3. Shi, Q., Chen, H., Wang, Y., Xu, J., Liu, Z. and Zhang, C. Recent advances in drug polymorphs: Aspects of pharmaceutical properties and selective crystallization. *International Journal of Pharmaceutics.* 2022, **611**, p.121320.
4. Cölfen, H. and Mann, S. Higher-Order Organization by Mesoscale Self-Assembly and Transformation of Hybrid Nanostructures. *Angewandte Chemie International Edition.* 2003, **42**(21), pp.2350-2365.
5. Crystal forms. In: Sunagawa, I. ed. *Crystals: Growth, Morphology, & Perfection*. Cambridge: Cambridge University Press, 2005, pp.10-19.
6. Mullin, J.W. *Crystallisation.* 4 ed. Oxford: Butterworth-Heinemann, 2001.
7. Gibbs, J.W. On the Equilibrium of Heterogeneous Substances. *Trans. Connect. Acad. Sci.* 1876, **3**, p.140.
8. Polte, J. Fundamental growth principles of colloidal metal nanoparticles – a new perspective. *CrystEngComm.* 2015, **17**(36), pp.6809-6830.
9. Kossel, W. Zur Theorie des Kristallwachstums. *Nachrichten von der Gesellschaft der Wissenschaften zu Göttingen, Mathematisch-Physikalische Klasse.* 1927, **1927**, p.8.
10. Crystal growth. In: Sunagawa, I. ed. *Crystals: Growth, Morphology, & Perfection*. Cambridge: Cambridge University Press, 2005, pp.20-59.
11. Hartman, P. and Perdok, W.G. On the Relations Between Structure and Morphology of Crystals. I. *Acta Crystallographica* 1955, **8**, p.4.
12. Burton, W.K., Cabrera, N. and Frank, F.C. The Growth of Crystals and the Equilibrium Structure of their Surfaces. *Philosophical Transactions of the Royal Society of London. Series A, Mathematical and Physical Sciences.* 1951, **243**(866), pp.299-358.

13. Tsukamoto, K. In-situ observation of crystal growth and the mechanism. *Progress in Crystal Growth and Characterization of Materials.* 2016, **62**(2), pp.111-125.
14. Cubillas, P. and Anderson, M.W. Synthesis Mechanism: Crystal Growth and Nucleation. In: Cejka, J. et al. eds. *Zeolites and Catalysis*. Weinheim: John Wiley & Sons, 2010, p.11.
15. Desarnaud, J., Derluyn, H., Carmeliet, J., Bonn, D. and Shahidzadeh, N. Hopper Growth of Salt Crystals. *The Journal of Physical Chemistry Letters.* 2018, **9**(11), pp.2961-2966.
16. Oaki, Y. and Imai, H. Experimental Demonstration for the Morphological Evolution of Crystals Grown in Gel Media. *Crystal Growth & Design.* 2003, **3**(5), pp.711-716.
17. Dove, P.M., Han, N. and De Yoreo, J.J. Mechanisms of classical crystal growth theory explain quartz and silicate dissolution behavior. *Proc Natl Acad Sci U S A.* 2005, **102**(43), pp.15357-15362.
18. Dove, P.M., Han, N. and De Yoreo, J.J. Mechanisms of classical crystal growth theory explain quartz and silicate dissolution behavior. *Proceedings of the National Academy of Sciences.* 2005, **102**(43), pp.15357-15362.
19. Dove, P.M. and Han, N. Kinetics of Mineral Dissolution and Growth as Reciprocal Microscopic Surface Processes Across Chemical Driving Force. *AIP Conference Proceedings.* 2007, **916**(1), pp.215-234.
20. Ostwald, W. Über die vermeintliche Isomerie des roten und gelben Quecksilberoxyds und die Oberflächenspannung fester Körper. *Zeitschrift für Physikalische Chemie.* 1900, **34U**(1), pp.495-503.
21. Gebauer, D. and Cölfen, H. Prenucleation clusters and non-classical nucleation. *Nano Today.* 2011, **6**(6), pp.564-584.
22. Gebauer, D., Völkel, A. and Cölfen, H. Stable Prenucleation Calcium Carbonate Clusters. *Science.* 2008, **322**(5909), pp.1819-1822.
23. Vekilov, P.G. The two-step mechanism of nucleation of crystals in solution. *Nanoscale.* 2010, **2**(11), pp.2346-2357.
24. Cölfen, H. Nonclassical Nucleation and Crystallization. *Crystals.* 2020, **10**(2), p.61.
25. Erdemir, D., Lee, A.Y. and Myerson, A.S. Nucleation of Crystals from Solution: Classical and Two-Step Models. *Accounts of Chemical Research.* 2009, **42**(5), pp.621-629.
26. Gebauer, D. How Can Additives Control the Early Stages of Mineralisation? *Minerals.* 2018, **8**(5), p.179.

27. Mitra, M.K. and Muthukumar, M. Theory of spinodal decomposition assisted crystallization in binary mixtures. *The Journal of Chemical Physics.* 2010, **132**(18), p.184908.
28. De Yoreo, J.J., Gilbert, P.U.P.A., Sommerdijk, N.A.J.M., Penn, R.L., Whitelam, S., Joester, D., Zhang, H., Rimer, J.D., Navrotsky, A., Banfield, J.F., Wallace, A.F., Michel, F.M., Meldrum, F.C., Cölfen, H. and Dove, P.M. Crystallization by particle attachment in synthetic, biogenic, and geologic environments. *Science.* 2015, **349**(6247), p.6760.
29. Niederberger, M. and Cölfen, H. Oriented attachment and mesocrystals: Non-classical crystallization mechanisms based on nanoparticle assembly. *Physical Chemistry Chemical Physics.* 2006, **8**(28), pp.3271-3287.
30. Liu, Y., Geng, H., Qin, X., Yang, Y., Zeng, Z., Chen, S., Lin, Y., Xin, H., Song, C., Zhu, X., Li, D., Zhang, J., Song, L., Dai, Z. and Kawazoe, Y. Oriented Attachment Revisited: Does a Chemical Reaction Occur? *Matter.* 2019, **1**(3), pp.690-704.
31. Yuwono, V.M., Burrows, N.D., Soltis, J.A. and Penn, R.L. Oriented Aggregation: Formation and Transformation of Mesocrystal Intermediates Revealed. *Journal of the American Chemical Society.* 2010, **132**(7), pp.2163-2165.
32. Wang, T., Cölfen, H. and Antonietti, M. Nonclassical Crystallization: Mesocrystals and Morphology Change of $CaCO_3$ Crystals in the Presence of a Polyelectrolyte Additive. *Journal of the American Chemical Society.* 2005, **127**(10), pp.3246-3247.
33. Kulak, A.N., Iddon, P., Li, Y., Armes, S.P., Cölfen, H., Paris, O., Wilson, R.M. and Meldrum, F.C. Continuous Structural Evolution of Calcium Carbonate Particles: A Unifying Model of Copolymer-Mediated Crystallization. *Journal of the American Chemical Society.* 2007, **129**(12), pp.3729-3736.
34. Jun, Y.-S., Zhu, Y., Wang, Y., Ghim, D., Wu, X., Kim, D. and Jung, H. Classical and Nonclassical Nucleation and Growth Mechanisms for Nanoparticle Formation. *Annual Review of Physical Chemistry.* 2022, **73**(1), pp.453-477.
35. Penn, R.L. and Banfield, J.F. Morphology development and crystal growth in nanocrystalline aggregates under hydrothermal conditions: insights from titania. *Geochimica et Cosmochimica Acta.* 1999, **63**(10), pp.1549-1557.
36. Peters, J.L., van den Bos, K.H.W., Van Aert, S., Goris, B., Bals, S. and Vanmaekelbergh, D. Ligand-Induced Shape Transformation of PbSe Nanocrystals. *Chemistry of Materials.* 2017, **29**(9), pp.4122-4128.

37. Salzmann, B.B.V., van der Sluijs, M.M., Soligno, G. and Vanmaekelbergh, D. Oriented Attachment: From Natural Crystal Growth to a Materials Engineering Tool. *Accounts of Chemical Research.* 2021, **54**(4), pp.787-797.
38. Zitoun, D., Pinna, N., Frolet, N. and Belin, C. Single Crystal Manganese Oxide Multipods by Oriented Attachment. *Journal of the American Chemical Society.* 2005, **127**(43), pp.15034-15035.
39. Sturm, E.V. and Cölfen, H. Mesocrystals: structural and morphogenetic aspects. *Chem Soc Rev.* 2016, **45**(21), pp.5821-5833.
40. Ridgwell, A. and Zeebe, R.E. The role of the global carbonate cycle in the regulation and evolution of the Earth system. *Earth and Planetary Science Letters.* 2005, **234**(3), pp.299-315.
41. Lowenstam, H.A. Minerals Formed by Organisms. *Science.* 1981, **211**(4487), pp.1126-1131.
42. Calvert, P.D. Biomineralization and Biomimetic Materials. In: Meyers, R.A. ed. *Encyclopedia of Physical Science and Technology (Third Edition)*. New York: Academic Press, 2003, pp.193-205.
43. Driessens, F.C.M. and Verbeeck, R.K. *Biominerals.* Boca Raton: CRC Press, 1990.
44. Niu, Y.-Q., Liu, J.-H., Aymonier, C., Fermani, S., Kralj, D., Falini, G. and Zhou, C.-H. Calcium carbonate: controlled synthesis, surface functionalization, and nanostructured materials. *Chem Soc Rev.* 2022.
45. Meldrum, F.C. Calcium carbonate in biomineralisation and biomimetic chemistry. *International Materials Reviews.* 2003, **48**(3), pp.187-224.
46. Oates, J.A.H. *Lime and Limestone: Chemistry and Technology, Production and Uses.* Hoboken: John Wiley & Sons, 2008.
47. Tegethoff, F.W. *Calcium Carbonate: From the Cretaceous Period into the 21st Century.* Basel: Birkhauser, 2012.
48. Zhang, M., Li, J., Zhao, J., Cui, Y. and Luo, X. Comparison of $CH_4$ and $CO_2$ Adsorptions onto Calcite(10.4), Aragonite(011)Ca, and Vaterite(010)$CO_3$ Surfaces: An MD and DFT Investigation. *ACS Omega.* 2020, **5**(20), pp.11369-11377.
49. Wray, J.L. and Daniels, F. Precipitation of Calcite and Aragonite. *Journal of the American Chemical Society.* 1957, **79**(9), pp.2031-2034.
50. Morse, J.W. and Mackenzie, F.T. *Geochemistry of sedimentary carbonates.* Amsterdam ;: Elsevier, 1990.
51. Fermani, S., Njegić Džakula, B., Reggi, M., Falini, G. and Kralj, D. Effects of magnesium and temperature control on aragonite crystal

aggregation and morphology. *CrystEngComm.* 2017, **19**(18), pp.2451-2455.
52. Bragg, W.L. The structure of aragonite. *Proceedings of the Royal Society of London. Series A, Containing Papers of a Mathematical and Physical Character.* 1924, **105**(729), pp.16-39.
53. Konopacka-Łyskawa, D. Synthesis Methods and Favorable Conditions for Spherical Vaterite Precipitation: A Review. *Crystals.* 2019, **9**(4), p.223.
54. Wang, J., Zhang, F., Zhang, J., Ewing, R.C., Becker, U. and Cai, Z. Carbonate orientational order and superlattice structure in vaterite. *Journal of Crystal Growth.* 2014, **407**, pp.78-86.
55. Christy, A.G. A Review of the Structures of Vaterite: The Impossible, the Possible, and the Likely. *Crystal Growth & Design.* 2017, **17**(6), pp.3567-3578.
56. Pouget, E.M., Bomans, P.H.H., Dey, A., Frederik, P.M., de With, G. and Sommerdijk, N.A.J.M. The Development of Morphology and Structure in Hexagonal Vaterite. *Journal of the American Chemical Society.* 2010, **132**(33), pp.11560-11565.
57. Sawada, K. The mechanisms of crystallization and transformation of calcium carbonates. *Pure and Applied Chemistry.* 1997, **69**(5), pp.921-928.
58. Gower, L.B. Biomimetic Model Systems for Investigating the Amorphous Precursor Pathway and Its Role in Biomineralization. *Chemical Reviews.* 2008, **108**(11), pp.4551-4627.
59. Raz, S., Hamilton, P.C., Wilt, F.H., Weiner, S. and Addadi, L. The Transient Phase of Amorphous Calcium Carbonate in Sea Urchin Larval Spicules: The Involvement of Proteins and Magnesium Ions in Its Formation and Stabilization. *Advanced Functional Materials.* 2003, **13**(6), pp.480-486.
60. Ihli, J., Wong, W.C., Noel, E.H., Kim, Y.-Y., Kulak, A.N., Christenson, H.K., Duer, M.J. and Meldrum, F.C. Dehydration and crystallization of amorphous calcium carbonate in solution and in air. *Nature Communications.* 2014, **5**(1), p.3169.
61. Rodriguez-Blanco, J.D., Shaw, S. and Benning, L.G. The kinetics and mechanisms of amorphous calcium carbonate (ACC) crystallization to calcite, viavaterite. *Nanoscale.* 2011, **3**(1), pp.265-271.
62. Gong, Y.U.T., Killian, C.E., Olson, I.C., Appathurai, N.P., Amasino, A.L., Martin, M.C., Holt, L.J., Wilt, F.H. and Gilbert, P.U.P.A. Phase transitions in biogenic amorphous calcium carbonate. *Proceedings of the National Academy of Sciences.* 2012, **109**(16), pp.6088-6093.

63. Politi, Y., Metzler, R.A., Abrecht, M., Gilbert, B., Wilt, F.H., Sagi, I., Addadi, L., Weiner, S. and Gilbert, P.U.P.A. Transformation mechanism of amorphous calcium carbonate into calcite in the sea urchin larval spicule. *Proceedings of the National Academy of Sciences.* 2008, **105**(45), pp.17362-17366.
64. Beniash, E., Aizenberg, J., Addadi, L. and Weiner, S. Amorphous Calcium Carbonate Transforms into Calcite during Sea Urchin Larval Spicule Growth. *Proceedings: Biological Sciences.* 1997, **264**(1380), pp.461-465.
65. Aizenberg, J., Muller, D.A., Grazul, J.L. and Hamann, D.R. Direct fabrication of large micropatterned single crystals. *Science.* 2003, **299**(5610), pp.1205-1208.
66. Loste, E. and Meldrum, F.C. Control of calcium carbonate morphology by transformation of an amorphous precursor in a constrained volume. *Chemical Communications.* 2001, (10), pp.901-902.
67. Zou, Z., Yang, X., Albéric, M., Heil, T., Wang, Q., Pokroy, B., Politi, Y. and Bertinetti, L. Additives Control the Stability of Amorphous Calcium Carbonate via Two Different Mechanisms: Surface Adsorption versus Bulk Incorporation. *Advanced Functional Materials.* 2020, **30**(23), p.2000003.
68. Sommerdijk, N.A.J.M. and With, G.d. Biomimetic $CaCO_3$ Mineralization using Designer Molecules and Interfaces. *Chemical Reviews.* 2008, **108**(11), pp.4499-4550.
69. Shaked, H., Polishchuk, I., Nagel, A., Bekenstein, Y. and Pokroy, B. Long-term stabilized amorphous calcium carbonate—an ink for bio-inspired 3D printing. *Materials Today Bio.* 2021, **11**, p.100120.
70. Rodriguez-Blanco, J.D., Shaw, S., Bots, P., Roncal-Herrero, T. and Benning, L.G. The role of pH and Mg on the stability and crystallization of amorphous calcium carbonate. *Journal of Alloys and Compounds.* 2012, **536**, pp.S477-S479.
71. Schmidt, I., Zolotoyabko, E., Lee, K., Gjardy, A., Berner, A., Lakin, E., Fratzl, P. and Wagermaier, W. Effect of Strontium Ions on Crystallization of Amorphous Calcium Carbonate. *Crystal Research and Technology.* 2019, **54**(6), p.1900002.
72. Rao, C., Li, M., Sun, X., Li, M., Lian, X., Wang, H., Jia, L., Niu, B. and Li, W. Preparation and characterization of phosphate-stabilized amorphous calcium carbonate nanoparticles and their application in curcumin delivery. *Materials Chemistry and Physics.* 2020, **255**, p.123552.
73. Kababya, S., Gal, A., Kahil, K., Weiner, S., Addadi, L. and Schmidt, A. Phosphate–Water Interplay Tunes Amorphous Calcium Carbonate Metastability: Spontaneous Phase Separation

and Crystallization vs Stabilization Viewed by Solid State NMR. *Journal of the American Chemical Society.* 2015, **137**(2), pp.990-998.
74. Rao, A., Drechsler, M., Schiller, S., Scheffner, M., Gebauer, D. and Cölfen, H. Stabilization of Mineral Precursors by Intrinsically Disordered Proteins. *Advanced Functional Materials.* 2018, **28**(37), p.1802063.
75. Xu, Y., Tijssen, K.C.H., Bomans, P.H.H., Akiva, A., Friedrich, H., Kentgens, A.P.M. and Sommerdijk, N.A.J.M. Microscopic structure of the polymer-induced liquid precursor for calcium carbonate. *Nature Communications.* 2018, **9**(1), p.2582.
76. Gower, L.A. and Tirrell, D.A. Calcium carbonate films and helices grown in solutions of poly(aspartate). *Journal of Crystal Growth.* 1998, **191**(1), pp.153-160.
77. Gower, L.B. and Odom, D.J. Deposition of calcium carbonate films by a polymer-induced liquid-precursor (PILP) process. *Journal of Crystal Growth.* 2000, **210**(4), pp.719-734.
78. Nielsen, M.H., Aloni, S. and De Yoreo, J.J. In situ TEM imaging of $CaCO_3$ nucleation reveals coexistence of direct and indirect pathways. *Science.* 2014, **345**(6201), pp.1158-1162.
79. Pouget, E.M., Bomans, P.H.H., Goos, J.A.C.M., Frederik, P.M., de With, G. and Sommerdijk, N.A.J.M. The Initial Stages of Template-Controlled $CaCO_3$ Formation Revealed by Cryo-TEM. *Science.* 2009, **323**(5920), pp.1455-1458.
80. Cartwright, J.H.E., Checa, A.G., Gale, J.D., Gebauer, D. and Sainz-Díaz, C.I. Calcium Carbonate Polyamorphism and Its Role in Biomineralization: How Many Amorphous Calcium Carbonates Are There? *Angewandte Chemie International Edition.* 2012, **51**(48), pp.11960-11970.
81. Clark, S.M., Colas, B., Jacob, D.E., Neuefeind, J.C., Wang, H.-W., Page, K.L., Soper, A.K., Schodder, P.I., Duchstein, P., Zubiri, B.A., Yokosawa, T., Pipich, V., Zahn, D., Spiecker, E. and Wolf, S.E. The nano- and meso-scale structure of amorphous calcium carbonate. *Scientific Reports.* 2022, **12**(1), p.6870.
82. Duchstein, P., Schodder, P.I., Leupold, S., Dao, T.Q.N., Kababya, S., Cicconi, M.R., de Ligny, D., Pipich, V., Eike, D., Schmidt, A., Zahn, D. and Wolf, S.E. Small-Molecular-Weight Additives Modulate Calcification by Interacting with Prenucleation Clusters on the Molecular Level**. *Angewandte Chemie International Edition.* 2022, **n/a**(n/a), p.e202208475.
83. Demichelis, R., Raiteri, P., Gale, J.D., Quigley, D. and Gebauer, D. Stable prenucleation mineral clusters are liquid-like ionic polymers. *Nature Communications.* 2011, **2**(1), p.590.

84. Mohammed, A.S.A., Carino, A., Testino, A., Andalibi, M.R. and Cervellino, A. In Situ Liquid SAXS Studies on the Early Stage of Calcium Carbonate Formation. *Particle & Particle Systems Characterization.* 2019, **36**(6), p.1800482.
85. Gebauer, D., Gunawidjaja, P.N., Ko, J.Y.P., Bacsik, Z., Aziz, B., Liu, L., Hu, Y., Bergström, L., Tai, C.-W., Sham, T.-K., Edén, M. and Hedin, N. Proto-Calcite and Proto-Vaterite in Amorphous Calcium Carbonates. 2010, **49**(47), pp.8889-8891.
86. Lam, R.S.K., Charnock, J.M., Lennie, A. and Meldrum, F.C. Synthesis-dependant structural variations in amorphous calcium carbonate. *CrystEngComm.* 2007, **9**(12), pp.1226-1236.
87. Fernandez-Martinez, A., Kalkan, B., Clark, S.M. and Waychunas, G.A. Pressure-Induced Polyamorphism and Formation of 'Aragonitic' Amorphous Calcium Carbonate. *Angewandte Chemie International Edition.* 2013, **52**(32), pp.8354-8357.
88. Hesse, K.F., Küppers, H. and Suess, E. Refinement of the structure of Ikaite, CaCO3 - 6H2O. *Zeitschrift für Kristallographie - Crystalline Materials.* 1983, **163**(1-4), pp.227-232.
89. Effenberger, H. Kristallstruktur und Infrarot-Absorptionsspektrum von synthetischem Monohydrocalcit, $CaCO_3 \cdot H_2O$. *Monatshefte für Chemie / Chemical Monthly.* 1981, **112**(8), pp.899-909.
90. Rodriguez-Blanco, J.D., Shaw, S., Bots, P., Roncal-Herrero, T. and Benning, L.G. The role of Mg in the crystallization of monohydrocalcite. *Geochimica et Cosmochimica Acta.* 2014, **127**, pp.204-220.
91. Bischoff, J.L., Fitzpatrick, J.A. and Rosenbauer, R.J. The Solubility and Stabilization of Ikaite ($CaCO_3 \cdot 6H_2O$) from 0° to 25°C: Environmental and Paleoclimatic Implications for Thinolite Tufa. *The Journal of Geology.* 1993, **101**(1), pp.21-33.
92. Tollefsen, E., Stockmann, G., Skelton, A., Mörth, C.-M., Dupraz, C. and Sturkell, E. Chemical controls on ikaite formation. *Mineralogical Magazine.* 2018, **82**(5), pp.1119-1129.
93. Marland, G. The stability of $CaCO_3 \cdot 6H_2O$ (ikaite). *Geochimica et Cosmochimica Acta.* 1975, **39**(1), pp.83-91.
94. Tollefsen, E., Balic-Zunic, T., Mörth, C.-M., Brüchert, V., Lee, C.C. and Skelton, A. Ikaite nucleation at 35 °C challenges the use of glendonite as a paleotemperature indicator. *Scientific Reports.* 2020, **10**(1), p.8141.
95. Hu, Y.-B., Wolf-Gladrow, D.A., Dieckmann, G.S., Völker, C. and Nehrke, G. A laboratory study of ikaite ($CaCO_3 \cdot 6H_2O$) precipitation as a function of pH, salinity, temperature and phosphate concentration. *Marine Chemistry.* 2014, **162**, pp.10-18.

96. Dey, A., de With, G. and Sommerdijk, N.A.J.M. In situ techniques in biomimetic mineralization studies of calcium carbonate. *Chem Soc Rev.* 2010, **39**(2), pp.397-409.
97. Patterson, J.P., Xu, Y., Moradi, M.-A., Sommerdijk, N.A.J.M. and Friedrich, H. CryoTEM as an Advanced Analytical Tool for Materials Chemists. *Accounts of Chemical Research.* 2017, **50**(7), pp.1495-1501.
98. De Yoreo, J.J. and N. A. J. M, S. Investigating materials formation with liquid-phase and cryogenic TEM. *Nature Reviews Materials.* 2016, **1**(8), p.16035.
99. Nudelman, F., de With, G. and Sommerdijk, N.A.J.M. Cryo-electron tomography: 3-dimensional imaging of soft matter. *Soft Matter.* 2011, **7**(1), pp.17-24.
100. Wu, H., Friedrich, H., Patterson, J.P., Sommerdijk, N.A.J.M. and de Jonge, N. Liquid-Phase Electron Microscopy for Soft Matter Science and Biology. *Advanced Materials.* 2020, **32**(25), p.2001582.
101. Parent, L.R., Bakalis, E., Proetto, M., Li, Y., Park, C., Zerbetto, F. and Gianneschi, N.C. Tackling the Challenges of Dynamic Experiments Using Liquid-Cell Transmission Electron Microscopy. *Accounts of Chemical Research.* 2018, **51**(1), pp.3-11.
102. Ilett, M., Freeman, H.M., Aslam, Z., Galloway, J.M., Klebl, D.P., Muench, S.P., McPherson, I.J., Cespedes, O., Kim, Y.-Y., Meldrum, F.C., Yeandel, S.R., Freeman, C.L., Harding, J.H. and Brydson, R.M.D. Evaluation of correlated studies using liquid cell and cryo-transmission electron microscopy: Hydration of calcium sulphate and the phase transformation pathways of bassanite to gypsum. *Journal of Microscopy.* p.14.
103. Li, M. and Ling, L. Visualizing Dynamic Environmental Processes in Liquid at Nanoscale via Liquid-Phase Electron Microscopy. *ACS Nano.* 2022.
104. Rieger, J., Hädicke, E., Rau, I.U. and Boeckh, D. A rational approach to the mechanisms of incrustation inhibition by polymeric additives / Wirkungsweise von polymeren Inkrustrationsinhibitoren. *Tenside Surfactants Detergents.* 1997, **34**(6), pp.430-435.
105. Rieger, J., Frechen, T., Cox, G., Heckmann, W., Schmidt, C. and Thieme, J. Precursor structures in the crystallization/precipitation processes of $CaCO_3$ and control of particle formation by polyelectrolytes. *Faraday Discussions.* 2007, **136**(0), pp.265-277.
106. Pichon, B.P., Bomans, P.H.H., Frederik, P.M. and Sommerdijk, N.A.J.M. A Quasi-Time-Resolved CryoTEM Study of the Nucleation of $CaCO_3$ under Langmuir Monolayers. *Journal of the American Chemical Society.* 2008, **130**(12), pp.4034-4040.

107. Nudelman, F., Sonmezler, E., Bomans, P.H.H., de With, G. and Sommerdijk, N.A.J.M. Stabilization of amorphous calcium carbonate by controlling its particle size. *Nanoscale.* 2010, **2**(11), pp.2436-2439.
108. Walker, J.M., Marzec, B. and Nudelman, F. Solid-State Transformation of Amorphous Calcium Carbonate to Aragonite Captured by CryoTEM. *Angewandte Chemie International Edition.* 2017, **56**(39), pp.11740-11743.
109. Kröger, R. and Verch, A. Liquid Cell Transmission Electron Microscopy and the Impact of Confinement on the Precipitation from Supersaturated Solutions. *Minerals.* 2018, **8**(1), p.21.
110. Meldrum, F.C. and O'Shaughnessy, C. Crystallization in Confinement. *Advanced Materials.* 2020, **32**(31), p.2001068.
111. Smeets, P.J.M., Cho, K.R., Kempen, R.G.E., Sommerdijk, N.A.J.M. and De Yoreo, J.J. Calcium carbonate nucleation driven by ion binding in a biomimetic matrix revealed by in situ electron microscopy. *Nature Materials.* 2015, **14**(4), pp.394-399.
112. Liu, Z., Zhang, Z., Wang, Z., Jin, B., Li, D., Tao, J., Tang, R. and De Yoreo, J.J. Shape-preserving amorphous-to-crystalline transformation of $CaCO_3$ revealed by in situ TEM. *Proceedings of the National Academy of Sciences.* 2020, **117**(7), pp.3397-3404.
113. Tao, J., Zhou, D., Zhang, Z., Xu, X. and Tang, R. Magnesium-aspartate-based crystallization switch inspired from shell molt of crustacean. *Proceedings of the National Academy of Sciences.* 2009, **106**(52), pp.22096-22101.
114. Wang, D., Wallace, A.F., De Yoreo, J.J. and Dove, P.M. Carboxylated molecules regulate magnesium content of amorphous calcium carbonates during calcification. *Proceedings of the National Academy of Sciences.* 2009, **106**(51), pp.21511-21516.
115. Kelly, D.J., Clark, N., Zhou, M., Gebauer, D., Gorbachev, R.V. and Haigh, S.J. In Situ TEM Imaging of Solution-Phase Chemical Reactions Using 2D-Heterostructure Mixing Cells. *Advanced Materials.* 2021, **33**(29), p.2100668.
116. Ramnarain, V., Georges, T., Ortiz Peña, N., Ihiawakrim, D., Longuinho, M., Bulou, H., Gervais, C., Sanchez, C., Azaïs, T. and Ersen, O. Monitoring of $CaCO_3$ Nanoscale Structuration through Real-Time Liquid Phase Transmission Electron Microscopy and Hyperpolarized NMR. *Journal of the American Chemical Society.* 2022, **144**(33), pp.15236-15251.
117. De Yoreo, J.J., Jin, B., Chen, Y., Pyles, H., Baer, M., Legg, B., Wang, Z., Washton, N., Mueller, K., Baker, D., Schenter, G. and Mundy, C. Formation, Chemical Evolution, and Solidification of the

Calcium Carbonate Dense Liquid Phase [PREPRINT (Version 1)]. 2022, (Accessed 30th July 2022. Available from: https://doi.org/10.21203/rs.3.rs-1743346/v1).
118. Goodhew, P.J., Humphreys, J. and Beanland, R. *Electron Microscopy and Analysis.* London: Taylor & Francis, 2001.
119. Inkson, B.J. 2 - Scanning electron microscopy (SEM) and transmission electron microscopy (TEM) for materials characterization. In: Hübschen, G. et al. eds. *Materials Characterization Using Nondestructive Evaluation (NDE) Methods*. Woodhead Publishing, 2016, pp.17-43.
120. Williams, D.B. and Carter, C.B. *Transmission Electron Microscopy: A Textbook for Materials Science.* Boston: Springer, 2009.
121. NobelPrize.org. *The Nobel Prize in Chemistry 2017.* [Online]. 2017. [Accessed 16.06.2020]. Available from: https://www.nobelprize.org/prizes/chemistry/2017/summary/
122. Dubochet, J., Adrian, M., Chang, J.-J., Homo, J.-C., Lepault, J., McDowall, A.W. and Schultz, P. Cryo-electron microscopy of vitrified specimens. *Quarterly Reviews of Biophysics.* 1988, **21**(2), pp.129-228.
123. Murata, K. and Wolf, M. Cryo-electron microscopy for structural analysis of dynamic biological macromolecules. *Biochimica et Biophysica Acta (BBA) - General Subjects.* 2018, **1862**(2), pp.324-334.
124. Schneider, N.M. Electron Beam Effects in Liquid Cell TEM and STEM. In: Ross, F.M. ed. *Liquid Cell Electron Microscopy*. Cambridge: Cambridge University Press, 2016, pp.140-163.
125. de Jonge, N. and Ross, F.M. Electron microscopy of specimens in liquid. *Nature Nanotechnology.* 2011, **6**(11), pp.695-704.
126. Jones, R.R., Hooper, D.C., Zhang, L., Wolverson, D. and Valev, V.K. Raman Techniques: Fundamentals and Frontiers. *Nanoscale Res Lett.* 2019, **14**(1), p.231.
127. Das, R.S. and Agrawal, Y.K. Raman spectroscopy: Recent advancements, techniques and applications. *Vibrational Spectroscopy.* 2011, **57**(2), pp.163-176.
128. Gabbott, P. *Principles and Applications of Thermal Analysis.* New Jersey: John Wiley & Sons, 2008.
129. Pope, C.G. X-Ray Diffraction and the Bragg Equation. *Journal of Chemical Education.* 1997, **74**(1), p.129.
130. Smart, L. and Moore, E. *Solid State Chemistry: An Introduction.* 3rd ed. Oxford: Taylor & Francis, 2014.
131. Meenan, P.A., Anderson, S.R. and Klug, D.L. 3 - The influence of impurities and solvents on crystallization. In: Myerson, A.S. ed.

*Handbook of Industrial Crystallization (Second Edition)*. Woburn: Butterworth-Heinemann, 2002, pp.67-100.
132. Pirouzian, H.R., Konar, N., Palabiyik, I., Oba, S. and Toker, O.S. Pre-crystallization process in chocolate: Mechanism, importance and novel aspects. *Food Chemistry.* 2020, **321**, p.126718.
133. Llinàs, A. and Goodman, J.M. Polymorph control: past, present and future. *Drug Discovery Today.* 2008, **13**(5), pp.198-210.
134. Taylor, L.S., Braun, D.E. and Steed, J.W. Crystals and Crystallization in Drug Delivery Design. *Molecular Pharmaceutics.* 2021, **18**(3), pp.751-753.
135. Lowenstam, H.A. and Weiner, S. *On Biomineralization.* New York: Oxford University Press, 1989.
136. Shtukenberg, A.G., Lee, S.S., Kahr, B. and Ward, M.D. Manipulating Crystallization with Molecular Additives. *Annual Review of Chemical and Biomolecular Engineering.* 2014, **5**(1), pp.77-96.
137. Meldrum, F.C. and Cölfen, H. Controlling Mineral Morphologies and Structures in Biological and Synthetic Systems. *Chemical Reviews.* 2008, **108**(11), pp.4332-4432.
138. Sommerdijk, N.A.J.M. and Cölfen, H. Lessons from Nature—Biomimetic Approaches to Minerals with Complex Structures. *MRS Bulletin.* 2010, **35**(2), pp.116-121.
139. Romé de L'Isle, J.B.L.d. *Essai de cristallographie, ou Description des figures géométriques, propres à différens corps du regne minéral, connus vulgairement sous le nom de cristaux : avec figures et développemens.* A Paris: Chez Didot Jeune, Libraire, 1772.
140. Factors determining the morphology of polyhedral crystals. In: Sunagawa, I. ed. *Crystals: Growth, Morphology, & Perfection*. Cambridge: Cambridge University Press, 2005, pp.60-88.
141. Cabrera, N. and Vermilyea, D. *Proceedings of the International Conference Cooperstown, NY*. Wiley New York. 1958.
142. Yoreo, J.J.D. and Vekilov, P.G. Principles of Crystal Nucleation and Growth. *Reviews in Mineralogy and Geochemistry.* 2003, **54**(1), pp.57-93.
143. Ristic, R.I., DeYoreo, J.J. and Chew, C.M. Does Impurity-Induced Step-Bunching Invalidate Key Assumptions of the Cabrera−Vermilyea Model? *Crystal Growth & Design.* 2008, **8**(4), pp.1119-1122.
144. Lutsko, J.F., González-Segredo, N., Durán-Olivencia, M.A., Maes, D., Van Driessche, A.E.S. and Sleutel, M. Crystal Growth Cessation Revisited: The Physical Basis of Step Pinning. *Crystal Growth & Design.* 2014, **14**(11), pp.6129-6134.

145. Zhang, J. and Nancollas, G.H. Kink densities along a crystal surface step at low temperatures and under nonequilibrium conditions. *Journal of Crystal Growth.* 1990, **106**(2), pp.181-190.
146. De Yoreo, J.J., Zepeda-Ruiz, L.A., Friddle, R.W., Qiu, S.R., Wasylenki, L.E., Chernov, A.A., Gilmer, G.H. and Dove, P.M. Rethinking Classical Crystal Growth Models through Molecular Scale Insights: Consequences of Kink-Limited Kinetics. *Crystal Growth & Design.* 2009, **9**(12), pp.5135-5144.
147. Bliznakow, G. Crystal habit and adsorption of cosolutes. *Fortsch Min.* 1958, **36**, p.149.
148. Ranganathan, M. and Weeks, J.D. Theory of Impurity Induced Step Pinning and Recovery in Crystal Growth from Solutions. *Physical Review Letters.* 2013, **110**(5), p.055503.
149. Kim, Y.-Y., Freeman, C.L., Gong, X., Levenstein, M.A., Wang, Y., Kulak, A., Anduix-Canto, C., Lee, P.A., Li, S., Chen, L., Christenson, H.K. and Meldrum, F.C. The Effect of Additives on the Early Stages of Growth of Calcite Single Crystals. *Angewandte Chemie International Edition.* 2017, **56**(39), pp.11885-11890.
150. Kim, Y.-Y., Ganesan, K., Yang, P., Kulak, A.N., Borukhin, S., Pechook, S., Ribeiro, L., Kröger, R., Eichhorn, S.J., Armes, S.P., Pokroy, B. and Meldrum, F.C. An artificial biomineral formed by incorporation of copolymer micelles in calcite crystals. *Nature Materials.* 2011, **10**, p.890.
151. Kim, Y.-Y., Carloni, J.D., Demarchi, B., Sparks, D., Reid, D.G., Kunitake, Miki E., Tang, C.C., Duer, M.J., Freeman, C.L., Pokroy, B., Penkman, K., Harding, J.H., Estroff, L.A., Baker, S.P. and Meldrum, F.C. Tuning hardness in calcite by incorporation of amino acids. *Nature Materials.* 2016, **15**, p.903.
152. Paul, D. and Das, G. Bio-inspired synthesis of flavonoids incorporated $CaCO_3$: Influence on the phase, morphology and mechanical strength of the composites. *Colloids and Surfaces A: Physicochemical and Engineering Aspects.* 2022, **642**, p.128720.
153. Kahr, B. and Shtukenberg, A.G. Dyeing crystals since 2000. *CrystEngComm.* 2016, **18**(47), pp.8988-8998.
154. Liu, Y., Zang, H., Wang, L., Fu, W., Yuan, W., Wu, J., Jin, X., Han, J., Wu, C., Wang, Y., Xin, H.L., Chen, H. and Li, H. Nanoparticles Incorporated inside Single-Crystals: Enhanced Fluorescent Properties. *Chemistry of Materials.* 2016, **28**(20), pp.7537-7543.
155. Rae Cho, K., Kim, Y.-Y., Yang, P., Cai, W., Pan, H., Kulak, A.N., Lau, J.L., Kulshreshtha, P., Armes, S.P., Meldrum, F.C. and De Yoreo, J.J. Direct observation of mineral–organic composite formation reveals occlusion mechanism. *Nature Communications.* 2016, **7**(1), p.10187.

156. van Enckevort, W.J.P. and van den Berg, A.C.J.F. Impurity blocking of crystal growth: a Monte Carlo study. *Journal of Crystal Growth.* 1998, **183**(3), pp.441-455.
157. Nicoud, L.H. and Myerson, A.S. The Influence of Impurities and Additives on Crystallization. In: Lee, A.Y. et al. eds. *Handbook of Industrial Crystallization*. 3 ed. Cambridge: Cambridge University Press, 2019, pp.115-135.
158. Ma, W., Lutsko, J.F., Rimer, J.D. and Vekilov, P.G. Antagonistic cooperativity between crystal growth modifiers. *Nature.* 2020, **577**(7791), pp.497-501.
159. Marzec, B., Green, D.C., Holden, M.A., Coté, A.S., Ihli, J., Khalid, S., Kulak, A., Walker, D., Tang, C., Duffy, D.M., Kim, Y.-Y. and Meldrum, F.C. Amino Acid Assisted Incorporation of Dye Molecules within Calcite Crystals. *Angewandte Chemie International Edition.* 2018, **57**(28), pp.8623-8628.
160. Teng, H.H., Dove, P.M. and De Yoreo, J.J. Kinetics of calcite growth: surface processes and relationships to macroscopic rate laws. *Geochimica et Cosmochimica Acta.* 2000, **64**(13), pp.2255-2266.
161. Darkins, R., Kim, Y.-Y., Green, D.C., Broad, A., Duffy, D.M., Meldrum, F.C. and Ford, I.J. Calcite Kinetics for Spiral Growth and Two-Dimensional Nucleation. *Crystal Growth & Design.* 2022, **22**(7), pp.4431-4436.
162. Xu, J., Wang, J., Hong, M. and Teng, H.H. Solution-chemistry control of $Mg^{2+}$-calcite interaction mechanisms: Implication for biomineralization. *American Mineralogist.* 2016, **101**(5), pp.1104-1112.
163. Nielsen, L.C., De Yoreo, J.J. and DePaolo, D.J. General model for calcite growth kinetics in the presence of impurity ions. *Geochimica et Cosmochimica Acta.* 2013, **115**, pp.100-114.
164. Davis, K.J., Dove, P.M. and De Yoreo, J.J. The Role of $Mg^{2+}$ as an Impurity in Calcite Growth. *Science.* 2000, **290**(5494), pp.1134-1137.
165. Berner, R.A. The role of magnesium in the crystal growth of calcite and aragonite from sea water. *Geochimica et Cosmochimica Acta.* 1975, **39**(4), pp.489-504.
166. Davis, K.J., Dove, P.M., Wasylenki, L.E. and De Yoreo, J.J. Morphological consequences of differential $Mg^{2+}$ incorporation at structurally distinct steps on calcite. *American Mineralogist.* 2004, **89**(5-6), pp.714-720.
167. Ihli, J., Clark, J.N., Kanwal, N., Kim, Y.Y., Holden, M.A., Harder, R.J., Tang, C.C., Ashbrook, S.E., Robinson, I.K. and Meldrum, F.C. Visualization of the effect of additives on the nanostructures

of individual bio-inspired calcite crystals. *Chem Sci.* 2019, **10**(4), pp.1176-1185.
168. Wasylenki, L.E., Dove, P.M., Wilson, D.S. and De Yoreo, J.J. Nanoscale effects of strontium on calcite growth: An in situ AFM study in the absence of vital effects. *Geochimica et Cosmochimica Acta.* 2005, **69**(12), pp.3017-3027.
169. Rajam, S. and Mann, S. Selective stabilization of the (001) face of calcite in the presence of lithium. *Journal of the Chemical Society, Chemical Communications.* 1990, (24), pp.1789-1791.
170. Wang, L., Ruiz-Agudo, E., Putnis, C.V. and Putnis, A. Direct observations of the modification of calcite growth morphology by $Li^+$ through selectively stabilizing an energetically unfavourable face. *CrystEngComm.* 2011, **13**(12), pp.3962-3966.
171. Song, R.-Q. and Cölfen, H. Additive controlled crystallization. *CrystEngComm.* 2011, **13**(5), pp.1249-1276.
172. Kim, Y.Y., Ganesan, K., Yang, P., Kulak, A.N., Borukhin, S., Pechook, S., Ribeiro, L., Kroger, R., Eichhorn, S.J., Armes, S.P., Pokroy, B. and Meldrum, F.C. An artificial biomineral formed by incorporation of copolymer micelles in calcite crystals. *Nat Mater.* 2011, **10**(11), pp.890-896.
173. Ning, Y., Armes, S.P. and Li, D. Polymer-Inorganic Crystalline Nanocomposite Materials via Nanoparticle Occlusion. *Macromolecular Rapid Communications.* 2022, **n/a**(n/a), p.2100793.
174. Borukhin, S., Bloch, L., Radlauer, T., Hill, A.H., Fitch, A.N. and Pokroy, B. Screening the Incorporation of Amino Acids into an Inorganic Crystalline Host: the Case of Calcite. *Advanced Functional Materials.* 2012, **22**(20), pp.4216-4224.
175. Green, D.C., Ihli, J., Thornton, P.D., Holden, M.A., Marzec, B., Kim, Y.-Y., Kulak, A.N., Levenstein, M.A., Tang, C., Lynch, C., Webb, S.E.D., Tynan, C.J. and Meldrum, F.C. 3D visualization of additive occlusion and tunable full-spectrum fluorescence in calcite. *Nature Communications.* 2016, **7**(1), p.13524.
176. Green, D.C., Darkins, R., Marzec, B., Holden, M.A., Ford, I.J., Botchway, S.W., Kahr, B., Duffy, D.M. and Meldrum, F.C. Dichroic Calcite Reveals the Pathway from Additive Binding to Occlusion. *Crystal Growth & Design.* 2021, **21**(7), pp.3746-3755.
177. Kahr, B. and Gurney, R.W. Dyeing Crystals. *Chemical Reviews.* 2001, **101**(4), pp.893-952.
178. Nahi, O., Kulak, A.N., Kress, T., Kim, Y.-Y., Grendal, O.G., Duer, M.J., Cayre, O.J. and Meldrum, F.C. Incorporation of nanogels within calcite single crystals for the storage, protection and

controlled release of active compounds. *Chemical Science.* 2021, **12**(28), pp.9839-9850.
179. Li, H. and Estroff, L.A. Porous calcite single crystals grown from a hydrogel medium. *CrystEngComm.* 2007, **9**(12), pp.1153-1155.
180. Nudelman, F. and Sommerdijk, N.A.J.M. Biomineralization as an Inspiration for Materials Chemistry. *Angewandte Chemie International Edition.* 2012, **51**(27), pp.6582-6596.
181. Teng, H.H., Dove, P.M., Orme, C.A. and de Yoreo, J.J. Thermodynamics of Calcite Growth: Baseline for Understanding Biomineral Formation. *Science.* 1998, **282**(5389), pp.724-727.
182. Gebauer, D., Cölfen, H., Verch, A. and Antonietti, M. The Multiple Roles of Additives in $CaCO_3$ Crystallization: A Quantitative Case Study. *Advanced Materials.* 2009, **21**(4), pp.435-439.
183. Weiner, S. and Hood, L. Soluble protein of the organic matrix of mollusk shells: a potential template for shell formation. *Science.* 1975, **190**(4218), pp.987-989.
184. Addadi, L., Moradian, J., Shay, E., Maroudas, N.G. and Weiner, S. A chemical model for the cooperation of sulfates and carboxylates in calcite crystal nucleation: Relevance to biomineralization. *Proceedings of the National Academy of Sciences.* 1987, **84**(9), pp.2732-2736.
185. Orme, C.A., Noy, A., Wierzbicki, A., McBride, M.T., Grantham, M., Teng, H.H., Dove, P.M. and DeYoreo, J.J. Formation of chiral morphologies through selective binding of amino acids to calcite surface steps. *Nature.* 2001, **411**, p.775.
186. Wu, C., Zhao, K., Wang, X., Cao, M., Xu, H. and Lu, J.R. Dissolution of the Calcite (104) Face under Specific Calcite–Aspartic Acid Interaction As Revealed by in Situ Atomic Force Microscopy. *Crystal Growth & Design.* 2012, **12**(5), pp.2594-2601.
187. Nada, H. Difference in the Conformation and Dynamics of Aspartic Acid on the Flat Regions, Step Edges, and Kinks of a Calcite Surface: A Molecular Dynamics Study. *The Journal of Physical Chemistry C.* 2014, **118**(26), pp.14335-14345.
188. Orme, C.A., Noy, A., Wierzbicki, A., McBride, M.T., Grantham, M., Teng, H.H., Dove, P.M. and DeYoreo, J.J. Formation of chiral morphologies through selective binding of amino acids to calcite surface steps. *Nature.* 2001, **411**(6839), pp.775-779.
189. Montanari, G., Lakshtanov, L.Z., Tobler, D.J., Dideriksen, K., Dalby, K.N., Bovet, N. and Stipp, S.L.S. Effect of Aspartic Acid and Glycine on Calcite Growth. *Crystal Growth & Design.* 2016, **16**(9), pp.4813-4821.

190. Magdans, U., Torrelles, X., Angermund, K., Gies, H. and Rius, J. Crystalline Order of a Water/Glycine Film Coadsorbed on the (104) Calcite Surface. *Langmuir.* 2007, **23**(9), pp.4999-5004.
191. Tobler, D.J., Blanco, J.D.R., Dideriksen, K., Sand, K.K., Bovet, N., Benning, L.G. and Stipp, S.L.S. The Effect of Aspartic Acid and Glycine on Amorphous Calcium Carbonate (ACC) Structure, Stability and Crystallization. *Procedia Earth and Planetary Science.* 2014, **10**, pp.143-148.
192. Picker, A., Kellermeier, M., Seto, J., Gebauer, D. and Cölfen, H. The multiple effects of amino acids on the early stages of calcium carbonate crystallization. *Zeitschrift für Kristallographie - Crystalline Materials.* 2012, **227**(11), pp.744-757.
193. Finney, A.R., Innocenti Malini, R., Freeman, C.L. and Harding, J.H. Amino Acid and Oligopeptide Effects on Calcium Carbonate Solutions. *Cryst Growth Des.* 2020, **20**(5), pp.3077-3092.
194. Mijowska, S., Polishchuk, I., Lang, A., Seknazi, E., Dejoie, C., Fermani, S., Falini, G., Demitri, N., Polentarutti, M., Katsman, A. and Pokroy, B. High Amino Acid Lattice Loading at Nonambient Conditions Causes Changes in Structure and Expansion Coefficient of Calcite. *Chemistry of Materials.* 2020, **32**(10), pp.4205-4212.
195. Li, C. and Qi, L. Bioinspired Fabrication of 3D Ordered Macroporous Single Crystals of Calcite from a Transient Amorphous Phase. *Angewandte Chemie International Edition.* 2008, **47**(13), pp.2388-2393.
196. Kim, Y.-Y., Ribeiro, L., Maillot, F., Ward, O., Eichhorn, S.J. and Meldrum, F.C. Bio-Inspired Synthesis and Mechanical Properties of Calcite–Polymer Particle Composites. *Advanced Materials.* 2010, **22**(18), pp.2082-2086.
197. Lu, C., Qi, L., Cong, H., Wang, X., Yang, J., Yang, L., Zhang, D., Ma, J. and Cao, W. Synthesis of Calcite Single Crystals with Porous Surface by Templating of Polymer Latex Particles. *Chemistry of Materials.* 2005, **17**(20), pp.5218-5224.
198. Ning, Y., Han, Y., Han, L., Derry, M.J. and Armes, S.P. Exerting Spatial Control During Nanoparticle Occlusion within Calcite Crystals. *Angewandte Chemie International Edition.* 2020, **59**(41), pp.17966-17973.
199. Ning, Y., Fielding, L.A., Ratcliffe, L.P.D., Wang, Y.-W., Meldrum, F.C. and Armes, S.P. Occlusion of Sulfate-Based Diblock Copolymer Nanoparticles within Calcite: Effect of Varying the Surface Density of Anionic Stabilizer Chains. *Journal of the American Chemical Society.* 2016, **138**(36), pp.11734-11742.

200. Kim, Y.-Y., Semsarilar, M., Carloni, J.D., Cho, K.R., Kulak, A.N., Polishchuk, I., Hendley IV, C.T., Smeets, P.J.M., Fielding, L.A., Pokroy, B., Tang, C.C., Estroff, L.A., Baker, S.P., Armes, S.P. and Meldrum, F.C. Structure and Properties of Nanocomposites Formed by the Occlusion of Block Copolymer Worms and Vesicles Within Calcite Crystals. *Advanced Functional Materials.* 2016, **26**(9), pp.1382-1392.
201. Sanson, C., Schatz, C., Le Meins, J.-F., Soum, A., Thévenot, J., Garanger, E. and Lecommandoux, S. A simple method to achieve high doxorubicin loading in biodegradable polymersomes. *Journal of Controlled Release.* 2010, **147**(3), pp.428-435.
202. Boucher-Jacobs, C., Rabnawaz, M., Katz, J.S., Even, R. and Guironnet, D. Encapsulation of catalyst in block copolymer micelles for the polymerization of ethylene in aqueous medium. *Nature Communications.* 2018, **9**(1), p.841.
203. Yu, Q., Sun, N., Hu, D., Wang, Y., Chang, X., Yan, N., Zhu, Y. and Li, Y. Encapsulation of inorganic nanoparticles in a block copolymer vesicle wall driven by the interfacial instability of emulsion droplets. *Polymer Chemistry.* 2021, **12**(29), pp.4184-4192.
204. Ning, Y., Whitaker, D.J., Mable, C.J., Derry, M.J., Penfold, N.J.W., Kulak, A.N., Green, D.C., Meldrum, F.C. and Armes, S.P. Anionic block copolymer vesicles act as Trojan horses to enable efficient occlusion of guest species into host calcite crystals. *Chemical Science.* 2018, **9**(44), pp.8396-8401.
205. Ning, Y., Fielding, L.A., Doncom, K.E.B., Penfold, N.J.W., Kulak, A.N., Matsuoka, H. and Armes, S.P. Incorporating Diblock Copolymer Nanoparticles into Calcite Crystals: Do Anionic Carboxylate Groups Alone Ensure Efficient Occlusion? *ACS Macro Letters.* 2016, **5**(3), pp.311-315.
206. Hendley, C.T., Fielding, L.A., Jones, E.R., Ryan, A.J., Armes, S.P. and Estroff, L.A. Mechanistic Insights into Diblock Copolymer Nanoparticle–Crystal Interactions Revealed via in Situ Atomic Force Microscopy. *Journal of the American Chemical Society.* 2018, **140**(25), pp.7936-7945.
207. Nahi, O., Broad, A., Kulak, A.N., Freeman, H.M., Zhang, S., Turner, T.D., Roach, L., Darkins, R., Ford, I.J. and Meldrum, F.C. Positively Charged Additives Facilitate Incorporation in Inorganic Single Crystals. *Chemistry of Materials.* 2022, **34**(11), pp.4910-4923.
208. Schenk, A.S., Cantaert, B., Kim, Y.-Y., Li, Y., Read, E.S., Semsarilar, M., Armes, S.P. and Meldrum, F.C. Systematic Study

of the Effects of Polyamines on Calcium Carbonate Precipitation. *Chemistry of Materials.* 2014, **26**(8), pp.2703-2711.
209. Woldetsadik, A.D., Sharma, S.K., Khapli, S., Jagannathan, R. and Magzoub, M. Hierarchically Porous Calcium Carbonate Scaffolds for Bone Tissue Engineering. *ACS Biomaterials Science & Engineering.* 2017, **3**(10), pp.2457-2469.
210. Xu, W., Zhao, R., Wu, T., Li, G., Wei, K. and Wang, L. Biodegradable calcium carbonate/mesoporous silica/poly(lactic-glycolic acid) microspheres scaffolds with osteogenesis ability for bone regeneration. *RSC Advances.* 2021, **11**(9), pp.5055-5064.
211. Ohgushi, H., Okumura, M., Yoshikawa, T., Inboue, K., Senpuku, N., Tamai, S. and Shors, E.C. Bone formation processin porous calcium carbonate and hydroxyapatite. *Journal of Biomedical Materials Research.* 1992, **26**(7), pp.885-895.
212. Singh, P. and Sen, K. Drug delivery of sulphanilamide using modified porous calcium carbonate. *Colloid and Polymer Science.* 2018, **296**(10), pp.1711-1718.
213. Yang, H., Wang, Y., Liang, T., Deng, Y., Qi, X., Jiang, H., Wu, Y. and Gao, H. Hierarchical porous calcium carbonate microspheres as drug delivery vector. *Progress in Natural Science: Materials International.* 2017, **27**(6), pp.674-677.
214. Zhang, J., Yao, B., Ping, H., Fu, Z., Li, Y., Wang, W., Wang, H., Wang, Y., Zhang, J. and Zhang, F. Template-free synthesis of hierarchical porous calcium carbonate microspheres for efficient water treatment. *RSC Advances.* 2016, **6**(1), pp.472-480.
215. Trushina, D.B., Borodina, T.N., Belyakov, S. and Antipina, M.N. Calcium carbonate vaterite particles for drug delivery: Advances and challenges. *Materials Today Advances.* 2022, **14**, p.100214.
216. Feoktistova, N., Rose, J., Prokopović, V.Z., Vikulina, A.S., Skirtach, A. and Volodkin, D. Controlling the Vaterite $CaCO_3$ Crystal Pores. Design of Tailor-Made Polymer Based Microcapsules by Hard Templating. *Langmuir.* 2016, **32**(17), pp.4229-4238.
217. Trofimov, A.D., Ivanova, A.A., Zyuzin, M.V. and Timin, A.S. Porous Inorganic Carriers Based on Silica, Calcium Carbonate and Calcium Phosphate for Controlled/Modulated Drug Delivery: Fresh Outlook and Future Perspectives. *Pharmaceutics.* 2018, **10**(4), p.167.
218. Abebe, M., Hedin, N. and Bacsik, Z. Spherical and Porous Particles of Calcium Carbonate Synthesized with Food Friendly Polymer Additives. *Crystal Growth & Design.* 2015, **15**(8), pp.3609-3616.

219. Yu, J., Yu, J.C., Zhang, L., Wang, X. and Wu, L. Facile fabrication and characterization of hierarchically porous calcium carbonate microspheres. *Chemical Communications.* 2004, (21), pp.2414-2415.
220. Guo, X., Liu, L., Wang, W., Zhang, J., Wang, Y. and Yu, S.-H. Controlled crystallization of hierarchical and porous calcium carbonate crystals using polypeptide type block copolymer as crystal growth modifier in a mixed solution. *CrystEngComm.* 2011, **13**(6), pp.2054-2061.
221. Ichikawa, K. Buffering dissociation/formation reaction of biogenic calcium carbonate. *Chemistry.* 2007, **13**(36), pp.10176-10181.
222. Ridgway, C.J., Gane, P.A.C. and Schoelkopf, J. Modified calcium carbonate coatings with rapid absorption and extensive liquid uptake capacity. *Colloids and Surfaces A: Physicochemical and Engineering Aspects.* 2004, **236**(1), pp.91-102.
223. Preisig, D., Haid, D., Varum, F.J.O., Bravo, R., Alles, R., Huwyler, J. and Puchkov, M. Drug loading into porous calcium carbonate microparticles by solvent evaporation. *European Journal of Pharmaceutics and Biopharmaceutics.* 2014, **87**(3), pp.548-558.
224. Stirnimann, T., Di Maiuta, N., Gerard, D.E., Alles, R., Huwyler, J. and Puchkov, M. Functionalized Calcium Carbonate as a Novel Pharmaceutical Excipient for the Preparation of Orally Dispersible Tablets. *Pharmaceutical Research.* 2013, **30**(7), pp.1915-1925.
225. Stirnimann, T., Atria, S., Schoelkopf, J., Gane, P.A.C., Alles, R., Huwyler, J. and Puchkov, M. Compaction of functionalized calcium carbonate, a porous and crystalline microparticulate material with a lamellar surface. *International Journal of Pharmaceutics.* 2014, **466**(1), pp.266-275.
226. Roth, R., Schoelkopf, J., Huwyler, J. and Puchkov, M. Functionalized calcium carbonate microparticles for the delivery of proteins. *European Journal of Pharmaceutics and Biopharmaceutics.* 2018, **122**, pp.96-103.
227. Lundin Johnson, M., Noreland, D., Gane, P., Schoelkopf, J., Ridgway, C. and Millqvist Fureby, A. Porous calcium carbonate as a carrier material to increase the dissolution rate of poorly soluble flavouring compounds. *Food & Function.* 2017, **8**(4), pp.1627-1640.
228. Haruta, S., Hanafusa, T., Fukase, H., Miyajima, H. and Oki, T. An effective absorption behavior of insulin for diabetic treatment following intranasal delivery using porous spherical calcium carbonate in monkeys and healthy human volunteers. *Diabetes Technol Ther.* 2003, **5**(1), pp.1-9.

229. Peng, C., Zhao, Q. and Gao, C. Sustained delivery of doxorubicin by porous $CaCO_3$ and chitosan/alginate multilayers-coated $CaCO_3$ microparticles. *Colloids and Surfaces A: Physicochemical and Engineering Aspects.* 2010, **353**(2), pp.132-139.
230. Xiang, Y., Han, J., Zhang, G., Zhan, F., Cai, D. and Wu, Z. Efficient Synthesis of Starch-Regulated Porous Calcium Carbonate Microspheres as a Carrier for Slow-Release Herbicide. *ACS Sustainable Chemistry & Engineering.* 2018, **6**(3), pp.3649-3658.
231. Hetherington, N.B.J., Kulak, A.N., Kim, Y.-Y., Noel, E.H., Snoswell, D., Butler, M. and Meldrum, F.C. Porous Single Crystals of Calcite from Colloidal Crystal Templates: ACC Is Not Required for Nanoscale Templating. *Advanced Functional Materials.* 2011, **21**(5), pp.948-954.
232. Park, R.J. and Meldrum, F.C. Synthesis of Single Crystals of Calcite with Complex Morphologies. *Advanced Materials.* 2002, **14**(16), pp.1167-1169.
233. Park, R.J. and Meldrum, F.C. Shape-constraint as a route to calcite single crystals with complex morphologies. *Journal of Materials Chemistry.* 2004, **14**(14), pp.2291-2296.
234. Li, L., Yang, Y., Lv, Y., Yin, P. and Lei, T. Porous calcite $CaCO_3$ microspheres: Preparation, characterization and release behavior as doxorubicin carrier. *Colloids and Surfaces B: Biointerfaces.* 2020, **186**, p.110720.
235. Yu, H., Wang, D. and Han, M.-Y. Top-Down Solid-Phase Fabrication of Nanoporous Cadmium Oxide Architectures. *Journal of the American Chemical Society.* 2007, **129**(8), pp.2333-2337.
236. Yu, H.-D., Tee, S.Y. and Han, M.-Y. Preparation of porosity-controlled calcium carbonate by thermal decomposition of volume content-variable calcium carboxylate derivatives. *Chemical Communications.* 2013, **49**(39), pp.4229-4231.
237. Rodriguez-Navarro, C., Ruiz-Agudo, E., Luque, A., Rodriguez-Navarro, A.B. and Ortega-Huertas, M. Thermal decomposition of calcite: Mechanisms of formation and textural evolution of CaO nanocrystals. *American Mineralogist.* 2009, **94**(4), pp.578-593.
238. Karunadasa, K.S.P., Manoratne, C.H., Pitawala, H.M.T.G.A. and Rajapakse, R.M.G. Thermal decomposition of calcium carbonate (calcite polymorph) as examined by in-situ high-temperature X-ray powder diffraction. *Journal of Physics and Chemistry of Solids.* 2019, **134**, pp.21-28.
239. Tsuboi, Y. and Koga, N. Thermal Decomposition of Biomineralized Calcium Carbonate: Correlation between the Thermal Behavior and Structural Characteristics of Avian Eggshell. *ACS Sustainable Chemistry & Engineering.* 2018, **6**(4), pp.5283-5295.

240. Albéric, M., Zolotoyabko, E., Spaeker, O., Li, C., Tadayon, M., Schmitt, C.N.Z., Politi, Y., Bertinetti, L. and Fratzl, P. Heat-Mediated Micro- and Nano-pore Evolution in Sea Urchin Biominerals. *Crystal Growth & Design.* 2022, **22**(6), pp.3727-3739.
241. Sun, J., Bhushan, B. and Tong, J. Structural coloration in nature. *RSC Advances.* 2013, **3**(35), pp.14862-14889.
242. Andrew Richard, P. 515 million years of structural colour. *Journal of Optics A: Pure and Applied Optics.* 2000, **2**(6), p.R15.
243. Bagnara, J.T., Fernandez, P.J. and Fujii, R. On the blue coloration of vertebrates†. *Pigment Cell Research.* 2007, **20**(1), pp.14-26.
244. Jacucci, G., Schertel, L., Zhang, Y., Yang, H. and Vignolini, S. Light Management with Natural Materials: From Whiteness to Transparency. *Advanced Materials.* 2021, **33**(28), p.2001215.
245. Chen, F., Huang, Y., Li, R., Zhang, S., Wang, B., Zhang, W., Wu, X., Jiang, Q., Wang, F. and Zhang, R. Bio-inspired structural colors and their applications. *Chemical Communications.* 2021, **57**(99), pp.13448-13464.
246. Bragg, W.L. The Refractive Indices of Calcite and Aragonite. *Proceedings of the Royal Society of London. Series A, Containing Papers of a Mathematical and Physical Character.* 1924, **105**(732), pp.370-386.
247. Agency, E.C. *Titanium dioxide proposed to be classified as suspected of causing cancer when inhaled.* [Online]. 2017. [Accessed]. Available from: https://echa.europa.eu/-/titanium-dioxide-proposed-to-be-classified-as-suspected-of-causing-cancer-when-inhaled
248. Gohar I. Dar, Madiha Saeed and Wu, A. Toxicity of $TiO_2$ Nanoparticles. In: Aiguo Wu and Ren, W. eds. *TiO2 Nanoparticles*. 2020, pp.67-103.
249. Wu, Y., Chen, L., Chen, F., Zou, H. and Wang, Z. A key moment for $TiO_2$: Prenatal exposure to $TiO_2$ nanoparticles may inhibit the development of offspring. *Ecotoxicology and Environmental Safety.* 2020, **202**, p.110911.
250. Braakhuis, H.M., Gosens, I., Heringa, M.B., Oomen, A.G., Vandebriel, R.J., Groenewold, M. and Cassee, F.R. Mechanism of Action of $TiO_2$: Recommendations to Reduce Uncertainties Related to Carcinogenic Potential. *Annual Review of Pharmacology and Toxicology.* 2021, **61**(1), p.null.
251. Li, K., Li, C., Li, H., Li, M. and Song, Y. Designable structural coloration by colloidal particle assembly: from nature to artificial manufacturing. *iScience.* 2021, **24**(2), p.102121.
252. Wiersma, D.S. Disordered photonics. *Nature Photonics.* 2013, **7**(3), pp.188-196.

253. H., S.T.B., Jared, H., D., W.B. and Michael, M. It's Not a Bug, It's a Feature: Functional Materials in Insects. *Advanced Materials.* 2018, **30**(19), p.1705322.
254. Poloni, E., Bouville, F., Schmid, A.L., Pelissari, P.I.B.G.B., Pandolfelli, V.C., Sousa, M.L.C., Tervoort, E., Christidis, G., Shklover, V., Leuthold, J. and Studart, A.R. Carbon ablators with porosity tailored for aerospace thermal protection during atmospheric re-entry. *Carbon.* 2022, **195**, pp.80-91.
255. Yu, S., Guo, B., Johnsen, S., Wiegand, G., Lemmer, U., Guo, X., Zhang, M., Li, Y., Sprau, C., Hölscher, H., Colsmann, A. and Gomard, G. Nanoporous Polymer Reflectors for Organic Solar Cells. *Energy Technology.* 2022, **10**(2), p.2100676.
256. Yang, Z., Sun, H., Xi, Y., Qi, Y., Mao, Z., Wang, P. and Zhang, J. Bio-inspired structure using random, three-dimensional pores in the polymeric matrix for daytime radiative cooling. *Solar Energy Materials and Solar Cells.* 2021, **227**, p.111101.
257. Julia, S., Gianni, J., D., O.O., Hendrik, H. and Silvia, V. Bio-inspired Highly Scattering Networks via Polymer Phase Separation. *Advanced Functional Materials.* 2018, **28**(24), p.1706901.
258. Wilts, B.D., Sheng, X., Holler, M., Diaz, A., Guizar-Sicairos, M., Raabe, J., Hoppe, R., Liu, S.-H., Langford, R., Onelli, O.D., Chen, D., Torquato, S., Steiner, U., Schroer, C.G., Vignolini, S. and Sepe, A. Evolutionary-Optimized Photonic Network Structure in White Beetle Wing Scales. *Advanced Materials.* 2018, **30**(19), p.1702057.
259. Vukusic, P., Hallam, B. and Noyes, J. Brilliant Whiteness in Ultrathin Beetle Scales. *Science.* 2007, **315**(5810), pp.348-348.
260. Iwasaka, M. and Mizukawa, Y. Magneto-optical properties of biogenic photonic crystals in algae. *Journal of Applied Physics.* 2014, **115**(17), p.17B501.
261. Santana, P. and Aldana Aranda, D. Nacre morphology and chemical composition in Atlantic winged oyster Pteria colymbus (Röding, 1798). *PeerJ.* 2021, **9**, pp.e11527-e11527.
262. Nagai, Y., Uematsu, K., Wani, R. and Toyofuku, T. Reading the Fine Print: Ultra-Microstructures of Foraminiferal Calcification Revealed Using Focused Ion Beam Microscopy. *Frontiers in Marine Science.* 2018, **5**.
263. Weiss, I.M., Muth, C., Drumm, R. and Kirchner, H.O.K. Thermal decomposition of the amino acids glycine, cysteine, aspartic acid, asparagine, glutamic acid, glutamine, arginine and histidine. *BMC Biophysics.* 2018, **11**(1), p.2.

264. Mehta, S., Biederman, S. and Shivkumar, S. Thermal degradation of foamed polystyrene. *Journal of Materials Science.* 1995, **30**(11), pp.2944-2949.
265. Green, D.C., Ihli, J., Kim, Y.-Y., Chong, S.Y., Lee, P.A., Empson, C.J. and Meldrum, F.C. Rapid Screening of Calcium Carbonate Precipitation in the Presence of Amino Acids: Kinetics, Structure, and Composition. *Crystal Growth & Design.* 2016, **16**(9), pp.5174-5183.
266. Zuman, P. Reactions of Orthophthalaldehyde with Nucleophiles. *Chemical Reviews.* 2004, **104**(7), pp.3217-3238.
267. Schindelin, J., Arganda-Carreras, I., Frise, E., Kaynig, V., Longair, M., Pietzsch, T., Preibisch, S., Rueden, C., Saalfeld, S., Schmid, B., Tinevez, J.-Y., White, D.J., Hartenstein, V., Eliceiri, K., Tomancak, P. and Cardona, A. Fiji: an open-source platform for biological-image analysis. *Nature Methods.* 2012, **9**(7), pp.676-682.
268. Berg, S., Kutra, D., Kroeger, T., Straehle, C.N., Kausler, B.X., Haubold, C., Schiegg, M., Ales, J., Beier, T., Rudy, M., Eren, K., Cervantes, J.I., Xu, B., Beuttenmueller, F., Wolny, A., Zhang, C., Koethe, U., Hamprecht, F.A. and Kreshuk, A. ilastik: interactive machine learning for (bio)image analysis. *Nature Methods.* 2019, **16**(12), pp.1226-1232.
269. Habibzadeh, F. Statistical Data Editing in Scientific Articles. *Journal of Korean medical science.* 2017, **32**(7), pp.1072-1076.
270. Lafuente, B., Downs, R.T., Yang, H. and Stone, N. 1. The power of databases: The RRUFF project. In: Thomas, A. and Rosa Micaela, D. eds. *Highlights in Mineralogical Crystallography*. De Gruyter (O), 2015, pp.1-30.
271. Hintze, J.L. and Nelson, R.D. Violin Plots: A Box Plot-Density Trace Synergism. *The American statistician.* 1998, **52**(2), pp.181-184.
272. Chen, H. and Liu, N. Application of Non-Arrhenius Equations in Interpreting Calcium Carbonate Decomposition Kinetics: Revisited. *Journal of the American Ceramic Society.* 2010, **93**(2), pp.548-553.
273. Gockenbach, M. and Schmidtke, K. Newton's law of heating and the heat equation. *Involve: A Journal of Mathematics.* 2009, **2**(4), pp.419-437, 419.
274. Saeed, R.M., Schlegel, J.P., Castano, C. and Sawafta, R. Uncertainty of Thermal Characterization of Phase Change Material by Differential Scanning Calorimetry Analysis. *International Journal of Engineering Research & Technology.* 2016, **5**(1).

275. RRUFF. *Database of Raman Spectroscropy.* [Online]. 2017. [Accessed 10/02/2017]. Available from: http://rruff.info/
276. Chen, Y. and Bond, T.C. Light absorption by organic carbon from wood combustion. *Atmos. Chem. Phys.* 2010, **10**(4), pp.1773-1787.
277. HARRIS JR., F.S. Particle characteristics from light scattering measurements1. *Tellus.* 1969, **21**(2), pp.223-229.
278. Onimisi A. Jimoh, Kamar Shah Ariffin, Hashim Bin Hussin and Temitope, A.E. Synthesis of Precipitated Calcium Carbonate: A Review. *Carbonates and Evaporites.* 2018, **33**(2), p.15.
279. Boyjoo, Y., Pareek, V.K. and Liu, J. Synthesis of micro and nano-sized calcium carbonate particles and their applications. *Journal of Materials Chemistry A.* 2014, **2**(35), pp.14270-14288.
280. Huwald, E. From rock to filler. In: Tegethoff, F.W. ed. *Calcium Carbonate: From the Cretaceous Period into the 21st Century*. Basel: Birkhäuser Basel, 2001, pp.170-195.
281. Ghosh, S. Advances in cement technology: chemistry, manufacture and testing. 2003.
282. Xanthos, M. *Functional fillers for plastics.* John Wiley & Sons, 2010.
283. Harrison, D. Industrial minerals laboratory manual. *Limestones, UK, BGS, 111pp.* 1993.
284. Kumar, G.S., Ramakrishnan, A. and Hung, Y.-T. Lime Calcination. In: Wang, L.K. et al. eds. *Advanced Physicochemical Treatment Technologies*. Totowa, NJ: Humana Press, 2007, pp.611-633.
285. Ghosh, S. *Advances in cement technology: critical reviews and case studies on manufacturing, quality control, optimization and use.* Elsevier, 2014.
286. Spiropoulos, J. *Small scale production of lime for building.* F. Vieweg, 1985.
287. Simoni, M., Wilkes, M.D., Brown, S., Provis, J.L., Kinoshita, H. and Hanein, T. Decarbonising the lime industry: State-of-the-art. *Renewable and Sustainable Energy Reviews.* 2022, **168**, p.112765.
288. Mattila, H.-P., Hudd, H. and Zevenhoven, R. Cradle-to-gate life cycle assessment of precipitated calcium carbonate production from steel converter slag. *Journal of Cleaner Production.* 2014, **84**, pp.611-618.
289. Vance, K., Falzone, G., Pignatelli, I., Bauchy, M., Balonis, M. and Sant, G. Direct Carbonation of $Ca(OH)_2$ Using Liquid and Supercritical $CO_2$: Implications for Carbon-Neutral Cementation. *Industrial & Engineering Chemistry Research.* 2015, **54**(36), pp.8908-8918.

290. Eguchi, K., Satake, T., Tajika, M., Kuwamoto, S., Yokoyama, K., Matsui, J., Issiki, T. and Umesaki, N. Formation and Growth Mechanism of Calcium Carbonate Nanoparticles via a Bubbling Method. *IOP Conference Series: Materials Science and Engineering.* 2011, **18**(6), p.062001.
291. Chapnerkar, V.D. and Badgujar, M.N. *Process for production of rhombic shaped precipitated calcium carbonate*. Google Patents. 1994.
292. Chelazzi, D., Poggi, G., Jaidar, Y., Toccafondi, N., Giorgi, R. and Baglioni, P. Hydroxide nanoparticles for cultural heritage: Consolidation and protection of wall paintings and carbonate materials. *Journal of Colloid and Interface Science.* 2013, **392**, pp.42-49.
293. Chang, R., Kim, S., Lee, S., Choi, S., Kim, M. and Park, Y. Calcium Carbonate Precipitation for $CO_2$ Storage and Utilization: A Review of the Carbonate Crystallization and Polymorphism. *Frontiers in Energy Research.* 2017, **5**.
294. Montes-Hernandez, G., Chiriac, R., Toche, F. and Renard, F. Gas–solid carbonation of $Ca(OH)_2$ and CaO particles under non-isothermal and isothermal conditions by using a thermogravimetric analyzer: Implications for $CO_2$ capture. *International Journal of Greenhouse Gas Control.* 2012, **11**, pp.172-180.
295. Chang, R., Choi, D., Kim, M.H. and Park, Y. Tuning Crystal Polymorphisms and Structural Investigation of Precipitated Calcium Carbonates for $CO_2$ Mineralization. *ACS Sustainable Chemistry & Engineering.* 2017, **5**(2), pp.1659-1667.
296. Harutyunyan, V.S., Kirchheim, A.P., Monteiro, P.J.M., Aivazyan, A.P. and Fischer, P. Investigation of early growth of calcium hydroxide crystals in cement solution by soft X-ray transmission microscopy. *Journal of Materials Science.* 2009, **44**(4), pp.962-969.
297. Hajilar, S. and Shafei, B. Assessment of structural, thermal, and mechanical properties of portlandite through molecular dynamics simulations. *Journal of Solid State Chemistry.* 2016, **244**, pp.164-174.
298. Busing, W.R. and Levy, H.A. Neutron Diffraction Study of Calcium Hydroxide. *The Journal of Chemical Physics.* 1957, **26**(3), pp.563-568.
299. Jain, A., Ong, S.P., Hautier, G., Chen, W., Richards, W.D., Dacek, S., Cholia, S., Gunter, D., Skinner, D., Ceder, G. and Persson, K.A. Commentary: The Materials Project: A materials genome approach to accelerating materials innovation. *APL Materials.* 2013, **1**(1), p.011002.

300. Gillott, J.E. Carbonatation of $Ca(OH)_2$ investigated by thermal and x-ray diffraction methods of analysis. *Journal of Applied Chemistry.* 1967, **17**(7), pp.185-189.
301. Powers, T.C. A Hypothesis on Carbonation Shrinkage. *Journal of the Portland Cement Association Research and Development Laboratories.* 1962, pp.40-50.
302. Putnis, A. Mineral Replacement Reactions. *Reviews in Mineralogy and Geochemistry.* 2009, **70**(1), pp.87-124.
303. Pollok, K., Putnis, C.V. and Putnis, A. Mineral replacement reactions in solid solution-aqueous solution systems: Volume changes, reactions paths and end-points using the example of model salt systems. *American Journal of Science.* 2011, **311**(3), pp.211-236.
304. Putnis, A. and Putnis, C.V. The mechanism of reequilibration of solids in the presence of a fluid phase. *Journal of Solid State Chemistry.* 2007, **180**(5), pp.1783-1786.
305. Renard, F., Røyne, A. and Putnis, C.V. Timescales of interface-coupled dissolution-precipitation reactions on carbonates. *Geoscience Frontiers.* 2019, **10**(1), pp.17-27.
306. Cardew, P.T., Davey, R.J. and Birchall, J.D. The kinetics of solvent-mediated phase transformations. *Proceedings of the Royal Society of London. A. Mathematical and Physical Sciences.* 1985, **398**(1815), pp.415-428.
307. Wayman, C.M. Solid-State Phase Transformations. *Annual Review of Materials Science.* 1971, **1**(1), pp.185-218.
308. Ruiz-Agudo, E., Putnis, C.V. and Putnis, A. Coupled dissolution and precipitation at mineral–fluid interfaces. *Chemical Geology.* 2014, **383**, pp.132-146.
309. J. R. Johnstone and Glasser, F.P. Carbonation of Portlandite Single Crystals and Portlandite in Cement Paste. In: *9th International Congress on the Chemistry of Cement*, 1992, pp.370-376.
310. Ruiz-Agudo, E., Kudłacz, K., Putnis, C.V., Putnis, A. and Rodriguez-Navarro, C. Dissolution and Carbonation of Portlandite [$Ca(OH)_2$] Single Crystals. *Environmental Science & Technology.* 2013, **47**(19), pp.11342-11349.
311. Yang, T., Keller, B., Magyari, E., Hametner, K. and Günther, D. Direct observation of the carbonation process on the surface of calcium hydroxide crystals in hardened cement paste using an Atomic Force Microscope. *Journal of Materials Science.* 2003, **38**(9), pp.1909-1916.
312. Rodriguez-Navarro, C., Cazalla, O., Elert, K. and Sebastian, E. Liesegang pattern development in carbonating traditional lime

mortars. *Proceedings of the Royal Society of London. Series A: Mathematical, Physical and Engineering Sciences.* 2002, **458**(2025), pp.2261-2273.
313. Cizer, Ö., Van Balen, K., Elsen, J. and Van Gemert, D. Real-time investigation of reaction rate and mineral phase modifications of lime carbonation. *Construction and Building Materials.* 2012, **35**, pp.741-751.
314. Beruto, D.T. and Botter, R. Liquid-like $H_2O$ adsorption layers to catalyze the $Ca(OH)_2/CO_2$ solid–gas reaction and to form a non-protective solid product layer at 20°C. *Journal of the European Ceramic Society.* 2000, **20**(4), pp.497-503.
315. Beruto, D.T., Barberis, F. and Botter, R. Calcium carbonate binding mechanisms in the setting of calcium and calcium–magnesium putty-limes. *Journal of Cultural Heritage.* 2005, **6**(3), pp.253-260.
316. Mehta, P.K. *Concrete: Structure, Properties and Materials.* London: Englewood Cliffs, 1986.
317. Montes-Hernandez, G., Pommerol, A., Renard, F., Beck, P., Quirico, E. and Brissaud, O. In situ kinetic measurements of gas–solid carbonation of $Ca(OH)_2$ by using an infrared microscope coupled to a reaction cell. *Chemical Engineering Journal.* 2010, **161**(1), pp.250-256.
318. Günter, J.R. Attempt to a Systematic Classification of Topotactic Reactions. *Bulletin of the Institute for Chemical Research, Kyoto University.* 1975, **53**(2), p.6.
319. Stepkowska, E.T. Hypothetical transformation of $Ca(OH)_2$ into $CaCO_3$ in solid-state reactions of portland cement. *Journal of Thermal Analysis and Calorimetry.* 2005, **80**(3), pp.727-733.
320. Putnis, C.V., Wang, L., Ruiz-Agudo, E., Ruiz-Agudo, C. and Renard, F. Crystallization via Nonclassical Pathways: Nanoscale Imaging of Mineral Surfaces. In: *Crystallization via Nonclassical Pathways Volume 2: Aggregation, Biomineralization, Imaging & Application*. American Chemical Society, 2021, pp.1-35.
321. Rodriguez-Navarro, C., Kudłacz, K., Cizer, Ö. and Ruiz-Agudo, E. Formation of amorphous calcium carbonate and its transformation into mesostructured calcite. *CrystEngComm.* 2015, **17**(1), pp.58-72.
322. McGinty, J., Yazdanpanah, N., Price, C., ter Horst, J.H. and Sefcik, J. CHAPTER 1 Nucleation and Crystal Growth in Continuous Crystallization. In: *The Handbook of Continuous Crystallization*. The Royal Society of Chemistry, 2020, pp.1-50.
323. Rodriguez-Navarro, C., Elert, K. and Ševčík, R. Amorphous and crystalline calcium carbonate phases during carbonation of

nanolimes: implications in heritage conservation. *CrystEngComm.* 2016, **18**(35), pp.6594-6607.
324. Kirboga, S. and Oner, M. Effect of the Experimental Parameters on Calcium Carbonate Precipitation. *Chemical Engineering Transactions.* 2013, **32**, p.6.
325. Ramakrishna, C., Thenepalli, T. and Ahn, J.-W. A Brief Review of Aragonite Precipitated Calcium Carbonate (PCC) Synthesis Methods and its Applications. *Korean Journal of Chemical Engineering.* 2017, **55**(4), p.12.
326. Trushina, D.B., Bukreeva, T.V., Kovalchuk, M.V. and Antipina, M.N. CaCO3 vaterite microparticles for biomedical and personal care applications. *Materials Science and Engineering: C.* 2014, **45**, pp.644-658.
327. Cizer, Ö., Rodriguez-Navarro, C., Ruiz-Agudo, E., Elsen, J., Van Gemert, D. and Van Balen, K. Phase and morphology evolution of calcium carbonate precipitated by carbonation of hydrated lime. *Journal of Materials Science.* 2012, **47**(16), pp.6151-6165.
328. Hartman, P. and Perdok, W.G. On the Relations between Structure and Morphology of Crystals. II. *Acta Crystallographica.* 1955, **8**, p.4.
329. Paquette, J. and Reeder, R.J. Relationship between surface structure, growth mechanism, and trace element incorporation in calcite. *Geochimica et Cosmochimica Acta.* 1995, **59**(4), pp.735-749.
330. García Carmona, J., Gómez Morales, J. and Rodríguez Clemente, R. Rhombohedral–scalenohedral calcite transition produced by adjusting the solution electrical conductivity in the system $Ca(OH)_2$–$CO_2$–$H_2O$. *Journal of Colloid and Interface Science.* 2003, **261**(2), pp.434-440.
331. García-Carmona, J., Gómez-Morales, J., Fraile-Sainz, J. and Rodríguez-Clemente, R. Morphological characteristics and aggregation of calcite crystals obtained by bubbling $CO_2$ through a $Ca(OH)_2$ suspension in the presence of additives. *Powder Technology.* 2003, **130**(1), pp.307-315.
332. García-Carmona, J., Morales, J.G. and Clemente, R.R.g. Morphological control of precipitated calcite obtained by adjusting the electrical conductivity in the $Ca(OH)_2$–$H_2O$–$CO_2$ system. *Journal of Crystal Growth.* 2003, **249**(3), pp.561-571.
333. Harja, M., Cretescu, I., Rusu, L. and Ciocinta, R.C. The Influence of Experimental Factors on Calcium Carbonate Morphology Prepared by Carbonation. *Revista de Chemie.* 2009, **60**(12).
334. Ukrainczyk, M., Kontrec, J., Babić-Ivančić, V., Brečević, L. and Kralj, D. Experimental design approach to calcium carbonate

precipitation in a semicontinuous process. *Powder Technology.* 2007, **171**(3), pp.192-199.
335. Xiang, L., Xiang, Y., Wang, Z.G. and Jin, Y. Influence of chemical additives on the formation of super-fine calcium carbonate. *Powder Technology.* 2002, **126**(2), pp.129-133.
336. Altiner, M. Influences of $CO_2$ Bubbling Types on Preparation of Calcite Nanoparticles by Carbonation Process. *Periodica Polytechnica Chemical Engineering.* 2018, **62**(2), p.5.
337. Bang, J.-H., Jang, Y.N., Kim, W., Song, K.S., Jeon, C.W., Chae, S.C., Lee, S.-W., Park, S.-J. and Lee, M.G. Precipitation of calcium carbonate by carbon dioxide microbubbles. *Chemical Engineering Journal.* 2011, **174**(1), pp.413-420.
338. Westin, K.-J. and Rasmuson, Å.C. Precipitation of calcium carbonate in the presence of citrate and EDTA. *Desalination.* 2003, **159**(2), pp.107-118.
339. Fortier, S.M., Jackson, W.B., O'Rorke, P.B., Perez, R. and Bryan, D.P. *Precipitated Calcium Carbonate and Its Production and Use*. 1999.
340. Westin, K.J. and Rasmuson, Å.C. Crystal growth of aragonite and calcite in presence of citric acid, DTPA, EDTA and pyromellitic acid. *Journal of Colloid and Interface Science.* 2005, **282**(2), pp.359-369.
341. RAO, A., Berg, J.K., Kellermeier, M. and Gebauer, D. Sweet on biomineralization: effects of carbohydrates on the early stages of calcium carbonate crystallization. *European Journal of Mineralogy.* 2014, **26**(4), pp.537-552.
342. Kim, G., Kim, S. and Kim, M.-J. Effect of sucrose on $CO_2$ storage, vaterite content, and $CaCO_3$ particle size in indirect carbonation using seawater. *Journal of CO2 Utilization.* 2022, **57**, p.101894.
343. Park, W.K., Ko, S.-J., Lee, S.W., Cho, K.-H., Ahn, J.-W. and Han, C. Effects of magnesium chloride and organic additives on the synthesis of aragonite precipitated calcium carbonate. *Journal of Crystal Growth.* 2008, **310**(10), pp.2593-2601.
344. Konopacka-Łyskawa, D., Kościelska, B. and Karczewski, J. Controlling the size and morphology of precipitated calcite particles by the selection of solvent composition. *Journal of Crystal Growth.* 2017, **478**, pp.102-110.
345. Kaessberger, M. and Pohl, M. *Precipitated Calcium Carbonate Pigment, Especially for Use in Inkjet Printing Paper Coatings*. 2006.
346. Virtanen, P. *Precipitated Calcium Carbonate and Method for the Production Thereof*. 1997.

347. Shen, J., Song, Z., Qian, X. and Liu, W. Modification of Papermaking Grade Fillers: A Brief Review. *BioRes.* 2009, **4**(3), p.19.
348. Ambrosi, M., Dei, L., Giorgi, R., Neto, C. and Baglioni, P. Colloidal Particles of $Ca(OH)_2$: Properties and Applications to Restoration of Frescoes. *Langmuir.* 2001, **17**(14), pp.4251-4255.
349. Downs, R.T. and Hall-Wallace, M. *The American Mineralogist Crystal Structure Database.* [Online]. 2003. [Accessed 24/01/2017]. Available from: http://rruff.geo.arizona.edu/AMS/amcsd.php
350. Glaeser, Robert M., Han, B.-G., Csencsits, R., Killilea, A., Pulk, A. and Cate, Jamie H.D. Factors that Influence the Formation and Stability of Thin, Cryo-EM Specimens. *Biophysical Journal.* 2016, **110**(4), pp.749-755.
351. Wang, J.U.N., Keener, T.C., Li, G. and Khang, S.-J. The Dissolution Rate of $Ca(OH)_2$ in Aqueous Solutions. *Chemical Engineering Communications.* 1998, **169**(1), pp.167-184.
352. Hooley, R., Brown, A. and Brydson, R. Factors affecting electron beam damage in calcite nanoparticles. *Micron.* 2019, **120**, pp.25-34.
353. Hooley, R.W.M., Brown, A.P., Kulak, A.N., Meldrum, F.C. and Brydson, R.M.D. A Quantitative Evaluation of Electron Beam Sensitivity in Calcite Nanoparticles. *Journal of Physics: Conference Series.* 2017, **902**, p.012005.
354. Tobler, D.J., Rodriguez-Blanco, J.D., Dideriksen, K., Bovet, N., Sand, K.K. and Stipp, S.L.S. Citrate Effects on Amorphous Calcium Carbonate (ACC) Structure, Stability, and Crystallization. *Advanced Functional Materials.* 2015, **25**(20), pp.3081-3090.
355. Salah Uddin, K.M., Izadifar, M., Ukrainczyk, N., Koenders, E. and Middendorf, B. Dissolution of Portlandite in Pure Water: Part 1 Molecular Dynamics (MD) Approach. *Materials (Basel).* 2022, **15**(4).
356. Snyder, R.C. and Doherty, M.F. Faceted crystal shape evolution during dissolution or growth. *AIChE Journal.* 2007, **53**(5), pp.1337-1348.
357. Arends, J. and Jongebloed, W.L. Ultrastructural Studies of Synthetic Apatite Crystals. *Journal of Dental Research.* 1979, **58**(2_suppl), pp.837-843.
358. Frank, F.C. Capillary equilibria of dislocated crystals. *Acta Crystallographica.* 1951, **4**(6), pp.497-501.
359. Hirth, J.P. and Srolovitz, D.J. Shape of hollow dislocation cores. *Philosophical Magazine A.* 1994, **69**(2), pp.341-347.

360. Juilland, P., Nicoleau, L., Arvidson, R.S. and Gallucci, E. Advances in dissolution understanding and their implications for cement hydration. *RILEM Technical Letters.* 2017, **2**(0), pp.90-98.
361. Cabrera, N. and Levine, M.M. XLV. On the dislocation theory of evaporation of crystals. *The Philosophical Magazine: A Journal of Theoretical Experimental and Applied Physics.* 1956, **1**(5), pp.450-458.
362. Noiriel, C., Oursin, M. and Daval, D. Examination of crystal dissolution in 3D: A way to reconcile dissolution rates in the laboratory? *Geochimica et Cosmochimica Acta.* 2020, **273**, pp.1-25.
363. Noiriel, C., Oursin, M., Saldi, G. and Haberthür, D. Direct Determination of Dissolution Rates at Crystal Surfaces Using 3D X-ray Microtomography. *ACS Earth and Space Chemistry.* 2019, **3**(1), pp.100-108.
364. Kudłacz, K. *Phase Transitions within the Lime Cycle: Implications in Stone Conversation*. thesis, Universidad de Granada, 2014.
365. Rodriguez-Navarro, C., Burgos-Cara, A., Lorenzo, F.D., Ruiz-Agudo, E. and Elert, K. Nonclassical Crystallization of Calcium Hydroxide via Amorphous Precursors and the Role of Additives. *Crystal Growth & Design.* 2020, **20**(7), pp.4418-4432.
366. Glasson, D.R. Reactivity of lime and related oxides. II. Sorption of water vapour on calcium oxide. *Journal of Applied Chemistry.* 1958, **8**(12), pp.798-803.
367. Haslam, R.T., Calingaert, G. and Taylor, C.M. THE HYDRATES OF LIME. *Journal of the American Chemical Society.* 1924, **46**(2), pp.308-311.
368. Gebauer, D., Gunawidjaja, P.N., Ko, J.Y.P., Bacsik, Z., Aziz, B., Liu, L., Hu, Y., Bergström, L., Tai, C.-W., Sham, T.-K., Edén, M. and Hedin, N. Proto-Calcite and Proto-Vaterite in Amorphous Calcium Carbonates. *Angewandte Chemie International Edition.* 2010, **49**(47), pp.8889-8891.
369. Agency, I.E. *Global Energy Review 2021.* Paris: IEA, 2021.
370. Agency, I.E. *The Future of Hydrogen.* Paris: IEA, 2019.
371. Veziroğlu, T.N. and Barbir, F. Hydrogen: the wonder fuel. *International Journal of Hydrogen Energy.* 1992, **17**(6), pp.391-404.
372. Edwards, P.P., Kuznetsov, V.L., David, W.I.F. and Brandon, N.P. Hydrogen and fuel cells: Towards a sustainable energy future. *Energy Policy.* 2008, **36**(12), pp.4356-4362.
373. Chen, J., Li, Q., Wang, L., Fan, C. and Liu, H. Advances in Whole-Cell Photobiological Hydrogen Production. *Advanced NanoBiomed Research.* 2021, **1**(4), p.2000051.

374. Oey, M., Sawyer, A.L., Ross, I.L. and Hankamer, B. Challenges and opportunities for hydrogen production from microalgae. *Plant Biotechnology Journal.* 2016, **14**(7), pp.1487-1499.
375. Lewis, N.S. and Nocera, D.G. Powering the planet: Chemical challenges in solar energy utilization. *Proceedings of the National Academy of Sciences.* 2006, **103**(43), pp.15729-15735.
376. Chen, S., Takata, T. and Domen, K. Particulate photocatalysts for overall water splitting. *Nature Reviews Materials.* 2017, **2**(10), p.17050.
377. Diffey, B.L. Sources and measurement of ultraviolet radiation. *Methods.* 2002, **28**(1), pp.4-13.
378. Maeda, K. and Domen, K. Photocatalytic Water Splitting: Recent Progress and Future Challenges. *J. Phys. Chem. Lett.* 2010, **1**, p.7.
379. Hisatomi, T., Kubota, J. and Domen, K. Recent advances in semiconductors for photocatalytic and photoelectrochemical water splitting. *Chem Soc Rev.* 2014, **43**(22), pp.7520-7535.
380. Maeda, K. Photocatalytic water splitting using semiconductor particles: History and recent developments. *Journal of Photochemistry and Photobiology C: Photochemistry Reviews.* 2011, **12**(4), pp.237-268.
381. Kudo, A. and Miseki, Y. Heterogeneous photocatalyst materials for water splitting. *Chem Soc Rev.* 2009, **38**(1), pp.253-278.
382. Wu, H., Tan, H.L., Toe, C.Y., Scott, J., Wang, L., Amal, R. and Ng, Y.H. Photocatalytic and Photoelectrochemical Systems: Similarities and Differences. *Advanced Materials.* 2020, **32**(18), p.1904717.
383. Marwat, M.A., Humayun, M., Afridi, M.W., Zhang, H., Abdul Karim, M.R., Ashtar, M., Usman, M., Waqar, S., Ullah, H., Wang, C. and Luo, W. Advanced Catalysts for Photoelectrochemical Water Splitting. *ACS Applied Energy Materials.* 2021, **4**(11), pp.12007-12031.
384. Cox, N., Pantazis, D.A., Neese, F. and Lubitz, W. Biological Water Oxidation. *Accounts of Chemical Research.* 2013, **46**(7), pp.1588-1596.
385. Yano, J. and Yachandra, V. $Mn_4Ca$ Cluster in Photosynthesis: Where and How Water is Oxidized to Dioxygen. *Chemical Reviews.* 2014, **114**(8), pp.4175-4205.
386. Cox, N., Retegan, M., Neese, F., Pantazis, D.A., Boussac, A. and Lubitz, W. Electronic structure of the oxygen-evolving complex in photosystem II prior to O-O bond formation. *Science.* 2014, **345**(6198), pp.804-808.

387. Umena, Y., Kawakami, K., Shen, J.-R. and Kamiya, N. Crystal structure of oxygen-evolving photosystem II at a resolution of 1.9 Å. *Nature.* 2011, **473**(7345), pp.55-60.
388. Cox, N., Pantazis, D.A., Neese, F. and Lubitz, W. Artificial photosynthesis: understanding water splitting in nature. *Interface Focus.* 2015, **5**(3), p.20150009.
389. Faunce, T.A., Lubitz, W., Rutherford, A.W., MacFarlane, D., Moore, G.F., Yang, P., Nocera, D.G., Moore, T.A., Gregory, D.H., Fukuzumi, S., Yoon, K.B., Armstrong, F.A., Wasielewski, M.R. and Styring, S. Energy and environment policy case for a global project on artificial photosynthesis. *Energy & Environmental Science.* 2013, **6**(3), pp.695-698.
390. Chen, Q.-F., Guo, Y.-H., Yu, Y.-H. and Zhang, M.-T. Bioinspired molecular clusters for water oxidation. *Coordination Chemistry Reviews.* 2021, **448**, p.214164.
391. Tan, H.L., Amal, R. and Ng, Y.H. Alternative strategies in improving the photocatalytic and photoelectrochemical activities of visible light-driven $BiVO_4$: a review. *Journal of Materials Chemistry A.* 2017, **5**(32), pp.16498-16521.
392. He, H. 2 - Metal oxide semiconductors and conductors. In: Cui, Z. and Korotcenkov, G. eds. *Solution Processed Metal Oxide Thin Films for Electronic Applications*. Elsevier, 2020, pp.7-30.
393. Fujishima, A. and Honda, K. Electrochemical Photolysis of Water at a Semiconductor Electrode. *Nature.* 1972, **238**(5358), pp.37-38.
394. Liao, C.-H., Huang, C.-W. and Wu, J.C.S. Hydrogen Production from Semiconductor-based Photocatalysis via Water Splitting. *Catalysts.* 2012, **2**(4), pp.490-516.
395. Post, J.E. Manganese oxide minerals: Crystal structures and economic and environmental significance. *Proceedings of the National Academy of Sciences.* 1999, **96**(7), pp.3447-3454.
396. Najafpour, M.M. and Allakhverdiev, S.I. Manganese compounds as water oxidizing catalysts for hydrogen production via water splitting: From manganese complexes to nano-sized manganese oxides. *International Journal of Hydrogen Energy.* 2012, **37**(10), pp.8753-8764.
397. Ghosh, S.K. Diversity in the Family of Manganese Oxides at the Nanoscale: From Fundamentals to Applications. *ACS Omega.* 2020, **5**(40), pp.25493-25504.
398. Harriman, A., Pickering, I.J., Thomas, J.M. and Christensen, P.A. Metal oxides as heterogeneous catalysts for oxygen evolution under photochemical conditions. *Journal of the Chemical Society, Faraday Transactions 1: Physical Chemistry in Condensed Phases.* 1988, **84**(8), pp.2795-2806.

399. Harriman, A., Richoux, M.-C., Christensen, P.A., Mosseri, S. and Neta, P. Redox reactions with colloidal metal oxides. Comparison of radiation-generated and chemically generated $RuO_2 \cdot 2H_2O$. *Journal of the Chemical Society, Faraday Transactions 1: Physical Chemistry in Condensed Phases.* 1987, **83**(9), pp.3001-3014.
400. Morris, N.D. and Mallouk, T.E. A High-Throughput Optical Screening Method for the Optimization of Colloidal Water Oxidation Catalysts. *Journal of the American Chemical Society.* 2002, **124**(37), pp.11114-11121.
401. Limburg, B., Bouwman, E. and Bonnet, S. Rate and Stability of Photocatalytic Water Oxidation using $[Ru(bpy)_3]^{2+}$ as Photosensitizer. *ACS Catalysis.* 2016, **6**(8), pp.5273-5284.
402. Najafpour, M.M., Rahimi, F., Aro, E.-M., Lee, C.-H. and Allakhverdiev, S.I. Nano-sized manganese oxides as biomimetic catalysts for water oxidation in artificial photosynthesis: a review. *Journal of The Royal Society Interface.* 2012, **9**(75), pp.2383-2395.
403. Robinson, D.M., Go, Y.B., Mui, M., Gardner, G., Zhang, Z., Mastrogiovanni, D., Garfunkel, E., Li, J., Greenblatt, M. and Dismukes, G.C. Photochemical Water Oxidation by Crystalline Polymorphs of Manganese Oxides: Structural Requirements for Catalysis. *Journal of the American Chemical Society.* 2013, **135**(9), pp.3494-3501.
404. Boppana, V.B.R. and Jiao, F. Nanostructured $MnO_2$: an efficient and robust water oxidation catalyst. *Chemical Communications.* 2011, **47**(31), pp.8973-8975.
405. Pokhrel, R., Goetz, M.K., Shaner, S.E., Wu, X. and Stahl, S.S. The “Best Catalyst” for Water Oxidation Depends on the Oxidation Method Employed: A Case Study of Manganese Oxides. *Journal of the American Chemical Society.* 2015, **137**(26), pp.8384-8387.
406. Menezes, P.W., Indra, A., Littlewood, P., Schwarze, M., Göbel, C., Schomäcker, R. and Driess, M. Nanostructured Manganese Oxides as Highly Active Water Oxidation Catalysts: A Boost from Manganese Precursor Chemistry. 2014, **7**(8), pp.2202-2211.
407. Najafpour, M.M., Rahimi, F., Amini, M., Nayeri, S. and Bagherzadeh, M. A very simple method to synthesize nano-sized manganese oxide: an efficient catalyst for water oxidation and epoxidation of olefins. *Dalton Transactions.* 2012, **41**(36), pp.11026-11031.
408. Jiao, F. and Frei, H. Nanostructured cobalt and manganese oxide clusters as efficient water oxidation catalysts. *Energy & Environmental Science.* 2010, **3**(8), pp.1018-1027.
409. Najafpour, M.M. Self-assembled layered hybrid $[Ru(bpy)_3]^{2+}$/manganese(iii,iv) oxide: a new and efficient strategy

for water oxidation. *Chemical Communications.* 2011, **47**(42), pp.11724-11726.
410. Morris, N.D., Suzuki, M. and Mallouk, T.E. Kinetics of Electron Transfer and Oxygen Evolution in the Reaction of $[Ru(bpy)_3]^{3+}$ with Colloidal Iridium Oxide. *The Journal of Physical Chemistry A.* 2004, **108**(42), pp.9115-9119.
411. Ahmad, H., Kamarudin, S.K., Minggu, L.J. and Kassim, M. Hydrogen from photo-catalytic water splitting process: A review. *Renewable and Sustainable Energy Reviews.* 2015, **43**, pp.599-610.
412. Jafari, T., Moharreri, E., Amin, A.S., Miao, R., Song, W. and Suib, S.L. Photocatalytic Water Splitting-The Untamed Dream: A Review of Recent Advances. *Molecules.* 2016, **21**(7).
413. Kubota, J. and Domen, K. Photocatalytic Water Splitting Using Oxynitride and Nitride Semiconductor Powders for Production of Solar Hydrogen. *Interface magazine.* 2013, **22**(2), pp.57-62.
414. Maeda, K., Takata, T., Hara, M., Saito, N., Inoue, Y., Kobayashi, H. and Domen, K. GaN:ZnO Solid Solution as a Photocatalyst for Visible-Light-Driven Overall Water Splitting. *Journal of the American Chemical Society.* 2005, **127**(23), pp.8286-8287.
415. Nurlaela, E., Ziani, A. and Takanabe, K. Tantalum nitride for photocatalytic water splitting: concept and applications. *Materials for Renewable and Sustainable Energy.* 2016, **5**(4), p.18.
416. Ingram, D.B. and Linic, S. Water Splitting on Composite Plasmonic-Metal/Semiconductor Photoelectrodes: Evidence for Selective Plasmon-Induced Formation of Charge Carriers near the Semiconductor Surface. *Journal of the American Chemical Society.* 2011, **133**(14), pp.5202-5205.
417. Kazuhiko, M., Kentaro, T., Daling, L., Nobuo, S., Yasunobu, I. and Kazunari, D. Noble-Metal/$Cr_2O_3$ Core/Shell Nanoparticles as a Cocatalyst for Photocatalytic Overall Water Splitting. *Angewandte Chemie International Edition.* 2006, **45**(46), pp.7806-7809.
418. Thomann, I., Pinaud, B.A., Chen, Z., Clemens, B.M., Jaramillo, T.F. and Brongersma, M.L. Plasmon Enhanced Solar-to-Fuel Energy Conversion. *Nano Letters.* 2011, **11**(8), pp.3440-3446.
419. Furube, A., Du, L., Hara, K., Katoh, R. and Tachiya, M. Ultrafast Plasmon-Induced Electron Transfer from Gold Nanodots into $TiO_2$ Nanoparticles. *Journal of the American Chemical Society.* 2007, **129**(48), pp.14852-14853.
420. Standridge, S.D., Schatz, G.C. and Hupp, J.T. Distance Dependence of Plasmon-Enhanced Photocurrent in Dye-Sensitized Solar Cells. *Journal of the American Chemical Society.* 2009, **131**(24), pp.8407-8409.

421. Cushing, S.K., Li, J., Meng, F., Senty, T.R., Suri, S., Zhi, M., Li, M., Bristow, A.D. and Wu, N. Photocatalytic Activity Enhanced by Plasmonic Resonant Energy Transfer from Metal to Semiconductor. *Journal of the American Chemical Society.* 2012, **134**(36), pp.15033-15041.
422. Liu, Z., Hou, W., Pavaskar, P., Aykol, M. and Cronin, S.B. Plasmon Resonant Enhancement of Photocatalytic Water Splitting Under Visible Illumination. *Nano Letters.* 2011, **11**(3), pp.1111-1116.
423. Wang, X., Long, R., Liu, D., Yang, D., Wang, C. and Xiong, Y. Enhanced full-spectrum water splitting by confining plasmonic Au nanoparticles in N-doped $TiO_2$ bowl nanoarrays. *Nano Energy.* 2016, **24**, pp.87-93.
424. Kuo, C.-H., Li, W., Pahalagedara, L., El-Sawy, A.M., Kriz, D., Genz, N., Guild, C., Ressler, T., Suib, S.L. and He, J. Understanding the Role of Gold Nanoparticles in Enhancing the Catalytic Activity of Manganese Oxides in Water Oxidation Reactions. *Angewandte Chemie International Edition.* 2015, **54**(8), pp.2345-2350.
425. Gorlin, Y., Chung, C.-J., Benck, J.D., Nordlund, D., Seitz, L., Weng, T.-C., Sokaras, D., Clemens, B.M. and Jaramillo, T.F. Understanding Interactions between Manganese Oxide and Gold That Lead to Enhanced Activity for Electrocatalytic Water Oxidation. *Journal of the American Chemical Society.* 2014, **136**(13), pp.4920-4926.
426. Seitz, L.C., Hersbach, T.J.P., Nordlund, D. and Jaramillo, T.F. Enhancement Effect of Noble Metals on Manganese Oxide for the Oxygen Evolution Reaction. *The Journal of Physical Chemistry Letters.* 2015, **6**(20), pp.4178-4183.
427. Wyckoff, R.W.G. The crystal structures of some carbonates of the calcite group. *American Journal of Science.* 1920, **s4-50**(299), pp.317-360.
428. Radha, A.V. and Navrotsky, A. Direct Experimental Measurement of Water Interaction Energetics in Amorphous Carbonates $MCO_3$ (M = Ca, Mn, and Mg) and Implications for Carbonate Crystal Growth. *Crystal Growth & Design.* 2015, **15**(1), pp.70-78.
429. Leukel, S. and Tremel, W. Water-Controlled Crystallization of $CaCO_3$, $SrCO_3$, and $MnCO_3$ from Amorphous Precursors. *Crystal Growth & Design.* 2018, **18**(8), pp.4662-4670.
430. Wolf, S.E., Müller, L., Barrea, R., Kampf, C.J., Leiterer, J., Panne, U., Hoffmann, T., Emmerling, F. and Tremel, W. Carbonate-coordinated metal complexes precede the formation of liquid amorphous mineral emulsions of divalent metal carbonates. *Nanoscale.* 2011, **3**(3), pp.1158-1165.

431. Parakhonskiy, B.V., Yashchenok, A.M., Konrad, M. and Skirtach, A.G. Colloidal micro- and nano-particles as templates for polyelectrolyte multilayer capsules. *Advances in Colloid and Interface Science.* 2014, **207**, pp.253-264.
432. Abreu, A.d.S., Carvalho, J.A., Tedesco, A.C., Beltrame Junior, M. and Simioni, A.R. Fabrication of polyelectrolyte microspheres using porous manganese carbonate as sacrificial template for drug delivery application. *Journal of Materials Research.* 2019, **34**(8), pp.1353-1362.
433. Zhu, H., Stein, E.W., Lu, Z., Lvov, Y.M. and McShane, M.J. Synthesis of Size-Controlled Monodisperse Manganese Carbonate Microparticles as Templates for Uniform Polyelectrolyte Microcapsule Formation. *Chemistry of Materials.* 2005, **17**(9), pp.2323-2328.
434. Xu, L., Li, J., Shi, W., Bao, N. and Yu, C. Immobilization of hemoglobin on $MnCO_3$ sphere-loaded Au nanoparticles as highly efficient sensing platform towards hydrogen peroxide. *Nanotechnology.* 2020, **32**(2), p.025503.
435. Udayabhanu, Muralikrishna, S., Kishore, B., Nagabhushana, H., Suresh, D., Sharma, S.C. and Nagaraju, G. One pot green synthesis of $MnCO_3$–rGO composite hybrid superstructure: application to lithium ion battery and biosensor. *New Journal of Chemistry.* 2017, **41**(21), pp.12854-12865.
436. Zhang, N., Ma, J., Li, Q., Li, J. and Ng, D.H.L. Shape-controlled synthesis of $MnCO_3$ nanostructures and their applications in supercapacitors. *RSC Advances.* 2015, **5**(100), pp.81981-81985.
437. Tang, Y., Chen, S., Chen, T., Guo, W., Li, Y., Mu, S., Yu, S., Zhao, Y., Wen, F. and Gao, F. Synthesis of peanut-like hierarchical manganese carbonate microcrystals via magnetically driven self-assembly for high performance asymmetric supercapacitors. *Journal of Materials Chemistry A.* 2017, **5**(8), pp.3923-3931.
438. Aragón, M.J., León, B., Pérez Vicente, C. and Tirado, J.L. A new form of manganese carbonate for the negative electrode of lithium-ion batteries. *Journal of Power Sources.* 2011, **196**(5), pp.2863-2866.
439. Xiao, L., Wang, S., Wang, Y., Meng, W., Deng, B., Qu, D., Xie, Z. and Liu, J. High-Capacity and Self-Stabilized Manganese Carbonate Microspheres as Anode Material for Lithium-Ion Batteries. *ACS Applied Materials & Interfaces.* 2016, **8**(38), pp.25369-25378.
440. Kesavan, T., Suresh, S., Arulraj, I., Ragupathy, P. and Dheenadayalan, S. Facile synthesis of hollow sphere $MnCO_3$: A

cheap and environmentally benign anode material for Li-ion batteries. *Materials Letters.* 2014, **136**, pp.411-415.
441. Liu, L., Yang, Z., Liang, H., Yang, H. and Yang, Y. Facile synthesis of $MnCO_3$ hollow dumbbells and their conversion to manganese oxide. *Materials Letters.* 2010, **64**(19), pp.2060-2063.
442. Liu, L., Zhang, X., Wang, R. and Liu, J. Facile synthesis of $Mn_2O_3$ hollow and core–shell cube-like nanostructures and their catalytic properties. *Superlattices and Microstructures.* 2014, **72**, pp.219-229.
443. Biernacki, L. and Pokrzywnicki, S. The Thermal Decomposition of Manganese Carbonate Thermogravimetry and Exoemission of Electrons. *Journal of Thermal Analysis and Calorimetry.* 1999, **55**(1), pp.227-232.
444. Reyes, I.A., Flores, M., Palacios, E.G., Islas, H., Juárez, J.C., Reyes, M., Teja, A.M. and Pérez, C.A. Kinetics of the Thermal Decomposition of Rhodochrosite. *Minerals.* 2021, **11**(1), p.34.
445. Ma, R., Bando, Y., Zhang, L. and Sasaki, T. Layered $MnO_2$ Nanobelts: Hydrothermal Synthesis and Electrochemical Measurements. *Advanced Materials.* 2004, **16**(11), pp.918-922.
446. Duan, L., Xu, Y., Zhang, P., Wang, M. and Sun, L. Visible Light-Driven Water Oxidation by a Molecular Ruthenium Catalyst in Homogeneous System. *Inorg. Chem.* 2010, **49**(1), p.7.
447. Prier, C.K., Rankic, D.A. and MacMillan, D.W.C. Visible Light Photoredox Catalysis with Transition Metal Complexes: Applications in Organic Synthesis. *Chemical Reviews.* 2013, **113**(7), pp.5322-5363.
448. Walsh, D., Sanchez-Ballester, N.M., Ariga, K., Tanaka, A. and Weller, M. Chelate stabilized metal oxides for visible light photocatalyzed water oxidations. *Green Chemistry.* 2015, **17**(2), pp.982-990.
449. Walsh, D., Patureau, P., Walton, J., Potticary, J., Hall, S.R. and Weller, M.T. Visible light promoted photocatalytic water oxidation: effect of fluctuating light intensity upon reaction efficiency. *RSC Advances.* 2016, **6**(99), pp.97363-97366.
450. Kim, Y.-Y., Williams, D., Meldrum, F.C. and Walsh, D. Simple Photosystem II Water Oxidation Centre Analogues in Visible Light Oxygen and $H^+$ Generation. *Small.* 2013, **9**(1), pp.61-66.
451. Najafpour, M.M., Ehrenberg, T., Wiechen, M. and Kurz, P. Calcium Manganese(III) Oxides ($CaMn_2O_4 \cdot x\,H_2O$) as Biomimetic Oxygen-Evolving Catalysts. *Angewandte Chemie International Edition.* 2010, **49**(12), pp.2233-2237.

452. Kim, Y.Y., Williams, D., Meldrum, F.C. and Walsh, D. Simple photosystem II water oxidation centre analogues in visible light oxygen and $H^+$ generation. *Small.* 2013, **9**(1), pp.61-66.
453. Walsh, D., Sanchez-Ballester, N.M., Ting, V.P., Hall, S.R., Terry, L.R. and Weller, M.T. Visible light promoted photocatalytic water oxidation: effect of metal oxide catalyst composition and light intensity. *Catal. Sci. Technol.* 2015, **5**, p.4.
454. Brunauer, S., Emmett, P.H. and Teller, E. Adsorption of Gases in Multimolecular Layers. *Journal of the American Chemical Society.* 1938, **60**(2), pp.309-319.
455. Dollimore, D., Spooner, P. and Turner, A. The BET method of analysis of gas adsorption data and its relevance to the calculation of surface areas. *Surface Technology.* 1976, **4**(2), pp.121-160.
456. Thommes, M., Kaneko, K., Neimark, A.V., Olivier, J.P., Rodriguez-Reinoso, F., Rouquerol, J. and Sing, K.S.W. Physisorption of gases, with special reference to the evaluation of surface area and pore size distribution (IUPAC Technical Report). *Pure and Applied Chemistry.* 2015, **87**(9-10), pp.1051-1069.
457. Sing, K.S.W. Adsorption methods for the characterization of porous materials. *Advances in Colloid and Interface Science.* 1998, **76-77**, pp.3-11.
458. Pyroscience. *Sensing Principle Oxygen Sensors.* [Online]. 2022. [Accessed 16/04/2022]. Available from: https://www.pyroscience.com/en/products/theory/optical-oxygen-sensors
459. Yang, P., Liang, X., Wu, C., Cui, T. and Wang, Y. Study on Adding Ammonium Hydrogen Fluoride to Improve Manganese Leaching Efficiency of Ammonia Leaching Low-Grade Rhodochrosite. *Metals.* 2021, **11**(9), p.1496.
460. Kim, Y., Caumon, M.-C., Barres, O., Sall, A. and Cauzid, J. Identification and composition of carbonate minerals of the calcite structure by Raman and infrared spectroscopies using portable devices. *Spectrochimica Acta Part A: Molecular and Biomolecular Spectroscopy.* 2021, **261**, p.119980.
461. Seguin, M.K. Study of the stability of $MnCO_3$ in inert atmospheres and in air. *American Mineralogist.* 1972, **57**(3-4_Part_1), pp.511-523.
462. Downs, R.T. and Hall-Wallace, M. The American Mineralogist Crystal Structure Database. *American Mineralogist.* 2003, **88**, p.3.
463. Stern, K.H. High Temperature Properties and Decomposition of Inorganic Salts Part 2, Carbonates. *Journal of Physical and Chemical Reference Data.* 1969, **1**, pp.747-772.

464. Nicholson, D. Variation of surface area during the thermal decomposition of solids. *Transactions of the Faraday Society.* 1965, **61**(0), pp.990-998.
465. Gregg, S.J. 806. The production of active solids by thermal decomposition. Part I. Introduction. *Journal of the Chemical Society (Resumed).* 1953, (0), pp.3940-3944.
466. Shalkevich, N., Escher, W., Bürgi, T., Michel, B., Si-Ahmed, L. and Poulikakos, D. On the Thermal Conductivity of Gold Nanoparticle Colloids. *Langmuir.* 2010, **26**(2), pp.663-670.
467. Ishida, T., Murayama, T., Taketoshi, A. and Haruta, M. Importance of Size and Contact Structure of Gold Nanoparticles for the Genesis of Unique Catalytic Processes. *Chemical Reviews.* 2020, **120**(2), pp.464-525.
468. Lian, S., Browne, M.P., Domínguez, C., Stamatin, S.N., Nolan, H., Duesberg, G.S., Lyons, M.E.G., Fonda, E. and Colavita, P.E. Template-free synthesis of mesoporous manganese oxides with catalytic activity in the oxygen evolution reaction. *Sustainable Energy & Fuels.* 2017, **1**(4), pp.780-788.
469. Li, J., Xi, B., Zhu, Y., Li, Q., Yan, Y. and Qian, Y. A precursor route to synthesize mesoporous γ-$MnO_2$ microcrystals and their applications in lithium battery and water treatment. *Journal of Alloys and Compounds.* 2011, **509**(39), pp.9542-9548.
470. Zhao, J., Tao, Z., Liang, J. and Chen, J. Facile Synthesis of Nanoporous γ-MnO2 Structures and Their Application in Rechargeable Li-Ion Batteries. *Crystal Growth & Design.* 2008, **8**(8), pp.2799-2805.
471. Pal, P., Pahari, S.K., Giri, A.K., Pal, S., Bajaj, H.C. and Panda, A.B. Hierarchically order porous lotus shaped nano-structured $MnO_2$ through $MnCO_3$: chelate mediated growth and shape dependent improved catalytic activity. *Journal of Materials Chemistry A.* 2013, **1**(35), pp.10251-10258.
472. Kozuch, S. and Martin, J.M.L. “Turning Over” Definitions in Catalytic Cycles. *ACS Catalysis.* 2012, **2**(12), pp.2787-2794.
473. Hüttig, G.F. Die Reaktionsarten von dem Typus A starr+B starr→AB starr. *Kolloid-Zeitschrift.* 1942, **99**(3), pp.262-277.
474. Boppana, V.B.R., Yusuf, S., Hutchings, G.S. and Jiao, F. Nanostructured Alkaline-Cation-Containing δ-$MnO_2$ for Photocatalytic Water Oxidation. *Advanced Functional Materials.* 2013, **23**(7), pp.878-884.